

Mario Capitelli · Roberto Celiberto
Gianpiero Colonna · Fabrizio Esposito
Claudine Gorse · Khaled Hassouni
Annarita Laricchiuta · Savino Longo

Fundamental Aspects of Plasma Chemical Physics

Kinetics



Springer

Springer Series on Atomic, Optical, and Plasma Physics

Volume 85

Editor-in-Chief

Gordon W.F. Drake, Windsor, Canada

Series editors

Andre D. Bandrauk, Sherbrooke, Canada

Klaus Bartschat, Des Moines, USA

Philip George Burke, Belfast, UK

Robert N. Compton, Knoxville, USA

M.R. Flannery, Atlanta, USA

Charles J. Joachain, Bruxelles, Belgium

Peter Lambropoulos, Iraklion, Greece

Gerd Leuchs, Erlangen, Germany

Pierre Meystre, Tucson, USA

The Springer Series on Atomic, Optical, and Plasma Physics covers in a comprehensive manner theory and experiment in the entire field of atoms and molecules and their interaction with electromagnetic radiation. Books in the series provide a rich source of new ideas and techniques with wide applications in fields such as chemistry, materials science, astrophysics, surface science, plasma technology, advanced optics, aeronomy, and engineering. Laser physics is a particular connecting theme that has provided much of the continuing impetus for new developments in the field. The purpose of the series is to cover the gap between standard undergraduate textbooks and the research literature with emphasis on the fundamental ideas, methods, techniques, and results in the field.

More information about this series at <http://www.springer.com/series/411>

Mario Capitelli • Roberto Celiberto
Gianpiero Colonna • Fabrizio Esposito
Claudine Gorse • Khaled Hassouni
Annarita Laricchiuta • Savino Longo

Fundamental Aspects of Plasma Chemical Physics

Kinetics



Springer

Mario Capitelli University of Bari and CNR Bari, Italy	Roberto Celiberto Dipartimento di Ingegneria Civile, Ambientale, del Territorio, Edile e di Chimica (DICATECh) Polytechnic of Bari Bari, Italy
Gianpiero Colonna CNR Bari, Italy	Fabrizio Esposito
Claudine Gorse University of Bari and CNR Bari, Italy	CNR Bari, Italy
Annarita Laricchiuta CNR Bari, Italy	Khaled Hassouni Laboratoire des Sciences des Procédés et des Matériaux, CNRS-INSIS Paris, France
	Savino Longo University of Bari and CNR Bari, Italy

ISSN 1615-5653 ISSN 2197-6791 (electronic)
 Springer Series on Atomic, Optical, and Plasma Physics
 ISBN 978-1-4419-8184-4 ISBN 978-1-4419-8185-1 (eBook)
 DOI 10.1007/978-1-4419-8185-1

Library of Congress Control Number: 2015945655

Springer New York Heidelberg Dordrecht London
 © Springer New York 2016

This work is subject to copyright. All rights are reserved by the Publisher, whether the whole or part of the material is concerned, specifically the rights of translation, reprinting, reuse of illustrations, recitation, broadcasting, reproduction on microfilms or in any other physical way, and transmission or information storage and retrieval, electronic adaptation, computer software, or by similar or dissimilar methodology now known or hereafter developed.

The use of general descriptive names, registered names, trademarks, service marks, etc. in this publication does not imply, even in the absence of a specific statement, that such names are exempt from the relevant protective laws and regulations and therefore free for general use.

The publisher, the authors and the editors are safe to assume that the advice and information in this book are believed to be true and accurate at the date of publication. Neither the publisher nor the authors or the editors give a warranty, express or implied, with respect to the material contained herein or for any errors or omissions that may have been made.

Printed on acid-free paper

Springer Science+Business Media LLC New York is part of Springer Science+Business Media (www.springer.com)

There are well-known conditions in which translational, vibrational, and rotational temperatures differ and/or various components of a system (electrons, ions, and neutral molecules, for instance) have different temperatures, and/or a system cannot be described at all using the concept of temperature (nonequilibrium, stationary, and relaxing systems). Strictly speaking, Arrhenius-type kinetics cannot be used in these cases and the ordinary expression for the rate of a chemical reaction is inapplicable.

L. Polak

Preface

In the first two books of the series *Fundamental Aspects of Plasma Chemical Physics*, we have discussed thermodynamics¹ and transport² of thermal plasmas characterized by equilibrium or quasi-equilibrium conditions. Plasma technology often uses working conditions very far from the equilibrium ones so that kinetic approaches are to be used to describe the properties of these plasmas. In this way we enter the scenario of *cold plasmas* which can present strong deviations from equilibrium of the internal energy distribution functions implying a loss of validity of the concept of temperature. A peculiar situation holds for electrons, which present a non-Maxwellian energy distribution function to be described by a suitable Boltzmann equation. Moreover the presence of non-Boltzmann vibrational and electronic distributions generates non-Arrhenius behavior of reaction rates, a point not easily perceived by researchers which extensively use the Arrhenius law for the relevant rates. Cold plasmas present average electron energies in the range 0.1–10 eV, while the translational temperature of heavy components ranges from room temperature to about 2,000 K. Ionization degrees well below 10^{-3} characterize this kind of plasmas which run in the torr and sub-torr pressure range even though it is nowadays possible to form atmospheric nonequilibrium plasmas. Cold plasmas are widely used in material science for cleaning, film deposition, plasma etching, surface activation, as well as to produce gas lasers (e.g., the CO₂ and excimer lasers) and negative and positive ion beams. Plasma medicine, biomaterial activation, plasma-assisted combustion, and numerous aerospace applications do extensively use cold plasmas for reaching important goals.

The present book tries to rationalize the description of cold plasmas through a chemical physics approach, in particular by using the state-to-state plasma kinetics which considers each internal state as a new species with its own cross sections.

¹M. Capitelli, G. Colonna and A. D'Angola "Fundamental Aspects of Plasma Chemical Physics. Thermodynamics" Springer Series in Atomic, Optical and Plasma Physics (2012) Vol.66.

²M. Capitelli, D. Bruno and A. Laricchiuta "Fundamental Aspects of Plasma Chemical Physics. Transport" Springer Series in Atomic, Optical and Plasma Physics (2013) Vol.74.

This approach needs complete sets of state-resolved cross sections, the knowledge of which at least for the most common diatomic species (O_2 , N_2 , and H_2) is continuously increasing. In addition kinetic approaches based on the solution of Boltzmann equation and/or by Monte Carlo methods are being discussed especially for the description of the electron and ion energy distribution function. Coupling between electron energy distribution functions (eedf) and nonequilibrium internal (rotational, vibrational, and electronic states) distributions through second kind collisions are such to superimpose interesting structures on eedf with large consequences on plasma reactivity. This coupling should be also extended to the dissociation and ionization kinetics promoted either by electron impact or by heavy particle collisions involving excited states.

The book can be considered divided into three parts: the first part is dedicated to the dynamics of elementary processes including also heterogeneous ones and the second part to the description of plasma kinetics through the construction of suitable master equations for both atomic and molecular plasmas. Finally the third part includes different applications in applied fields such as microelectronics, fusion, and aerospace. As in the first two books of the series, some overlaps occur in the different chapters to keep part of them self-consistent allowing undergraduate and PhD students as well as researchers to construct a personal road in the understanding of the relevant topics. It is worth noting that the book can be considered complementary to other books published by one of the present authors,^{3,4} on nonequilibrium plasma kinetics. An appropriate selection of the reported chapters can be used for courses on the kinetics of cold plasmas addressed to undergraduate and PhD students.

Bari, Italy

Mario Capitelli
Roberto Celiberto
Gianpiero Colonna
Fabrizio Esposito
Claudine Gorse
Khaled Hassouni
Annarita Laricchiuta
Savino Longo

³M. Capitelli Ed. “Non-equilibrium Vibrational Kinetics” Topics in Current Physics Springer (1986) Vol.39.

⁴M. Capitelli, B.F. Gordiets, C.M. Ferreira and A.I. Osipov “Plasma Kinetics in Atmospheric Gases” Springer Series in Atomic, Optical and Plasma Physics (1986) Vol.31.

Acknowledgments

This book is dedicated to Ettore Molinari, the founder of the plasma chemistry school in Bari, and to Gert D. Billing, Boris F. Gordiets, Aleksei I. Osipov, and Carlos Matos Ferreira for their contribution to the topics discussed in the book.

Moreover we wish to thank Giuliano D'Ammando, Paola Diomede, Vincenzo Laporta, Lucia Daniela Pietanza, Francesco Taccogna, and Massimo Tomellini for their involvement in revising the chapters (6, 8, 1, 6, 10, 3), respectively, as well as all the other Italian and international colleagues quoted in the references.

Contents

Introduction	xv
1 Electron-Molecule Collision Cross Sections and Rate Coefficients	1
1.1 Theoretical Model of Resonant Collisions	2
1.2 Resonant Collisions Involving Atmospheric Molecules.....	7
1.2.1 N ₂ , O ₂ and NO Molecules	7
1.2.2 CO and CO ₂ Molecules	13
1.3 Electron-Molecule Collisions in Fusion Plasmas	17
1.3.1 CH, BeH ⁺ , and BeH Molecules	18
1.3.2 Resonant Processes Involving H ₂ Molecule.....	24
References.....	27
2 Reactivity and Relaxation of Ro-Vibrationally Excited Molecules	31
2.1 Computational Method.....	31
2.2 H+H ₂	34
2.2.1 Isotopes and Scaling Relations.....	37
2.3 N+N ₂	37
2.4 O+O ₂	51
2.5 Future Developments.....	52
References.....	53
3 Atom Recombination at Surfaces	57
3.1 Hydrogen on Graphite Surface	60
3.2 Hydrogen on Metals.....	65
3.3 Oxygen and Nitrogen on Silica	69
3.4 vdfs in Catalysis: A Phenomenological Approach.....	71
References.....	76
4 Kinetic and Monte Carlo Approaches to Solve Boltzmann Equation for eedf	79
4.1 Boltzmann Equation in Two-Term Approximation	80
4.1.1 Theoretical Model	80
4.1.2 Numerical Aspects in the Solution of BE	98

4.1.3	Negative Electron Conductivity	100
4.2	Monte Carlo Method for Electron Transport	100
References		109
5	Superelastic Collisions and Electron Energy Distribution Function	113
5.1	Boltzmann Equation for Atomic and Molecular Plasmas	114
5.1.1	Inelastic Collisions	115
5.1.2	Superelastic Collisions	115
5.1.3	A Golden Rule for Superelastic Collisions	116
5.2	Atomic and Molecular Plasmas	118
5.2.1	Case 1: Pure CO	118
5.2.2	Case 2: Pure He	119
5.2.3	Case 3: He-CO Mixture	120
5.3	Time Evolution of eedf	122
5.3.1	Post-discharge Conditions	122
5.3.2	eedf Evolution During Discharges	127
5.3.3	Abrupt Change of E/N	127
5.3.4	RF Bulk Discharges	131
5.3.5	Case Study: Excimer Laser Kinetics	135
5.3.6	Photoresonant Plasmas	137
5.4	Experimental Determination of eedf	138
References		140
6	Collisional-Radiative Models for Atomic H Plasmas	143
6.1	Equilibrium Relations	144
6.1.1	Boltzmann Relation	144
6.1.2	Saha Relation	145
6.1.3	Maxwell Distribution	145
6.1.4	Planck Spectral Distribution	146
6.2	Non-equilibrium Atomic Plasma	146
6.2.1	Electron Impact Excitation	147
6.2.2	Radiative Transitions	148
6.2.3	Master Equations for Spatially Homogenous Plasma	150
6.3	Cross Sections and Rate Coefficients	151
6.3.1	Excitation by Electron Impact	151
6.3.2	Electron Impact Ionization	153
6.3.3	Spontaneous Emission	155
6.4	Radiative Recombination	156
6.5	QSS Approximation	157
6.5.1	QSS Approximation (General Equations)	157
6.5.2	Interpretation of X_i^0 e R_i^1	160
6.6	QSS Results for Optically-Thin Atomic H Plasmas	161
6.7	Time-Dependent Results	162
6.7.1	Ionizing Plasma $\gamma < 0$	164
6.7.2	Large Deviations from Equilibrium	166
References		171

7	Vibrational Kinetics	175
7.1	Vibrational Kinetics of Diatomic Molecules	176
7.1.1	VT Terms	176
7.1.2	VV Terms	178
7.1.3	Dissociation-Recombination Terms	181
7.2	Vibrational Relaxation Kinetics	183
7.2.1	Sudden Decrease of Gas Temperature	184
7.2.2	Laser Pumping of CO	186
7.2.3	Pumping of CO by Vibrationally Excited N ₂	187
7.2.4	Boundary Layer	191
7.3	Vibrational Kinetics Under Plasma Conditions	195
7.3.1	Laser-Plasma Interaction	198
Appendix 1:	Non-equilibrium Vibrational Distributions:	
	General Considerations	199
Appendix 2	201
References	202
8	Particle Models for Low Pressure Plasmas	205
8.1	Time Scales	206
8.2	Particle Models	207
8.3	Dynamic Particle List	208
8.4	Self-Consistent Approach	209
8.5	Worked Example: RF Model for Hydrogen	211
8.5.1	The Model	212
8.5.2	Solutions to Reduce the Computational Effort	214
8.5.3	Test Case	215
8.5.4	Some Results for Hydrogen	215
8.5.5	Ion Energy Distribution Functions (iedf) in H ₂ RF Discharge	217
References	221
9	Self-Consistent Kinetics of Molecular Plasmas: The Nitrogen Case	223
9.1	Database of N ₂ Processes	224
9.2	Excited State Kinetics and eedf Under Discharge Conditions	227
9.3	Excited State Kinetics and eedf Under Post-discharge (Afterglow) Conditions	236
9.3.1	Short Time Pulsed Discharges	237
9.3.2	Nitrogen Afterglow Following Continuous Discharges ..	238
References	241
10	Negative Ion H⁻ for Fusion	247
10.1	The Kinetic Model	248
10.2	Time-Dependent Pulsed Discharges	257
10.3	Rydberg States	260
10.4	RF Coupled Negative Ion Sources	262

10.5 Negative Ion Energy Distribution Function	266
References	269
11 Non Equilibrium Plasma in High Enthalpy Flows	275
11.1 Fluid Dynamic Model for State-to-State Kinetics	276
11.2 N ₂ Vibrational Kinetics in Nozzle	278
11.3 Air Vibrational Kinetics in Nozzle	282
11.4 Ionizing Nitrogen Mixture	285
11.5 Nozzle Expansion in the Presence of Electric and Magnetic Field	288
11.6 The Role of Radiation in High Enthalpy Flows	293
11.6.1 Shock Tube	293
11.6.2 Nozzle Flow	298
References	301
12 Toward the Activation of Polyatomic Molecules by eV Processes: The CO₂ Case Study	305
References	311
Index	313

Introduction

NON EQUILIBRIUM PLASMA KINETICS is an emerging interdisciplinary discipline describing plasma conditions characterized by large deviations from the equilibrium in both the plasma components and their internal distribution functions. In particular the state-to-state description of the different components including the energy distribution functions of free electrons demands an interdisciplinary approach including quantum and classical dynamics of elementary processes, statistical mechanics and Monte Carlo particle methods ending with more or less sophisticated fluid dynamic approaches. These methods are extensively presented in the present book, which can be considered divided into three parts: the first part is dedicated to the dynamics of elementary processes and of free electrons and the second part to the description of plasma kinetics through the construction of suitable master equations for both atomic and molecular plasmas. Finally the third part includes different applications in applied fields such as microelectronics, fusion, and aerospace.

In particular Chap. 1 is dedicated to the description of electron-molecule cross sections and rates for direct and resonant processes by using semiclassical and quantum approaches. Emphasis is given to the dependence of cross sections and rates on the vibrational quantum number of the target. Particular attention is devoted to the scattering of electrons and diatomic molecules (H_2 , N_2 , O_2) as well as with other molecules of interest in plasma fusion. Chapter 2 reports cross sections and rates of atom-molecule interaction mainly based on QCT (Quasi Classical Trajectory) as a function of initial and final ro-vibrational quantum numbers of the target and products. Vibrational excitation rates of $H-H_2(v,j)$, $N-N_2(v)$, $O-N_2(v)$, and $O-O_2(v)$ are discussed in the whole ro-vibrational range. Chapter 3 reports the formation of nonequilibrium ro-vibrational distributions coming from heterogeneous recombination of atoms on metallic and ceramic surfaces. The results are obtained by using both quantum mechanical and kinetic approaches.

Chapter 4 introduces the reader to the solution of the Boltzmann equation by using both kinetic and Monte Carlo approaches. The two-term expansion of Boltzmann equation, which will be extensively used in the bulk of the book, is

fully described in the chapter. The Monte Carlo approach to solve the Boltzmann equation is then taken into account and also used to check the two-term expansion.

The next three chapters are dedicated to nonequilibrium plasma kinetics. In particular Chap. 5 reports several examples of coupling between excited states and eedf for different discharge and post-discharge conditions emphasizing the role of second kind (super-elastic) collisions from vibrationally and electronically excited states in structuring eedf. Chapter 6 describes in detail the collisional radiative model for atomic hydrogen under quasistationary, stationary, and time-dependent situations. The first part of this chapter uses a Maxwell distribution function for free electrons, while the second part uses non-Boltzmann eedf especially for recombining plasma situations. In the same chapter, we discuss the dependence of excitation and ionization cross sections on the principal quantum number of atomic hydrogen. Chapter 7 describes in detail the nonequilibrium vibrational kinetics of diatomic molecules emphasizing the redistribution of vibrational quanta, introduced by different interactions, by VV (vibration-vibration) and VT (vibration-translation) energy exchange transfer processes.

The third part of the book deals with the applications. Chapter 8 discusses parallel plate RF reactors for microelectronics applications by using a self-consistent PIC (Particle in Cell) model able to yield eedf and vibrational distributions as a function of the distance of electrodes. In the same chapter, we report nonequilibrium translational distributions of ions derived by collisional sheath dynamics. Chapter 9 describes in detail the nonequilibrium vibrational kinetics of nitrogen discharges emphasizing in particular the possibility of vibrational mechanisms in affecting the dissociation rates of nitrogen. Chapter 10 reports the kinetics of negative ion H⁻ sources under different plasma configurations (multipole magnetic plasma, RF discharges) to be used for injecting intense neutral beams in tokamak facilities for fusion. Emphasis is given to the collisional production of negative H⁻ ions either through the dissociative attachment from vibrationally excited molecules or through dissociative attachment for Rydberg states, and Chap. 11 is dedicated to the description of the plasma kinetics during nozzle expansion and shock wave interaction for miming conditions met under reentry conditions for aerospace applications. Under these conditions we recover eedf and vdf very far from Maxwell and Boltzmann distributions.

Finally Chap. 12 considers the challenge of properly accounting the vibrational issue in the kinetics of polyatomic molecules, as CO₂ plasmas, nowadays collecting a large interest in the community for their relevance to technological applications in the fields of energy and environment.

Chapter 1

Electron-Molecule Collision Cross Sections and Rate Coefficients for Processes Involving Excited States

The formulation of a theoretical model for non-equilibrium plasmas relies primarily on the knowledge of cross section information on collisional processes involving excited species. This is particularly true for molecular plasmas where the presence of molecules, characterized by a large spectrum of rovibronic states, gives rise to an enormous number of scattering processes where momentum or energy transfers, as well as reactive events, can occur. This implies, then, the determination of the corresponding cross sections for each process and for a suitable range of relative kinetic energy of the collision partners, which results in the need of large cross section databases.

A first example of low-temperature non-equilibrium molecular plasma is provided, in space explorations, by the atmospheric gases interacting with the thermal shield of a space vehicle during the immersion in the atmosphere of a planet at hypersonic speed (re-entry conditions). The energy exchanges, consequent to the shock wave generated in the impact, induce the formation of a molecular plasma in thermal and chemical non-equilibrium conditions, characterized by a non-Boltzmann population of the internal states. Then redistribution of energy takes place through a complex collision physics where a role of primary importance is played by the electron-molecule collisions (Capitelli et al. 2009).

Hydrogen/deuterium plasmas in fusion technology offer a second relevant example of a non-equilibrium systems. Here the hydrogen, used for the nuclear energy production, getting into the low-temperature regions of the containing vessel (edge and divertor plasmas) condenses in H₂ excited molecules which play a role of capital importance in affecting the performance of the nuclear devices (Clark and Reiter 2005; Capitelli et al. 2006).

This Chapter deals with internal transitions, induced by electron impact, of diatomic molecules initially in a given quantum state, with particular emphasis on the vibrational excitations, which play a prominent role in the energy balance of the molecular plasmas (Capitelli et al. 2011). An efficient process for the activation of the vibrational degrees of freedom is represented by the resonant collisions whose

mechanism involves the capture from the molecule of the incident electron, with the concomitant formation of a molecular anion. This is a transient species, better described as a resonant state, which can either decay, by electron emission, back into some excited vibrational level of the neutral molecule, giving rise to the so-called resonant vibrational excitation (RVE), or can dissociate by production of a neutral atom and a negative atomic ion. This last process, known as dissociative electron attachment (DEA), can occur if the atomic negative ion exists in a stable state. Unlike the *direct* inelastic vibrational excitation, which is an inefficient process usually involving few vibrational levels, particularly for homonuclear molecules owing no permanent dipole moment, multi-quantum vibrational transitions can occur, on the contrary, through the above resonant mechanism which can promote effectively the activation of high vibrational levels.

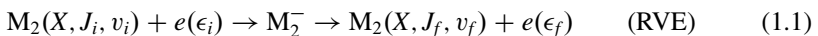
Hence the importance of reliable information on the corresponding state-to-state cross sections in the construction of realistic models of molecular plasmas. Beside the laboratory measurements, which can provide precious cross section information on electron-impact vibrational excitation, at least for those levels experimentally accessible, cross section calculations can be performed with no particular limitations, being the theoretical description of the resonant collisions within the range of the present state-of-the-art of the scattering theories. So complete sets of cross sections for electron-impact processes, involving all the vibrational levels of a given molecule, can be obtained.

One of the outcomes of a modeling in molecular plasma is the electron energy distribution function (eedf) which can be strongly affected, beside the other processes, by the electron collisions with vibrationally excited molecules, so that, in stationary conditions, the eedf can significantly deviate from the Maxwellian distribution (see Chaps. 5 and 9–11). Maxwellian state-specific rate coefficients are in any case helpful to model the dependence on the vibrational quantum number in equilibrium plasmas.

In the next section we will formulate the resonance theory for electron-molecule collision cross section calculations for both RVE and DEA processes, while in the subsequent sections we will review the main results pertinent for molecular plasmas in aerospace and fusion applications.

1.1 Theoretical Model of Resonant Collisions

When a diatomic molecule, M_2 , in its ground electronic state, X , and in a given ro-vibrational level, denoted by (J_i, v_i) , interacts with an electron of incident energy ϵ_i , the following processes can occur (Bardsley and Mandl 1968):



where (J_f, v_f) denotes a final ro-vibrational level and ϵ_f the kinetic energy of the outgoing electron. The first process leads to a ro-vibrational excitation and the second to dissociation. In both cases a resonant state of the M_2^- molecular ion is formed after the trapping of the incident electron within the target molecule M_2 . RVE includes also the excitation to the vibrational continuum of the neutral molecule, followed by dissociation, according to the process



This channel (Laporta et al. 2014, 2015) will not be considered in the present Chapter.

The theoretical description of the resonant collision process starts from the Schrödinger equation,

$$H\Psi(\mathbf{r}_M, \mathbf{r}_e, \mathbf{R}) = [H_{el} + T_N]\Psi(\mathbf{r}_M, \mathbf{r}_e, \mathbf{R}) = E\Psi(\mathbf{r}_M, \mathbf{r}_e, \mathbf{R}), \quad (1.4)$$

where the Hamiltonian operator H is expressed as a sum of the electronic Hamiltonian, H_{el} , and the nuclear operator T_N . Ψ is the wave function for the $M_2 + e$ scattering system depending on the target electron coordinates, denoted collectively with \mathbf{r}_M , on the incident electron vector position \mathbf{r}_e , and on the internuclear distance vector \mathbf{R} . E is the total energy. The solution of Eq.(1.4) can be searched by resorting to a standard treatment where the scattering wave function is expressed in terms of a close-coupling expansion, including bound and continuum states. The orthonormal basis set is formed by wave functions factorized, according to the Born-Oppenheimer approximation, in an electronic and nuclear part. In the applications a simplified model is usually adopted where only one discrete electronic state is selected, which can be written as $\Phi(\mathbf{r}_M, \mathbf{r}_e; R)\xi(\mathbf{R})$. Here Φ is the electronic eigenfunction of the Hamiltonian H_{el} , depending on the electron coordinates and, parametrically, on the internuclear distance R , while $\xi(\mathbf{R})$ is the resonant nuclear wave function. No limitations, instead, are imposed to the continuum spectrum whose expansion can be written in terms of the product $\Psi_\epsilon^n(\mathbf{r}_M, \mathbf{r}_e; R)\chi_\nu^n(\mathbf{R})$, where Ψ_ϵ^n is the wave function for the electronic state n , depending on the continuum energy ϵ , and $\chi_\nu^n(\mathbf{R})$ is the nuclear wave function of the target molecule, where $\nu = (J, v)$ denotes the ro-vibrational quantum numbers. These wave functions are solution of the target nuclear equation given by

$$[T_N + V_M^n(R) - E_\nu^n]\chi_\nu^n(\mathbf{R}) = 0, \quad (1.5)$$

where $V_M^n(R)$ is the potential energy of the electronic state of the neutral molecule and E_ν^n the associated ro-vibrational eigenvalues. Thus the scattering wave function is written as (Wadehra 1986),

$$\Psi(\mathbf{r}_M, \mathbf{r}_e, \mathbf{R}) \approx \Phi(\mathbf{r}_M, \mathbf{r}_e; R)\xi(\mathbf{R}) + \sum_{n,\nu} d\epsilon f_\nu^n(\epsilon) \Psi_\epsilon^n(\mathbf{r}_M, \mathbf{r}_e; R) \chi_\nu^n(\mathbf{R}) \quad (1.6)$$

where $f_v^n(\epsilon)$ is a linear combination coefficient and the electronic wave functions are assumed antisymmetrized. Equation (1.6) obeys to the boundary condition:

$$\begin{aligned} \Psi(r_e \rightarrow \infty) &\longrightarrow e^{i\mathbf{k}_{v_i}^{n_i}(\epsilon_i) \cdot \mathbf{r}_e} \Psi^{n_i}(\mathbf{r}_M; R) \chi_{v_i}^{n_i}(\mathbf{R}) + \\ &+ \sum_{n,v} \Psi^n(\mathbf{r}_M; R) \chi_v^n(\mathbf{R}) \int d\epsilon f_v^n(\epsilon) e^{i\mathbf{k}_v^n(\epsilon) \cdot \mathbf{r}_e} = \\ &= \sum_{n,v} \Psi^n \chi_v^n \int d\epsilon [\delta(\epsilon - \epsilon_i) \delta_{nn_i} \delta_{vv_i} + f_v^n(\epsilon)] e^{i\mathbf{k}_v^n(\epsilon) \cdot \mathbf{r}_e} \quad (1.7) \end{aligned}$$

where the index i denotes the initial state of the system. $k(\epsilon) = (2m\epsilon/\hbar)^{1/2}$ is the momentum of the free electron. m is the electron mass and \hbar the Dirac constant. $\Psi^n(\mathbf{r}_M; R)$ is the target electronic wave function. In the last line we have shortened the notation by including the first term under the sum-integral and omitted the arguments in the wave functions. In writing Eq. (1.7) we have used the fact that $\Phi(r_e \rightarrow \infty) = 0$ due to the bound nature of the discrete wave function. From the last line of Eq. (1.7) it is immediate to deduce:

$$f_{v_i}^{n_i}(\epsilon_i) = \delta(\epsilon - \epsilon_i) \delta_{nn_i} \delta_{vv_i}. \quad (1.8)$$

Inserting now the expansion (1.6) in Eq. (1.4), and assuming, according to the fixed-nuclei approximation, $T_N \Phi = T_N \Psi_\epsilon^n \approx 0$, we obtain:

$$\begin{aligned} &\xi(\mathbf{R}) H_{el} \Phi(\mathbf{r}_M, \mathbf{r}_e; R) + \Phi(\mathbf{r}_M, \mathbf{r}_e; R) T_N \xi(\mathbf{R}) + \\ &+ \sum_{\hbar, v} \int d\epsilon f_v^n(\epsilon) \chi_v^n(\mathbf{R}) H_{el} \Psi_\epsilon^n(\mathbf{r}_M, \mathbf{r}_e; R) + \\ &+ \sum_{\hbar, v} \int d\epsilon f_v^n(\epsilon) \Psi_\epsilon^n(\mathbf{r}_M, \mathbf{r}_e; R) T_N \chi_v^n(\mathbf{R}) = \\ &= E \left[\Phi(\mathbf{r}_M, \mathbf{r}_e; R) \xi(\mathbf{R}) + \sum_{\hbar, v} \int d\epsilon f_v^n(\epsilon) \Psi_\epsilon^n(\mathbf{r}_M, \mathbf{r}_e; R) \chi_v^n(\mathbf{R}) \right]. \quad (1.9) \end{aligned}$$

Multiplying now this equation on the left by $\int d\mathbf{r}_M d\mathbf{r}_e \Phi^*(\mathbf{r}_M, \mathbf{r}_e; R)$ and using the orthonormality of the basis set, we get finally:

$$[T_N + V^-(R) - E] \xi(\mathbf{R}) = - \sum_{n,v} \chi_v^n(\mathbf{R}) \int d\epsilon f_v^n(\epsilon) V_{dc}^n(\epsilon; R), \quad (1.10)$$

where $V^-(R) = \langle \Phi | H_{el} | \Phi \rangle$ is the *adiabatic* potential energy of the bound electronic state of M_2^- molecular ion. Equation (1.10) shows the role of the *discrete-continuum coupling matrix element* $V_{dc}^n(\epsilon; R) = \langle \Phi | H_{el} | \Psi_\epsilon^n \rangle$. This describes the interaction

between the discrete and continuum spectrum of the $M_2 + e$ system and determines the existence of the resonance. If the bound-continuum coupling is weak, in fact, the right-hand side of Eq. (1.10) becomes negligibly small, so that the whole expression reduces to the nuclear Schrödinger equation of a non-resonant stable state of the M_2^- molecular ion, where E and $\xi(\mathbf{R})$ are now its stable ro-vibrational eigenvalue and eigenfunction respectively.

The coefficient $f_v^n(\epsilon)$ also depends on the coupling matrix. It can be found by premultiplying Eq. (1.9) by $\int d\mathbf{R} d\mathbf{r}_M d\mathbf{r}_e \Psi_{\epsilon'}^{n'*}(\mathbf{r}_M, \mathbf{r}_e; R) \chi_{v'}^{n'*}(\mathbf{R})$. One has:

$$f_v^n(\epsilon) = \lim_{\eta \rightarrow 0} \int d\mathbf{R} \chi_v^{n*}(\mathbf{R}) \frac{V_{dc}^{n*}(\epsilon, R)}{E - E_v^n - \epsilon + i\eta} \xi(\mathbf{R}) + \delta(\epsilon - \epsilon_i) \delta_{nn_i} \delta_{vv_i}, \quad (1.11)$$

where we have suppressed the prime superscript and added the last term on the right coming from Eq. (1.8). Using Eq. (1.11) in Eq. (1.10) we have:

$$[T_N + V^-(R) - E] \xi(\mathbf{R}) = -V_{dc}^{n_i}(\epsilon_i, R) \chi_{v_i}^{n_i}(\mathbf{R}) - \int d\mathbf{R}' K(\mathbf{R}, \mathbf{R}') \xi(\mathbf{R}') \quad (1.12)$$

where

$$K(\mathbf{R}, \mathbf{R}') = \sum_{n,v} \chi_v^{n*}(\mathbf{R}') \chi_v^n(\mathbf{R}) \left[\Delta_v^n(R', R, E - E_v^n) - \frac{i}{2} \Gamma_v^n(R', R, E - E_v^n) \right]. \quad (1.13)$$

The *level shift*, Δ_v^n , and the *resonance width*, Γ_v^n , are defined by:

$$\Delta_v^n(R, R', E - E_v^n) = P \int_0^\infty d\epsilon \frac{1}{2\pi} \frac{\Gamma_v^n(R, R', E - E_v^n)}{E - E_v^n - \epsilon}, \quad (1.14)$$

where P denotes the principal value of the integral and

$$\Gamma_v^n(R', R, E - E_v^n) = 2\pi V_{dc}^{n*}(E - E_v^n, R') V_{dc}^n(E - E_v^n, R). \quad (1.15)$$

Equation (1.12) is usually referred to as the *non-local form* of the resonant nuclear equation. This denomination comes from the fact the value in a given point \mathbf{R} of the unknown function $\xi(\mathbf{R})$ on the left-hand side, depends on the values of the same function in the whole range of the integration variable, \mathbf{R}' , on the right. In this form the non-local coupling matrix elements, $V_{dc}^n(E - E_v^n, R)$, are function of both the internuclear distance R and the energy $E - E_v^n$. The lack of information in literature on these non-local quantities for many molecules of applicative interest, and also the need of the production of large cross section databases, which imposes fast computational methods, can make convenient the use of a *local* approximate form of Eq. (1.12). This can be obtained if we assume that the quantity in the square bracket in Eq. (1.13) can be considered as independent of the ro-vibrational levels v . This is true for example when $E \gg E_v^n$, so that the level shift and the width become a weak function of E_v^n . In this conditions, instead to suppress the eigenvalue E_v^n , it can

be replaced by a constant value opportunely selected. Assuming then $E_v^n \approx E_{\bar{v}}^n$, and putting $E - E_v^n \approx \bar{\epsilon}$, Eq. (1.13) can be rewritten as:

$$\begin{aligned} K(\mathbf{R}, \mathbf{R}') &\approx \sum_n \left[\Delta_{\bar{v}}^n(R', R, \bar{\epsilon}) - \frac{i}{2} \Gamma_{\bar{v}}^n(R', R, \bar{\epsilon}) \right] \times \\ &\quad \times \sum_v \chi_v^{n*}(\mathbf{R}') \chi_v^n(\mathbf{R}) = \\ &= \sum_n \left[\Delta_{\bar{v}}^n(R', R, \bar{\epsilon}) - \frac{i}{2} \Gamma_{\bar{v}}^n(R', R, \bar{\epsilon}) \right] \delta_n(R - R'), \end{aligned} \quad (1.16)$$

where we have used the completeness of the ro-vibrational basis set. Inserting this approximate form of the kernel $K(\mathbf{R}, \mathbf{R}')$ in Eq. (1.12), and using the δ -function properties in the right-hand side integration, we get the local resonant nuclear equation,

$$\left[T_N + V^-(R) + \Delta_{tot}(R) - \frac{i}{2} \Gamma_{tot}(R) - E \right] \xi(\mathbf{R}) = -V_{dc}^{n_i}(\epsilon_i, R) \chi_{v_i}^{n_i}(\mathbf{R}), \quad (1.17)$$

where for brevity we have put,

$$\Delta_{tot} = \sum_n \Delta_{\bar{v}}^n(R), \quad \Gamma_{tot} = \sum_n \Gamma_{\bar{v}}^n(R). \quad (1.18)$$

The complex quantity in Eq. (1.17), $V^- + \Delta_{tot} - i\Gamma_{tot}/2$, is known as *optical potential*.

The last step for the solution of Eq. (1.17) is the expansion of both $\xi(\mathbf{R})$ and $\chi_{v_i}^{n_i}(\mathbf{R})$ in terms of spherical harmonics where $\xi(R)/R$ and $\chi_{v_i}^{n_i}(R)/R$ are the radial parts. After some manipulation (Wadehra 1986) the final local form for the radial equation is obtained,

$$\left[T_N + V^-(R) + \Delta_{tot}(R) - \frac{i}{2} \Gamma_{tot}(R) - E \right] \xi(R) = -V_{dc}^{n_i}(\epsilon_i, R) \chi_{v_i}^{n_i}(R). \quad (1.19)$$

This is the equation used for cross section calculations discussed in next sections and will be referred to as the *local complex-potential* (LCP) approximation. Once this equation is solved, with the appropriate boundary conditions for $\xi(R)$, the cross sections for DEA and RVE can be calculated (Wadehra 1986).

The widths can be obtained from the local form of Eq. (1.15) as $\Gamma_{\bar{v}}^n(\bar{\epsilon}; R) = 2\pi |V_{dc}^n(\bar{\epsilon}; R)|^2$. The input quantities for solving Eq. (1.19) are then represented by the adiabatic potential $V^-(R)$, the coupling matrix elements $V_{dc}^n(\bar{\epsilon}; R)$ and the initial electronic state potential $V_M^{n_i}(R)$ of the neutral molecule, which allows for the calculation of ro-vibrational eigenvalues and eigenfunctions through Eq. (1.5). The total scattering energy is then expressed as $E = E_{v_i}^{n_i} + \epsilon_i$.

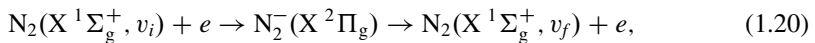
1.2 Resonant Collisions Involving Atmospheric Molecules

When a spacecraft, after a space mission, returns back to the Earth, its thermal shield interacts with the terrestrial atmosphere. The modeling of the plasma created at the vehicle surface requires cross sections and rate coefficients for the collision processes involving N₂ and O₂ molecules, which are the main components of the atmospheric gas, as well as those for other molecular species like NO, CO, CO₂ present in small fractions. In planetary explorations, however, also the atmospheres of other planets, with their own compositions, must be considered. Relevant examples are the Venus and Mars atmospheres, which consist mostly of CO and CO₂ species, or the gaseous giant planets, like Jupiter or Saturn, where hydrogen is the most abundant constituent.

In this section we will review the resonant vibrational excitation cross sections and rate coefficients calculated in our group, relevant for atmospheric modeling, for electron-collision processes involving the above molecules in excited vibrational levels (Laporta et al. 2012a,b, 2013, 2014; Celiberto et al. 2014). A special place is occupied by hydrogen because of its importance also in nuclear energy researches, and will be discussed in this Chapter in connection with fusion technology.

1.2.1 N₂, O₂ and NO Molecules

Resonant vibrational cross sections (RVE) have been calculated for the process (Laporta et al. 2012b, 2014):



Recent calculations for the above process were performed in Laporta et al. (2014) by using an accurate potential curve for the ground state N₂(X¹Σ_g⁺) (Le Roy et al. 2006), while that of the N₂⁻(X²Π_g) state were obtained by ab initio calculations using the R-matrix method, which provided also the resonance width. The obtained results are shown in Fig. 1.1.

The RVE cross sections have been calculated for all the possible transitions $v_i \rightarrow v_f$ linking the 59 vibrational levels supported by the N₂ ground state potential curve (Laporta et al. 2014). Figure 1.2 shows a comparison with the experiments (Allan 1985) for the transitions 0 → 1, 5, 10. Quite satisfactory is the agreement theory-experiment for the 0 → 1 and 0 → 5 transitions, while some discrepancy arises for the 0 → 10 excitation, probably due to the very small absolute cross section values which implies a reduced accuracy. However, for large multi-quantum excitations we can expect that the LCP approximation is no longer valid so that a non-local treatment of the dynamical model could be more appropriate (Cederbaum and Domcke 1981).

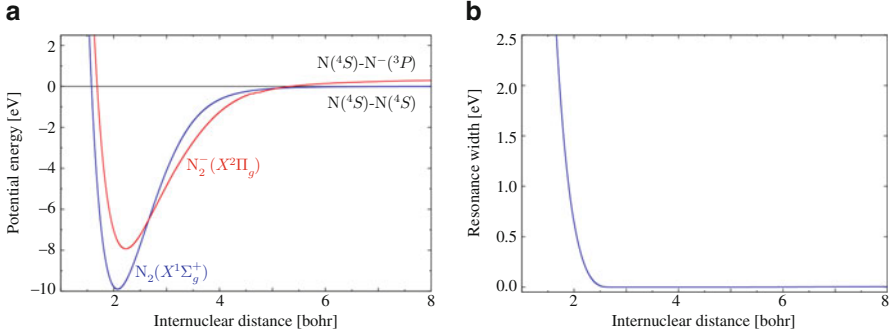


Fig. 1.1 (a) Potential curves for $N_2(X^1\Sigma_g^+)$ and $N_2^-(X^2\Pi_g)$ states and (b) the resonance width (Laporta et al. 2014)

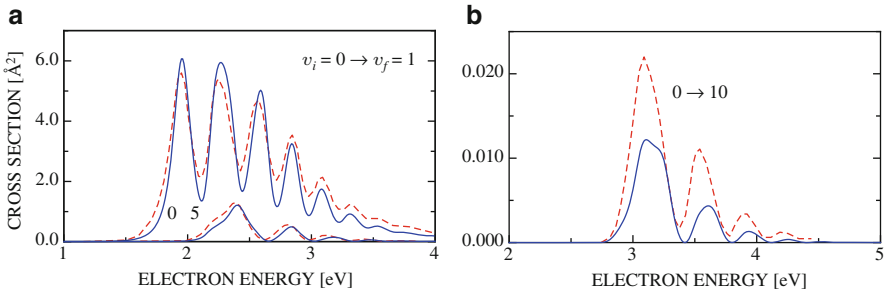
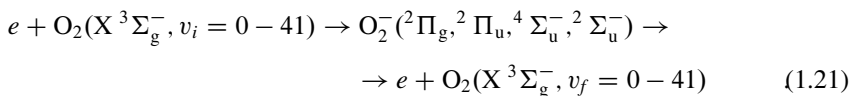


Fig. 1.2 Comparison of the theoretical cross sections (Laporta et al. 2014) (full-blue line) with the experiments (Allan 1985) (dashed-red lines) for the transitions shown in the panels

Very good agreement is instead observed in Fig. 1.3 where the theoretical cross sections are compared with the experimental results of Wong, as reported by Dubé and Herzenberg (1979), for the $0 \rightarrow 1$ and $0 \rightarrow 2$ transitions. A comparison of the cross sections calculated by the LCP approximation with the R -matrix results is shown in Fig. 1.4. A shift in the peak positions is observed in this case, probably determined by the different input parameters used in the two calculations.

Figure 1.5a, b show elastic and inelastic RVE cross sections for some transitions as a function of the incident electron energy. The oscillating structures observed in all the curves, follow mainly the behavior of the bound vibrational wave functions of $N_2^-(X^2\Pi_g)$ ion and disappear in the continuum region above the dissociation limit of the resonant state (Celiberto et al. 2013b). Figure 1.5c, d show the corresponding rate coefficients, calculated by assuming a Maxwellian electron energy distribution function and found in good agreement with previous calculations (Laporta et al. 2012b; Huo et al. 1986, 1987).

The RVE collisions involving the oxygen molecule can be written as:



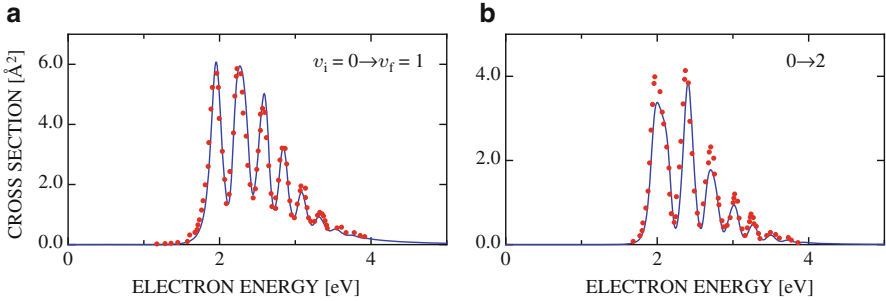


Fig. 1.3 Comparison of the theoretical cross sections (Laporta et al. 2014) (full-blue line) with the experiments of Wong, as cited by Dubé and Herzenberg (1979) (markers), for the transitions shown in the panels

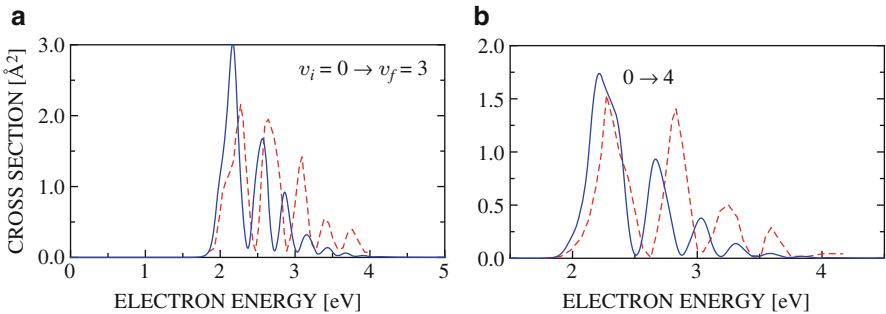


Fig. 1.4 Comparison of the theoretical cross sections calculated by the LCP model (Laporta et al. 2014) (full-blue line) and the *R*-matrix method (Schneider et al. 1979) (dashed-red lines) for the transitions shown in the panels

where four resonant states are implicated in the process. The potential curves for the O₂ and O₂⁻ electronic states were obtained by using the MOLPRO chemistry code (Werner et al. 2010) and by exploiting existing data in literature. Details of the calculations are given elsewhere (Laporta et al. 2013) and the results are shown in Fig. 1.6. Forty two vibrational levels, belonging to the ground electronic state of the neutral molecule were found, and cross sections and rates were calculated for all transitions. A comparison of the theoretical calculations with the experiments is shown in Fig. 1.7. A good agreement is observed between the LCP calculations (Laporta et al. 2013) with the experimental results (Noble et al. 1996) for the 0 → 1, 2 transitions, while some discrepancy is observed with the *R*-matrix results (Noble et al. 1996), for the 0 → 1, 2, 3, 4 excitations, probably due to the fact that these last calculations included the ⁴S_u⁻ resonance only. A little worse is the comparison with the experiments for the 0 → 3, 4 transitions, where the LCP calculations show larger cross sections. We should stress here the fact that the experimental cross sections shown in Fig. 1.7, were obtained from the measured differential cross sections by assuming for the incident electron a pure *p*-wave

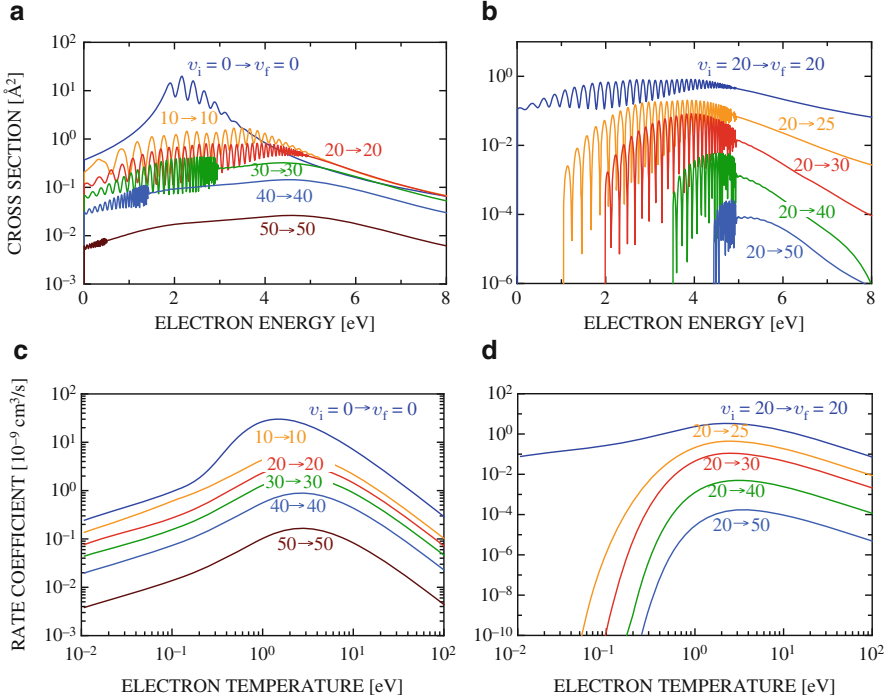


Fig. 1.5 Electron-N₂ elastic (a) and inelastic (b) cross sections and the corresponding rate coefficients (c)–(d), for the transitions shown in the panels

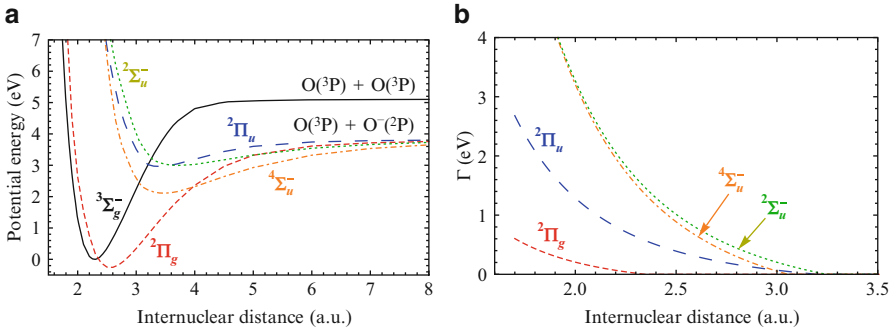


Fig. 1.6 (a) Potential curves for the O₂ ground state and for the four O₂⁻ resonant states as shown in the figure. (b) The corresponding resonance widths

behavior ($l = 1$) while, according to the analysis of Allan (1995), a d -wave ($l = 2$) contribution should be considered (Laporta et al. 2013).

Cross sections and rate coefficients for some transitions are shown in Fig. 1.8. The different features exhibited by the cross sections in different range of electron energies, are determined by the different contributions coming from the four

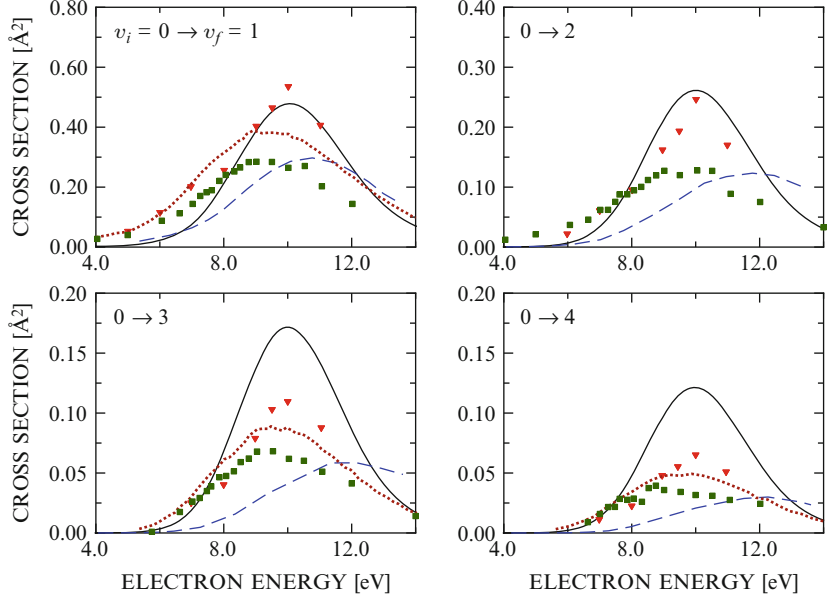


Fig. 1.7 Comparison of calculated and measured RVE cross sections in $e\text{-O}_2$ collisions. Theoretical: solid lines (Laporta et al. 2013), long-dashed lines (Noble et al. 1996). Experimental: triangles (Noble et al. 1996), squares (Wong et al. 1973) and dotted lines (Allan 1995)

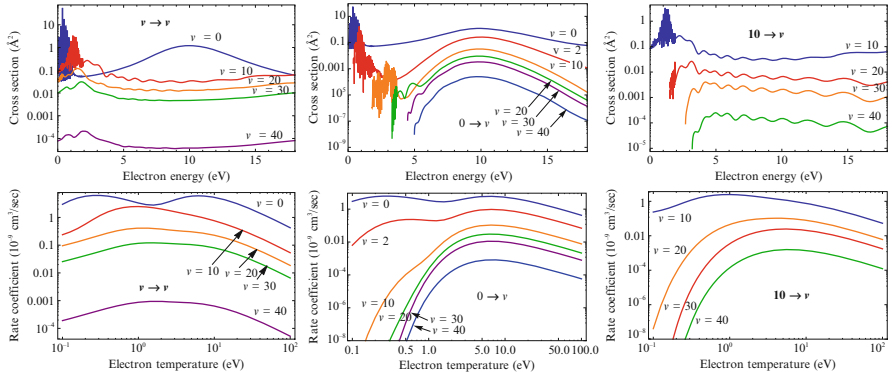


Fig. 1.8 Electron- O_2 elastic and inelastic cross sections (upper panels) and the corresponding rate coefficients (lower panels), for the shown transitions

resonant states. The rapid oscillations, in fact, observed at very low energies (<4 eV) comes from the dominance of the $^2\Pi_g$ symmetry (see Fig. 1.6a), while at larger energy (~ 10 eV) the $^4\Sigma_u^-$ gives the main contribution. The structures present in the $10 \rightarrow v'$ transitions, as well as those for the $v \rightarrow v$ case for large v , are probably due to the overlap of the vibrational wave functions of the O_2 molecule with the continuum of the O_2^- resonant states (Laporta et al. 2013).

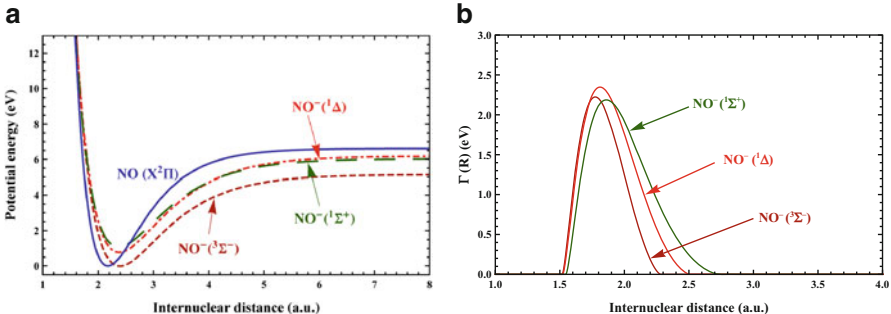
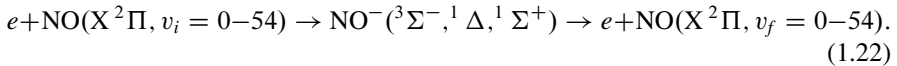


Fig. 1.9 (a) Potential curves for the NO ground state and for the three NO⁻ resonant states as shown in the figure. (b) The corresponding resonance widths

Dissociative electron attachment cross sections were also calculated for O₂ molecule, along with those for the resonant dissociative vibrational excitation by electron impact. The interested reader is referred to Laporta et al. (2015) for a discussion of these processes.

RVE cross section calculations were performed also for the following process involving the nitric oxide molecule (Laporta et al. 2012b):



which involves three different resonant NO⁻ states. In this case the potential curves for the resonant and neutral electronic states were expressed as Morse functions optimized to fit the calculated values (Gilmore 1965), while the widths were adjusted in order to reproduce the experimental cross sections (Allan 2005). The obtained potentials and widths are shown in Fig. 1.9. The $\Gamma(R)$ of Fig. 1.9b were found in good agreement with the ab initio results of Trevisan et al. (2005) in the available range of internuclear distances (Laporta et al. 2012b). The cross sections for process (1.22) are shown in Fig. 1.10. The figure shows that the peak position is well reproduced by the theoretical calculations, while some difference is observed in their intensity. However, except for the elastic case, our cross section are on the contrary in very good agreement with the theoretical cross sections of Trevisan et al. (2005), as shown in Fig. 1.11 for the same transitions. Example of RVE cross sections and rate coefficients are shown in Fig. 1.12 for some elastic and inelastic transitions.

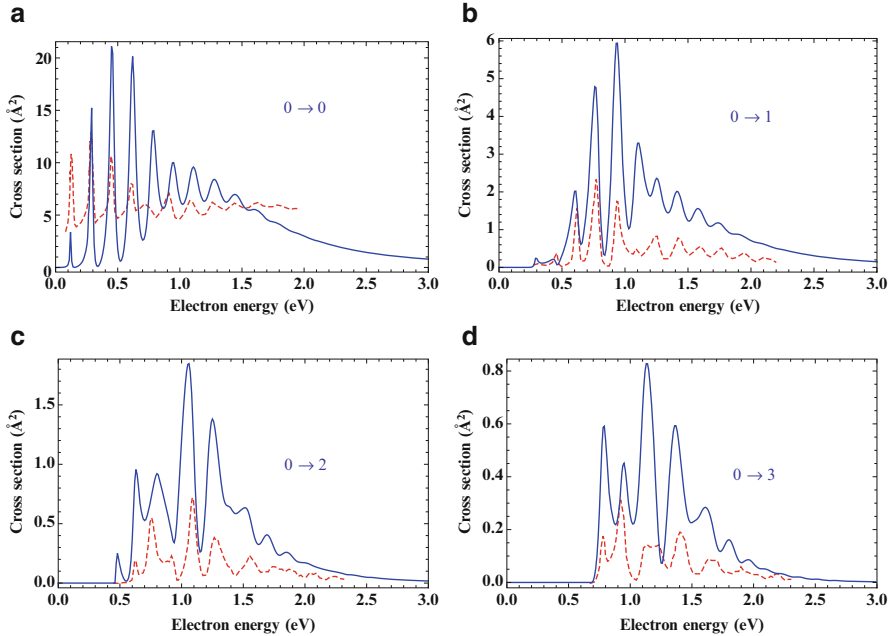
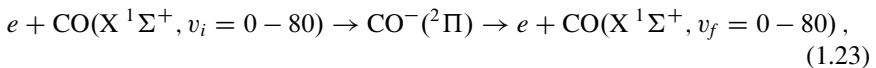


Fig. 1.10 Comparison of the calculated RVE cross sections in e -NO collisions (Laporta et al. 2012b) (solid lines) with the experiments (Allan 2005) (dashed lines) for the transitions shown in the figures

1.2.2 CO and CO₂ Molecules

RVE cross sections calculations have been extended also to the process (Laporta et al. 2012a)



which proceeds through the ${}^2\Pi$ resonant states. Potential energy curves for this state, as well as for $\text{CO}(\text{X}^1\Sigma^+)$ state and the resonance width, were calculated ab initio by using MOLPRO and R -matrix method (Laporta et al. 2012a). Figure 1.13 shows the results. In particular in the right panel are represented the calculated points and the analytical fit obtained by assuming for $\Gamma(R)$ the polynomial expression,

$$\begin{aligned} \Gamma(R) = & (-302.66 + 635.8R - 480.06R^2 + 156.9R^3 - 18.88R^4) \times \\ & \times \Theta[V^-(R) - V_M^0(R)] (\text{eV}), \end{aligned} \quad (1.24)$$

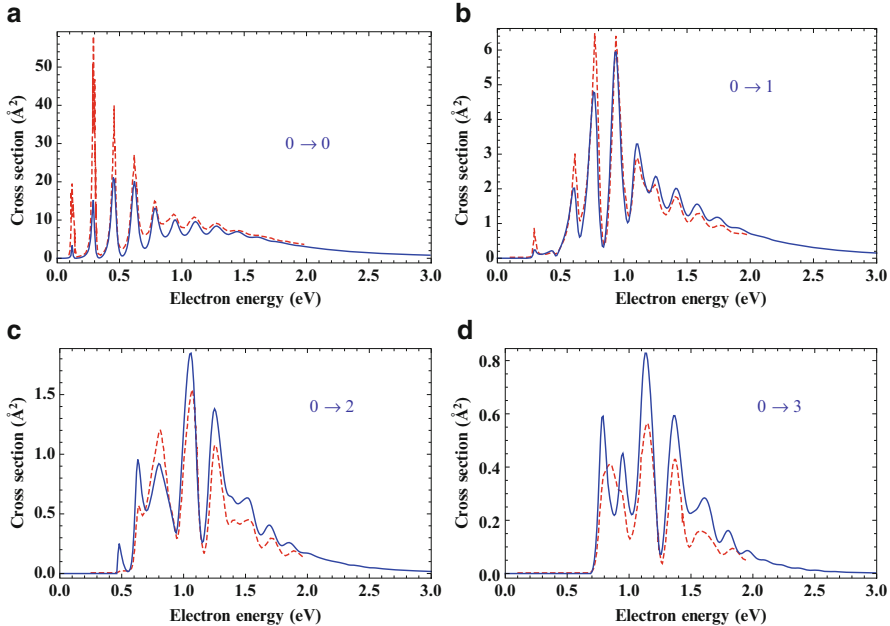


Fig. 1.11 Comparison of the LCP theoretical RVE cross sections in e -NO collisions (Laporta et al. 2012b) (solid lines) with non-local calculations (Trevisan et al. 2005) (dashed lines) for the transitions shown in the figures

where Θ is the step-function and $V^-(R)$ and $V_M^0(R)$ represent, respectively, the neutral and resonant state potential curves.

A comparison of the LCP calculated cross sections with the R -matrix results (Morgan 1991) and with the experiments (Allan 2010) is shown in Fig. 1.14.

The agreement among the various results is excellent for all the transitions but the $0 \rightarrow 10$. As already noted, for these large multi-quantum excitations the LCP model is probably insufficient and a more accurate non-local description of the resonant scattering, involving an energy-dependent Γ , could be necessary.

Cross sections for some elastic and inelastic transitions, with the corresponding Maxwellian rate coefficients, are shown in Fig. 1.15.

RVE cross sections were calculated also for electron-CO₂ collisions (Celiberto et al. 2014). Carbon dioxide is a polyatomic molecule owing three normal vibrational modes (symmetric and asymmetric stretching and bending modes), which would require a multidimensional formulation for the resonant scattering (Rescigno et al. 2002). However, following the analysis of the experimental observations of Čadez et al. (1977), suggesting that a decoupling scheme can be assumed for the stretching mode, the cross sections have been calculated for the RVE process (Celiberto et al. 2014):

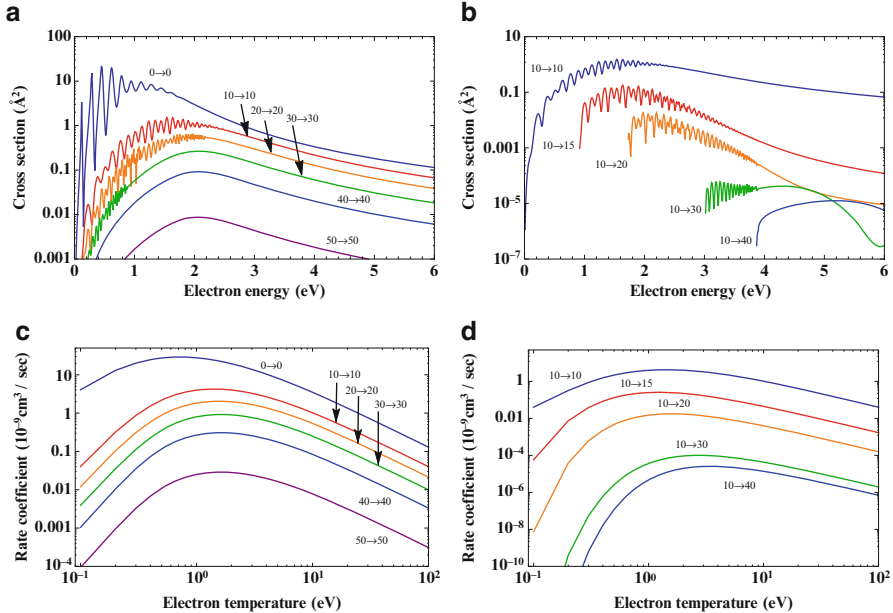


Fig. 1.12 Electron-NO elastic (**a**) and inelastic (**b**) cross sections and the corresponding rate coefficients (**c**)–(**d**), for the transitions shown in the panels

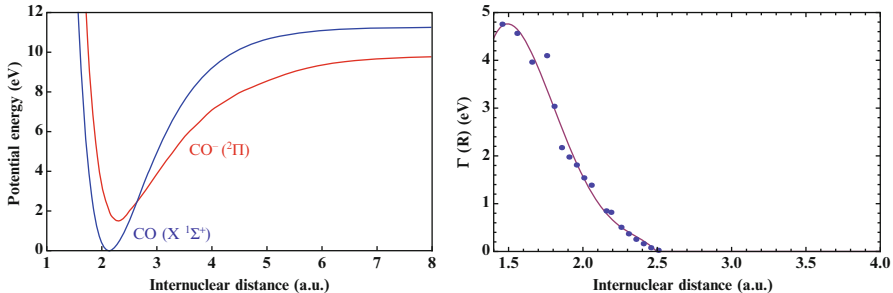
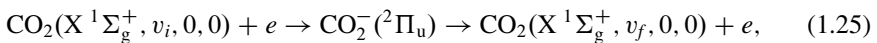


Fig. 1.13 *Left panel:* potential curves for the CO ground state and the CO⁻ resonant states. *Right panel:* the corresponding resonance width. This panel shows the R-matrix points along with the analytical fit (*full line*)



involving the $2\Pi_u$ resonant state and limited to the symmetric stretch vibrational excitations only, for which the usual one-dimensional LPC approximation, for the dynamical model, has been adopted.

The potential energy curves and widths, shown in Fig. 1.16, were calculated by using MOLPRO and the R-matrix codes. The obtained cross sections and rate

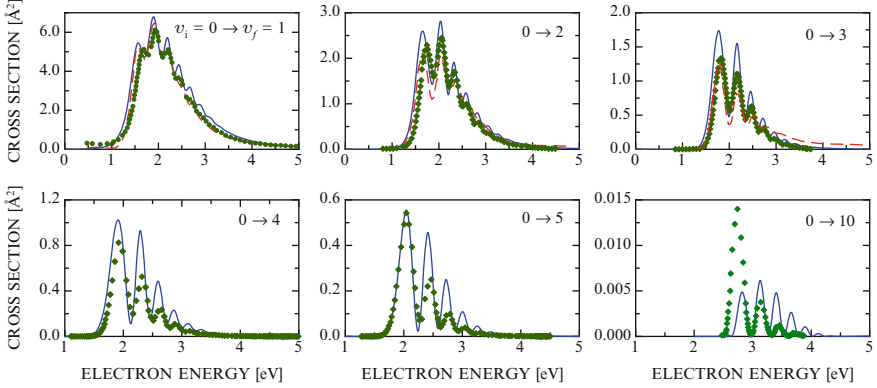


Fig. 1.14 Comparison of LCP electron-CO RVE cross sections in $e\text{-NO}$ collisions (Laporta et al. 2012a) (solid lines) with the R -matrix calculations (dashed lines) (Morgan 1991) and experimental data (Allan 2010) (markers)

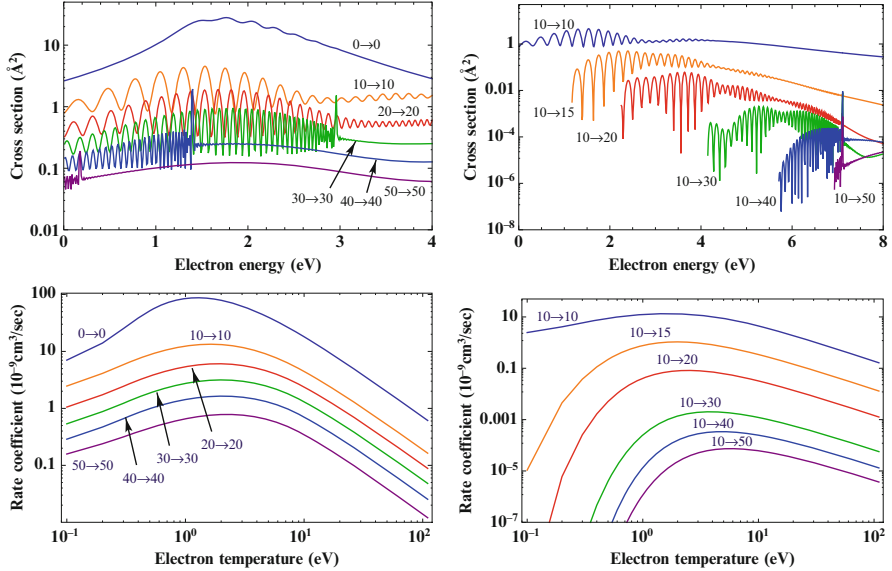


Fig. 1.15 Electron-CO elastic and inelastic cross sections (upper panels) and the corresponding rate coefficients (lower panels), for the shown transitions

coefficients are shown in Fig. 1.17 for some $(v_i, 0, 0) \rightarrow (v_f, 0, 0)$ transitions, involving the symmetric stretch coordinate. Superimposed to the usual boomerang oscillations, two and three broad maxima appear for the transitions with $v_i = 1$ and 2 respectively, probably generated by the oscillating structure of the corresponding vibrational levels of the neutral molecule. The rate coefficients, on the other hand,

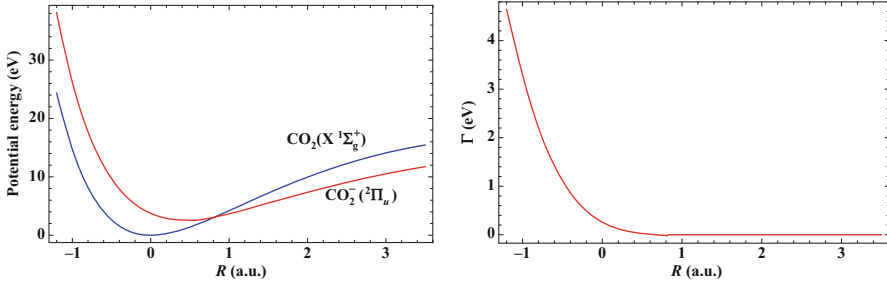


Fig. 1.16 Left panel: potential curves for the CO_2 ground and the CO_2^- resonant states. Right panel: the corresponding resonance width

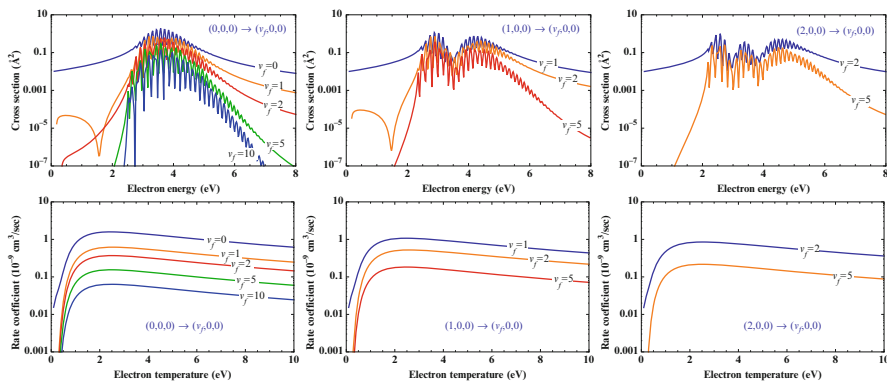


Fig. 1.17 Electron- CO_2 cross sections (upper panels) and the corresponding rate coefficients (lower panels), for the shown $(v_i, 0, 0) \rightarrow (v_f, 0, 0)$ transitions involving the symmetric stretching mode (Celiberto et al. 2014)

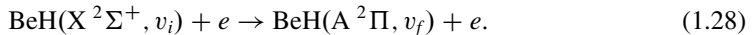
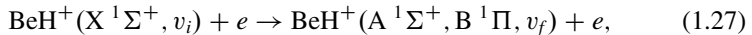
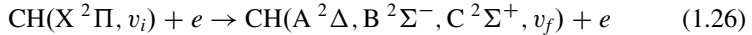
do not show any particular feature and follow the usual decreasing trend with the final vibrational level, typical of the diatomic molecules.

1.3 Electron-Molecule Collisions in Fusion Plasmas

The tokamak technology, developed in controlled nuclear fusion researches, is based on the magnetic confinement of hydrogen gas, brought at very high temperatures needed for the nuclear reactions to occur, so that a fully ionized plasma is created. In the outermost region, however, close to the reactor walls, where the temperature drops down from hundreds to few eV or less (edge and divertor regions), the plasma gets in direct contact with the wall-material. Recombination processes then start to take place and the formation of hydrogen molecules, as well as that of new compounds generated by the plasma-wall chemical reactions, may occur.

Beryllium and carbon graphite are among the first-wall materials used in current studies for the main chamber of the tokamak reactors and divertor plates respectively. The formation of beryllium hydrates and hydrocarbons is then expected, so that molecular and collisional data are required also for these species.

In this section we will review recent cross section and rate coefficient calculations for non-resonant, vibro-electronic excitations, induced by electron impact on vibrationally excited molecules, according to the processes (Celiberto et al. 2009a, 2012b, 2013a; Baluja and Msezane 2001; Chakrabarti and Tennyson 2012)



A brief discussion will finally be devoted to some dissociative electron attachment and resonant vibrational excitations, involving vibrationally excited hydrogen molecules and occurring through a Rydberg-excited resonant state.

1.3.1 CH, BeH⁺, and BeH Molecules

R-matrix cross sections for the processes (1.26) were reported by Baluja and Msezane (2001) in a range of energies from the threshold to 10 eV obtained in the fixed-nuclei approximation. In order to extend the cross section calculations to all the vibrational transitions and to a larger range of energies, the Born-Bethe (BB) approximation has been applied to the vibro-electronic transition of process (1.26) (Celiberto et al. 2009a). The BB cross section is given by:

$$\sigma_{v_i, v_f}^{\text{X,F}}(\epsilon_i) = \frac{2\pi}{3\epsilon_i} g \left| M_{v_i, v_f}^{\text{X,F}} \right|^2 \ln \left[\frac{4I_{v_i}\epsilon_i}{(\Delta E_{v_i, v_f}^{\text{X,F}})^2} \right] (a_0^2), \quad (1.29)$$

where a_0 is Bohr's radius. F stands for one of the excited electronic states involved in the vibronic transition $\text{X}(v_i) \rightarrow \text{F}(v_f)$, i.e. $\text{F} \equiv ^2\Delta, \text{B}^2\Sigma^-, \text{C}^2\Sigma^+$. ϵ_i is the incident electron energy, g is a state-multiplicity factor, I_{v_i} is the ionization potential counted from the level v_i and $\Delta E_{v_i, v_f}^{\text{X,F}}$ is the transition energy. The vibrational transition dipole moment matrix element is defined as $M_{v_i, v_f}^{\text{X,F}} = \langle v_f | D_{\text{X,F}}(R) | v_i \rangle$, where $D_{\text{X,F}}(R)$ is the transition dipole moment.

The cross section calculation needs, along the transition dipole moments, also the potential energy curve for each electronic state. These last quantities, available in literature van Dishoeck (1987), are required for the calculations of the vibrational wave functions and eigenvalues entering the definition of the matrix elements $M_{v_i, v_f}^{\text{X,F}}$ and transition energies $\Delta E_{v_i, v_f}^{\text{X,F}}$ respectively.

As is well known, the BB approximation is appropriate for high energies but diverges towards the threshold. In order to obtain reliable cross sections in all the

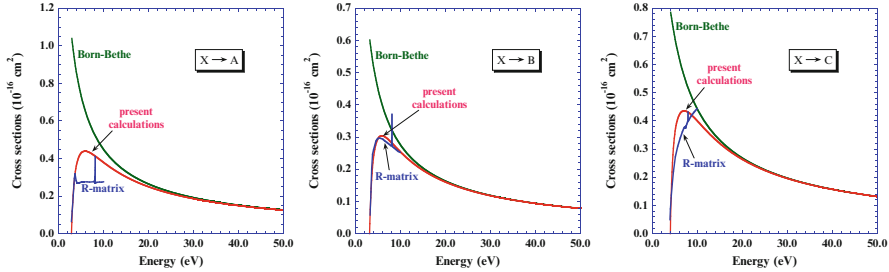


Fig. 1.18 Born-Bethe, *R*-matrix and interpolated cross sections for the transitions $X(0) \rightarrow A ^2\Delta(0)$, $X(0) \rightarrow B ^2\Sigma^-(0)$ and $X(0) \rightarrow C ^2\Sigma^+$, as indicated in the panels

required range of energies (from the threshold to 100 eV), an interpolation procedure has been adopted to link the BB cross sections, for the three electronic transitions $X(0) \rightarrow F(0)$ at high energies, with the available *R*-matrix cross section near the threshold (Celiberto et al. 2009a). The interpolating function is written as:

$$\sigma_{0,0}^{X,F}(x) = \left(1 - \frac{1}{x^a}\right) \left[\sigma_{0,0}^{X,F}(x)_{BB} + \frac{ba_0^2}{x^c} \right], \quad (1.30)$$

where $\sigma_{0,0}^{X,F}(x)_{BB}$ is the BB cross sections given by Eq. (1.29). x , the reduced energy, is defined as $x = \epsilon_i / \Delta E_{v_i, v_f}^{X,F}$ and a, b and c are fitting coefficients optimized in order to best-fit the *R*-matrix values (Celiberto et al. 2009a). Equation (1.30) reduces to the *R*-matrix cross sections for $\epsilon_i \rightarrow \Delta E_{v_i, v_f}^{X,F}$ and to the BB results for $\epsilon_i \rightarrow \infty$, as required. The resulting cross sections, for the $X(0) \rightarrow F(0)$ transitions are shown in Fig. 1.18.

In order to extend the cross sections to all the vibrational transitions, we may assume in Eq. (1.29) that $I_v \approx \Delta E_{v_i, v_f}^{X,F}$ (Mott and Massey 1965). This allows to express the ratio $\sigma_{v_i, v_f}^{X,F} / \sigma_{0,0}^{X,F}$ in terms of the corresponding ratios of transition energies and matrix elements $M_{v_i, v_f}^{X,F}$, which leads to the scaling expression

$$\sigma_{v_i, v_f}^{X,F}(x \cdot \Delta E_{v_i, v_f}^{X,F}) = \frac{\Delta E_{0,0}^{X,F}}{\Delta E_{v_i, v_f}^{X,F}} \left| \frac{M_{v_i, v_f}^{X,F}}{M_{0,0}^{X,F}} \right|^2 \sigma_{0,0}^{X,F}(x \cdot \Delta E_{0,0}^{X,F}). \quad (1.31)$$

Transition energies and matrix elements are reported in Celiberto et al. (2009a) and $\sigma_{0,0}^{X,F}$ is given by Eq. (1.30). It can be shown also, by using Eq. (1.31), that a similar scaling law holds for the Maxwellian rate coefficients, i.e.

$$\kappa_{v_i, v_f}^{X,F}(T) = \left(\frac{\Delta E_{0,0}^{X,F}}{\Delta E_{v_i, v_f}^{X,F}} \right)^{1/2} \left| \frac{M_{v_i, v_f}^{X,F}}{M_{0,0}^{X,F}} \right|^2 \kappa_{0,0}^{X,F} \left(T \cdot \frac{\Delta E_{0,0}^{X,F}}{\Delta E_{v_i, v_f}^{X,F}} \right). \quad (1.32)$$

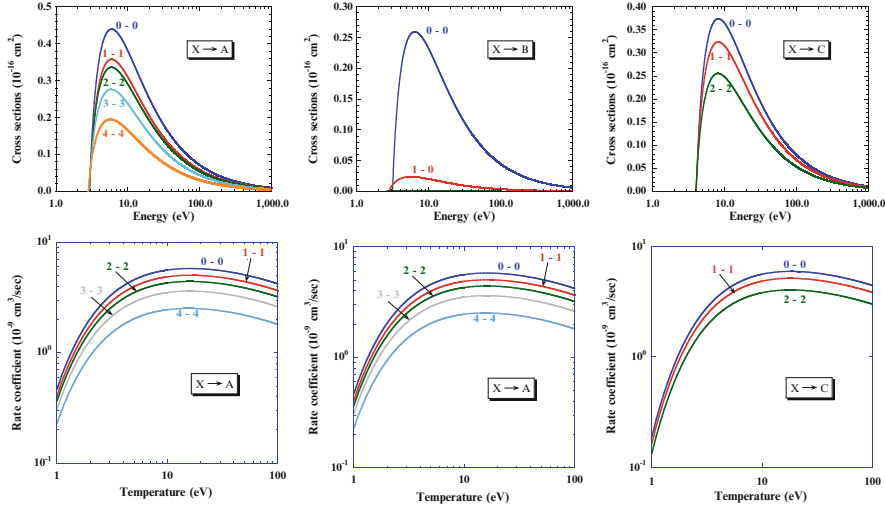


Fig. 1.19 Electron-CH cross sections (*upper panels*) and corresponding rate coefficients (*lower panels*) for the indicated transitions

Cross sections and rate coefficients, for some $X(v_i) \rightarrow F(v_f)$ transitions, are shown in Fig. 1.19.

Cross sections for process (1.27) were calculated by using the Coulomb-Born approximation (Chu and Dalgarno 1974) which, for vibro-electronic excitations, gives the expression (Celiberto et al. 2012b):

$$\sigma_{v_i, v_f}^{X, F}(\epsilon_i) = \frac{3g}{4\pi k_i^2} \left| M_{v_i, v_f}^{X, F} \right|^2 f_E(\eta_i, \zeta)(a_0^2), \quad (1.33)$$

where $\zeta = \eta_f - \eta_i$ and $\eta_{i,f} = k_{i,f}^{-1}$. $k_{i,f} = (2\epsilon_{i,f})^{1/2}(a_0^{-1})$ are the initial and final free electron momenta and $\epsilon_{i,f}$ its corresponding energies. Again $M_{v_i, v_f}^{X, F}$ are the vibrational transition dipole moment matrix elements defined in Eq. (1.29). The quantity $f_E(\eta_i, \zeta)$, expressed in terms of hypergeometric functions, is given elsewhere (Chu and Dalgarno 1974).

The transition dipole moments, as well as the potential curves for the $X^1\Sigma^+$, $A^1\Sigma^+$ and $B^1\Pi$ electronic states involved in process (1.27), necessary for vibrational wave function and eigenvalue calculations, were taken from Machado and Ornellas (1991).

Figure 1.20a-d shows the cross sections calculated by Eq. (1.33) for the electronic transitions $X \rightarrow A$ and $X \rightarrow B$ and for some v_i, v_f values (full-blue lines). The cross sections for the vibrational transitions with $v_i, v_f > 0$ were obtained by using again Eq. (1.31). The transition energies and matrix elements are provided in Celiberto et al. (2012b). The cross sections, for the $X(0) \rightarrow A(0)$ transition, required in Eq. (1.31), can be expressed by the following analytical formula,

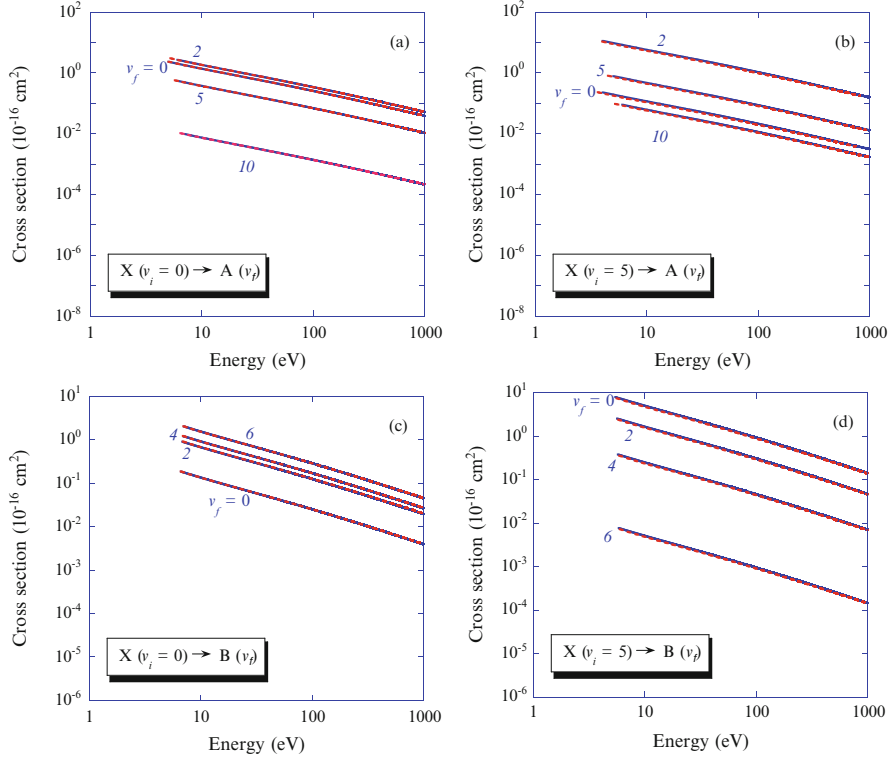


Fig. 1.20 Calculated (full-blue lines) and scaled (dashed-red lines) electron- BeH^+ cross sections for the transitions $\text{X}(v_i = 0, 5) \rightarrow \text{A}(v_f)$ (upper panels) and $\text{X}(v_i = 0, 5) \rightarrow \text{B}(v_f)$ (lower panels). The v_f values are shown in the figure for each curve

$$\sigma_{0,0}^{\text{X,A}}(x) = 1.1646 \frac{\ln(0.4181 + 2.3002x)}{0.87915x - 0.39751x^{0.1}} (10^{-16} \text{ cm}^2), \quad (1.34)$$

while the cross section for the $\text{X}(0) \rightarrow \text{B}(0)$ transition can be obtained by the simple proportionality relation

$$\sigma_{0,0}^{\text{X,B}}(x) = 0.07746 \sigma_{0,0}^{\text{X,A}}(x). \quad (1.35)$$

Once the $\sigma_{0,0}^{\text{X,A}}(x)$ is calculated, the cross sections for all the other vibro-electronic transitions can then be obtained by Eqs. (1.35) and (1.31). The accuracy of the analytical formulas can be appreciated in Fig. 1.20a-d, where the dashed-red curves, representing the fitted and scaled cross sections, almost overlap with the values calculated by the Coulomb-Born approximation.

The corresponding rate coefficients were calculated by using Eq. (1.32) with $\kappa_{0,0}^{\text{X,F}}(T)$ given by,

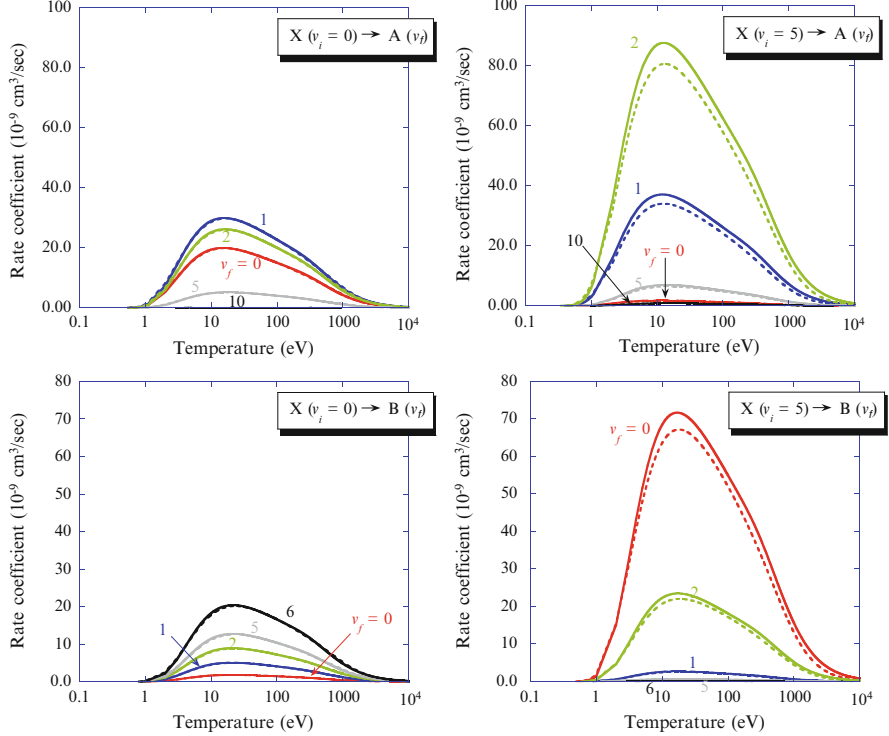


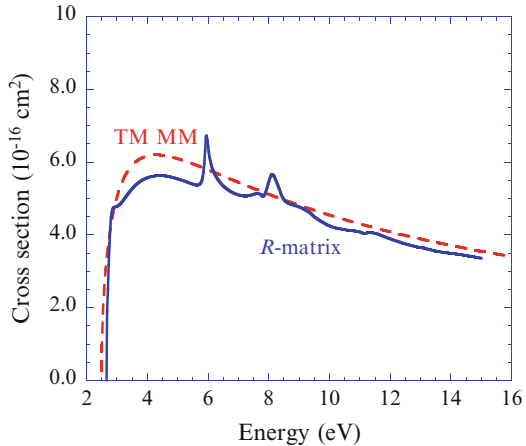
Fig. 1.21 Calculated (full lines) and scaled (dashed lines) electron- BeH^+ rate coefficients for the transitions $X(v_i = 0, 5) \rightarrow A(v_f)$ (upper panels) and $X(v_i = 0, 5) \rightarrow B(v_f)$ (lower panels). The v_f values are shown in the figure for each curve

$$\kappa_{0,0}^{\text{X,F}}(T) = c_1 \frac{e^{-c_2/T}}{1 + c_3 T^{c_4} + c_5 T^{c_6}} \left(10^{-9} \text{cm}^3 \text{s}^{-1}\right), \quad (1.36)$$

where the fitting coefficients, c_i , are given in Celiberto et al. (2012b) for both the transitions $X(0) \rightarrow A(0)$ and $X(0) \rightarrow B(0)$. The rates for some transitions are displayed in Fig. 1.21a-d. The figures show both the calculated rates and those obtained by Eq. (1.32). The scaling works quite well, being the largest discrepancy, at the maximum, not greater than 10 %.

The cross sections for process (1.28) have been calculated by using the R -matrix method in the fixed-nuclei approximation (Celiberto et al. 2013a) and for a range of energies from the threshold up to 16 eV. The internuclear distance was set at the equilibrium bond-length of 2.487 a.u. The calculations were then extended to high energies and to all the vibro-electronic excitations by using the Mott and Massey approximation (Mott and Massey 1965) modified in order to avoid threshold divergence. The explicit cross section formula is given by (Celiberto et al. 2013a):

Fig. 1.22 Comparison of the *R*-matrix (full-blue lines) and TMMM (dashed-red lines) cross section for the process $X^2\Sigma^+(v_i = 0) \rightarrow A^2\Pi(v_f = 0)$



$$\sigma_{v_i, v_f}(\epsilon_i) = \frac{4\pi}{3\epsilon_i} g |M_{v_i, v_f}|^2 \ln \frac{\sqrt{\Delta E_{v_i, v_f}}}{|\sqrt{\epsilon_i} - \sqrt{\epsilon_i - \Delta E_{v_i, v_f}}|} (a_0^2). \quad (1.37)$$

This expression, which vanishes at the threshold ($\epsilon_i \rightarrow \Delta E_{v_i, v_f}$), in the following will be referred to as the threshold-modified Mott and Massey (TMMM) cross section approximation.

Equation (1.37) requires the dipole transition moment matrix elements, $M_{v_i, v_f} = \langle v_f | D(R) | v_i \rangle$, and the transition energies for the electronic excitation $X^2\Sigma^+ \rightarrow A^2\Pi$ of process (1.28). These quantities can be calculated once the transition dipole moments $D(R)$ and the potential curves are provided. They were taken from the literature (Pitarch-Ruiz et al. 2008) and, in addition, the transition dipole moments were normalized in order to reproduce that obtained by the *R*-matrix method at the equilibrium bond-length (Celiberto et al. 2013a).

Figure 1.22 shows a comparison of the TMMM cross sections with the *R*-matrix results for the $X^2\Sigma^+(v_i = 0) \rightarrow A^2\Pi(v_f = 0)$ transition. We should stress preliminarily here, that while the TMMM approximation is applied to the $0 \rightarrow 0$ vibrational transition, the *R*-matrix calculations, performed in the fixed-nuclei approximation at the equilibrium bond-length, do not include the vibrational motion. However, we may assume that the nuclear motion, in the *R*-matrix results, is confined in the multiplicative Franck-Condon factors which, for the $v_i = v_f$ transitions, have all been found very close to the unity (Celiberto et al. 2013a). So that the comparison in Fig. 1.22 can be considered consistent.

The figure shows that the two calculations agree very well in the range of considered energies. This validates the TMMM method which can thus be extended confidently to high energies, where its accuracy is expected to increase. Figure 1.23 shows the cross sections and the corresponding rate coefficients for some vibrational transitions and for a range of energies from the threshold to 1,000 eV. In the same

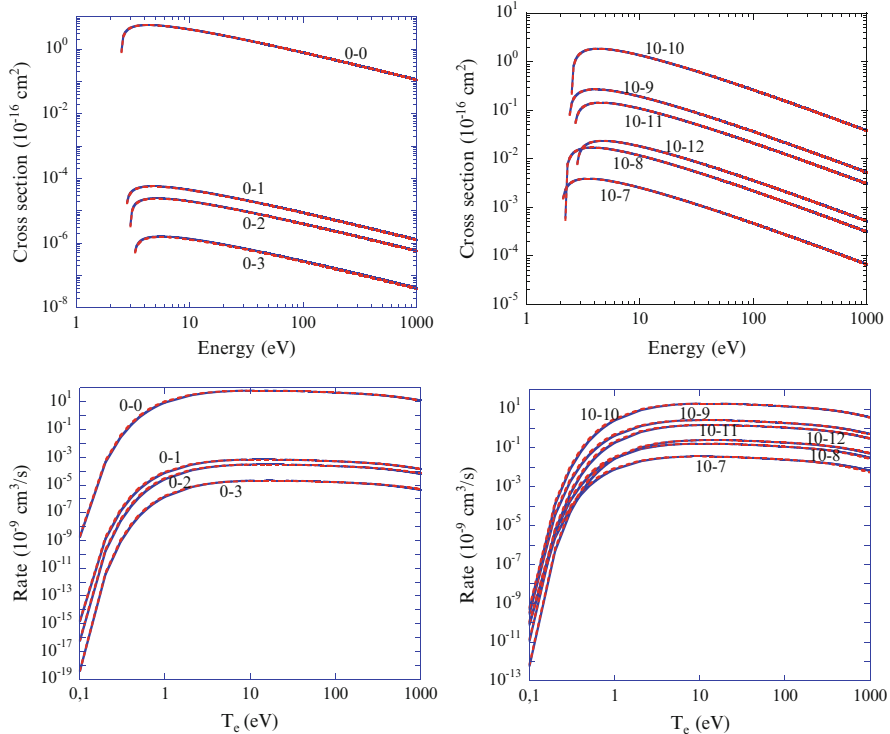
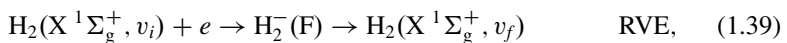
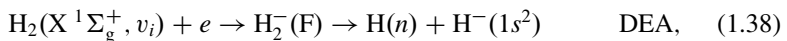


Fig. 1.23 Calculated (full-blue lines) and scaled (dashed-red lines) electron-BeH cross sections (upper panels) and the corresponding rate coefficients (lower panels) for the transitions $X(v_i = 0, 10) \rightarrow A(v_f)$ as indicated in the figure

figures are shown also cross sections and rates obtained by the analytical formulas of Eqs. (1.31)–(1.32).

1.3.2 Resonant Processes Involving H₂ Molecule

Dissociative electron attachment and resonant vibrational excitation in hydrogen molecule occur through the following processes:



where F denotes a resonant electronic state of the H_2^- molecular ion and n is the principal quantum number of the neutral hydrogen atom produced in the DEA process along with a negative ion in the $1s^2$ state.

DEA and RVE cross sections, involving the lowest H_2^- electronic state, $F = \text{X } ^2\Sigma_u^+$, have been calculated and measured since the early studies on resonant collisions and a vast literature is now available on the subject. This state, generated by the capture of the incident electron inside the centrifugal barrier formed by the $l = 1$ partial wave (*shape resonance*), beyond its purely theoretical interest in resonant scattering, plays, in fact, a role of great importance in fusion devices. In particular, both DEA and RVE occurring through this state are involved in the efficient production of H^- ions and in the recombination processes in negative ion sources, divertor and edge plasmas (Bacal 2012; Clark and Reiter 2005).

More limited calculations were performed also for the processes (1.38) and (1.39) occurring through the excited $F = \text{B } ^2\Sigma_g^+$ valence state (Wadehra 1979; Atems and Wadehra 1993).

More recently, the calculations were extended to the DEA and RVE processes proceeding through the Rydberg-excited $F = ^2\Sigma_g^+$ state (Celiberto et al. 2008, 2009b, 2012a, 2013b). The formation of this resonance, whose Rydberg nature appears clearly in the DEA process where an excited hydrogen atom ($n = 2$) is produced, occurs through the trapping of the incident electron inside the target molecule which, acquiring the collision energy, gets electronically excited (*Feshbach resonance*). Evidence of the formation of this Rydberg state was provided by experimental observations in both RVE and DEA cross section measurements (Comer and Read 1971; Rapp et al. 1965; Schulz 1959).

Extensive work on ab initio potential curves and widths, for a large spectrum of H_2^- resonances, including the excited $^2\Sigma_g^+$ state, has been done in literature Stibbe and Tennyson (1997a,b, 1998), and the availability of these information allowed for a first application of the LCP model to process (1.39) for the case $v_i = 0$ (Celiberto et al. 2008). Differential cross sections were obtained for the $0 \rightarrow v_f$ transitions, which were found in very good agreement with the available experimental measurements (Comer and Read 1971).

Comparison with the experimental data was also performed for the DEA process starting from $v_i = 0$ (Schulz 1959; Rapp et al. 1965), which however was made problematic by the discrepancy between the different measurements (Celiberto et al. 2009b).

The calculations were finally extended to the DEA process involving vibrationally excited H_2 molecules ($v_i > 0$) (Celiberto et al. 2012a). Figure 1.24a shows the cross sections for the dissociative attachment starting from some selected v_i values as a function of the incident electron energy, while Fig. 1.24b shows also the Maxwellian rates coefficients, as a function of the electron temperature, for the same process and for all 15 values of the vibrational quantum number.

RVE cross sections, as well as the rate coefficients, have also been calculated, by using the LCP approximation, for process (1.39) and for the vibrational transitions with $v_f \geq v_i$ (Celiberto et al. 2013b). The cross section for the reversed processes ($v_f < v_i$) can be obtained by the detailed balance (Celiberto et al. 2012b). An

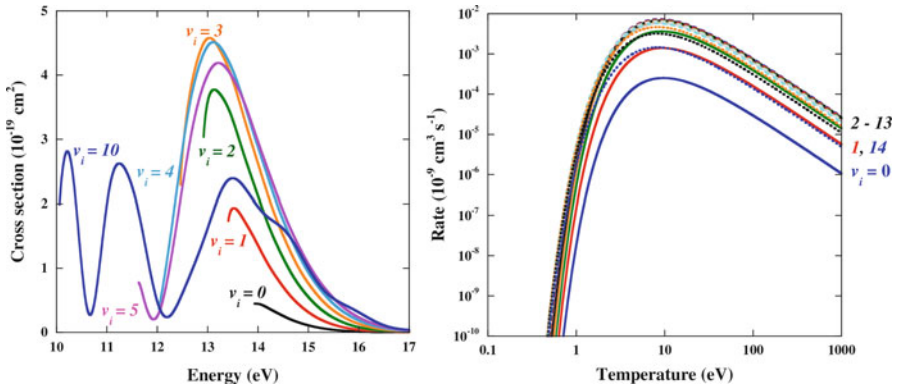


Fig. 1.24 Electron-H₂ DEA cross sections for process (1.38) with $v_i = 0, 1, 2, 3, 4, 5$ and 10 (a) and Maxwellian rate coefficients for the same process with v_i ranging from 0 through 14 (b)

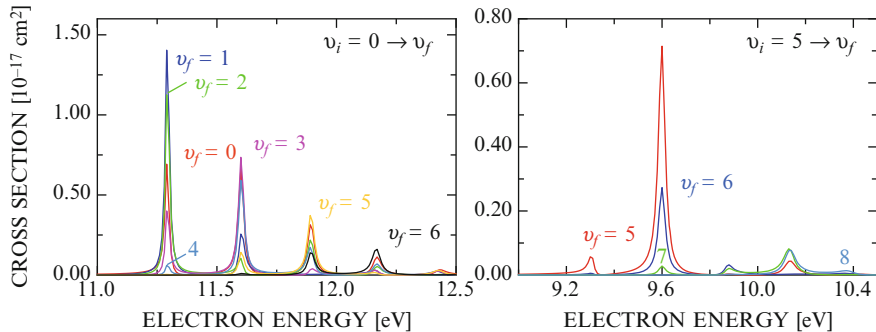


Fig. 1.25 Electron-H₂ RVE cross sections for the transitions $0 \rightarrow v_f$ (left panel) and $5 \rightarrow v_f$ (right panel) with $v_f = 0 - 14$. Each curve is labeled by the value of v_f

example of RVE cross sections for the $v_i = 0, 5 \rightarrow v_f$ excitations is shown in Fig. 1.25. The sharp nature of the cross section peaks, placed at the vibrational energy eigenvalues of the H₂⁻(²S_g⁺) Rydberg state, confirm the long-lived Feshbach nature of the resonance.

Figure 1.26 shows the rate coefficients for the transitions $v_i = 0, 1, 5, 12 \rightarrow v_f = 0 - 14$ (full-blue lines). All the shown curves exhibit the same behavior as a function of the temperatures, being the difference of quantitative nature only. These curves can be reproduced by a fitting function of the form

$$\kappa_{v_i, v_f}(\Delta E_p^L \tau) = \kappa_{v_i, v_f}^{\text{Max}} \left(\frac{1}{\tau} \right)^{3/2} e^{-\frac{1}{\tau}}, \quad (1.40)$$

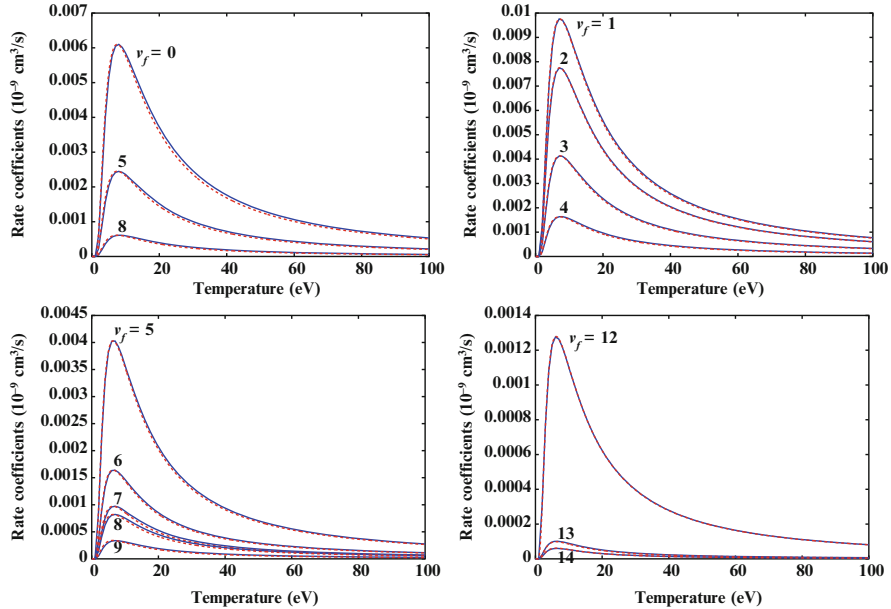


Fig. 1.26 Electron-H₂ RVE rate coefficients (full-blue lines) for the transitions $v_i = 0, 1, 5, 12 \rightarrow v_f$ where the values of $v_f (\geq v_i)$ are indicated in the panels. The figure shows also the fitted rates for the same transitions (dashed-red lines)

where ΔE_p^L gives the position of the vibrational eigenvalues with respect to the v_i -th vibrational level and the reduced temperature, τ , is defined by $\tau = T/\Delta E_p^L$. $\kappa_{v_i, v_f}^{\text{Max}}$ is the rate maximum. Both the numerical values of the two parameters, ΔE_p^L and $\kappa_{v_i, v_f}^{\text{Max}}$, are provided in Celiberto et al. (2013b). Equation (1.40) has been derived by assuming, in the analytical formula for the Maxwellian rate coefficients, a δ -function form for the cross sections, justified by the sharp and well separated peaks observed in their graphical representation (see Celiberto et al. 2013b for details). The above fitting expression proved to be very accurate. This can be clearly seen in Fig. 1.26 where, along with the calculated rates, are shown also the corresponding fits (dashed-red curves).

References

- Allan M (1985) Excitation of vibrational levels up to $v=17$ in N₂ by electron impact in the 0–5 eV region. J Phys B At Mol Opt Phys 18(22):4511
 Allan M (1995) Measurement of absolute differential cross sections for vibrational excitation of O₂ by electron impact. J Phys B At Mol Opt Phys 28(23):5163
 Allan M (2005) Electron collisions with NO: elastic scattering, vibrational excitation and ${}^2\Pi_{1/2} \rightarrow {}^2\Pi_{3/2}$ transitions. J Phys B At Mol Opt Phys 38(5):603

- Allan M (2010) Electron collisions with CO: elastic and vibrational excitation cross sections. *Phys Rev A* 81:042706
- Atems DE, Wadehra JM (1993) Resonant contributions to dissociation of H₂ by low-energy electron impact. *J Phys B At Mol Opt Phys* 26(21):L759
- Bacal M (2012) Negative hydrogen ion production in fusion dedicated ion sources. *Chem Phys* 398:3
- Baluja KL, Msezane AZ (2001) Electron collisions with methylidyne (CH) radical using the R-matrix method. *J Phys B At Mol Opt Phys* 34:3157
- Bardsley JN, Mandl F (1968) Resonant scattering of electrons by molecules. *Rep Prog Phys* 31(2):471
- Cádez I, Gresteau F, Tronc M, Hall RI (1977) Resonant electron impact excitation of CO₂ in the 4 eV region. *J Phys B At Mol Phys* 10(18):3821
- Capitelli M, Cacciato M, Celiberto R, De Pascale O, Diomede P, Esposito F, Gicquel A, Gorse C, Hassouni K, Laricchiuta A, Longo S, Pagano D, Rutigliano M (2006) Vibrational kinetics, electron dynamics and elementary processes in H₂ and D₂ plasmas for negative ion production: modelling aspects. *Nucl Fusion* 46(6):S260–S274
- Capitelli M, Celiberto R, Esposito F, Laricchiuta A (2009) Molecular dynamics for state-to-state kinetics of non-equilibrium molecular plasmas: state of art and perspectives. *Plasma Process Polym* 6(5):279–294
- Capitelli M, Celiberto R, Colonna G, D'Ammando G, De Pascale O, Diomede P, Esposito F, Gorse C, Laricchiuta A, Longo S, Pietanza LD, Taccogna F (2011) Plasma kinetics in molecular plasmas and modeling of reentry plasmas. *Plasma Phys Control Fusion* 53(12):124007
- Cederbaum LS, Domicke W (1981) Local against non-local complex potential in resonant electron-molecule scattering. *J Phys B At Mol Phys* 14:4665–4689
- Celiberto R, Janev RK, Wadehra JM, Laricchiuta A (2008) Cross sections for 11–14-eV *e*-H₂ resonant collisions: vibrational excitation. *Phys Rev A* 77(1):012714
- Celiberto R, Janev RK, Reiter D (2009a) Basic molecular processes for hydrocarbon spectroscopy in fusion edge plasmas: vibrationally state-selective excitation of A ²Δ, B ²Σ[−] and C ²Σ⁺ states of CH by electron impact. *Plasma Phys Control Fusion* 51:085012
- Celiberto R, Janev RK, Wadehra JM, Laricchiuta A (2009b) Cross sections for 14-eV *e*-H₂ resonant collisions: dissociative electron attachment. *Phys Rev A* 80:012712
- Celiberto R, Janev R, Wadehra J, Tennyson J (2012a) Dissociative electron attachment to vibrationally excited H₂ molecules involving the resonant rydberg electronic state. *Chem Phys* 398(0):206–213
- Celiberto R, Janev RK, Reiter D (2012b) State-to-state electron impact cross sections for BeH⁺ molecular ions in ITER-like fusion edge plasmas with Be walls. *Plasma Phys Control Fusion* 54:035012
- Celiberto R, Baluja KL, Janev RK (2013a) Electron-impact state-to-state resolved cross sections and rate coefficients for the X(v) → A(v') excitation in BeH molecules. *Plasma Sources Sci Technol* 22:015008
- Celiberto R, Janev JK, Laporta V, Tennyson J, Wadehra JM (2013b) Electron-impact vibrational excitation of vibrationally excited H₂ molecules involving the resonant ²Σ_g⁺ Rydberg-excited electronic state. *Phys Rev A* 88(6):062701
- Celiberto R, Laporta V, Laricchiuta A, Wadehra J, Tennyson J (2014) Molecular physics of elementary processes relevant to hypersonics: electron-molecule collisions. *Open Plasma Phys J* 7(Suppl 1: M1):33–47
- Chakrabarti K, Tennyson J (2012) Electron collisions with the BeH⁺ molecular ion in the R-matrix approach. *Eur Phys J D* 66(1):31
- Chu SI, Dalgarno A (1974) Rotational excitation of CH⁺ by electron impact. *Phys Rev A* 10:788
- Clark REH, Reiter D (eds) (2005) Nuclear fusion research: understanding plasma-surface interactions. Springer Series in Chemical Physics, vol 78. Springer, Heidelberg
- Comer J, Read FH (1971) Potential curves and symmetries of some resonant states of H₂[−]. *J Phys B* 4:368

- Dubé L, Herzenberg A (1979) Absolute cross sections from the “boomerang model” for resonant electron-molecule scattering. *Phys Rev A* 20(1):194–213
- Gilmore FR (1965) Potential energy curves for N₂, NO, O₂ and corresponding ions. *J Quant Spectrosc Radiat Transf* 5(2):369–389. IN1-IN3
- Huo WM, McCoy V, Lima MAP, Gibson TL (1986) Electron-nitrogen molecule collisions in high temperature nonequilibrium air. In: Moss JN, Scott CD (eds) Thermochemical aspects of re-entry flows. Progress in astronautics and aeronautics, vol 103. AIAA, New York, pp 152–196
- Huo WM, Gibson TL, Lima MAP, McKoy V (1987) Schwinger multichannel study of the $^2\Pi_g$ shape resonance in N₂. *Phys Rev A* 36(4):1632–1641
- Laporta V, Cassidy CM, Tennyson J, Celiberto R (2012a) Electron-impact resonant vibration excitation cross sections and rate coefficients for carbon monoxide. *Plasma Sources Sci Technol* 21(4):045005
- Laporta V, Celiberto R, Wadehra JM (2012b) Theoretical vibrational-excitation cross sections and rate coefficients for electron-impact resonant collisions involving rovibrationally excited N₂ and NO molecules. *Plasma Sources Sci Technol* 21(5):055018
- Laporta V, Celiberto R, Tennyson J (2013) Resonant vibrational-excitation cross sections and rate constants for low-energy electron scattering by molecular oxygen. *Plasma Sources Sci Technol* 22(2):025001
- Laporta V, Little DA, Celiberto R, Tennyson J (2014) Electron-impact resonant vibrational excitation and dissociation processes involving vibrationally excited N₂ molecules. *Plasma Sources Sci Technol* 23(6):065002
- Laporta V, Celiberto R, Tennyson J (2015) Dissociative electron attachment and electron-impact resonant dissociation of vibrationally excited O₂ molecules. *Phys Rev A* 91:012701
- Le Roy RJ, Huang Y, Jary C (2006) An accurate analytic potential function for ground-state N₂ from a direct-potential-fit analysis of spectroscopic data. *J Chem Phys* 125(16):164310
- Machado FBC, Ornellas R (1991) A theoretical investigation of the low-lying electronic states of the molecule BeH⁺. *J Chem Phys* 94:7237
- Morgan LA (1991) Low-energy electron scattering by CO. *J Phys B At Mol Opt Phys* 24(21):4649
- Mott NF, Massey HSW (1965) The theory of atomic collisions. Oxford University Press, Oxford
- Noble CJ, Higgins K, Wöste G, Duddy P, Burke PG, Teubner PJO, Middleton AG, Brunger MJ (1996) Resonant mechanisms in the vibrational excitation of ground state O₂. *Phys Rev Lett* 76(19):3534–3537
- Pitarch-Ruiz J, Sanchez-Marin J, Velasco AM, Martin I (2008) Full configuration interaction calculation of BeH adiabatic states. *J Chem Phys* 129:054310
- Rapp D, Sharp E, Briglia DD (1965) Large isotope effect in the formation of H⁻ od D⁻ by electron impact on H₂, HD, and D₂. *Phys Rev Lett* 14:533
- Rescigno TN, Isaacs WA, Orel AE, Meyer HD, McCurdy CW (2002) Theoretical study of resonant vibrational excitation of CO₂ by electron impact. *Phys Rev A* 65:032716
- Schneider BI, Le Dourneuf M, Lan VK (1979) Resonant vibrational excitation of N₂ by low-energy electrons: an ab initio R-matrix calculation. *Phys Rev Lett* 43(26):1926–1929
- Schulz GJ (1959) Formation of H⁻ ions by electron impact on H₂. *Phys Rev* 113:816
- Stibbe DT, Tennyson J (1997a) Ab initio calculations of vibrationally resolved resonances in electron collisions with H₂, HD, and D₂. *Phys Rev Lett* 79:4116
- Stibbe DT, Tennyson J (1997b) Parent state swapping of resonances in electron-hydrogen molecule scattering. *J Phys B At Mol Opt Phys* 30:L301–L307
- Stibbe DT, Tennyson J (1998) Electron-H₂ scattering resonances as a function of bond length. *J Phys B At Mol Opt Phys* 31:815–844
- Trevisan CS, Houfek K, Zhang Z, Orel AE, McCurdy CW, Rescigno TN (2005) Nonlocal model of dissociative electron attachment and vibrational excitation of NO. *Phys Rev A* 71(5):052714
- van Dishoeck EF (1987) Photodissociation processes in the CH molecule. *J Chem Phys* 86:196
- Wadehra JM (1979) Rates of dissociative attachment of electrons to excited H₂ and D₂. *Appl Phys Lett* 35:917

- Wadehra JM (1986) Vibrational excitation and dissociative attachment. In: Capitelli M (ed) Non-equilibrium vibrational kinetics. Topics in Current Physics, vol 39. Springer, Heidelberg, pp 191–232
- Werner HJ, Knowles PJ, Knizia G, Manby FR, Schütz M et al (2010) Molpro, version 2010.1, a package of ab initio programs
- Wong SF, Boness MJW, Schulz GJ (1973) Vibrational excitation of O₂ by electron impact above 4 eV. Phys Rev Lett 31(16):969–972

Chapter 2

Reactivity and Relaxation of vibrationally/rotationally excited molecules with open shell atoms

Vibrational kinetics is built around detailed data of molecular collisions. One of the most important processes determining vibrational non-equilibrium is the collision of open shell atoms with molecules. In this case, in addition to non-reactive outcome and dissociation, also the reactive channel should be considered, because it can significantly contribute to vibrational non-equilibrium. Historically, state-to-state kinetics has been used long before reliable state-to-state data were available. To this aim, simple models of *non-reactive* rate coefficients have been used for long times, often neglecting the reactive process as well as the dissociation, or using further approximations (Capitelli 1986). These models are essentially based on atom induced small perturbations on *harmonic* oscillators. Of course, this kind of results are limited to low-lying vibrational states, and under the hypothesis of negligible reactive processes. As a matter of fact, comparisons with more accurate data show the unsatisfactory performance of these methods, in particular for atom-molecule collisions, also by orders of magnitude. Accurate quantum mechanical methods are available (Skouteris et al. 2000; Launay 1991; Gray and Balint-Kurti 1998), but their requirements of computational resources are really huge, and they are not free from important drawbacks concerning dissociation (Skouteris et al. 2000; Launay 1991) and low-energy regime (Gray and Balint-Kurti 1998). This is the motivation for using the quasiclassical trajectory method (QCT), which represents a good compromise between reliability of results and feasibility of calculations, and is the most used method for large scale cross section calculations.

2.1 Computational Method

The quasiclassical trajectory method dates back to 1965, with the publication of the paper on H+H₂ reaction cross sections by Karplus et al. (1965), using a simple LEPS PES for this system. The method has been refined by many other

authors, and some reviews can be found for example in Porter and Raff (1976) and Pattengill (1979). Here only a brief outline will be presented, with particular emphasis on some practical details of relevance in order to obtain reliable and also affordable results, considering the large amounts of data required in the context of kinetic studies. In QCT method, nuclear dynamics is completely classical on the adiabatic potential energy surface of the scattering problem. The underneath hypothesis is the smallness of the De Broglie length in comparison with the typical dimensions of the problem. However, it is clear from the large amount of comparisons in literature that this criterion alone is not very useful to discriminate reliable results from very approximate ones. It is often the case that averaged quantities, such as cross sections and rate coefficients, are in quite good agreement with accurate theoretical and experimental results, despite significant discrepancies of very detailed results (such as transition probabilities in collinear case or with zero total angular momentum). Of course, QCT is not the method of choice for low total energies, but it can be extremely useful to continue low energy results obtained with accurate methods, considering that these methods require a huge computational effort, rapidly growing as the total energy increases, the reverse being true for quasiclassical trajectories. Characterization of molecular reagents and products is of course a central point in QCT. Concerning the first ones, the common way of performing quasiclassical dynamics is to prepare reagents by pseudoquantizing the initial molecule, in order to obtain a vibrating and rotating classical body whose rovibrational actions can be put in direct relation with the corresponding quantal values by simple pseudoquantization rules (Langer 1937):

$$j_1^{cl} = \sqrt{\ell(\ell + 1)\hbar^2} \quad (2.1)$$

or

$$j_2^{cl} = (\ell + \frac{1}{2})\hbar \quad (2.2)$$

and

$$v^{cl} = \oint p \, dq = (v + \frac{1}{2})h \quad (2.3)$$

The meaning of these relations is linked to the principle of correspondence, so they can be considered exact in the limit of high quantum numbers (this is the reason for coexistence in literature of two possible angular momentum quantization rules: their values at high rotational quantum numbers tend to be the same). A much more accurate analysis of the correspondences between quantal and classical motion can be found in Miller (1970), where the basis is the classical approximation to the Feynmann path integral. In QCT the operation to perform for reagents is to impose a molecular angular momentum given by Eq. (2.1) or (2.2), and then to prepare the molecule in order to have a classical action given by Eq. (2.3). This is done generally

by pre-computing the whole set of useful quantities for rovibrational states for the given molecule in the proper diatomic asymptote of the PES. This last operation, in turn, can be made by recursively finding the classical inversion points for an initial guess of internal energy, and then calculating the action integral (2.3) and comparing with the searched integer value (the quantized value to be simulated). A trial and error procedure brings the calculus towards the solution with the desired level of approximation. At that point, a complete table of classical inversion points is available for each pseudoquantized couple of rovibrational quantum numbers, therefore the classical motion can always start from one of these two points and a very simple dynamics can be performed for a fraction of the vibrational period, in order to set up the initial vibrational phase. Other operations to complete the preparation of the initial molecule are the setting up of the rotational phase and initial orientation of rotational axis, as well as the impact parameter of the atomic projectile, that is the distance of the initial atom velocity from the parallel line passing through the center of mass of the diatom. The impact parameter can be pseudoquantized or not (more frequently), in the first case it can be obtained by pseudoquantizing the orbital angular momentum. No quantum counterpart exists of rotational and vibrational phase, as well as the precession angle around angular momentum. They are undetermined, being their conjugated momenta quantized, i.e. known without uncertainty. Quasiclassically these coordinates are uniformly distributed, using a vector of independent random variables (the statistics associated to QCT rises from distributions of these random input parameters). Concerning products, an analysis of final properties is needed, because of course no quantization is found after a purely classical dynamics. Therefore a method for pseudoquantizing the final (possible) molecular outcome of the collision is required. Here the problem is more subtle and complex, because a continuous distribution of final rovibrational actions obtained from QCT have to be put in some relation with a discrete quantal distribution. The easiest (and by far the most used) way to treat the problem is to find the nearest integers in final angular momentum and vibrational action, by simply inverting Eqs. (2.1)–(2.3) (histogram binning). The correspondence with quantal motion can be not very accurate, in particular for the first rovibrational levels (in accord with the correspondence principle). The theoretical justification of this procedure is in Miller (1971), where it is possible to recognize that the procedure consists in averaging final actions instead of taking only the exact quantized values (whose calculation would be statistically impossible). In that paper it is possible also to understand the level of approximation of the histogram binning, due to both the action averaging as well as lack of amplitude superposition (this is substituted by superposition of probabilities). Concerning the first issue, the gaussian binning can really improve the quasiclassical result, as explained in Bonnet and Rayez (2004) and Bonnet (2008). It is directly derived from the purely classical probability of Miller, with the substitution of the Dirac delta with a gaussian of suited width (Bonnet 2008). Its application is extremely simple at the trajectory analysis stage, with the only drawback of some increase of statistical noise due to the very low importance attributed to trajectories too far from exact quantized values. Concerning the lack of trajectory interference, on the contrary, the problem

is much more complex, because the classical probability should be replaced by more sophisticated formulations (primitive, or uniform, or initial value representation semiclassical approximations Miller 2001). However, the examples of application of these semiclassical methods in literature are really scarce, and never for systematic calculations of cross sections, as those ones needed in kinetic models. This kind of calculations could be very effective in the ranges of low energy where QCT does not give accurate results for state-to-state cross sections. A very accurate QM calculation is offered by two quite popular codes, ABC (Skouteris et al. 2000) and the code of (Launay 1991). They are both time independent, require a huge amount of computational resources, and are currently limited by total energies below dissociation limit. As a consequence they are insufficient to perform complete calculations for kinetic models, but they are extremely important for assessing lower limits of total energy for the reliability of calculations performed by QCT method. Once the quasiclassical results connect smoothly to exact QM calculations in a restricted range of relatively low energies, it is very likely they will be reliable for higher energies, where the classical approximations get better and better and exact QM calculations become more demanding. In the following paragraphs, some relevant aspects of calculation of cross sections for atom-molecule collisions will be illustrated by using real systems of large theoretical as well as technological interest.

2.2 H+H₂

This is one of the most studied systems, for its relative simplicity and the availability of experimental results, since the 1960 of the past century. Actually, an accurate PES has been obtained for this system only in 1978 (LSTH Truhlar and Horowitz 1978). Important papers have been devoted to presentation of new methods for molecular dynamics tested on this system (Karplus et al. 1965; Schatz and Kuppermann 1976b,a; Althorpe 2001; Hankel et al. 2006). As a consequence, some sparse very accurate results have been obtained, even recently, on new PESs, considering higher order effects (Mielke et al. 2002). When dealing with application of molecular dynamics results to kinetic models, where complete sets of cross sections or rate coefficients are needed, it is practically impossible to apply an accurate method for the entire range of total energy needed (typically from room temperature to many tenths of thousands of Kelvin). In fact, complete sets of cross sections have been obtained only using approximations. Essentially three sets have been obtained by QCT method by Martin and Mandy (1993) on the cited LSTH PES, by Kim et al. (2009) on BKMP2, and by Esposito et al. (1999) and Esposito and Capitelli (2001, 2005) on both surfaces. Approximated quantal methods have been applied to this collisional system spanning the whole vibrational ladder (Krštić and Schultz 1999b). It is important to underline, however, that the use of an *approximated* quantal method *does not guarantee better accuracy* than methods based on classical mechanics. It strongly depends on the level of approximation used in the methods adopted, the range of collisional energy explored in calculations, the (light or heavy)

collisional system, the level of detail that is needed in final results. Dealing with (ro)vibrationally detailed cross sections for atom-molecule collisions to be used in kinetic models, these issues are all present, because the energy range is very large (from 1 meV to 10 eV or more), the whole detailed (ro)vibrational ladder is preferably required, and the systems considered can have very different masses. As an example, the largely used infinite order sudden approximation (Krstić and Schultz 1999a) consists of calculating transition probability for collisions neglecting rotation, both for reagents and products. If it is possible to study kinetic conditions which do not require initial excited rotational states (they are anyway a subset of those ones of interest), it is quite problematic to neglect final rotation in products, because it is the dynamics that should assess its irrelevance, given the initial conditions. In a vibrational transition it could be possible (as it often happens) that final rotation is significant, even if initial rotation does not. Rotation is also extremely important in dissociation and recombination processes, as can be seen in Esposito and Capitelli (2009). Generally speaking, the best strategy would be surely to merge results obtained from different methods in different and partially overlapping ranges of parameters, checking for smooth continuity of data and reasonable accord with available experimental results. This is a challenging task requiring experience in quite different methods for molecular dynamics and a huge availability of computational resources. As an example of application of successful accurate quasiclassical calculations to this light system the reader is referred to Esposito and Capitelli (2009), where collisional three-body recombination is studied by means of two mechanisms, including state-to-state processes. It appears that the final result is quite appreciable, with reliable results with good comparisons with the available data of experimental and theoretical origin. Actually a successful application of QCT needs high accuracy in its implementation when a complete state-to-state database of cross section or rate coefficients is required. In this case, it is not possible to tune the computational parameters of the simulation for a specific process. As a consequence, for some low probability processes it is possible to find a completely misleading result on the base of very few useful trajectories badly calculated. To avoid this effect, it is important to check each trajectory with a systematic method. In Esposito and Capitelli (2002) the choice is simply the reintegration of each trajectory step with a smaller time step, for example one half of the starting value. If the check is positive, a new time step is generated, otherwise only the lower time step result is retained and compared with a new more accurate integration, and so on. Even if this can appear a very expensive method, it allows a fine tuning of the time step along each integration, which has the result of statistically decreasing significantly the total computational time, and avoids integration of unuseful wrong and very long trajectories when the potential has a deep well, as in case of O+O₂ collisions (Esposito and Capitelli 2002). The present collisional system is of interest in many fields of technological application, in particular considering the lightest isotopes of hydrogen. However, it is much easier to obtain detailed experimental data about non-symmetrical isotopes, as in H+D₂ or D+H₂. As a consequence, the majority of comparisons between computational and experimental results are with that kind of isotopic combinations. Detailed data

for identical isotopes, on the contrary, should be taken from computational results, being their reliability assessed indirectly by means of experimental and theoretical data comparison with other isotope combinations. This is not the right place to digress about the overwhelming literature about these comparisons, the reader is referred to Aoiz et al. (2005) for a wide survey on the topic. The main findings that can be extracted from these comparisons concern the following points:

1. Reliability of the most recent PESs about this system, BKMP2 (Boothroyd et al. 1996) and CC (Mielke et al. 2002). They are very accurate (indeed they are the most accurate PESs ever calculated), and the last one (CC) has negligible differences with the older BKMP2, on which the majority of results has been calculated. This reliability comes from comparisons with many experiments. The famous significant discrepancy of the exothermal reactive rate $v = 1 \rightarrow 0$ (Mayne and Toennies 1981) between theory and experiment is now solved in favor of theoretical results, being the experiment with the excited vibrational state not completely reliable (Götting et al. 1987).
2. Accurate and quasiclassical methods have been applied, and in general the comparisons are quite good for averaged quantities, as initially guessed by Miller (1970) on the basis of his semiclassical theory. Following his explanation, it is clear the effect of neglecting the superposition of amplitudes. In fact, while the probability is “conserved” throughout the distribution in different final rovibrational channels, it is distributed with a sort of unpredictable randomness, due to lack of superposition of each trajectory contribution with the correct phase (which is completely lacking in a quasiclassical calculation).
3. This quasiclassical drawback must anyway obey the correspondence principle: in fact, when higher states are considered, faster oscillations tend to cancel with higher probability in the superposition, and as a consequence QCT results tend to be more accurate.
4. Also the dynamics can influence the importance of lack of correct superposition in QCT. In fact, it is known (Aoiz et al. 2005) that non-reactive results tend to be less accurate than reactive ones when compared with “exact” QM data. Even in this case it is possible to rationalize the effect: a significative part of non-reactive trajectories can come from a recrossing of reactive barrier. As a consequence, there can be a systematic superposition of two sets of trajectories with two quite different paths in the unreactive case, with important phase effects, of course absent for reactive trajectories.
5. Another independent source of errors in QCT is the presence of classically forbidden transitions. When the vibrational phase of reactant molecule is uniformly varied in its whole range, as is normal in a QCT calculation by means of the appropriate random numbers, the final products reach a range of possible values of final vibrational action, that is unquantized vibrational number times \hbar . The range of this vibrational outcome can be smaller than the possible vibrational range of products, therefore there can be some final values of vibrational quantum number never reached by the classical collision at the specified collisional energy: the transition is said “classically forbidden”. This has nothing to do

with energy forbidden transitions, in fact a well known case is found for He+H₂ non-reactive collisions in the exothermal direction (Balakrishnan et al. 1999). In that case, for collisional energies lower than about 1.0 eV the rovibrational cross section drops, contrarily to the accurate quantum mechanical result. Classically forbidden rovibrational transitions are naturally present at a certain low energy value for every collisional system, but a general method to know the lower limit of applicability of classical calculations is not available.

These observations are mainly obtained with calculations and comparisons about H+H₂ collisions, because of the availability of many data about it. However, it is the lightest atom-molecule collisional system, therefore quasiclassical calculations are expected to perform also better on heavier systems.

2.2.1 Isotopes and Scaling Relations

For the very light H+H₂ collisional system the isotope effect can be particularly important. In addition, a real interest into heavier isotopes is due to their applications in nuclear fusion technological development. As a consequence scaling relations to obtain rate coefficients for a different set of isotopes have been developed (Krštić and Schultz 1999b). Concerning quasiclassical calculations and simultaneous change of the three atomic masses by the same factor, there is the possibility of obtaining an exact (in the quasiclassical sense) scaling relation, by scaling the time of the simulation proportionally to the square root of the mass ratio, as considered in Capitelli et al. (2007). This can be applied at the level of trajectories (more accurately), or at the level of cross sections. The reader is referred to the literature for the details of the procedure (Capitelli et al. 2007).

2.3 N+N₂

This is one of the most important collision processes in atmospheric kinetics, with technological applications in the field of entry into planetary atmospheres. It has been studied initially only from a non-reactive point of view (i.e., without atom exchange between the projectile and the initial molecule, but only rovibrational energy exchange), because of the application of approximated schemes of calculation (SSH, FHO) (Schwartz et al. 1952; Husimi 1953; Kerner 1958; Treanor 1965). Actually, the reactive part is of large importance, as can be shown, and must be summed to the non-reactive part in order to obtain reliable results for rovibrational energy transfer processes, also at moderate temperatures. The first reliable PES for this collisional system was the semiempirical LEPS (London-Eyring-Polanyi-Sato) PES by Laganà and Garcia (1994). Many calculations have been done on that PES, with fairly good comparisons with the few experimental

results available. In particular, the same authors provided the first calculations on their PES (Laganà and Garcia 1994; Laganà et al. 1997). Extensive calculations of state-to-state cross sections for vibrational energy exchange and dissociation have been performed, including the whole ladder of rovibrational states in an approximate way (Esposito and Capitelli 1999, 2006; Esposito et al. 2006). Actually, the results of those calculations represent one of the most extensive databases on that system from low (1 meV) to intermediate (10 eV) collisional energy. The limits of this database are the following:

1. The lower energy limit, determined by the problems of quasiclassical method already stressed, as well as the inaccuracy of the large range interaction in the PES calculation, which becomes important at low energies. On the contrary, tunneling problems are probably of negligible importance (Caridade et al. 2010).
2. The upper limit, determined by problems of possible interaction with excited electronic states, which implies the use of a non-adiabatic method for dynamics, and the consequent requirement of larger computational resources. Recently new excited PESs have been proposed in literature (Galvão et al. 2012), of large interest for possible applications. From preliminary calculations in Galvão et al. (2012), it appears that this upper limit could be negligible, at least for energy ranges of some eVs.
3. The huge number of states of the molecule (about 10,000) imposes an approximation strategy. In Esposito and Capitelli (1999) this strategy was based on calculating dynamics starting from a limited number of rotational initial states, including the whole ladder of initial vibrational states. All the possible final states energetically accessible are in principle reached by trajectories, but to have a sufficient statistics for reliable results it is necessary to sum on final rotational states. This strategy allows one to have the whole vibrational ladder, which is fundamental for detailed kinetic studies, but introduces an approximation on initial rotation, that can be relevant (Capitelli et al. 2000). Another possibility is of course to approximate the initial vibrational ladder, considering on the contrary the whole initial rotational ladder, as in Esposito and Capitelli (2006). In this case it is possible to interpolate the rate coefficients in a relatively easy way on vibrational distribution, as in Esposito et al. (2006), but a global interpolation of cross sections is much more challenging, due to the relevant variations among cross sections originating from different vibrational states. If rate coefficients are suitable for the applications, vibrational interpolation of rates can be a good solution, but this is not true for DSMC (Direct simulation Monte Carlo) applications, as in Bruno et al. (2002). A better solution for this important case is to try to directly interpolate cross sections on initial rotation, as will be briefly illustrated in Fig. 2.1. In this case, rotationally averaged cross section for collisions of O with $N_2(v,j)$ is obtained, using only one initial rotational state in 15. A simple linear interpolation on j is then used to generate all the lacking initial state cross sections to add into the Boltzmann weighted sum for the rotational temperature:

Fig. 2.1 Rotationally averaged cross sections (*line with markers*) for vibrational energy exchange in collisions of ground state atomic oxygen with ground state molecular nitrogen. (*red*) $T_{\text{rot}} = 300 \text{ K}$, (*blue*) $T_{\text{rot}} = 10,000 \text{ K}$; (*lines without markers*) corresponding interpolated cross sections (see text for details)

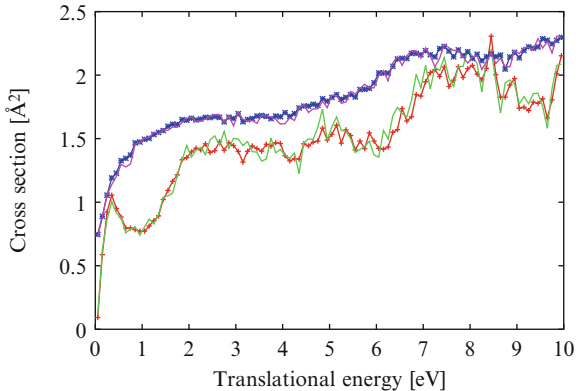
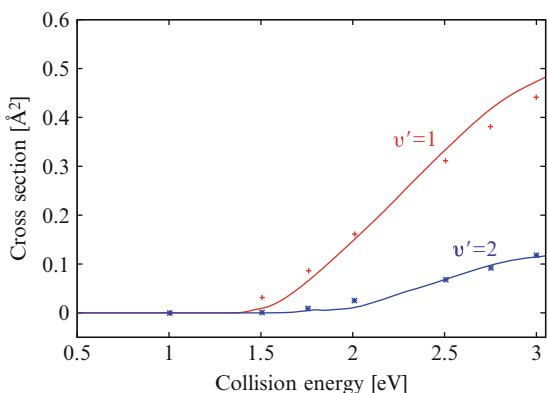


Fig. 2.2 Comparison of (*solid line*) quasiclassical and (*markers*) semiclassical (Balakrishnan et al. 1998) cross section calculations of N+N₂($v = 0, j = 7$) to different v' as a function of collision energy



$$\sigma(\varepsilon, T_{\text{rot}}) = \sum_j (\sigma(\varepsilon, j) \exp(-E_{vj}/k_B T_{\text{rot}})) / Q \quad (2.4)$$

being E_{vj} the energy of the (v, j) rovibrational level, k_B Boltzmann constant, Q rotational partition function.

In Fig. 2.1 the comparison is done between interpolated and completely calculated cross sections, at two quite different rotational temperatures, 300 and 10,000 K, for vibrational state-to-state cross sections. The results are quite good and reliable, with a clear gain in computational resources required.

In Fig. 2.2 the cross sections for inelastic vibrational excitation in N+N₂ collisions from ($v = 0, j = 7$) to final ($v' = 1, 2$) are shown, as calculated in Esposito and Capitelli (2006) on the LEPS PES (Laganà and Garcia 1994). For comparison the data (Balakrishnan et al. 1998) are shown, calculated on the same PES with a semiclassical method, essentially consisting in a quasiclassical method in which the vibrational degree of freedom of the molecule is treated quantum mechanically, with a feedback on the classical dynamics by means of an average potential (Billing 1984). This method copes with the problem of the quasiclassical inaccuracy in

presence of large spacings of energy levels, as for low-lying vibrational states. The comparison in Fig. 2.2 appears globally good. However, some apparently minor discrepancies in the threshold region could eventually have catastrophic consequences on low temperature rate coefficients. This depends on two reasons. The first one is that for processes with a threshold as in this case rate coefficients are extremely sensitive to tiny details in the threshold region, particularly if the mean energy of the translational energy distribution is lower than the threshold. The statistical errors on the semiclassical calculation in Fig. 2.2 have not been published, therefore it is not possible to appreciate if the discrepancy in the threshold region is due to statistical uncertainty or to a fundamental difference in the application of the quasiclassical and semiclassical methods. The second problem is in the approximation of the cross sections by points. Once the dynamical calculation has been performed in this way, it is hard to guess what analytical function should be used to interpolate the points in order to get a continuous cross section, for example in order to calculate the rate coefficient (but also to use it in a DSMC code). Being not unique, any interpolation could be good, but really in the threshold region this is a catastrophe, and can bring to very large errors on rate coefficients. A better strategy is the one of Aoiz and coworkers in (1997), where the whole energy range is continuously and uniformly scanned, and the cross section is calculated on the whole range using a suitable number of terms of Legendre polynomials, obtained directly from the trajectory results. In this way, no ambiguity is present in the cross section results, because the cross section is ab initio represented by a unique functional form. Another possible strategy is presented in Esposito (2011), where a particular kind of interpolation is performed on a very large number of discretized bins along the energy axis of each cross section, obtained with a continuous collisional energy distribution. The large number of bins results in better energy resolution, but of course also in an extremely noisy cross section. A procedure is then applied to perform a “feature extraction” from these noisy results in order to recover in an optimized way the “meaningful” information obscured by the statistical noise. This feature extraction is adaptive, recursive and strictly dependent on the level of statistical error of each point. The first attempt of the algorithm is to find a simple segment that initially approximates the full cross section on the whole range, then the segment is broken in two pieces connected by one point, and the two segments are free to adjust themselves with the constraint of the common point. This point can move both in value (cross section) and in collision energy. The procedure is then iterated with each of the two segments, and so on, with a convergence criterion linked to the statistical noise. In fact, the final number of segments depends on this noise and on the average local curvature of the distribution. The typical final result is illustrated in Fig. 2.3a, where it is possible to note that many small segments are present in the region near the threshold, while long segments are able to accurately describe the cross section in the regions where this one shows a quasi-rectilinear trend.

In Fig. 2.3b the rate coefficient calculated from the cross section interpolated by the polygonal is compared with the same rate obtained directly from the noisy cross section. It is clear the perfect agreement on many orders of magnitude. It is worth

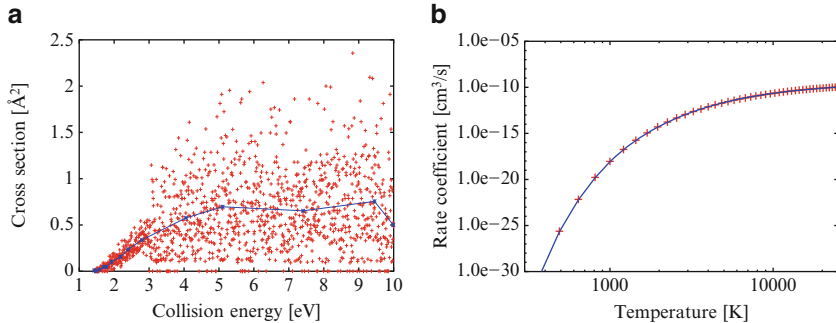


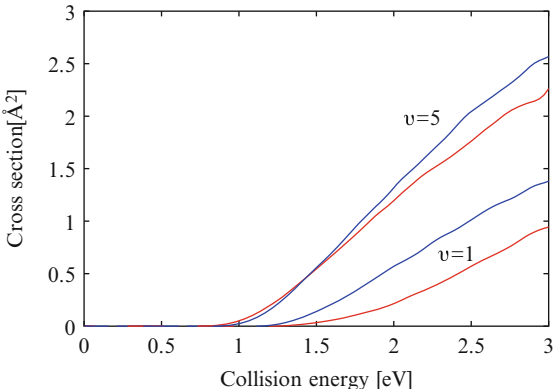
Fig. 2.3 (a) Original (noisy) cross section as a function of collision energy (red markers) and interpolation (blue polygonal line). (b) Comparison of rate coefficient calculated from the original points (red markers) and from the interpolation (blue line)

noting the small number of points used in the polygonal that allow to describe accurately the noisy cross section, retaining all the fundamental details (thresholds, plateaus, linear trends, etc.) and discarding the statistical fluctuations (hence the name “feature extraction”). Reaching the same level of accuracy using only discrete points along the energy axis would require much more calculations, for example in the threshold region. The use of this particular interpolation allows to manage a large mass of cross sections with high level of detail, using very compact data.

Concerning atom-molecule collisions with all atoms of the same species, the sum of reactive and non-reactive processes should be considered when dealing with vibrational energy transfer. On the contrary, old data used in kinetic models are based only on non-reactive data, as well as data coming from recent quantum calculations are often limited to non-reactive processes, because this can be obtained with a relatively simpler method. Any method limited in this way can be safely used only when the reactive channels are really closed, otherwise it is clear that the non-reactive result will be affected by the limitation, in addition to the lack of reactive contribution. But the question is: to what extent reactive processes are significant with respect to non-reactive ones? With quasiclassical calculations it is easy to obtain both contributions, provided the PES is adequate, with the only limitation of classically forbidden transitions (Miller 1970). In the H+H₂ case, the work of Martin and Mandy (1993) has been considered by other authors (Flower and Roueff 1998) to conclude that a ratio of 2 between reactive and non-reactive rates should be considered. The justification given in Flower and Roueff (1998) is quite simple, linked just to selection rule for orto-para states in H+H₂ system. However, a more fundamental reason can explain the general predominance of reactive processes on non-reactive ones in rovibrational energy exchange, as will be explained in the following.

A comparison of reactive and inelastic quasiclassical cross sections for N+N₂ collisions is performed in Fig. 2.4, where the diatom starts from $v=1$ and $v=5$ at a rotational temperature of 300 K, and the removal process is considered (that is

Fig. 2.4 Comparison of cross sections for (red) reaction and (blue) inelastic processes from $v = 1$ and $v = 5$, with final $v' \neq v$, at a rotational temperature of 300 K, for $\text{N} + \text{N}_2$ collisions



final $v' \neq v$). It is clear the strong similarity of the two contributions in the whole energy range, with a higher value of the non-reactive cross section for $v=1$ with respect to the reactive one. Considering that $v=5$ energy level is very near to the reaction barrier height, while $v=1$ level is well below, this similarity suggests that the majority of non-reactive trajectories are indeed missed reactive ones (recrossing trajectories). The presence of a threshold for an exothermal process could appear strange (removal process is dominated by de-excitation), and this effect might be ascribed just to a deficiency of the classical method of calculation. Low probability in the exothermal direction for low energy values can be easily justified on the basis of very general considerations. It is possible to consider two extreme conditions, the first one in which the time for traversing the SCR (strong coupling region), t_{SCR} , which depends on energy projectile as well as on potential features, is much higher than the vibrational period t_{vib} (which tends to slightly increase with vibrational quantum number), and the second condition in which t_{SCR} is comparable to or less than t_{vib} . In the first case, translational motion is by definition adiabatic with respect to vibration, so no transition is expected (its probability might be very low). In the second case, on the contrary, it is quite likely that vibration-translation transitions take place, because the characteristic times of the two motions are similar and the interaction of the two degrees of freedom is expected to be strong. Summarizing, vibrational adiabaticity is expected at low collision energy and low initial vibrational quantum number, and viceversa. These considerations (essentially the Massey criterion for adiabatic-diabatic processes applied to vibration-translation exchange (Massey 1949)) are quite general, therefore the same behavior can be expected from a classical as well as a quantum calculation. However, it is clear that this qualitative criterion cannot assure that a given cross section is exactly zero in a range of translational energy, but only that it should be very low. It is well known the inability of QCT to calculate very low probabilities, as well as its inadequacy in describing vibrational quasi-adiabaticity (Bonnet 2008) (i.e. quite low probability of final vibrational outcome different from the initial one in inelastic cases). As a consequence, quasiclassical results can be essentially considered reliable, excluding

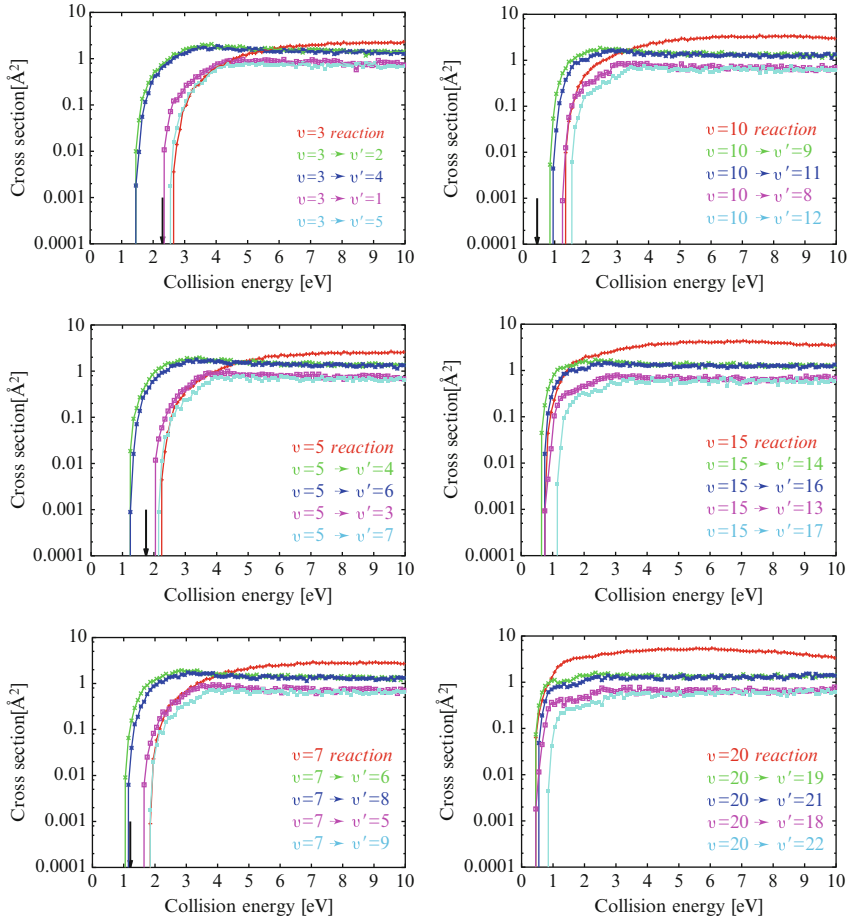


Fig. 2.5 Reactive (red) and non-reactive ($v \rightarrow v'$) cross sections of vibrational energy exchange for O+N₂($v, j = 0$) collisions, as a function of collision energy. The downward arrow, when present, is the threshold for reactive processes. Non-reactive processes appear quite similar to reactive ones in the threshold region, excluding only mono-quantum processes. See text for comments

the very low energy values, for which quite low values of probability are anyway expected. A better description of this point will be presented in the following, introducing the criterion of discrimination of two- and three-body collisions.

In Fig. 2.5 the collisions of ground state oxygen atom with nitrogen molecule is considered on the $^2A''$ PES of Gamallo et al. (2003). The initial vibrational state is indicated in the panels, while initial rotation is zero. For $v < 12$ the reactive process is endothermal, without a reaction barrier (apart from the purely endothermal step) along this PES (a reaction barrier is present along the C_{2v} minimum, at an energy higher than the endothermal step, see Akpinar et al. 2012). The energy threshold

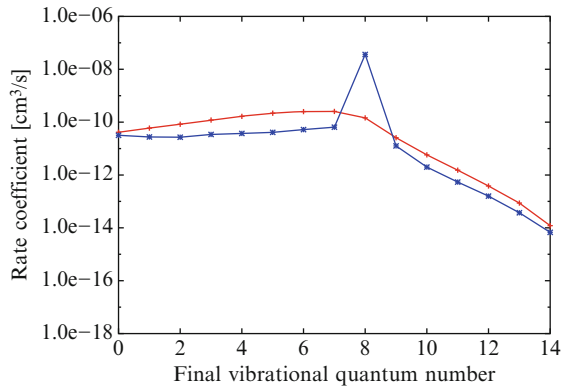
for reaction, which depends on initial (ro)vibrational state considered, is indicated by a downward arrow on the collision energy axis. This system has been chosen because of its high endothermicity (3.3 eV), in order to compare easily the typical behavior of reactive and inelastic cross sections. In Fig. 2.5, the reaction cross section is represented by the red curves, the blue and green curves represent the inelastic mono-quantum deexcitation and excitation, respectively, while the magenta and turquoise are bi-quantum deexcitation and excitation, respectively. The scale is logarithmic, in order to show clearly the threshold behavior. In panel (a), where initial $v = 3$, the inelastic mono-quantum cross sections are clearly dominant on the reaction one and on the bi-quantum ones up to 4 eV. The bi-quantum case (both deexcitation and excitation) is quite similar to the reactive case, with similar thresholds, while the mono-quantum case is significantly under the reactive threshold (about 1 eV). These two trends of mono- and bi-quantum cross section in comparison with reaction continue also for higher initial vibrational quantum numbers, as it is clear in lower panels (b),(c), from $v = 5$ and 7 respectively, but progressively reducing the discrepancy in the thresholds.

In panel (d), with $v = 10$, all the considered cross sections are completely on the right of the energy threshold for reaction. In panel (e) the case from $v = 15$ is shown, which is exothermal. The dynamical thresholds tend clearly to coalesce into a unique value, as stressed also in the last panel (f) from $v = 20$. The reaction cross section starts to be higher than inelastic cross sections at a collisional energy decreasing with initial v . Only for $v \geq 20$ reaction tends to be the dominant process on the whole range explored. The observation to extract from this comparison is that non-reactive processes are indeed quite similar to reactive ones with the exclusion of the elastic and quasi-elastic ones (i.e. mono-quantum deexcitation-excitation processes). Excluding these last processes, it is possible to say that the whole non-reactive processes take place only when reaction threshold is overcome, as one of the possible outcomes of a strong interaction. In fact, it is possible to appreciate that for symmetric systems like H+H₂ (Fig. 2.6) and N+N₂ (Fig. 2.8), there are two independent equivalent reactive channels, and the inelastic channel, excluding elastic and quasielastic processes, has a rate coefficient quite near to each reactive channel rate coefficient. This is the origin of the 1:2 ratio between non-reactive and reactive rate coefficients for symmetric collisional systems. It is anticipated here that all the discrepancies between non-reactive and reactive rates, apart from the elastic and quasi-elastic ones, could be attributed to non-reactive non-recrossing trajectories (see below).

On the contrary, it is clear the completely different trend of elastic and quasielastic processes, with a very high elastic peak with two rapidly decaying shoulders of quasielastic transitions. This behavior is typical of a harmonic oscillator perturbed by an atomic projectile, where there is an exponential decay of probability of vibrational energy exchange as a function of vibrational energy ε_{vib} transferred to the classical oscillator. The well known formula for transition probability of a forced harmonic oscillator is:

$$P_{n,m} = n! m! e^{-\varepsilon} \varepsilon^{(m+n)} (S_{n,m})^2$$

Fig. 2.6 Comparison of (red) reactive and (blue) non-reactive rate coefficients as a function of final vibrational quantum number at $T_{\text{coll}} = T_{\text{rot}} = 3,000$ K for collision of H with H₂(v = 8). The elastic peak is only qualitatively approximated. The non-reactive contribution is doubled to compare with the two reactive channels for this kind of symmetric systems



$$S_{n,m} = \sum_{j=0} \frac{(-1)^j \varepsilon^{-j}}{(n-j)! j! (m-j)!} \quad (2.5)$$

where ε is the ratio of the ε_{vib} to one quantum of energy of the harmonic oscillator, being n, m initial and final vibrational quantum number, respectively. This transition probability has been exploited many times in different approximated methods for molecular dynamics, in particular in FHO (Husimi 1953; Kerner 1958; Treanor 1965) and DECENT (Giese and Gentry 1974) methods. This formula was obtained for a harmonic oscillator by Husimi (1953) and Kerner (1958) for a special potential:

$$U(x) = \frac{1}{2} kx^2 - xF(t) \quad (2.6)$$

This potential has the property of allowing the quantal and classical motion to be put in exact correspondence. Once the vibrational energy ε_{vib} transferred to the oscillator, initially at rest, is known from classical mechanics, it is possible to use directly formula (2.5) with this classical value of ε_{vib} , and the probability result is what can be obtained in an exact quantum calculation. Of course, the potential of realistic cases can be quite different from Eq. (2.6), therefore some restrictions must be put on the applicability of the method (even if it is not a perturbation method in principle). In particular, it is clear that during an atom-molecule collision the perturbing force cannot have a spatial dependence on the typical scale of the vibrational motion, otherwise it would not be expressible in the (2.6) way (Treanor 1965). In order to fulfill this condition the R distance between the atom and the center of mass of the diatom should be sufficiently larger than r , the internuclear distance of the diatom. This kind of collision could be indicated as “purely non-reactive” (PNR), essentially a *two body collision* between the atom and the diatom as a whole. Of course, the minimum acceptable value of $z = R/r$ depends on the true atom-diatom interaction potential. In order to correctly apply the formula (2.5), one should only consider PNR trajectories, defined as those ones having a ratio z never less than a certain two-body parameter $z_{2b} \sim 1.5$ during time evolution.

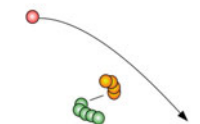
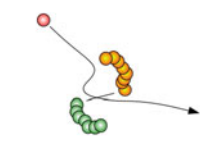
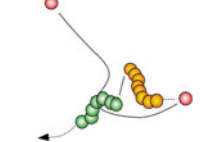
This is done only implicitly and approximately, by limiting the maximum value of collisional energy considered in the calculation. However, the limitation is not stringent, because the model is not a first order perturbation method, as already pointed out. It is clear that the value of z_{2b} is arbitrary to a certain extent, like R_{\max} for the maximum radius of interaction in a collision. If the collisional system has a barrier to reaction, PNR trajectories are those ones with energy sufficiently below the barrier, or trajectories above the barrier but with a sufficiently high impact parameter, so that the atomic projectile is only slightly deviated from the original straight line.

As a consequence, under the conditions of Fig. 2.5 purely non-reactive trajectories are the only ones below the reactive barrier, of course, but give also a contribution above the barrier, with high impact parameter trajectories. The remaining large contribution comes from non-reactive but not-PNR trajectories: in this case the collisional system has a significant interaction, that is the encounter is a true *three body collision*, not a simple two body interaction. Non-reactive but not-PNR trajectories are those ones for which $z < z_{2b}$ somewhere along time evolution. In this set there are surely the recrossing trajectories, that could be defined as those non-reactive trajectories for which $z_{\min} < z_{3b}$ (three-body parameter $z_{3b} \approx 1$; a more accurate definition is based on considering the couples of internuclear distances). These trajectories recross the ideal surface dividing reactants from products. It is easy to realize that these trajectories have necessarily entered the strong coupling region. However, it is clear from the preceding discussion that these trajectories should be much more similar to reactive trajectories than to purely non-reactive ones. This is confirmed by the striking similarity of trends in rate coefficients between reactive and non-reactive cases already illustrated in Figs. 2.6 and 2.8.

In Table 2.1 a scheme of the classification is sketched. The subdivision of non-reactive trajectories in recrossing and non-recrossing is necessary because z_{PNR} is obviously arbitrary, and there is an intermediate condition between PNR and recrossing. PNR and non-reactive non-recrossing trajectories take place with a weak interaction, the reverse being true for recrossing and reactive trajectories.

A better illustration of the existence of all these kind of trajectories can be observed in Fig. 2.7, where some trajectories for $\text{O}+\text{N}_2(v = 5, j = 0)$ collisions are monitored for their minimum ratio $z_{\min} = (R/r)_{\min}$ (along time evolution) against their final vibrational actions (the quasiclassical analog of quantum number), at increasing values of collisional energy. At 1.0 eV (Fig. 2.7a) the range of possible z_{\min} values varies only from about 2.0 down to 1.5, with a range of final vibrational number well below 1. This means exactly the existence of a PNR condition for the whole set of trajectories shown, where the vibrational adiabaticity that obviously derives from the application of QCT final analysis is indeed incorrect, because QCT is here unable to see the very low (but not necessarily zero) probability of vibrational exchange. This condition would be perfect for application of forced harmonic oscillator model. When energy is increased, the response changes with a wider final action distribution, in a way that is now correctly detectable by QCT analysis (Fig. 2.7b at 1.5 eV, with a vibrational width greater than 1). The range of z_{\min} now is displaced towards lower values. At 2 eV (Fig. 2.7c) the

Table 2.1 Scheme of the classification for trajectories

purely non-reactive	$z_{\min} > z_{2b}$	2-body collision (weak)	
non-reactive non-recrossing	$z_{3b} < z_{\min} < z_{2b}$	3-body collision (weak)	
non-reactive recrossing	$z_{\min} < z_{3b}$	3-body collision (strong)	
reactive	$z_{\min} < z_{3b}$	3-body collision (strong)	

new element is the presence of few trajectories with z_{\min} near to 1 (essentially recrossing trajectories) with very low values of final vibration. This condition is then replicated with much more trajectories when collisional energy is increased to 2.5 eV (Fig. 2.7d) (beyond the reaction threshold), together with the appearance of reactive trajectories at z_{\min} significantly lower (<0.6). It is important to realize that this kind of analysis stresses the presence of a threshold for accurate quasiclassical calculation of transition probability. In fact, for a collisional energy of 1 eV the O+N₂ system does not produce any vibrational result detectable by a standard binning procedure, while for larger energy values this is feasible. This threshold for quasiclassical vibrational adiabaticity cannot be anticipated from purely energetic considerations, in fact this threshold is lower for He+H₂ collisional system, even if the vibrational quantum is higher than the analogous quantity for O+N₂. This vibrational response to translational energy input is typical of each collisional system and can be studied phenomenologically with the analysis presented here. Under this vibrational threshold, of course, the quasiclassical transition probability is, erroneously, zero, and could be corrected by using for example DECENT method limited to trajectories quasiclassically adiabatic in the vibrational sense.

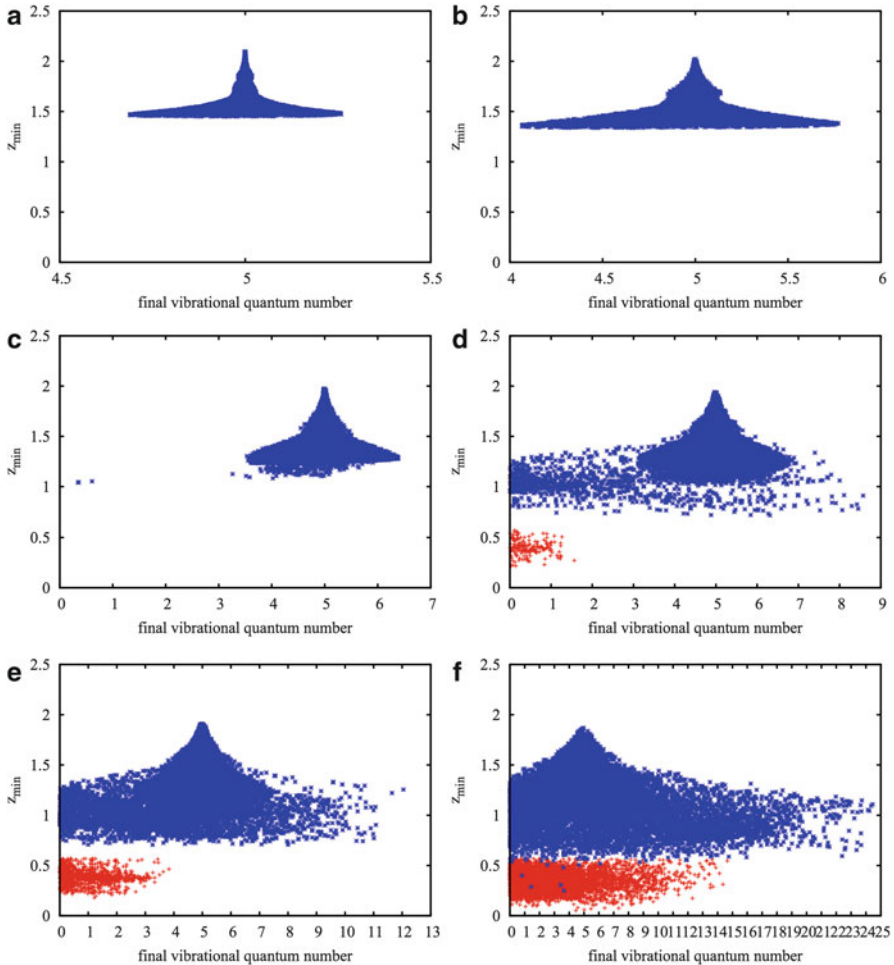
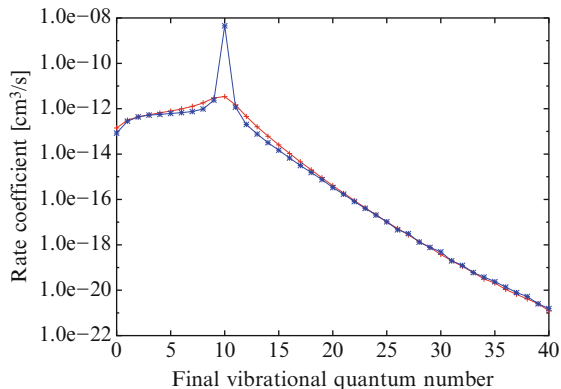


Fig. 2.7 Relation between minimum ratio of R/r along each trajectory, z_{\min} , and final vibrational quantum number (in quasi-classical sense) for $O+N_2(v=5, j=0)$ collisions, at various collisional energies **(a)** 1.0, **(b)** 1.5, **(c)** 2.0, **(d)** 2.5, **(e)** 3.0, **(f)** 5.0 eV. In red: reactive, in blue: non-reactive trajectories. At 1.0 eV **(a)** QCT method is unable to detect any vibrational variation from $v=5$, because final action does not differ more than half quantum from the original value. At 2.0 eV **(c)** very few trajectories near the $z_{\min}=1$ limit present a very low value of final vibrational action. Many other trajectories present this feature when collisional energy is increased beyond the reaction threshold

It is clear from preceding discussion that recrossing trajectories should not be modeled with harmonic oscillator models like FHO and DECENT, because the simple forced harmonic oscillator model that is the base of these methods is inapplicable for strong interaction of the projectile with the target, as already stressed in Shuler and Zwanzig (1960) and Treanor (1965). Fortunately, recrossing

Fig. 2.8 Comparison of (red) reactive and (blue) non-reactive vibrational energy transfer rate coefficients for N+N₂(v = 10) collisions as a function of final vibrational quantum number, at $T_{\text{coll}} = T_{\text{rot}} = 3,000$ K. The non-reactive contribution is doubled, in order to show its ratio 1:2 with the reactive contribution



trajectories and reactive trajectories can be successfully treated with QCT. On the contrary, QCT is not accurate on PNR trajectories, as can be seen for example in the already cited He-H₂ collisions in Balakrishnan et al. (1999), where QCT vibrational cross sections in the exothermal direction for collisional energy less than about 1 eV are zero, while the accurate quantum mechanical calculations give values as high as 0.1 Å². Being the potential of the collisional system completely repulsive, there are no reactive trajectories, but all the possible kinds of non-reactive trajectories are present. In fact, it is clear that the classification presented is valid, because trajectories with sufficient energy will bring the three atoms sufficiently close to classify the encounter as a three body one. Therefore in this important case the same considerations should apply, with a possible cooperation of FHO model with quasiclassical trajectories in low and high energy ranges respectively.

Why reactive and mixed inelastic transitions should be well reproduced by QCT, contrarily to what happens to purely inelastic transitions? The answer is in the approximation introduced by histogram binning in QCT. As clear from the preceding discussion, when less than a vibrational quantum is classically exchanged, QCT is inaccurate. This inaccuracy is present also for reactive trajectories and for inelastic ones passing through transition state (recrossing), but in those cases a quite continuous and smooth distribution of final actions is expected, as can be appreciated in the preceding figures, the opposite of the dramatic elastic peak with quasielastic exponentially decaying shoulders. In this last case, the inaccuracy on quasielastic transitions tends to be largely overemphasized, while in the former case it is generally negligible.

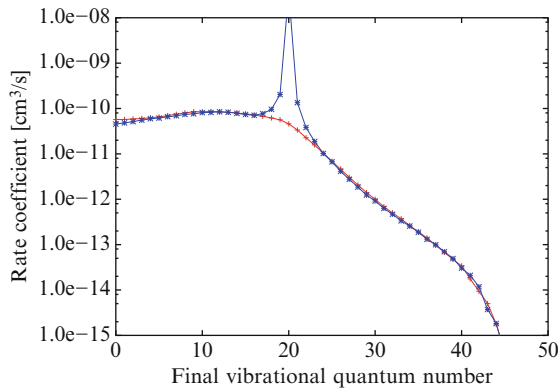
This is also shown in Fig. 2.8, where reactive and non-reactive rate coefficients as a function of final vibrational quantum number are presented from $v = 10$ for the collisional system N+N₂(v). It is clear the similarity of reactive and non-reactive trends, if just the elastic and quasielastic rates are excluded. This is confirmed by analogous quasiclassical calculations on many other systems (O+N₂, O+O₂, N+O₂) (Esposito and Capitelli 2002, 2007; Laganà et al. 2014). A word of caution should be spent about the quasiclassical elastic cross section. This one should be without convergence, because the method normally is not able to

distinguish between trajectories without interaction and trajectories in which the only modification is in the kinematics of the projectile (and no change in molecular rovibrational actions). As a consequence, the elastic peak shown here is due only to the accumulation of results in the elastic channel, with the convergence due to any other different channel. Therefore, it is only a very rough value to evaluate only qualitatively. It is important, however, to point out that a purely classical elastic cross section is obtainable, by introducing an ad-hoc modification of the final analysis of projectile motion (essentially the Heisenberg uncertainty principle reintroduced in the classical context to eliminate non-interacting trajectories). This has been probably presented for the first time by Polanyi et al. (1977).

From these observations, one could suggest to apply standard QCT method for reactive and recrossing non-reactive trajectories, discarding purely non-reactive trajectories. The non-reactive part of the calculation so obtained should be summed to the results of the application of forced harmonic oscillator method with classical trajectories (like DECENT method Giese and Gentry 1974), limited to purely non-reactive trajectories. In this way the best results of the two methods can be usefully exploited. Some uncertainty remains about the treatment of non-reactive non-recrossing trajectories, however it should not be a major issue, because both methods should be able to treat correctly those trajectories.

New PESs have been recently proposed in literature since the semiempirical LEPS PES. The one of the NASA AMES group (Wang et al. 2003) has introduced an important feature in the barrier region (“Lake Eyring”), potentially capable of significantly changing the reactive properties of the collisional system with respect to the simple LEPS PES. The height of the barrier to reaction is also quite different, about 2 eV against 1.56 of the semiempirical PES. Unfortunately, this PES has been used only by its authors for dynamical calculations, but it has never been publicly available. Other groups (Garcia et al. 2008; Caridade et al. 2010) have calculated accurate PESs for this system, with a particular attention to the barrier region as described by the NASA group. It is likely that the purely non-reactive part of the calculations on these new PESs are quite similar to preceding calculations on LEPS PES, partially because that part of the calculations are poorly treated by QCT method, but also because it should not be too sensitive to the PES features. The significantly new part is surely what is concerned with the *new* transition state. Following the preceding observations, however, this should not affect only the reactive calculations, but also the non-reactive ones, because these last ones are for the most part recrossing ones and not purely non-reactive trajectories. An accurate comparison should be performed in order to assess this point. However, a quite reliable database of quasiclassical cross sections and rate coefficients is available for this collisional system, obtained on the cited LEPS PES with a high degree of accuracy from the statistical point of view, and good comparisons with literature. The reader is referred to the literature for the details and the data (Esposito and Capitelli 1999, 2006; Capitelli et al. 2000; Esposito et al. 2006).

Fig. 2.9 Comparison of (red) reactive and (blue) non-reactive (multiplied by 2) vibrational energy transfer rate coefficients for O+O₂(v = 20) collisions as a function of final vibrational quantum number, at $T_{\text{coll}} = T_{\text{rot}} = 3,000$ K



2.4 O+O₂

What happens in the case of an attractive potential between the atom and the molecular target, as for O+O₂ collisions? Following the explanation of the preceding paragraph, it should be clear that all the considerations remain unaltered, with the observation that in this case it is much more likely that only a small part of trajectories will be purely non-reactive and, as a consequence, reactive and non-reactive trajectories should behave in a quite similar way. This is confirmed in Fig. 2.9, where rate coefficients for collisions of O+O₂(v = 20) as a function of final vibrational quantum number are shown, while rotational and translational temperatures are fixed at 3,000 K. The PES used is the one of Varandas and Pais (1988), and the series of calculations have been performed in Esposito and Capitelli (2002, 2007). It is clear the strong similarity of the reactive and non-reactive trends, taking into account the 2:1 ratio and excluding the elastic peak and its surroundings. Another observation is the relatively flat behavior of de-excitation rates, due to the mixing effect of the attractive potential. In this case, in fact, the collisional system is temporarily trapped into the attractive potential, escaping at the end with a statistical distribution of final products. It is important to take into account this behavior when evaluating approximation of rates, because it is clear that in this case simple models of mono-quantum rates are strongly inadequate.

The figure is an important confirmation of the very striking similarity of reactive and non-reactive trajectories, because in this case it would be very easy to see differences due to statistical or non-statistical behavior, differences that are completely absent. On the other side, the elastic and quasielastic peak is anyway present and important, and it could be successfully modelled with forced harmonic oscillator methods, but realizing anyway that in this case only a quite small part of dynamics is captured, while the multi-quantum transitions are due to three body interactions, more correctly modelled by QCT method. The best way of comparing data obtained by various computational procedures is of course to compare with experiments. However, very often there is a problem in this comparison, rarely stressed, that can

significantly alter the conclusions. In fact, it is quite common to obtain vibrational data from shockwave experiments, where the original measured quantity is a slight pressure deviation from equilibrium. The connection between this macroscopic quantity and the state-to-state rate coefficients (Dove and Teitelbaum 1974) is quite laborious and, principally, is based on some very crude approximations, first of all the Bethe-Teller law (Bethe and Teller 1941) for low-lying vibrational states. This law is another model based on transitions in a forced harmonic oscillator, and it is clear from the preceding discussion what can be actually modelled from these models, and what should not. For O+O₂(v) this approximation appears completely inadequate, because of the large majority of trajectories coming from strong three body encounters, with a small contribution from weak two body ones. The flat distribution of multi-quantum rate coefficients, on the other side, is another clear indication that forced harmonic oscillator models, with their exponential decay of probability as a function of vibrational energy exchanged, cannot be adequate for this collisional system. As a consequence, also comparisons with experiments based on these simplifications in the deconvolution of data should be considered with caution. The recommended rate coefficients for this system for both vibrational energy exchange and dissociation can be found in Esposito et al. (2008), where complete analytic fits of the relevant quantities are available.

2.5 Future Developments

The increasing computational power available for computational chemistry allows new detailed calculations using accurate methods for molecular dynamics. However, with increasing collisional energy the computational requirements for exact methods scales unfavorably, while in the same conditions quasiclassical calculations scale very efficiently. It is obvious, as a consequence, to search for a correct compromise between the two approaches. This will be the best strategy for obtaining reliable data in a large range of collisional energy. In order to perform this program, it is important to know the lower limits of applicability of quasiclassical method, in particular with respect to vibrational adiabaticity, a relatively less studied aspect, often much more relevant than tunneling in distorting the classical results in comparison to an exact quantum treatment. Some relevant notes about this point have been presented here, with an analysis of molecular collisions based on the distance of closest approach during each classical encounter. As a consequence, a new proposal of merging in a peculiar way the quasiclassical results with forced harmonic oscillator model applied to classical trajectories has been presented, in order to obtain reliable results also for low energy values, useful for kinetic models of technological interest. However, for collisional energies larger than 0.5–1 eV quasiclassical calculations can be considered reliable also for light atoms, and the relevant sets of data have been indicated for some important atom-diatom collisional

systems. The next challenge is now to introduce a more accurate treatment for high energies, which in general implies the consideration of non-adiabatic transitions. The difficulties in this case consist of the construction of excited PESs, the couplings among them and, last but not least, the suited method for performing the dynamics, considering the large number of processes required for a subsequent kinetic study. Trajectory surface hopping (Tully and Preston 1971) is the most natural extension of quasiclassical method for this kind of problems, but many methods (Jasper et al. 2004) based on classical trajectories have been developed, including an original proposal by Esposito (2013).

References

- Akpınar S, Armenise I, Defazio P, Esposito F, Gamallo P, Petrongolo C, Sayós R (2012) Quantum mechanical and quasiclassical Born-Oppenheimer dynamics of the reaction $N_2(X^1\Sigma_g^+)+O(^3P)\rightarrow N(^4S)+NO(X^2\Pi)$ on the $N_2O\tilde{a}^3A''$ and \tilde{b}^3A' surfaces. *Chem Phys* 398:81–89
- Althorpe SC (2001) Quantum wavepacket method for state-to-state reactive cross sections. *J Chem Phys* 114:1601
- Aoiz FJ, Bañares L, Herrero VJ, Sàez Ràbanos V, Tanarro I (1997) The $H+D_2\rightarrow HD+D$ reaction. Quasiclassical trajectory study of cross sections, rate constants, and kinetic isotope effect. *J Phys Chem A* 101(35):6165–6176
- Aoiz FJ, Bañares L, Herrero VJ (2005) The $H+H_2$ reactive system. progress in the study of the dynamics of the simplest reaction. *Int Rev Phys Chem* 24(1):119–190
- Balakrishnan N, Kharchenko V, Dalgarno A (1998) Quantum mechanical and semiclassical studies of $N+N_2$ collisions and their application to thermalization of fast N atoms. *J Chem Phys* 108(3):943–949
- Balakrishnan N, Vieira M, Babb J, Dalgarno A, Forrey R, Lepp S (1999) Rate coefficients for ro-vibrational transitions in H_2 due to collisions with He. *Astrophys J* 524:1122
- Bethe HA, Teller E (1941) Deviations from thermal equilibrium in shock waves. Technical report X-117, Ballistic Research Labs
- Billing G (1984) The semiclassical treatment of molecular roto/vibrational energy transfer. *Comput Phys Rep* 1(5):239–296
- Bonnet L (2008) The method of Gaussian weighted trajectories. III. An adiabaticity correction proposal. *J Chem Phys* 128(4):044109
- Bonnet L, Rayez J (2004) Gaussian weighting in the quasiclassical trajectory method. *Chem Phys Lett* 397(1–3):106–109
- Boothroyd AI, Keogh WJ, Martin PG, Peterson MR (1996) A refined H_3 potential energy surface. *J Chem Phys* 104(18):7139
- Bruno D, Capitelli M, Esposito F, Longo S, Minelli P (2002) Direct simulation of non-equilibrium kinetics under shock conditions in nitrogen. *Chem Phys Lett* 360(1–2):31–37
- Capitelli M (1986) Nonequilibrium vibrational kinetics. Topics in current physics, vol 39. Springer-Verlag, Berlin Heidelberg
- Capitelli M, Esposito F, Kustova E, Nagnibeda E (2000) Rate coefficients for the reaction $N_2(i)+N\rightarrow 3N$: a comparison of trajectory calculations and the Treanor-Marrone model. *Chem Phys Lett* 330(1–2):207–211
- Capitelli M, Celiberto R, Esposito F, Laricchiuta A (2007) Cross section data for negative ion sources. *AIP Conf Proc* 925(1):3–10

- Caridade PJSB, Galvão BRL, Varandas AJC (2010) Quasiclassical trajectory study of atom-exchange and vibrational relaxation processes in collisions of atomic and molecular nitrogen. *J Phys Chem A* 114:6063–6070
- Dove JE, Teitelbaum H (1974) The vibrational relaxation of H₂. I. Experimental measurements of the rate of relaxation by H₂, He, Ne, Ar, and Kr. *Chem Phys* 6(3):431–444
- Esposito F (2011) Atom-Diatom collision processes: rovibrationally detailed cross sections for models. In: Levin DA, Wysocki JJ, Garcia AL (eds) AIP conference proceedings, AIP Publishing, vol 1333, pp 1357–1364
- Esposito F (2013) Non-adiabatic dynamics with quasiclassical trajectories: a trajectory surface sliding method. Quantum reactive scattering workshop, Bordeaux, 10–14 June 2013
- Esposito F, Capitelli M (1999) Quasiclassical molecular dynamic calculations of vibrationally and rotationally state selected dissociation cross-sections: N+ N₂(*v,j*) → 3N. *Chem Phys Lett* 302(1–2):49–54
- Esposito F, Capitelli M (2001) Dynamical calculations of state-to-state and dissociation cross sections for atom-molecule collision processes in hydrogen. *At Plasma-Mater Interact Data Fusion* 9:65–73
- Esposito F, Capitelli M (2002) Quasiclassical trajectory calculations of vibrationally specific dissociation cross-sections and rate constants for the reaction O+O₂(*v*)→3O. *Chem Phys Lett* 364:180–187
- Esposito F, Capitelli M (2005) Detailed cross section calculations of atom-molecule energy transfer processes and dissociation for hydrogen, nitrogen and oxygen. *AIP Conf Proc* 771(1):246–254
- Esposito F, Capitelli M (2006) QCT calculations for the process N₂(*v*)+N→N₂(*v'*)+N in the whole vibrational range. *Chem Phys Lett* 418:581–585
- Esposito F, Capitelli M (2007) The relaxation of vibrationally excited O₂ molecules by atomic oxygen. *Chem Phys Lett* 443:222–226
- Esposito F, Capitelli M (2009) Selective vibrational pumping of molecular hydrogen via gas phase atomic recombination. *J Phys Chem A* 113:15307–15314
- Esposito F, Gorse C, Capitelli M (1999) Quasi-classical dynamics calculations and state-selected rate coefficients for H+ H₂(*v,j*) →3H processes: application to the global dissociation rate under thermal conditions. *Chem Phys Lett* 303(5–6):636–640
- Esposito F, Armenise I, Capitelli M (2006) N-N₂ state to state vibrational-relaxation and dissociation rates based on quasiclassical calculations. *Chem Phys* 331(1):1–8
- Esposito F, Armenise I, Capitta G, Capitelli M (2008) O-O₂ state-to-state vibrational relaxation and dissociation rates based on quasiclassical calculations. *Chem Phys* 351(1–3):91–98
- Flower D, Roueff E (1998) Vibrational relaxation in H-H₂ collisions. *J Phys B At Mol Opt Phys* 31:L955
- Galvão BRL, Caridade PJSB, Varandas AJC (2012) N(⁴S/²D)+N₂: accurate ab initio-based DMBE potential energy surfaces and surface-hopping dynamics. *J Chem Phys* 137(22):22A515
- Gamallo P, González M, Sayós R (2003) Ab initio derived analytical fits of the two lowest triplet potential energy surfaces and theoretical rate constants for the N(⁴S)+NO(X²Π) system. *J Chem Phys* 119(5):2545
- García E, Saracibar A, Gómez-Carrasco S, Laganà A (2008) Modeling the global potential energy surface of the N+N₂ reaction from ab initio data. *Phys Chem Chem Phys* 10:2552
- Giese CF, Gentry WR (1974) Classical trajectory treatment of inelastic scattering in collisions of H⁺ with H₂, HD, and D₂. *Phys Rev A* 10(6):2156
- Götting R, Herrero V, Toennies J, Vodegel M (1987) Determination of the absolute scattering cross section for the reaction D+H₂(*v*=1) →HD+H at 0.33 eV. *Chem Phys Lett* 137(6):524–532
- Gray SK, Balint-Kurti GG (1998) Quantum dynamics with real wave packets, including application to three-dimensional (J=0)D+H₂ →HD+H reactive scattering. *J Chem Phys* 108(3):950
- Hankel M, Smith SC, Allan RJ, Gray SK, Balint-Kurti GG (2006) State-to-state reactive differential cross sections for the H+H₂ →H₂+H reaction on five different potential energy surfaces employing a new quantum wavepacket computer code: DIFFREALWAVE. *J Chem Phys* 125:164303

- Husimi K (1953) Miscellanea in elementary quantum mechanics, II. *Prog Theor Phys* 9(4):381–402
- Jasper AW, Zhu C, Nangia S, Truhlar DG (2004) Introductory lecture: nonadiabatic effects in chemical dynamics. *Faraday Discuss* 127:1–22
- Karplus M, Porter R, Sharma R (1965) Exchange reactions with activation energy. I. Simple barrier potential for (H, H_2). *J Chem Phys* 43:3259
- Kerner EH (1958) Note on the forced and damped oscillator in quantum mechanics. *Can J Phys* 36(3):371–377
- Kim JG, Kwon OJ, Park C (2009) Master equation study and nonequilibrium chemical reactions for $H+H_2$ and $He+H_2$. *J Thermophys Heat Transf* 23(3):443–453
- Krstić P, Schultz D (1999a) Elastic and vibrationally inelastic slow collisions: $H+H_2$, H^++H_2 . *J Phys B At Mol Opt Phys* 32:2415
- Krstić PS, Schultz DR (1999b) Consistent definitions for, and relationships among, cross sections for elastic scattering of hydrogen ions, atoms, and molecules. *Phys Rev A* 60(3):2118
- Laganà A, Garcia E (1994) Temperature dependence of nitrogen atom-molecule rate coefficients. *J Phys Chem* 98(2):502–507
- Laganà A, Crocchianti S, Aspuru G, Riganelli A, García E (1997) Accurate calculations of cross sections and rate coefficients of some atom-diatom reactions relevant to plasma chemistry. *Plasma Sources Sci Technol* 6:270
- Laganà A, Lombardi A, Pirani F, Gamallo P, Sayós R, Armenise I, Cacciatore M, Esposito F, Rutigliano M (2014) Molecular physics of elementary processes relevant to hypersonics: atom-molecule, molecule-molecule and atoms-surface processes. *Open Plasma Phys J* 7(Suppl 1):M1):48–59
- Langer RE (1937) On the connection formulas and the solutions of the wave equation. *Phys Rev* 51(8):669–676
- Launay JM (1991) Computation of cross sections for the $F+H_2(v=0,j=0)\rightarrow FH(v',j)+H$ reaction by the hyperspherical method. *Theoretica chimica acta* 79(3–4):183–190
- Mandy M, Martin P (1993) Collisional excitation of H_2 molecules by H atoms. *Astrophys J Suppl Ser* 86:199–210
- Massey HSW (1949) Collisions between atoms and molecules at ordinary temperatures. *Rep Prog Phys* 12:248
- Mayne HR, Toennies JP (1981) Quasiclassical trajectory studies of the $H+H_2$ reaction on an accurate potential-energy surface. III. Comparison of rate constants and cross sections with experiment. *J Chem Phys* 75(4):1794
- Mielke SL, Garrett BC, Peterson KA (2002) A hierarchical family of global analytic Born-Oppenheimer potential energy surfaces for the $H+H_2$ reaction ranging in quality from double-zeta to the complete basis set limit. *J Chem Phys* 116(10):4142
- Miller WH (1970) Semiclassical theory of atom-diatom collisions: path integrals and the classical S matrix. *J Chem Phys* 53(5):1949
- Miller WH (1971) Classical S matrix for rotational excitation; quenching of quantum effects in molecular collisions. *J Chem Phys* 54(12):5386
- Miller WH (2001) The semiclassical initial value representation: a potentially practical way for adding quantum effects to classical molecular dynamics simulations. *J Phys Chem A* 105(13):2942–2955
- Pattengill M (1979) Rotational excitation III: classical trajectory methods. In: Atom-molecule collision theory. Springer US, pp 359–375
- Polanyi JC, Sathyamurthy N, Schreiber JL (1977) Rotational energy transfer (theory). I. Comparison of quasiclassical and quantum mechanical results for elastic and rotationally inelastic $HCl-Ar$ collisions. *Chem Phys* 24(1):105–110
- Porter RN, Raff LM (1976) Classical trajectory methods in molecular collisions. In: Dynamics of molecular collisions. Springer Series Modern Theoretical Chemistry, vol. 2. Springer US
- Schatz GC, Kuppermann A (1976a) Quantum mechanical reactive scattering for three-dimensional atom plus diatom systems. I. Theory. *J Chem Phys* 65(11):4642

- Schatz GC, Kuppermann A (1976b) Quantum mechanical reactive scattering for three-dimensional atom plus diatom systems. II. Accurate cross sections for H+H₂. *J Chem Phys* 65(11):4668
- Schwartz RN, Slawsky ZI, Herzfeld KF (1952) Calculation of vibrational relaxation times in gases. *J Chem Phys* 20(10):1591
- Shuler KE, Zwanzig R (1960) Quantum-mechanical calculation of harmonic oscillator transition probabilities in a one-dimensional impulsive collision. *J Chem Phys* 33(6):1778
- Skouteris D, Castillo JF, Manolopoulos DE (2000) ABC: a quantum reactive scattering program. *Comput Phys Commun* 133(1):128–135
- Treanor CE (1965) Vibrational energy transfer in high-energy collisions. *J Chem Phys* 43(2):532
- Truhlar DG, Horowitz CJ (1978) Functional representation of Liu and Siegbahn's accurate ab initio potential energy calculations for H+H₂. *J Chem Phys* 68(5):2466
- Tully JC, Preston RK (1971) Trajectory surface hopping approach to nonadiabatic molecular collisions: the reaction of H⁺ with D₂. *J Chem Phys* 55(2):562–572
- Varandas A, Pais A (1988) A realistic double many-body expansion (DMBE) potential energy surface for ground-state O₃ from a multiproperty fit to ab initio calculations, and to experimental spectroscopic, inelastic scattering, and kinetic isotope thermal rate data. *Mol Phys* 65(4):843–860
- Wang D, Stallcop JR, Huo WM, Dateo CE, Schwenke DW, Partridge H (2003) Quantal study of the exchange reaction for N+N₂ using an ab initio potential energy surface. *J Chem Phys* 118:2186

Chapter 3

Formation of vibrationally and rotationally excited molecules during atom recombination at surfaces

The kinetic modeling of plasmo-chemical systems to be realistic must account for the heterogeneous interaction of gas-phase with surfaces, i.e. the reactor walls or, in the case of atmosphere entry condition, the ceramic tiles on the nose of space vehicles used in thermal protection systems (TPS). The presence of the surface actually activates a number of different elementary processes, including atom/molecule elastic scattering, sticking, surface diffusion, dissociative adsorption, vibrational deactivation or recombination mechanisms. The assessment of the catalyticity of the surface (Herdreich et al. 2012) depends on the chemical interaction of gas-phase species with the atoms in the crystal lattice and on the morphology of the surface at a microscopic level. Experimentally the recombination coefficient γ is defined as the ratio of the number of particles undergoing recombination to the total number of particles that flow to the surface per time unit. Therefore γ assumes values from 0, for a non-catalytic, to 1 for fully-catalytic surface. However, to properly account for the gas-surface interaction, an effective recombination coefficient is defined as $\gamma \cdot \beta$, where β is the energy accommodation coefficient, i.e. the fraction of energy released in recombination that actually goes to the surface. β is usually taken as 1, however an actual inefficient coupling with the surface could instead determine the formation of molecules translationally hot or characterized by a significant amount of internal energy. In this context theoretical methods in molecular dynamics could be exploited to estimate the γ values for a number of systems, giving also an insight into the elementary mechanism of recombination and a complex information about the energy sharing among the different degrees of freedom of the system leading to non-equilibrium nascent ro-vibrational distributions that are relevant to a state-to-state kinetic approach.

For the recombination, two mechanisms are generally invoked: the direct, two-step Eley-Rideal (ER) and the indirect Langmuir-Hinshelwood (LH) mechanisms

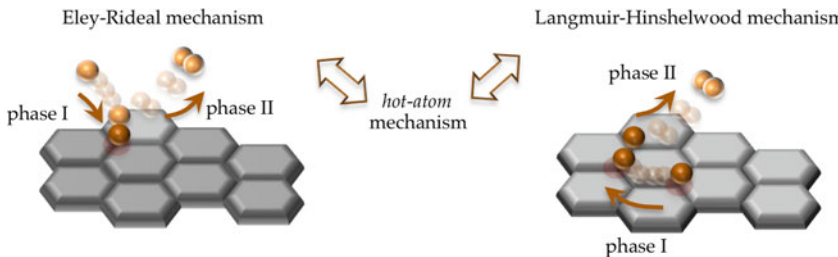
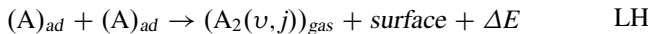
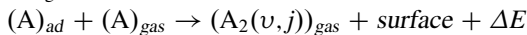


Fig. 3.1 Pictorial view of phases in surface-recombination mechanisms



Both models are to different extent exothermic, ΔE representing the energy released in desorption of molecule from the surface. In the ER recombination an atom in the gas-phase approaches the surface at a site where another atom is adsorbed and the interaction leads to molecule formation released back into the gas-phase. The LH mechanism, on the contrary, involves two atoms adsorbed at the surface, mainly physisorbed so as to allow their migration through the surface until the molecule formation and the eventual desorption (different phases are schematically depicted in Fig. 3.1). However these two mechanisms could be regarded as two ideal limits, the realistic heterogeneous recombination actually entailing a third scheme, the so-called *hot-atom* mechanism (Harris and Kasemo 1981). In this last case the molecule is formed in the interaction of an atom from the gas-phase, that comes to be weakly bound at the surface and can quite easily migrate on the surface, reacting before full thermalization (*hot atom*) with a second adsorbed atom.

The energetics of adsorption could be explained using a simplified 1D model for the interaction potential of a atom/molecule approaching a clean surface, depending only on the distance along the normal to the surface as in Fig. 3.2. The physisorption interactions, almost site-independent, is characterized by a shallow well, typically located at distances greater than 0.3 nm, and is due to the van der Waals or electrostatic dipole long-range attraction forces. The chemisorption entails the formation of a chemical bond (ionic or covalent) with atoms in the surface with wells of depths depending on the bond strength, in any case larger than 0.4 eV. Thus during the collision time of the gas-phase species hitting the surface the interaction can evolve through a minimum energy path from a transient state of physisorption to the chemisorption well and this last step might require overcoming a potential barrier.

The actual multidimensional gas-solid potential energy surface (PES) is shaped by the periodicity of the crystal substrate, affected locally by the presence of defects, sites occupied by impurities, and the specific-site interactions depend

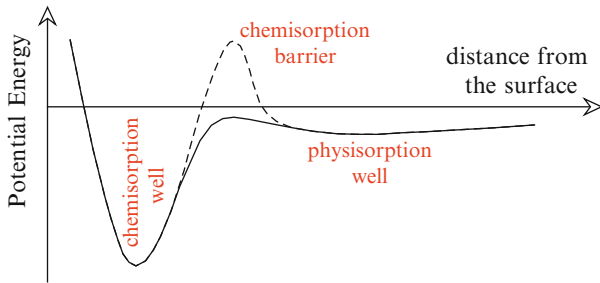


Fig. 3.2 Simplified picture of atom/molecule-surface interaction potential for chemisorption and physisorption

on the angular coordinates in the approaching trajectory. The modern quantum density function theory, within the generalized gradient approximation (DFT-GGA) and using a slab-supercell approach, offers the reasonable level of accuracy for the calculation of relevant configurations, relying on local or global interpolation methods to obtain a physically-sound mathematical representation of the surface with correct asymptotic behaviors (Gamallo et al. 2013). In the frame of analytical fitting schemes an adaptive periodic model of the LEPS (London-Eyring-Polanyi-Sato) potential, widely used in the gas-phase triatomic reactions, has been proposed and proved to be reliable in the dissociative/recombination dynamics of hydrogen at metallic surface. However a modified flexible PLEPS has been recently developed in order to accommodate the corrugated structure of the PES in case of heavy diatomic molecules. It should be also recalled the use of *reactive force field* potentials, bond-order based potentials constructed adding up all the contributions to the interaction. The approach is limited by the difficulty in evaluating bond-order parameters, accounting for the modification of the electronic structure in the bond-formation/breaking dynamics (Gamallo et al. 2013).

The state-specific recombination probability, $P_r^{v,j}(E, T_S)$, can be obtained in the framework of semiclassical (Billing 1982, 1990) or quantum wavepacket dynamics investigation, studying the dependence on the collision energy, E , and on the surface temperature T_S . The theoretical value of the thermal macroscopic recombination coefficient, γ , can be estimated by integrating the probability over the translational energy distribution of atoms in the gas phase, assuming this last as a Boltzmann one, and summing up over the final ro-vibrational distribution. It should be stressed that the recombination coefficient can be also estimated by modeling the surface kinetics in the frame of different approaches, as the mesoscopic approach, leading to asymptotic analytical solutions accounting for the dependence of γ on the surface characteristics (elementary process activation energies, density of adsorption sites, wall temperature) (Kim and Boudart 1991; Guerra 2007; Guaitella et al. 2011), or the MonteCarlo technique, used for the simulation of surface evolution (Reese et al. 2001).

In this Chapter a survey is presented of the results obtained in the investigation of ro-vibrationally excited molecules formed in heterogeneous atomic recombination, selecting few systems of interest in technological application: hydrogen at graphite and crystal metals surfaces, due to their relevance in plasma reactors for nuclear fusion (Čadež et al. 2008; Rutigliano and Caciato 2011) and interstellar chemistry (Latimer et al. 2008; Bourlot et al. 2012), and of oxygen and nitrogen at silica surface, relevant to the estimation of heat overload on the nose of space vehicles during the Earth re-entry phase. In the last section of this Chapter a brief description is given of a different phenomenological method proposed by Molinari and Tomellini (2006a) and Tomellini (2005) for describing the recombination of atomic species on different surfaces.

3.1 Hydrogen on Graphite Surface

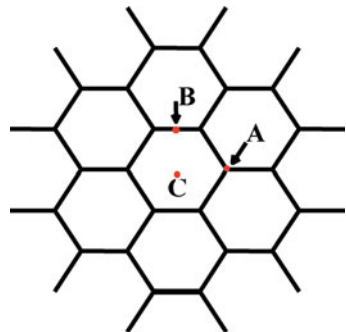
The catalytic activity of the graphite surface in favoring the recombination of adsorbed hydrogen atoms has been deeply investigated from a theoretical point of view by using different approaches (Rutigliano et al. 2001; Sha et al. 2002; Ree et al. 2002; Morisset et al. 2004, 2005; Hornekær et al. 2006; Rutigliano and Caciato 2008), modeling the graphite surface with a period slab approach (Farebrother et al. 2000; Sha and Jackson 2002; Ferro et al. 2003), coronene or graphene (Jeloaica and Sidis 1999; Morisset et al. 2003; Sizun et al. 2010; Bonfanti et al. 2011). The temperature of the surface is critically relevant to different environments, very low temperatures (10–100 K) characteristic of studies of hydrogen recombination on dust grains in interstellar medium, while higher values (500–800 K) are considered in many plasma applications, including fusion. Another point is the investigation on isotopic effects (Caciato and Rutigliano 2006; Rutigliano and Caciato 2008), expected to be significant due to the soft phonon structure of graphite, in fact fusion reactors usually operate with deuterium-tritium.

The ER recombination of atomic hydrogen on (0001) graphite has been studied in the framework of the semiclassical collisional method (Billing 1982, 1990). The method assumes the dynamics of gas-phase species described classically by solving the relevant Hamilton's equations of motion, while the phonons modes of the surface are treated quantum-mechanically. The coupling between the classical degrees of freedom with the phonons dynamics is made via a time-dependent effective potential V_{eff} , of the mean-field type, entering the Hamiltonian

$$H_{\text{eff}} = \frac{1}{2} \sum_{i,\gamma} \frac{1}{m_i} P_{i,\gamma}^2 + V_{\text{H}_2}(\mathbf{r}) + \Delta E_{ph} + V_{\text{eff}} \quad (3.1)$$

$P_{i,\gamma}$ the γ th component of momentum of atom i of mass m_i , V_{H_2} the intramolecular potential of non-interacting H_2 and ΔE_{ph} the energy exchange with surface phonons, directly obtained from the transition probabilities for the excitation/deexcitation phonon processes. The effective potential is defined as the

Fig. 3.3 Graphite surface structure and adsorption sites.
A: top, B: bridge, C: hollow



expectation value of the interaction potential over the total phonon wave function corresponding to the surface temperature, i.e.

$$V_{\text{eff}}(t, T_S) = \langle \psi_{ph} | V_{int} | \psi_{ph} \rangle \quad (3.2)$$

The time evolution of the wavefunction for the phonon states is obtained by solving the time-dependent Schrödinger equations (in the second quantization scheme) in the interaction potential for atoms in the lattice, treated as independent harmonic oscillators. It should be noted that the semiclassical model does not account for quantum effects in the dynamics, as the low-kinetic energy tunneling of the activation barrier.

A semi empirical PES has been constructed for the hydrogen-graphite system, smoothly switching from H₂- to H-graphite interaction potential according to the H-H interatomic separation (Rutigliano et al. 2001). H₂ is physisorbed on graphite in the perpendicular geometry (for on-top perpendicular configuration the physisorption well depth is 51 meV), as confirmed both by experimental and theoretical results (Mattera et al. 1980; Novaco and Wroblewski 1989), the adsorption energy being negligible regardless the adsorption site. On the contrary the H-graphite interaction is characterized by a strongly site-dependent chemisorption, the most favorable interaction occurring on top of carbon atom, i.e. at the lattice site A in Fig. 3.3, at a distance of 1.58 Å with a chemisorption well-depth of 0.52 eV, modeled with the potential from Jeloaica and Sidis (1999) obtained performing DFT-GGA cluster calculations for a coronene-like system.

The adsorbed H atom is placed at the equilibrium distance and in thermal equilibrium with the surface at the temperature T_S , the molecular dynamic code simulates the H atom in the gas phase impinging on the surface with polar angles ($\theta; \phi$) with a kinetic energy E_{kin} , giving the recombination probabilities, the nascent vibrational and rotational distribution of formed H₂ molecules. Furthermore the semiclassical probability of other competing inelastic exit channels, activated in the interaction with the surface, are estimated

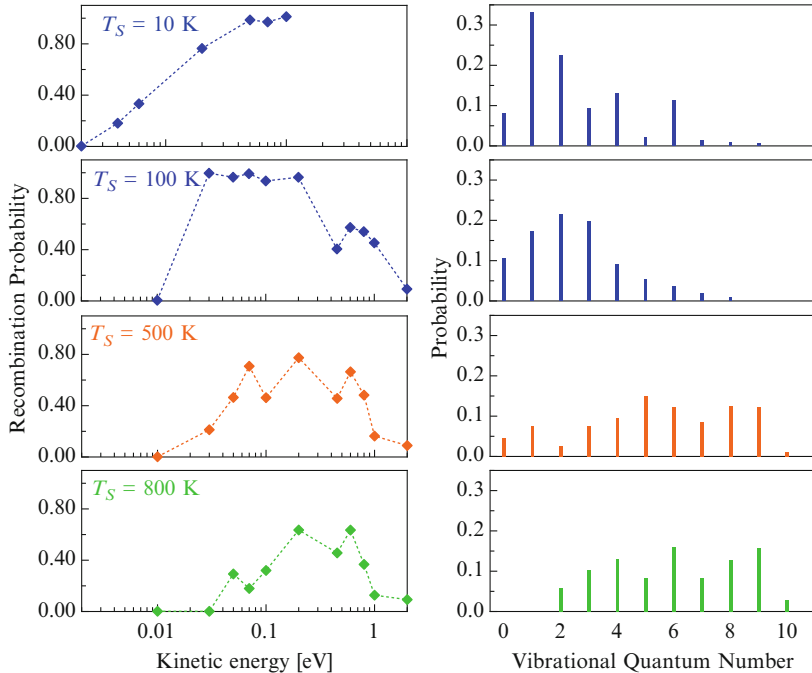
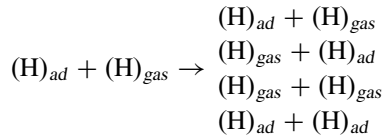


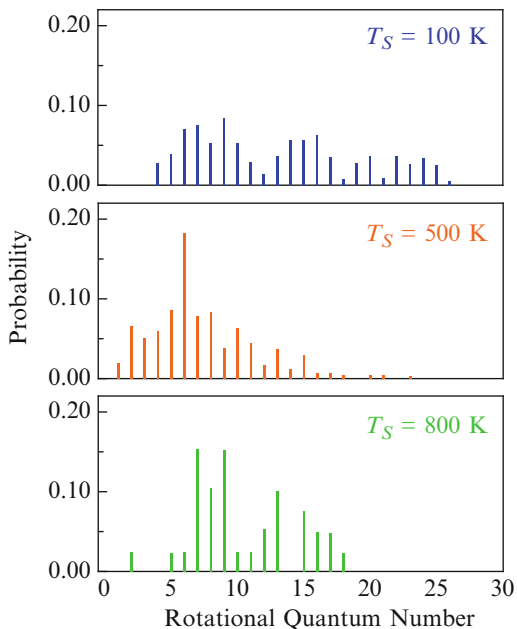
Fig. 3.4 (left) Recombination probability as a function of incident kinetic energy of the impinging atom and (right) vibrational distributions of H_2 formed at graphite surface, through ER mechanism, at $E_{\text{kin}} = 0.07\text{ eV}$ for different values of the surface temperature. $T_S = 10\text{ K}$ (Rutigliano et al. 2001), $T_S = 100\text{--}800\text{ K}$ (Rutigliano and Caciato 2008)



The regime considered in these studies is near thermal kinetic energies, with neutral atoms and molecules in their ground electronic states, and surface damage processes relevant in the investigation of plasma reactor walls performances, as physical sputtering and chemical etching, are not considered.

The surface temperature is quite effective on the recombination probability, as depicted in Fig. 3.4. Results for $T_S = 10\text{ K}$ (Rutigliano et al. 2001) show a sharp increase in the threshold region $E_{\text{kin}} \sim 0.04\text{ eV}$, reaching the limiting unitary value that remains constant up to 0.1 eV . Further increase in the T_S value results in the shift of the kinetic energy threshold to higher values and in a decrease of the probability value. The analysis of the trajectories shows that at high surface temperatures the atom adsorbed at the surface gains enough translational energy in the interaction

Fig. 3.5 Rotational distributions of H_2 formed at graphite surface, through ER mechanism, at $E_{kin} = 0.07$ eV for different values of the surface temperature (Rutigliano and Caciato 2008)



with the gas-phase atom to favorably escape from the surface before recombination. For higher kinetic energies above 0.2 eV, the competing inelastic channels become more effective, inhibiting the recombination.

The energy distribution analysis shows that a large fraction of the exothermic energy released in H_2 formation is transferred to vibration. The corresponding nascent distributions, shown in Fig. 3.4 at the impact kinetic energy of 0.07 eV and obtained summing up the contribution coming from the rotational ladder, are significantly excited, the non-equilibrium character being emphasized at high surface temperatures, with depletion of the first levels in favor of the medium and tail regions of the distribution. The opposite is observed for the rotational distributions (Fig. 3.5), higher rotational levels being significantly populated at lower surface temperature values, when the rotation-vibration coupling is more effective.

The existence of isotopic effect in recombination have been investigated (Caciato and Rutigliano 2006, Rutigliano and Caciato 2008), studying the formation of D_2 and HD molecules and considering the heteroisotope dimer formation from two different dynamical paths



In Fig. 3.6 the temperature profile of the recombination coefficient, γ , has been displayed for H_2 and its heavier isotopic variants at $T_S = 500\text{ K}$. The recombination is progressively less effective along the series H_2 , DH , D_2 , HD , corresponding to

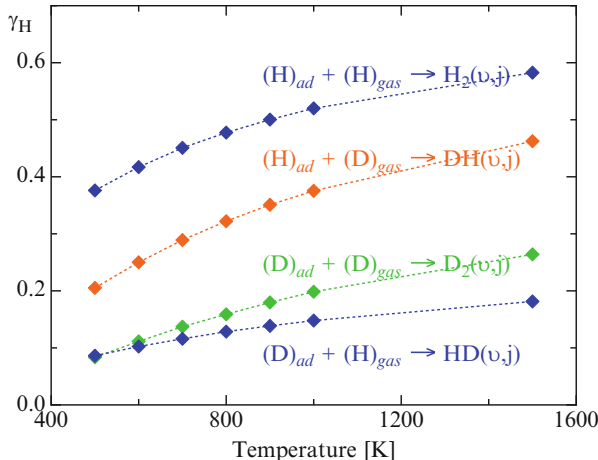


Fig. 3.6 Recombination coefficient $\gamma(T_S, T_{\text{gas}})$ as a function of gas temperature, leading to the formation of H_2 , D_2 (Cacciatore and Rutigliano 2006) and HD (Rutigliano and Cacciatore 2008), through ER mechanism on graphite surface, at $T_S = 500$ K

a shift in the kinetic energy threshold value for the corresponding recombination probability. Another significant evidence is that recombination is enhanced when the lighter atom is chemisorbed at the surface, in fact this is expected, being the energy loss in surface-phonon excitation processes for deuterium larger and thus reducing the available energy for desorption. The energetics of the two paths is also different, with a significant transfer to vibration in the case of HD recombination, thus leading to pumped ro-vibrational distributions with respect to the DH case, where the newly formed molecules are translationally hot, though the energy partitioning among internal degrees of freedom still favors the vibration.

Though most of theoretical studies on H_2 formation on graphite are devoted to ER mechanism, the dynamics of HL recombination has been proved to be efficient in originating highly vibrationally excited molecules. The mechanism, entailing the migration of recombining atoms on the surface, is governed by the physisorption at rather large distance from the surface, the process being, differently from chemisorption, not hindered by any potential barrier, thus favoring the sticking of gas-phase atoms. The recombination probability has been calculated in a 3D quantum dynamics, following the temporal propagation of a three-dimensional wave-packet on a semi empirical model PES, characterized by a physisorption well of 8 meV at 4.18 Å, and considering kinetic energies from 2 to 50 meV (Morisset 2004; Morisset et al. 2004).

The balance of the energy available, accounting for the kinetic term and the energy released in H_2 formation ($D_0 = 4.475$ eV), and energetic cost for desorption, leaves a large fraction actually stored in the internal degrees of freedom of the molecule and therefore leads to non-equilibrium highly excited nascent rovibrational distributions, displayed in Fig. 3.7 for $E_{\text{kin}} = 8.16$ meV. The rotational

Fig. 3.7 Rotational (j even) and vibrational population distributions of H_2 formed in the LH recombination process at $E_{kin} = 8.16$ meV (Morisset et al. 2004)

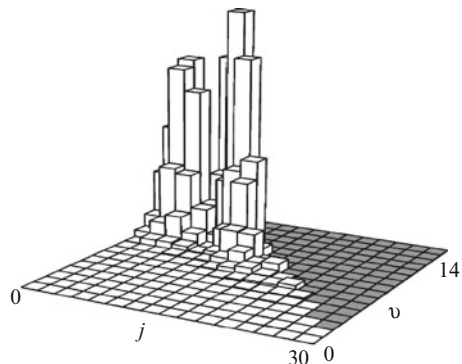
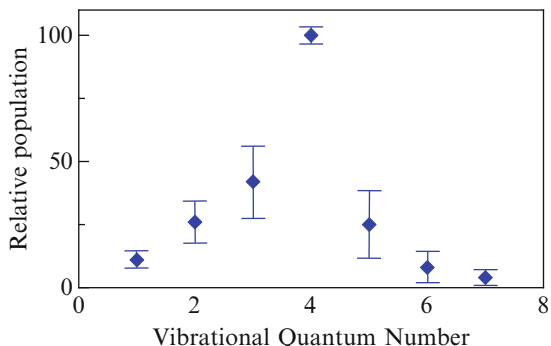


Fig. 3.8 Experimentally estimated nascent vibrational distribution for HD formed on a HOPG surface at 15 K (Latimer et al. 2008)



distribution is broad and centered around $j = 6$, while highest j values are rapidly depleted due to coupling with translation. The vibrational excitation is very effective leading to a strong non-equilibrium distribution peaked at high vibrational quantum numbers.

In Fig. 3.8 the nascent vibrational distribution (Latimer et al. 2008) of $\text{HD}(v)$ molecule formed at catalytic HOPG (Highly Oriented Pyrolytic Graphite) surface at 15 K is reported, the relative population being estimated from ro-vibrational distributions ($1 < v < 7$ and $0 < j < 6$) experimentally detected with REMPI (resonance Enhanced Multi-Photon Ionisation) technique. Though not directly comparable with theory, results show that molecules formed in the recombination possess a considerable internal excitation, confirming the general conclusions from different theoretical investigations.

3.2 Hydrogen on Metals

The recombination/relaxation dynamics of hydrogen on copper surface has been studied in the past in the frame of semiclassical dynamical model (Hansen and Billing 1997; Caciato and Billing 1990).

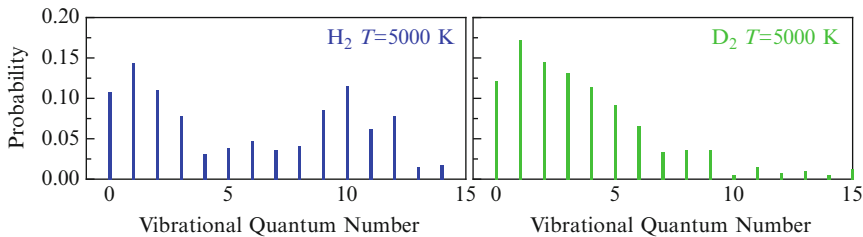
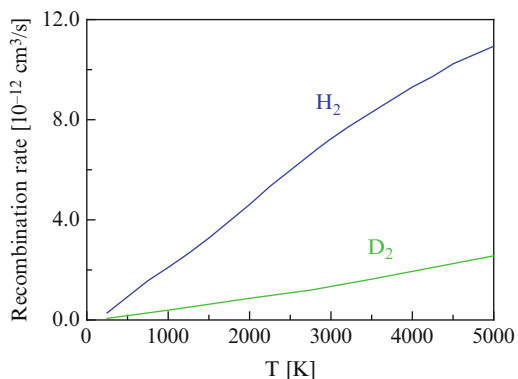


Fig. 3.9 Normalized vibrational contributions to the rate constant for H_2 and D_2 recombination at copper surface, at the translation temperature of gas-phase H atoms $T = 5,000 \text{ K}$ and at surface temperature $T_s = 300 \text{ K}$ (Hansen and Billing 1997)

Fig. 3.10 Recombination rates for hydrogen and deuterium as a function of temperature, at surface temperature $T_s = 300 \text{ K}$ (Hansen and Billing 1997)



In Fig. 3.9 the vibrational distributions for recombination on Cu(100) crystal, through ER mechanism, are shown. The interaction potential surface, reconstructed within the EDIM (embedded diatomics in molecules) model, was characterized by a chemisorption well of 0.6 eV and a barrier of 0.5 eV, allowing in the trajectory simulation the approach of gas-phase atom along the coordinate perpendicular to the surface. The adsorbed atom is in thermal equilibrium with the surface and is placed randomly within the aiming area at a distance characterizing the physisorption condition, in fact for chemisorption the recombination probability was found to be severely reduced. Furthermore the analysis of the fractional energy distribution to the available degrees of freedom, enlightens the role of phonon excitation in the realistic description of the dynamics.

In Fig. 3.10 the recombination rate for hydrogen and deuterium are displayed as a function of the gas temperature for a surface temperature of 300 K. The large differences could be explained in terms of the strong sensitivity of the recombination to the available kinetic energy, in fact for the heavier deuterium atom the adsorption is more favorable, reducing the free kinetic energy. Different vibrational distributions originates as it can be appreciated in Fig. 3.9, where the normalized vibrational contributions for the two isotopes are displayed at $T = 5,000 \text{ K}$.

The ER recombination of atomic hydrogen on a clean, perfect W(001) tungsten crystal has been theoretically investigated in the frame of a fully three-dimensional semiclassical collisional approach (Rutigliano and Caciato 2011), modeling the hydrogen-tungsten interaction at the most favorable absorption site, four-fold (4F) with an accurate PES, obtained in the tight binding approximation, the potential being the sum of a Born-Mayer-type term, accounting for H-H and H-W repulsive interactions, and of a *band* contribution, for the change in local density of states width on substrate atoms due to the adsorption of hydrogen (Forni et al. 1992a,b). This PES, characterized by a chemisorption energy of 3.03 eV at equilibrium distance from the surface of 0.52 Å, well fits the spectroscopic constants for adsorbed chemical species and suitably describes a metallic substrate with electron density strongly delocalized with respect to valence-bond-based LEPS. Furthermore the dynamical coupling between the tungsten phonons and the adsorbed hydrogen atoms has been accounted, in fact the study of H recombination on Cu (Caciato and Billing 1990) have demonstrate the role played by lattice phonons and electron-hole excitation mechanism in the bond formation or breaking at the surface.

The semiclassical ER recombination probability, calculated for an impact kinetic energy of gas-phase hydrogen atom in the interval 0.05–5.0 eV, shows that two collisional regimes can be identified, for E_{kin} below 2.5 eV the recombination governs the surface dynamic, while at higher energies the adsorption/desorption scattering becomes the most relevant process. The recombination is a direct, single step, largely exothermic process and the energy released is shared among the degrees of freedom of desorbing H₂, mainly transferred to the translational motion and equally activating the rotation and vibration, while in this case the exchange with surface phonons is small.

In Fig. 3.11 the vibrational distributions for different kinetic energy values are reported, showing that while for low values the distribution is peaked at $v = 0$ and only the first three levels are significantly populated, the only ones energetically accessible, increasing the energy a broader distribution appears populating higher vibrational levels up to $v = 7$.

The recombination on hot polycrystalline tungsten filament exposed to a flow of partially dissociated hydrogen in a cell has been experimentally investigated (Markelj and Čadež 2011) and the H₂ vibrational population has been measured by means of the vibrational spectroscopy based on low-energy-threshold dissociative attachment process. In Fig. 3.12 theoretical and experimental distributions are compared, showing differences for high vibrational quantum numbers. However it should be pointed out that semiclassical recombination is estimated on a perfect crystal and on the preferential absorption site, the (4F), while with a real polycrystalline surface also the other non-equivalent sites, characterized by lower adsorption energies, on W(001), W(110) and W(111) crystals are simultaneously involved. Furthermore the deconvolution of the spectrum of H⁻ yield, showed evidences of ro-vibrational populations well described by Boltzmann distributions with characteristic temperatures higher than those for recombination on copper, suggesting the role of recombination mechanism involving a *hot* atom interacting with adsorbed hydrogen at surface

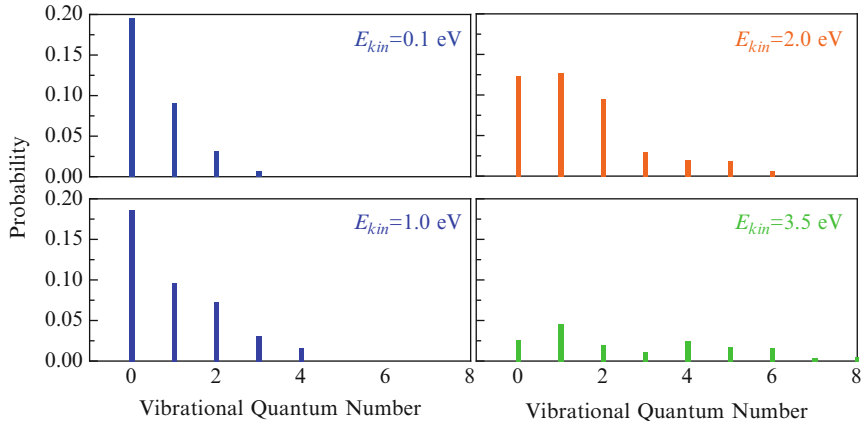


Fig. 3.11 Nascent vibrational distribution of H_2 recombined at tungsten surface ($T_S = 500 \text{ K}$), at different values of the collision energy, for the atom impinging the surface (Rutigliano and Caciato 2011). The distribution is not normalized, giving the actual value for the vibrational-level-specific recombination probability

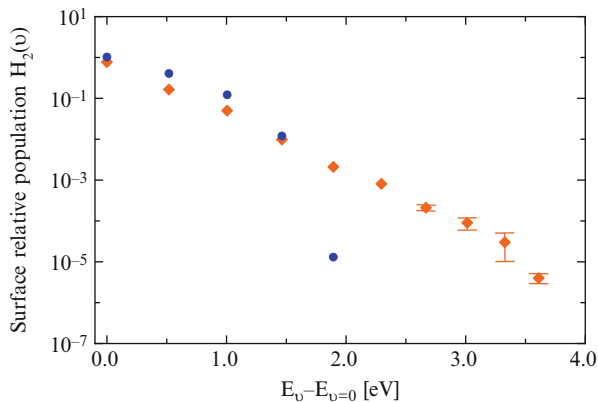


Fig. 3.12 Relative H_2 vibrational distribution formed through ER mechanism on $\text{W}(001)$ surface (Rutigliano and Caciato 2011) (closed circles), compared with experimental results (closed diamonds) (Markelj and Čadež 2011)

sites with different desorption energies (Markelj and Čadež 2011). Finally the theoretical analysis of the trajectories reveals that the molecules are formed close to the surface, thus the discrepancy with experiments could result by a distribution detected after multiple gas-surface and gas-phase collisions.

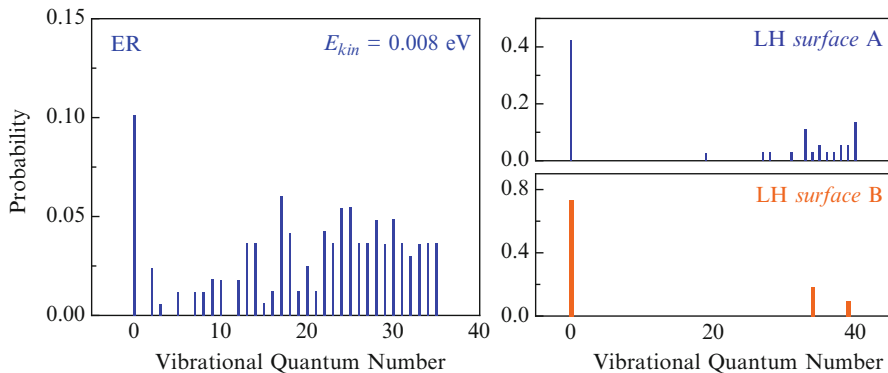


Fig. 3.13 Vibrational population distribution of O_2 molecules formed by atomic recombination at β -cristobalite surface, $T_S = 1,000$ K, for ER mechanism at surface B (Balat-Pichelin et al. 2003b) and for LH mechanism at surface A and B (Caciato et al. 1999)

3.3 Oxygen and Nitrogen on Silica

The recombination dynamics of oxygen atoms on β -cristobalite, the stable phase of silica at $T_S = 1,000$ K, has been theoretically investigated with semiclassical (Caciato et al. 1999) and classical trajectory (Arasa et al. 2009; Morón et al. 2011) methods.

Both ER and HL mechanisms have been considered in the frame of the semi-classical collisional theory, constructing an empirical PES for the O/O_2 -silica interaction (Caciato et al. 1999).

The dynamics of gas-phase atom interacting with a oxygen atom randomly adsorbed at the surface unit cell, at $T_S = 1,000$ K, shows that in the low kinetic energy regime the probability for both the incoming and the adsorbed atom to be reflected from the surface into the gas phase is the most relevant process. The ER recombination probability is rather low, being practically prevented at energies higher than 3.8 eV, due to the increasing importance of the competing channels. The fraction of the reaction exothermicity transferred as heat to the surface is small, especially in the low kinetic energy regime, and O_2 molecules are formed in highly excited vibrational levels, as can be appreciated in Fig. 3.13. The LH mechanism plays a minor role at high surface temperatures. Considering different structures of the top-most crystal layer, i.e. a silica surface covered by bonded oxygen atoms (surface A) and with unoccupied silicon sites (surface B), the recombination probability, for two oxygen atoms placed on the top of silicon atoms of the surface, is higher by a factor 3 for surface A (0.11) with respect to surface B ($3.85 \cdot 10^{-2}$) as also the energy flow to the surface. In both cases the oxygen molecules are mainly formed in the ground vibrational level, though the pumping of highly excited vibrational levels cannot be neglected (Caciato et al. 1999) (Fig. 3.13).

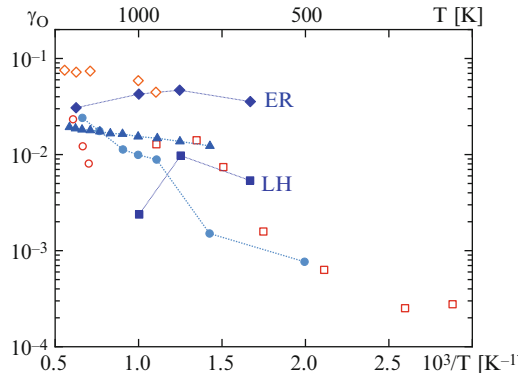


Fig. 3.14 Temperature profile of recombination coefficient of oxygen at β -cristobalite surface. (close squares) semiclassical LH recombination (Balat-Pichelin et al. 2003b), (close diamonds) semiclassical ER recombination (Balat-Pichelin et al. 2003b), classical trajectory ER recombination (close circles) (Arasa et al. 2009) and (close triangles) (Morón et al. 2011). Experiments: (open diamonds) (Balat-Pichelin et al. 2003b), (open circles) (Scott 1983), (open squares) (Greaves and Linnett 1959)

In Fig. 3.14 the recombination coefficients γ estimated with different theoretical approaches (Cacciatore et al. 1999; Balat-Pichelin et al. 2003b; Arasa et al. 2009) are compared with experimental values (Greaves and Linnett 1959; Scott 1983; Balat-Pichelin et al. 2003a,b). The semiclassical recombination compared with experimental results (Greaves and Linnett 1959; Balat-Pichelin et al. 2003b) indicates the mechanism-switch from LH to ER when the surface temperature increases, the ER mechanism governing the dynamics for temperatures in the range 800–2,000 K, while in the lower temperature region, 600–800 K, the LH results predict experimental γ (Greaves and Linnett 1959).

However the dynamical results for ER recombination obtained by classical trajectory method (Arasa et al. 2009; Morón et al. 2011), assuming a quasithermal condition $T \approx T_s$, predict a lower recombination coefficient, the discrepancy to be attributed to the different topology of the new PES, interpolating DFT ab-initio results, and also to the selected initial position of adsorbed oxygen atom.

It should be mentioned that the dynamics of oxygen on quartz surface has been recently theoretically investigated, the recombination coefficient being found both theoretically and experimentally significantly lower than in the case of β -cristobalite substrate (Bedra et al. 2006; Zazza et al. 2012).

The ER recombination of nitrogen at silica surface has been studied, using an accurate DFT calculations for N and N_2 interactions with clusters cleaved form the β -cristobalite crystalline structure and constructing a LEPS fitting the ab-initio results. The LEPS predicts a binding energy for N atoms chemisorbed on top of active silicon atom of 2.72 eV at equilibrium distance from the surface of 1.65 Å, in good agreement with DFT results in Arasa et al. (2005). The semiclassical dynamics shows that the recombination process is favored only in a narrow interval of impact

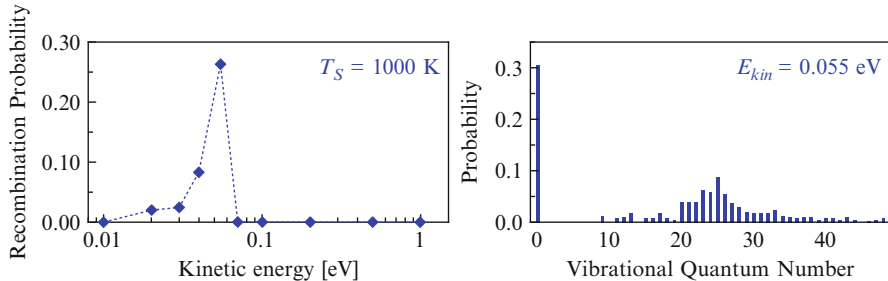


Fig. 3.15 (left) Recombination probability as a function of impact kinetic energy of atom impinging the surface and (right) vibrational population distribution of N_2 formed through ER recombination at silica surface, at temperature $T_S = 1,000 \text{ K}$ (Rutigliano et al. 2006)

energies peaked at 0.055 eV, increasing the energy the chemisorbed atom remains preferably trapped at the surface and the probability becomes vanishingly small, as shown in Fig. 3.15.

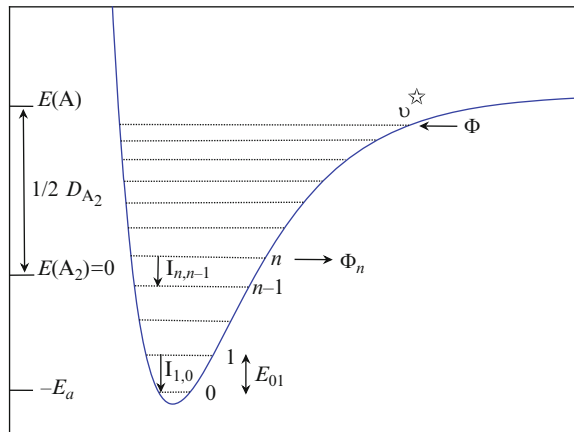
In the same figure the nascent vibrational profile of N_2 molecules at the kinetic energy of the peak is reported. The distribution has a sharp maximum at $v = 0$ while a larger number of molecules present are broadly formed in the medium-lying vibrational levels. The trajectory analysis clarified that the recombination takes place when the two atoms are close to the surface, thus coupling strongly with surface phonon modes and transferring only a small energy fraction to the vibrational degree of freedom. The excitation of rotational levels is very inefficient in the whole impact-energy range. The estimated value for the recombination coefficient is $\gamma = 3.99 \times 10^{-2}$. A direct comparison with experiments is not straightforward, being the surface other than β -cristobalite, i.e. quartz (Marshall 1962) or pure silica (Kim and Boudart 1991), however the measured value of γ , at $T_S = 1,000 \text{ K}$, is lower than 10^{-3} , suggesting the existence of an activation barrier to recombination.

It should be noted that results reported in Fig. 3.15 do not take into account the possibility of heterogeneous formation of $\text{N}_2(A^3\Sigma_u^+)$ metastable state, playing an important role in the nitrogen afterglow (Petrovic et al. 2001; Guerra et al. 2003; Colonna et al. 2015).

3.4 The Vibrational Energy Distributions Functions in Catalysis: A Phenomenological Approach

The vibrational energy distribution function plays an important role also in the field of the Heterogeneous Catalysis, assuming nowadays a strategic importance in plasma chemistry. Here we briefly discuss the main ideas, which brought these two

Fig. 3.16 Schematic representation of the vibrational ladder in the adsorption potential well. The case of atom recombination is considered. In the drawing E_a is the adsorption energy, Φ is the adsorption (recombination) flux of ad-atoms, $\frac{1}{2}D_{A_2}$ is the binding energy of the diatom (A_2). The vibrational energy is measured from the bottom of the well and the adsorption energy of the atom is equal to $E_a + \frac{1}{2}D_{A_2}$



topics into close contact and the way they have been developed in order to describe experimental data on reaction kinetics.

The first step of a catalytic reaction taking place on a solid surface is the accommodation of the reacting species at the adsorption sites. This process is ruled by the dissipation of the excess energy of the ad-species into the solid, the excess energy depending on the depth of the adsorption potential well. Competition between energy disposal and adsorption of reacting species may lead, under catalytic conditions, to non-equilibrium vibrational energy distribution functions of the ad-species (Molinari and Tomellini 2000). To be specific, for a mobile ad-layer the ad-species are considered as a 1D quantum oscillator along the normal to the surface (z degree of freedom), which behaves as a free particle on the surface plane (x,y degrees of freedom). On this basis, the vibrational energy of the ad-species trapped in the adsorption potential well acquires importance to gain insight into the dynamics of the catalytic reaction. In other words, a complete description of the kinetics of a catalytic reaction under steady state conditions requires the knowledge of the energy distribution function of the reacting ad-species, i.e. of how the species are distributed in energy in the adsorption potential well (Fig. 3.16).

The interplay between the vibrational distribution functions and the reaction rate has been the main topic of a series of papers, published during the last decades (Molinari and Tomellini 2000, 2001, 2002, 2006a,b, 2010a,b; Tomellini 2005), aimed at describing experimental data by means of theoretical modelling. The approach discussed in Tomellini (2005) and Molinari and Tomellini (2006b) employs rate equations for the population (σ_n) of the ad-species in the anharmonic vibrational ladder according to the following (see Fig. 3.16 for the notation):

$$\dot{\sigma}_n = I_{n+1,n} - (\Phi_n + I_{n,n-1}) \quad (3.3)$$

where Φ_n is the flux of ad-species which leave the n -level of the ladder owing to recombination (i.e. reaction and desorption), $\Phi = \sum_{j=0}^{v^*} \Phi_j$ is the total reaction

rate and $I_{n,n-1} = (K_n + P_n^r)\sigma_n - (K_{-(n-1)} + P_{(n-1)}^f)\sigma_{n-1}$, where K_n and $K_{-(n-1)}$ are direct and reverse rate constants for quantum exchange with the solid (thermal bath), respectively. In the equation for $I_{n,n-1}$ the pseudo first-order rate coefficients P_n^f and P_n^r are given by $P_n^f = \sum_{s=1}^{v^*} P_{n,s \rightarrow n+1,s-1}\sigma_s$ and $P_n^r = \sum_{s=0}^{v^*-1} P_{n,s \rightarrow n-1,s+1}\sigma_s$, where $P_{n,s \rightarrow n+1,s-1}$ is the rate constant for the VV quantum scattering (Tomellini 2005; Molinari and Tomellini 2006b). The steady state solution of Eq. (3.3) reads (Tomellini 2005)

$$\sigma_n = \sigma_0 e^{\beta a_n} \prod_{k=1}^n \gamma_k + \sum_{j=1}^{n-1} \left[\alpha_j I_{j,j-1} e^{\beta(a_n-a_j)} \prod_{k=j+1}^n \gamma_k \right] + \alpha_n I_{n,n-1} \quad (3.4)$$

$$\gamma_n = \frac{e^{-\beta E_{01}} + \frac{1}{K_n} \sum_{s=0}^{v^*-1} P_s(n) \sigma_{s+1} e^{-\beta(a_{s+1}-a_s)}}{1 + \frac{1}{K_n} \sum_{s=0}^{v^*-1} P_s(n) \sigma_s} \quad (3.5)$$

where $\beta = \frac{1}{k_B T}$, $\alpha_n = \frac{1}{K_n + P_n^r}$, $E_n = nE_{01} - a_n$ is the energy spectrum of the anharmonic oscillator ($a_0 = a_1 = 0$) and the short notation $P_s(n) = P_{n,s \rightarrow n-1,s+1}$ has also been used. At the steady state the currents, $I_{n+1,n} = \sum_{j=0}^n \Phi_j$, depend on the σ_s 's through the recombination fluxes Φ_j . In fact, on the basis of the associative model the relationship holds: $\Phi_k = \sigma_k \sum_{m=\mu(k)}^{v^*} Z_{mk} \sigma_m (1 + \delta_{mk})$ where δ_{mk} is the Kronecker delta, Z_{mk} is the rate constant for recombination and the $\mu(k)$ function ensures energy conservation (Molinari and Tomellini 2000; Tomellini 2005). Besides, also the $\alpha_n = \frac{1}{K_n + P_n^r}$ term depends on the σ_n 's. Accordingly, the populations should be computed by solving the non-linear system of algebraic equations (3.4) and (3.5) in the σ_n unknowns ($n = 1, 2, \dots, v^*$). In addition, for the complete determination of the vibrational distribution the σ_0 surface density is also needed. To this end one more equation is required, that is the balance between the adsorption and the desorption rates at steady state. For example, in case of random, non-precursor mediated adsorption of atoms this equation reads, $J(1 - \sigma) = \sum_k \Phi_k = \Phi$.

From the discussion above it stems that the determination of the population is a formidable task which cannot be accomplished analytically. However, solution in closed form can be attained by employing approximations, leading to more manageable expressions certainly suitable to interpret experimental data. By assuming rate coefficients independent of quantum numbers Eq. (3.4) gives (Tomellini 2005; Molinari and Tomellini 2006b)

$$\sigma_n = \sigma_0 \gamma^n e^{\beta a_n} + \alpha \sum_{j=1}^n [I_{j,j-1} \gamma^{n-j} e^{\beta(a_n-a_j)}] \quad (3.6)$$

where $\gamma = \gamma_B + \frac{P_{VV}}{K} \alpha \sum_{s=0}^{v^*-1} e^{-\beta(a_{s+1}-a_s)} I_{s+1,s}$ and $\gamma_B = e^{-\beta E_{01}}$. Equation (3.6) shows that the vibrational distribution function is made up of two terms. The first

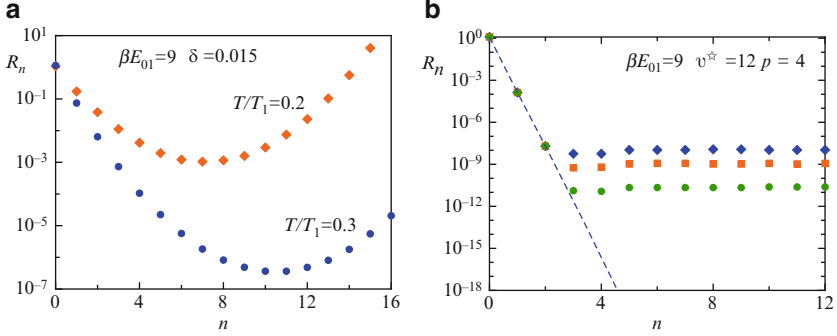


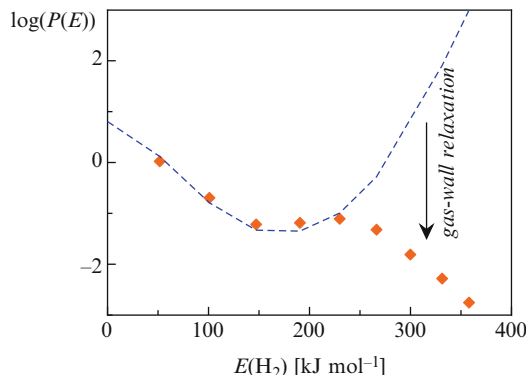
Fig. 3.17 Typical behavior of the vibrational distribution, $R_n = \frac{\sigma_n}{\sigma_0}$, as given by Eq. (3.7). In this equation, the first term is related to the VV process and requires $P_{VV} \neq 0$; the second one is proportional to the reaction rate. (a) Non-equilibrium distribution function in the case of prevailing VV scattering process ($K \rightarrow 0$) for a system of Morse oscillators with anharmonicity $E_{01}\delta(a_n = n(n-1)E_{01}\delta)$. This distribution has been reported for two values of the T/T_1 ratio. (b) Non-equilibrium distribution function in the case of prevailing VL scattering process ($\gamma = \gamma_B$). Parameters values are: $\Phi/\sigma_0 = 0.2 \text{ s}^{-1}$ (diamonds); 10 s^{-1} (squares); 100 s^{-1} (circles)

is strongly dependent on the VV process; in fact it reduces to the Boltzmann distribution function, $\sigma_0 e^{\beta(nE_{01}-a_n)}$ provided $P_{VV} = 0$. The second is proportional to the currents of ad-species “moving down” the vibrational levels of the ladder owing to the quantum exchange with the solid (energy dissipation into the bath, VL process). It is worth stressing that in the computation above both VV and VL processes are operative. The importance of these two processes, on the shape of the distribution function, is worthy of note. In fact, in the limiting case $K \rightarrow \infty$ the distribution function gives the Boltzmann distribution. On the other hand, in the case of negligible energy disposal to the solid, $K \rightarrow 0$, Eqs. (3.4) and (3.6) (owing to the conservation of the number of vibrational quanta in the VV process) give the distribution derived by Treanor et al. (1968), that is, for an anharmonic ladder, $\sigma_n = \sigma_0 e^{-\beta a_n} \gamma^n = \sigma_0 e^{-\beta[nE_{01}\frac{T}{T_1}-a_n]}$ with $T_1 > T$ the vibrational temperature. Typical behaviors of the vibrational distribution function, in the case of prevailing VV or VL quantum exchanges, have been displayed in Fig. 3.17a, b. Noteworthy the shapes of these distributions are quite different.

Equation (3.6) has been employed for describing experimental data on the kinetics of reactions at solid surfaces. To this end, the expression of the distribution is further simplified by retaining the leading term in the sum entering Eq. (3.6) (i.e. at $j = n$) and considering a few reaction channels, only. For instance, in the case of diatom recombination from level $n = 0$ and $n = p$, the energy distribution function becomes (Molinari and Tomellini 2006b)

$$\begin{aligned} \sigma_{n \leq p} &= \sigma_0 \gamma^n + \frac{1}{2} \alpha \Phi \\ \sigma_{n > p} &= \sigma_0 \gamma^n + \alpha \Phi \end{aligned} \quad (3.7)$$

Fig. 3.18 Vibrational distribution function of H_2 (gas) produced by recombinative desorption at a Ta surface:
 $P(E) = N_{\text{H}_2}(E)/N_{\text{H}_2}$. Experimental points (*close diamonds*) and Treanor distribution function (*dashed line*) of the H ad-atoms (From Molinari and Tomellini 2001)



where Φ is the recombination rate. The relevance of Eq.(3.7) for catalysis is discussed in the following. Let us consider the case (quite frequent) of prevailing VL scattering. The rate constant for energy disposal in a VL process is usually in the range 10^9 – 10^{12} s⁻¹ implying low values of the $\alpha\Phi$ term in Eq. (3.7). However, since in catalytic processes the important reaction channels usually involve ad-species in high energy levels, the term $\alpha\Phi$ can be the dominant one for the performing levels, namely $\alpha\Phi \gg \sigma_0\gamma^n$ in Eq. (3.7). Moreover, the reaction rate depends on vibrational distribution function through a relationship of the form $\Phi \approx Z\sigma_0\sigma_p$, where σ_0 is a function of the reaction rate as well (Molinari and Tomellini 2006b).

The present modeling has been employed for describing experimental data on the kinetics of various reactions at solid surfaces. The approach actually deals with a reaction mechanism intermediate between the ER (Eley Rideal) and the LH (Langmuir Hinshelwood); it has been named LH*, that is a multilevel hot ad-species mechanism (Molinari and Tomellini 2001). Equation (3.7) has been used to interpret experimental data on H recombination on solid surfaces (Molinari and Tomellini 2001), the D-atom abstraction by H-atoms (Molinari and Tomellini 2006a), and the oxidation of CO (Molinari and Tomellini 2002).

For H recombination on metal surfaces, the vibrational distribution function of the product molecules have been interpreted as the “image” of the non-equilibrium vibrational distribution function of the H ad-atoms under steady state conditions. The distribution function of H_2 gas produced by H recombination on Ta surface has been reported in Fig. 3.18. In this figure the dashed line is the distribution function expected for a Treanor distribution function of the ad-atoms. Besides, vibrational relaxation has to be considered to properly describe the experimental data (Molinari and Tomellini 2001). It should be noted the close correlation of the results reported in Fig. 3.18 with the corresponding ones in the gas phase (Capitelli et al. 1977), which will be extensively treated in Chap. 7. The analysis of the kinetic data allows one to obtain information on the rate coefficients for energy exchange to the solid. In particular, the mechanism of energy disposal via electron-hole pair excitation, in catalytic reaction on metals, has been also investigated in Molinari and Tomellini (2010a,b). Recently, the theoretical model has been applied to the

complex reaction of CO oxidation on Pt group metals with the purpose of analyzing the “*high rate*” and the “*low rate*” regimes which characterize the hysteresis loop of such an important reaction (Molinari and Tomellini 2011).

References

- Arasa C, Gamallo P, Sayós R (2005) Adsorption of atomic oxygen and nitrogen at β -cristobalite (100): a density functional theory study. *J Phys Chem B* 109(31):14954–14964
- Arasa C, Morón V, Busnengo H, Sayós R (2009) Eley-Rideal reaction dynamics between O atoms on β -cristobalite (100) surface: a new interpolated potential energy surface and classical trajectory study. *Surf Sci* 603(17):2742–2751
- Balat-Pichelin M, Badie J, Berjoan R, Boubert P (2003a) Recombination coefficient of atomic oxygen on ceramic materials under Earth re-entry conditions by optical emission spectroscopy. *Chem Phys* 291(2):181–194
- Balat-Pichelin M, Badie JM, Cacciato M, Rutigliano M (2003b) Catalyticcity of silica surfaces at high temperature: comparison between experimental recombination coefficient and molecular dynamic simulation. *Hot Structures and Thermal Protection Systems for Space Vehicles*, A. Wilson (ed.), vol. ESA SP-521. European Space Agency, Paris
- Bedra L, Rutigliano M, Balat-Pichelin M, Cacciato M (2006) Atomic oxygen recombination on quartz at high temperature: experiments and molecular dynamics simulation. *Langmuir* 22(17):7208–7216
- Billing GD (1982) On a semiclassical approach to energy transfer by atom/molecule-surface collisions. *Chem Phys* 70(3):223–239
- Billing GD (1990) The dynamics of molecule-surface interaction. *Comput Phys Rep* 12(6):383–450
- Bonfanti M, Casolo S, Tantardini GF, Martinazzo R (2011) Surface models and reaction barrier in Eley-Rideal formation of H_2 on graphitic surfaces. *Phys Chem Chem Phys* 13(37):16680
- Bourlot JL, Petit FL, Pinto C, Roueff E, Roy F (2012) Surface chemistry in the interstellar medium. I. H_2 formation by Langmuir-Hinshelwood and Eley-Rideal mechanisms. *Astron Astrophys* 541:A76
- Cacciato M, Billing GD (1990) Dynamical relaxation of $H_2(v,j)$ on a copper surface. *Surf Sci* 232(1):35–50
- Cacciato M, Rutigliano M (2006) Recombination processes involving H and D atoms interacting with a graphite surface: collisional data relevant to fusion plasma devices. *Phys Scr* T124:80–85
- Cacciato M, Rutigliano M, Billing GD (1999) Eley-Rideal and Langmuir-Hinshelwood recombination coefficients for oxygen on silica surfaces. *J Thermophys Heat Transf* 13(2):195–203
- Čadež I, Markelj S, Rupnik Z, Pelicon P (2008) Processes with neutral hydrogen and deuterium molecules relevant to edge plasma in tokamaks. *J Phys Conf Ser* 133:012029
- Capitelli M, Dilonardo M, Molinari E (1977) A theoretical calculation of dissociation rates of molecular hydrogen in electrical discharges. *Chem Phys* 20(3):417–429
- Colonna G, Laporta V, Celiberto R, Capitelli M, Tennyson J (2015) Non equilibrium vibrational and electron energy distribution functions in atmospheric nitrogen ns discharges: the role of electron-molecule vibrational excitation scaling laws. *Plasma Sources Sci Technol* 24:035004
- Farebrother AJ, Meijer AJ, Clary DC, Fisher AJ (2000) Formation of molecular hydrogen on a graphite surface via an Eley-Rideal mechanism. *Chem Phys Lett* 319(3):303–308
- Ferro Y, Marinelli F, Allouche A (2003) Density functional theory investigation of the diffusion and recombination of H on a graphite surface. *Chem Phys Lett* 368:609–615
- Forni A, Desjonquères M, Spanjaard D, Tantardini G (1992a) Dynamical study of the adsorption of hydrogen on the W(001) surface. *Surf Sci* 269–270:201–206

- Forni A, Desjonquères M, Spanjaard D, Tantardini G (1992b) A monte carlo quasi-classical trajectories study of the chemisorption of hydrogen on the W(001) surface. *Surf Sci* 274(1):161–172
- Gamallo P, Martin-Gondre L, Sayós R, Crespos C, Larrégaray P (2013) Potential energy surfaces for the dynamics of elementary gas-surface processes. In: Dynamics of gas-surface interactions. Springer Series in Surface Sciences, Springer-Verlag Berlin Heidelberg, vol. 50, pp 25–50
- Greaves JC, Linnett JW (1959) Recombination of atoms at surfaces. part 6. Recombination of oxygen atoms on silica from 20° C to 600° C. *Trans Faraday Soc* 55:1355–1361
- Guaitella O, Hübner M, Marinov D, Guerra V, Pintassilgo C, Welzel S, Röpcke J, Rousseau A (2011) Oxidation of NO into NO₂ by surface adsorbed O atoms. *Contrib Plasma Phys* 51(2–3):176–181
- Guerra V (2007) Analytical model of heterogeneous atomic recombination on silicalike surfaces. *IEEE Trans Plasma Sci* 35(5):1397–1412
- Guerra V, Dias F, Loureiro J, Sa PA, Supiot P, Dupret C, Popov T (2003) Time-dependence of the electron energy distribution function in the nitrogen afterglow. *IEEE Trans Plasma Sci* 31(4):542–551
- Hansen BF, Billing GD (1997) Hydrogen and deuterium recombination rates on a copper surface. *Surf Sci* 373(1):L333–L338
- Harris J, Kasemo B (1981) On precursor mechanisms for surface reactions. *Surf Sci Lett* 105(2):L281–L287
- Herdrich G, Fertig M, Petkow D, Steinbeck A, Fasoulas S (2012) Experimental and numerical techniques to assess catalysis. *Prog Aerosp Sci* 48–49:27–41
- Hornekær L, Šljivančanin Ž, Xu W, Otero R, Rauls E, Stensgaard I, Lægsgaard E, Hammer B, Besenbacher F (2006) Metastable structures and recombination pathways for atomic hydrogen on the graphite (0001) surface. *Phys Rev Lett* 96(15):156104
- Jeloaica L, Sidis V (1999) DFT investigation of the adsorption of atomic hydrogen on a cluster-model graphite surface. *Chem Phys Lett* 300(1):157–162
- Kim YC, Boudart M (1991) Recombination of oxygen, nitrogen, and hydrogen atoms on silica: kinetics and mechanism. *Langmuir* 7(12):2999–3005
- Latimer ER, Islam F, Price SD (2008) Studies of HD formed in excited vibrational states from atomic recombination on cold graphite surfaces. *Chem Phys Lett* 455(4–6):174–177
- Markelj S, Čadež I (2011) Production of vibrationally excited hydrogen molecules by atom recombination on Cu and W materials. *J Chem Phys* 134(12):124707
- Marshall T (1962) Surface recombination of nitrogen atoms upon quartz. *J Chem Phys* 37(10):2501
- Mattera L, Rosatelli F, Salvo C, Tommasini F, Valbusa U, Vidali G (1980) Selective adsorption of ¹H₂ and ²H₂ on the (0001) graphite surface. *Surf Sci* 93(2–3):515–525
- Molinari E, Tomellini M (2000) Non-equilibrium vibrational kinetics in adlayers: outline of an alternative approach to catalytic processes. *Chem Phys* 253(2–3):367–388
- Molinari E, Tomellini M (2001) Non-equilibrium vibrational kinetics and ‘hot atom’ models in the recombination of hydrogen atoms on surfaces. *Chem Phys* 270(3):439–458
- Molinari E, Tomellini M (2002) Vibrational non-equilibrium and ‘hot atoms’ in the oxidation of carbon monoxide on catalytic surfaces. *Chem Phys* 277(3):373–386
- Molinari E, Tomellini M (2006a) The dissipation of vibrational quanta in exoergic surface processes and its impact on reaction rates: a case study. *Surf Sci* 600(2):273–286
- Molinari E, Tomellini M (2006b) Kinetics of atom recombination at catalytic surfaces ruled by hot atom energy distributions. *Catal Today* 116(1):30–37
- Molinari E, Tomellini M (2010a) Evidence for vibrational excitation of the adlayer in exoergic processes at metal surfaces: H-atom abstraction and recombination and adsorption-stimulated desorption of CO. *Zeitschrift für Physikalische Chemie* 224:743
- Molinari E, Tomellini M (2010b) The interplay of energy disposal and reaction rates in exoergic processes at metal surfaces: desorption rates in vibrationally excited adlayers. *Zeitschrift für Physikalische Chemie* 224:761
- Molinari E, Tomellini M (2011) Kinetic analysis of high-rate and of low-rate regimes in CO oxidation on Pt group metals: evidence for vibrational excitation of the O-rich adlayer and for thermal equilibrium of the CO-rich phase. *Zeitschrift für Physikalische Chemie* 225:139

- Morisset S (2004) Dynamique de la formation d'hydrogène moléculaire sur une poussière interstellaire. PhD thesis, Université de Paris XI U.F.R. Scientifique D'Orsay
- Morisset S, Aguillon F, Sizun M, Sidis V (2003) The dynamics of H₂ formation on a graphite surface at low temperature. *Phys Chem Chem Phys* 5(3):506–513
- Morisset S, Aguillon F, Sizun M, Sidis V (2004) Quantum dynamics of H₂ formation on a graphite surface through the Langmuir Hinshelwood mechanism. *J Chem Phys* 121(13):6493–6501
- Morisset S, Aguillon F, Sizun M, Sidis V (2005) Wave-packet study of H₂ formation on a graphite surface through the Langmuir-Hinshelwood mechanism. *J Chem Phys* 122(19):194702
- Morón V, Gamallo P, Martin-Gondre L, Crespos C, Larregay R, Sayós R (2011) Recombination and chemical energy accommodation coefficients from chemical dynamics simulations: O/O₂ mixtures reacting over a β -cristobalite (001) surface. *Phys Chem Chem Phys* 13(39):17494
- Novaco AD, Wroblewski JP (1989) Rotational states of H₂, HD, and D₂ on graphite. *Phys Rev B* 39:11364–11371
- Petrovic ZL, Markovic VL, Pejovic MM, Gocic SR (2001) Memory effects in the afterglow: open questions on long-lived species and the role of surface processes. *J Phys D Appl Phys* 34(12):1756
- Ree J, Kim YH, Shin HK (2002) Dynamics of H₂ formation on a graphite surface. *Chem Phys Lett* 353(5):368–378
- Reese J, Raimondeau S, Vlachos D (2001) Monte Carlo algorithms for complex surface reaction mechanisms: efficiency and accuracy. *J Comput Phys* 173(1):302–321
- Rutigliano M, Caciato M (2008) Isotope and surface temperature effects for hydrogen recombination on a graphite surface. *Chem Phys Phys Chem* 9(1):171–181
- Rutigliano M, Caciato M (2011) Eley-Rideal recombination of hydrogen atoms on a tungsten surface. *Phys Chem Chem Phys* 13(16):7475
- Rutigliano M, Caciato M, Billing GD (2001) Hydrogen atom recombination on graphite at 10 K via the Eley-Rideal mechanism. *Chem Phys Lett* 340(1–2):13–20
- Rutigliano M, Pieretti A, Caciato M, Sanna N, Barone V (2006) N atoms recombination on a silica surface: a global theoretical approach. *Surf Sci* 600(18):4239–4246
- Scott C (1983) Effects of nonequilibrium and surface catalysis on shuttle heat transfer-a review. AIAA paper 83-1485, 18th thermophysics conference. American Institute of Aeronautics and Astronautics, US
- Sha X, Jackson B (2002) First-principles study of the structural and energetic properties of H atoms on a graphite (0001) surface. *Surf Sci* 496(3):318–330
- Sha X, Jackson B, Lemoine D (2002) Quantum studies of Eley-Rideal reactions between H atoms on a graphite surface. *J Chem Phys* 116(16):7158–7169
- Sizun M, Bachellerie D, Aguillon F, Sidis V (2010) Investigation of ZPE and temperature effects on the Eley-Rideal recombination of hydrogen atoms on graphene using a multidimensional graphene-H-H potential. *Chem Phys Lett* 498(1–3):32–37
- Tomellini M (2005) Modeling of adatom vibrational populations and recombination rates in exoergic reactions. *Surf Sci* 577(2–3):200–210
- Treanor CE, Rich JW, Rehm RG (1968) Vibrational relaxation of anharmonic oscillators with exchange-dominated collisions. *J Chem Phys* 48(4):1798–1807
- Zazza C, Rutigliano M, Sanna N, Barone V, Caciato M (2012) Oxygen adsorption on β -quartz model surfaces: some insights from density functional theory calculations and semiclassical time-dependent dynamics. *J Phys Chem A* 116(9):1975–1983

Chapter 4

Kinetic and Monte Carlo Approaches to Solve Boltzmann Equation for the Electron Energy Distribution Functions

In modeling plasmas, the characterization of free electrons is a fundamental aspect to determine the thermodynamic state of the system and its departure from LTE. In non-equilibrium conditions, electron distribution is far from the Maxwell one, due to the complex interplay between the composition, internal level distributions of heavy species and free electrons. Superelastic collisions, transferring energy from excited species to the electrons, create plateaux and structures in the distribution tails, determining the rate coefficients of electron induced processes. As a consequence, the knowledge of the distribution is a key aspect in modeling the chemistry of a plasma.

To calculate the velocity (energy) distribution of free electrons it is necessary to solve the *Boltzmann Equation* which describes the time evolution of the distribution of particles in the 6-dimension phase space. This equation, derived directly from the Liouville theorem of statistical mechanics, cannot be solved in its general form, and different approximate method have been developed. The most famous approximate solution was the Chapman-Enskog equation (CEE) (Hirschfelder et al. 1966; Chapman and Cowling 1970; Capitelli et al. 2013). This approach, which supposes small deviations from the Maxwell distribution, is commonly used to determine the transport coefficients of gas mixtures and plasmas.

However, in non-equilibrium plasmas, the assumptions of CEE are not valid and the numerical solution of a reduced BE must be used. The common approach to the solution of free electron BE is the expansion in spherical harmonics, often stopped to the first order. This is the so called *two-term* approximation, known also as *P1*. The *P1* is very popular: it gives good accuracy if the applied electric field is not too high. It can be self-consistently coupled with the state-to-state chemical kinetics, needing reasonable computational resources. The *P1* approximation has also been used to model plasma in non-homogeneous systems (Busch and Kortshagen 1995; Dujko et al. 2011; Kortshagen 1993; Kortshagen et al. 1996; Tsendar 1995; Uhrlandt and Winkler 1996; Dujko et al. 2011).

Moreover the method can be extended to higher order in the spherical harmonics expansion, obtaining a hierarchy of equations, more difficult to be solved, if many terms in the expansion are needed (Yachi et al. 1988, 1991; Maeda and Makabe 1994; Loffhagen et al. 1996; Braglia et al. 1985; Leyh et al. 1998; Ness 1994). On the other hand a Monte Carlo method can be used to solve the Boltzmann equation, this approach being equivalent to consider $P\infty$ expansion (Dujko et al. 2011).

The solution of the Boltzmann equation, especially in $P1$ approximation, is used also to determine the electron-impact cross sections from experimental swarm data (Morgan 1991, 1992, 1993; Petrović et al. 2009; Phelps 1968). This useful application, introduced by Phelps (Engelhardt and Phelps 1963; Frost and Phelps 1962, 1964), was capable to predict the shape of resonances in the vibrational excitation of homonuclear diatomic molecules such as N_2 (Phelps 1991; Phelps and Pitchford 1985; Pitchford and Phelps 1982).

To conclude this introduction, it is worth noticing that the problem of calculating electron transport by solving the Boltzmann equation is widely applied also to investigate the properties of the electron phonon gas in semiconductors and metals (Apostolova et al. 2015; Greenwood 1958; Majorana 1991; Pietanza et al. 2004a,b, 2005, 2007; Shivanian et al. 2014), where the collision integral must consider the interaction with the phonon gas and the quantum statistic of the species considered (Fermi-Dirac for electrons and Bose-Einstein for phonons).

4.1 Boltzmann Equation in Two-Term Approximation

4.1.1 Theoretical Model

The Boltzmann equation (BE) describes the time evolution of the distribution function f in the phase space (\mathbf{r}, \mathbf{v})

$$\frac{\partial f(\mathbf{r}, \mathbf{v}, t)}{\partial t} + \mathbf{v} \cdot \nabla_{\mathbf{r}} f(\mathbf{r}, \mathbf{v}, t) + \mathbf{a} \cdot \nabla_{\mathbf{v}} f(\mathbf{r}, \mathbf{v}, t) = \left(\frac{\delta f}{\delta t} \right)_{coll} \quad (4.1)$$

The left-hand term of the equation describes the change of particle density due to movement and acceleration. The right-hand side, the collision integral (CI), describes the redistribution of particles in the velocity space due to collisions. The CI verifies mass, moment and energy conservation laws, so that the Navier-Stokes equations can be directly derived from the BE. The existence of equilibrium solution (Boltzmann distribution, BD) is granted by the detailed balance principle, asserting that a collision path has the same probability if time and space are reversed.

From the distribution function it is possible to calculate the macroscopic properties of the gas i.e. particle density (N), mean velocity (\mathbf{v}_d) and mean energy (ϵ_{med})

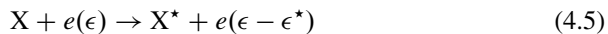
$$N = \iiint_v f(\mathbf{r}, \mathbf{v}, t) d^3 v \quad (4.2)$$

$$\mathbf{v}_d = \frac{1}{N} \iiint_v \mathbf{v} f(\mathbf{r}, \mathbf{v}, t) d^3 v \quad (4.3)$$

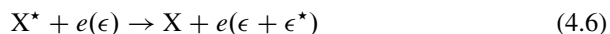
$$\varepsilon_{med} = \frac{1}{N} \iiint_v \frac{m}{2} v^2 f(\mathbf{r}, \mathbf{v}, t) d^3 v \quad (4.4)$$

For ionized gases, the contribution of free electrons can be separated from that of heavy particles, as a consequence of the large mass difference. The largest cross sections are usually those of elastic collisions between electrons and heavy species. However, as a consequence of the small electron mass, the efficiency in the energy transfer is strongly mitigated. In the presence of electric field, the elastic collisions are responsible of the Joule heating of the gas due to the electron current. Another relevant process is electron-electron elastic collisions, whose contribution is appreciable for ionization degrees above 10^{-3} . Their effect is to favor the formation of a Maxwell distribution, conserving the total energy of the electron gas.

The contribution of inelastic collisions to the distribution function is very important, resulting in strong deviations from the BD, causing an abrupt change in the distribution at the threshold energy of the corresponding process. The word *inelastic* is usually referred to *first-kind* collisions



which transfer energy from electrons to atomic or molecular excitation. The *second-kind* collisions, also called *superelastic*



are the reverse of the first-kind collisions, transferring energy from excited heavy particles to electrons. These last processes are the main responsible of the formation of structures in the electron distribution, such as plateaux and peaks. The complex interaction between all these processes, some of them in competition between each other, can be described only with the solution of the BE. A good compromise between accuracy and complexity is the two-term approximation, or *P1*, that will be described in this section.

4.1.1.1 Two-Term Approximation

The two-term approximation considers the electron distribution to be almost isotropic

$$f(\mathbf{r}, \mathbf{v}, t) = f_0(\mathbf{r}, v, t) + \frac{\mathbf{v}}{v} \cdot \mathbf{f}_1(\mathbf{r}, v, t) \quad (4.7)$$

The unitary vector $\frac{\mathbf{v}}{v}$ can be expressed in term of three director cosines, considering the angles $\vartheta_x, \vartheta_y, \vartheta_z$ between the vector \mathbf{v} with respect to the x, y, z axis

$$\varphi_i = \frac{v_i}{v} = \cos \vartheta_i \quad (4.8)$$

The anisotropy is determined by the electric field direction. In general, a single angle is necessary because, by a rotation transformation, the electric field can be oriented along z axis. If also a magnetic field is present, two preferential directions are determined by the fields: considering as $x - z$ the plane determined by the \mathbf{E} and \mathbf{B} vectors, the z axis is oriented in the direction of the electric field, the x axis in the direction perpendicular to \mathbf{E} and the y axis perpendicular to the plane $x - z$ (Mitchner and Kruger 1973). In this work we prefer the general form of the $P1$ that considers an arbitrary direction of the fields.

When the electric field is oriented in the z direction, only f_z in Eq. (4.7) is different from zero. In this case it is more appropriate to transform the integrals in spherical coordinates ($\cos \vartheta_z = \varphi_z$) and, for a generic function F , depending only on v and φ_z , we have

$$\iiint_{-\infty}^{\infty} F(v, \varphi_z) d^3 v = \int_0^{\infty} v^2 dv \oint F(v, \varphi_z) d\Omega \quad (4.9)$$

and in spherical coordinates the integral over the solid angle Ω is given by

$$\oint F(v, \varphi_z) d\Omega = \int_0^{2\pi} d\alpha \int_{-1}^1 F(v, \varphi_z) d\varphi_z = 2\pi \int_{-1}^1 F(v, \varphi_z) d\varphi_z \quad (4.10)$$

Considering that

$$\int_{-1}^1 d\varphi_x = \int_{-1}^1 d\varphi_y = 2 \quad (4.11)$$

Eq. (4.9) becomes

$$\begin{aligned} \int_{-1}^1 F(v, \varphi_z) d\varphi_z &= \frac{1}{4} \int_{-1}^1 d\varphi_x \int_{-1}^1 d\varphi_y \int_{-1}^1 F(v, \varphi_z) d\varphi_z \\ &= \frac{1}{4} \iiint_{-1}^1 F(v, \varphi_z) d^3 \varphi \end{aligned} \quad (4.12)$$

The use of (v, φ_z) variables is adequate only if the electric field is oriented in z direction. For field oriented in the x direction, the functions depend only on φ_x as

well as on φ_y if oriented in the y direction. In these conditions it is more proficient to write Eq. (4.10) with respect to the relative director cosine.

Equation (4.12) can be applied also to functions of the type $F = F_x(v, \varphi_x) + F_y(v, \varphi_y) + F_z(v, \varphi_z)$. In the spherical harmonic expansion, functions containing mixed power terms as $\varphi_x^a \varphi_y^b \varphi_z^c$ can appear; from symmetry considerations, if at least one among a, b or c is odd, it can be easily demonstrated that

$$\iiint_{-\infty}^{\infty} \varphi_x^a \varphi_y^b \varphi_z^c d^3 v = 0 \Leftrightarrow \int_{-\infty}^{\infty} v^2 dv \iiint_{-1}^1 \varphi_x^a \varphi_y^b \varphi_z^c d^3 \varphi = 0 \quad (4.13)$$

extending the validity of Eq. (4.12) also to this class of functions. This vectorial notation leads to a considerable simplification of the formalism. It must be pointed out that in all the other cases the integrals must be calculated solving the equation using the exact expression of the solid angle.

All the integrals over the φ variables are of the type

$$\int_{-1}^1 \varphi_i^{a-1} d\varphi_i = 2 \frac{a|2}{a} \quad (4.14)$$

where the symbol $a|2$ is the remainder of $a/2$ (0 for even numbers and 1 for odd numbers). In particular for $a=1,2,3$ the integral assumes respectively the values $2, 0, \frac{2}{3}$.

Let's calculate some integrals relevant for the mathematical foundation of the two-term expansion, following directly from Eq. (4.14). As an example, the isotropic (f_0) term can be obtained integrating Eq. (4.7) over the director cosines, giving

$$\begin{aligned} \iiint_{-1}^1 f(\mathbf{r}, \mathbf{v}, t) d^3 \varphi &= \iiint_{-1}^1 [f_0(\mathbf{r}, v, t) + \boldsymbol{\varphi} \cdot \mathbf{f}_1(\mathbf{r}, v, t)] d^3 \varphi \\ &= f_0(\mathbf{r}, v, t) \iiint_{-1}^1 d^3 \varphi + \mathbf{f}_1(\mathbf{r}, v, t) \cdot \iiint_{-1}^1 \boldsymbol{\varphi} d^3 \varphi \\ &= f_0 \int_{-1}^1 d\varphi_x \int_{-1}^1 d\varphi_y \int_{-1}^1 d\varphi_z + \\ &\quad f_{1x} \int_{-1}^1 \varphi_x d\varphi_x \int_{-1}^1 d\varphi_y \int_{-1}^1 d\varphi_z + \\ &\quad f_{1y} \int_{-1}^1 d\varphi_x \int_{-1}^1 \varphi_y d\varphi_y \int_{-1}^1 d\varphi_z + \\ &\quad f_{1z} \int_{-1}^1 d\varphi_x \int_{-1}^1 d\varphi_y \int_{-1}^1 \varphi_z d\varphi_z \\ &= 8f_0(\mathbf{r}, v, t) \end{aligned} \quad (4.15)$$

Analogous procedure must be followed for each component of the vector (\mathbf{f}_1), such as

$$\begin{aligned} \iiint_{-1}^1 \varphi_x f(\mathbf{r}, \mathbf{v}, t) d^3 \varphi &= \iiint_{-1}^1 [\varphi_x f_0(\mathbf{r}, v, t) + \varphi_x \boldsymbol{\varphi} \cdot \mathbf{f}_1(\mathbf{r}, v, t)] d^3 \varphi \\ &= f_0(\mathbf{r}, v, t) \iiint_{-1}^1 \varphi_x d^3 \varphi + \mathbf{f}_1(\mathbf{r}, v, t) \cdot \iiint_{-1}^1 \varphi_x \boldsymbol{\varphi} d^3 \varphi \\ &= f_0 \int_{-1}^1 \varphi_x d\varphi_x \int_{-1}^1 d\varphi_y \int_{-1}^1 d\varphi_z + \\ &\quad f_{1x} \int_{-1}^1 \varphi_x^2 d\varphi_x \int_{-1}^1 d\varphi_y \int_{-1}^1 d\varphi_z + \\ &\quad f_{1y} \int_{-1}^1 \varphi_x d\varphi_x \int_{-1}^1 \varphi_y d\varphi_y \int_{-1}^1 d\varphi_z + \\ &\quad f_{1z} \int_{-1}^1 d\varphi_x \varphi_x \int_{-1}^1 d\varphi_y \int_{-1}^1 \varphi_z d\varphi_z \\ &= \frac{8}{3} f_{1x}(\mathbf{r}, v, t) \end{aligned} \quad (4.16)$$

giving the general relations

$$\begin{aligned} f_0(\mathbf{r}, v, t) &= \frac{1}{8} \iiint_{-1}^1 f(\mathbf{r}, \mathbf{v}, t) d^3\varphi \quad (a) \\ \mathbf{f}_1(\mathbf{r}, v, t) &= \frac{3}{8} \iiint_{-1}^1 \mathbf{\varphi} f(\mathbf{r}, \mathbf{v}, t) d^3\varphi \quad (b) \end{aligned} \quad (4.17)$$

The first three moments of the distribution (particle density, mean velocity and mean energy in eV), following the same procedure as for Eqs. (4.15) and (4.16), are given by

$$N_e = \iiint_v f(\mathbf{r}, \mathbf{v}, t) d^3v = 4\pi \int_0^\infty v^2 f_0(\mathbf{r}, v, t) dv \quad (4.18)$$

$$\mathbf{v}_d = \frac{1}{N_e} \iiint_v \mathbf{v} f(\mathbf{r}, \mathbf{v}, t) d^3v = \frac{4\pi}{3N_e} \int_0^\infty v^3 \mathbf{f}_1(\mathbf{r}, v, t) dv \quad (4.19)$$

$$\varepsilon_{med} = \frac{m_e}{2eN_e} \iiint_v v^2 f(\mathbf{r}, \mathbf{v}, t) d^3v = \frac{4\pi m_e}{eN_e} \int_0^\infty v^4 f_0(\mathbf{r}, v, t) dv \quad (4.20)$$

It should be noted that the scalar properties, such as density and mean energy, are obtained from the f_0 while the vectorial properties, such as the mean velocity, are calculated from the \mathbf{f}_1 .

4.1.1.2 Differential Equations

The integrals presented in the previous section will help us to derive the differential equations for free electron kinetics. Let's consider the BE (Eq.(4.1)) for free electrons in magnetized plasma; the acceleration a is given by

$$\mathbf{a} = \mathcal{A} + \mathbf{v} \wedge \mathcal{R} \quad (4.21)$$

where \mathcal{A} is the contribution of conservative forces i.e. electric (\mathbf{E}) and gravity fields (\mathbf{g}), usually negligible,

$$\mathcal{A} = -\frac{e}{m_e} \mathbf{E} + \mathbf{g} \quad (4.22)$$

and \mathcal{R} is proportional to magnetic induction \mathbf{B}

$$\mathcal{R} = -\frac{e}{m_e} \mathbf{B} \quad (4.23)$$

In the $P1$, four differential equations are obtained, one for f_0 and three for \mathbf{f}_1 . The first equation is obtained integrating the BE over the φ 's variables. For the time derivative we have

$$\iiint_{-1}^1 \frac{\partial f}{\partial t} d^3\varphi = \frac{\partial}{\partial t} \iiint_{-1}^1 f d^3\varphi = \frac{\partial f_0}{\partial t} \iiint_{-1}^1 d^3\varphi + \\ + \sum_{i=1}^3 \frac{\partial f_{1i}}{\partial t} \iiint_{-1}^1 \varphi_i d^3\varphi = 8 \frac{\partial f_0}{\partial t} \quad (4.24)$$

being the integrals in the sum all null (see Eq. (4.14)). For the space gradient it is

$$\mathbf{v} \cdot \nabla_r f = v \boldsymbol{\varphi} \cdot \nabla_r f_0 + v \boldsymbol{\varphi} \cdot \nabla_r \boldsymbol{\varphi} \cdot \mathbf{f}_1 \quad (4.25)$$

where the integral of the first addendum is null, because contains only the first power of the φ 's. Noticing that the second addendum contains product of the type $\varphi_i \varphi_j$, only the integrals with $i = j$ survive obtaining

$$\iiint_{-1}^1 \mathbf{v} \cdot \nabla_r f d^3\varphi = v \sum_{i=1}^3 \frac{\partial f_{1i}}{\partial x_i} \iiint_{-1}^1 \varphi_i^2 d^3\varphi \\ = v \sum_{i=1}^3 \frac{\partial f_{1i}}{\partial x_i} \frac{8}{3} = \frac{8v}{3} \nabla_r \cdot \mathbf{f}_1 \quad (4.26)$$

The velocity gradient of the distribution is given by

$$\nabla_v f = \frac{\mathbf{v}}{v} \frac{\partial f_0}{\partial v} + \frac{\mathbf{f}_1}{v} + \frac{\mathbf{v}}{v} \mathbf{v} \cdot \frac{\partial}{\partial v} \frac{\mathbf{f}_1}{v} = \boldsymbol{\varphi} \frac{\partial f_0}{\partial v} + \frac{\mathbf{f}_1}{v} + \boldsymbol{\varphi} v \boldsymbol{\varphi} \cdot \frac{\partial}{\partial v} \frac{\mathbf{f}_1}{v} \quad (4.27)$$

Two different contributions are obtained, one due to electric field

$$\iiint_{-1}^1 \mathcal{A} \cdot \nabla_v f d^3\varphi = \mathcal{A} \cdot \left(8 \frac{\mathbf{f}_1}{v} + \frac{8v}{3} \frac{\partial}{\partial v} \frac{\mathbf{f}_1}{v} \right) = \frac{8\mathcal{A}}{3v^2} \cdot \frac{\partial v^2 \mathbf{f}_1}{\partial v} \quad (4.28)$$

and the other one due to magnetic induction, where all the terms proportional to $\boldsymbol{\varphi}$ in Eq. (4.27) are null for the properties of the vector product and the contribution of \mathbf{f}_1/v is null for Eq. (4.14)

$$\iiint_{-1}^1 \mathbf{v} \wedge \mathcal{R} \cdot \nabla_v f d^3\varphi = 0 \quad (4.29)$$

The contribution of the collision integral, described in detail in Mitchner and Kruger (1973), Golant et al. (1980) and Rockwood (1973), is given by

$$S_0 = \frac{1}{8} \iiint_{-1}^1 \left(\frac{\delta f}{\delta t} \right)_{coll} d^3\varphi \quad (4.30)$$

To determine the differential equation for \mathbf{f}_1 , the BE is multiplied by $\boldsymbol{\varphi}$ and then integrated as for f_0

$$\iiint_{-1}^1 \boldsymbol{\varphi} \frac{\partial f}{\partial t} d^3 \varphi = \frac{8}{3} \frac{\partial \mathbf{f}_1}{\partial t} \quad (4.31)$$

$$\iiint_{-1}^1 \boldsymbol{\varphi} \mathbf{v} \cdot \nabla_r f d^3 \varphi = \frac{8}{3} v \nabla_r f_0 \quad (4.32)$$

$$\iiint_{-1}^1 \boldsymbol{\varphi} \mathcal{A} \cdot \nabla_v f d^3 \varphi = \frac{8}{3} \mathcal{A} \frac{\partial f_0}{\partial v} \quad (4.33)$$

$$\iiint_{-1}^1 \boldsymbol{\varphi} \mathbf{v} \wedge \mathcal{R} \cdot \nabla_v f d^3 \varphi = \frac{8}{3} \mathcal{R} \wedge \mathbf{f}_1 \quad (4.34)$$

$$\mathbf{S}_1 = \frac{3}{8} \iiint_{-1}^1 \boldsymbol{\varphi} \left(\frac{\delta f}{\delta t} \right)_{coll} d^3 \varphi \quad (4.35)$$

Combining all these terms we have the system of equations

$$\begin{cases} \frac{\partial f_0}{\partial t} + \frac{v}{3} \nabla_r \cdot \mathbf{f}_1 + \frac{\mathcal{A}}{3v^2} \cdot \frac{\partial v^2 \mathbf{f}_1}{\partial v} = S_0 \\ \frac{\partial \mathbf{f}_1}{\partial t} + v \nabla_r f_0 + \mathcal{A} \frac{\partial f_0}{\partial v} + \mathcal{R} \wedge \mathbf{f}_1 = \mathbf{S}_1 \end{cases} \quad (4.36)$$

The expression for \mathbf{S}_1 has been derived in Mitchner and Kruger (1973), Golant et al. (1980) and Rockwood (1973)

$$\mathbf{S}_1 = -\nu_e \mathbf{f}_1 \quad (4.37)$$

where ν_e is the frequency of the elastic collisions

$$\nu_e = \sum_s v \sigma_s^{mt} N_s \quad (4.38)$$

being σ_s^{mt} the momentum transfer cross section. Other processes, such as inelastic, superelastic and electron-electron collisions, must be taken into account in \mathbf{S}_1 (see Mitchner and Kruger 1973), but their contribution is usually negligible.

From basic vector algebra it is known that the vector product can be written in matrix form as

$$\mathbf{a} \wedge \mathbf{b} = \begin{pmatrix} 0 & -a_z & a_y \\ a_z & 0 & -a_x \\ -a_y & a_x & 0 \end{pmatrix} \begin{pmatrix} b_x \\ b_y \\ b_z \end{pmatrix} \quad (4.39)$$

Combining the terms $\mathcal{R} \wedge \mathbf{f}_1$ and \mathbf{S}_1 we have

$$\mathcal{R} \wedge \mathbf{f}_1 + v_e \mathbf{f}_1 = \begin{pmatrix} v_e & -\mathcal{R}_z & \mathcal{R}_y \\ \mathcal{R}_z & v_e & -\mathcal{R}_x \\ -\mathcal{R}_y & \mathcal{R}_x & v_e \end{pmatrix} \begin{pmatrix} f_{1x} \\ f_{1y} \\ f_{1z} \end{pmatrix} = \hat{\Omega} \mathbf{f}_1 \quad (4.40)$$

Grouping in the second equation all the terms that depends only on the isotropic distribution f_0

$$\mathbf{Q}_0 = - \left(v \nabla_r f_0 + \mathcal{A} \frac{\partial f_0}{\partial v} \right) \quad (4.41)$$

Eq. (4.36) can be rewritten as

$$\begin{cases} \frac{\partial f_0}{\partial t} + \frac{v}{3} \nabla_r \cdot \mathbf{f}_1 + \frac{\mathcal{A}}{3v^2} \cdot \frac{\partial v^2 \mathbf{f}_1}{\partial v} = S_0 \\ \frac{\partial \mathbf{f}_1}{\partial t} + \hat{\Omega} \mathbf{f}_1 = \mathbf{Q}_0 \end{cases} \quad (4.42)$$

In the second equation of the system above, $\hat{\Omega} \mathbf{f}_1$ behaves like a dissipation term while \mathbf{Q}_0 is the driving force. As a consequence the electron current is generated by the conservative field \mathcal{A} and by space gradients of f_0 (i.e. diffusion). On the other hand, the dissipation terms are due to collisions and to the magnetic field. This last contribution is very important because the magnetic field operates in opposition with the electric field. We must point out that this is only a partial view because for flowing plasmas other terms due to magnetic field must be considered i.e. the Faraday electromotive field and the MHD interaction

$$\mathbf{E}_F = \mathbf{u} \wedge \mathbf{B} \quad (4.43)$$

$$\mathbf{F}_{MHD} = \mathbf{J} \wedge \mathbf{B} = -eN_e \mathbf{v}_d \wedge \mathbf{B} \quad (4.44)$$

4.1.1.3 Quasi-stationary Approximation

For slowly varying fields, \mathbf{f}_1 relaxes very rapidly, relatively to the isotropic distribution. In this conditions, the quasi-stationary approximation ($\frac{\partial \mathbf{f}_1}{\partial t} \approx 0$) can be used and the second equation in (4.42) becomes

$$\hat{\Omega} \mathbf{f}_1 = \mathbf{Q}_0 \quad (4.45)$$

Eq. (4.45) is a linear system relating \mathbf{f}_1 to f_0

$$\mathbf{f}_1 = \hat{\Omega}^{-1} \mathbf{Q}_0 = \hat{\omega} \mathbf{Q}_0 \quad (4.46)$$

The matrix $\hat{\omega}$ can be easily calculated and is given by

$$\hat{\omega} = \frac{1}{v_e(v_e^2 + \mathcal{R}^2)} \begin{pmatrix} v_e^2 + \mathcal{R}_x^2 & \mathcal{R}_x \mathcal{R}_y + v_e \mathcal{R}_z \mathcal{R}_x \mathcal{R}_z - v_e \mathcal{R}_y \\ \mathcal{R}_x \mathcal{R}_y - v_e \mathcal{R}_z & v_e^2 + \mathcal{R}_y^2 \mathcal{R}_y \mathcal{R}_z + v_e \mathcal{R}_x \\ \mathcal{R}_x \mathcal{R}_z + v_e \mathcal{R}_y \mathcal{R}_y \mathcal{R}_z - v_e \mathcal{R}_x & v_e^2 + \mathcal{R}_z^2 \end{pmatrix} \quad (4.47)$$

Substituting Eq. (4.46) in the equation for f_0 we have an expression that does not depend on \mathbf{f}_1

$$\frac{\partial f_0}{\partial t} + \frac{v}{3} \nabla_r \cdot \hat{\omega} \mathbf{Q}_0 + \frac{\mathcal{A}}{3v^2} \cdot \frac{\partial v^2 \hat{\omega} \mathbf{Q}_0}{\partial v} = S_0 \quad (4.48)$$

For homogeneous systems all the space gradients vanish obtaining

$$\frac{\partial f_0}{\partial t} - \frac{1}{3v^2} \frac{\partial}{\partial v} \mathcal{A} \cdot \hat{\omega} \mathcal{A} v^2 \frac{\partial f_0}{\partial v} = S_0 \quad (4.49)$$

4.1.1.4 Electrons in Flow

The model described above has been obtained for a plasma at rest. In flow conditions, some corrections are necessary. As first step let's find the transform relations of the distribution function when changing inertial frame of reference. It is reasonable to suppose that (4.48) and (4.49) are valid in a reference frame that moves together with the flow having velocity \mathbf{u} . The particle velocity in this new frame (v') is related to the velocity in the laboratory system (v) by $v' = \mathbf{v} - \mathbf{u}$ (for non-relativistic flows). Changing frame of reference also changes the shape of the distribution, but the probability of having a particle with velocity \mathbf{v}' in the frame of reference flow-fixed, is the same as a particle of velocity \mathbf{v} in the laboratory. This means that

$$f'(\mathbf{v}') = f(\mathbf{v}) \quad (4.50)$$

In the flow-fixed frame of reference and under the two-term formalism, the transformed distribution is given by

$$f'(\mathbf{v}') = f(\mathbf{v}) = f_0(\mathbf{v}' + \mathbf{u}) + \frac{\mathbf{v}' + \mathbf{u}}{|\mathbf{v}' + \mathbf{u}|} \cdot \mathbf{f}_1(\mathbf{v}' + \mathbf{u}) \quad (4.51)$$

Assuming that the flow speed is much lower than the thermal velocity ($\mathbf{v}' \approx \mathbf{v}$), we can expand the terms in Eq. (4.51) in a Taylor series truncated at the first order,

$$\begin{aligned} f_0(\mathbf{v}' + \mathbf{u}) &\approx f_0(\mathbf{v}') + \mathbf{u} \cdot \boldsymbol{\varphi}' \frac{\partial f_0(\mathbf{v}')}{\partial v} \\ \frac{\mathbf{v}' + \mathbf{u}}{|\mathbf{v}' + \mathbf{u}|} &\approx \boldsymbol{\varphi}' \\ \mathbf{f}_1(\mathbf{v}' + \mathbf{u}) &\approx \mathbf{f}_1(\mathbf{v}') + \mathbf{u} \cdot \boldsymbol{\varphi}' \frac{\partial \mathbf{f}_1(\mathbf{v}')}{\partial v} \end{aligned} \quad (4.52)$$

and applying the definition of f_0 and \mathbf{f}_1 in Eq. (4.17) we have

$$\begin{aligned} f'_0(v') &= \frac{1}{8} \iiint_{-1}^1 f'(\mathbf{v}') d^3\varphi' = f_0(v') + \frac{1}{3}\mathbf{u} \cdot \frac{\partial \mathbf{f}_1(v')}{\partial v} \\ \mathbf{f}'_1(v') &= \frac{3}{8} \iiint_{-1}^1 \boldsymbol{\varphi}' f'(\mathbf{v}') d^3\varphi' = \mathbf{f}_1(v') + \mathbf{u} \frac{\partial f_0(v')}{\partial v} \end{aligned} \quad (4.53)$$

Also the collision terms must be corrected, being Eq. (4.37) valid only in the flow-fixed frame of reference. Considering that the collision terms must have the same value independently of the transformation

$$\mathbf{S}_1 = -\nu_e \mathbf{f}'_1 = -\nu_e \mathbf{f}_1 - \nu_e \mathbf{u} \frac{\partial f_0(v)}{\partial v} \quad (4.54)$$

which has one more term with respect to the gas at rest. Rewriting Eq. (4.36) for \mathbf{f}_1 including this additional term, Eqs. (4.42) and (4.45)–(4.48) do not change form if the quantity \mathbf{Q}_0 is redefined as

$$\mathbf{Q}_0 = - \left[v \nabla_v f_0 + (\mathcal{A} + \nu_e \mathbf{u}) \frac{\partial f_0}{\partial v} \right] \quad (4.55)$$

where the flow speed acts as a driving force for the electron current. In quasi-steady state condition Eq. (4.49) becomes

$$\frac{\partial f_0}{\partial t} - \frac{1}{3v^2} \frac{\partial}{\partial v} \mathcal{A} \cdot \hat{\omega} (\mathcal{A} + \nu_e \mathbf{u}) v^2 \frac{\partial f_0}{\partial v} = S_0 \quad (4.56)$$

Similar procedure must be followed to correct the term S_0 for flowing plasma. As a first step, neglecting electron-electron collisions, the CI is a linear operator (\hat{S}_{LC}) of f_0 in the flow-fixed frame

$$S_0 = \hat{S}_{LC}[f'_0(v)] = \hat{S}_{LC} \left[f_0(v) + \frac{1}{3} \mathbf{u} \cdot \frac{\partial \mathbf{f}_1(v)}{\partial v} \right] \quad (4.57)$$

and in quasi-steady state approximation

$$S_0 = \hat{S}_{LC}[f'_0(v)] = \hat{S}_{LC} \left[f_0(v) + \frac{1}{3} \mathbf{u} \cdot \frac{\partial \hat{\omega} \mathbf{Q}_0}{\partial v} \right] \quad (4.58)$$

To calculate the contribution of electron-electron collisions to S_0 and \mathbf{S}_1 (Mitchner and Kruger 1973), the distribution must be transformed in a reference frame that moves with the electron current so that $\mathbf{f}'_1 = \mathbf{0}$. However, the contribution of the flow to the collision integrals S_0 and \mathbf{S}_1 is a second order correction.

The approach described above can be applied to multi-fluid models of plasmas, determining the coupling between the electron gas and heavy particles. The two systems mutually exchange both energy and momentum. The energy balance is already considered in S_0 , providing one includes the corresponding terms in the

fluid dynamic equations. On the other hand, the momentum exchange is usually neglected, due to the small electron mass. To estimate the momentum exchange between electrons and heavy particles, rewrite the equation neglecting terms due to fields and spatial gradients

$$\frac{\partial \mathbf{f}_1}{\partial t} = -v_e \mathbf{u} \frac{\partial f_0}{\partial v} - v_e \mathbf{f}_1 \quad (4.59)$$

The momentum equation for electrons is given by

$$\rho_e \mathbf{u}_e = m_e N_e \mathbf{v}_d \quad (4.60)$$

and combining Eq. (4.59) with Eq. (4.19), the drag of free electrons due to heavy particles flow is given by

$$\begin{aligned} \left(\frac{\partial \rho_e \mathbf{u}_e}{\partial t} \right)_{drag} &= N_e m_e \frac{\partial \mathbf{v}_d}{\partial t} = \frac{4\pi m_e}{3} \int_0^\infty v^3 \frac{\partial \mathbf{f}_1}{\partial t} dv \\ &= -\frac{4\pi m_e}{3} \int_0^\infty v^3 v_e \left(\mathbf{u} \frac{\partial f_0}{\partial v} + \mathbf{f}_1 \right) dv \end{aligned} \quad (4.61)$$

4.1.1.5 Electron Energy Distribution

The two-term Boltzmann equation, more than for the velocity distribution, is usually written for the electron energy distribution function (Rockwood 1973) (eedf) defined as

$$n_0(\epsilon) = 4\pi \sqrt{\frac{2e^3 \epsilon}{m_e^3}} f_0(v) \quad (4.62)$$

$$\mathbf{n}_1(\epsilon) = \frac{8\pi \epsilon e^2 \epsilon}{3m_e^2} \mathbf{f}_1(v) \quad (4.63)$$

transforming Eqs. (4.18)–(4.20) as

$$N_e = \int_0^\infty n_0(\epsilon) d\epsilon \quad (4.64)$$

$$\mathbf{v}_d = \frac{1}{N_e} \int_0^\infty \mathbf{n}_1(\epsilon) d\epsilon \quad (4.65)$$

$$\varepsilon_{med} = \frac{1}{N_e} \int_0^\infty \epsilon n_0(\epsilon) d\epsilon \quad (4.66)$$

where the electron energy, expressed in eV, is $\epsilon = \frac{m_e}{2e} v^2$. Changing the variable from v to ϵ transforms derivative and differential as

$$\frac{\partial}{\partial v} = \sqrt{\frac{2m_e \epsilon}{e}} \frac{\partial}{\partial \epsilon} \quad (4.67)$$

$$dv = \sqrt{\frac{e}{2m_e \epsilon}} d\epsilon \quad (4.68)$$

resulting in the differential equations (see Eq. (4.36))

$$\begin{cases} \frac{\partial n_0}{\partial t} + \nabla_r \cdot \mathbf{n}_1 + \frac{m_e \mathcal{A}}{e} \cdot \frac{\partial \mathbf{n}_1}{\partial \epsilon} = S_0 \\ \frac{\partial \mathbf{n}_1}{\partial t} + \frac{2e\epsilon}{3m_e} \nabla_r n_0 + \frac{2\epsilon}{3} (\mathcal{A} + v_e \mathbf{u}) \left(\frac{\partial n_0}{\partial \epsilon} - \frac{n_0}{2\epsilon} \right) + \hat{\mathcal{Q}} \mathbf{n}_1 = \mathbf{0} \end{cases} \quad (4.69)$$

and in quasi-stationary approximation we have

$$\mathbf{n}_1 = -\frac{2e\epsilon}{3m_e} \hat{\omega} \left[\nabla_r n_0 + \frac{m_e}{e} (\mathcal{A} + v_e \mathbf{u}) \left(\frac{\partial n_0}{\partial \epsilon} - \frac{n_0}{2\epsilon} \right) \right] \quad (4.70)$$

Neglecting the contribution of the gradients we obtain the classical expression reported by Rockwood (Rockwood 1973; Mitchner and Kruger 1973; Golant et al. 1980; Colonna and Capitelli 2008b, 2003)

$$\begin{aligned} \frac{\partial n_0(\epsilon)}{\partial t} &= -\frac{\partial J_{el}(\epsilon)}{\partial \epsilon} - \frac{\partial J_f(\epsilon)}{\partial \epsilon} - \frac{\partial J_{ee}(\epsilon)}{\partial \epsilon} - \frac{\partial J_{ne}(\epsilon)}{\partial \epsilon} \\ &\quad + S_{in}(\epsilon) + S_{sup}(\epsilon) + S_{ion}(\epsilon) + S_{rec}(\epsilon). \end{aligned} \quad (4.71)$$

The different terms in Eq. (4.71) are due to the contribution of the fields (see Eqs. (4.69) and (4.70))

$$J_f = \frac{2m_e}{3e} \mathcal{A} \hat{\omega}(\mathbf{B}) (\mathcal{A} + v_e \mathbf{u}) \sqrt{\epsilon^3} \frac{\partial}{\partial \epsilon} \left(\frac{n_0}{\sqrt{\epsilon}} \right), \quad (4.72)$$

being

$$\left(\frac{\partial n_0}{\partial \epsilon} - \frac{n_0}{2\epsilon} \right) = \sqrt{\epsilon} \frac{\partial}{\partial \epsilon} \left(\frac{n_0}{\sqrt{\epsilon}} \right), \quad (4.73)$$

the elastic collisions (J_{el})

$$\begin{cases} J_{el} = c(\varepsilon) \left(\frac{kT}{2} - \varepsilon \right) n_0 - \varepsilon k T c(\varepsilon) \frac{\partial n_0}{\partial \varepsilon} \\ c(\varepsilon) = \bar{v}(\varepsilon) = 2\sqrt{2e\varepsilon m_e} \sum_s \frac{N_s \sigma_s^{mt}}{m_s} \end{cases} \quad (4.74)$$

the electron-electron collisions (J_{ee})

$$\begin{cases} J_{ee} = \alpha \left[P(\varepsilon) \left(\frac{n_0}{2\varepsilon} - \frac{\partial n_0}{\partial \varepsilon} \right) - Q(\varepsilon) n_0 \right] \\ \alpha = \frac{2\pi}{3} N_e (K_e e)^2 \sqrt{\frac{2e}{m_e} \ln \Lambda} = 2.5821 \cdot 10^{-12} N_e \ln \Lambda \\ \Lambda = \frac{\varepsilon_{med}}{K_e e} \sqrt{\frac{\varepsilon_{car}}{4\pi K_e e N_e}} = 5.1527 \cdot 10^{12} \varepsilon_{med} \sqrt{\frac{\varepsilon_{car}}{N_e}} \\ P(\varepsilon) = \frac{2}{\sqrt{\varepsilon}} \int_0^\varepsilon x n_0 dx + 2\varepsilon \int_\varepsilon^\infty \frac{n_0}{\sqrt{(x)}} dx \\ Q(\varepsilon) = \frac{3}{\sqrt{\varepsilon}} \int_0^\varepsilon n_0 dx \end{cases} \quad (4.75)$$

and the inelastic (S_{in}) and superelastic (S_{sup}) collisions

$$S_{in} = \sum_{s,l,u} N_{sl} \left[v(\varepsilon + \varepsilon_{sul}^*) \sigma_{sul}^{in} (\varepsilon + \varepsilon_{sul}^*) n_0 (\varepsilon + \varepsilon_{sul}^*) - v(\varepsilon) \sigma_{sul}^{in} (\varepsilon) n_0 (\varepsilon) \right] \quad (4.76)$$

$$S_{sup} = \sum_{s,l,u} N_{su} \left[v(\varepsilon - \varepsilon_{sul}^*) \sigma_{sul}^{sup} (\varepsilon - \varepsilon_{sul}^*) n_0 (\varepsilon - \varepsilon_{sul}^*) - v(\varepsilon) \sigma_{sul}^{sup} (\varepsilon) n_0 (\varepsilon) \right]. \quad (4.77)$$

The superelastic cross section, σ_{sul}^{sup} is related to σ_{sul}^{in} through the micro-reversibility principle

$$\sigma_{sul}^{sup} (\varepsilon) = \frac{g_l(\varepsilon + \varepsilon_{sul}^*)}{g_u \varepsilon} \sigma_{sul}^{in} (\varepsilon + \varepsilon_{sul}^*) \quad (4.78)$$

For small threshold transitions,¹ such as rotational excitation, the definition in Eqs. (4.76) and (4.77) should be adapted to account for the size of the discretized energy grid. Under the assumption that $\varepsilon^* \ll \Delta\varepsilon$, it is possible to approximate the source term of the considered process with the derivative with respect to the energy

¹A threshold is considered small if its value is smaller than the grid size.

$$\bar{S}_{in} \approx \varepsilon^* \lim_{\varepsilon^* \rightarrow 0} \frac{S_{in}}{\varepsilon_{sul}^*} = \varepsilon_{sul}^* N_{sl} \frac{\partial v(\varepsilon) \sigma_{sul}^{in}(\varepsilon) n_0(\varepsilon)}{\partial \varepsilon} \quad (4.79)$$

and analogously, for the superelastic source term

$$\bar{S}_{sup} \approx \varepsilon^* \lim_{\varepsilon^* \rightarrow 0} \frac{S_{sup}}{\varepsilon_{sul}^*} = -\varepsilon_{sul}^* N_{su} \frac{\partial v(\varepsilon) \sigma_{sul}^{sup}(\varepsilon) n_0(\varepsilon)}{\partial \varepsilon} \quad (4.80)$$

transforming the source terms in fluxes in the energy space.

Ionization (S_{ion}) term is equal to the inelastic term, considering the corresponding threshold energies and cross sections. On the other hand, recombination source terms should be rearranged considering the following cross section for the recombination process, i.e. $A + e \rightarrow A^+ + 2e$

$$\sigma^{rec}(\varepsilon - \varepsilon^*) = \frac{g_A + \varepsilon}{g_A(\varepsilon - \varepsilon^*)} \frac{Q_A + Q_e}{Q_A K_{eq}} e^{-\Delta H_{ion}/kT} \sigma^{ion}(\varepsilon) \quad (4.81)$$

The term J_{ne} , introduced for the first time in (Colonna and Capitelli 2003) (see also Colonna and Capitelli 2008b), accounts for the plasma expansion or compression and will be described in the next section.

4.1.1.6 Electron Kinetics in Nozzle Flow

In recent papers (Colonna and Capitelli 2001a,b, 2003, 2005, 2008b) we have investigated the state-to-state non-equilibrium during the supersonic expansion through converging-diverging nozzles. For this system, good accuracy can be achieved by quasi-1D Euler equations

$$\begin{cases} \frac{d\rho u A}{dx} = 0 \\ \frac{dP}{dx} + \rho u \frac{du}{dx} = \dot{S}_u \\ u \frac{du}{dx} + \frac{dh_T}{dx} + \frac{dh_{in}}{dx} = \dot{S}_T \\ P = \frac{\rho R T}{m} \end{cases} \quad (4.82)$$

where \dot{S}_u is the source term for the momentum equation, due for example to MHD interaction (see Eq. (4.44)) or electron drug (see Eq. (4.61)), and \dot{S}_T is a source term for energy, due to Joule heating or radiative losses

$$\dot{Q}_J = \mathbf{J} \cdot \mathbf{E} = -e N_e \mathbf{v}_d \cdot \mathbf{E} \quad (4.83)$$

$$\dot{Q}_{rad} = \sum_{s,u,l} \dot{A}_{sul} h v_{sul} N_{su} \quad (4.84)$$

An algorithm to solve the system in Eq.(4.82) can be found in Colonna et al. (2001). The general solution of nozzle equations describes the transformation of thermal energy, given to the gas at the nozzle inlet, in flow speed, resulting in a low pressure and low temperature flow moving at supersonic speed. To calculate the enthalpic contributions (h_T, h_{in}) the gas composition must be known. In the state-to-state approach, a continuity equation

$$\frac{d\rho_{sl}Au}{dx} = \dot{\rho}_{sl} \quad (4.85)$$

is added to Eqs.(4.82) for each level of each species, where $\dot{\rho}_{sl}$ is a source term due to chemical reactions and internal transitions. Due to finite rate coefficients, chemical processes and internal transitions become almost frozen at the nozzle exit, resulting in internal temperatures much higher than the gas one.

The discretized BE in (4.71) has the form of a master equation, considering the electrons in different intervals as different levels of the same species. This parallelism is not perfect because, being the electron energy representing a disordered translational motion, the electron gas cools down during the expansion as the heavy particles, even in absence of reactions and collisional processes. To adapt the $P1$ for quasi 1D nozzle flow, the space gradients must be substituted with

$$\nabla_r f \equiv \begin{pmatrix} \frac{1}{A} \frac{\partial A f}{\partial x} \\ 0 \\ 0 \end{pmatrix} \quad (4.86)$$

This approach makes the BE very complex, containing mixed derivatives in space and energy. It can be easily verified that the term J_{ne} in Eq. (4.71) written as

$$J_{ne}(\epsilon) = \frac{m_e}{e} n_0(\epsilon) u \frac{\partial u}{\partial t} \quad (4.87)$$

balances the mean electron energy with the variation of the electron kinematic energy. In fact, the variation in electron energy due to increase of flow speed is given by

$$\delta \varepsilon_{med} = \delta \int_0^\infty \epsilon n_0(\epsilon) d\epsilon = \int_0^\infty \epsilon \delta n_0(\epsilon) d\epsilon = \frac{m_e}{e} u \delta u \int_0^\infty \epsilon \frac{\partial n_0}{\partial \epsilon} d\epsilon \quad (4.88)$$

and integrating by parts we have

$$\int_0^\infty \epsilon \frac{\partial n_0}{\partial \epsilon} d\epsilon = \epsilon n_0(\epsilon)|_0^\infty - \int_0^\infty n_0(\epsilon) d\epsilon = 0 - 0 - 1 = -1 \quad (4.89)$$

$$\delta \varepsilon_{med} = - \frac{m_e}{e} u \delta u \quad (4.90)$$

which is the variation of mean electron kinematic energy. Equation (4.87) is compatible with the energy variation in Eq.(4.90), and implicitly considers that the contribution of the expansion acts homogeneously in all the energy range. This approach makes the equation much simpler and can give to the BE for free electrons (Eq. (4.71)) the same structure as the state-to-state master equation (see Eq. (4.85)) if the time derivative is substituted by the substantial derivative i.e.

$$\frac{\partial F}{\partial t} \rightarrow \frac{\partial uF}{\partial x} \quad (4.91)$$

simplifying the problem of coupling the free electron kinetics with nozzle flows equations.

4.1.1.7 Transport Properties

In this section we will describe how to obtain the transport properties of a plasma in the framework of $P1$ approach. We will consider the general case of a magnetized plasma. The electron mean velocity is calculated integrating \mathbf{n}_1 (see Eq. (4.65)) and, considering the expression given in Eq. (4.70), we have

$$\begin{aligned} \mathbf{v}_d = & -\frac{2e}{3m_e N_e} \left(\int_0^\infty \hat{\omega} \epsilon n_0 d\epsilon \right) \nabla_r N_e - \frac{2e}{3m_e} \left(\int_0^\infty \epsilon \hat{\omega} \nabla_r \frac{n_0}{N_e} d\epsilon \right) \\ & - \frac{2}{3N_e} \left(\int_0^\infty \hat{\omega} \sqrt{\epsilon^3 \frac{\partial}{\partial \epsilon} \frac{n_0}{\sqrt{\epsilon}}} d\epsilon \right) \mathcal{A} - \frac{2}{3N_e} \left(\int_0^\infty \hat{\omega} v_e \sqrt{\epsilon^3 \frac{\partial}{\partial \epsilon} \frac{n_0}{\sqrt{\epsilon}}} d\epsilon \right) \mathbf{u} \end{aligned} \quad (4.92)$$

We can recognize four contributions that can be related to different transport properties: diffusion, thermal diffusion, electrical conductivity and flow drag, being this last relevant only in presence of the magnetic field. In fact, for $\mathbf{B} \neq 0$ this contribution is responsible of the Faraday current. For $\mathbf{B} = 0$ it gives the trivial result that the electrons moves together with the flow.

Comparing with the classical transport theory, the electron-diffusion coefficient is given by

$$\hat{D}_e = \frac{2e}{3m_e N_e} \left(\int_0^\infty \hat{\omega} \epsilon n_0 d\epsilon \right) \quad (4.93)$$

In non-equilibrium case the thermal diffusion cannot be represented by a single coefficient because it is necessary to know the real gradient of the distribution. In the case of Maxwell distribution, the gradient of the distributions is transformed in a gradient of the temperature as

$$\nabla_r \frac{n_0}{N_e} = \frac{\epsilon}{T_e^2 N_e} \nabla_r T_e \quad (4.94)$$

giving for the thermal diffusion coefficient

$$\hat{D}_e^T = \frac{2e}{3m_e N_e T_e^2} \left(\int_0^\infty \epsilon^2 \hat{\omega} n_0 d\epsilon \right) \quad (4.95)$$

The electrical conductivity $\hat{\sigma}_e$ is related to the electron mobility $\hat{\mu}_e$ by the simple relation $\hat{\sigma}_e = -eN_e \hat{\mu}_e$. From the third term in Eq. (4.92) we have

$$\hat{\mu}_e = -\frac{2}{3N_e} \left(\int_0^\infty \hat{\omega} \sqrt{\epsilon^3} \frac{\partial}{\partial \epsilon} \frac{n_0}{\sqrt{\epsilon}} d\epsilon \right) \quad (4.96)$$

These transport coefficients have tensorial character induced by the matrix $\hat{\omega}$. It must be noted that, differently from the Chapman-Enskog method, which build the tensors considering the Hall parameter, the matrix $\hat{\omega}$ is inside the integral. In case of null magnetic field the tensors become diagonal and isotropic, resulting in scalar coefficients. In this case we can define the characteristic energy as

$$\varepsilon_{car} = \frac{D_e}{\mu_e} \quad (4.97)$$

and, for a theorem due to Einstein (Mitchner and Kruger 1973; Golant et al. 1980; Rockwood 1973), in presence of Maxwellian distributions, it is $\varepsilon_{car} = T_e$.

To clarify the role of the matrix $\hat{\omega}$ let's discuss the case of the current produced by electric and magnetic fields perpendicular to each other. Considering the magnetic field oriented in the z direction, $\mathbf{B} = (0, 0, B)$, and defining

$$\begin{aligned} \beta &= \frac{eB}{v_e m_e} \\ \alpha &= \frac{\beta}{v_e(1+\beta^2)} \\ \gamma &= \frac{1}{v_e(1+\beta^2)} \end{aligned} \quad (4.98)$$

we have

$$\hat{\omega} = \frac{1}{v_e(1+\beta^2)} \begin{pmatrix} 1 & \beta & 0 \\ -\beta & 1 & 0 \\ 0 & 0 & 1+\beta^2 \end{pmatrix} = \begin{pmatrix} \gamma & \alpha & 0 \\ -\alpha & \gamma & 0 \\ 0 & 0 & 1/v_e \end{pmatrix} \quad (4.99)$$

Referring to the expression of \mathbf{n}_1 in Eq. (4.70) and considering that the current density is

$$\mathbf{j} = N_e e \mathbf{v}_d = N_e e \int_0^\infty \mathbf{n}_1 d\epsilon \quad (4.100)$$

for $\mathbf{E} = (0, E, 0)$, we have the appearance of Hall current, oriented in the x direction; its value is given by

$$j_{Hall} = -\frac{2N_e e^2}{3m_e} \int_0^\infty \epsilon \sqrt{\epsilon} \frac{\partial}{\partial \epsilon} \frac{n_0}{\sqrt{\epsilon}} \alpha E d\epsilon \quad (4.101)$$

4.1.1.8 When Quasi-steady Approximation Fails

The mathematical description of previous sections are based on the assumption that the anisotropic part of the distribution relaxes very rapidly. In many applications this approximation is not valid, as in the case where the electric field changes very rapidly. In this case the equations in (4.42) (or equivalently in (4.69)) must be solved separately for f_0 and \mathbf{f}_1 .

For sake of simplicity, let's consider an example with $\mathbf{B} = 0$. The general solution of the equation of the anisotropic part is given by

$$\mathbf{f}_1(t) = [\mathbf{c}(t) - \mathbf{c}(0)]e^{-v_e t} + \mathbf{f}_1(0)e^{-v_e t} \quad (4.102)$$

$$\mathbf{c}(t) = \frac{e}{m_e} \int_{-\infty}^t \mathbf{E} \frac{\partial f_0}{\partial v} e^{v_e z} dz = \frac{e}{m_e} \frac{\partial f_0}{\partial v} \int_{-\infty}^t \mathbf{E} e^{v_e z} dz \quad (4.103)$$

supposing, reasonably, that the variation of $\frac{\partial f_0}{\partial v}$ is much slower than f_1 . For a constant \mathbf{E} field we have

$$\begin{aligned} \mathbf{c}(t) &= \frac{e}{m_e v_e} \frac{\partial f_0}{\partial v} \mathbf{E} e^{v_e t} \\ \mathbf{f}_1(t) &= \frac{e}{m_e v_e} \frac{\partial f_0}{\partial v} \mathbf{E} + \left[\mathbf{f}_1(0) - \frac{e}{m_e v_e} \frac{\partial f_0}{\partial v} \mathbf{E} \right] e^{-v_e t} \end{aligned} \quad (4.104)$$

This result shows that the anisotropic distribution reaches the quasi-stationary value in a time of the order of $\frac{1}{v_e}$, independently on the initial value.

Let's now consider the case of an oscillating field

$$\mathbf{E} = \mathbf{E}_0 \cos(\omega_E t) \quad (4.105)$$

the integral in Eq. (4.103) is given by

$$\begin{aligned} \mathbf{c}(t) &= \frac{e}{m_e} \frac{\partial f_0}{\partial v} \mathbf{E}_0 \int_{-\infty}^t \cos(\omega_E t) e^{v_e z} dz = \\ &= \frac{e}{m_e} \frac{\partial f_0}{\partial v} \mathbf{E}_0 e^{v_e t} \frac{v_e \cos(\omega_E t) + \omega_E \sin(\omega_E t)}{v_e^2 + \omega_E^2} \end{aligned} \quad (4.106)$$

Substituting in Eq. (4.102) and neglecting the terms decaying exponentially we have

$$\mathbf{f}_1(t) = \frac{e}{m_e} \frac{\partial f_0}{\partial v} \mathbf{E}_0 \frac{v_e \cos(\omega_E t) + \omega_E \sin(\omega_E t)}{v_e^2 + \omega_E^2} \quad (4.107)$$

Comparing Eq. (4.107) with Eq. (4.104) for $t \gg 1/v_e$, the equation for quasi-steady solution can still be used by substituting the electric field with the expression

$$\begin{aligned} \mathbf{E}_{eff} &= \mathbf{E}_0 \frac{v_e^2}{v_e^2 + \omega_E^2} \left[\cos(\omega_E t) + \frac{\omega_E}{v_e} \sin(\omega_E t) \right] \\ &= \mathbf{E}_0 \cos \phi \cos(\omega_E t - \phi) \end{aligned} \quad (4.108)$$

where $\phi = \tan^{-1}(\omega_E/v_e)$. If $v_e \gg \omega_E$ the effective field is equal to the applied field, otherwise they are different, with the amplitude reduced by the factor $\cos \phi$ and with a phase shift with respect to the applied field; in the limit case $v_e \ll \omega_E$ it is $\mathbf{E}_{eff} \approx \mathbf{E}_0 \frac{v_e}{\omega_E} \sin(\omega_E t)$, showing amplitude decrease and a phase shift of 90°. The effective field E_{eff} takes into account the inertia of the current if the field changes very rapidly.

4.1.2 Numerical Aspects in the Solution of BE

From now on, we will consider the Boltzmann equation in the form given in Eq. (4.71). A finite difference approach is considered to rewrite the equation on a discrete energy grid (Rockwood 1973; Elliot and Greene 1976), transforming $n_0(\epsilon)$ in a vector \mathbf{n} . Independently on the discretization rule, Eq. (4.71) present the general form

$$\frac{d\mathbf{n}}{dt} = \hat{C}\mathbf{n} + \hat{T}(\mathbf{n})\mathbf{n} \quad (4.109)$$

where \hat{C} is a matrix that includes all the J 's and S 's, except J_{ee} , and it depends only on the heavy particle composition and level population. The matrix $\hat{T}(\mathbf{n})$, obtained from J_{ee} , introduces a nonlinear term, depending on the distribution vector. The $\hat{T}(\mathbf{n})\mathbf{n}$ term must conserve the total energy of the electron gas and has a Maxwellian distribution as fixed point.

In many applications the electron kinetics is much faster than chemical kinetics; in this case, considering a fixed composition and internal level population, the stationary solution of the Boltzmann equation can be calculated directly solving the equation

$$\hat{C}\mathbf{n} + \hat{T}(\mathbf{n})\mathbf{n} = [\hat{C} + \hat{T}(\mathbf{n})]\mathbf{n} = \mathbf{0} \quad (4.110)$$

This equation has infinite solutions, being its determinant null, because it conserves the number of electrons. To overcome this problem, an independent relation must replace the first equation of the system; that is the normalization relation i.e.

$$\sum_{i=0}^{N_e} n_i \Delta \epsilon_i = N_e \quad (4.111)$$

making the matrix $[\hat{C} + \hat{T}(\mathbf{n})]$ non-singular. This approach is very fast, especially when the electron-electron collisions are not considered, when Eq. (4.110) is linear. In presence of free electrons iterative methods must be used as *Newton* or *Fixed Point* algorithms.

A more complex problem is to solve the electron kinetics self-consistently with the master equation for heavy particle state-to-state kinetics and in particular in flow conditions. In this case the time-dependent solution must be calculated (see Eq. (4.109)). In presence of electron-electron collisions it is very important that the solution algorithm makes the term $\hat{T}(\mathbf{n})\mathbf{n}$ to really conserve the electron energy. Considering the simple *Implicit Euler* time integration algorithm

$$\mathbf{n}_t = [\hat{I} - \Delta t \hat{C} - \Delta t \hat{T}(\mathbf{n}_{t-\Delta t})]^{-1} \mathbf{n}_{t-\Delta t} \quad (4.112)$$

does not conserve the total energy. A better algorithm is to use an operator splitting, separating the linear term by the non-linear one, that will be solved by an iterative approach

$$\begin{aligned} \mathbf{n}_t^0 &= [\hat{I} - \Delta t \hat{C}]^{-1} \mathbf{n}_{t-\Delta t} \\ \mathbf{n}_t^1 &= [\hat{I} - \Delta t \hat{T}(\mathbf{n}_t^0)]^{-1} \mathbf{n}_t^0 \\ \mathbf{n}_t^k &= [\hat{I} - \Delta t \hat{T}(\mathbf{n}_t^{k-1})]^{-1} \mathbf{n}_t^0 \end{aligned} \quad (4.113)$$

up to convergence. This method is very efficient because the matrix \hat{T} is tridiagonal and can be solved very rapidly (Press et al. 1992). According to Rockwood (1973), the diagonals of the matrix \hat{T} can be calculated as the product of a full matrix with the eedf vector. A faster approach can be obtained starting from the original definition of the \hat{T} matrix as an integral of the eedf; After some mathematics, it can be shown that \hat{T} can be obtained by solving linear systems represented by bidiagonal matrices, resulting in a considerably gain in efficiency (D'Angola et al. 2010).

In these years we have solved the Boltzmann equation in the two term approximation for several situations including applied oscillating fields (Capitelli et al. 1987), post-discharge (Gorse et al. 1986), nozzle expansion (Colonna and Capitelli 2001a, 2008a) and many other conditions (Capitelli et al. 2000). Many chapters in this book will be devoted to the illustration of different results.

4.1.3 Negative Electron Conductivity

In this section we will limit to an interesting example, where the solution of the Boltzmann equation predicts a negative electron mobility in decaying plasma. The strong deviations of the eedf from the equilibrium distribution make possible the phenomenon of absolute negative conductivity (ANG). This phenomenon, which has also been observed experimentally, can be predicted on the basis of the Crompton formula for the electron mobility deduced in the framework of the two-term approximation, i.e.

$$\mu = -\frac{e}{3N} \sqrt{\frac{2}{m_e}} \int_0^\infty \frac{\varepsilon}{\sigma_{mt}(\varepsilon)} \frac{d}{d\varepsilon} f_0(\varepsilon) d\varepsilon \quad (4.114)$$

From the formula in Eq. (4.114) it can be seen that the electron mobility can become negative if the eedf has an increasing trend in a energy region where the momentum transfer cross section has a low value. A natural candidate for the study of this phenomenon is argon, because of the wide and deep Ramsauer minimum in the e -Ar momentum transfer cross section. The increasing trend of the eedf can be produced by removing electrons in the appropriate energy range by an attaching species, taking advantage that attachment cross sections have usually a sharp peak in the resonant region. The mixture Ar:NF₃ has been studied by using the two-term approximation for the velocity distribution function (Dyatko et al. 1998). The most appropriate conditions for observing the phenomenon by these simulations are those of decaying plasmas, where electrons have initially a Maxwell distribution and a constant electric field is applied. The electrons are gradually removed by attachment to NF₃ molecules: this effect, together with the electric field, produces an eedf with a maximum at a few eV's (Fig. 4.1). As a result, a negative drift of electrons, in the direction of the electric field, is observed (Fig. 4.2). The fact that an inelastic process plays a critical role in this model requires a check of the two term approximation used. This check was performed by MC simulations (Dyatko et al. 2000) which confirmed the effect found by two-term calculations, although some small relative deviations of the values of mobility calculated by MC and two-term approximation were detected in the regime of negative conductivity.

4.2 Monte Carlo Method for Electron Transport

The *Monte Carlo* (MC) method is an approach to solve the problem of electron and ion transport based on the numerical simulation of the motion of a large particle ensemble where the collision processes are introduced by generating appropriately distributed random numbers. Monte Carlo simulations are characterized by high computational cost but also by straightforward implementation and can be used to

Fig. 4.1 eedf calculated in decaying Ar:NF₃ (97:3) plasma at $E/N = 2$ Td, $T_{e0} = 10,000$ K at $t = (1)$ 0 (2) 2.5×10^{-10} (3) 10^{-9} (4) 3×10^{-9} (5) 5×10^{-9} (6) 10^{-8} s (From Dyatko et al. 1998)

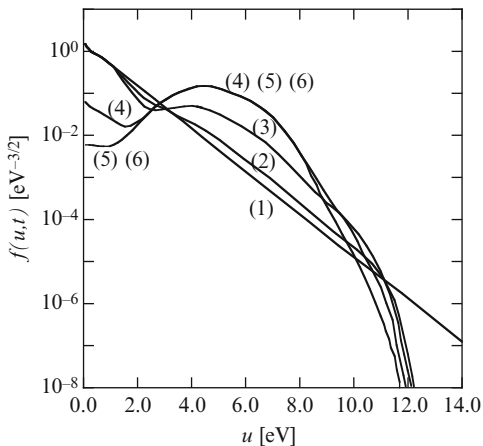
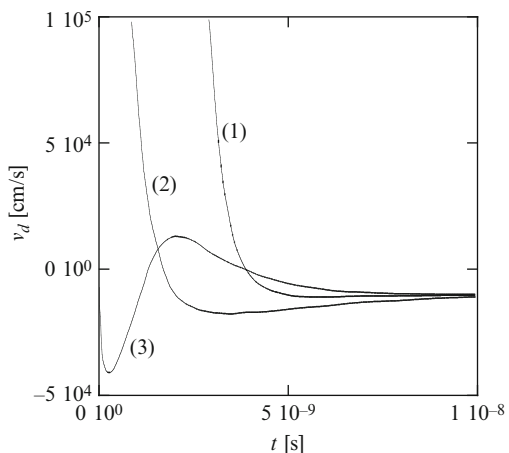


Fig. 4.2 Time evolution of the drift velocity, same condition of Fig. 4.1, for $T_{e0} = 10,000$ K (1), 50,000 K (2), for a rectangular eedf (3) (From Dyatko et al. 1998)



calculate the eedf and other electron quantities when the deterministic solution of Boltzmann equation is less practical, namely in two cases:

1. When the two-term approximation for the velocity distribution is not reliable,
2. When space-dependent quantities are sought and the approximation based on the local E/N cannot be applied because of diffusion effects (i.e. in the so-called *non local regime*).

Historically this method was developed to solve the problem of neutron transport (Spanier and Gelbard 1969), and later applied to charged species. It is important to establish from the beginning the fundamental difference between Monte Carlo particle methods and the so-called Molecular Dynamics approach. This last method simulates explicitly both ‘test particles’ and ‘target particles’, and if the distance between them is low enough it tracks a collision event, by some kind of ‘hard sphere’ approach or better by introducing an appropriate potential and solving the equations

of motion while the distance between the two particles is within the range of the interaction potential. The Monte Carlo method is based on a different principle: only the electrons are simulated and the effect of background particles is included by introducing random numbers, sampled from an appropriate distribution intended to mimic the underlying physics or to implement a stochastic solution method of the transport equation. Furthermore, collision processes are assumed to be binary and instantaneous, in the spirit of the Boltzmann equation. The particle dynamics becomes the solution of the stochastic differential equation for the stochastic process (\mathbf{r}, \mathbf{v}) , while in the framework of the molecular dynamics approach is the solution of the Liouville equation for the phase space distribution $f(\{\mathbf{r}_i, \mathbf{v}_i\})$ describing both the electrons and the target particles.

A computer simulation can consider only a small fraction of the real number of electrons in a real plasma: this is not a problem for the simulation of uniform systems where the number of electrons needs not be specified, but otherwise it is assumed that any simulated electron represents a large number of real electrons following the same trajectory. The ratio between the numbers of real to simulated electrons is the particle weight w . The collision times can be calculated by using the following theorem from probability theory: given a collection of random numbers $0 < r_i < 1$ with uniform distribution, a collection of random numbers $a < x_i < b$ distributed according to the function $p(x)$ is given by

$$\int_a^{x_i} p(x') dx' = r_i \quad (4.115)$$

After calculating the integral, (4.115) becomes an equation for x_i that must be solved. Depending on the case the integration in (4.115) as well as the solution of the resulting equation will be performed either analytically or numerically. The collection $\{r_i\}$ can be provided by standard random number generators.

The time to the next electron-molecule collision must be calculated knowing the collision frequency as a function of the electron velocity, but the electron velocity changes during the free flight due to the electric field. This problem is solved in the simplest way by introducing a *null species* such that in an electron-null species collision (*null process*) the electron velocity does not change. While the idea of a null isotope was already well known in neutron transport where it was used to solve the problem of non uniform media (Spanier and Gelbard 1969), its application to the problem of velocity change in charged particle transport is attributed to H. Skullerud (1968). Using this method, the cross section for the electron-null species collision is chosen to obtain a constant total collisions frequency ν_{tot} , given by

$$\nu_{\text{tot}} = \max_{r \in D, 0 \leq \varepsilon \leq \varepsilon_{\text{lim}}} \left(\sqrt{\frac{2\varepsilon}{m_e}} \sum_k n_k(\mathbf{r}) \sigma_k(\varepsilon) \right) \quad (4.116)$$

where k 's are electron-neutral collision processes, $\sigma_k(\varepsilon)$ is the corresponding cross section, n_k the number density of the collision partner, D the simulation domain, and ε_{lim} is a limit of the scale of kinetic energy based on physical considerations.

The introduction of a null species produces a strong simplification of the problem. With a constant collision frequency, the collision times are distributed according to:

$$p(t) = v_{\text{tot}} \exp(-v_{\text{tot}} t) \quad (4.117)$$

The time to the next collision is then obtained using (4.115). The specific collision process k (including the *null* one) which occurs after the free flight is selected based on the discrete distribution:

$$\sqrt{\frac{2\varepsilon}{m_e} \frac{\sigma_k(\varepsilon) n_k(\mathbf{r})}{v_{\text{tot}}}} \quad (4.118)$$

The null process is eliminated in this stage since, if selected, it has no effect on the electron trajectory. In some cases the computational cost of eliminating most of the collision processes as null can be very high, as when the cross sections have sharp peaks in a narrow energy range or when the gas density has sharp gradients (like in shock waves). To solve this problem the energy range and the domain D can be partitioned into several subsets (Longo and Capitelli 1994), and the corresponding maximum collision frequency is used in every subset. Electrons can cross the boundaries between subsets during the free flight: this problem is solved by allowing some superposition of the subsets and by using the higher collision frequency in the intersections.

After any collision, the new electron energy and the scattering angle is easily determined depending on the nature of the collision itself. The versor of the post collision velocity is found from those of the pre-collision one, the scattering angle ϑ and the azimuth angle φ , used as Euler angles: sections based on

$$\begin{aligned} v'_x &= v_x \cos \vartheta + A \sin \varphi \sin \vartheta \\ v'_y &= v_y \cos \vartheta - \frac{v_z v}{\beta} \cos \varphi \sin \vartheta - \frac{v_y v_x}{\beta} \sin \varphi \sin \vartheta \\ v'_z &= v_z \cos \vartheta + \frac{v_y v}{\beta} \cos \varphi \sin \vartheta - \frac{v_z v_x}{\beta} \sin \varphi \sin \vartheta \\ \beta &= (v_{y0}^2 + v_{z0}^2)^{1/2} \end{aligned} \quad (4.119)$$

The scattering angle is generated according to the differential cross section using Eq. (4.115) with $a = 0$, $b = \pi$ and

$$p(\vartheta) = 2\pi \frac{\sigma(\varepsilon, \vartheta) \sin \vartheta}{\sigma(\varepsilon)} \quad (4.120)$$

while $\varphi = 2\pi r_i$, being uniformly distributed.

In view of the possibility, offered by Monte Carlo methods, to include details of the collision anisotropy in the calculations, the problem of how to interpolate and compress and relevant data becomes important. Solutions include the use of model phase functions $\Theta(\theta)$ (for isotropic scattering $\Theta(\theta) = 1$) to interpolate data. An example is the one obtained theoretically for Born's scattering, e.g.

$$\Theta(\theta) = \frac{1 - \alpha^2}{2(1 - \alpha \cos \theta)^2} \quad (4.121)$$

where α is an anisotropy parameter, $\alpha = 0$ corresponds to isotropic scattering, while the limit $\alpha \rightarrow 1$ to complete forward scattering. Another approach is to build up an artificial differential cross section which is able to match the values of the total elastic and momentum transfer cross sections, which are usually the most available and accurate c.s. data. This can be done in several ways. A very simple solution (Longo and Capitelli 1994) is based on assuming a differential cross section with two isotropic lobes, for forward scattering and backward scattering respectively, whose entity is determined by the c.s. matching. This amounts to using the following phase function:

$$\Theta(\theta, \epsilon) = (A(\epsilon) - B(\epsilon))H(\cos \theta) + B(\epsilon) \quad (4.122)$$

where A and B are energy-dependent coefficients and H is the Heaviside step function. The matching is obtained assuming that the probability of (semi-isotropic) forward scattering ($\cos \theta \geq 0$) is related to c.s.'s by the formula

$$p_f = 0.5 + \frac{\sigma_{el}(\epsilon) - \sigma_{mt}(\epsilon)}{\sigma_{el}(\epsilon)} \quad (4.123)$$

while the total cross section (to be used in (4.115)) is simply given by σ_{el} . In a paper by Okhrimovskyy et al. (2002) a phase function based on Born's scattering is assumed.

Using these matching methods only two data vectors for values of the two cross sections $\sigma_{el}(\epsilon)$ and $\sigma_{mt}(\epsilon)$, at several values of ϵ , need to be stored and eventually interpolated to implement anisotropic scattering. They have been used for example in the open source, fortran code MagBoltz (Biagi 1999) which allows to calculate the eedf for many gases thanks to a large database of momentum transfer and total elastic scattering cross sections embedded in the visible fortran code (as an extended sequence of *data* statements).

Of course all these methods assume that some information on the anisotropic cross section is available. This is not always the case, for example when considering not very well known gas components. In this case a first guess can be provided by using Born's scattering theory again for quantitative *estimate* of the anisotropy parameter α using the expression:

$$\alpha \sim \frac{1}{1 + (21\text{eV})Z^{3/2}\epsilon^{-1}} \quad (4.124)$$

where Z is the number of valence electrons of the atom or molecule under consideration. This expression predicts a higher degree of forward scattering when the energy increases.

Although these approaches allow to include anisotropic scattering conveniently, for many electron transport problems it is often appropriate to assume isotropic scattering: this happens e.g. when the method is used to solve the problem of space-dependent electron transport while the hypothesis of weak anisotropy is assumed to hold, or far from the sheath or reactor surfaces like in the bulk, homogeneous plasma. This hypothesis strongly simplifies calculations since Eq. (4.115) becomes $\cos \vartheta_i = 1 - 2r$; but specially because under isotropic scattering the new velocity is expressed in the laboratory system using ϑ and φ as polar angles. In this case the elastic collision frequency is calculated using the momentum transfer cross section instead of the total elastic one, since by adopting this procedure the resulting eedf for the uniform and steady-state case is consistent with the results obtained by the two-term approximation of the Boltzmann equation in the case of predominant elastic collisions.

Having generated appropriate scattering angles, the electron energy must be updated.

The new kinetic energy is obtained from the dynamics of binary collisions. In the case of electron-neutral elastic scattering it is usually appropriate to neglect the translational distribution of neutrals, this leads to the following relation for the electron kinetic energy loss

$$\frac{\Delta \varepsilon}{\varepsilon} = -2 \frac{m}{M} (1 - \cos \vartheta) \quad (4.125)$$

For isotropic scattering this expression can be replaced by its angular average $-2m/M$. For inelastic collisions the electron energy is changed appropriately. Some collisions are able to change the number of electrons, for example ionization and attachment. One simple way to treat these collisions is to neglect the effect on the number density and consider them as inelastic collisions: this solution is usually appropriate for many applications. A better approach allows the number of simulated electrons to change: to this aim a dynamic list of simulated electrons can be implemented. The total number of particles in the list can be adjusted while the particle w is modified accordingly, as shown later in Sect. 8.3.

In the course of the simulation particles are used to calculate the desired results. The details of this process will be outlined in the following, but the general principle can be anticipated: particles quantities constitute a statistical sampling for the determination of the mean value of a mathematical quantity called an estimator. Any estimator is devised in such a way that its mean value correspond to the value of a physical quantity of interest, and in the continuum case can be expressed as the kernel of an appropriate functional of the general electron distribution function

$f(\mathbf{r}, \mathbf{v}, t)$. This function is defined in such a way that the number of electrons in the (one particle) phase volume $d^3 r d^3 v$ at the time t is given by $f(\mathbf{r}, \mathbf{v}, t) d^3 r d^3 v$.

By the MC approach a functional of the form

$$\langle K(\{\lambda\}) | f \rangle = \int K(\{\lambda\}, \mathbf{r}, \mathbf{v}, t) f(\mathbf{r}, \mathbf{v}, t) d^3 r d^3 v \quad (4.126)$$

(where $K(\{\lambda\}, \mathbf{r}, \mathbf{v}, t)$ is a set of suitable nuclei distinguished by the set of variables $\{\lambda\}$) is determined by estimating the integral above as a mean value, based on the assumption that any simulated electron at a given time t gives a contribution $w \delta^3(\mathbf{r}_i - \mathbf{r}) \delta^3(\mathbf{v}_i - \mathbf{v})$ to the distribution f .

For example the average rate of a chemical reaction $e+A$ in the space region V_ℓ at the time t is obtained by setting

$$K(\ell) = v \sigma(v) n_A \Omega_{V_\ell}(\mathbf{r}) \mu^{-1}(V_\ell) \quad (4.127)$$

where $\Omega_{V_\ell}(\mathbf{r})$ is the characteristic function of V_ℓ , equal to 1 if $\mathbf{r} \in V_\ell$ and 0 otherwise and $\mu(V_\ell)$ is the measure of V_ℓ . The electron energy distribution function in V_ℓ is obtained as a discrete distribution on a discrete energy axis $(i + \frac{1}{2}) \Delta \varepsilon$, by setting

$$K(\ell, i) = \frac{\Omega_{V_\ell}(\mathbf{r}) \Omega_i(\mathbf{v})}{\sqrt{\varepsilon} \mu^{-1}(V_\ell) \Delta \varepsilon} \quad (4.128)$$

and $\Omega_i(\mathbf{v})$ is the characteristic function of the set $(\{\mathbf{v}\} : i \Delta \varepsilon < mv^2/2 < (i+1) \Delta \varepsilon)$. The same principle allows to calculate the energy dependent coefficients which express the angular dependence of the local velocity distribution by an expansion in Legendre polynomials, e.g.

$$f(\varepsilon, \vartheta) = \sum_n P_n(\cos \vartheta) f_n(\varepsilon) \quad (4.129)$$

The calculation is based on the formula for coefficients of expansion in Legendre polynomials applied to the angle-dependent energy distribution:

$$c_{n,i} = \frac{2n+1}{2} \frac{1}{\Delta \varepsilon \sqrt{i + \frac{1}{2} \Delta \varepsilon}} \int_{-1}^{+1} P_n(\cos \vartheta) \int_{i \Delta \varepsilon}^{(i+1) \Delta \varepsilon} \sqrt{\varepsilon} f(\varepsilon, \cos \vartheta) d\varepsilon d \cos \vartheta \quad (4.130)$$

where $c_{n,i}$ is the average of $f_n(\varepsilon)$ in the i -th energy range and the integral is estimated based on simulated electrons as above. Based on this method it has been possible to use MC calculations to determine systematically the functions $f_n(\varepsilon)$ (Braglia et al. 1982).

The hypothesis that a simulated electron at a time t gives a contribution $w \delta^3(\mathbf{r}_i - \mathbf{r}) \delta^3(\mathbf{v}_i - \mathbf{v})$ to the distribution f can be justified by two different methods. The first one is the so-called physical analogy: an argument based on the

fact that the free flight times, collision quantities and electromagnetic forces in the model are a close description of the physical ones, therefore a swarm of simulated particles must retain the same statistics of a solution of the Boltzmann equation which is based on the same physics. A more formal but also more productive argument is based on the fact that the MC method can be deduced from the application of the Neumann-Ulam MC method to the solution of the integral form of the Boltzmann equation: the original argument (Spanier and Gelbard 1969) was formulated for neutron transport. For electron transport the demonstration needs to be extended to account for velocity changes due to the electric field: this has been done using the Green function (Longo 2000).

The direct derivation of the MC method from the transport equation has the advantage of a generally simpler implementation of variance reduction techniques: these last are modifications of the basic method aimed at reducing the statistical variance in the calculation of functionals, often based on the recognition of the purely mathematical nature of the simulated particles. For example, a particle weight w can be decreased during the propagation to describe a destruction process, instead of removing the particle at a given time (Spanier and Gelbard 1969). These techniques allow to reduce much the computational cost of a simulation, which is otherwise high since the relative error on macroscopic quantities due to statistical fluctuations decreases slowly with the number n of contributing events, as $n^{-1/2}$, as can be shown from the law of large numbers. It is not uncommon for an accurate determination of transport quantities for electrons to require several hours of computational time on a modern workstation.

A highly efficient example of variance reduction technique is the *Monte Carlo Flux* method (Schaefer and Hui 1990). In this method the phase space of electrons is partitioned into cells, and the problem of electron transport is reformulated in the following form:

$$n_i(t + \Delta t) = \sum_j q_{ji}(\Delta t) n_j(t) - n_i(t) \sum_j q_{ij}(\Delta t) \quad (4.131)$$

where n_i is the number of electrons in the i -th cell, and Δt is a time step which is selected in order to fulfill the inequalities $\tau_{\text{coll}} \ll \Delta t \ll \tau_{\text{eedf}}$ (for electrons $\tau_{\text{eedf}}/\tau_{\text{coll}} \approx M/m$) involving the characteristics times for electron-neutral collisions and the relaxation of the eedf. A set of MC simulations is performed in order to evaluate the coefficients $q_{ij}(\Delta t)$ by placing systematically sample electrons in the i -th cell and collecting the number of electrons found in any j -cell after the time Δt . Then Eq. (4.131) is solved for any time $t = N\Delta t$ starting from an initial condition $\{n_i(0)\}$ by straightforward iteration. Alternatively the steady state solution of Eq. (4.131) is found by an eigenvalue method. The advantage of the Monte Carlo Flux method is that the eedf can be evaluated with uniform statistical accuracy in low density regions which cannot be treated by the straightforward MC method since the probability that a simulated electron is found in the region is negligible.

In Figs. 4.3 and 4.4 two examples of calculation of the eedf are given (Longo and Capitelli 1994). In the first case the eedf for a mixture Ne/Xe/HCl (mostly Ne)

Fig. 4.3 Steady state eedf calculated for electrons in a Ne/Xe/HCl (99.5 : 0.44 : 0.06 mole ratio) mixture and $E/N=2$ Td, by using the two-term approximation (solid line) and the MC method (markers)

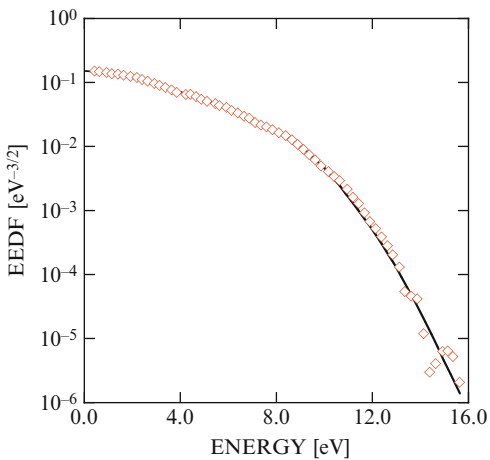
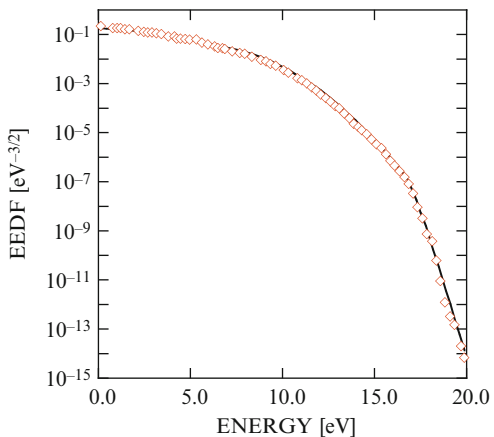


Fig. 4.4 Steady state eedf for electrons in the system of Fig. 4.3 calculated by using the two-term approximation (solid line) and the Monte Carlo Flux method (markers)



used for XeCl lasers (see Sect. 5.3.5) is calculated, and compared to the solution of the two-term Boltzmann equation in the same conditions. In the second case an example of calculation by the Monte Carlo Flux method in the same conditions is given, illustrating the possibility of calculating a wide range of values of eedf. In both cases a good agreement was observed with the numerical solution of the two-term Boltzmann equation as expected for this case since the elastic collision frequency is always higher than the inelastic. By inspecting the high energy region in Fig. 4.4 it can be seen how use of the Monte Carlo Flux allows to determine values of the eedf exceedingly low to be detected by the conventional MC method: this feature can be important in order to calculate ionization and excitation rates at low values of the reduced electric field E/N .

The MC method can be modified in order to include electron-electron collisions, these last lead to a nonlinear transport equation. These collisions can be implemented approximately as binary processes, where the target electron is sampled

from the eedf (a simple way to do it is to use sample another electron from the same simulated ensemble) and using the momentum transfer cross section for screened Coulomb interaction

$$\sigma_{mt} = \frac{16\pi e^4}{m_e^2(\mathbf{v}' - \mathbf{v})^4} \ln \Lambda \quad (4.132)$$

where $\ln \Lambda$ is the Coulomb logarithm. The corresponding partial collision frequency is

$$\nu_{ee} = \sigma_{mt} n_e |\mathbf{v}' - \mathbf{v}| \quad (4.133)$$

Under the action of e - e collisions only, the eedf relaxes to a Maxwell distribution.

References

- Apostolova T, Perlado J, Rivera A (2015) Femtosecond laser irradiation induced-high electronic excitation in band gap materials: a quantum-kinetic model based on Boltzmann equation. *Nucl Instrum Methods Phys Res Sect B: Beam Interact Mater Atoms* 352:167–170
- Biagi SF (1999) Monte Carlo simulation of electron drift and diffusion in counting gases under the influence of electric and magnetic fields. *Nucl Instrum Methods Phys Res Sect A* 421:234
- Braglia G, Wilhelm J, Winkler E (1985) Multi-term solutions of Boltzmann's equation for electrons in the real gases Ar, CH₄ and CO₂. *Lettore Al Nuovo Cimento (1971–1985)* 44(6):365–378
- Braglia GL, Romanò L, Diligenti M (1982) Comment on “comparative calculations of electron-swarm properties in N₂ at moderate E/N values”. *Phys Rev A* 26(6):3689
- Busch C, Kortshagen U (1995) Numerical solution of the spatially inhomogeneous Boltzmann equation and verification of the nonlocal approach for an argon plasma. *Phys Rev E* 51(1):280
- Capitelli M, Celiberto R, Gorse C, Winkler R, Wilhelm J (1987) Electron energy distribution function in He-CO radio-frequency plasmas: the role of vibrational and electronic superelastic collisions. *J Appl Phys* 62:4398
- Capitelli M, Ferreira CM, Gordiets BF, Osipov R (2000) Plasma kinetics in atmospheric gases. Springer Series on Atomic, Optical, and Plasma Physics, vol. 31. Springer-Verlag Berlin Heidelberg
- Capitelli M, Bruno D, Laricchiuta A (2013) Fundamental aspects of plasma chemical physics: transport. Springer series on atomic, optical, and plasma physics, vol 74. Springer, New York
- Chapman S, Cowling TG (1970) The mathematical theory of non-uniform gases. Cambridge University Press, Cambridge
- Colonna G, Capitelli M (2001a) The influence of atomic and molecular metastable states in high enthalpy nozzle expansion nitrogen flows. *J Phys D: Appl Phys* 34:1812–1818
- Colonna G, Capitelli M (2001b) Self-consistent model of chemical, vibrational, electron kinetics in nozzle expansion. *J Thermophys Heat Transf* 15:308–316
- Colonna G, Capitelli M (2003) The effects of electric and magnetic fields on high enthalpy plasma flows. AIAA paper 2003–4036, AIAA
- Colonna G, Capitelli M (2005) Plasma expansion in presence of electric and magnetic fields. In: Capitelli M (ed) 24th international symposium on rarefied gas dinamics, AIP conference proceedings, vol 762, American Institute of Physics, New York, pp 1295–1300
- Colonna G, Capitelli M (2008a) Boltzmann and master equations for magnetohydrodynamics in weakly ionized gases. *J Thermophys Heat Transf* 22(3):414–423

- Colonna G, Capitelli M (2008b) Boltzmann and master equations for mhd in weakly ionized gases. *J Thermophys Heat Transf* 22(3):414–423
- Colonna G, Tuttafesta M, Giordano D (2001) Numerical methods to solve Euler equations in one-dimensional steady nozzle flow. *Comput Phys Commun* 138:213–221
- D'Angola A, Coppa G, Capitelli M, Gorse C, Colonna G (2010) An efficient energy-conserving numerical model for the electron energy distribution function in the presence of electron-electron collisions. *Comput Phys Commun* 181(7):1204–1211
- Dujko S, White R, Petrović ZL, Robson R (2011) A multi-term solution of the nonconservative Boltzmann equation for the analysis of temporal and spatial non-local effects in charged-particle swarms in electric and magnetic fields. *Plasma Sources Sci Technol* 20(2):024013
- Dyatko NA, Capitelli M, Longo S, Napartovich AP (1998) Negative electron mobility in a decaying plasma. *Plasma Phys Rep* 24(8):691 (translated from *Fizika Plasmy*)
- Dyatko NA, Napartovich AP, Sakadzic S, Petrovich Z, Raspovovich Z (2000) On the possibility of negative electron mobility in a decaying plasma. *J Phys D* 33(4):375
- Elliot CJ, Greene AE (1976) Electron energy distribution in *e*-beam generated Xe and Ar plasmas. *J Appl Phys* 47(7):2946–2953
- Engelhardt A, Phelps A (1963) Elastic and inelastic collision cross sections in hydrogen and deuterium from transport coefficients. *Phys Rev* 131(5):2115
- Frost L, Phelps A (1962) Rotational excitation and momentum transfer cross sections for electrons in H₂ and N₂ from transport coefficients. *Phys Rev* 127(5):1621
- Frost L, Phelps A (1964) Momentum-transfer cross sections for slow electrons in He, Ar, Kr, and Xe from transport coefficients. *Phys Rev* 136(6A):A1538
- Golant VE, Zilinskij AP, Sacharov IE (1980) Fundamentals of plasma physics. Wiley, New York
- Gorse C, Paniccia F, Ricard A, Capitelli M (1986) Electron energy distribution functions in He-CO vibrationally excited post discharges. *J Chem Phys* 84:4717
- Greenwood D (1958) The Boltzmann equation in the theory of electrical conduction in metals. *Proc Phys Soc* 71(4):585
- Hirschfelder JO, Curtiss CF, Bird RB (1966) Molecular theory of gases and liquids. John Wiley, New York
- Kortshagen U (1993) A non-local kinetic model applied to microwave produced plasmas in cylindrical geometry. *J Phys D: Appl Phys* 26(10):1691
- Kortshagen U, Parker G, Lawler J (1996) Comparison of Monte Carlo simulations and nonlocal calculations of the electron distribution function in a positive column plasma. *Phys Rev E* 54(6):6746
- Leyh H, Loffhagen D, Winkler R (1998) A new multi-term solution technique for the electron Boltzmann equation of weakly ionized steady-state plasmas. *Comput Phys Commun* 113(1):33–48
- Loffhagen D, Winkler R, Braglia G (1996) Two-term and multi-term approximation of the nonstationary electron velocity distribution in an electric field in a gas. *Plasma Chem Plasma Process* 16(3):287–300
- Longo S (2000) Monte Carlo models of electron and ion transport in non-equilibrium plasmas. *Plasma Sources Sci Technol* 9:468
- Longo S, Capitelli M (1994) A simple approach to treat anisotropic elastic collisions in Monte Carlo calculations of the electron energy distribution function in cold plasmas. *Plasma Chem Plasma Process* 14(1):1
- Maeda K, Makabe T (1994) Radiofrequency electron swarm transport in reactive gases and plasmas. *Physica Scripta* 1994(T53):61
- Majorana A (1991) Space homogeneous solutions of the Boltzmann equation describing electron-phonon interactions in semiconductors. *Transp Theory Stat Phys* 20(4):261–279
- Mitchner M, Kruger CHJ (1973) Partially ionized gases. Wiley and Sons, New York
- Morgan W (1992) A critical evaluation of low-energy electron impact cross sections for plasma processing modeling. i: Cl₂, F₂, and HCl. *Plasma Chem Plasma Process* 12(4):449–476
- Morgan WL (1991) Use of numerical optimization algorithms to obtain cross sections from electron swarm data. *Phys Rev A* 44(3):1677

- Morgan WL (1993) Test of a numerical optimization algorithm for obtaining cross sections for multiple collision processes from electron swarm data. *J Phys D Appl Phys* 26(2):209
- Ness K (1994) Multi-term solution of the Boltzmann equation for electron swarms in crossed electric and magnetic fields. *J Phys D Appl Phys* 27(9):1848
- Okhrimovskyy A, Bogaerts A, Gijbels R (2002) Electron anisotropic scattering in gases: a formula for Monte Carlo simulations. *Phys Rev E* 65:037402
- Petrović ZL, Dujko S, Marić D, Malović G, Nikitović Ž, Šaši O, Jovanović J, Stojanović V, Radmilović-Rađenović M (2009) Measurement and interpretation of swarm parameters and their application in plasma modelling. *J Phys D Appl Phys* 42(19):194002
- Phelps A (1968) Rotational and vibrational excitation of molecules by low-energy electrons. *Rev Mod Phys* 40(2):399
- Phelps A (1991) Cross sections and swarm coefficients for nitrogen ions and neutrals in N₂ and argon ions and neutrals in Ar for energies from 0.1 eV to 10 keV. *J Phys Chem Ref Data* 20(3):557–573
- Phelps A, Pitchford L (1985) Anisotropic scattering of electrons by N₂ and its effect on electron transport. *Phys Rev A* 31(5):2932
- Pietanza LD, Colonna G, Longo S, Capitelli M (2004a) Electron and phonon distribution relaxation in metal films under a femtosecond laser pulse. *Thin Solid Films* 453:506–512
- Pietanza LD, Colonna G, Longo S, Capitelli M (2004b) Electron and phonon relaxation in metal films perturbed by a femtosecond laser pulse. *Appl Phys A* 79(4–6):1047–1050
- Pietanza LD, Colonna G, Capitelli M (2005) Electron and phonon dynamics in laser short pulses-heated metals. *Appl Surf Sci* 248(1):103–107
- Pietanza LD, Colonna G, Longo S, Capitelli M (2007) Non-equilibrium electron and phonon dynamics in metals under femtosecond laser pulses. *Eur Phys J D-Atomic Mol Optical Plasma Phys* 45(2):369–389
- Pitchford L, Phelps A (1982) Comparative calculations of electron-swarm properties in N₂ at moderate E/N values. *Phys Rev A* 25(1):540
- Press WH, Flannery BP, Teukolsky SA, Vetterling WT (1992) Numerical recipes in C: the art of scientific computing. Cambridge University Press, Cambridge
- Rockwood SD (1973) Elastic and inelastic cross sections for electron-Hg scattering from Hg transport data. *Phys Rev A* 8(5):2348–2360
- Schaefer G, Hui P (1990) The Monte Carlo flux method. *J Comput Phys* 89(1):1
- Shivanian E, Abbasbandy S, Alhuthali MS (2014) Exact analytical solution to the Poisson-Boltzmann equation for semiconductor devices. *Eur Phys J Plus* 129(6):1–8
- Skullerud HR (1968) The stochastic computer simulation of ion motion in a gas subjected to a constant electric field. *J Phys D* 1(11):1567
- Spanier J, Gelbard EM (1969) Monte Carlo principles and neutron transport problems. Addison-Wesley, Reading
- Tsendin L (1995) Electron kinetics in non-uniform glow discharge plasmas. *Plasma Sources Sci Technol* 4(2):200
- Uhrlandt D, Winkler R (1996) Radially inhomogeneous electron kinetics in the dc column plasma. *J Phys D Appl Phys* 29(1):115
- Yachi S, Kitamura Y, Kitamori K, Tagashira H (1988) A multi-term Boltzmann equation analysis of electron swarms in gases. *J Phys D Appl Phys* 21(6):914
- Yachi S, Date H, Kitamori K, Tagashira H (1991) A multi-term Boltzmann equation analysis of electron swarms in gases-the time-of-flight parameters. *J Phys D Appl Phys* 24(4):573

Chapter 5

Superelastic Collisions and Electron Energy Distribution Function

Electron energy distribution function (eedf) in non equilibrium plasmas is a key quantity which determines many properties of the medium including the transport coefficients of electrons and the rates of elementary processes. Still now the experimental determination of eedf is a difficult task (Blagoev et al. 1992; Plasil et al. 2009), so that theory is often used to get informations on eedf. Pioneers in this description can be considered numerous authors; among them we want to remind the historical contributions of Phelps (Engelhardt et al. 1964; Frost and Phelps 1964), Nighan (1970, 1972), Rockwood (1973), and Rockwood et al. (1973) and more recently by Morgan and Penetrante (1990) and Hagelaar and Pitchford (2005) who numerically solved the homogeneous Boltzmann equation (BE) with stationary and non-stationary methods. Phelps pioneered the deconvolution of experimental transport properties by a Boltzmann analysis to get complete set of elastic and inelastic cross sections. Nighan (1970, 1972) on the other hand was one of the first researchers to show the role of second-kind vibrational collisions (superelastic vibrational collisions) in affecting eedf in molecular nitrogen. The concentration of vibrationally excited molecules was considered as a parameter by imposing a given vibrational temperature for the nitrogen molecules. Rockwood (1973) presented a powerful time-dependent algorithm to solve the BE which was the basis to calculate eedf under transient situations (transitions from a given E/N value to an other E/N including $E/N = 0$, bulk RF discharges, time-dependent discharges (Gorse et al. 1990b; Capitelli et al. 1983, 1984, 1988; Bretagne et al. 1987; Gorse et al. 1988b)). Soon it appeared clear that to understand the role of excited states in affecting eedf one should solve a BE coupled to a system of rate equations for vibrationally and electronically excited states. Nowadays this approach is commonly used by researchers in plasma chemistry and plasma physics thanks also to the contributions given by many researchers (Adamovich and Rich 1997; Jelenak et al. 1995; Ferreira et al. 1985; Gorse et al. 1988b; Capitelli et al. 2009). This approach is forgotten when applied to 1D and 2D codes used to represent more realistic plasma situations.

As an example only few PIC MCC (particle in cell with Monte Carlo collisions) codes introduce second-kind collisions in their kinetic models. The first attempt in this direction was made by Longo et al. (1998) in describing by a PIC MCC code the RF parallel plate plasma reactor working with molecular nitrogen. The role of superelastic vibrational collisions in this kind of discharges was discussed with the non-local effects on eedf.

5.1 Boltzmann Equation for Atomic and Molecular Plasmas

The Boltzmann equation for the distribution function of electrons can be written in compact form as (see Chap. 4)

$$\frac{\partial n(\varepsilon, t)}{\partial t} = -\frac{\partial J_E(\varepsilon)}{\partial \varepsilon} - \frac{\partial J_{el}(\varepsilon)}{\partial \varepsilon} - \frac{\partial J_{ee}(\varepsilon)}{\partial \varepsilon} - \frac{\partial J_r(\varepsilon)}{\partial \varepsilon} + S_{in}(\varepsilon) + S_{sup}(\varepsilon) \quad (5.1)$$

where $n(\varepsilon, t)d\varepsilon$ is the number of electrons in the energy range $[\varepsilon, \varepsilon + d\varepsilon]$ at time t . The different terms on the right hand side of Eq. (5.1) describe the flux of electrons in the energy space due to

$\frac{\partial J_E}{\partial \varepsilon}$	the electric field E
$\frac{\partial J_{el}}{\partial \varepsilon}$	the elastic electron-heavy particle collisions
$\frac{\partial J_{ee}}{\partial \varepsilon}$	the electron-electron elastic collisions
$\frac{\partial J_r}{\partial \varepsilon}$	the rotational collisions
S_{in}	the inelastic collisions
S_{sup}	the superelastic (second-kind) collisions

The units of $n(\varepsilon, t)$ are eV^{-1} , linked to the electron energy distribution function in $\text{eV}^{-3/2}$ by the Eq. (4.62). The source terms are due to inelastic and superelastic collisional processes



involving internal transitions, where M is an atom or a molecule in its ground state while M^* indicates the corresponding excited species. However, being the energy threshold of the rotational transitions very small, the rotational contribution, J_r can be obtained from Eqs. (4.79) and (4.80), i.e. by a continuous type term. On the other hand Eqs. (4.79) and (4.80) can be simplified in the following form (Hake and Phelps 1967; Gorse and Capitelli 1984)

$$\frac{\partial J_r}{\partial \varepsilon} = -\frac{\partial}{\partial \varepsilon} \left[N_S \Gamma \left(\frac{15}{8} \right) Ry 2^{7/4} B_0^{7/8} (k_B T)^{-1/8} \varepsilon^{-1/4} \sqrt{\frac{2}{m}} n(\varepsilon, t) 8\pi D^{2/3} a_0^{2/3} \right] \quad (5.3)$$

where B_0 and D are the rotational constant and the dipole moment of the diatomic molecule, and Ry the Rydberg constant.

5.1.1 Inelastic Collisions

The inelastic source terms can be obtained by energy balance equations. We have essentially two contributions; the first one is due to electrons with energy ε jumping to the $\varepsilon - \varepsilon^*$



giving the contribution

$$S_{in}^1(\varepsilon) = -N_M n(\varepsilon) v(\varepsilon) \sigma_{in}(\varepsilon) \quad (5.5)$$

where $\sigma_{in}(\varepsilon)$ is the inelastic cross section and ε^* is the threshold energy of the process. The second contribution comes from electrons with energy $\varepsilon + \varepsilon^*$ jumping to ε

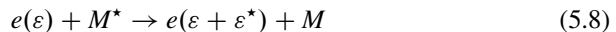


giving

$$S_{in}^2(\varepsilon) = N_M n(\varepsilon + \varepsilon^*) v(\varepsilon + \varepsilon^*) \sigma_{in}(\varepsilon + \varepsilon^*) \quad (5.7)$$

5.1.2 Superelastic Collisions

In superelastic collisions cold electrons receive energy from excited states reversing the previous elementary processes. Similarly to the inelastic processes the superelastic source term is due to molecular deactivation



The kinetic term for depopulating electrons at energy ε is then written

$$S_{sup}^1 = -N_{M^*} n(\varepsilon) v(\varepsilon) \sigma_{sup}(\varepsilon) \quad (5.9)$$

where σ_{sup} is the superelastic cross section and N_{M^*} is the concentration of the excited state. On the other hand the kinetic term populating electrons at energy ε arises from the following elementary process



and can be written as

$$S_{sup}^2 = N_M \cdot n(\varepsilon - \varepsilon^*) v(\varepsilon - \varepsilon^*) \sigma_{sup}(\varepsilon - \varepsilon^*) \quad (5.11)$$

The cross section of the superelastic collisions are related to the corresponding inelastic one, applying the micro-reversibility principle¹

$$\sigma_{sup}(\varepsilon - \varepsilon^*) = \frac{g_0}{g^*} \frac{\varepsilon}{\varepsilon - \varepsilon^*} \sigma_{in}(\varepsilon) \quad (5.12)$$

where g_0 and g^* represent respectively the statistical weight of ground and excited states.

5.1.3 A Golden Rule for Superelastic Collisions

This section is devoted to understand the relative contribution of inelastic and superelastic collisions in affecting the eedf. In principle, being superelastic collisions the reverse process of the inelastic one, to have an effective contribution on the eedf we should have $S_{sup}^2(\varepsilon) \geq -S_{in}^1(\varepsilon)$,² i.e.

$$N_M \cdot n(\varepsilon - \varepsilon^*) v(\varepsilon - \varepsilon^*) \sigma_{sup}(\varepsilon - E^*) \geq N_M n(\varepsilon) v(\varepsilon) \sigma_{in}(\varepsilon) \quad (5.13)$$

Limiting our discussion to a single process and considering the fraction of excited molecules

$$\chi = \frac{N_{M^*}}{N_M} \quad (5.14)$$

the velocity ratio

$$\frac{v(\varepsilon - \varepsilon^*)}{v(\varepsilon)} = \sqrt{\frac{\varepsilon - \varepsilon^*}{\varepsilon}} \quad (5.15)$$

and the eedf in [eV^{-3/2}]

$$f(\varepsilon) \propto \frac{n(\varepsilon)}{\sqrt{\varepsilon}} \quad (5.16)$$

Eq. (5.13) can be rearranged, considering also Eq. (5.12), as

$$f(\varepsilon) \leq \chi \frac{g_0}{g^*} f(\varepsilon - \varepsilon^*) \quad (5.17)$$

¹This principle assure the existence of the equilibrium distribution.

²We should note that $S_{sup}^2(\varepsilon) = -S_{sup}^1(\varepsilon - \varepsilon^*)$ and $S_{in}^2(\varepsilon) = -S_{in}^1(\varepsilon + \varepsilon^*)$.

Posing $\eta = \chi g_0/g^*$, and considering the limiting case $S_{sup}^2(\varepsilon) = -S_{in}^1(\varepsilon)$, which should be the stationary condition, we can estimate the value of the distribution at the threshold energy

$$f(\varepsilon^*) = f(0)\eta \quad (5.18)$$

i.e. the location and magnitude of the first maximum in the eedf.

A second maximum can occur at $\varepsilon = 2\varepsilon^*$ with the following amplitude

$$f(2\varepsilon^*) = f(\varepsilon^*)\eta = f(0)\eta^2 \quad (5.19)$$

Applying the relation recursively, we can estimate the amplitude of n -th maximum, located at $n\varepsilon^*$

$$f(n\varepsilon^*) = f((n-1)\varepsilon^*)\eta = \dots = f(0)\eta^n \quad (5.20)$$

The critical value of metastable concentration able to affect the eedf can be estimated from Eq. (5.17) in the form

$$\chi \geq \frac{f(\varepsilon)}{f(\varepsilon - \varepsilon^*)} \frac{g^*}{g_0} \quad (5.21)$$

Assuming χ as a free parameter and considering a Maxwell distribution function for low-energy electrons at T_e we get

$$\frac{f(\varepsilon)}{f(\varepsilon - \varepsilon^*)} \approx \frac{f(\varepsilon^*)}{f(0)} \approx \exp\left(-\frac{\varepsilon^*}{k_B T_e}\right) \quad (5.22)$$

so that the superelastic term can be important when

$$\chi \geq \frac{g^*}{g_0} \exp\left(-\frac{\varepsilon^*}{k_B T_e}\right) \quad (5.23)$$

We report in Table 5.1 the exponential term appearing in Eq. (5.22) for different values of T_e and threshold energies corresponding to the CO metastable state ($\varepsilon^* = 6.2$ eV), to the He metastable state ($\varepsilon^* = 19.6$ eV) and to the first vibrational level of CO ($\varepsilon^* = 0.25$ eV). We can see that the concentration of excited state must strongly increase with T_e in all the cases. Favorable conditions for the action of the excited states are for $T_e \rightarrow 0$, i.e. when $E/N \rightarrow 0$ corresponding to post-discharge conditions.

Equation (5.20) (see also Osiac et al. 2007) has been recently used to rationalize the plateaux in eedf in low temperature and afterglow plasmas (D'Ammando et al. 2015). Note that our approach solves the Boltzmann Equation in the *local approximation*. *Non-local* effects will be discussed in Chap. 8. Here It is interesting to note that the following equation (Demidov et al. 2006), similar to Eq. (5.18)

Table 5.1 Exponential term in Eq. (5.22) as a function of T_e , for different metastable states

T_e (eV)	CO($E^* = 6.2$ eV)	He($E^* = 19.6$ eV)	CO($E^* = 0.25$ eV)
0	0.0	0.0	0.0
0.4	1.85×10^{-7}	5.24×10^{-22}	0.53
0.5	4.11×10^{-6}	9.25×10^{-18}	0.60
1.0	2.11×10^{-3}	3.07×10^{-9}	0.78
3.0	1.26×10^{-1}	1.45×10^{-3}	0.92

$$\frac{N_{\text{ef}}}{N_{\text{eb}}} \approx \frac{N_{A^*}}{N_A} \quad (5.24)$$

where N_{ef} and N_{eb} are the densities of fast and bulk electrons, respectively, and N_A^* and N_A the number densities of metastable and ground state atoms, has been used in the description of non-local eedf in bounded afterglow plasmas.

5.2 Atomic and Molecular Plasmas

In this section we will present the electron energy distributions calculated in pure molecular and atomic gases and in some mixtures. To better understand the numerous results presented in this chapter we define two conditions:

1. *Cold plasma*, where the concentration of excited states is very small so that superelastic collisions can be neglected;
2. *Hot plasma*, where appreciable concentration of excited states does exist and superelastic collisions plays a relevant role;

In the *cold gas* approximation the inelastic term is due to the redistribution of electron energy via collisions with atoms and molecules in their ground state.

The main difference between atomic and molecular plasmas stands in the absence in atomic plasma of the contribution of rotational states as well as of inelastic and superelastic collisions involving vibrational states.

5.2.1 Case 1: Pure CO

The metastable states of CO can affect eedf only when the first part of eedf presents very low temperature, the post-discharge conditions $T_e \rightarrow 0$ being the ideal room to see the effect of second-kind collisions. On the other hand the superelastic vibrational collisions acting at low energy should present much higher concentrations of vibrationally excited states to affect eedf. These points will appear

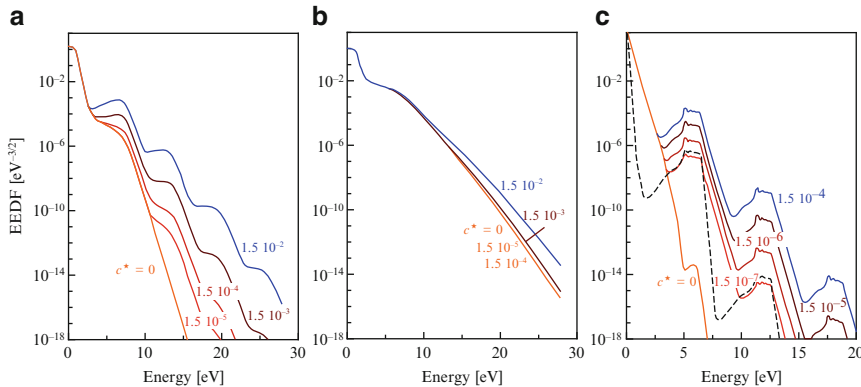


Fig. 5.1 Electron energy distribution functions vs. energy at different concentrations of CO($a^3\Pi$) metastable state, c^* , in the discharge and post-discharge regime (all the curves have been calculated with a vibrational distribution at $\vartheta_1 = 2,000$ K). **(a)** $E/N = 2 \cdot 10^{-16}$ V cm 2 ; **(b)** $E/N = 6 \cdot 10^{-16}$ V cm 2 ; **(c)** post-discharge, $E/N = 0$ (dashed line: $\vartheta_1 = 0$ K and $c^* = 2 \times 10^{-7}$) (From Gorse et al. 1986)

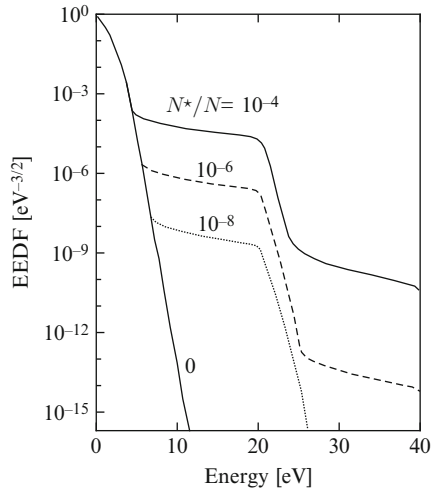
clear in many chapters of the book. We anticipate some results by discussing eedf in pure CO at different E/N and metastable concentration values having fixed the vibrational temperature of CO, $\vartheta_1 = E_{10}/K \ln(N_0/N_1)$, at 2,000 K.

Figure 5.1a, b report the cases at $E/N = 20$ and 60 Td, which to a first approximation correspond to electron temperatures of about 0.5 and 1 eV (Gorse et al. 1986). Inspection of Table 5.1 tell us that at $T_e = 0.5$ eV we expect that the effect of second-kind collisions from CO metastable will occur only when its concentration is of the order of 4×10^{-6} , increasing up to 2×10^{-3} for $T_e = 1$ eV. We can see that eedf structures created by second-kind collisions between cold electrons and metastable states appear at 20 Td at metastable concentrations much lower than the 60 Td case. Figure 5.1c on the other hand reports the corresponding results at $E/N = 0$ showing that in this case very low concentrations of metastable states create large structures in eedf. It is worth noting that in this case Eqs. (5.18)–(5.20) quantitatively reproduce the sequence of maxima and their magnitude. The bulk of the results have been obtained with $\vartheta_1 = 2,000$ K which practically imposes the same temperature to the low-energy part of eedf, the same with $c^* = 0$. In the same figure we have reported the eedf at $\vartheta_1 = 0$ K and $c^* = 2 \times 10^{-7}$, which shows the persistence of the plateaux created by superelastic collisions with metastable states as well as pronounced dips before the plateau region.

5.2.2 Case 2: Pure He

Similar results are reported in Fig. 5.2 (Gorse et al. 1988a) for an helium plasma at $E/N = 2 \times 10^{-17}$ V cm 2 . Different concentrations of He(3S) are used to understand the role of the reaction

Fig. 5.2 Electron energy distribution functions versus energy, at $E/N = 2 \times 10^{-17} \text{ V cm}^2$, for different concentrations of He(3S) metastable state (Gorse et al. 1988a)



in affecting eedf. This reaction produces electrons at $E^* = 19.6 \text{ eV}$ which are then spread in a plateau by elastic collisions. The first plateau is then reproduced at higher energies following qualitatively and quantitatively Eqs. (5.18)–(5.20)

5.2.3 Case 3: He-CO Mixture

In this case the simultaneous presence of the metastable states of both CO and He and the presence of vibrational excited states of CO can be qualitatively understood with the previous arguments, even though we can expect more structured eedf due to synergic effects of both second-kind and inelastic collisions. As anticipated, the superelastic terms mainly come from the following reactions



Taking into account that we consider vibrational levels up to $v = 10$, we can anticipate that processes (a) will affect eedf up to 3 eV, while processes (b) and (c) will form beams of electrons at $E^* = 6.2$ and 19.6 eV . Elastic and inelastic collisions will spread these beams over all eedf ending in a very structured eedf. The excited state concentrations are considered as independent variables ($C_1 = \text{CO}({}^3\Pi)/\text{CO}$;

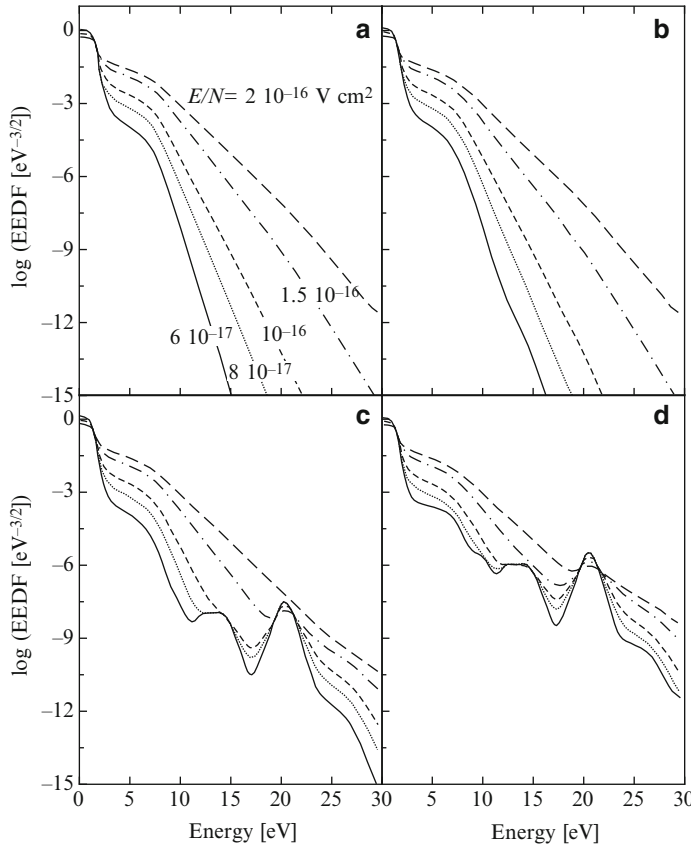
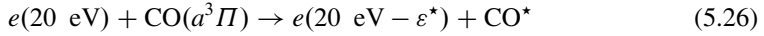


Fig. 5.3 Electron energy distribution functions versus energy at different values of the reduced electric field E/N and for different concentrations of metastable states ($C_1 = \text{CO}(a^3\Pi)/\text{CO}$; $C_2 = \text{He}({}^3S)/\text{He}$) for 10:90 CO-He mixture. **(a)** $C_1 = C_2 = 0$; **(b)** $C_1 = 10^{-6}$, $C_2 = 0$; **(c)** $C_1 = C_2 = 10^{-6}$; **(d)** $C_1 = C_2 = 10^{-4}$. The CO vibrational distribution in all curves corresponds to a Treanor's law at $\vartheta_1 = 2,000$ K and $T = 300$ K (Gorse et al. 1989)

$C_2 = \text{He}({}^3S)/\text{He}$). No electron-electron collisions have been considered, while the vibrational distribution describing the 10 vibrational levels of CO is a Treanor one (Treanor et al. 1968) at $\vartheta_1 = 2,000$ K and $T_g = 300$ K. Details of the input data can be found in Gorse et al. (1989).

Figure 5.3a-d (Gorse et al. 1989) report the results for a 10:90 CO/He mixture at $E/N = 20$ $Td = 2 10-16$ V cm^2 and four different sets of C_1 , C_2 concentrations. A well-structured eedf results by the interplay of numerous superelastic and inelastic collisions. In particular the maximum at $\varepsilon = 20$ eV is caused by process (c), while process (b) practically does not affect eedf (see Fig. 5.3b). Process (a), which is present in all figures, on the contrary, acts for $\varepsilon < 4$ eV. The increase of the concentration of metastable states (Fig. 5.3d) is able not only to increase the peak at 20 eV (approximately by two orders of magnitude by going from $C_2 = 10^{-6}$ to

10^{-4} , but also to generate a structure in eedf at $\varepsilon = 12$ eV. This structure is the result of an inelastic process involving electrons $\varepsilon = 20$ eV (those formed by process *c*) colliding with CO, i.e.



5.3 Time Evolution of eedf

The relaxation of the eedf in the ambient gas is usually very fast, therefore a quasi-stationary approach can be considered, calculating directly the stationary solution of the Boltzmann equation considering constant the gas composition, internal distributions and the electric field. In some cases, it is interesting to analyze the evolution of the eedf.

5.3.1 Post-discharge Conditions

An operational condition where the superelastic collisions play a fundamental role, is the post-discharge. In this case the electron temperature rapidly decreases due to elastic scattering and the golden rule in Eq. (5.23) is fulfilled, because the population of excited species, especially in metastable states, survive for much longer time.

5.3.1.1 Penning Ionization and Superelastic Electronic Collisions

We consider in this section the time evolution of eedf from a given initial Maxwellian distribution at $T_e = 1.5$ eV to another condition characterized by a sudden increase of E/N up to 1 Td. We select an argon plasma with two excited states Ar^* , Ar^{**} , the first describing the $4s$ state and the other one a lumped level including $4p$, $3d$ and $5s$ states. We select at time $t = 0$ concentrations of excited states $N^*/N_0 = 4 \times 10^{-9}$ and $N^{**}/N_0 = 4 \times 10^{-10}$, N^* and N^{**} denoting the concentrations of the two groups of levels. The time evolution of eedf is reported in Fig. 5.4a (Bretagne et al. 1987) and compared with the corresponding values obtained by neglecting the presence of electronic states, i.e. by neglecting superelastic and Penning ionization. We find that after $\tau = Nt = 2.5 \times 10^{11} \text{ cm}^{-3} \text{ s}$ a quasi-stationary condition is achieved for the eedf. We must note that in the energy range $\varepsilon > 7$ eV the presence of excited states strongly modifies the eedf, in particular the quasi-stationary distribution, due to both superelastic electron collisions and Penning ionizations. We can see that neglecting these processes depletes the eedf in the energy range $\varepsilon > 8$ eV. The structures which appear on the distribution when these processes are considered must be identified as follows: the two steps appearing near $\varepsilon \sim 7.5$ and 10 eV are mainly due to Penning ionizations

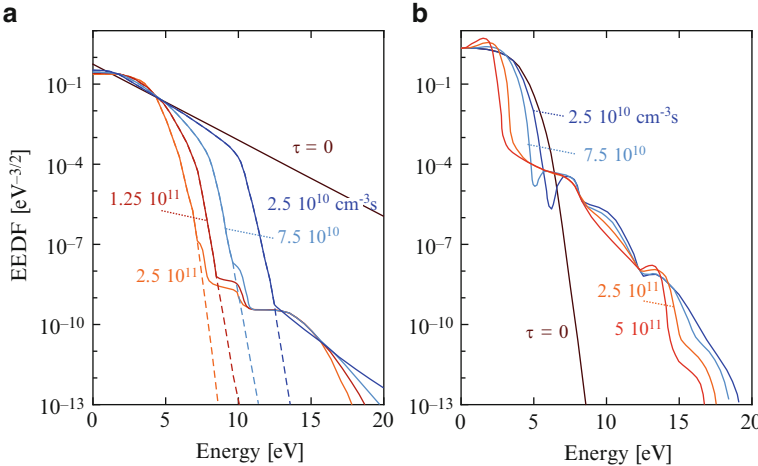
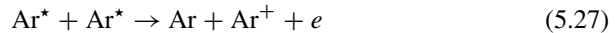
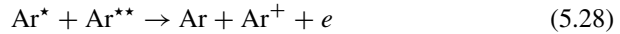


Fig. 5.4 Relaxation of the eedf at different values of the reduced times τ . **(a)** $E/N = 10^{-17} \text{ V cm}^2$ and with $n_e/N_0 = 4 \times 10^{-9}$, relative excited-state densities are $N^*/N_0 = 4 \times 10^{-9}$ and $N^{**}/N_0 = 4 \times 10^{-10}$, the dotted lines correspond to eedf calculated without excited states. **(b)** $E/N = 0 \text{ V cm}^2$, the initial eedf is the quasi-stationary one obtained for $E/N = 10^{-17} \text{ V cm}^2$ without excited states (From Bretagne et al. 1987)



and



while the tail of the distribution ($\varepsilon > 10 \text{ eV}$) is controlled by superelastic collisions. A more structured eedf is found when we impose a post-discharge condition at $E/N = 0$ starting from $E/N = 1 \text{ Td}$ (see Fig. 5.4b). The role of excited states is well evident by looking at the reported eedf at different times.

These observations were qualitatively confirmed by the experimental eedf measurements by Hopkins et al. (1989) and by theoretical results by Adams et al. (2012).

5.3.1.2 Post-discharge and Electron-Electron Collisions

The case studies previously reported were obtained in the absence of electron-electron collisions, which however can play an important role in thermalizing eedf, either in discharge or post-discharge conditions. It is indeed difficult to give a golden rule for estimating the ionization degree, α , necessary to thermalize eedf, because α is strongly dependent on the presence of excited states. In general the Coulomb cross sections decrease with increasing the energy so that these collisions will play

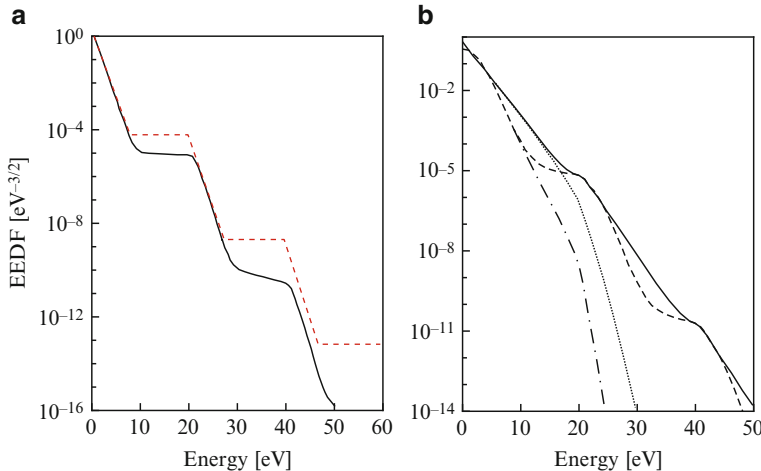


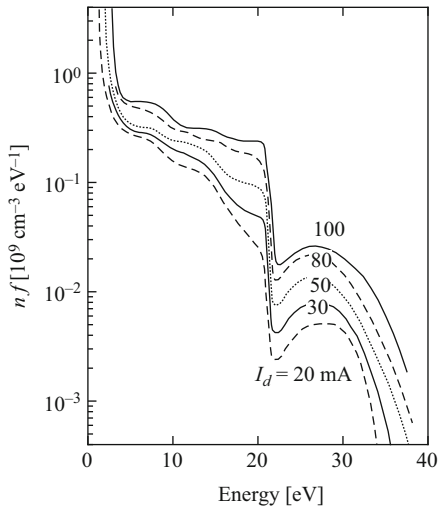
Fig. 5.5 (a) eedf at $E/N = 2 \text{ Td}$, $\alpha = 10^{-4}$, $[\text{He}(2^3S)]/[\text{He}(^1S)] = 10^{-4}$, $[\text{He}(2^1S)]/[\text{He}(^1S)] = 10^{-5}$ and $[\text{He}(2^1P)]/[\text{He}(^1S)] = 10^{-6}$; (solid line) solution of Boltzmann equation, (dashed line) reconstruction of eedf through Eq. (5.20). (b) eedf at $E/N = 4 \text{ Td}$, $\alpha = 10^{-3}$, $[\text{He}(2^3S)] = 10^{-4}$, in the presence of the following kinds of collisions: (dashed-dotted line) only elastic and inelastic collisions; (dotted line) elastic, inelastic, and $e-e$ collisions; (dashed line) elastic, inelastic and superelastic collisions; (solid line) elastic, inelastic, superelastic, and $e-e$ collisions (From Capriati et al. 1992)

a major role in affecting the low energy part of eedf. In the presence of excited states we can expect a difficulty in the thermalization of eedf when the action of second-kind collisions occurs at high energy as in the case of helium, the reverse being true when the second-kind collisions are preferentially due to vibrational energy exchanges and metastable states with low energy threshold, as in the case of nitrogen or carbon monoxide.

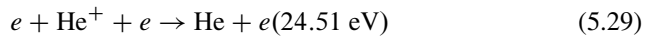
As an example Fig. 5.5a (Capriati et al. 1992, 1993) shows that an ionization degree of 10^{-4} is not sufficient to thermalize the plateau in an helium plasma at $E/N = 2 \text{ Td}$ created by second-kind collisions from He metastable states with the same concentration. On the other hand an ionization degree of 10^{-3} at $E/N = 4 \text{ Td}$ is able to smooth the plateau created by a concentration of 10^{-4} of metastable states (see Fig. 5.5b). The same ionization degree in the absence of excited states is not able to thermalize the corresponding eedf (same figure). In Fig. 5.5a is also reported (dashed line) the reconstruction of eedf through Eq. (5.20) and assuming an f_0 value corresponding to a Maxwell distribution function for low-energy electrons at $T_e = 8,400 \text{ K}$ (D'Ammando et al. 2015).

The results reported in the two figures can find a similarity with the experimental eedf in transverse Hollow Cathode Discharges (HCD). Figure 5.6 reports the high energy experimental eedf obtained by Mizeraczyk and Urbanik (1983) for a pressure of 10 hPa and an electron density of $3.5 \times 10^{12} \text{ cm}^{-3}$, i.e. for an ionization degree of 1.4×10^{-5} . Inspection of the figure shows the long plateau in eedf due to

Fig. 5.6 Electron energy distribution (high-energy part) for transverse HCD in helium, Helium pressure 10 hPa, for different values of the discharge current (From Mizeraczyk and Urbanik 1983)



second-kind collisions from the metastable He atom and a second maximum which can be due either to second-kind collisions involving high energy electrons or to ion recombination



The HCD discharge represents an ideal situation to the experimental detection of second-kind collisions because the corresponding eedf at low energy presents very low electron temperatures of the same order of magnitude of our calculations reported in Fig. 5.5a, b. Note however that the plateau in HCD discharges can be also formed by a source of secondary electrons, generated by high-energy electrons coming from the cathode-fall region (Arslanbekov and Kudryavtsev 1998, 1999).

As a second example of the influence of e - e collisions in affecting eedf we report results for nitrogen in post-discharge and discharge conditions at different values of ionization degrees. Table 5.2 (Colonna et al. 1993) reports the concentration of the different excited states which in combination with different concentration of electrons will be used in the solution of Boltzmann equation. Inspection of the corresponding data shows us large concentrations of vibrationally excited states which, while exalting the role of superelastic vibrational collisions, decrease the corresponding role of superelastic electronic collisions.

Figure 5.7a reports the stationary eedf in the post-discharge regime calculated by neglecting, and including e - e collisions at different ionization degrees. Let us first consider the eedf calculated by neglecting e - e collisions. In the absence of e - e collisions we can see that the low-energy part of the distribution ($\epsilon < 4$ eV) is controlled by superelastic vibrational collisions, while the two plateaus starting at 8 and 16 eV are the consequence of superelastic electronic collisions. The different plateaus are linked by abrupt changes in eedf. Let us now examine the influence

Table 5.2 Elastic and inelastic processes inserted in the Boltzmann equation for N₂ molecule, together with their threshold energies, ϵ_{th} , and the population densities of different vibrational and electronic states (Colonna et al. 1993)

Levels	ϵ_{th} (eV)	N/N_{tot}
$v = 0$	0	0.185
$v = 1$	0.29	0.167
$v = 2$	0.59	0.148
$v = 3$	0.88	0.130
$v = 4$	1.17	0.111
$v = 5$	1.41	0.093
$v = 6$	1.76	0.074
$v = 7$	2.06	0.056
$v = 8$	2.35	0.037
$A^3\Sigma_u^+$	6.17	1.7×10^{-5}
$B^3\Pi_g$	7.35	8.3×10^{-6}
$W^3\Delta$	7.36	2.8×10^{-6}
$B'^3\Sigma_u^-$	8.16	1.5×10^{-5}
$d'^1\Sigma_u^-$	8.40	4.6×10^{-5}
$a^1\Pi_g$	8.55	1.9×10^{-6}
$w^1\Delta_u$	8.89	6.5×10^{-7}
$C^3\Pi_u$	11.03	5.9×10^{-9}
$E^3\Sigma_g^+$	11.88	0.0
$d''^1\Sigma$	12.25	0.0
Sum of singlets	13.00	0.0
Ionization	15.60	

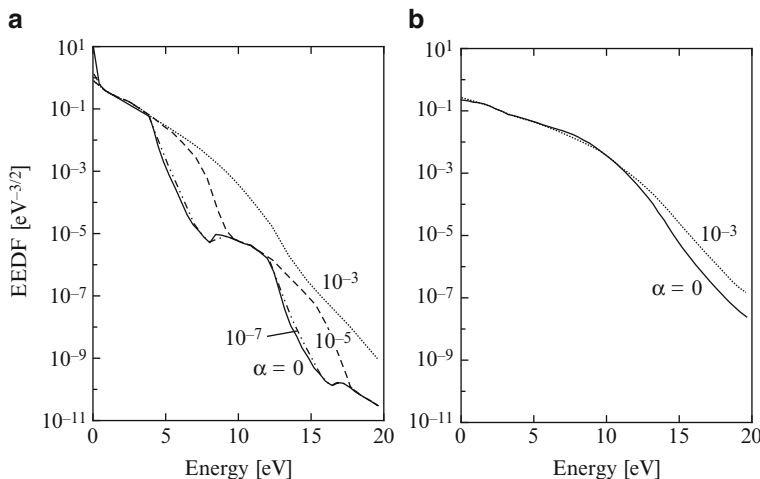


Fig. 5.7 Electron energy distribution functions in N₂ calculated with (dotted and dashed lines) and without (solid and dotted-dashed lines) e-e collisions for different ionization degrees. (a) post-discharge, $E/N = 0$ Td, and (b) discharge, $E/N = 50$ Td (From Colonna et al. 1993)

of $e\text{-}e$ collisions on the eedf. We can see that the plateaux of the eedf are not affected by the presence of $e\text{-}e$ collisions if the ionization degree (α) does not exceed 10^{-5} , while the linking of the different plateaus strongly depends on the presence of $e\text{-}e$ collisions already at $\alpha = 10^{-5}$. In particular, these collisions tend to fill the gap between the different plateaus. On increasing the electron concentration ($\alpha = 10^{-3}$) the eedf has a more regular shape, and the plateaus tend to disappear. Another interesting effect occurs at low energy ($\varepsilon < 0.3$ eV), where the presence of $e\text{-}e$ collisions strongly affects the distribution, an effect first shown by Dyatko et al. (1993). The same ionization degrees are not sufficient to affect eedf in discharge conditions. This point can be appreciated by looking at Fig. 5.7b where eedf at $E/N = 50$ Td have been reported at different ionization degrees with fixed concentrations of excited states from Table 5.2. Only high ionization degrees ($\alpha = 10^{-3}$) can weakly affect eedf and only at high electron energy ($\varepsilon > 10$ eV). To conclude this section we can reiterate that $e\text{-}e$ collisions play a role which changes from a system to an another one in any case strongly depending on the concentration of excited states (see also Matveyev and Silakov 2001; Capitelli et al. 1996).

5.3.2 *eedf Evolution During Discharges*

Another case study considers the evolution of the eedf when the electric field is not constant in time. It should be noted that the Boltzmann equation can be written in term of normalized quantities. In this case the collision frequencies are divided by the particle density (or pressure), the electric field is reduced by the density (or pressure), while the time is multiplied by the corresponding quantity. We will consider two test cases, one with an abrupt change in the electric field between two stationary values, and one with the a periodic electric field.

5.3.3 *Abrupt Change of E/N*

We want to examine the temporal behavior of a non-isothermal plasma as response of an abrupt change of the electric field in the presence of a given distribution of vibrationally excited states (Capitelli et al. 1984; Wilhelm and Winkler 1976, 1979), solving Eq. (5.1). The electron kinetics includes the following contributions: heating by the electric field, elastic collisions of electrons with molecules in all vibrational states of the electronic ground state, excitation and de-excitation of rotational states of the various vibrationally excited molecules in the conventional *continuous approximation*. Furthermore, the excitation of various higher vibrational states of the electronic ground state, the electronic excitation, dissociation and ionization from different vibrational levels as well as de-excitation of vibrationally excited molecules of the electronic ground state to various lower vibrational levels in second-kind collisions (superelastic collisions) are taken into account.

The ionizing collisions are described as excitation processes neglecting secondary electrons and therefore considering constant the total electron density n_e . In this case 47 vibrational levels have been considered. In the calculation we used the same momentum transfer cross sections for all the vibrational states and the same assumption has been applied to the cross sections of the effective rotational processes. The evolution of the mean electron energy is calculated as

$$\frac{d\bar{\varepsilon}}{dt} = \frac{1}{n_e} \int_0^\infty \frac{\partial n(\varepsilon, t)}{\partial t} \varepsilon d\varepsilon = \frac{1}{n_e} (\bar{U}_E - \bar{U}_c) \quad (5.30)$$

where \bar{U}_E the power injected by the electric field

$$\begin{aligned} \bar{U}_E &= - \int_0^\infty \frac{\partial J_E(\varepsilon)}{\partial \varepsilon} \varepsilon d\varepsilon = - \varepsilon J_E(\varepsilon)|_0^\infty + \int_0^\infty J_E(\varepsilon) d\varepsilon = \\ &= \int_0^\infty J_E(\varepsilon) d\varepsilon = v_d E \end{aligned} \quad (5.31)$$

and \bar{U}_c is power redistributed in the different channels

$$\bar{U}_c = \bar{U}_{el} + \bar{U}_r + \sum_k \bar{U}_k^{in} - \sum_k \bar{U}_k^{sup} \quad (5.32)$$

where \bar{U}_{el} and \bar{U}_r are respectively the contribution of elastic and rotational collisions, that, considering the integration by part as in Eq. (5.31), become

$$\begin{aligned} \bar{U}_{el} &= - \int_0^\infty J_{el}(\varepsilon) d\varepsilon \\ \bar{U}_r &= - \int_0^\infty J_r(\varepsilon) d\varepsilon \end{aligned} \quad (5.33)$$

while \bar{U}_k^{in} and \bar{U}_k^{sup} are the contribution of inelastic and superelastic collisions in different processes

$$\begin{aligned} \bar{U}_k^{in} &= \int_0^\infty S_{in,k} \varepsilon_k^* d\varepsilon = N_{kl} \varepsilon_k^* \int_0^\infty v \sigma_k^{in} n(\varepsilon) d\varepsilon = n_e N_{kl} \varepsilon_k^* K_k^{in} \\ \bar{U}_k^{sup} &= - \int_0^\infty S_{sup,k} \varepsilon_k^* d\varepsilon = N_{ku} \varepsilon_k^* \int_0^\infty v \sigma_k^{sup} n(\varepsilon) d\varepsilon = n_e N_{ku} \varepsilon_k^* K_k^{sup} \end{aligned} \quad (5.34)$$

It should be noted that all the \bar{U} 's are proportional to the total particle densities (N), therefore it is more useful to report this quantities divided by N , correspondingly considering reduced time $\bar{t} = tN$. It is interesting to analyze the inelastic source terms by channels, grouping processes of similar nature, such as vibrational excitation (ve), electronic excitation (ee), ionization and dissociation (id) and so on. The inelastic and superelastic transitions considered in the present study are reported in Table 5.1 of Cacciato et al. (1982).

Fig. 5.8 The population distribution of vibrational states for N_2 (From Capitelli et al. 1984)

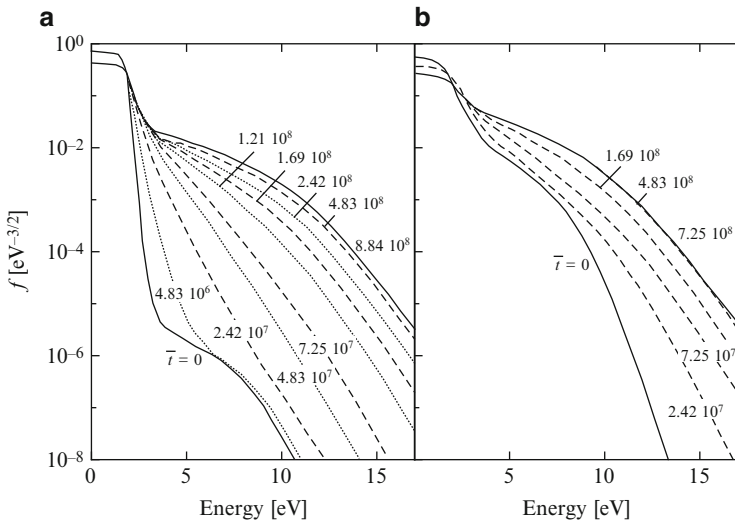
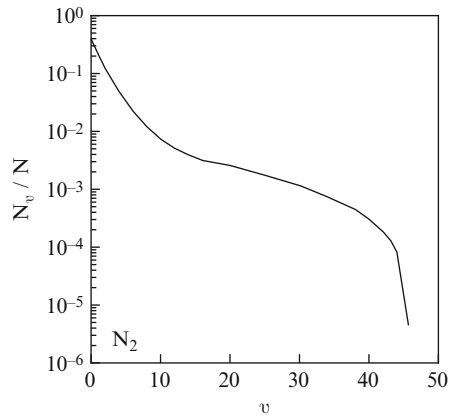


Fig. 5.9 The temporal evolution of $f(\varepsilon, \bar{t})$ in N_2 with \bar{t} [cm^{-3}s] as a parameter for the transition of E/N from 30 to 100 Td for vnp (a) and vp (b) conditions (From Capitelli et al. 1983)

Figure 5.8 (Capitelli et al. 1984, 1981) reports the non-equilibrium vibrational distribution of N_2 typical of an electrical discharge at E/N of 30 Td and electron density of 10^{10} cm^{-3} . We assume that this distribution remains frozen during the jump-like change of reduced field from 30 to 100 Td and we compare the relevant results (vibrationally populated, vp) with the corresponding ones obtained by disregarding the vibrational excitation (vibrationally non-populated, vnp). Figure 5.9a, b (Capitelli et al. 1983) show the temporal evolution of the energy distribution function f for the jump-like transition at vnp and at vp conditions for different normalized times. In both cases the curves given for the largest time values in each figure represents the distribution in the new stationary state at the final field

strength (E/N). As can be seen, at higher energies the distribution increases by several orders of magnitude as a consequence of the higher electrical field and of the presence of excited states in the vp case. The new stationary state is reached in nearly the same relaxation time of about $\bar{t} = 10^9 \text{ cm}^{-3} \text{ s}$ in the normalized time scale in both cases but the total increase of the energy distribution is markedly reduced in the vp case compared with the vnp case. Absolute relaxation times of $10^{-10} - 10^{-8} \text{ s}$ are then expected for particle densities of $10^{19} - 10^{17} \text{ cm}^{-3}$. It is interesting to examine how the contributions of the different kinds of energy transfer channels to the total power loss during the relaxation process investigated. For this purpose the many individual power losses by inelastic collisions $\frac{\bar{U}_{\mu\ell}}{N}$ are summarized in groups to the power losses $\frac{\bar{U}_{\mu}}{N}$ for total vibrational excitation (denoted by the index ve), for total electronic excitation and dissociation ($ee + di$) as well as for the ionization (i). If these processes are further subdivided with respect to the vibrational ground state alone or with respect to all higher vibrational states the corresponding power losses are denoted by the additional index $v = 0$ or $v > 0$. In addition, the total power gain due to all collisions of second-kind is denoted by $\frac{\bar{U}_{vde}}{N}$ and the effective power loss due to the total action of the vibrational excitation as well as de-excitation is indicated by the index $ve - vde$. The behavior of these quantities as a function of time is presented for the transition 30–100 Td under vnp and vp conditions in Fig. 5.10a, b.

Inspection of Fig. 5.10a shows that the dominant energy transfer channel during the relaxation process is the power loss due to vibrational excitation. Only at the final establishment of the new stationary state the power loss due to electronic excitation

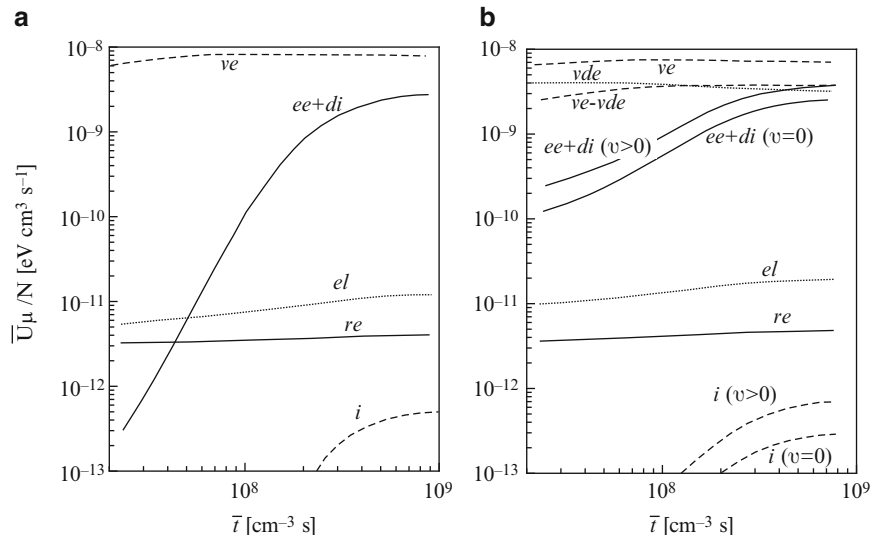


Fig. 5.10 The different power losses \bar{U}_{μ}/N during the relaxation process in N_2 for the transition of E/N from 30 to 100 Td for vnp (a) and vp (b) conditions (From Capitelli et al. 1984)

and dissociation achieves the same order of magnitude as that by vibrational excitation. In contrast the inclusion of vibrationally excited molecules (Fig. 5.10b) leads to a marked enhancement of the total power loss by electronic excitation and dissociation and to a reduction of the effective vibrational loss. However during the further relaxation both losses become comparable with one another. Note also the predominance of $v > 0$ transitions in the vp case.

5.3.4 RF Bulk Discharges

This topics has been widely studied in the past in collaboration with the Greifswald group. The main results of these studies can be understood by looking at the behavior of eedf during half a cycle of an RF discharge in the presence of vibrationally and electronically excited states. To this end we solve the time-dependent Boltzmann equation. A radio-frequency field, acting upon the bulk-plasma, spatially homogeneous and weakly ionized, can be written as a function of normalized quantities

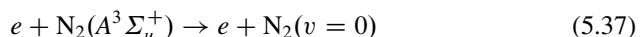
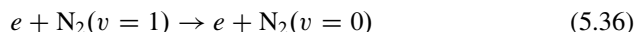
$$\bar{E}(t) = \bar{E}_0 \cos(\varpi \bar{t}) \quad (5.35)$$

where $\bar{E} = E/P$ denotes the reduced field amplitude ($\text{V cm}^{-1} \text{Torr}^{-1}$), $\varpi = \omega/P$ and $\bar{t} = tP$, the reduced angular frequency ($\text{s}^{-1} \text{Torr}^{-1}$) and a reduced time scale (s Torr), respectively. We consider two case studies, pure nitrogen and the excimer laser mixture, in the presence of different concentrations of vibrationally and electronically excited states.

Similar numerical studies have been considered by Jiang and Economou (1993) and Loureiro (1993), while more recently experimental determination of transient eedf has been presented by Seo (2006).

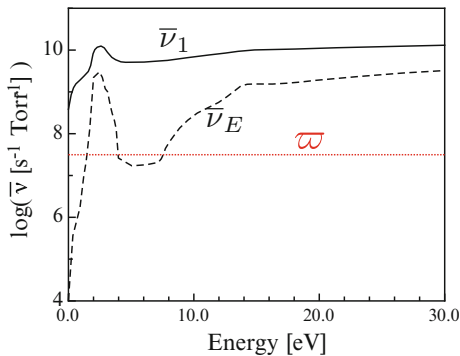
5.3.4.1 Nitrogen Plasma

In this case we consider elastic and inelastic cross sections as available in Phelps and Pitchford (1985), Phelps (2005), and LXcat (2015) i.e. all starting from the ground state of nitrogen molecules. In addition we consider second-kind collisions from these two reactions



The concentrations of the two excited states are taken as parameters. In particular the vibrational temperature is varied from 2,000 to 4,000 K while the molar fraction of the metastable state ranges from 10^{-6} to 10^{-4} . The understanding of

Fig. 5.11 The normalised collision frequency for impulse dissipation (full curve) and for energy dissipation (broken curve) in the N₂ system as a function of electron energy (Capitelli et al. 1988)



the modulation of eedf to the variation of electrical field can be better understood by comparing the reduced field frequency with the corresponding frequencies for momentum $\bar{\nu}_1$ and energy transfer $\bar{\nu}_E$.

Figure 5.11 (Capitelli et al. 1988) shows the behavior of these two quantities as a function of electron energy. We can expect a large modulation of eedf with respect to the RF field when $\varpi < \bar{\nu}_E$. Let us consider the case $\varpi = \pi \times 10^7 \text{ s}^{-1} \text{Torr}^{-1}$. Inspection of Fig. 5.11 shows us that the inequality holds for energy $> 10 \text{ eV}$ in a narrow energy range between $2 < \varepsilon < 4 \text{ eV}$, this energy range being characterized by strong inelastic vibrational energy losses. On the other hand there are two energy regions $\varepsilon < 2 \text{ eV}$ and $4 < \varepsilon < 8 \text{ eV}$ in which the applied field frequency is larger than the energy dissipation frequency (i.e. $\varpi > \bar{\nu}_E$). In these last regions we must expect a reduced modulation of the eedf with respect to the applied field, while a large modulation is expected for $\varepsilon \geq 10 \text{ eV}$ and for $2 < \varepsilon < 4 \text{ eV}$. This is indeed the case as can be appreciated by looking at Fig. 5.12a where the periodic behavior of eedf is reported as a function of energy at different times for a semiperiod of the RF field. According to the reduced time $t' = \varpi t / (2\pi)$ (i.e. $\bar{E}(t) = \bar{E}_0 \cos(2\pi t')$), $t' = 0$ and 0.5 represent instants at which the electric field is at its maximum ($E = E_0$) and its minimum ($E = -E_0$) while $t' = 0.25$ to the zero passage of the field, i.e. ($E = 0$) (see Fig. 5.13). Inspection of Fig. 5.12a shows a large modulation of the eedf in the region of strong inelastic losses (i.e. $2 < \varepsilon < 4 \text{ eV}$, $\varepsilon \geq 10 \text{ eV}$) while no modulation exists in the energy range characterize by low values of inelastic losses (i.e. $\varepsilon < 2 \text{ eV}$ and $4 < \varepsilon < 8 \text{ eV}$). Let us consider now the effect of superelastic vibrational collisions (SVC) and superelastic electronic collisions (SEC) on the temporal behavior of the eedf. Figure 5.12b–d report different cases obtained by changing the population densities of excited states. We can see that the insertion of SVC reduces the modulation and enlarges the population of eedf in the region 1–4 eV, while SEC drain electrons mainly from the energy range 4–8 eV to the energy interval 10–16 eV (note that the energy threshold of the metastable triplet state is 6.7 eV), thus reducing the modulation of eedf in the last energy range. Interesting is also the strong decrease of the minimum of eedf in the presence of large concentration of vibrationally excited states (Fig. 5.12d) due to

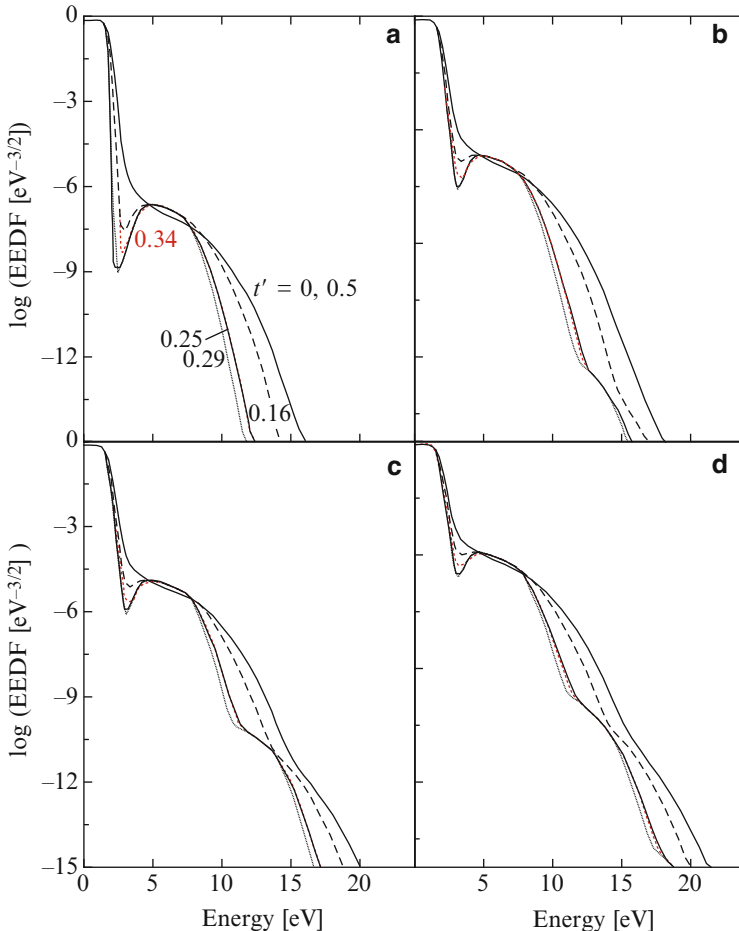


Fig. 5.12 Temporal evolution of eedf for different populations of excited states ($t' = \pi i / (2\pi)$). $E_0/p_0 = 9.9 \text{ V cm}^{-1} \text{ Torr}^{-1}$, $\omega/p_0 = \pi \times 10^7 \text{ s}^{-1} \text{ Torr}^{-1}$. (a) $N_2^* = 0$, $\vartheta_1 = 0 \text{ K}$; (b) $N_2^* = 10^{-6}$, $\vartheta_1 = 2,000 \text{ K}$; (c) $N_2^* = 10^{-4}$, $\vartheta_1 = 2,000 \text{ K}$; (d) $N_2^* = 10^{-4}$, $\vartheta_1 = 4,000 \text{ K}$ (From Capitelli et al. 1988)

the compensation of SEC in filling the loss of electrons in this energy range from inelastic vibrational collisions.

It should be noted that the *hole* and the *hump* in the nitrogen electron energy distribution function has been experimentally detected in RF and ICP plasmas by different authors (Hopkins et al. 1989; Lee et al. 2010). The results previously reported have been obtained by neglecting electron-electron Coulomb collisions. These collisions have been considered in RF cold CO and H₂ plasmas (Winkler et al. 1992) showing the effect only for ionization degrees higher than 10⁻⁴.

Fig. 5.13 Electric field as a function of reduced time t' in RF discharges

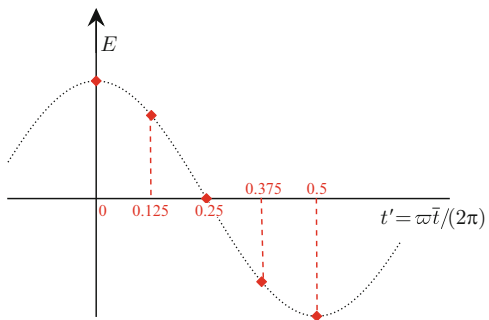


Table 5.3 Molar fractions of the different Ne/Xe/HCl species in various mixtures (Gorse et al. 1990a)

	Mixture 1	Mixture 2	Mixture 3
Ne	0.985	0.985	0.985
Xe	0.01	0.01	0.0099
HCl($v = 0$)	0.005	4.04×10^{-3}	4.04×10^{-3}
Ne*		0.985×10^{-6}	0.985×10^{-6}
Xe*		1.0×10^{-6}	1.0×10^{-4}
HCl($v = 1$)	0.005	0.895×10^{-3}	0.895×10^{-3}
HCl($v = 2$)	0.005	0.580×10^{-4}	0.580×10^{-4}

5.3.4.2 Excimer Laser Mixture

We consider a Ne/Xe/HCl RF plasma in the presence of different concentrations of excited states HCl($v = 1$), HCl($v = 2$), Xe* and Ne* taken as free parameters. Table 5.3 (Gorse et al. 1990a) shows the chosen densities characterizing the three mixtures. We note an increase of concentration of excited states passing from mixture 1 to mixture 3, mixture 1 completely disregarding the presence of excited states.

Figure 5.14a–c give the periodic behavior of eedf for the considered mixtures, together with the corresponding self-consistent E_0/p_0 values. Eedf oscillates with double the field frequency. The self-consistent field is obtained by considering that in the steady state, on average over one field period electron production and loss must become equal. This is the implicit condition for the maintenance of steady state RF bulk plasma, which implicitly selects the consistent reduced field amplitude E_0/p_0 in the solution approach. Of course a more realistic self-consistent model should solve the Boltzmann equation with the Poisson equation as well as with non-equilibrium plasma kinetics occurring in the active medium (see Chap. 8).

The parameter of the curves is the normalised time t' in the RF field (Fig. 5.13), thus curve A: $t' = 0$ and $t' = 0.5$ corresponding to the maximum and the minimum of the field; C: $t' = 0.25$ to the zero passage of the field, while curves B: $t' = 0.125$ and D: $t' = 0.375$ characterize cases located symmetrically in energy (eV) (see Fig. 5.13). For mixture 1 (Fig. 5.14a) a relatively large modulation of eedf exists. Furthermore there is a remarkable delay between curves B and D, which refer to

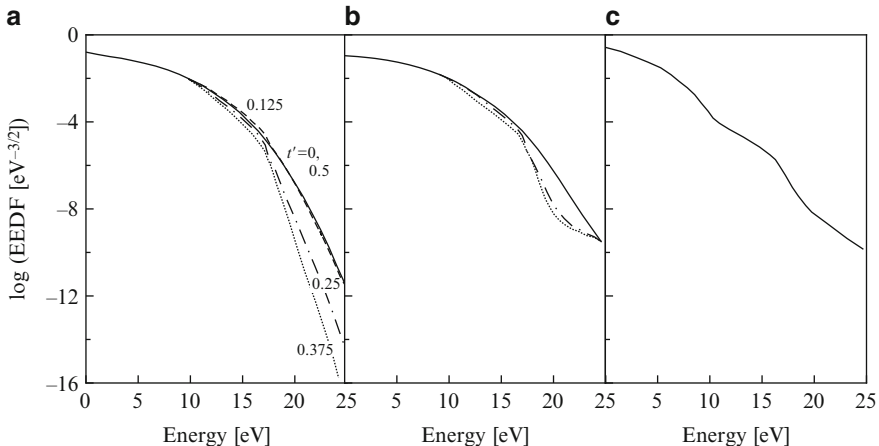


Fig. 5.14 Temporal evolution of eedf for different concentrations of excited states (Table 5.3) at $\omega/p_0 = \pi \times 10^7 \text{ s}^{-1} \text{ Torr}^{-1}$. (a) Mixture 1, $E_0/p_0 = 3.28 \text{ V cm}^{-1} \text{ Torr}^{-1}$; (b) Mixture 2, $E_0/p_0 = 3.66 \text{ V cm}^{-1} \text{ Torr}^{-1}$; (c) Mixture 3, $E_0/p_0 = 0.87 \text{ V cm}^{-1} \text{ Torr}^{-1}$ (From Gorse et al. 1990a)

the same magnitude of the electric field with opposite sign. This means that we have a situation which is remarkably non-stationary. The addition of increasing concentrations of excited states (Fig. 5.14b, c) strongly decreases the modulation of eedf as a result of the action of second-kind collisions. These collisions have a global effect of reducing the total energy dissipation frequency, while at the same time they enlarge the tail of eedf draining electrons from low- to high-energy. These two effects are seen in Fig. 5.14c where we observe the disappearance of modulation and the increase of the eedf tail by several orders of magnitude as compared with the results reported in Fig. 5.14a. Another interesting aspect lies in the fact that the self-consistent E_0/p_0 amplitude slightly increases passing from mixture 1 to mixture 2; a reduction of a factor 4 occurring in mixture 3. The reduction in mixture 3 is due to the increased importance of the ionizing frequency from Xe^* , while the slight increase of E_0/p_0 in mixture 2 is due to the modification of the bulk of eedf due to second-kind collisions.

5.3.5 Case Study: Excimer Laser Kinetics

We present in this section a study on the time-dependent eedf in a self-sustained RLC discharge XeCl laser operating at high pressure with the aim to emphasize the role of second-kind collisions in the presence of electron-electron collisions with a time variable E/N reduced field. Moreover problems of quasi-stationarity of eedf are discussed due to the similarity of the study to the streamer evolution. The results are obtained from a model based on the simultaneous solution of

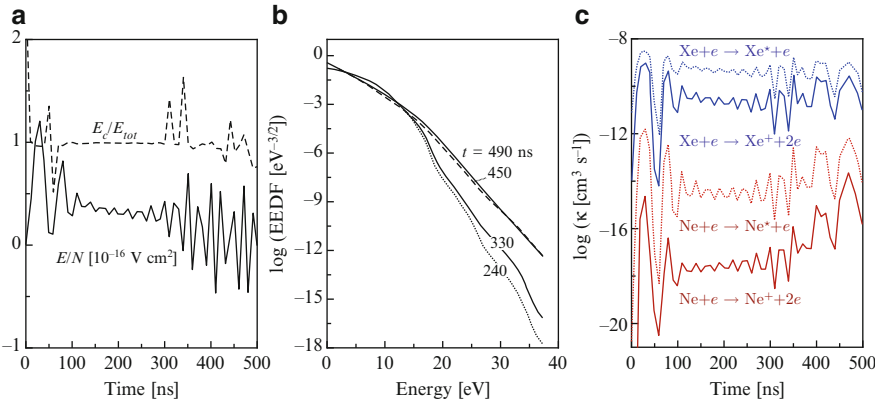


Fig. 5.15 (a) Temporal evolution of reduced electric field (E/N) and of the ratio between electron collisional power loss (E_c) and gain by electric field and superelastic collision (E_{tot}) in Ne/Xe/HCl (2268.5/10/1.5 Torr) mixture. (b) Electron energy distribution function in Ne/Xe/HCl mixture at different times. (c) Temporal evolution of selected rate coefficients (From Gorse et al. 1990b)

- The time-dependent eedf
- The RLC circuit equations
- Plasmachemistry including also excited state kinetics
- Photon kinetics.

The plasmachemistry includes 26 species [$\text{HCl}(v = 0)$, $\text{HCl}(v = 1)$, $\text{HCl}(v = 2)$, Ne , Xe , Ne^* , Xe^* , Ne_2^* , Xe_2^* , Ne_2^+ , Xe_2^+ , Ne^+ , Xe^+ , H , Cl , Cl^- , Cl^+ , Cl_2 , Cl_2^* , NeCl^* , XeCl^* , NeXe^+ , XeCl^+ , e , $h\nu$ (laser) and $h\nu$] involved in 76 reactions occurring in a $10-\ell$ discharge with the following initial composition (Ne/Xe/HCl 2268.5/10/1.5 Torr). Details of the method can be found in Gorse et al. (1990b).

The Boltzmann equation is solved time-dependently, taking into account superelastic and electron-electron collisions. The former come from deactivation of vibrationally excited HCl molecules as well as from metastable Xe^* and Ne^* species. Let us first investigate the problem of quasi-stationarity. To this end Fig. 5.15a shows the temporal evolution of the ratio between the power loss by electrons in all collisional processes (E_c) and the corresponding power gained by electrons from electric field and superelastic collisions (E_{tot}). In the same figure we also have reported the behavior of reduced electric field (E/N) in the laser cell, which has been obtained by solving the relevant circuit equations with a self-consistent laser resistance. Keeping in mind that this ratio should be one for quasi-stationary conditions, we can observe that deviations from quasi-stationarity occur in different zones of temporal evolution of laser kinetics, despite the high pressure operating in the system.

Figure 5.15b shows the temporal evolution of electron energy distribution function during the laser discharge. The four curves shown in this figure refer to approximately the same reduced electric field, but different concentrations of electrons and excited species (both calculated self-consistently, see Table 5.4).

Table 5.4 Fraction of metastable state of Xenon and density of free electrons for different time of the simulation (see Fig. 5.15). The times have been chosen to result in similar values of the reduced electric field (Data from Gorse et al. 1990b)

time t (ns)	$E/N \times 10^{17}$ (V cm 2)	$Xe^*/Xe \times 10^3$	$n_e \times 10^{-14}$ cm $^{-3}$
240	3.30	2.4	1.93
330	3.37	4.8	4.10
450	3.31	48.	7.27
490	3.14	78.	67.3

Combined effects of electron-electron ($e\text{-}e$) and superelastic collisions (SC) are evident in this figure. In particular, $e\text{-}e$ collisions tend to Maxwellize eedf, having large effects on both the bulk and the tail of eedf.

These effects propagate on the temporal evolution of rate coefficients, as can be appreciated in Fig. 5.15c, where we have reported the excitation (toward the metastable Ne^* and Xe^* species) and ionization rates. From this figure we can see both the effects of non-stationarity of eedf and of $e\text{-}e$ and SC. The first point can be appreciated by noting that the modulation of rate coefficients does not completely follow the alteration of electric field, having high values when the electric field crosses the zero point. This situation is similar to the one occurring in radio frequency discharges. The effect of SC is evident in Fig. 5.15c, where we have marked four points corresponding to approximately the same E/N as in Fig. 5.15b. Note that while the excitation and the ionization of Xe, at fixed E/N , slightly decreases with both increasing electron density and concentration of excited states, the reverse is dramatically true for the same processes involving neon species. This behavior reflects the corresponding one of the bulk of eedf (important for the rate coefficients involving Xe) and of the tail of eedf (important for the rate coefficients involving Ne).

5.3.6 Photoresonant Plasmas

A lot of interest is devoted to laser excitation and ionization of alkali-metal vapors (Eletskii et al. 1988). The absorption of laser photons in these media is possible by tuning the laser frequency to the resonant transition, quasi-resonant transitions, and two-photon resonant transitions. Then different microscopic processes can transport the laser excitation up to the ionization limit. In the context of the present book we want to show the structured eedf resulting from different microscopic processes including associative ionization, Penning ionization, electron-impact excitation and ionization, photoionization, excited atom-excited atom collisions, and radiative recombination, as well as three-body recombinations. Moreover second-kind collisions involving cold electrons and excited atoms are of primary importance to produce structures (Morgan et al. 1981; Morgan 1983).

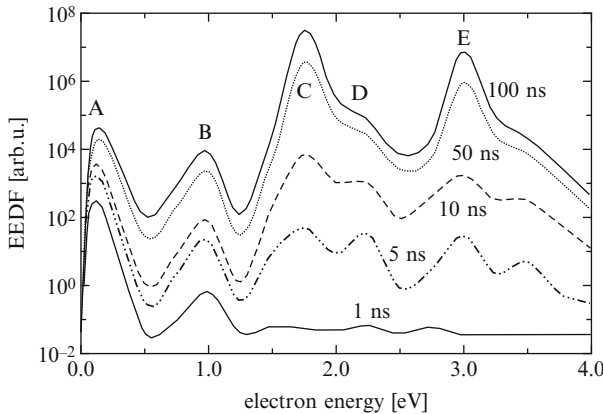


Fig. 5.16 Time development of the electron energy distribution function in caesium vapor excited with cw laser at a laser power of 150 mW (From Mahmoud and Gamal 2010)

Figure 5.16 (Mahmoud and Gamal 2010) shows a calculated electron energy distribution function (eedf) at a laser power of 150 mW at various time intervals, namely 1, 5, 10, 50 and 100 ns in high pressure caesium. Certain peaks (A, B, C, D and E) lying at energies 0.12, 1, 1.75, 2.25 and 3 eV, respectively can be attributed (A) to associative ionization (AI) process, (B),(C) to Penning ionization and photoionization, (D),(E) to the superelastic collisions (1SEC and 2SEC) between the free electrons produced by associative ionization and Penning ionization processes with atoms in the Cs($6p$) state. These time-dependent calculations are confirmed by the experimental observations of De Tomasi et al. (1997) and Pappas et al. (2000). Note that the eedf of these photo-resonant plasmas can produce, when mixed with rare gases, an interesting phenomenon called negative ion conductivity (Measures and Cardinal 1981; Gorbunov et al. 1999, 2001) (see Chap. 4).

5.4 Experimental Determination of eedf

One of the most clear experimental evidence of the role of superelastic collisions in affecting the eedf in the afterglow plasma was reported by Blagoev et al. (1992). The afterglow plasma was produced by 10–20 μ s DC pulses applied with a repetition rate of 2.4 kHz on the electrodes of a glass tube (diameter 2.6 cm), the current between 50 and 250 mA, for a Ar-Hg mixture. The experimental eedf shown in Fig. 5.17 exhibits the maxima due to the processes

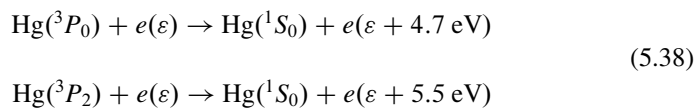


Fig. 5.17 Electron energy distribution function in mercury afterglow plasma. (Solid line) experimental curve, (markers) after deconvolution (From Blagoev et al. 1992)

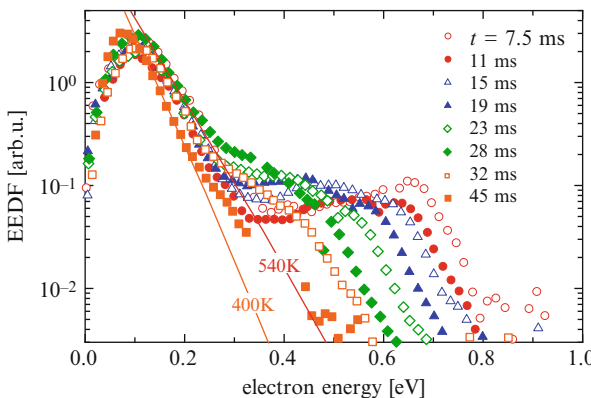
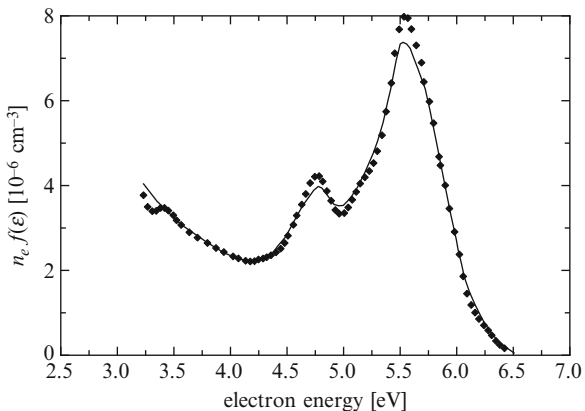


Fig. 5.18 Evolution of eedf in He/Ar/Xe/H₂ plasma obtained from measured characteristics of Langmuir probe (experimental conditions in the text). In low energy region (<0.15 eV), the eedfs are expected to be Maxwellian. The solid curves correspond to Maxwellian electron energy distributions fitted to the measured data for the decay time 7.5 and 45 ms. The plotted eedfs are normalised to 1 (From Plasil et al. 2009)

A recent paper (Plasil et al. 2009) reports the role of low-lying electronically excited states on the relaxation of the eedf in post-discharge conditions. In Fig. 5.18 an example for the He/Ar/Xe/H₂ plasma ($p = 1,600$ Pa, $T = 250$ K, $[\text{Ar}] = 7 \times 10^{12} \text{ cm}^{-3}$, $[\text{H}_2] = 5.6 \times 10^{12} \text{ cm}^{-3}$, $[\text{Xe}] = 4.3 \times 10^{12} \text{ cm}^{-3}$) is reported. In this case the excited $(\text{XeH}^+)^*$ state creates the plateaus in the eedf in an energy region below 1 eV.

Finally we want to emphasize the large interest for the experimental determination of eedf in capacitively coupled RF plasmas as well as in low pressure ICP (Inductive Coupled Plasmas) (Dilecce et al. 1991; Song et al. 2011; Godyak and Demidov 2011).

References

- Adamovich IV, Rich JW (1997) The effect of superelastic electron-molecule collisions on the vibrational energy distribution function. *J Phys D: Appl Phys* 30(12):1741
- Adams SF, Bogdanov EA, Demidov VI, Koepke ME, Kudryavtsev AA, Williamson JM (2012) Metastable atom and electron density diagnostic in the initial stage of a pulsed discharge in Ar and other rare gases by emission spectroscopy. *Phys Plasmas* (1994-present) 19(2):023510
- Arslanbekov RR, Kudryavtsev AA (1998) Energy balance of the bulk, Maxwellian electrons in spatially inhomogeneous negative-glow plasmas. *Phys Rev E* 58:6539–6552
- Arslanbekov RR, Kudryavtsev AA (1999) Modeling of nonlocal slow-electron kinetics in a low-pressure negative-glow plasma. *Phys Plasmas* 6(3):1003–1016
- Blagoev A, Kovachev S, Petrov G, Popov T (1992) Superelastic collisions between slow electrons and excited Hg atoms. *J Phys B* 25(7):1599
- Bretagne J, Capitelli M, Gorse C, Puech V (1987) Influence of excited states on the electron distribution function in an argon plasma for discharge and post-discharge conditions. *EPL (Europhys Lett)* 3(11):1179
- Cacciatore M, Capitelli M, Gorse C (1982) Non-equilibrium dissociation and ionization of nitrogen in electrical discharges: the role of electronic collisions from vibrationally excited molecules. *Chem Phys* 66(1–2):141–151
- Capitelli M, Dilonardo M, Gorse C (1981) Coupled solutions of the collisional Boltzmann equations for electrons and the heavy particle master equation in nitrogen. *Chem Phys* 56(1):29–42
- Capitelli M, Gorse C, Wilhelm J, Winkler R (1983) Collision dominated relaxation of electrons in a weakly ionized nitrogen plasma after abrupt change of the electric field. *Chem Phys* 79(1):1–7
- Capitelli M, Gorse C, Wilhelm J, Winkler R (1984) The electron relaxation to stationary states in collision dominated plasmas in molecular gases. *Annalen der Physik* 496(2):119–138
- Capitelli M, Celiberto R, Gorse C, Winkler R, Wilhelm J (1988) Electron energy distribution functions in radio-frequency collision dominated nitrogen discharges. *J Phys D: Appl Phys* 21(5):691
- Capitelli M, Colonna G, Gicquel A, Gorse C, Hassouni K, Longo S (1996) Maxwell and non-Maxwell behavior of electron energy distribution function under expanding plasma jet conditions: the role of electron-electron, electron-ion, and superelastic electronic collisions under stationary and time-dependent conditions. *Phys Rev E* 54(2):1843
- Capitelli M, Colonna G, De Pascale O, Gorse C, Hassouni K, Longo S (2009) Electron energy distribution functions and second kind collisions. *Plasma Sources Sci Technol* 18(1):014014
- Capriati G, Colonna G, Gorse C, Capitelli M (1992) A parametric study of electron energy distribution functions and rate and transport coefficients in nonequilibrium helium plasmas. *Plasma Chem Plasma Process* 12(3):237–260
- Capriati G, Boeuf J, Capitelli M (1993) A self-consistent one-dimensional model for He nonequilibrium kinetics in RF discharges. *Plasma Chem Plasma Process* 13(3):499–519
- Colonna G, Gorse C, Capitelli M, Winkler R, Wilhelm J (1993) The influence of electron-electron collisions on electron energy distribution functions in N₂ post discharge. *Chem Phys Lett* 213(1):5–9
- D'Ammando G, Colonna G, Capitelli M, Laricchiuta A (2015) Superelastic collisions under low temperature plasma and afterglow conditions: a golden rule to estimate their quantitative effects. *Phys Plasmas* 22:034501
- Demidov V, DeJoseph C, Kudryavtsev A (2006) Nonlocal effects in a bounded afterglow plasma with fast electrons. *IEEE Trans Plasma Sci* 34(3):825–833
- De Tomasi F, Milosevic S, Verkerk P, Fioretti A, Allegrini M, Jabbour ZJ, Huennekens J (1997) Experimental study of caesium energy pooling collisions and modelling of the excited atom density in the presence of optical pumping and radiation trapping. *J Phys B: Atomic, Molecular and Optical Physics* 30(21):4991

- Dilecce G, Capitelli M, De Benedictis S (1991) Electron-energy distribution function measurements in capacitively coupled RF discharges. *J Appl Phys* 69(1):121–128
- Dyatko NA, Kochetov IV, Napartovich AP (1993) Electron energy distribution function in decaying nitrogen plasmas. *J Phys D: Appl Phys* 26(3):418
- Eletskii AV, Zaitsev YN, Fomichev SV (1988) Formation kinetics and parameters of a photoresonant plasma. *Zh Eksp Teor Fiz* 94:98–106
- Engelhardt AG, Phelps AV, Risk CG (1964) Determination of momentum transfer and inelastic collision cross sections for electrons in nitrogen using transport coefficients. *Phys Rev* 135:A1566–A1574
- Ferreira CM, Loureiro J, Ricard A (1985) Populations in the metastable and the resonance levels of argon and stepwise ionization effects in a low-pressure argon positive column. *J Appl Phys* 57(1):82–90
- Frost LS, Phelps AV (1964) Momentum-transfer cross sections for slow electrons in He, Ar, Kr, and Xe from transport coefficients. *Phys Rev* 136:A1538–A1545
- Godyak VA, Demidov VI (2011) Probe measurements of electron-energy distributions in plasmas: what can we measure and how can we achieve reliable results? *J Phys D: Appl Phys* 44(23):233001
- Gorbunov N, Melnikov A, Movchan I, Smurov I, Flamant G (1999) Conductivity of a photoplasma of sodium vapor-inert gas mixtures. *IEEE Trans Plasma Sci* 27(1):182–192
- Gorbunov NA, Melnikov AS, Smurov I, Bray I (2001) Ionization kinetics of optically excited lithium vapour under conditions of negative electron mobility. *J Phys D: Appl Phys* 34(9):1379
- Gorse C, Capitelli M (1984) Kinetic processes in non-equilibrium carbon monoxide discharges. II. Self-consistent electron energy distribution functions. *Chem Phys* 85(2):177–187
- Gorse C, Paniccia F, Bretagne J, Capitelli M (1986) Electron energy distribution functions in carbon monoxide discharge and post-discharge conditions: the role of superelastic electronic collisions from $\text{CO}(A^3\Pi)$ state. *J Appl Phys* 59(3):731–735
- Gorse C, Bretagne J, Capitelli M (1988a) Electron energy distribution function in helium discharges: the role of superelastic collisions from He^3S . *Phys Lett A* 126(4):277–279
- Gorse C, Cacciatore M, Capitelli M, De Benedictis S, Dilecce G (1988b) Electron energy distribution functions under N_2 discharge and post-discharge conditions: a self-consistent approach. *Chem Phys* 119(1):63–70
- Gorse C, Paniccia F, Ricard A, Capitelli M (1989) Electron energy distribution functions in He-CO DC laser mixture: the role of superelastic electronic collisions. *Contrib Plasma Phys* 29(1):109–117
- Gorse C, Capitelli M, Celiberto R, Winkler R, Wilhelm J (1990a) Electron kinetics in radio-frequency plasmas: excimer Ne-Xe-HCl mixture. *J Phys D: Appl Phys* 23(8):1041
- Gorse C, Capitelli M, Dipace A (1990b) Time-dependent Boltzmann equation in a self-sustained discharge XeCl laser: influence of electron-electron and superelastic collisions. *J Appl Phys* 67(2):1118–1120
- Hagelaar GJM, Pitchford LC (2005) Solving the Boltzmann equation to obtain electron transport coefficients and rate coefficients for fluid models. *Plasma Sources Sci Technol* 14(4):722
- Hake RD, Phelps AV (1967) Momentum-transfer and inelastic-collision cross sections for electrons in O_2 , CO, and CO_2 . *Phys Rev* 158:70–84
- Hopkins MB, Anderson CA, Graham WG (1989) Time-resolved electron energy distribution function measurements in a low-frequency R.F. glow discharge. *EPL (Europhys Lett)* 8(2):141
- Jelenak A, Jovanović J, Bzenić S, Vrhovac S, Manola S, Tomčík B, Petrović ZLj (1995) The influence of excited states on the kinetics of excitation and dissociation in gas mixtures containing methane. *Diam Relat Mater* 4(9):1103–1112
- Jiang P, Economou DJ (1993) Temporal evolution of the electron energy distribution function in oxygen and chlorine gases under DC and AC fields. *J Appl Phys* 73(12):8151–8160
- Lee HC, Lee JK, Chung CW (2010) Evolution of the electron energy distribution and E-H mode transition in inductively coupled nitrogen plasma. *Phys Plasmas* (1994–present) 17(3):033506
- Longo S, Capitelli M, Hassouni K (1998) Nonequilibrium vibrational distributions of N_2 in radio-frequency parallel-plate reactors. *J Thermophys Heat Transf* 12(4):473–477

- Loureiro J (1993) Time-dependent electron kinetics in N₂ and H₂ for a wide range of the field frequency including electron-vibration superelastic collisions. *Phys Rev E* 47:1262–1275
- LXcat (2015) Plasma data exchange project database. <http://fr.lxcat.net/home/>
- Mahmoud MA, Gamal YEE (2010) Effect of energy pooling collisions in formation of a cesium plasma by continuous wave resonance excitation. *Optica Applicata* 40(1):129–141
- Matveyev AA, Silakov VP (2001) Electron energy distribution function in a moderately ionized argon plasma. *Plasma Sources Sci Technol* 10(2):134
- Measures RM, Cardinal PG (1981) Laser ionization based on resonance saturation – a simple model description. *Phys Rev A* 23:804–815
- Mizeraczyk J, Urbanik W (1983) Electron energy distribution function (0–40 eV range) in helium in transverse hollow-cathode discharge used for lasers. *J Phys D: Appl Phys* 16(11):2119
- Morgan WL (1983) Non-Maxwellian electrons in a laser produced sodium plasma. *Appl Phys Lett* 42(9):790–791
- Morgan W, Penetrante B (1990) Elendif: a time-dependent Boltzmann solver for partially ionized plasmas. *Comput Phys Commun* 58(1–2):127–152
- Morgan WL, Franklin RD, Haas RA (1981) Electron energy distribution in photolytically pumped lasers. *Appl Phys Lett* 38(1):1–3
- Nighan WL (1970) Electron energy distributions and collision rates in electrically excited N₂, CO, and CO₂. *Phys Rev A* 2:1989–2000
- Nighan WL (1972) Electron kinetic processes in CO lasers. *Appl Phys Lett* 20(2):96–99
- Osiac M, Schwarz-Selinger T, O'Connell D, Heil B, Petrovic ZL, Turner MM, Gans T, Czarnetzki U (2007) Plasma boundary sheath in the afterglow of a pulsed inductively coupled RF plasma. *Plasma Sources Sci Technol* 16(2):355
- Pappas D, Smith BW, Omenetto N, Winefordner JD (2000) Formation of a cesium plasma by continuous-wave resonance excitation. *Appl Spectrosc* 54(8):1245–1249
- Phelps AV (2005) JILA database. http://jila.colorado.edu/~avp/collision_data
- Phelps AV, Pitchford LC (1985) Anisotropic scattering of electrons by N₂ and its effect on electron transport. *Phys Rev A* 31:2932–2949
- Plasil R, Korolov I, Kotrik T, Dohnal P, Bano G, Donko Z, Glosik J (2009) Non-Maxwellian electron energy distribution function in He, He/Ar, He/Xe/H₂ and He/Xe/D₂ low temperature afterglow plasma. *Eur Phys J D* 54(2):391–398
- Rockwood SD (1973) Elastic and inelastic cross sections for electron-Hg scattering from Hg transport data. *Phys Rev A* 8:2348–2358
- Rockwood SD, Brau J, Proctor W, Canavan G (1973) Time-dependent calculations of carbon monoxide laser kinetics. *IEEE J Quantum Electron* 9(1):120–129
- Seo SH (2006) Experimental investigations of pulse-power-modulated inductive discharges. *J Korean Phys Soc* 48(3):414–421
- Song MA, Lee YW, Chung TH (2011) Characterization of an inductively coupled nitrogen-argon plasma by Langmuir probe combined with optical emission spectroscopy. *Phys Plasmas* 18(2):023504
- Treanor CE, Rich JW, Rehm RG (1968) Vibrational relaxation of anharmonic oscillators with exchange-dominated collisions. *J Chem Phys* 48(4):1798–1807
- Wilhelm J, Winkler R (1976) Die relaxation der geschwindigkeitsverteilungsfunktion der elektronen im homogenen feld mit elastischen und anregenden stößen i. theoretische grundlagen und erste ergebnisse für zeitunabhängiges elektrisches feld. Beiträge aus der Plasmaphysik 16(5):287–315
- Wilhelm J, Winkler R (1979) Progress in the kinetic description of non-stationary behaviour of the electron ensemble in non-isothermal plasmas. *J Phys Colloq* 40(C7):251–267
- Winkler R, Wilhelm J, Capitelli M, Gorse C (1992) Impact of electron-electron interaction on the electron energy distribution function in molecular plasmas under RF field action. *Plasma Chem Plasma Process* 12(1):71–87

Chapter 6

Collisional-Radiative Models for Atomic Hydrogen Plasmas

Collisional-radiative (CR) models of atomic hydrogen have a long history started with two pioneering papers by Bates et al. (1962a,b) and later expanded and generalized by Drawin (1969, 1970), Drawin and Emard (1971), Fujimoto et al. (1972), Fujimoto (1973, 2004), Biberman et al. (1967, 1973, 1987), Caciato and Capitelli (1974, 1976a,b), and Van Sijde et al. (1984). In those works, stationary or quasi-steady state (QSS) approaches were employed, assuming fast relaxation of excited states and slow varying free electron and ground state concentrations. At the same time, some papers started to exploit a time-dependent approach (Gudzenko and Shelepin 1964; Gordiets et al. 1968; Limbaugh and Mason 1971; Caciato and Capitelli 1975; Caciato et al. 1976; Gorse et al. 1978; Tallents 1977), in order to investigate the possibility of using the population inversion created in a recombining regime to generate laser pulses in atomic hydrogen plasma.

A common assumption in CR models is to consider the electrons to follow a Maxwell distribution, obtaining in this case electron impact rate coefficients depending on the electron temperature T_e only. This approximation is still used in recent applications (Bultel and Annaloro 2013; Munafò et al. 2013). Large efforts are being made (Colonna et al. 2001, 2012; Capitelli et al. 2013; Vleek and Pelikan 1985) in self-consistently coupling the CR models with a Boltzmann equation for the non-equilibrium electron energy distribution function. This self-consistent approach, recently also applied to metal plasmas produced by ns laser pulse (Pietanza et al. 2010), gives a more realistic description of atomic hydrogen kinetics, including in the model the effect of superelastic collisions.

In this chapter we discuss different situations described by equilibrium and non-equilibrium eedf, limiting our study to a $H(n)$, H^+ plasma i.e. we consider a completely dissociated system. More advanced collisional-radiative models for both atoms and molecules have been reported by various authors (Hassouni et al. 1999a,b, 2006; Capitelli et al. 1996; Longo et al. 1998).

6.1 Equilibrium Relations

For equilibrium atomic plasmas we can calculate the composition, the thermodynamic properties and the population of excited states by using Boltzmann and Saha equations i.e. by using equilibrium thermodynamics (Capitelli et al. 2012). In the next sections the most important equilibrium relations are summarized.

6.1.1 Boltzmann Relation

The ratio of the number density n_j , of particles of a particular species (molecule, atom, or ion) in a higher energy level j to the number density n_i in a lower energy level i is given by the Boltzmann relation

$$\frac{n_j}{n_i} = \frac{g_j}{g_i} e^{-\varepsilon_{ij}/kT} \quad (6.1)$$

Here g_i and g_j denote the degeneracies of the i -th and j -th levels, respectively and

$$\varepsilon_{ij} = \varepsilon_j - \varepsilon_i$$

To relate n_j to the total number of particles $n = n_1 + n_2 + \dots + n_k$ we employ

$$\frac{n}{n_1} = \sum_{i=1}^k \frac{n_i}{n_1} = \frac{1}{g_1} \sum_{i=1}^k g_i e^{-\varepsilon_i/kT} = \frac{Q(T)}{g_1} \quad (6.2)$$

where

$$Q(T) = \sum_{i=1}^{\infty} g_i e^{-\varepsilon_i/kT} \quad (6.3)$$

is the partition function. The atomic partition function diverges if the sum includes infinite number of levels,¹ as obtained when solving the electronic Schrödinger equation for the isolated atom. In a gas or in a plasma, interactions with neighboring particles impose an effective finite upper limit N_{\max} to the number of bound energy levels, so that Q is a finite number (Capitelli et al. 2012). It should be noted that the problem of the number of atomic levels compatible with a given cutoff criterion is usually disregarded in CR models, while it is an unavoidable issue when applying statistical methods to calculated the equilibrium thermodynamics properties of a system (Cacciatore and Capitelli 1974).

¹It should be noted that for $i \rightarrow \infty$ $\varepsilon_i \rightarrow I$ where I is the ionization energy and $g_i \rightarrow \infty$.

6.1.2 Saha Relation

In case of ionization equilibrium, for each species in a plasma, the number density of an ionized species in the ground level n_1^+ and the corresponding number density of neutral particles in the k -th level n_k are related to the free electron number density n_e by the Saha equation²

$$\frac{n_e n_1^+}{n_k} = 2 \frac{g_1^+}{g_k} \left(\frac{2\pi m_e k T_e}{h^2} \right)^{3/2} e^{-(I - \varepsilon_k)/k T_e} \quad (6.4)$$

Considering the global atomic concentration n_a and introducing the partition functions Q_a for the neutral atom and Q_+ for the ion, we may also write the Saha equation in the form

$$\frac{n_e n_+}{n_a} = 2 \frac{Q_+}{Q_a} \left(\frac{2\pi m_e k T}{h^2} \right)^{3/2} e^{-\varepsilon_I/k T} \quad (6.5)$$

6.1.3 Maxwell Distribution

The velocity distribution of the particles obeys the Maxwell law

$$f(v) = 4\pi \left(\frac{m}{2\pi k T} \right)^{3/2} v^2 \exp \left(-\frac{mv^2}{2kT} \right) \quad (6.6)$$

The Maxwell distribution in energy space is obtained changing the integration variable $n(\varepsilon)d\varepsilon = f(v)dv(\varepsilon)$

$$n(\varepsilon) = f(v) \frac{dv(\varepsilon)}{d\varepsilon} = \frac{1}{\sqrt{2m_e \varepsilon}} f \left(\sqrt{\frac{2\varepsilon}{m_e}} \right)$$

resulting in the following expression for the electron energy distribution function (eedf) in inverse energy units [eV⁻¹]

$$n(\varepsilon) = \frac{2}{\pi^{1/2} (k T)^{3/2}} \sqrt{\varepsilon} \exp \left(-\frac{\varepsilon}{k T} \right) \quad (6.7)$$

Dividing Eq. (6.7) by $\sqrt{\varepsilon}$ another representation (in [eV^{-3/2}]), commonly found in literature, is obtained

²The coefficient 2 in the equation is the statistical weight of free electrons due to the spin.

$$f(\varepsilon) = \frac{n_e(\varepsilon)}{\sqrt{\varepsilon}} = \frac{2}{\pi^{1/2}(kT)^{3/2}} \exp\left(-\frac{\varepsilon}{kT}\right) \quad (6.8)$$

Using the latter normalization, a Maxwell distribution function is represented by a linear function in a semi-log plot of $f(\varepsilon)$ vs ε .

6.1.4 Planck Spectral Distribution

The three previous equilibrium relations associated with the names of Boltzmann, Saha, and Maxwell pertain to matter. When the radiation field is also in thermodynamic equilibrium the photons are characterized by a temperature-dependent equilibrium distribution, the Planck function

$$B_v(T) = \frac{2hv^3}{c^2} \frac{1}{e^{hv/kT} - 1} \quad (6.9)$$

The distribution has the units of a radiation intensity, i.e. energy (W) crossing the unit surface (m^{-2}) per unit solid angle (sr^{-1}) per unit frequency (Hz^{-1}).

6.2 Non-equilibrium Atomic Plasma

Most laboratory-generated plasmas as well as plasmas used in industrial and technological applications and space plasmas are characterized by large losses of energy by radiation or by transient regimes (laser plasmas) and cannot be described by the previous equilibrium relations. As a consequence, a kinetic approach must be used to find the plasma composition as well as population densities of excited states for atomic and molecular plasmas. This kind of approach, which closely follows the chemical kinetic approach, was developed many years ago for atomic plasmas by the Belfast school (Bates et al. 1962a,b) and was in particular called collisional-radiative (CR) model.

Let us start to describe the kinetic approach considering the atomic hydrogen plasma, composed by free electrons e^- , protons H^+ and atomic hydrogen in the different electronic states. This is the simplest system that can be investigated with the CR approach, because the ion does not have an internal structure and atomic hydrogen electronic levels can be identified by the principal quantum number n , i.e. $H(n)$, because of the degeneracy of levels with respect to angular and magnetic quantum numbers.³ To simplify the problem, we assume the following hypotheses

³Obviously this is valid only for an isolated atom, and in presence of electric and magnetic field, as it can happen in a plasma, the degeneracy is broken due to the Stark and Zeeman effects.

1. Radiation transfer is approximately described by reducing the Einstein coefficient for spontaneous emission by a factor (called escape factor) to account for local reabsorption of radiation emitted by an atomic transition.
2. The plasma is homogeneous i.e. diffusion processes are completely disregarded
3. Only collisional processes induced by electrons are considered.⁴

In the following we discuss the most important classes of elementary processes governing the kinetics of excited states of hydrogen atoms. Each process introduces a term in the kinetic equation of the i -th electronic level, that can be written in the following form

$$\frac{dn_i}{dt} = \sum_p S_i^p \quad (6.10)$$

where n_i is the level concentration (usually a number density) and S_i^p is the source term for the i -th level due to the p -th elementary process.

Note that, if assumption 2 is removed, one should take into account the dependence of the diffusion coefficients of hydrogen excited states on the principal quantum number (Capitelli et al. 2004; Bruno et al. 2007).

6.2.1 Electron Impact Excitation

An electron interacting with an atom in a given state i can induce an electronic transition to a higher energy level j . The reverse de-excitation process is also possible because of the detailed balance principle. These processes can be written as



The source term for this process is given by

$$S_i^{ex} = -n_i n_e \sum_{j \neq i} k_{ij} + n_e \sum_{j \neq i} k_{ji} n_j \quad (6.12)$$

where n_e is the electron density and k_{ij} and k_{ji} are the rate coefficients for the excitation and de-excitation processes respectively. A characteristic collisional relaxation time τ_c can be defined by

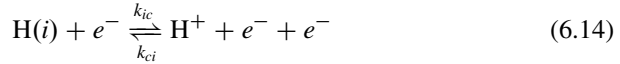
$$\tau_c = \left(n_e \sum_{j \neq i} k_{ij} \right)^{-1} \quad (6.13)$$

⁴In some cases (for example, low initial electron density), atom-atom collisions can be important and must also be considered in the kinetic scheme as also shown in the last examples of the present chapter.

corresponding to the characteristic time-scale of the relaxation of the level if only the first term in Eq. (6.12) is considered.⁵ It should be noted that, if n_e is constant the electron impact excitation is a first order kinetic process, characterized by an exponentially decaying trend.

6.2.1.1 Electron Impact Ionization/Recombination

Electron impact ionization and the corresponding three-body recombination process are described by the following kinetic equation



giving the source term

$$S_i^{ion} = -n_i n_e k_{ic} + n_e^2 n_+ k_{ci} \quad (6.15)$$

where n_+ is the number density of the ion, and k_{ic} and k_{ci} the electron impact ionization and three-body recombination rate coefficients. Taking into account excitation and ionization processes together, we can define an overall collisional relaxation time by

$$\tau_c = \left[n_e \left(k_{ic} + \sum_{j \neq i} k_{ij} \right) \right]^{-1} \quad (6.16)$$

This process introduces also source terms for free electron and ion number densities

$$S_e^{ion} = S_{H^+}^{ion} = - \sum_i S_i^{ion} \quad (6.17)$$

6.2.2 Radiative Transitions

We characterize the spontaneous emission through the Einstein probabilities A_{ij} (s^{-1}); the reabsorption is simply inserted in the original collisional-radiative model by decreasing the Einstein probabilities by the escape factor λ_{ij} .



⁵The definition given here must be considered an estimation of the relaxation time. Noticing that, if n_e is constant, this kind of process results in a linear system of equation, therefore, more rigorously, the eigenvalue of the kinetic matrix must be considered as relaxation times, while Eq. (6.13) consider only the diagonal elements.

In particular, thin and thick plasmas are characterized by the following assumptions

$$\begin{aligned}\lambda_{ij} &= 1 \quad \forall (i,j) \quad \text{thin plasma} \\ \lambda_{ij} &< 1 \quad \forall (i,j) \quad \text{thick plasma}\end{aligned}\tag{6.19}$$

This approach assumes that the mean photon free path is so short that practically all reabsorption happens at the same position of emission. Note that if an atomic line is completely reabsorbed we have $\lambda_{ij} = 0$, i.e. $\lambda_{ij}A_{ij} = 0$. Let us introduce the quantity $A_{ij}^* = \lambda_{ij}A_{ij}$.

The source term for radiative transitions taking into account the Einstein coefficient adjusted by the escape factor is

$$S_i^{rad} = \sum_{j>i} n_j A_{ji}^* - n_i \sum_{i>j} A_{ij}^* \tag{6.20}$$

The radiative relaxation time is then defined as

$$\tau_r = \left(\sum_{j<i} A_{ij}^* \right)^{-1} \tag{6.21}$$

It is worth noting that the above parametric and local approximation for radiation reabsorption can be avoided coupling the CR model to the radiation transport equation (Colonna et al. 2012).

6.2.2.1 Radiative Recombination

Another important radiative process in the hydrogen plasma is radiative recombination in which a free electron is captured by a proton forming a bound state with the simultaneous emission of a photon



By introducing the rate constant β_i we can write for the source term of level i

$$S_i^{rr} = n_e n_+ \beta_i \tag{6.23}$$

The reverse process can be neglected for weak optical quantum fields. The source terms for the ion and electron populations can be written as

$$S_e^{rr} = S_{H^+}^{rr} = - \sum_i S_i^{rr} \tag{6.24}$$

6.2.3 Master Equations for Spatially Homogenous Plasma

The complete equation for the level population of an hydrogen electronic level (including the ground one) can be written by collecting the previous terms in the so called Master Equation for the i -th hydrogen level

$$\begin{aligned} \frac{dn_i}{dt} = & n_e \sum_{j \neq i} n_j k_{ji} + n_e^2 n_+ k_{ci} - n_i n_e \sum_{j \neq i} k_{ij} - n_e n_i k_{ic} \\ & + n_e n_+ \beta_i + \sum_{j > i} n_j A_{ji}^* - n_i \sum_{i > j} A_{ij}^* \quad i, j = 1, 2, \dots, n_{\max} \end{aligned} \quad (6.25)$$

It should be noted that all the source terms are a linear function of the density of atoms in each internal state.

Let us introduce the quantity $X_i = n_i / n_i^b$, where n_i^b is an ideal concentration of the i -th excited hydrogen level calculated as a function of n_e , n_+ and T_e through the Saha equation (see Eq. (6.4)). Therefore $n_i^b = f(T_e, n_e, n_+)$ and $X_i = n_i / n_i^b = 1$ at thermodynamic equilibrium. The X_i thus represent deviations of the level population from the equilibrium values, caused by processes not balanced by the inverse ones. Expressing Eq. (6.25) in terms of the X_i variables, the following equation is obtained

$$\begin{aligned} \frac{dX_i}{dt} = & -X_i \left[n_e k_i^* + \sum_{j < i} A_{ij}^* \right] + n_e \sum_{j \neq i} X_j \frac{n_j^b}{n_i^b} k_{ji} \\ & + \sum_{j > i} X_j \frac{n_j^b}{n_i^b} A_{ji}^* + \frac{n_e n_+}{n_i^b} [\beta_i + n_e k_{ci}] \quad i, j = 1, 2, \dots, n_{\max} \end{aligned} \quad (6.26)$$

with

$$k_i^* = k_{ic} + \sum_{j \neq i} k_{ij} \quad (6.27)$$

Moreover we can write corresponding conservation equations for the electron and proton number densities

$$\frac{dn_e}{dt} = \frac{dn_+}{dt} = - \sum_i \frac{dn_i}{dt} \quad (6.28)$$

which directly follows from Eqs. (6.17) and (6.24).

The dimension of the system of differential equations depends on the number of excited states considered in addition to the equation for the electron density. We can solve this problem under different assumptions. The most general case is the solution of the complete set of differential equations. On the other hand the stationary solution is obtained setting all the temporal derivatives equal to zero. An intermediate approach, suitable in many practical applications, is called quasi-

steady state (QSS). In this case all the temporal derivatives of excited states equal to zero while the ground state is allowed to relax in time together with the electron density. This approximation is valid for hydrogenoid systems, while metastable states formed by electronic excitation of complex atoms, characterized by slow relaxation rates comparable to that of the ground state, also require a time dependent description as reported by different authors (Cacciatore and Capitelli 1976a,b; Gorse et al. 1978).

6.3 Cross Sections and Rate Coefficients

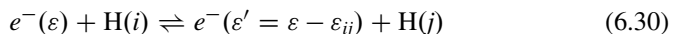
In this section we provide an overview of the elementary data, i.e. cross sections and rate coefficients describing electron impact and radiative processes necessary for solving the kinetic problem. In turn cross sections enter as rate coefficients k i.e. as cross sections averaged over the electron energy distribution function $n(\varepsilon)$

$$k = \int_{\varepsilon_p^*}^{\infty} n(\varepsilon) \sigma(\varepsilon) v(\varepsilon) d\varepsilon \quad (6.29)$$

as widely discussed in previous chapters. We assume an equilibrium (Maxwell) distribution function for $n(\varepsilon)$ in many sections of the present chapter, which concludes with a discussion of the methods needed when dealing with a non-equilibrium eedf. In the following pages the cross sections and rate coefficients entering the CR model are discussed introducing relatively simple analytical expressions, especially valid for hydrogenic systems and providing an intuitive understanding of their dependence on the electronic level principal quantum number. On the other hand, for accurate results, it is necessary to use accurate cross sections which are nowadays available and reported in open access databases (see ALADDIN (2013) as an example).

6.3.1 Excitation by Electron Impact

Let us consider the excitation process



Quantum mechanics (in the Born-Bethe approximation) gives the following equation for the cross section of an optically allowed transition

$$\sigma_{ij}^{\text{exc}}(\varepsilon) = 4\pi a_0^2 \left(\frac{I_H}{\varepsilon_{ij}} \right)^2 f_{ij} \frac{\ln(u+1)}{u+1}, \quad u = \frac{\varepsilon - \varepsilon_{ij}}{\varepsilon_{ij}} \quad (6.31)$$

The equation contains the Bohr radius a_0 , the ionization potential of hydrogen atom $I_{\text{H}} = 13.6 \text{ eV}$, the difference of energy $\varepsilon_{ij} = \varepsilon_j - \varepsilon_i$ of the relevant levels and the kinetic energy of the impinging electron ε and the absorption oscillator strength f_{ij} . In kinetic problems it is very important to establish how excitation cross section depends on the quantum numbers of the upper and lower levels. This dependence can be understood introducing the Kramers formula for the oscillator strength of the hydrogen atom in absorption ($i < j$):

$$f_{ij} = \frac{32}{3\pi\sqrt{3}} \frac{1}{i^5} \frac{1}{j^3} \frac{I_{\text{H}}^3}{(\varepsilon_j - \varepsilon_i)^3} \quad (6.32)$$

in Eq. (6.31)

$$\sigma_{ij}^{\text{exc}}(\varepsilon) = \frac{128a_0^2}{3\sqrt{3}} \frac{1}{i^5} \frac{1}{j^3} \frac{I_{\text{H}}^5 \ln(u+1)}{(\varepsilon_j - \varepsilon_i)^5(u+1)} \quad (6.33)$$

Keeping in mind that the energy of H levels, referred to the ionization limit, is given by $\varepsilon_i = -I_{\text{H}}/i^2$ we have

$$\sigma_{ij}^{\text{exc}}(\varepsilon) = \frac{128a_0^2}{3\sqrt{3}} \frac{i^5 j^7}{(j^2 - i^2)^5} \frac{\ln(u+1)}{u+1} \quad (6.34)$$

As we can see, the cross section is inversely proportional to $(j^2 - i^2)^5$. Therefore, the largest cross sections are those for transitions between adjacent levels, $i \rightarrow i+1$. Moreover, the cross section is proportional to $i^5 j^7$, thus the cross sections for transitions between excited states are higher than those starting from the ground state. Figure 6.1 compares accurate excitation cross sections (ALADDIN 2013; Janev and Smith 1993) for transitions starting from the ground state with the cross sections obtained using the approximate expression (6.34).

As expected, the largest cross section occurs for the transition $1 \rightarrow 2$ and the excitation cross section strongly decreases with the increase of the principal quantum number j of the final state. Moreover the cross sections for transitions between excited states are higher than the cross section for excitation from the ground state. This is particularly true for transition between nearby levels. Figure 6.2 shows the excitation cross sections for the transition $i \rightarrow i+1$ for different i as a function of the electron energy. As expected this cross section grows with the principal quantum number i .

Figure 6.3a, b report the rate coefficients as a function of the electron temperature corresponding to the cross sections of Figs. 6.1 and 6.2. These values have been calculated using Eq. (6.29) with a Maxwell distribution function for electrons and accurate electron impact cross sections (ALADDIN 2013). The rate coefficients increase with T_e and their behavior mirrors that of the cross sections: the higher rate coefficients are for transitions of the type $i \rightarrow i+1$, increasing with the principal quantum number i .

Fig. 6.1 Cross section for the process $H(i = 1) + e^-(\varepsilon) \rightarrow H(j > 1) + e^-(\varepsilon - \varepsilon_{ij})$ calculated using Eq. (6.34) (dotted lines) or taken from the ALADDIN database (ALADDIN 2013) (solid lines)

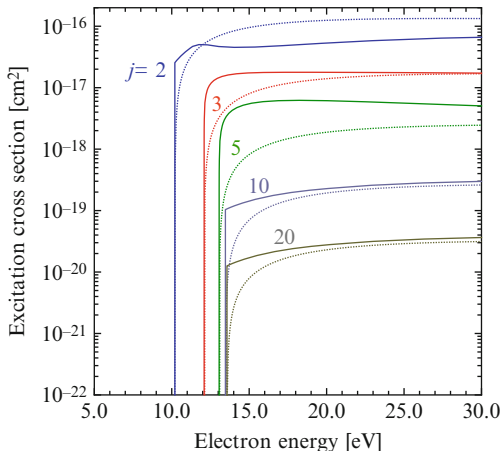
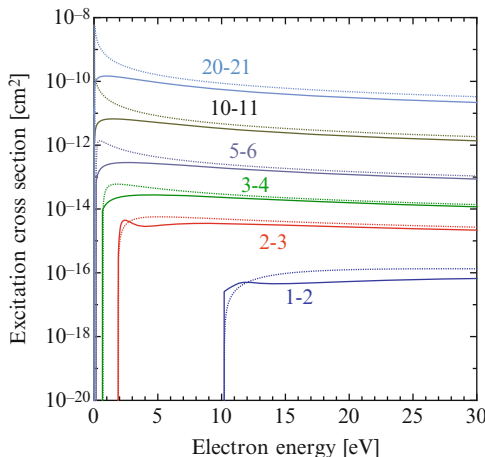
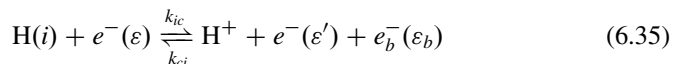


Fig. 6.2 Cross section for the process $H(i) + e^-(\varepsilon) \rightarrow H(j = i + 1) + e^-(\varepsilon - \varepsilon_{ij})$ calculated using Eq. (6.34) (dotted lines) or taken from the ALADDIN database (ALADDIN 2013) (solid lines)



6.3.2 Electron Impact Ionization

The ionization/recombination reaction is



The classical Thompson formula can be used to understand the dependence of ionization cross-section on the energy of electrons as well on the internal energy of the atom

$$\sigma_{\text{ion}}(\varepsilon) = 4\pi a_0^2 \frac{I_H^2(\varepsilon - I_i)}{I_i \varepsilon^2} \quad (6.36)$$

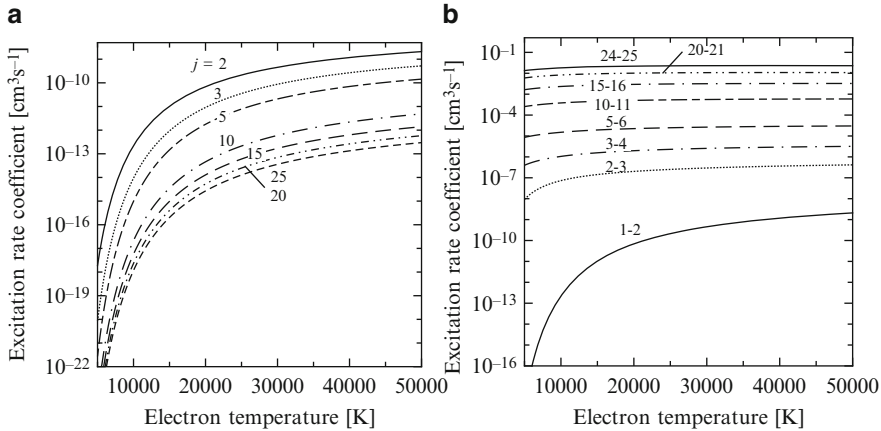
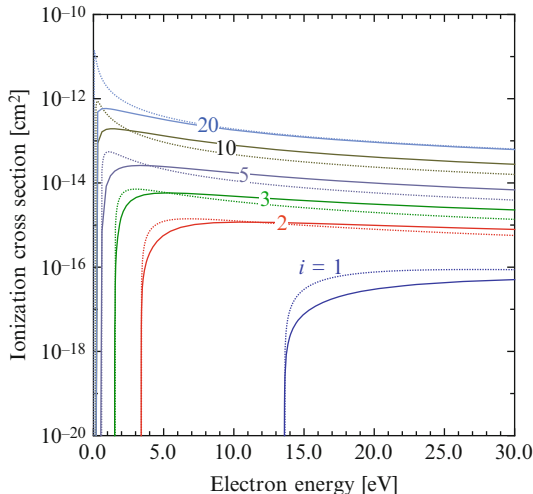


Fig. 6.3 Rate coefficient as a function of the electron temperature for the process (a) $H(i = 1) + e^-(\varepsilon) \rightarrow H(j > 1) + e^-(\varepsilon - \varepsilon_{ij})$ and (b) $H(i) + e^-(\varepsilon) \rightarrow H(j = i + 1) + e^-(\varepsilon - \varepsilon_{ij})$

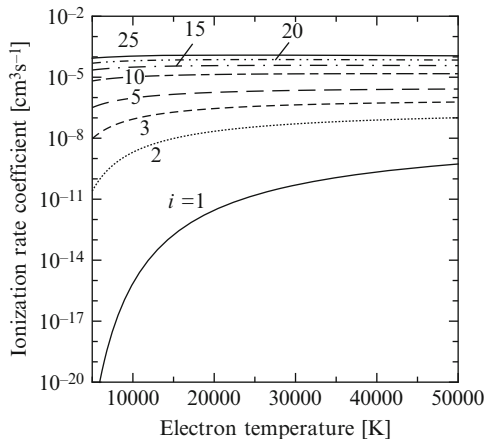
Fig. 6.4 Ionization cross sections of $H(i)$ as a function energy, for different values of the principal quantum number i , calculated using Eq. (6.36) (dotted lines) or taken from the ALADDIN database (ALADDIN 2013) (solid lines)



where I_i is the ionization energy from the i th level. Keeping in mind that I_i is proportional to i^{-2} , we can deduce that the ionization cross sections for $\varepsilon \gg I_i$ increases as i^2 .

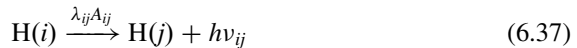
Figure 6.4 reports the ionization cross-sections of atomic hydrogen as a function of energy for different principal quantum number by ALADDIN (2013), compared to the values obtained from Eq. (6.36), showing a satisfactory agreement between the two sets of cross sections. The Maxwell ionization rate coefficients, calculated using accurate cross sections are reported as a function of T_e in Fig. 6.5.

Fig. 6.5 Ionization rate coefficients calculated using the ionization cross section in Fig. 6.4 and a Maxwell distribution function for different principal quantum number i as a function of the electron temperature



6.3.3 Spontaneous Emission

In spontaneous emission an atom found in state i with binding energy E_i undergoes a transition to a lower energy state j with binding energy $E_j > E_i$, emitting a photon of frequency ν_{ij} .



The probability of spontaneous emission is determined by the Einstein coefficient, which can be approximated by the following equation for hydrogen-like atoms of charge Z

$$A_{ij} = \frac{1.6 \times 10^{10} Z^4}{i^3 j (i^2 - j^2)} \quad (6.38)$$

It follows that for transitions to lower levels $j \ll i$

$$A_{ij} \approx \frac{1.6 \times 10^{10} Z^4}{i^5 j}$$

and for transition to an adjacent lower state ($j = i - 1$ with $i \gg 1$)

$$A_{i,i-1} \approx \frac{0.8 \times 10^{10} Z^4}{i^5}$$

The Einstein coefficient is approximately minimized setting $j = i/\sqrt{3}$

$$A_{i,i/\sqrt{3}} \approx \frac{4.15 \times 10^{10} Z^4}{i^6}$$

As we can see from the above equations, the most probable radiative transition is to the ground state. The transition to the adjacent lower level $i \rightarrow i - 1$ and to the level $j = 2$ have a probability one half as large. Transitions to states $i - 1 > j > 2$ are even less probable. For a fixed lower state j , the most probable transition to it is from the adjacent higher level $j + 1$. The probabilities of transitions from levels $i > j + 1$ are much smaller. Thus, spontaneous emission is more important for lower levels, and the effect of spontaneous emission in destroying the equilibrium state of the atomic energy level occurs essentially for lower levels and in particular for the fundamental one.

6.4 Radiative Recombination

Radiative recombination is the process in which an electron and anion form an atom and, in doing so, emit electromagnetic radiation. This process can be written schematically as



where the free electron kinetic energy ε , the frequency ν of the emitted photon and the binding energy I_i of level i are related by the energy conservation constraint

$$\varepsilon + I_i = h\nu \quad (6.40)$$

Kramers cross section for the recombination of a free electron with kinetic energy $\varepsilon = \frac{1}{2}mv^2$ into the level i of an hydrogenic ion with atomic number Z is given by Zel'dovich and Raizer (1967)

$$\sigma_{ci} = \frac{128\pi^4}{3\sqrt{3}} \frac{Z^4 e^{10}}{mc^3 h^4 v^2 \nu} \frac{1}{i^3} \quad (6.41)$$

The recombination rate coefficient towards level i is calculated integrating over the eedf

$$\beta_i = \int_0^\infty v(\varepsilon) n(\varepsilon) \sigma_{ci}(\varepsilon) d\varepsilon \quad (6.42)$$

Convenient computational approximations for the recombination rate coefficients, taking into account quantum mechanical corrections though the bound-free gaunt factor $g_{II}(i, \varepsilon)$ are described in Johnson (1972) and Seaton (1959).

6.5 QSS Approximation

Let us recall the equations of the collisional-radiative model, Eq. (6.26)

$$\begin{aligned} \frac{dX_i}{dt} &= -X_i \left[n_e k_i^* + \sum_{j < i} A_{ij} \right] + n_e \sum_{j \neq i} X_j \frac{n_j^b}{n_i^b} k_{ji} \\ &\quad + \sum_{j > i} X_j \frac{n_j^b}{n_i^b} A_{ji} + \frac{n_e n_+}{n_i^b} [\beta_i + n_e k_{ci}] \\ i, j &= 1, 2, \dots, n_{\max} \\ \frac{dn_e}{dt} &= \frac{dn_+}{dt} = - \sum_i \frac{dn_i}{dt} \end{aligned}$$

The purpose of this section is to present a simplified solution method for the above system called quasi-steady state (QSS) approximation. The QSS approximation is formulated setting to zero the temporal derivatives of excited states, while the ground state is allowed to relax in time with the electron density, resulting in the following system of equations

$$\frac{dn_i}{dt} = 0 \quad i \geq 2 \quad (6.43)$$

$$\frac{dn_e}{dt} = \frac{dn_+}{dt} = - \frac{dn_1}{dt} \neq 0 \quad (6.44)$$

The QSS model is usually justified on the basis of the much shorter relaxation times of the excited states compared to the ground state. Equation (6.43) yields a system of linear equation for $i \geq 1$, which can be solved by taking the electron number density n_e , the ground state number density n_1 and the free electron temperature T_e as parameters. Equation (6.44) yields a differential equation for the fundamental level. It is worth noticing that the solution of Eq. (6.44) requires an initial value for X_1 that depends on the assumed initial excited state distribution of the investigated system. Note also that in the presence of low-lying excited states, as in the case of N, O and C systems, the quasistationary condition is usually not valid for these states.

6.5.1 QSS Approximation (General Equations)

In the following we report the general equations to be solved in the QSS approximation. The system of linear equations for $i > 1$ can be compactly written as

$$\sum_{j=1}^{i^*} a_{ij} X_j = b_i \quad i = 2, 3, \dots, i^* \quad (6.45)$$

where i^* is the last level considered. The coefficients appearing in the equation can be written as

$$b_i = -\frac{n_e n_+}{n_i^b} [\beta_i + n_e k_{ci}] \quad (6.46)$$

$$a_{ii} = - \left[n_e k_i^* + \sum_{j < i} A_{ij} \right] \quad (6.47)$$

$$a_{ij} = \frac{n_j^b}{n_i^b} n_e k_{ji} \quad j < i \quad (6.48)$$

$$a_{ij} = \frac{n_j^b}{n_i^b} [A_{ji} + n_e k_{ji}] \quad j > i \quad (6.49)$$

The term a_{ii} represent loss of population of level i due to transitions to levels $j \neq i$ and to the continuum while terms a_{ij} with $j \neq i$ represent gain of population of level i due to electron impact excitation/de-excitation and spontaneous radiative decay from higher excited states. Finally the b_i coefficients represent the gain of population of level i due to three-body recombination and radiative recombination. Moreover, the a_{ij} coefficients depend on n_e and T_e (through the specific rate coefficients), while b_i depend on n_e , T_e and n_+ . For a pure atomic hydrogen plasma $n_+ = n_e$, but this is not the case when more than one ionic species is considered.

For the ground state we can write a differential equation

$$\frac{dX_1}{dt} = a_{11}X_1 + \sum_{j=2}^{i^*} a_{1j}X_j - b_1 \quad (6.50)$$

Equation (6.43) is linear in X_1 so that we can write the solutions in the following form

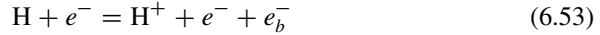
$$X_{i \geq 2} = X_{i \geq 2}^0 + R_{i \geq 2}^1 X_1 \quad (6.51)$$

Inserting this ansatz in Eq. (6.50) we obtain

$$\begin{aligned} \frac{dX_1}{dt} &= a_{11}X_1 + \sum_{j=2}^{i^*} a_{1j}[X_j^0 + R_j^1 X_1] - b_1 \\ &= a_{11}X_1 + \sum_{j=2}^{i^*} a_{1j}R_j^0 X_1 + \sum_{j=2}^{i^*} a_{1j}X_j^0 - b_1 \\ &= \left(a_{11} + \sum_{j=2}^{i^*} a_{1j}R_j^0 \right) X_1 + \left(\sum_{j=2}^{i^*} a_{1j}X_j^0 - b_1 \right) \end{aligned} \quad (6.52)$$

In this equation, the only unknown is X_1 , since the coefficients X_j^0 and R_j^0 have already been obtained solving Eq. (6.45) (see next sections).

It can be shown that the knowledge of coefficients X_j^0 and R_j^1 allows us to calculate average collisional-radiative ionization (S) and recombination (α) coefficients. These coefficients in turn are defined by considering a global ionization/recombination reaction



We therefore define a global ionization coefficient through

$$\left(\frac{dn_e}{dt} \right)_{\text{ion.}} = S n_e n_1 \quad (6.54)$$

a corresponding pseudo second-order global recombination coefficient through

$$\left(\frac{dn_e}{dt} \right)_{\text{rec.}} = -\alpha n_e n_+ \quad (6.55)$$

and a corresponding equation for the time derivatives of electron density and of ground state number density

$$-\frac{dn_e}{dt} = \frac{dn_1}{dt} = n_e n_+ \left(\alpha - S \frac{n_1}{n_+} \right) = \gamma n_e n_+ \quad (6.56)$$

The α and S coefficients are linked to X_i^0 and R_i^1 values by the following equations

$$\alpha = \frac{n_1^b}{n_e n_+} \left[-b_1 + \sum_{j>1} a_{1j} X_j^0 \right] \quad (6.57)$$

$$S = -\frac{1}{n_e} \left[a_{11} + \sum_{j>1} a_{1j} R_j^1 \right] \quad (6.58)$$

Note also that the coefficient γ dictates the nature of plasma

$$\begin{cases} \gamma = 0 & \text{stationary condition} \\ \gamma > 0 & \text{recombination condition} \\ \gamma < 0 & \text{ionization condition} \end{cases} \quad (6.59)$$

6.5.2 Interpretation of X_i^0 e R_i^1

In order to give an intuitive meaning to the X_i^0 e R_i^1 coefficients, let's rewrite the QSS system

$$\sum_{j=2}^{i^*} a_{ij} X_j = b_i - a_{i1} X_1 \quad i = 2, 3, \dots, i^* \quad (6.60)$$

where $a_{ij} = f(n_e, T_e)$ e $b_i = f(n_+, n_e, T_e)$ are independent from the excited state densities. Moreover, n_+, n_e are known data, the former two by the QSS approximation, the latter from the quasi-neutrality condition. For a fixed n_+ (entering the b_i coefficient only), set $X_1 = 0$ in the QSS system. We obtain

$$\sum_{j=2}^{i^*} a_{ij} X_j^0 = b_i \quad i = 2, 3, \dots, i^* \quad (6.61)$$

allowing the determination of $X_j^0, j = 2, 3, \dots, i^*$. Let's remark that the above system does not depend on the number density of the ground state, and parametrically depends on the electron and ion densities and T_e (through the various impact rate coefficients).

Similarly, let's fix $X_1 = 1$ e $n_+ = 0$ in the QSS system. Remembering that b_i are proportional to n_+ , the equations to be solved in this case are as follows

$$\sum_{j=2}^{i^*} a_{ij} R_j^1 = -a_{i1} \quad i = 2, 3, \dots, i^* \quad (6.62)$$

in the unknowns $R_j^1, j = 2, 3, \dots, i^*$. This time the solution does not depend on n_+ but only on n_e and T_e . Summing the solution of Eqs. (6.61) and (6.62) multiplied by X_1 we get

$$\sum_{j=2}^{i^*} a_{ij} (X_j^0 + X_1 R_j^1) = b_i - a_{i1} X_1 \quad i = 2, 3, \dots, i^* \quad (6.63)$$

It follows that the solution of the QSS system has been decomposed into

$$X_i = X_i^0 + R_i^1 X_1, \quad i > 1 \quad (6.64)$$

It is clear that X_i^0 is the part of the solution depending on the ion density only (ionization continuum) and independent of the ground state density, while the opposite is true for $R_i^1 X_1$. We see that the departure from equilibrium of the i -th state is made up of two contributions

- A contribution depending on the ground state density: $R_i^1 X_1$
- A contribution depending on the ion density: X_i^0

Moreover, the dependence on the the ground state density is linear. The essential features of the QSS solution are (van der Mullen 1990)

1. X_j^0 is obtained setting $X_1 = 0$, namely $n_1 = 0$ in the QSS system for fixed n_+, n_e, T_e , while R_j^1 is computed using $n_+ = 0$ and fixing n_e, T_e and $X_1 = 1$.
2. The condition $n_+ = 0$ means that the ionization process is not balanced by recombination, since b_i coefficients represent three-body (k_{ci}) and radiative recombination (β_i). This situation is typical of ionizing plasma.
3. Similarly, setting $X_1 = 0$ means that the rates of electron impact excitation and ionization from the ground state are zero in this case. This means that processes populating the ground state (electron impact de-excitation, three-body recombination, radiative decay and radiative recombination) are not balanced by the opposite ones. This is an extreme case of a recombining plasma.

The solution (6.64) tells us that at steady state the system is given by a linear combination of a purely ionizing and a purely recombining plasma. The system goes to equilibrium if $n_e \rightarrow \infty$ and $X_1 = 1$. In fact electron impact processes tend to establish a Saha-Boltzmann distribution among internal states at T_e , namely $X_i \rightarrow 1$ if $n_e \rightarrow \infty$. Therefore the coefficients X_i^0 e R_i^1 are such that $X_i^0 + R_i^1 \rightarrow 1$ when $n_e \rightarrow \infty$.

6.6 QSS Results for Optically-Thin Atomic H Plasmas

Let us examine the behavior of X_i^0 vs. n_e for $T_e = 16,000$ K (Fig. 6.6a) and $T_e = 32,000$ K (Fig. 6.6b). In both cases we see that an increase of electron density is such to strongly increase X_i^0 bringing it to the equilibrium value. The achievement of the equilibrium strongly depends on the considered quantum level. As an example at $T_e = 16,000$ K the $i = 2$ level reaches the equilibrium condition only at $n_e = 10^{17} \text{ cm}^{-3}$, while for $i = 5$ it is sufficient an electron density of 10^{13} cm^{-3} to bring the level to equilibrium.

Let us now examine the trend of R_i^1 values vs. n_e for different principal quantum numbers (Fig. 6.7a, b). R_i^1 reflects the contribution to the population of level i due to transitions from the ground state and low-lying excited states. We can see that the the trend of R_i^1 is opposite to that one presented by X_i^0 . They in fact decrease with increasing i . On the other hand the effect of temperature is similar to that one reported for X_i^0 .

Finally in Fig. 6.8a, b we report α (cm^3/s) and S (cm^3/s) vs. T_e for different electron densities n_e ($10^8 \div 10^{16} \text{ cm}^{-3}$). The trend of the two coefficients as a function of temperature is opposite. In particular the c-r recombination coefficient α decreases with T_e , the opposite being true for the c-r ionization coefficient.

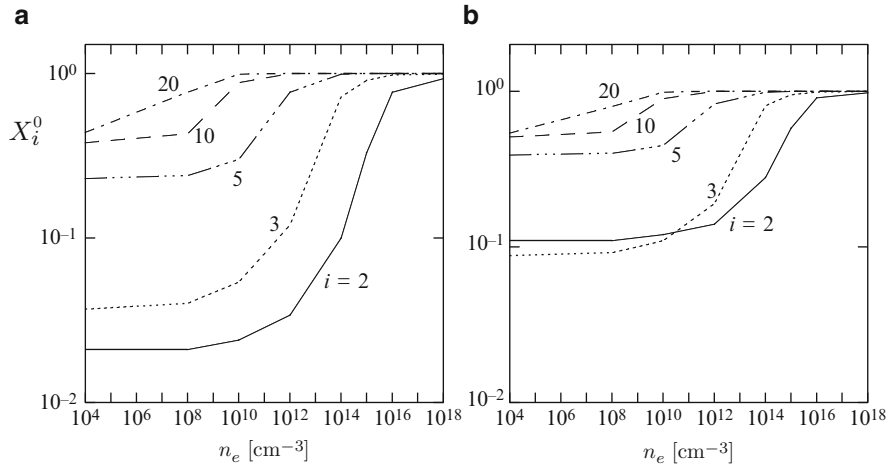


Fig. 6.6 X_i^0 as a function of the electron density n_e for different principal quantum number i at (a) $T_e = 16,000$ K and (b) $T_e = 32,000$ K

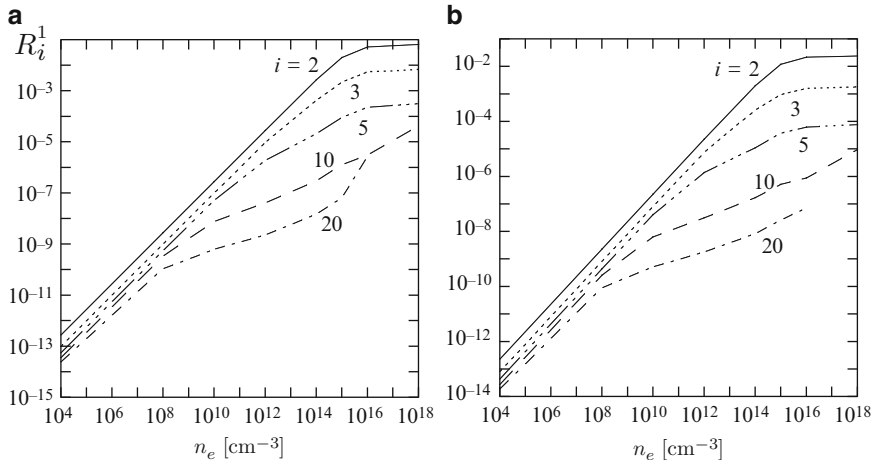


Fig. 6.7 R_i^1 as a function of the electron density n_e for different principal quantum number i at (a) $T_e = 16,000$ K and (b) $T_e = 32,000$ K

6.7 Time-Dependent Results

Time-dependent solutions of collisional-radiative model are indeed very instructive either from the basic point of view or from the impossibility to use the QSS approach under rapid time varying situations. Time-dependent results were presented more

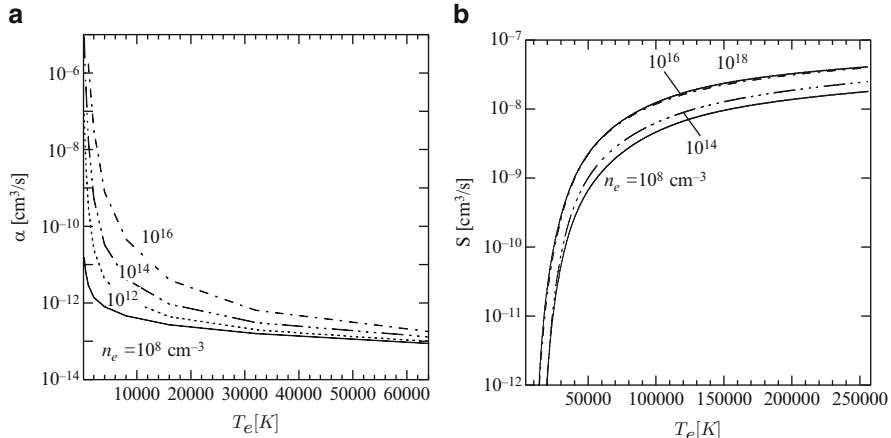


Fig. 6.8 Collisional-radiative (a) recombination coefficient α (cm³/s) and (b) ionization coefficient S (cm³/s) as a function of the electron temperature T_e for different electron densities n_e

than 40 years ago by Limbaugh and Mason (1971) for atomic helium plasmas, followed by the papers (Cacciatore and Capitelli 1975, 1976b; Gorse et al. 1978) for hydrogen, oxygen and nitrogen atomic plasmas. Nowadays the approach is straightforward due to the enormous development of applied mathematics and of computer science. In the following we will report examples taken from Pietanza (2000) and Colonna et al. (2001) who coupled the time-dependent collisional-radiative model with the Boltzmann equation for the electron energy distribution function (eedf). The results still refer to atomic hydrogen plasmas for the same conditions studied by Cacciatore and Capitelli (1975) assuming a Maxwellian eedf.

The relevant equations are those already presented for the collisional-radiative model

$$\begin{cases} \frac{dn_i}{dt} = M_{ij}n_j & \forall i \\ -\frac{dn_e}{dt} = -\frac{dn_+}{dt} = \gamma(t)n_en_+ \end{cases} \quad (6.65)$$

These equations are indeed coupled to a Boltzmann equation for the electron energy distribution function (see Chap. 4). The plasma can be essentially distinguished in two kinetic conditions, depending on dominant process between ionization and recombination, showing different behavior of the level distribution.

6.7.1 Ionizing Plasma $\gamma < 0$

The first condition concerns the so called ionizing plasma, in which the initial electron density is underpopulated with respect to the Saha-Boltzmann equilibrium. As an example of ionizing plasma let us choose the following parameters:

$$\begin{aligned} X_1 &= 10^6 \\ X_{i>1} &= 1 \\ n_e &= 10^{12} \text{ cm}^{-3} \\ T_e &= 16,000 \text{ K} \end{aligned}$$

The initial condition considers an overpopulation of the ground state with respect to the Saha-Boltzmann equilibrium so that during the evolution we should see a decrease of the population density of ground state, an increase of the electron density, and an overpopulation of the concentration of excited states. Let us consider the numerical results. In Fig. 6.9a we report the derivatives of the different species as a function of time. We see that after a short transient the derivatives of all excited states become very small thus evidencing the goodness of QSS approach. On the other hand the time derivatives of ground state and of electrons after approximately the same time become equal. Note however that despite the apparently large derivative both the electron density and the ground state keep their absolute values.

As an example the variation of electron density can be calculated by integrating the time derivative. We can perform this integration as follows

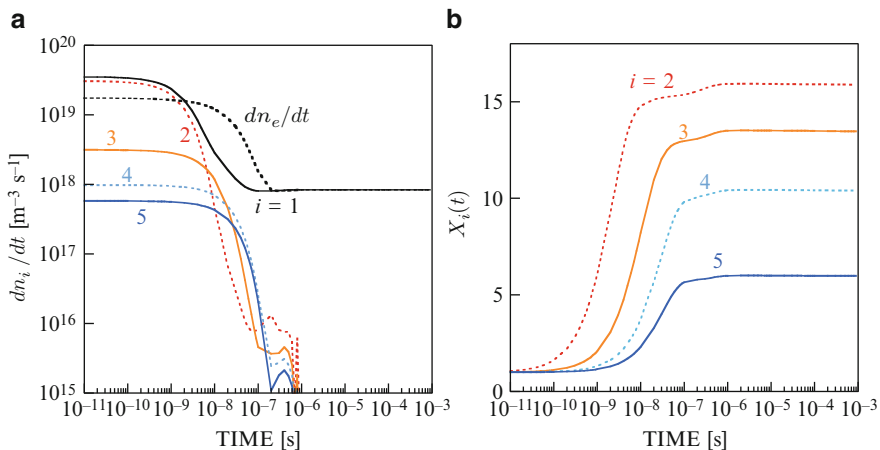


Fig. 6.9 Time evolution of (a) the derivatives of the concentrations, dn_i/dt , and of (b) X_i factors for selected levels

Table 6.1 X_i^0 and R_i^1 values for hydrogen plasma at $T_e = 16,000$ K and $n_e = 10^{12}$ cm $^{-3}$ calculated by Drawin (1970)

	$i = 2$	$i = 3$	$i = 4$	$i = 5$
X_i^0	$3.4 \cdot 10^{-2}$	$1.2 \cdot 10^{-1}$	$4.6 \cdot 10^{-1}$	$7.7 \cdot 10^1$
R_i^1	$2.8 \cdot 10^{-5}$	$9.6 \cdot 10^{-6}$	$4.8 \cdot 10^{-6}$	$1.9 \cdot 10^{-6}$

1. From $t_1 = 10^{-11}$ to $t_2 = 10^{-8}$ with a derivative of $2 \cdot 10^{13}$ cm $^{-3}$ s $^{-1}$.
 $\Delta n_e = 2 \cdot 10^5$ cm $^{-3}$.
2. From $t_3 = 10^{-8}$ to $t_4 = 10^{-7}$ with a derivative of 10^{13} cm $^{-3}$ s $^{-1}$.
 $\Delta n_e = 10^6$ cm $^{-3}$.
3. From $t_5 = 10^{-7}$ to $t_6 = 10^{-3}$ with a derivative of 10^{12} cm $^{-3}$ s $^{-1}$.
 $\Delta n_e = 10^9$ cm $^{-3}$.

The sum of these variations is much smaller than the initial electron density. Similar arguments apply to the ground state concentration.

Figure 6.9b reports the time evolution of the non-equilibrium factors for the same conditions of Fig. 6.9a. We can see that after a transient of 10^{-7} s the X_i factors reach their quasi-stationary values. In particular for the considered plasma the strong initial deviation (overpopulation) of ground state induces an overpopulation of excited states, this overpopulation decreases with increasing the principal quantum number. The stationary values obtained can be compared with the corresponding ones calculated by Drawin (1970) (Table 6.1). Combining the X_i^0 and the R_i^1 values of this author with the actual value of X_1 we obtain X_i values of 33, 11.8 and 3.1 for the levels 2, 3 and 5, these values being in satisfactory agreement with the results of Fig. 6.9b. The differences can be mainly attributed to the different choice of cross sections as well as to the different electron energy distribution functions used in the two calculations.

Let us report the trend of γ versus time for the same conditions (Fig. 6.10). We can see that after the same transient time γ reaches a negative constant value indicating the nature of ionizing plasma for the initial conditions considered in the test case. Again use of α and S calculated in the relevant figures gives a satisfactory agreement between time-dependent and stationary values.

Finally we report in the next figure the ratio of eedf(t)/eedf($t = 0$) as a function of time, showing only small deviations of eedf from the Maxwell distribution at the least for the considered conditions. Deviations are more important for a recombining plasma ($X_i(\gamma > 0) = 1$, including $\gamma = 1$, $T_e = 16,000$ K, $n_e = 10^{12}$ cm $^{-3}$) as it can be observed in Fig. 6.11. In this case we observe a depletion of the concentration of excited states as also shown in Cacciatore and Capitelli (1974).

Fig. 6.10 Time evolution of γ value

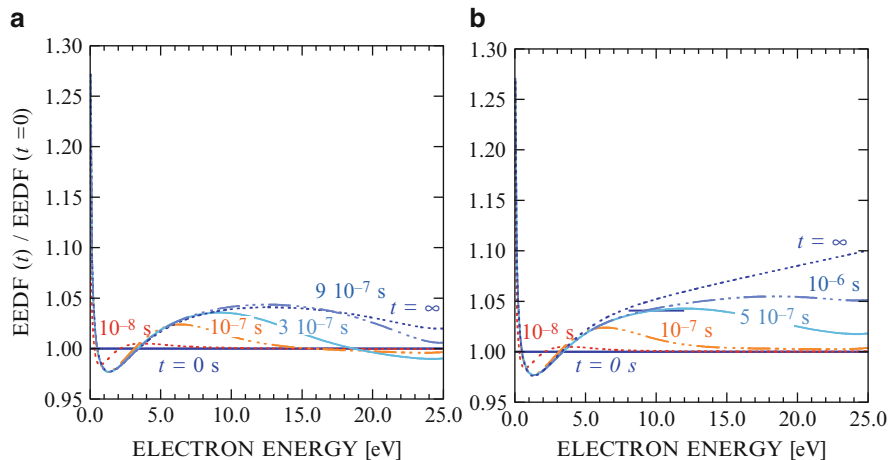
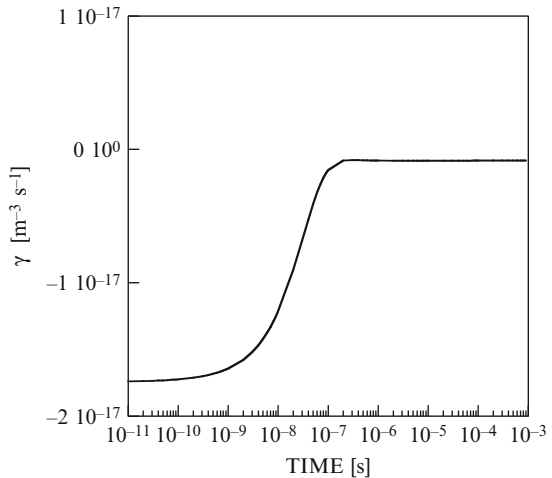


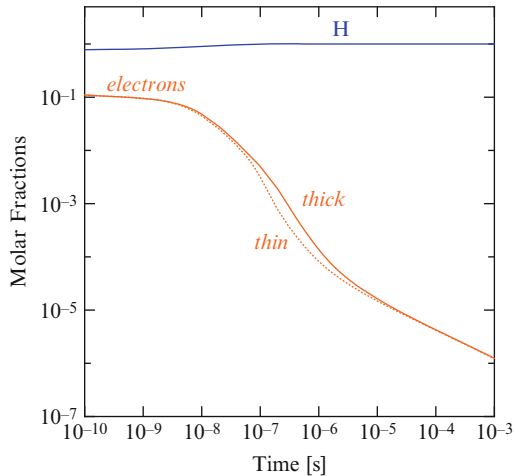
Fig. 6.11 Deviation of the actual electron energy distribution function from the Maxwell one
(a) ionizing plasma, $\gamma < 0$, and **(b)** recombining plasma, $\gamma > 0$

6.7.2 Large Deviations from Equilibrium

In this section we will examine some case studies in which there is a strong deviation of the electron energy distribution function (eedf) and atomic distribution from equilibrium. These cases derive from different initial conditions which then evolve towards stationary situations. The initial state is defined by

- T_g the (translational) gas temperature
- P_0 the total gas pressure
- ID_0 the initial value of the ionization degree

Fig. 6.12 Time evolution of the molar fractions of an hydrogen plasma under the following initial conditions: $T_e(0) = T_H(0) = 15,000$ K, $T_g = 1,000$ K and $ID_0 = 0.1$ at $P_0 = 1$ atm. Optically thick (solid line) and optically thin (dashed line) results are reported



- $T_H(0)$ the initial excitation temperature of the energy level distribution assumed as Boltzmann
- $T_e(0)$ the initial electron temperature, characterizing the electron energy distribution function, assumed as Maxwellian

Calculations are performed maintaining fixed both the gas temperature T_g and the total particle density ($n_{\text{tot}} = n_H + n_+ + n_e$ with $n_+ = n_e$) during all temporal evolution

We consider two initial conditions, the first one typical of a recombining plasma and the second corresponding to an ionizing one. As a concrete example of recombining plasma, we study an atmospheric pressure atomic hydrogen plasma with initial ionization degree of 0.1, while the initial population distribution over electronic states of H is a Boltzmann one at $T_{H=0} = 15,000$ K and the initial eedf is Maxwell at the same temperature $T_e(0) = T_H(0)$. The plasma is suddenly cooled at $T_g = 1,000$ K and both eedf and excited state internal distribution (isd) start relaxing. The two limit cases of thin ($\lambda_{ij} = 1$) and thick ($\lambda_{ij} = 0$) plasmas are compared in Figs. 6.12–6.14.

Before examining the results we want to anticipate the behavior of both isd (internal state distribution) and eedf we expect for this case. In the first place we expect a strong cooling of the electron temperature through the elastic and inelastic collisions with the atomic species, ultimately resulting in a Maxwellian eedf at the imposed gas temperature T_g . Moreover we can expect a strong decrease of the electron density and a corresponding decrease of the concentration of electronically excited states. Low electron temperature and low ionization degrees are the ideal conditions for the action of the second-kind collisions which tend to move low energy electrons to high energy ones through the processes

Fig. 6.13 Time evolution of the hydrogen atom 1s of the recombining hydrogen plasma of Sect. 6.7.2, comparing the optically thick (solid line) and optically thin (dashed line) cases

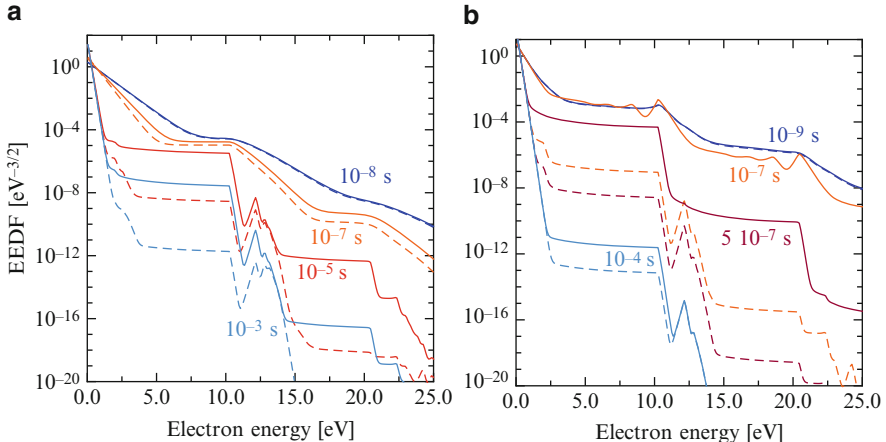
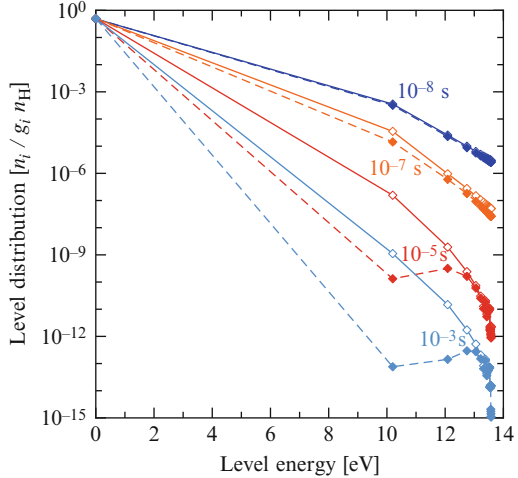
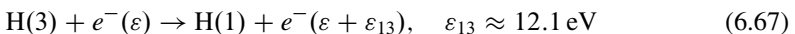
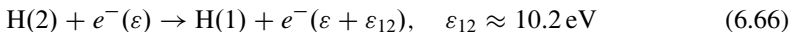


Fig. 6.14 Time evolution of the eedf in the recombining hydrogen plasma of Sect. 6.7.2 (a) neglecting and (b) accounting for atom-atom collisions, (solid line) optically thick and (dashed line) optically thin cases



and so on. These two processes depend on the concentration of excited states which are expected higher in the thick plasma case.

These qualitative observations are recovered in the following figures where we report the time dependence of electron density and of concentration of atomic hydrogen (Fig. 6.12) as well as the behavior of the whole distribution of

excited states (Fig. 6.13) and of eedf (Fig. 6.14a) against energy at different times. Inspection of Fig. 6.12 shows the strong decrease of the electron density in the recombination regime: small differences are observed between the two cases i.e. thin and thick plasmas. On the other hand the concentration of atomic hydrogen does not practically change due to neglecting of molecular hydrogen formation, which can be important for $t > 10^{-5}$ s in the reported results.

Figure 6.13 reports the normalized concentration of excited atomic hydrogen at different times. We observe that at $t = 10^{-8}$ s there are no noticeable differences between the thin and thick cases (the two distributions reflect the initial condition) while already at $t > 10^{-7}$ s large differences appear in the concentration of excited states for the two cases. As an example the concentration of the first excited state at $t = 10^{-5}$ s for the thick case is about 3 orders of magnitude higher than the corresponding concentration of the thin case. These differences strongly decrease for $n = 3$, becoming negligible for $n > 3$. This behavior can be associated to the fact that electron collisions on higher excited states overcome the corresponding radiative processes. The spontaneous radiative transition $n = 2 \rightarrow n = 1$ is responsible of the reported population inversion of the $n = 2$ level at $t = 10^{-3}$ s in the optically thin plasma. This process is not considered in the optically thick plasma (i.e. $\lambda_{21} = 0$), causing the population inversion to disappear in the latter case. The behavior of excited states together with the corresponding decrease of electron density and therefore of their thermalizing action on eedf through Coulomb collisions will be responsible of the time evolution of eedf.

Figure 6.14a compares the eedf for thin and thick conditions at different times. We can see that the two situations start giving different results already at $t = 10^{-7}$ s, the differences becoming extremely important from 10^{-5} s on. In this last case the eedf presents a very low temperature as can be appreciated by looking at the eedf for $\varepsilon < 3$ eV, thus magnifying the role of second-kind collisions. The long plateaux existing in both thin and thick cases are due to the initial build-up of a peak in the eedf at $\varepsilon = 10.2$ eV followed by redistribution through elastic (including electron-electron) and inelastic collisions. The differences in the two cases are due to the corresponding differences in the concentration of the first excited state. From $t = 10^{-5}$ s on other peaks in eedf due to the second-kind collision from the second and the third excited state of atomic hydrogen start appearing. In this case the differences in the thin and thick cases are less important due the corresponding small differences in the population densities. It should be also noted that second-kind collisions act also at early times, i.e. 10^{-8} s, despite the initial large electron concentration.

The results previously reported have been calculated without taking into account the influence of atom-atom interaction either in the excitation process or in the recombination one. Recently the CR model has been improved by inserting these processes (Colonna et al. 2012). Figure 6.14b reports the time evolution of eedf in the presence of atom-atom interaction in the recombination regime. The results qualitatively reproduce those reported in Fig. 6.14a even though the second-kind collisions play a major role in affecting eedf due the preferential pumping of high-lying states in the recombination of proton-electron pairs in the presence of atomic hydrogen.

Fig. 6.15 Time evolution of the molar fractions of an hydrogen plasma under the following initial conditions: $T_e = T_H = 1,000$ K, $T_g = 15,000$ K and $ID = 10^{-6}$ at $p = 1$ atm. Optically thick (solid line) and optically thin (dashed line) result are reported

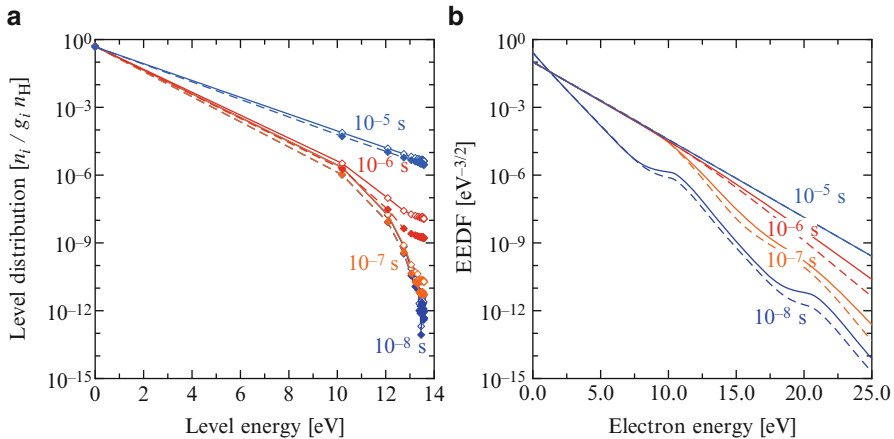
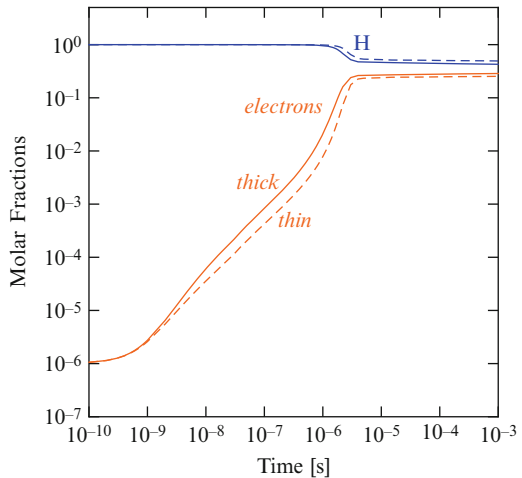


Fig. 6.16 Time evolution of (a) the hydrogen isd and (b) eedf of the ionizing hydrogen plasma of Sect. 6.7.2, comparing the optically thick (solid line) and optically thin (dashed line) cases

Let us now consider an ionization situation occurring in an atmospheric pressure hydrogen plasma characterized by a very small initial electron temperature $T_e = 1,000$ K which is suddenly submitted to a gas temperature of 15,000 K. In this case we also include the atom-atom collisions and we re-examine the time evolution of the different quantities. Figure 6.15 reports the time evolution of the molar fractions of electrons and atomic hydrogen in the thin and thick cases. We observe, as expected, an exponential increase of the electron concentration as well as a decrease by about an order of magnitude of the atom molar fraction. The role of radiation in the two cases is well evident. Figure 6.16a reports the time evolution of the excited state concentrations. It is worth noting that in the first stage of the evolution $t = 10^{-8} \div 10^{-7}$ s the excited state distribution is strongly non-Boltzmann

and scarcely affected by radiation reabsorption. Only at $t = 10^{-6}$ s the role of reabsorption starts affecting the distribution ending its role at $t = 10^{-5}$ s when the system is dominated by electron collision processes. This behavior is reflected on the trend of eedf (see Fig. 6.16b) where the reabsorption is well evident even though not dramatic.

In conclusion of this section we can say that the reabsorption process, acting on the population of electronically excited states affects the evolution of eedf, this process being more important in the recombination regime.

These results have been recently recovered in the study of nozzle flows of partially ionized He/H₂ mixture (Colonna et al. 2015; D'Ammando et al. 2014) as also shown in Sect. 11.6.2.

References

- ALADDIN (2013) Numerical database maintained by the IAEA nuclear data section A + M data unit. <https://www-amdis.iaea.org/ALADDIN/>
- Bates DR, Kingston AE, McWhirter RWP (1962a) Recombination between electrons and atomic ions. I. Optically thin plasmas. Proc R Soc Lond Ser A Math Phys Sci 267(1330):297–312
- Bates DR, Kingston AE, McWhirter RWP (1962b) Recombination between electrons and atomic ions. II. Optically thick plasmas. Proc R Soc Lond Ser A Math Phys Sci 270(1341):155–167
- Biberman LM, Vorob'ev VS, Yakubov IT (1967) High Temp (Teplofizika Vysokikh Temperatur) 5:177
- Biberman LM, Vorob'ev VS, Yakubov IT (1973) Sov Phys Uspekhi 15:375
- Biberman LM, Vorob'ev VS, Yakubov IT (1987) Kinetics of nonequilibrium low-temperature plasmas. Springer US
- Bruno D, Capitelli M, Catalfamo C, Laricchiuta A (2007) Transport of internal electronic energy in atomic hydrogen thermal plasmas. Phys Plasmas (1994–present) 14(7):072308
- Bultel A, Annaloro J (2013) Elaboration of collisional-radiative models for flows related to planetary entries into the Earth and Mars atmospheres. Plasma Sources Sci Technol 22(2):025008
- Cacciatore M, Capitelli M (1974) Non L.T.E. populations and related quantities for H-H⁺-e plasmas as a function of the cut-off level. Zeitschrift für Naturforschung A 29:1507–1509
- Cacciatore M, Capitelli M (1975) Population densities and ionization coefficients of fast transient hydrogen plasmas. Zeitschrift für Naturforschung A 30:48–54
- Cacciatore M, Capitelli M (1976a) Non L.T.E. properties of quasistationary oxygen plasmas. Zeitschrift für Naturforschung A 31:362–368
- Cacciatore M, Capitelli M (1976b) The temporal evolution of population densities of excited states in atomic oxygen thin plasmas. J Quant Spectrosc Radiat Transf 16(4):325–334
- Cacciatore M, Capitelli M, Drawin H (1976) Relaxation times for establishing quasi-stationary state populations in non-thermal plasmas. Physica B+C 84(2):267–274
- Capitelli M, Colonna G, Gicquel A, Gorse C, Hassouni K, Longo S (1996) Maxwell and non-Maxwell behavior of electron energy distribution function under expanding plasma jet conditions: the role of electron-electron, electron-ion, and superelastic electronic collisions under stationary and time-dependent conditions. Phys Rev E 54(2):1843
- Capitelli M, Celiberto R, Gorse C, Laricchiuta A, Pagano D, Traversa P (2004) Transport properties of local thermodynamic equilibrium hydrogen plasmas including electronically excited states. Phys Rev E 69:026412

- Capitelli M, Colonna G, D'Angola A (2012) Fundamental aspects of plasma chemical physics: thermodynamics. Springer series on atomic, optical, and plasma physics, vol 66. Springer, New York
- Capitelli M, Colonna G, Pietanza LD, D'Ammando G (2013) Coupling of radiation, excited states and electron energy distribution function in non equilibrium hydrogen plasmas. *Spectrochim Acta-Part B At Spectrosc* 83–84:1–13
- Colonna G, Pietanza LD, Capitelli M (2001) Coupled solution of a time-dependent collisional-radiative model and Boltzmann equation for atomic hydrogen plasmas: possible implications with LIBS plasmas. *Spectrochim Acta-Part B At Spectrosc* 56(6):587–598
- Colonna G, Pietanza LD, D'Ammando G (2012) Self-consistent collisional-radiative model for hydrogen atoms: atom-atom interaction and radiation transport. *Chem Phys* 398:37–45
- Colonna G, D'Ammando G, Pietanza LD, Capitelli M (2015) Excited-state kinetics and radiation transport in low-temperature plasmas. *Plasma Phys Control Fusion* 57:014009
- D'Ammando G, Capitelli M, Esposito F, Laricchiuta A, Pietanza LD, Colonna G (2014) The role of radiative reabsorption on the electron energy distribution functions in H₂/He plasma expansion through a tapered nozzle. *Phys Plasmas* 21(9):093508
- Drawin HW (1969) Collisional-radiative ionization and recombination coefficients for quasi-stationary homogeneous hydrogen and hydrogenic ion plasmas. *Zeitschrift für Physik* 225(5):470–482
- Drawin HW (1970) Thermodynamic properties of the equilibrium and non equilibrium states of plasmas. In: Venugopalan M (ed) Reactions under plasma conditions, Chapter 3. Wiley Interscience, New York/London
- Drawin H, Emard F (1971) Collisional-radiative volume recombination and ionization coefficients for quasi-stationary helium plasmas. *Zeitschrift für Physik* 243(4):326–340
- Fujimoto T (1973) Validity criteria for local thermodynamic equilibrium and coronal equilibrium. *J Phys Soc Jpn* 34(1):216–224
- Fujimoto T (2004) Plasma spectroscopy. Clarendon Press, Oxford
- Fujimoto T, Ogata Y, Sugiyama I, Tachibana K, Fukuda K (1972) Population density and LTE of excited atoms in a positive-column plasma I. Calculation on hydrogen. *Jpn J Appl Phys* 11(5):718–725
- Gordiets BF, Gudzenko LI, Shelepin LA (1968) *J Quant Spectrosc Radiat Transf* (in Russian) 8(2):791–804
- Gorse C, Cacciatore M, Capitelli M (1978) Some aspects in recombining transient nitrogen plasmas. *Zeitschrift für Naturforschung A* 33:895–902
- Gudzenko LI, Shelepin LA (1964) Negative absorption in a nonequilibrium hydrogen plasma. *JETP* 18(4):998. (Russian original - (1964) *ZhETF* 45:1445)
- Hassouni K, Gicquel A, Capitelli M (1999a) Self-consistent relaxation of the electron energy distribution function in excited H₂ postdischarges. *Phys Rev E* 59:3741–3744
- Hassouni K, Gicquel A, Capitelli M, Loureiro J (1999b) Chemical kinetics and energy transfer in moderate pressure H₂ plasmas used in diamond MPACVD processes. *Plasma Sources Sci Technol* 8(3):494
- Hassouni K, Lombardi G, Duten X, Haagelar G, Silva F, Gicquel A, Grotjohn TA, Capitelli M, Röpcke J (2006) Overview of the different aspects in modelling moderate pressure H₂ and H₂ CH₄ microwave discharges. *Plasma Sources Sci Technol* 15(1):117–125
- Janev RK, Smith J (1993) Cross sections for collision processes of hydrogen atoms with electrons, protons and multiply charge ions. International Atomic Energy Agency (ed) Atomic and plasma-material interaction data for fusion, vol 4. IAEA, Vienna
- Johnson LC (1972) Approximations for collisional and radiative transition rates in atomic hydrogen. *Astrophys J* 174:227–236
- Limbaugh CC, Mason AA (1971) Validity of the quasisteady state and collisional-radiative recombination for helium plasmas. I. Pure afterglows. *Phys Rev A* 4(6):2368
- Longo S, Capitelli M, Hassouni K (1998) Nonequilibrium vibrational distributions of N₂ in radio-frequency parallel-plate reactors. *J Thermophys Heat Transf* 12(4):473–477

- Munafò A, Lani A, Bultel A, Panesi M (2013) Modeling of non-equilibrium phenomena in expanding flows by means of a collisional-radiative model. *Phys Plasmas* 20(7):073501
- Pietanza LD (2000) Coupling of a collisional-radiative model with the electron Boltzmann equations for the study of hydrogen plasma in transient regime. Degree Thesis, Department of Physics, University of Bari
- Pietanza LD, Colonna G, De Giacomo A, Capitelli M (2010) Kinetic processes for laser induced plasma diagnostic: a collisional-radiative model approach. *Spectrochim Acta Part B: At Spectrosc* 65(8):616–626
- Seaton MJ (1959) Radiative recombination in hydrogenic ions. *Mon Not R Astron Soc* 119:81
- Tallents GJ (1977) Population inversions of soft X-ray transitions computed for rapidly cooling plasmas. *J Phys B: At Mol Phys* 10(9):1769
- van der Mullen JAM (1990) Excitation equilibria in plasmas; a classification. *Phys Rep* 191(2–3):109–220
- Van Sijde BD, van der Mullen JJAM, Schram DC (1984) Collisional radiative models in plasmas. Beiträge aus der Plasmaphysik 24(5):447–473
- Vlcek J, Pelikan V (1985) Electron energy distribution function in the collisional-radiative model of an argon plasma. *J Phys D: Appl Phys* 18(3):347
- Zel'dovich YB, Raizer YP (1967) Physics of shock waves and high-temperature hydrodynamic phenomena. Academic Press, New York and London

Chapter 7

Vibrational Kinetics

In this chapter we want to describe the vibrational kinetics of anharmonic diatomic molecule submitted to the action of different elementary processes including electron, molecule and heavy-particle collisions. A rich literature does exist on the subject including previous books written by different authors (Capitelli and Molinari 1980; Capitelli 1986; Gordiets et al. 1988; Capitelli et al. 2000; Fridman and Kennedy 2004; Fridman 2012). The chapter contains different experimental and theoretical examples which clarify the numerous applications of the vibrational kinetics under non equilibrium conditions.

We start with the kinetics of diatomic molecules in a thermal bath, i.e. the kinetics is limited to the presence of VT (vibration-translation) and VV (vibration-vibration) energy exchange processes as well as of the dissociation-recombination process (DR). Typical studied examples include the vibrational kinetics of diatomic molecules in expanding and compressing flows (Panesi et al. 2014; Munafò and Magin 2014; Candler et al. 1997) when the pumping of vibrational quanta can occur through a thermal bath as well as through the homogeneous and heterogeneous atomic recombination. In both cases the recombination process is a source of vibrational quanta over the top of vibrational ladder, these quanta being then redistributed over the whole ladder by VV and VT processes. This situation is typical of the kinetics occurring in the boundary layer of hypersonic flows with catalytic and non-catalytic surfaces. Another possibility is to pump vibrational quanta through VV' energy exchange processes (i.e. from different diatomic molecules) followed by VV and VT redistribution. An example is the pumping of vibrational levels of CO and CO₂ with the interaction of vibrationally excited nitrogen molecules. Similar results can be obtained by pumping vibrational quanta over the bottom of vibrational ladder through IR lasers, this process being followed by the VV up pumping mechanism which can generate non equilibrium vibrational distributions as well as non equilibrium chemical reactions. Again the CO system pumped by a CO laser has received large attention since the pioneering work of Rich (1971).

The role of free electrons is then introduced. In this case resonant electron-molecule processes (eV processes)¹ are able to introduce vibrational quanta into the bottom of vibrational ladder followed by VV and VT redistribution. This behavior has also been observed experimentally by Sanz et al. (2003).

Special attention has to be devoted to the coupling of plasma kinetics with the Boltzmann equation for free electrons. The pumping of vibrational quanta through eV collisions is at the same time accompanied by the parallel action of free electrons in directly dissociating the molecules. The formed atoms usually increase the VT relaxation of vibrationally excited molecules dramatically affecting the formation of long plateaux in the corresponding distribution functions. The synergic effect of plasma and laser introduction of vibrational quanta is another field, still open to improvement, where non-equilibrium vibrational kinetics plays an important role.

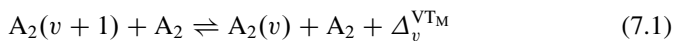
In general this chapter can be considered as an useful tool to understand basic problems in the non equilibrium vibrational kinetics of diatomic molecules preparing the reader to more complicated systems discussed in Chaps. 8–11.

7.1 Vibrational Kinetics of Diatomic Molecules

Let us start to describe the vibrational kinetics of an homonuclear diatomic molecule, in its simplest form. The most common approach is to consider three kind of processes: *Vibration-Translation* (VT) and *Vibration-Vibration* (VV) energy transfer and the *Dissociation-Recombination* (DR) chemical processes.

7.1.1 VT Terms

The VT process considers the energy exchange between the translational and vibrational degree of freedom. They can be distinguished in collisions with molecules (VT_M) or with atoms (VT_A). In the first case, only mono-quantum transitions are considered²

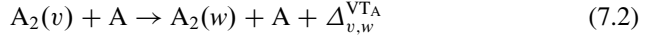


where the energy $\Delta_v^{\text{VT}_M} = \varepsilon_{v+1} - \varepsilon_v$, is exchanged with the translation.

In case of collisions with atoms the probability of multi-quantum transitions is much higher than in molecule-molecule collisions, therefore they must be considered

¹The resonant vibrational excitation processes, known as eV processes in the plasma modeling community, correspond to RVE discussed in Chap. 1.

²This assumption is commonly considered, even if it is valid only at low temperature.



where $\Delta_{v,w}^{\text{VT}_\text{A}} = \varepsilon_v - \varepsilon_w$.

Let us consider only VT_M (Eq.(7.1)) and a specific level v : the following transitions must be considered $v+1 \rightarrow v$, $v \rightarrow v+1$, $v-1 \rightarrow v$ and $v \rightarrow v$, giving, in the order, a term in the relative kinetic equation

$$\begin{aligned} \left(\frac{dN_v}{dt} \right)_{\text{VT}_\text{M}} &= +N_{v+1}N_{\text{A}_2}k_{v+1,v}^{\text{A}_2} - N_vN_{\text{A}_2}k_{v,v+1}^{\text{A}_2} \\ &\quad + N_{v-1}N_{\text{A}_2}k_{v-1,v}^{\text{A}_2} - N_vN_{\text{A}_2}k_{v,v-1}^{\text{A}_2} \end{aligned} \quad (7.3)$$

where N_v and N_{A_2} represent, in the order, the number density of the v -th level and of the molecule, while $k_{a,b}^{\text{A}_2}$ is the rate coefficient of the transition $a \rightarrow b$. The rate coefficients of the direct and reverse processes are related by the detailed balance to the rates giving

$$k_{v,v+1} = k_{v+1,v} \exp \left[-\frac{\varepsilon_{v+1} - \varepsilon_v}{k_B T} \right] \quad (7.4)$$

where ε_v is the level energy. As a consequence Eq.(7.3) becomes

$$\begin{aligned} \left(\frac{dN_v}{dt} \right)_{\text{VT}_\text{M}} &= N_{v+1}N_{\text{A}_2}k_{v+1,v}^{\text{A}_2} - N_vN_{\text{A}_2}k_{v+1,v}^{\text{A}_2} \exp \left[-\frac{\varepsilon_{v+1} - \varepsilon_v}{k_B T} \right] \\ &\quad - N_vN_{\text{A}_2}k_{v,v-1}^{\text{A}_2} + N_{v-1}N_{\text{A}_2}k_{v,v-1}^{\text{A}_2} \exp \left[-\frac{\varepsilon_v - \varepsilon_{v-1}}{k_B T} \right] \\ &= N_{\text{A}_2}k_{v+1,v}^{\text{A}_2} \left\{ N_{v+1} - N_v \exp \left[-\frac{\varepsilon_{v+1} - \varepsilon_v}{k_B T} \right] \right\} \\ &\quad - N_{\text{A}_2}k_{v,v-1}^{\text{A}_2} \left\{ N_v - N_{v-1} \exp \left[-\frac{\varepsilon_v - \varepsilon_{v-1}}{k_B T} \right] \right\} \end{aligned} \quad (7.5)$$

When we include the VT_A terms (Eq.(7.2)), we write the kinetic equation considering also multi-quantum transitions, i.e.

$$\left(\frac{dN_v}{dt} \right)_{\text{VT}_\text{A}} = -N_vN_\text{A} \sum_w k_{v,w}^\text{A} + N_\text{A} \sum_w N_w k_{w,v}^\text{A} \quad (7.6)$$

where N_A is the total number density of atoms and $k_{v,w}^\text{A}$. Also in this case the rates of the direct and reverse processes are connected by the detailed balance principle

$$k_{v,w}^A = k_{w,v}^A \exp \left[-\frac{\varepsilon_w - \varepsilon_v}{k_B T} \right] \quad (7.7)$$

ε_w and ε_v are the corresponding vibrational energies.

We can define VT relaxation times for a level v considering only exothermal transitions

$$\begin{aligned} \tau_v^{\text{VT}} &= \left[N_{A_2} \sum_{w=0}^{v-1} k_{v,w}^{A_2} + N_A \sum_{w=0}^{v-1} k_{v,w}^A \right]^{-1} \\ \tau_v^{\text{VT}_{A_2}} &= \left[N_{A_2} \sum_{w=0}^{v-1} k_{v,w}^{A_2} \right]^{-1} \\ \tau_v^{\text{VTA}} &= \left[N_A \sum_{w=0}^{v-1} k_{v,w}^A \right]^{-1} \end{aligned} \quad (7.8)$$

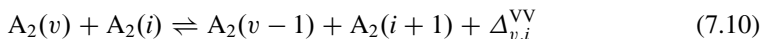
Particular important is the relaxation time of the first excited level linked i.e.

$$\begin{aligned} \tau_1^{\text{VT}_{A_2}} &= \left[N_{A_2} k_{1,0}^{A_2} \right]^{-1} \\ \tau_1^{\text{VTA}} &= \left[N_A k_{1,0}^A \right]^{-1} \end{aligned} \quad (7.9)$$

which determines the characteristic time of the formation of the vibrational distribution by VT processes.

7.1.2 VV Terms

Considering only mono-quantum transitions we can write



where

$$\Delta_{v,i}^{\text{VV}} = \varepsilon_{v-1} + \varepsilon_{i+1} - \varepsilon_v - \varepsilon_i \quad (7.11)$$

Focusing on the level v , four transitions are possible for VV processes, i.e. $v+1 \rightarrow v$, $v \rightarrow v+1$, $v \rightarrow v-1$, $v-1 \rightarrow v$,³ giving the following contribution to the kinetic equation

³VV rates are represented by four indexes, representing initial and final state of the two molecules. By convention here we will write as superscript the indexes of the molecule increasing its energy, and as subscript the indexes of the molecules loosing the vibrational quanta.

$$\left(\frac{dN_v}{dt} \right)_{VV} = N_{v+1} \sum_{i=1}^{v'} N_{i-1} k_{v+1,v}^{i-1,i} - N_v \sum_{i=1}^{v'} N_i k_{i,i-1}^{v,v+1} \\ - N_v \sum_{i=0}^{v'-1} N_i k_{v,v-1}^{i,i+1} + N_{v-1} \sum_{i=0}^{v'-1} N_{i+1} k_{i+1,i}^{v-1,v} \quad (7.12)$$

By applying the detailed balance on the rates, i.e.

$$k_{i,i-1}^{v,v+1} = k_{v+1,v}^{i-1,i} \exp \left[-\frac{\Delta_{v+1,i-1}^{VV}}{k_B T} \right] \quad (7.13)$$

$$\left(\frac{dN_v}{dt} \right)_{VV} = N_{v+1} \sum_{i=1}^{v'} N_{i-1} k_{v+1,v}^{i-1,i} - N_v \sum_{i=1}^{v'} N_i k_{v+1,v}^{i-1,i} \exp \left[-\frac{\Delta_{v+1,i-1}^{VV}}{k_B T} \right] \\ - N_v \sum_{i=0}^{v'-1} N_i k_{v,v-1}^{i,i+1} + N_{v-1} \sum_{i=0}^{v'-1} N_{i+1} k_{v,v-1}^{i,i+1} \exp \left[-\frac{\Delta_{v,i}^{VV}}{k_B T} \right] \quad (7.14)$$

7.1.2.1 Some Considerations About VV Processes

Let us discuss some peculiarities of the VV processes. First of all, while VT processes introduce linear terms in the kinetic equations of vibrational levels, VV are characterized by non-linear contribution, involving two molecules in the corresponding vibrational state. Moreover VV transitions does not change the global amount of quanta defined as

$$N_Q = \sum_{v=0}^{v'} v N_v \quad (7.15)$$

because one molecule increases its vibrational state by one while the other decreases its internal state by the same quantity. If the vibrational ladder of diatomic molecules were represented by an harmonic oscillator, the energy balance would be $\Delta_{v,i}^{VV} = 0$. However the vibrational energy, referred to the bottom of the potential curve, is expressed as a power series of $v + \frac{1}{2}$ i.e.

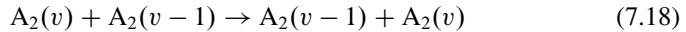
$$\varepsilon'_v = \varepsilon_{10} \left(v + \frac{1}{2} \right) - \omega_e \chi_e \left(v + \frac{1}{2} \right)^2 + \dots \quad (7.16)$$

where ε_{10} is the harmonic term and $\omega_e \chi_e$ is the coefficient of the second order correction and so on. To refer the energy to the ground vibrational state we just

consider $\varepsilon_v = \varepsilon'_v - \varepsilon'_0$. Stopping the expansion to the second order correction, considering the transition in Eq. (7.10), with the corresponding energy transfer in Eq. (7.11) we have

$$\begin{aligned} \frac{\Delta_{v,i}^{\text{VV}}}{\omega_e \chi_e} &= (v - 1 + \frac{1}{2})^2 - (v + \frac{1}{2})^2 + (i + 1 + \frac{1}{2})^2 - (i + \frac{1}{2})^2 \\ &= -2v + 2i + 2 = 2(i - v + 1) \end{aligned} \quad (7.17)$$

We can put in evidence the resonant VV transitions



giving the kinetic term

$$\left(\frac{dN_v}{dt} \right)_{\text{res}} = -k_{v,v-1}^{v-1,v} N_v N_{v-1} + k_{v,v-1}^{v-1,v} N_{v-1} N_v = 0 \quad (7.19)$$

i.e. it does not affect at all the vibrational kinetics because the initial and final states are the same.

Let us now consider the quasi-resonant processes



giving the kinetic term

$$\left(\frac{dN_v}{dt} \right)_{\text{q res}} = -k_{v,v-1}^{v,v+1} N_v N_v + k_{v+1,v}^{v-1,v} N_{v+1} N_{v-1} \quad (7.21)$$

The energy balance in this process is positive

$$\Delta_{v,v}^{\text{VV}} = 2\omega_e \chi_e \quad (7.22)$$

Again the detailed balance yields

$$k_{v,v-1}^{v,v+1} = k_{v+1,v}^{v-1,v} \exp \left[-\frac{\Delta_{v,v}^{\text{VV}}}{k_B T} \right] = k_{v+1,v}^{v-1,v} \exp \left[-\frac{2\omega_e \chi_e}{k_B T} \right] \quad (7.23)$$

In this case we have $k_{v,v-1}^{v,v+1} > k_{v+1,v}^{v-1,v}$ the differences strongly decreasing with increasing gas temperature. On the other hand, in the case of harmonic oscillator

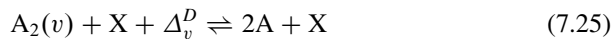
$$\varepsilon'_v = \varepsilon_{10} \left(v + \frac{1}{2} \right) \quad (7.24)$$

we get $k_{v,v-1}^{v,v+1} = k_{v+1,v}^{v-1,v}$.

Consider now non resonant transitions with $i > v$.⁴ The first behavior to notice is that $\Delta_{v,i}^{VV} > 0$ and the difference grows as larger the difference between i and v . Therefore, considering the detailed balance for these processes (see Eq. (7.13)) we have that $K_{v,v-1}^{i,i+1} > K_{i+1,i}^{v-1,v}$, the difference increasing as the temperature decreases. The main consequence of this property is that, especially at low temperature, the VV process force the molecules to move towards the extremes of the vibrational ladder (low v and high i) so that a minimum is observed in the vibrational distribution, the so called Treanor distribution (Treanor et al. 1968). This is relevant when the vibrational temperature is higher than the gas one. VV processes will try to reduce the vibrational temperature cooling the low energy distribution, but at the same time populate the distribution tail. This behavior lead to the conclusion that VV processes are a source of non equilibrium.⁵

7.1.3 Dissociation-Recombination Terms

The last contribution comes from the dissociation and recombination processes



where X is a molecule A₂ or an atom A and $\Delta_v^D = \varepsilon_D - \varepsilon_v$ is the dissociation energy from a given level. The corresponding kinetic equation is given by

$$\left\{ \begin{array}{l} \left(\frac{dN_v}{dt} \right)_{DR} = \sum_X \left[-k_v^{DX} N_v N_X + k_v^{RX} N_A^2 N_X \right] \\ \left(\frac{dN_A}{dt} \right)_{DR} = -2 \sum_X \sum_{v=0}^{v'} \left(\frac{dN_v}{dt} \right)_{DR,X} \end{array} \right. \quad (7.26)$$

It is possible to define global dissociation and recombination rates as

⁴The case with $v > i$ is obtained from this case by considering the reverse process and changing i with v .

⁵It would be interesting to compare this results with the electron-electron collisions in the free electron kinetics; even if both processes introduces non-linear terms and must fulfill a conservation principle (one for the quanta, one for the energy), $e-e$ collisions bring the distribution towards equilibrium, while VV processes causes non-equilibrium.

$$k_{A_2}^{DX} = \sum_{v=0}^{v'} k_v^{DX} \frac{N_v}{N_{A_2}} \quad (7.27)$$

$$k_{A_2}^{RX} = \sum_{v=0}^{v'} k_v^{RX}$$

Also in this case the detailed balance relates dissociation and recombination rates (Capitelli and Molinari 1980)

$$k_v^{RX} = k_v^{DX} \frac{e^{-\varepsilon_v/k_B T}}{K_{eq}^D \sum_v e^{-\varepsilon_v/k_B T}} \quad (7.28)$$

obtained considering dissociation/recombination equilibrium for each vibrational state, where K_{eq}^D is the equilibrium constant of the reaction $A_2 \rightleftharpoons 2A$.

It is also useful to define a pseudo first-order rate coefficient defined as

$$k_d^X = k_{A_2}^{DX} N_X \quad (7.29)$$

corresponding to the reverse of the characteristic time. We can define a global pseudo first-order rate as the sum of all the contributions.

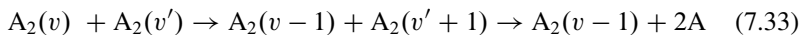
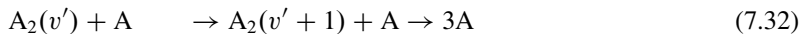
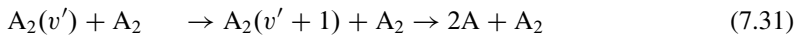
This approach, known as *direct dissociation* model, requires rate coefficients from each vibrational level, that often are missing, as also occurs for molecule-molecule collisions. On the other hand a lot of information is nowadays available for the state-selected dissociation rates of atom-diatom interactions. These data can be used for estimating the corresponding rates for molecule-molecule interactions. An interesting approach has been proposed in Esposito et al. (2006) and Colonna et al. (2006, 2008), where the rate coefficient for $N_2 + N_2$ dissociation has the same dependence from the vibrational quantum number as $N_2(v) + N$, scaled to reproduce experimental values of the thermal dissociation rate $k_{exp}^{D,N_2}(T)$

$$k_v^{DN_2} = k_v^{DN} \frac{k_{exp}^{DN_2} \sum_{v=0}^{v'} e^{-\varepsilon_v/k_B T}}{\sum_{v=0}^{v'} k_v^{DN}(T) e^{-\varepsilon_v/k_B T}} \quad (7.30)$$

When data are missing one has to use the *ladder climbing* model. The rescaling approach can also be applied to ladder climbing model, but in this case only dissociation from the last vibrational ladder is included.

7.1.3.1 Ladder Climbing Model

This approach includes in the vibrational kinetics a pseudo-level $v' + 1$ located above the last vibrational bound level of the molecule v' , representing the dissociation. In its original formulation VV and VT terms crossing level v' populate level $v' + 1$ immediately ending in the dissociation. The following chemical processes can be written



The dissociation rate is then written as

$$\left(\frac{dN_A}{dt} \right)_D = N_{v'} N_{A_2} k_{v', v'+1}^{\text{VTM}} + N_{v'} N_A k_{v', v'+1}^{\text{VTA}} + N_{v'} \sum_v N_v k_{v, v-1}^{v', v'+1} \quad (7.34)$$

A generalization of the ladder-climbing model has been presented in the work by Armenise et al. (1994), considering the multi-quantum dissociation for N_2+N collisions, extending multi-quantum VT rates. However, the ladder climbing model introduces very large errors in the estimation of the rates (Capitelli et al. 1999, 2004; Armenise et al. 2007), differencing from more accurate results of two orders of magnitude.

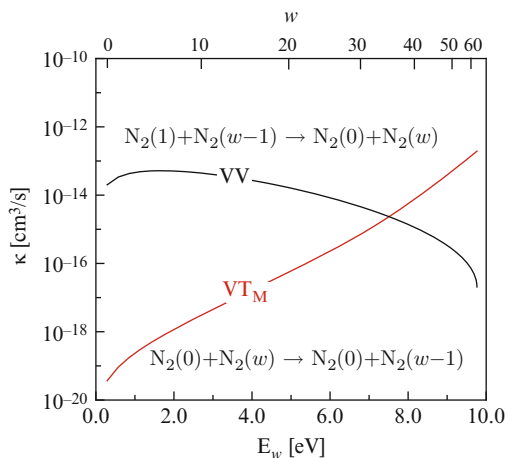
7.2 Vibrational Relaxation Kinetics

In the previous section we have presented the processes that must be included to investigate vibrational relaxation of the diatomic molecules. Taking into account the different contributions we can write the vibrational master equation (Caledonia and Center 1971) in the form

$$\frac{dN_v}{dt} = \left(\frac{dN_v}{dt} \right)_{\text{VV}} + \left(\frac{dN_v}{dt} \right)_{\text{VT}} + \left(\frac{dN_v}{dt} \right)_{\text{DR}} \quad (7.35)$$

In this section we will show the vibrational relaxation for different applications, such as vehicles entering planetary atmospheres, laser-plasma interaction, gas discharges and so on.

Fig. 7.1 Rate coefficients for VV and VT_M exothermic processes in N_2-N_2 collisions as a function of initial vibrational level, at $T = 500\text{ K}$



7.2.1 Sudden Decrease of Gas Temperature

Let us investigate the vibrational relaxation in presence of an abrupt change in the gas temperature. This condition can be considered a simplified model of high enthalpy flows, that will be discussed in detail in other sections see Chap. 11 and Sect. 7.2.4.

The case study reported in this section deals with a nitrogen gas heated at 7,000 K which is suddenly cooled at 500 K, at $p = 2\text{ Torr}$. The vibrational kinetics is solved in the presence of VV (mono-quantum), VT_M and VT_A energy exchange processes and dissociation-recombination processes. A sample of VV and VT_M rates at 500 K is reported in Fig. 7.1. The dissociation process uses direct dissociation rates obtained by QCT method when induced by atoms (Esposito et al. 2006) and the model reported in Eq. (7.30) for the dissociation by collisions with molecules, where the thermal rates has been taken from Ibragimova et al. (1999). We consider three initial conditions differing from the initial concentrations of atomic nitrogen as detailed below, to put in evidence the role of recombination during vibrational relaxations.

- (a) $\chi_N(t=0) = 0$;
- (b) $\chi_N(t=0) = 0.01$;
- (c) $\chi_N(t=0) = 0.35$;

Let us discuss in detail the time evolution of the system in the three cases, analyzing the vibrational distributions reported in Fig. 7.2a–c for the corresponding cases. In case (a), in absence of atoms, the vdf relaxation is determined by the interplay between VV and VT_M . The VV up-pumping dominates for low-lying states (see Fig. 7.1 comparing VV and VT_M rates), while VT_M depletion overcomes VV for high energy levels. The competition between the two processes determine the vdf evolution. At low v , the distribution cools down and a plateau is formed in the

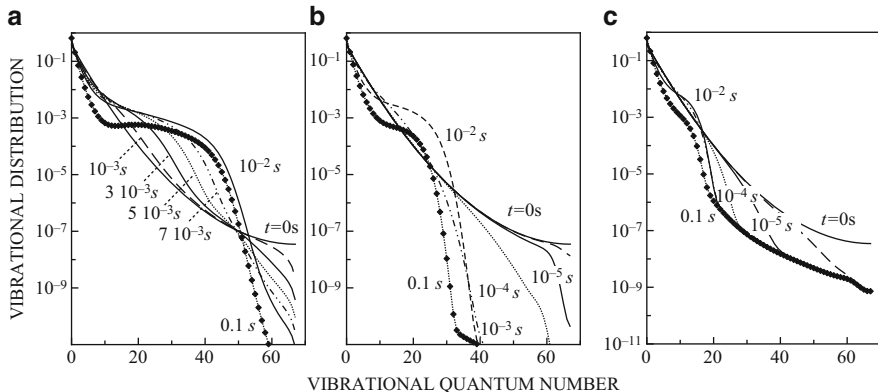


Fig. 7.2 Vibrational population distribution of N_2 ground state for different time-shots in the relaxation for different initial atomic nitrogen molar fraction. (a) $\chi_N(t = 0) = 0.0$ [case (1)]; (b) $\chi_N(t = 0) = 0.01$ [case (2)]; (c) $\chi_N(t = 0) = 0.35$ [case (3)] (From Capitelli et al. 2012)

interval $10 < v < 40$ due to VV processes, while for $v > 40$, starting from the last levels and propagating downward, the distribution tail is depleted by VT_M . At the beginning there is a small contribution of the dissociation favored by the highly excited distribution, however the atom production is limited ($\chi_N < 10^{-4}$), making the atom induced processes negligible. It is worth noting that the results reported in Fig. 7.2a are also typical of nitrogen relaxation in the post-discharge regime as shown theoretically (Capitelli et al. 1981) and experimentally (Akishev et al. 1982).

In case (b) the fraction of atoms is large enough to have a significant contribution of VT, but not sufficient to activate the recombination, that depends on χ_N^3 . What we observe is a larger contribution of VT, extended to the whole vibrational ladder, because of multi-quantum transitions introduced by VT, resulting in a faster relaxation of the tail and in the reduction of the extension of the plateau.

Finally, in case (c) the atom molar fraction is so high that also the recombination becomes effective. The low energy distribution still presents a plateau, even if just sketched, because the contribution of VT at low and intermediate levels is stronger, while the distribution tail is overpopulated by recombination, reaching a quasi-steady state condition determined by the balance among recombination, dissociation and VT (Colonna et al. 2006, 2008). In all the cases, the extension of the plateau depends on the set of the relevant rates used in the model as shown in Capitelli et al. (2012). Similar results can be found in Xu et al. (2014).

Qualitatively, these observations about vibrational distributions of diatomic species can be summarized as follows

- A long plateau at intermediate v , due to VV up pumping mechanism, can be expected when a strong input of vibrational quanta are pumped in the diatom when atomic molar fraction is very low ($\chi_N < 10^{-4}$);

- The plateau due to VV mechanism tends to disappear when the concentration of atoms increases ($\chi_N > 10^{-3}$);
- A long plateau is formed at high v through the selective pumping of vibrational quanta at the top of vibrational ladder ($\chi_N > 10^{-1}$).

In the following we will present different examples for the occurrence of conditions (a)–(c). We can anticipate that condition (a) can occur when the vibrational quanta are introduced during a resonant excitation of low-lying excited states by IR laser (CO is the typical example). The same condition can occur from the pumping of vibrational quanta from vibrationally hot molecules and cold molecules of an other species. Condition (b) can be obtained for an electrical discharge at low reduced electric fields E/N when eV (electron-vibration) energy transfer processes introduce vibrational quanta in the bottom of vibrational ladder and the electron energy is small enough to dissociate molecules by electron-impact collisions. Finally condition (c) can be obtained in an high vibrational reservoir with high concentrations of atomic species which then expand to lower pressures as well as in the boundary layer of an hypersonic object.

Similar problems can be met during a sudden increase of gas temperature as in a shock wave (see Chap. 11). In this context the Direct Simulation Monte Carlo (DSMC) with a state-to-state vibrational kinetics has been also used, showing the increase of the vibrational distribution function with the distance from the shock. Interesting results have been obtained dealing with a non-maxwell translational distribution function of heavy particles (Bruno et al. 1998, 2002).

7.2.2 *Laser Pumping of CO*

Non-equilibrium vibrational excitation under strong laser pulses have been obtained by different groups and rationalized by the master equation approach developed in the previous sections. The most studied system is CO mixed with rare gases (He,Ar); the pumping in this case is made over the first few levels by coupling the vibrational ladder with a IR resonant source (Flament et al. 1992). The idea was to exclude sources of atoms through electron impact dissociation (i.e. under plasma conditions) so that the VV up pumping mechanism could generate long plateaux in the vibrational distribution. The first experimental evidence of the non equilibrium vibrational distribution in CO pumped by a cw IR laser were rationalized by using a classical master equation approach including VV and VT terms. VT terms included the action of the gas noble (He,CO) and of CO itself. Long plateaux were created by this approach in disagreement with the experimental results (Schmailzl and Capitelli 1979) inducing to consider other relaxation channels. In particular large attention was devoted to the role of vibrational-electronic energy exchange (VE) reactions as well as dissociation from bimolecular dissociation involving highly excited states in depleting the vibrational distribution. In particular VE channels involve the following reactions

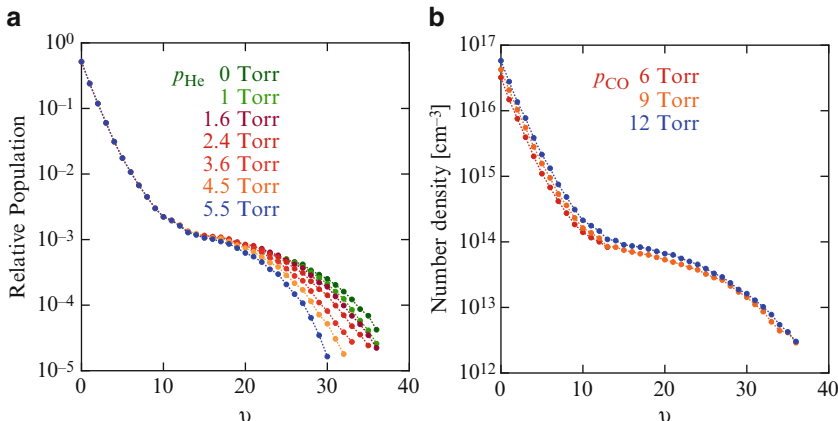
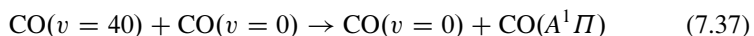
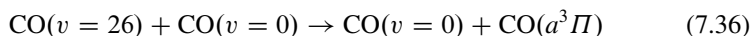


Fig. 7.3 (a) CO vdfs at $P_{\text{CO}} = 6$ Torr, at different helium partial pressures, (b) CO vdfs at different CO partial pressures, without helium (From Essenhigh et al. 2006)



The role of reaction in creating an hole in the vibrational range $20 < v < 30$ was experimentally proved in Farrenq and Rossetti (1985) and reproduced by other researchers. This hole however can be also created by the chemical reaction involving vibrationally excited molecules



This reaction is again receiving strong interest because can reduce the energy input for dissociation CO with extension to CO₂ (see Sect. 7.2.3).

One of the most recent experimental determination of the CO vibrational distribution pumped by an IR CO laser is reported in Fig. 7.3a for CO/Ar-He mixture and in Fig. 7.3b for CO/Ar.

7.2.3 Pumping of CO by vibrationally Excited N₂

An interesting example of non-equilibrium vibrational excitation is that one reported by our laboratory many years ago (De Benedictis et al. 1987) dealing with the pumping and redistribution of vibrational quanta in CO by molecular nitrogen vibrationally excited in a discharge. To a first approximation we can consider this case study as belonging to condition (1) even though during relaxation a chemical channel involving vibrationally excited molecules becomes open.

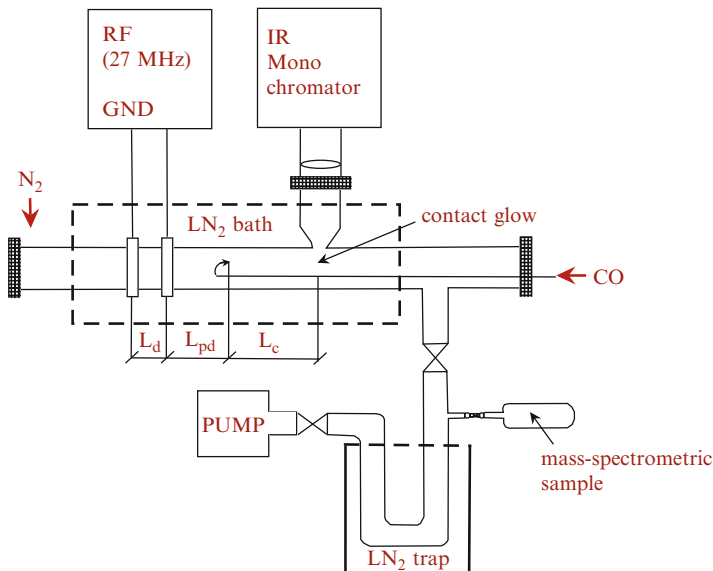


Fig. 7.4 Sketch of the experimental apparatus (De Benedictis et al. 1987)

A schematic drawing of the experimental apparatus is reported in Fig. 7.4. A capacitively RF discharge (27 MHz, 50 W) was produced in a tubular reactor (3.5 cm inner diameter). The infrared radiation of CO first overtone emitted from N₂-CO contact region was obtained by infrared spectroscopy at different N₂-CO contact lengths L_c (i.e. at different contact times) by changing the position of CO injection and of N₂ discharge with respect to the spectroscopic optical axis. A measurement of CO₂ concentration was also performed. In the experiments the distance of CO injection point from the ground electrode (post-discharge length) was fixed at 5 cm and its distance from the optical axis (contact length L_c) was varied from 2 to 30 cm. These lengths were then transformed in contact times.

The resulting CO vibrational distributions, obtained by the deconvolution of IR optical spectra have been reported in Fig. 7.5 and compared with the theoretical results. A qualitative agreement between theoretical and experimental is present in the trend of non-equilibrium vibrational distributions in the pumping (Fig. 7.5a) and relaxation (Fig. 7.5b) regimes. A careful examination of theory and experiments shows a time shift of a factor 2 in the different distribution functions. Moreover the concentrations of the theoretical tails are underestimated as compared with the experimental values. From the point of view of theory one should note that the reaction rates of the reaction



are important not only as chemical channel assisted by vibrational excitation but also as a deactivation process.

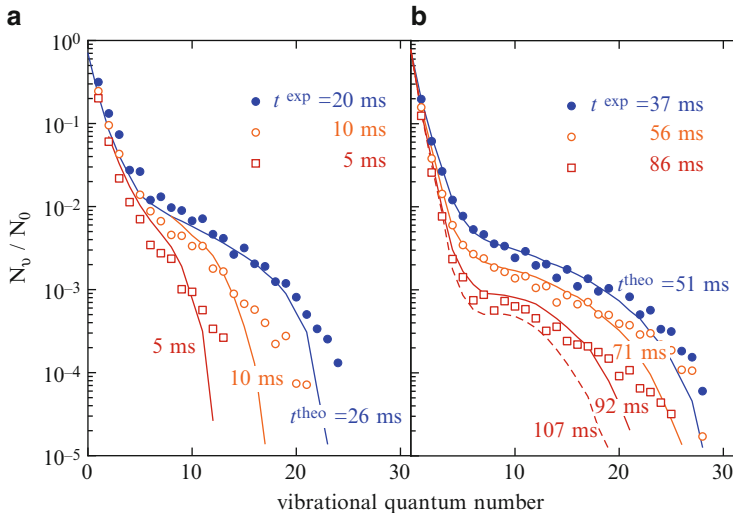


Fig. 7.5 CO vibrational distributions ($p = 1.4 \text{ Torr}$, $N_2/\text{CO} = 20$) at several contact times in the pumping (a) and relaxation (b) regimes. (markers) experiments; (solid lines) theory (From De Benedictis et al. 1987)

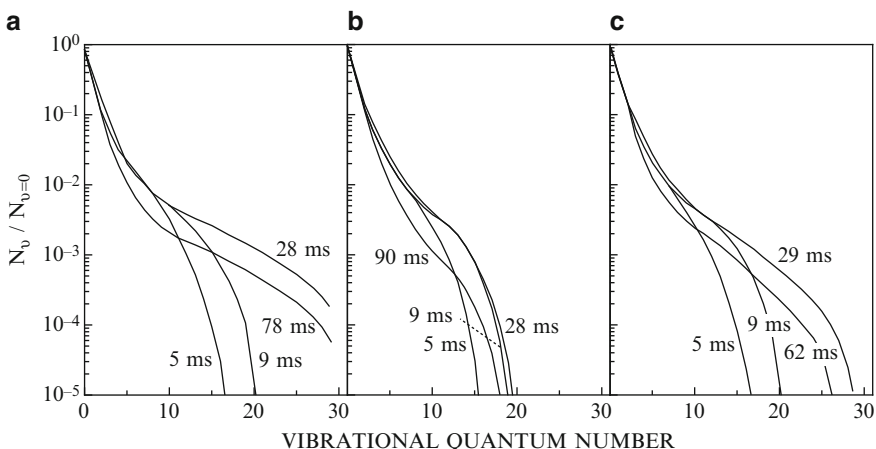


Fig. 7.6 Normalized CO vibrational distributions pumped by vibrationally excited N_2 molecules ($\text{CO}/\text{N}_2: 1/20$, $T_g: 500 \text{ K}$, $p: 2 \text{ Torr}$, $\vartheta_1(\text{N}_2)_{t=0}: 2,620 \text{ K}$) calculated according to different hypotheses on the $k_{v,w}^{\text{CO}_2}$ rates, (a) $k_{v,w}^{\text{CO}_2} = 0$; (b) $k_{v,w}^{\text{CO}_2}$ as in Gorse et al. (1984); (c) $k_{v,w}^{\text{CO}_2} = k_{v,v}^{\text{CO}_2}$ only diagonal terms (From Gorse et al. 1987)

This point can be understood by looking at Fig. 7.6 (Gorse et al. 1987) which reports the vibrational distributions of CO pumped by vibrationally excited N_2 molecules calculated according different assumptions on the rate coefficients of the process (7.39). In particular we note that more excited plateaux do exist when the

process (7.39) is disregarded i.e. when $k_{v,w}^{\text{CO}_2} = 0$ as compared to the use of the complete $k_{v,w}^{\text{CO}_2} \neq 0$. The situation with only the diagonal terms, i.e. $k_{v,v}^{\text{CO}_2} \neq 0$, is intermediate. The rates of process (7.39) have been obtained by using the following equation from the statistical theory developed by (Rusanov et al. 1979).

$$k_{v,w}^{\text{CO}_2} = k_g(T) \left[\frac{h\omega_{\text{CO}}(v+w) - \varepsilon_a}{h\omega_{\text{CO}}(v+w)} \right]^2 \left(\frac{\omega_{\text{CO}}}{\omega_{\text{CO}_2}} \right)^2 A_{v,w} \quad (7.40)$$

where $k_g(T) = 3 \times 10^{-10} T / 300 \text{ cm}^{-3} \text{s}^{-1}$ is the gas kinetic rate, $\omega_{\text{CO}} = 2,214.24 \text{ cm}^{-1}$ and $\omega_{\text{CO}_2} = 2,226.85 \text{ cm}^{-1}$ are the vibrational quanta of CO and of CO_2 asymmetric stretch, $\varepsilon_a = 6 \text{ eV}$ is the activation energy and $A_{v,w}$ is a step function taking the values 1 or zero if the total vibrational energy is larger or less than ε_a .

Coming back to the comparison of experimental and theoretical vibrational distributions reported in Fig. 7.5, we must remind that the theoretical calculations have been obtained by decreasing by a factor 100 (De Benedictis et al. 1987), the reaction rates from Eq. (7.40) as well as by decreasing the vibrational temperature of nitrogen in contact with cold oxygen to 1,260 K. Taking into account these points we can conclude that theoretical and experimental results present a satisfactory agreement showing in particular the same phenomenology during the different time regimes. Note also that a recent study of Essenhigh et al. (2006) estimate an activation energy of process (7.39) of 11.6 eV, a value which shifts the deactivation action of process (7.39) to higher vibrational levels. A comparison of the values of $k_{v,w=v}^{\text{CO}_2}$ calculated inserting in Eq. (7.40) $\varepsilon_a = 6 \text{ eV}$ and $\varepsilon_a = 11.6 \text{ eV}$ is reported in Fig. 7.7. We can appreciate differences up to a factor 2.5.

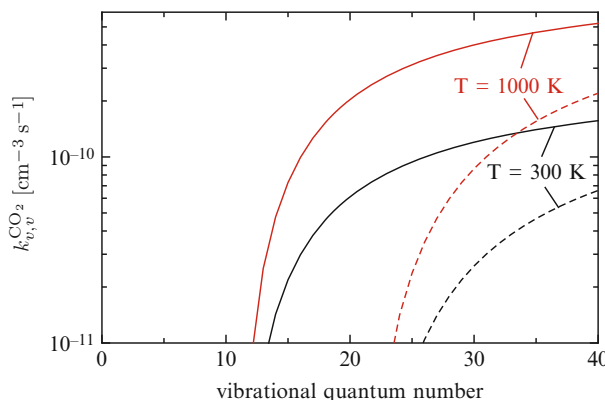


Fig. 7.7 Rates for CO_2 formation, i.e. process (7.39) in $w = v$ collisions, as a function of vibrational quantum number, calculated at two temperatures assuming different values for the threshold energy. (solid line) $\varepsilon_a = 6 \text{ eV}$; (dashed line) $\varepsilon_a = 11.6 \text{ eV}$

7.2.4 Boundary Layer

The non-equilibrium vibrational kinetics coupled to the dissociation recombination process described in the previous pages has been introduced in the fluidynamics of the boundary layer of a body flying at hypersonic velocity (Nagnibeda and Kustova 2009; Orsini et al. 2008; Armenise and Capitelli 2005). In this case the system of kinetic equations is transformed in a system of second order differential equations which describe the population density of each vibrational level and of atomic and molecular species along the coordinate η perpendicular to the body. In a compact form we write

$$c_v'' + f^* Sc^* c_v' = S_v \quad (7.41)$$

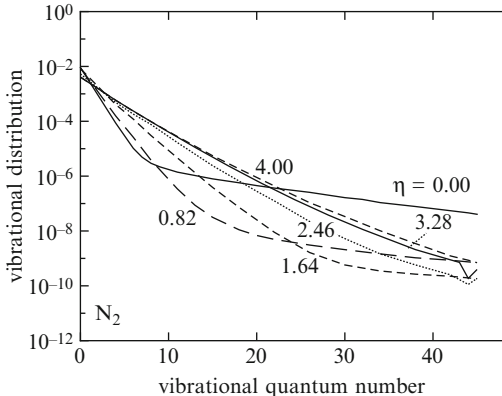
$$\vartheta'' + f^* Pr^* \vartheta' = S_T \quad (7.42)$$

where v denotes either the vibrational levels or atom and molecules without structure. c_v'' denotes the second derivative of the mass fraction of the different species $c_v = \frac{\rho_v}{\rho}$ as a function to the coordinate η normal to the surface and ϑ'' is the corresponding second derivative of the normalized translational temperature T in the boundary layer i.e. $\vartheta = \frac{T}{T_e}$ (T_e is the translational temperature at the edge of the boundary layer). Moreover Sc^* and Pr^* denote respectively the dimensionless Schmidt and Prandtl numbers and f is a stream function. The v equations denote the continuity equations of the vibrational levels of molecules and atoms while Eq. (7.42) is the energy continuity equation. The system of differential equations describe the chemical and thermal kinetics occurring in the boundary layer surrounding the hypersonic body in the self-similar reference system according to Lees-Dorodnitsyn transformations. Both vibrational kinetics and dissociation-recombination become source terms in the fluidynamic model together with an energy term which is responsible of the formation of the gas temperature profile along the boundary layer coordinate. The parameters entering the model are

- The gas temperature at the edge of the boundary layer and on the body surface
- The form of the vibrational distribution and the concentration of atoms at the edge of the boundary layer
- The catalytic nature of the body to the atomic recombination and vibrational energy accommodation
- The parameter β which describes the inverse of a residence time of a molecule in the boundary layer.

Details of the boundary layer (*b-l*) equations can be found in Armenise et al. (1998) and Armenise and Capitelli (2005). Here we want to describe typical results of non-equilibrium vibrational distributions and dissociation rates occurring as a function of the η coordinate. Two extreme conditions will be discussed (1) a non-catalytic surface to atom recombination (2) a catalytic one. In the first case the kinetics is controlled by the recombination of atoms in the gas phase followed by the

Fig. 7.8 N_2 vibrational distributions at different η values using the ladder climbing model with $T_{\text{wall}} = 1,000 \text{ K}$, $T_e = 7,000 \text{ K}$, $p_e = 1,000 \text{ N m}^{-2}$ and $\beta = 5,000 \text{ s}^{-1}$ (From Armenise et al. 1998)



redistribution by VV and VT energy exchange processes over the whole vibrational ladder. The atoms in fact entering the *b-l* are submitted to a temperature profile strongly decreasing from the *b-l* edge to the surface, i.e. they find ideal conditions to recombine preferentially pumping the high-lying levels of vibrational ladder. As a result long plateaux in the vibrational distribution are generated, not to be confused with the plateau due to pumping up mechanism.

Figure 7.8 (Armenise et al. 1998) shows this phenomenology reporting vibrational distributions along η for conditions typical of reentry conditions. Keeping in mind that $\eta = 4$ and $\eta = 0$ respectively denote the edge of the boundary layer and the surface, we can note the progressive increase of non-equilibrium effects in the vibrational distributions going from $\eta = 4$ to $\eta = 0$. In particular vdf passes from the imposed Boltzmann distribution at $\eta = 4$ to the non Boltzmann character near the surface. The corresponding long plateaux are the result of the recombination process in gas phase: the plateau in fact disappears in the absence of recombination process for the same conditions reported in Fig. 7.8. The strong non equilibrium character of vdf generates also non-equilibrium dissociation as can be understood by looking at Fig. 7.9. In this figure pseudo first-order dissociation constants of nitrogen are reported as a function of the inverse of gas temperature along the boundary layer. Low $1/T$ values means η values close to the edge of the boundary layer, high $1/T$ values indicating η values near to the surface. Inspection of Fig. 7.9 shows an Arrhenius behavior of the dissociation constant near the boundary layer edge, followed by an anti-Arrhenius behavior close to the surface. Again, we observe that the non-equilibrium vibrational distributions in all models are due to the recombination process. Solution of the fluid dynamic problem by completely neglecting the dissociation-recombination processes yields vibrational distributions that closely follow Boltzmann distributions at the local gas temperature. We must be aware, however, that non-equilibrium vibrational distributions can also occur in the boundary layer as a result of the VV up-pumping mechanism. The conditions suitable for this mechanism occur when the surface is kept at a low temperature and

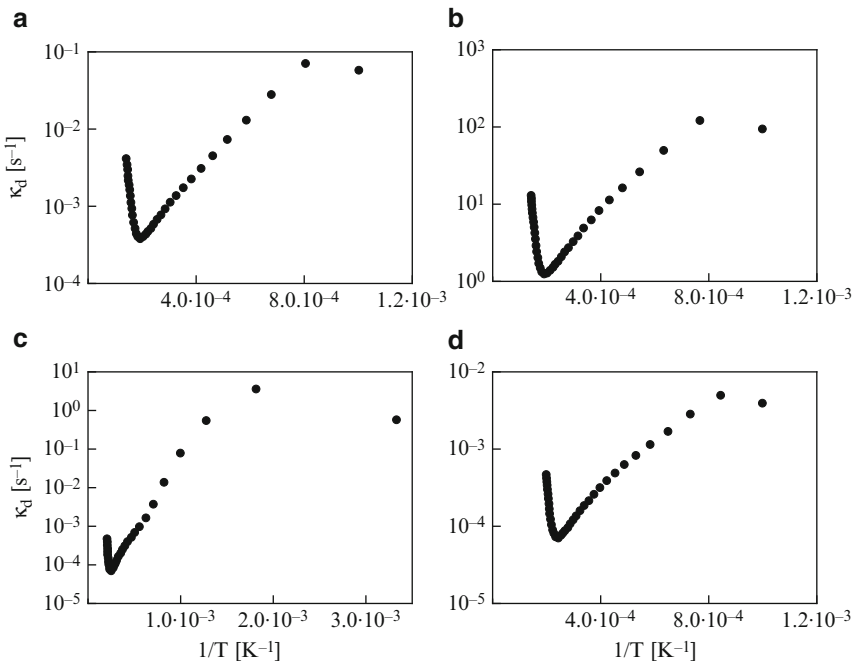


Fig. 7.9 Total pseudo first-order dissociation rate constants for different conditions. (a) $T_{\text{wall}} = 1,000 \text{ K}$, $T_e = 7,000 \text{ K}$, $p_e = 1,000 \text{ N m}^{-2}$ and $\beta = 5,000 \text{ s}^{-1}$; (b) $T_{\text{wall}} = 1,000 \text{ K}$, $T_e = 7,000 \text{ K}$, $p_e = 10^5 \text{ N m}^{-2}$ and $\beta = 10^5 \text{ s}^{-1}$; (c) $T_{\text{wall}} = 300 \text{ K}$, $T_e = 5,000 \text{ K}$, $p_e = 1,000 \text{ N m}^{-2}$ and $\beta = 5,000 \text{ s}^{-1}$; (d) $T_{\text{wall}} = 1,000 \text{ K}$, $T_e = 5,000 \text{ K}$, $p_e = 1,000 \text{ N m}^{-2}$ and $\beta = 5,000 \text{ s}^{-1}$ (From Armenise et al. 1998)

the concentration of atomic nitrogen is not important. The two conditions can be obtained by decreasing the temperatures at the edge of the boundary layer and on the surface.

Figure 7.10 (Armenise and Capitelli 2005) reports the non-equilibrium vibrational distributions for $T_{\text{wall}} = 300 \text{ K}$, $T_e = 5,000 \text{ K}$. Under these conditions, the VV up-pumping mechanism is able to create non-equilibrium vibrational distributions near to the surface. The results reported in the previous figures have been obtained by assuming a value of $\beta = 5,000 \text{ s}^{-1}$. As anticipated this parameter represents the inverse of the residence time of a fluid element in the boundary layer. This time should be compared with the relaxation times of the different chemical and physical processes occurring in the boundary layer. Two extreme cases can be envisaged; in the first case ($\beta = 10^7 \text{ s}^{-1}$) the flow time is much lower than the chemical and physical relaxation times and in the second case ($\beta = 10^1 \text{ s}^{-1}$) the flow time is much larger than the chemical and physical relaxation times. In the first case the chemical and physical processes have no time to change the edge vibrational distributions which remain practically frozen for all the boundary layer coordinate. In the second case the chemical and physical processes have the

Fig. 7.10 N_2 vibrational distributions at different η values using the ladder climbing model with
 $T_{\text{wall}} = 300 \text{ K}$, $T_e = 5,000 \text{ K}$,
 $p_e = 1,000 \text{ N m}^{-2}$ and
 $\beta = 5,000 \text{ s}^{-1}$ (From
Armenise et al. 1998)

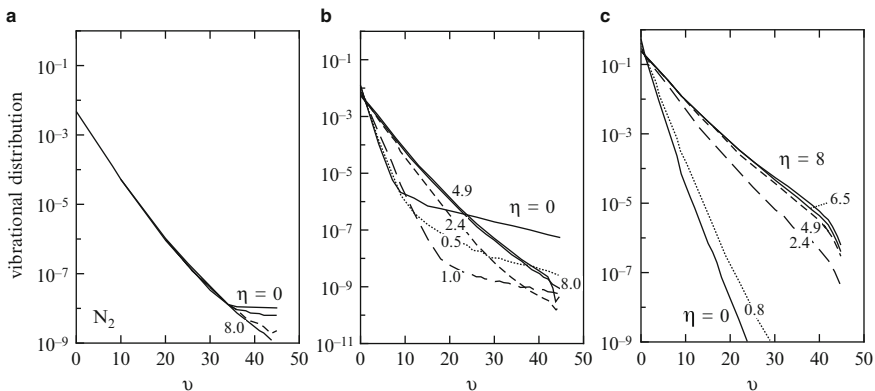
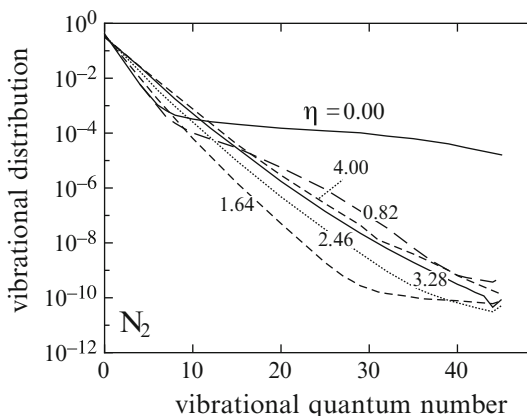


Fig. 7.11 The behavior of N_2 vibrational distributions ($\text{N}_2(v)/\text{N}$ mixture, non-catalytic surface) for different η values. (a) $\beta = 10^7 \text{ s}^{-1}$; (b) $\beta = 5,000 \text{ s}^{-1}$; (c) $\beta = 10^1 \text{ s}^{-1}$ (From Armenise and Capitelli 2005)

time to start and also to thermalize at the gas temperature, reaching equilibrium distributions along the temperature profile of the boundary layer. The two situations are well depicted in Fig. 7.11a–c (Armenise and Capitelli 2005). On the other hand the intermediate and most interesting case Fig. 7.11b allows the development of the non equilibrium vibrational distributions in all the boundary layer.

The results previously discussed have considered a surface not-catalytic to the atom recombination and to vibrational energy accommodation. Let us now consider the vibrational kinetics in the presence of a catalytic surface to atom recombination. We consider an air mixture in the dissociation-recombination regime with parameters equal to those reported in the previous case. Figure 7.12a, b (Armenise and Capitelli 2005) compare the non equilibrium vibrational distributions near to the surface, i.e. $\eta = 0$ for N_2 (Fig. 7.12a) and O_2 (Fig. 7.12b). The three curves refer in particular to the following conditions (1) non-catalytic surface, (2) catalytic surface

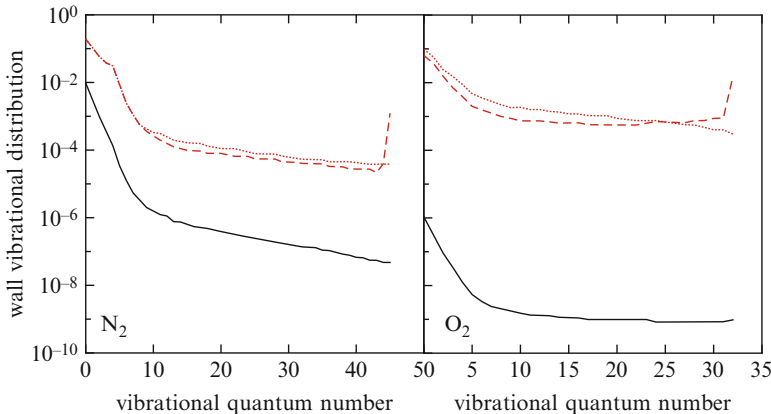


Fig. 7.12 N_2 (a) and O_2 (b) vibrational distributions close to the surface ($\eta = 0$) in an air mixture, for both the non-catalytic surface (solid line) and the SiO_2 surface, calculated according to different heterogeneous recombination models, i.e. (dashed line) recombination on the last vibrational level, (dotted line) recombination on all levels (From Armenise and Capitelli 2005)

with the experimental recombination process pumping only the last vibrational level of the molecules and (3) catalytic surface with the experimental recombination process equally pumping all the vibrational ladders of the molecules. Inspection of the figure shows that the surface catalyticicity increases by orders of magnitude the plateaux of non equilibrium vibrational distributions as compared with the non-catalytic case. Moreover models (2) and (3) give essentially the same results with the exclusion of the concentration of the last vibrational result due to the rapid rearrangement of the introduced vibrational quanta by the heterogeneous recombination process by VV and VT processes operating in the mixture.

The results reported in Fig. 7.12 are to be considered only from a qualitative point of view due to the crude approximations made for the heterogeneous recombination rates. Molecular dynamic calculations described in Chap. 3 should be considered to quantitatively improve the relevant results, as shown by Armenise et al. (2011).

7.3 Vibrational Kinetics Under Plasma Conditions

In the previous section we have discussed the vibrational kinetics in a neutral gas. To investigate the vibrational kinetics in a plasma we must add those processes promoted by collisions with free electrons. They include the electron energy-exchange processes, i.e. the vibrational excitation of molecules by electron impact (eV)



The kinetic term is written as

$$\left(\frac{dN_v}{dt} \right)_{eV} = -N_v N_e \sum_w k_{v,w}^e + N_e \sum_w N_w k_{w,v}^e \quad (7.44)$$

where N_e represents the electron density and $k_{w,v}^e$, the rate coefficient of the selected transition. The corresponding vibrational relaxation characteristic time can be written as

$$\tau_v^{eV} = \left[N_e \sum_{w=0}^{v-1} k_{v,w}^e \right]^{-1} \quad (7.45)$$

Particular important is the relaxation time of the first excited vibrational level

$$\tau_1^{eV} = (N_e k_{1,0}^e)^{-1} \quad (7.46)$$

which determines to a first approximation the characteristic time of the relaxation of vibrational temperature by eV process. The cross sections for these processes have been extensively discussed in Chap. 1.

Under non-equilibrium plasma conditions characterized by moderate electron temperature T_e , much higher in a discharge than T , new quanta are introduced in the vibrational ladder by eV processes, while VV and VT redistribute them through the whole vibrational ladder. Obviously, the importance of eV processes increases with the electron density, implying the necessity to have complete sets of eV cross sections (see Chap. 1).

On the other hand electrons can directly dissociate and ionize vibrationally excited molecules through the processes



which corresponding rates are $k_d^e(v)$ and $k_i^e(v)$, averaged when possible on a Boltzmann rotational distribution. The contribution of these processes to the kinetic equation are

$$\left(\frac{dN_v}{dt} \right)_{e d} = -N_v N_e k_d^e(v) \quad (7.49)$$

$$\left(\frac{dN_v}{dt} \right)_{e i} = -N_v N_e k_i^e(v) \quad (7.50)$$

defining the corresponding relaxation times as

$$\tau_v^{e d} = (N_e k_d^e(v))^{-1} \quad (7.51)$$

$$\tau_v^{e i} = (N_e k_i^e(v))^{-1} \quad (7.52)$$

The global dissociation and ionization rates by direct electron impact can be written as

$$\bar{k}_d^e = \frac{1}{2} \left(\frac{dN_A}{dt} \right)_{e,d} = \frac{1}{N_{A_2}} \sum_v N_v k_d^e(v) \quad (7.53)$$

$$\bar{k}_i^e = \left(\frac{dN_{A_2^+}}{dt} \right)_{e,i} = N_e \sum_v N_v k_i^e(v) \quad (7.54)$$

An (ab)used approximation is to take into account only the ground vibrational level of the diatom, that gives very crude results at low electron energy, such as in post-discharge, when the rate coefficients of vibrationally excited states, due to their lower energy thresholds, are orders of magnitude higher than the corresponding rates for $v = 0$. This statement is more and more true when well developed vibrational distributions are present in the plasma. Formally we can also define recombination terms by reverting Eqs. (7.47) and (7.48), i.e.



The kinetic terms assume the form

$$\left(\frac{dN_v}{dt} \right)_{e,dr} = N_A^2 N_e k_{dr}^e(v) \quad (7.57)$$

$$\left(\frac{dN_v}{dt} \right)_{e,ir} = N_{A_2^+}^2 N_e k_{ir}^e(v) \quad (7.58)$$

where the different coefficients are linked by detailed balance to the forward ones. Again total recombination rates are obtained by summing the different contributions

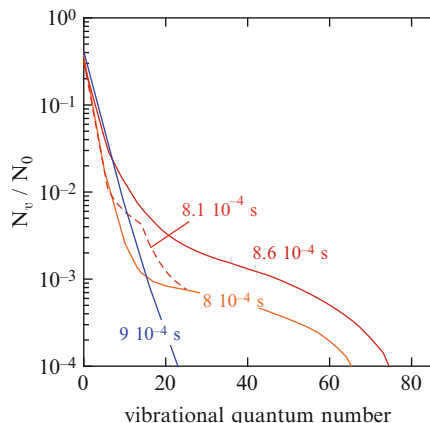
$$\bar{k}_{dr}^e = \sum_v k_{dr}^e(v) \quad (7.59)$$

$$\bar{k}_{ir}^e = \sum_v k_{ir}^e(v) \quad (7.60)$$

It should be noted that the detailed balance principle cannot be applied in this case because, due to the non equilibrium between the gas and the electron, especially in the presence of non-maxwellian eedf. In this case we should calculate recombination rates starting from superelastic collisions as described in Eq. (4.81).

In addition to these processes dissociation and ionization can occur through *pure vibrational* mechanisms (PVM) described in Chap. 9. These mechanisms can be more important than the corresponding processes induced by electron impact, especially considering intermediate vibrational levels.

Fig. 7.13 CO Vibrational distribution as a function of vibrational quantum number at different times before, during and after the laser pulse (Schmailzl and Capitelli 1979)

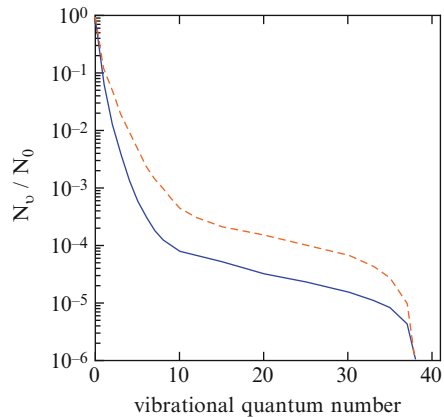


7.3.1 Laser-Plasma Interaction

An interesting new situation is represented by coupling two sources of vibrational quanta, discharge plus IR laser pulse. This situation was first studied theoretically by a master equation approach in pure CO (Schmailzl and Capitelli 1979). The vibrational kinetics contained also the deactivation by atomic carbon and oxygen generated by electron impact dissociation of CO. Moreover the interaction of a pulse IR laser with CO generated also a strong increase of gas temperature with consequences on the vibrational distribution. Figure 7.13 (Schmailzl and Capitelli 1979) shows the situation. The laser pulse begins 0.8 ms after the onset of the discharge. The interaction of the laser with CO vibrational levels occurs at a time when sufficient population in $v = 6$ to $v = 13$ do exist to observe appreciable absorption of the laser radiation. After 0.06 ms the introduced quanta by IR pulse are redistributed over the whole vibrational ladder showing an average increase by a factor 2.5 of the vibrational population densities compared with the discharge distributions. After 0.10 ms the increase of gas temperature destroys the pumping up mechanism generating a Boltzmann distribution.

An other interesting experiment rationalized by numerical calculations has been recently presented. In this case a cw IR laser is focused on an high pressure (600 Torr) N_2/CO (98:2) mixture, generating first the absorption of vibrational quanta on the first few vibrational quantum numbers followed by the VV up pumping mechanism. Then the system is coupled to a low E/N RF plasma to introduce additional vibrational quanta by electron impact excitation. A stable plasma is formed and well resolved infrared spectra are detected in the presence and absence of the electrical field. These infrared spectra are then de-convoluted to obtain the corresponding vibrational distributions which are reported in Fig. 7.14 (Lou and Adamovich 2009). The two plateaux differ up to a factor 7 qualitatively confirming results in Fig. 7.13. In particular the short plateaux reported in Fig. 7.14 as compared with the corresponding ones of Fig. 7.13 are due to the VT and VV relaxation of CO by nitrogen molecules which are majority in the mixture.

Fig. 7.14 Spatially averaged CO vdf without (solid blue line) and with (dashed orange line) RF field applied (Lou and Adamovich 2009)

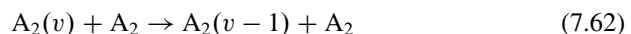


Appendix 1: Non-equilibrium Vibrational Distributions: General Considerations

A well developed vibrational distribution under non-equilibrium plasma conditions can be thought formed by three parts. The first part can be considered a Boltzmann one at ϑ_1 , followed by a plateau ending in another Boltzmann distribution at the gas temperature. They reflect the dominance of elementary processes acting in the plasma. As an example the plateau can be formed due to the interplay of VV quasi-resonant processes



and VT_M transitions.



Limiting our analysis to these two processes and considering quasi-stationary conditions we have the following relation

$$-N_v N_{A_2} k_{v,v-1} - N_v N_v k_{v,v-1}^{v,v+1} + N_{v+1} N_{v-1} k_{v+1,v}^{v-1,v} = 0 \quad (7.63)$$

Considering the detailed balance principle VV resonant rates (see Eq. (7.23)) we can write

$$-N_v N_{A_2} k_{v,v-1} - N_v N_v k_{v+1,v}^{v-1,v} \exp\left[-\frac{\Delta_{v,v}^{VV}}{k_B T}\right] + N_{v+1} N_{v-1} k_{v+1,v}^{v-1,v} = 0 \quad (7.64)$$

In the plateau we can assume, as a first approximation

$$N_v \approx N_{v+1} \approx N_{v-1} \quad (7.65)$$

so that Eq. (7.65) can be simplified as

$$-N_{A_2}k_{v,v-1} - N_v k_{v+1,v}^{v-1,v} \exp\left[-\frac{\Delta_{v,v}^{\text{VV}}}{k_B T}\right] + N_v k_{v+1,v}^{v-1,v} = 0 \quad (7.66)$$

giving

$$N_v = N_{A_2} \frac{k_{v,v-1}}{k_{v+1,v}^{v-1,v}} \left\{ 1 - \exp\left[-\frac{\Delta_{v,v}^{\text{VV}}}{k_B T}\right] \right\}^{-1} \quad (7.67)$$

Assuming harmonic oscillator rates (crude approximation)

$$k_{v,v-1} = v k_{1,0} \quad (7.68)$$

$$k_{v+1,v}^{v-1,v} = v^2 k_{1,0}^{0,1} \quad (7.69)$$

we get a v^{-1} dependence of the plateau

$$\frac{N_v}{N_{A_2}} = \frac{1}{v} \frac{k_{1,0}}{k_{1,0}^{0,1}} \left\{ 1 - \exp\left[-\frac{\Delta_{v,v}^{\text{VV}}}{k_B T}\right] \right\}^{-1} \quad (7.70)$$

i.e. a plateau slightly declining with v . It is interesting to develop the energy difference in the exponential factor assuming a simple anharmonic oscillator (see Eqs. (7.16)), (7.22), and expanding the exponential in power series, the equation at the plateau becomes

$$\frac{N_v}{N_{A_2}} = \frac{1}{v} \frac{k_{1,0}}{k_{1,0}^{0,1}} \left\{ 1 - \exp\left[-\frac{2\omega_e \chi_e}{k_B T}\right] \right\}^{-1} \approx \frac{1}{v} \frac{k_{1,0}}{k_{1,0}^{0,1}} \left[\frac{2\omega_e \chi_e}{k_B T} \right]^{-1}. \quad (7.71)$$

The VV kinetics in the presence of a source of vibrational quanta is such to create the so called Treanor distribution (Treanor et al. 1968) i.e.

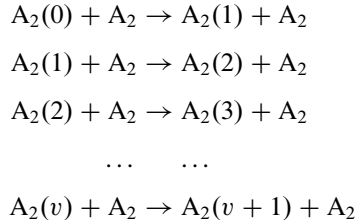
$$\left(\frac{N_v}{N_{v+1}} \right) = \exp\left[\frac{\varepsilon_1}{k_B \vartheta_1} - 2 \frac{\varepsilon_1 \chi_e v}{k_B T_g} \right] \quad (7.72)$$

χ_e is the anharmonicity constant and ϑ_1 and T_g are respectively the non-equilibrium vibrational temperature and the gas temperature. This distribution presents a minimum when the exponential becomes null, i.e.

$$(v)_{\min} = \frac{T_g}{2\chi_e \vartheta_1} + \frac{1}{2} \quad (7.73)$$

Appendix 2

Let us consider the VT terms restricting them to the mono-quantum transitions. The sequence of the following reactions can be considered



The different equations are interconnected so that we can write for the levels

$$\begin{aligned}
 \left(\frac{dN_0}{dt} \right) &= -N_0 N_{A_2} k_{0,1}^{A_2} + N_1 N_{A_2} k_{1,0}^{A_2} \\
 \left(\frac{dN_1}{dt} \right) &= N_0 N_{A_2} k_{0,1}^{A_2} - N_1 N_{A_2} k_{1,0}^{A_2} - N_1 N_{A_2} k_{1,2}^{A_2} + N_2 N_{A_2} k_{2,1}^{A_2} \\
 \left(\frac{dN_2}{dt} \right) &= N_1 N_{A_2} k_{1,2}^{A_2} - N_2 N_{A_2} k_{2,1}^{A_2} - N_2 N_{A_2} k_{2,3}^{A_2} + N_3 N_{A_2} k_{3,2}^{A_2}
 \end{aligned}$$

At the stationary conditions we can write

$$\begin{aligned}
 \left(\frac{dN_0}{dt} \right) &= -N_0 N_{A_2} k_{0,1}^{A_2} + N_1 N_{A_2} k_{1,0}^{A_2} = 0 \\
 \left(\frac{dN_1}{dt} \right) &= N_0 N_{A_2} k_{0,1}^{A_2} - N_1 N_{A_2} k_{1,0}^{A_2} - N_1 N_{A_2} k_{1,2}^{A_2} + N_2 N_{A_2} k_{2,1}^{A_2} = 0 \\
 \left(\frac{dN_2}{dt} \right) &= N_1 N_{A_2} k_{1,2}^{A_2} - N_2 N_{A_2} k_{2,1}^{A_2} - N_2 N_{A_2} k_{2,3}^{A_2} + N_3 N_{A_2} k_{3,2}^{A_2} = 0
 \end{aligned}$$

Summing the first two equations we get

$$-N_1 N_{A_2} k_{1,2}^{A_2} + N_2 N_{A_2} k_{2,1}^{A_2} = 0$$

while summing the first three equations we get

$$-N_2 N_{A_2} k_{2,3}^{A_2} + N_3 N_{A_2} k_{3,2}^{A_2} = 0$$

i.e.

$$N_1 k_{1,2}^{A_2} = N_2 k_{2,1}^{A_2}$$

$$N_2 k_{2,3}^{A_2} = N_3 k_{3,2}^{A_2}$$

and after applying the detailed balance principle on the rates we get

$$\frac{N_2}{N_1} = \frac{k_{1,2}^{A_2}}{k_{2,1}^{A_2}} = \exp \left[\frac{\varepsilon_2 - \varepsilon_1}{k_B T} \right]$$

$$\frac{N_1}{N_2} = \frac{k_{2,3}^{A_2}}{k_{3,2}^{A_2}} = \exp \left[\frac{\varepsilon_3 - \varepsilon_2}{k_B T} \right]$$

By making the same treatment on the first equation, we get

$$\frac{N_1}{N_0} = \frac{k_{0,1}^{A_2}}{k_{1,0}^{A_2}} = \exp \left[\frac{\varepsilon_1 - \varepsilon_0}{k_B T} \right]$$

The three levels submitted at the action of VT processes present at the stationary conditions a Boltzmann distribution at the gas temperature. This conclusion can be extended to the whole ladder of vibrational levels at the stationary conditions. It can be shown that also the time evolution of vibrational distributions under the action of VT mono-quantum transitions keeps its Boltzmann character if the initial condition is characterized by a Boltzmann distribution. More complex is the situation when multi-quantum VT transitions are inserted in the master equation.

References

- Akishev YS, Dem'yanov AV, Kochetov IV, Napartovich AP, Pashkin SV, Ponomarenko VV, Pevgov VG, Podobedov VB (1982) High Temp 20:658
- Armenise I, Capitelli M (2005) State to state vibrational kinetics in the boundary layer of an entering body in Earth atmosphere: particle distributions and chemical kinetics. *Plasma Sources Sci Technol* 14(2):S9–S17
- Armenise I, Capitelli M, Celiberto R, Colonna G, Gorse C, Laganà A (1994) The effect of N+N₂ collisions on the non-equilibrium vibrational distributions of nitrogen under reentry conditions. *Chem Phys Lett* 227(1):157–163
- Armenise I, Capitelli M, Gorse C (1998) Nitrogen nonequilibrium vibrational distributions and non-Arrhenius dissociation constants in hypersonic boundary layers. *J Thermophys Heat Transf* 12(1):45–51
- Armenise I, Esposito F, Capitelli M (2007) Dissociation–recombination models in hypersonic boundary layer flows. *Chem Phys* 336(1):83–90
- Armenise I, Rutigliano M, Cacciatore M, Capitelli M (2011) Hypersonic boundary layers: oxygen recombination on SiO₂ starting from ab initio coefficients. *J Thermophys Heat Transf* 25(4):627–632
- Bruno D, Capitelli M, Longo S (1998) DSMC modelling of vibrational and chemical kinetics for a reacting gas mixture. *Chem Phys Lett* 289(1–2):141–149
- Bruno D, Capitelli M, Esposito F, Longo S, Minelli P (2002) Direct simulation of non-equilibrium kinetics under shock conditions in nitrogen. *Chem Phys Lett* 360(1–2):31–37
- Caledonia GE, Center RE (1971) Vibrational distribution functions in anharmonic oscillators. *J Chem Phys* 55(2):552–561

- Candler GV, Olejniczak J, Harrold B (1997) Detailed simulation of nitrogen dissociation in stagnation regions. *Phys Fluids* (1994-present) 9(7):2108–2117
- Capitelli M (ed) (1986) Nonequilibrium vibrational kinetics. Springer series on Topics in current physics, vol 39. Springer-Verlag, Berlin Heidelberg
- Capitelli M, Molinari E (1980) Kinetics of dissociation processes in plasmas in the low and intermediate pressure range in Plasma Chemistry II, Springer Series Topics in Current Chemistry, vol.90, pp. 59–109. Springer, Berlin Heidelberg
- Capitelli M, Gorse C, Ricard A (1981) Influence of superelastic vibrational collisions on the relaxation of the electron energy distribution function in N₂ post discharge regimes. *J Phys Lett* 42(22):469–472
- Capitelli M, Colonna G, Gorse C, Esposito F (1999) State to state non-equilibrium vibrational kinetics: phenomenological and molecular dynamics aspects. AIAA paper 99–3568, AIAA
- Capitelli M, Ferreira CM, Gordiets BF, Osipov AI (2000) Plasma kinetics in atmospheric gases. Springer series on Atomic, optical, and plasma physics, vol 31. Springer, Berlin/Heidelberg
- Capitelli M, Colonna G, Esposito F (2004) On the coupling of vibrational relaxation with the dissociation-recombination kinetics: from dynamics to aerospace applications. *J Phys Chem A* 108(41):8930–8934
- Capitelli M, Armenise I, Bisceglie E, Bruno D, Celiberto R, Colonna G, D’Ammando G, De Pascale O, Esposito F, Gorse C, Laporta V, Laricchiuta A (2012) Thermodynamics, transport and kinetics of equilibrium and non-equilibrium plasmas: a state-to-state approach. *Plasma Chem Plasma Process* 32:427–450
- Colonna G, Armenise I, Bruno D, Capitelli M (2006) Reduction of state-to-state kinetics to macroscopic models in hypersonic flows. *J Thermophys Heat Transf* 20(3):477–486
- Colonna G, Pietanza LD, Capitelli M (2008) Recombination assisted nitrogen dissociation rates under nonequilibrium conditions. *J Thermophys Heat Transf* 22(3):399–406
- De Benedictis S, Capitelli M, Cramarossa F, Gorse C (1987) Non-equilibrium vibrational kinetics of CO pumped by vibrationally excited nitrogen molecules: a comparison between theory and experiment. *Chem Phys* 111(3):389–400
- Esposito F, Armenise I, Capitelli M (2006) N-N₂ state to state vibrational-relaxation and dissociation rates based on quasiclassical calculation. *Chem Phys* 331(1):1–8
- Essenhigh KA, Utkin YG, Bernard C, Adamovich IV, Rich JW (2006) Gas-phase Boudouard disproportionation reaction between highly vibrationally excited CO molecules. *Chem Phys* 330(3):506–514
- Farrenq R, Rossetti C (1985) Vibrational distribution functions in a mixture of excited isotopic CO molecules. *Chem Phys* 92(2–3):401–416
- Flament C, George T, Meister K, Tufts J, Rich J, Subramaniam V, Martin JP, Piar B, Perrin MY (1992) Nonequilibrium vibrational kinetics of carbon monoxide at high translational mode temperatures. *Chem Phys* 163(2):241–262
- Fridman A (2012) Plasma chemistry. Cambridge University Press, Cambridge
- Fridman A, Kennedy LA (2004) Plasma physics and engineering. CRC Press Taylor & Francis, UK
- Gordiets B, Osipov A, Shelepin L (1988) Kinetic processes in gases and molecular lasers. Gordon and Breach Science Publishers, US
- Gorse C, Cacciatore M, Capitelli M (1984) Kinetic processes in non-equilibrium carbon monoxide discharges. I. vibrational kinetics and dissociation rates. *Chem Phys* 85(2):165–176
- Gorse C, Billing GD, Cacciatore M, Capitelli M, De Benedictis S (1987) Non-equilibrium vibrational kinetics of CO pumped by vibrationally excited nitrogen molecules: general theoretical considerations. *Chem Phys* 111(3):371–387
- Ibragimova L, Smekhov G, Shatalov O (1999) Dissociation rate constants of diatomic molecules under thermal equilibrium conditions. *Fluid Dyn* 34(1):153–157
- Lou G, Adamovich IV (2009) Mechanism of laser and RF plasma in vibrational nonequilibrium CO-N₂ gas mixture. *J Appl Phys* 106(3):033304
- Munafò A, Magin TE (2014) Modeling of stagnation-line nonequilibrium flows by means of quantum based collisional models. *Phys Fluids* (1994-present) 26(9):097102

- Nagnibeda E, Kustova E (2009) Non-equilibrium reacting gas flows: kinetic theory of transport and relaxation processes. Springer series Heat and mass transfer. Springer, Berlin/Heidelberg
- Orsini A, Rini P, Taviani V, Fletcher D, Kustova E, Nagnibeda E (2008) State-to-state simulation of nonequilibrium nitrogen stagnation-line flows: fluid dynamics and vibrational kinetics. *J Thermophys Heat Transf* 22(3):390–398
- Panesi M, Munafò A, Magin TE, Jaffe RL (2014) Nonequilibrium shock-heated nitrogen flows using a rovibrational state-to-state method. *Phys Rev E* 90:013009
- Rich JW (1971) Kinetic modeling of the high-power carbon monoxide laser. *J Appl Phys* 42(7):2719–2730
- Rusanov VD, Fridman AA, Sholin GV (1979) Soviet Phys Tech Phys 24:1195
- Sanz ME, McCarthy MC, Thaddeus P (2003) Rotational transitions of SO, SiO, and SiS excited by a discharge in a supersonic molecular beam: vibrational temperatures, Dunham coefficients, Born-Oppenheimer breakdown, and hyperfine structure. *J Chem Phys* 119(22):11715
- Schmailzl U, Capitelli M (1979) Nonequilibrium dissociation of CO induced by electron-vibration and IR-laser pumping. *Chem Phys* 41(1–2):143–151
- Treanor CE, Rich JW, Rehm RG (1968) Vibrational relaxation of anharmonic oscillators with exchange-dominated collisions. *J Chem Phys* 48(4):1798–1807
- Xu D, Zeng M, Zhang W, Liu J (2014) Thermo-chemical nonequilibrium process in N₂/N mixture with state-to-state model. *ACTA Aerodyn Sin* 32(03):280

Chapter 8

Particle Models for Low Pressure Plasmas

Partially ionized gases produced by capacitively coupled parallel plate (CCPP), radio-frequency electric discharges, are used routinely for the surface treatments of materials ranging from thin film deposition to selective etching (Lieberman and Lichtenberg 1994; Chen and Chang 2003), and more recently including tailoring of the surface chemical properties (Kushner 1983; Diomede et al. 2011, 2012). In all these applications the special properties of species present in the ionized gas, in particular ions and radicals, play an essential role. The versatility of plasma treatment is linked with the possibility to feed a given plasma source with an endless variety of gas mixtures. At the same time and for much the same reasons, the understanding of the physics and chemistry of these systems is still in progress. In parallel with experimental studies, the computer models are of great help to get a view, although affected by uncertainties, of important aspects of the plasma dynamics and kinetics which are not realistically accessible through experimental measurements. In view of these considerations, the modeling of the discharge plasma in molecular gases represents an important benchmark for the computational techniques of the plasma discharge community. Most of the models developed until now are ‘fluid’ models based on a macroscopic description of the charged particle kinetics in the discharge. These models assume for the ionization coefficient, and in general for the rate coefficients of the electron/molecule reactions, values which are calculated by solving the Boltzmann equation by the two-term approximation as well as by Monte Carlo methods (see Chap. 4 and Kushner (2009), Fiala et al. (1994)). These are later interpolated in terms of the electron energy and applied locally depending on the calculated value of the electron temperature. This approach is fast and usually reliable, although it cannot handle accurately those cases where the electron component have a Knudsen number higher than ~ 0.01 and behave like a rarefied gas.

8.1 Time Scales

For a typical plasma dimension in the cm range, at room temperature, assuming an electron/neutral elastic cross section of 10^{-19} m^2 , the borderline pressure at which $Kn = 0.01$ is in the order of 0.5 Torr. When the pressure is significantly lower than this, only methods based on numerical solutions of kinetic equations for the translational distribution function $f(r, v, t)$ of the charged particles, can be applied in order to get accurate values for the rate coefficients of electron/molecule reactions. In general terms, the coupling of the neutral gas and plasma phase kinetics is always to be taken into account, especially for molecular gases: on one side in fact, the rate coefficients for electron/molecule reactions are functionals of the electron energy distribution function; on the other side, the Boltzmann collision integral is also a function of the gas composition, including the vibrational excitation. The necessity to take into account chemical kinetics as well as charged particle kinetics in the plasma phase at the same time creates an interesting problem of multiple time scales. In fact:

- The shortest electron particle kinetics time scale is the reverse of the electron plasma frequency, which in typical applicative cases is in the nanosecond range.
- The time scale for charged particle relaxation to the steady state is the ambipolar diffusion time, which in typical applicative cases is of the order of 0.1–1 ms
- The time scale for the stabilization of a steady state chemical composition of the plasma can reach (especially for electronegative plasmas) values of 0.01 s or higher.

So we have a time scale span of several orders of magnitude to be tackled by an appropriate technique, which must at the same time merge two different kinetic descriptions, one (for charged particles) based on transport kinetic equations, and the other (for neutral particles) based on chemical kinetics rate-diffusion equations. Several particle models of these kind of plasmas already appeared in the literature but as a rule they do not include the vibrational/chemical kinetics of gas phase molecules. A class of particle models including the kinetics of vibrationally excited molecules was considered in the past few years. These models include a state-to-state chemical kinetics for molecules, this last term meaning that molecules in different vibrational levels are treated as separate species. Another important problem not yet addressed for this system is an accurate, kinetic-level description of the several kinds of ions existing in the discharge, which should take into account also the thermal distribution of neutral particles in the bulk region of the plasma, where it cannot be neglected because of the thermal energy of ions. A fully self-consistent 1D model of the discharge plasma based on substantial improvements (to be described in details in the following) of previous models. The algorithm presented in this chapter includes several techniques to treat the different time scales described above, in particular the self-consistent treatment of neutral chemistry and plasma kinetics and a special scaling for the negative ion time scale.

8.2 Particle Models

Most non-equilibrium plasmas of interest are characterized by a large number of electrons in the Debye sphere: in these conditions the interaction between charged particles can be approximated by a particle-space charge field interaction. This point of view is assumed in the so-called Particle-in-Cell, or PIC approach (Birdsall and Langdon 1985; Birdsall 1991; Hockney and Eastwood 1991; Vahedi and Surendra 1995; Longo 2006; Tskhakaya et al. 2007; Donkó 2011). In the PIC approach the Newton equation for a large ensemble (10^4 – 10^6 particles) of electrons and positive ions are solved taking into account the local electric field as it results from local interpolation within a cell of a mathematical mesh (from what follows the name ‘Particle in Cell’). After any calculation step of the motion equations, the electric charge in any cell of the mesh is determined from the number of electrons and positive ions found in the cell itself, according to their statistical weight w . Known the electric charge density, the electric potential and field are determined by solving the Poisson equation on the same mesh. The PIC method is therefore fully equivalent to solve the Vlasov-Poisson plasma problem assuming a N-particle ensemble solution for any particle species:

$$f(\mathbf{r}, \mathbf{v}, t) = \Sigma_p \delta^3(\mathbf{r} - \mathbf{r}_p(t)) S(\mathbf{v} - \mathbf{v}_p(t)) \quad (8.1)$$

Where \mathbf{r}_p and \mathbf{v}_p are the single-particle position and velocity, satisfying the Newton equations, δ is the Dirac ‘delta function’ and S is a particle shape factor (a ‘smoothed’ δ). Depending on the explicit form of S one can have different sampling orders. For example, in the 1 dimensional case one can have in particular 0 order, or NGP (nearest grid point), which assigns the particle to the nearest grid point, and first order, or CIC (Cloud-in-Cell) which assigns the particle charge q to the two neighboring grid points in two fractions according to the particle position, proportional to the distance from the opposite point. The same formulas must be used to weight (interpolate) the electric field acting on any particle in order to grant the conservation of momentum in the limit of very small time steps. CIC sampling is more complex than NGP, but it should be preferred because it is by far less numerically noisy. Expressions for 2D can be found in Birdsall and Langdon (1985) and Birdsall (1991). The Newton equations in PIC are usually solved by using a simple scheme with interlaced grids for velocity and position, the so-called Leapfrog method:

$$\mathbf{v}_p(t + \frac{1}{2}\Delta t) = \mathbf{v}_p(t - \frac{1}{2}\Delta t) + \mathbf{a}_p(t)\Delta t \quad (8.2)$$

$$\mathbf{r}_p(t + \Delta t) = \mathbf{r}_p(t) + \mathbf{v}_p(t)\Delta t \quad (8.3)$$

Note that the difference with respect to the explicit Euler method is just the substitution of v with v' in the second equation. In fact the difference is deeper, because the two vectors \mathbf{r} and \mathbf{v} must be interpreted as $\mathbf{r}(t)$ and $\mathbf{v}(t + \Delta t/2)$, and the formulas to calculate for example the total kinetic energy must be modified

accordingly. This simple method is excellent in reproducing the electron plasma oscillations, provided it operates within its stability domain: to get a stable solution, it is necessary that $\Delta t < 1/\omega_e$ where ω_e is the electron plasma frequency. This stability problem at large time steps can be solved by using implicit solvers, which however meet some difficulties in bounded systems.

As regards the solution of the Poisson equation many methods are available. In the 1D case with boundary conditions for the electric potential (the Dirichlet problem) the solution is elementary, and after discretization of the space co-ordinate one gets:

$$\frac{-\varepsilon_0}{\Delta x^2} \begin{pmatrix} -2 & 1 & 0 & \dots & \dots \\ 1 & -2 & 1 & 0 & \dots \\ \dots & \dots & \dots & \dots & \dots \\ \dots & 0 & 1 & -2 & 1 \\ \dots & \dots & 0 & 1 & -2 \end{pmatrix} \begin{pmatrix} \varphi_1 \\ \varphi_2 \\ \dots \\ \varphi_{n-2} \\ \varphi_{n-1} \end{pmatrix} = \begin{pmatrix} \rho_1 - \varepsilon_0 \varphi_0 / \Delta x^2 \\ \rho_2 \\ \dots \\ \rho_{n-2} \\ \rho_{n-1} - \varepsilon_0 \varphi_n / \Delta x^2 \end{pmatrix}. \quad (8.4)$$

This system is tri-diagonal, and its numerical solution is straightforward (Birdsall and Langdon 1985). The boundary conditions can be for example

$$\varphi_0 = 0$$

$$\varphi_n = V_{rf} \cos \omega t$$

as in the case of a RF discharge. The grid spacing Δx cannot be chosen freely but it should be smaller than the electron Debye length. At the same time, however, the grid spacing should be sufficiently large to avoid average-speed electrons traveling more than Δx in a single time step. It is practically impossible to merge this last condition with resolution of the Debye length for thermal ions, therefore numerical ion instabilities due to finite Δx cannot be avoided; usually their effect is however small in collisional discharge models. In fact the charged particle energy is constantly flowing from the field to the molecules through the plasma phase, and we only need the spurious energy flux be lower than the physical one, this last being usually quite strong. These collision processes are included by MC method (Boeuf and Marode 1982; Pitchford and Phelps 1982), and the resulting technique is the PIC/MC method (Longo 2006). PIC/MC simulation of plasmas produced by high-frequency electric discharge has given results in remarkable agreement with experiments for electron dynamic quantities, in particular the eedf. These model are of different kinds, depending on the technique used to merge the free collision times t_c calculated from Eq. (4.117) for any particle with the fixed PIC time step.

8.3 Dynamic Particle List

As explained, the particle ensemble in a RF discharge simulation includes particles of different species with different properties: not only mass and charge are different,

but they are expected to behave differently in collision and chemical processes. Also, particles can disappear (i.e. charge species hitting the electrodes are neutralized) or appear (i.e. new electrons and ions are produced in ionization processes). Furthermore, the average number of simulated particles must be contained constantly in an ideal range in order to keep a good statistics without a too large computational cost per time step. For this purpose one can use a dynamic list of particles, i.e. a structure of the form

$$\{\mathbf{r}_i\}_{1 \leq i \leq N}, \{\mathbf{v}_i\}_{1 \leq i \leq N}, \{J_i\}_{1 \leq i \leq N},$$

where N is the number of particles and J_i is a logical variable that represents the species and state of the particle i -th, in the sense that when the particle is inactive, i.e. no longer a real particle $J_i = 0$, while when it is active the value of J_i sets the particles specie (e.g. $J_i = 1$ means that the i -th particle is an electron, 2 means a specified kind of positive ion, 3 is another kind of positive ion, etc.).

At each step of the calculation, it is assumed that only particles for which $J_i \neq 0$ are to be moved or taken into account for the calculation of average quantities or histograms.

To get rid of the i -th particle, for example because it is in contact with an absorbing surface, it is sufficient to put $J_i = 0$.

To produce a new particle with position \mathbf{r}_n and velocity \mathbf{v}_n is sufficient to increase N by 1, and after this change,

$$\mathbf{r}_N = \mathbf{r}_n, \mathbf{v}_N = \mathbf{v}_n$$

and J_N is set as appropriate. From time to time, the computer code must proceed to compress the list of particles, so that it does not fill the inactive particles. To this end what it has to be done is using the following algorithm: start from $i = 0$, scroll through the list with an index j , and only if $J_j \neq 0$ do the following:

$$\mathbf{r}_i \leftarrow \mathbf{r}_j, J_i \leftarrow J_j, i \leftarrow i + 1$$

At the end of the cycle N is set as $N \leftarrow i$. In this way, the list was compacted, and contains only active particles, with $J \neq 0$. This method can manage a list of particles of different kinds since all the necessary information is contained in the vector $\{J\}$.

8.4 Self-Consistent Approach

Despite the impressive power and success of PIC/MC approach, in order to apply it to the free electrons in low temperature plasmas it is necessary to include the interaction between the gas chemistry and the electron dynamics in the non-equilibrium case, that is, including state-to-state chemical kinetics with all the

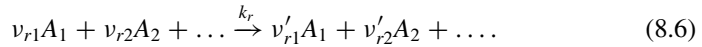
relevant electron-molecule collisions. The effect of chemistry on the electron transport is obvious, since the collision frequency (Eq. (4.116)) depends on the chemical composition of the gas. At the same time, the electron transport influences the chemical composition through plasmachemical processes involving electrons.

Therefore, it is necessary to couple *self-consistently* the electron transport with the chemical kinetics, i.e. to solve at the same time the electron transport and chemical kinetics problems taking into account their reciprocal connection. The method is very versatile and effective, allows to obtain an essentially exact solution of the kinetic problem for charged particles and has been described in many papers (Longo 2006; Diomede et al. 2007, 2008; Longo et al. 1997).

During the calculations, the densities of different species will be updated by solving appropriate equations. The approach is different for charged and neutral particles. Charged particle densities are obtained directly by the PIC/MC simulations. As for neutral densities, they are obtained by finding a stationary solution for the following set of non-linear reaction and diffusion equations

$$\frac{\partial \rho_s}{\partial t} = D_s \nabla^2 \rho_s + \sum_r (v'_{rs} - v_{rs}) k_r \prod_{s'} \rho_{s'}^{v_{rs'}}, \quad (8.5)$$

where D_s is the diffusion coefficient of the given species and k_r is the rate coefficient of the r -th chemical reaction process:



The chemistry of gas molecules interacting with the reactor walls is connected with boundary conditions of the system. Let us consider only pseudo first-order reactions



taking place on surface, with probability p_{rs} . The flux of A_s is

$$\phi_s = \frac{1}{4} \sqrt{\frac{8k_B T}{\pi m_s}} \rho_s (x = 0 \text{ or } l). \quad (8.8)$$

The catalytic boundary conditions are thus:

$$D_s \frac{\partial \rho_s}{\partial \xi} = - \sum_r p_{rs} \phi_s + \sum_{r's'} p_{r's'} v_{r's} \phi_{s'}, \quad (8.9)$$

where ξ is the vector locally normal to the surface. Since the charged particles densities are calculated by PIC/MC, they are not part of the unknowns of the system (Eqs. (8.5)–(8.9)). This system can be solved numerically after discretization on a grid. For a 1D problem, the equations for the density of any species in the form of vector $N_s = \{n_s(j)\}$ are written in the matrix form $A_s N_s = B_s$ where

A_s is a tridiagonal matrix containing coefficients of linear loss terms (for first order processes), diffusion terms and loss terms of the form $-kn_k(j)$ resulting from bimolecular reaction between species s and k , while $B_s(j)$ is the vector of chemical source terms. The matrix A is modified as usual in order to incorporate the catalytic boundary conditions. Since both A and B are actually functions of the set of unknown vectors $n_i(j)$, a relaxation technique is employed which can be described as Gauss Seidel block relaxation applied to the single system of equations $AN = B$ where N is the vector $n_{i,j}$. The system $A_1N_1 = B_1$ is solved for the first species vector $N_1 = \{n_1(i)\}$ assuming as starting point a uniform, thermal distribution for N_i . After that, the equation $A_2X_2 = B_2$ is solved for the second species with updated values for A_2 and B_2 , and so on to the last species and then back to the first, up to full relaxation. Based on the these ideas, fairly complete 1D models have been developed for RF discharges in pure nitrogen (Longo et al. 1997) and hydrogen (Longo 2000).

8.5 Worked Example: RF Model for Hydrogen

Hydrogen, besides being paradigmatic to chemistry and physics for obvious reasons, is an important component of the gas mixtures used in many real processes like diamond and amorphous silicon film deposition, because of the high reactivity of hydrogen atoms that can be produced in this non equilibrium plasma at low gas temperatures.

Furthermore, pure hydrogen is a challenging test case for several reasons. In view of its intermediate electronegativity the role of negative ions in this discharge is controversial. The ratio between negative ions and electrons in the bulk plasma, where negative ions accumulate, appears to be highly variable, albeit it is never much larger than one, as it happens instead in strongly electronegative gases like O₂ or Cl₂. Until very recently, H₂ has been regarded as an electropositive component in plasma processing discharge models in spite of the well known use of this discharge plasma as a source of negative ions in nuclear fusion technology (see Chap. 10). The neglecting of the electronegative properties of H₂ molecules by the plasma processing community is essentially due to the fact that the production of negative ions in this gas can not be described in closed form using the language of charged particle transport, but requires methods and concepts of molecular vibrational kinetics, since it involves excited states of H₂ molecules as an essential intermediate. To this picture one has to add a further complication, due to the fact that the electron energy distribution function is not a Maxwellian one but actually features a structured shape which is the result of the combined action of several kinds of electron-molecule collisions. Besides, a realistic model for parallel plate discharges cannot neglect the kinetics of atomic and molecular ions. In fact, while the gas feed is a single component (H₂ molecules), the plasma in the discharges is not, indeed molecules are dissociated by electron impact to radicals (H atoms) and ionized. The primary ionic species H₂⁺ reacts promptly with molecules to produce

the secondary ion H_3^+ , and non negligible fractions of atomic positive H^+ and, as mentioned above, negative ions H^- are produced by the network of chemical reactions.

8.5.1 The Model

The model version used is 1D in space and 3D in velocity space and represents the discharge neglecting radial field components and radial diffusion, both usually negligible in view of the small d/r aspect ratio of these systems. In this version of the model five charged components are considered, namely electrons, H^+ , H_2^+ , H_3^+ , and H^- ions. Elastic collision processes between these charged species and neutral components are included by using the Monte Carlo method in Chap. 4 with exact consideration of the interparticle collision statistics and the effect of the thermal velocity distribution of neutral particles. The field solver and the particle/Monte Carlo solver are coupled with exact consideration of collision statistics using the *modified time step* approach (Longo 2006). A large database of collision cross sections is enclosed in the plasma module, representing all the collision processes with consideration of the collision energy (Diomede et al. 2005) (all the cross sections used are discussed in the paper): more than 100 cross sections are stored and interpolated in view of the necessity to distinguish vibrational states of neutral molecules in collisions processes where the internal state of the molecule makes a very big difference (Diomede et al. 2007). Some reactions between charged species, e.g. electron/ion neutralization, are also included by a technique described in Longo (2006). The vibrational kinetics of H_2 molecules is included using a 1D reaction-diffusion model, where the diffusion of molecules is described under a continuous approximation i.e. with a diffusion term $D_v \partial^2 n_v / \partial x^2$ as explained earlier, where n_v is the number density of $\text{H}_2(v)$ and D_v is the corresponding diffusion coefficient calculated from the Chapman-Enskog theory (Capitelli et al. 2013).

This approximation is acceptable in view of the Knudsen number $Kn < 0.1$ although not excellent since Kn is still higher than 0.01.

Chemical reactions in gas phase are included by finite rates based on a database of rate coefficients which is included in the model. A list of reactions and rate coefficients sources is reported in Tables 8.1 and 8.2 (Panarese et al. 2013). We assume that H atoms are produced through direct dissociation of H_2 by electron impact via the repulsive triplet states like $\text{H}_2(\text{b}^3\Sigma_u^+)$, which are indeed the most important formation channels as confirmed later in the results section. The atom production rate from direct electron impact between electrons and H_2 molecules is given by $2\nu(x)$ where $\nu(x)$ ($\text{m}^{-3} \text{s}^{-1}$) is the reaction rate. This last is calculated as

$$\nu(x) = (2/m_e)^{1/2} n_m \int f_e(\epsilon, x) \epsilon^{1/2} \sigma_d(\epsilon) d\epsilon \quad (8.10)$$

where $f_e(\epsilon, x)$ is the translational distribution of electron normalized as

Table 8.1 Reactions included in the chemical kinetics for neutral particles

Process		Reference
$e + H_2(v = 0) \rightarrow e + H_2(v = 1, \dots, 5)$	eV ^a	JILA Database (2005)
$e + H_2(v = 1, \dots, 5) \rightarrow e + H_2(v = 0)$		JILA Database (2005)
$H_2(v) + H_2(w) \rightarrow H_2(v - 1) + H_2(w + 1)$	VV	Loureiro and Ferreira (1989)
$H_2(v) + H_2 \rightarrow H_2(v - 1) + H_2$	VT _M	Loureiro and Ferreira (1989)
$H_2(v) + H_2 \rightarrow H_2(v + 1) + H_2$		Loureiro and Ferreira (1989)
$H_2(v) + H \rightarrow H_2(w) + H$	VT	Gorse et al. (1987)
$e + H_2 \rightarrow e + 2H$ (via b ³ Σ _u ⁺ , c ³ Π _u , a ³ Σ _g ⁺ , d ³ Π _u)	Diss	JILA Database (2005)
$e + H_2(v) \rightarrow e + H_2(w)$ (via B ¹ Σ _u ⁺ , C ¹ Π _u)	EV	Celiberto et al. (2001)
$e + H_2 \rightarrow e + H + H(n = 2-3)$	Diss → H*	JILA Database (2005)
$e + H_2 \rightarrow H + H^+ + 2e$	Atom/ion channels	JILA Database (2005)
$e + H_2 \rightarrow H_2^+ + 2e$		JILA Database (2005)
$H_2^+ + H_2 \rightarrow H_3^+ + H(\text{fast})$		Phelps (1990)
$H_2(v > 0)\text{-wall} \rightarrow H_2(v = 0)$		Gorse et al. (1985)
$H\text{-wall} \rightarrow 1/2 H_2$	Rec	Kae-Nune et al. (1996)
$e + H \rightarrow 2e + H^+$	Ion	Kim and Rudd (1994)
$e + H_2(v = 0, \dots, 14) \rightarrow H + H^-$	DEA	Capitelli et al. (1994)
		Fabrikant et al. (2002)

^aThe resonant vibrational excitation processes, known as eV processes in the plasma modeling community, correspond to RVE discussed in Chap. 1

$$\int f_e(\epsilon, x) d\epsilon = n_e(x) \quad (8.11)$$

σ_d is the direct dissociation cross section, n_m and n_e are the number density of molecules and electrons respectively. The total atomic rate production R (s^{-1}) is therefore given by

$$R = 2 \int v(x) d^3x. \quad (8.12)$$

The treatment for ion-neutral processes like charge-exchange (not included in this paper) is essentially the same but the ion distribution replaces the eedf and the stoichiometric factor preceding the integral is equal to 1. Recombination processes which cannot fit the basic PIC/MC formalism since they involve two charged particles can be treated as a combination of two first order ones, each including one of two particle species involved in the process, during a PIC time step Δt . Charge neutrality is not enforced, but obtained on the average.

Table 8.2 Processes included in the PIC/MCC model

Charged/neutral particle	Collision processes	Reference
e/H_2	Elastic scattering	JILA Database (2005)
	eV-EV processes	JILA Database (2005) and Celiberto et al. (2001)
	Electronic excitation	JILA Database (2005)
	Dissociation	JILA Database (2005)
	Ionization	JILA Database (2005)
	Dissociative attachment	Capitelli et al. (1994) and Fabrikant et al. (2002)
$e/H_2(v)$	Elastic scattering	JILA Database (2005)
	Vibrational deactivation	JILA Database (2005)
e/H	Elastic scattering	JILA Database (2005)
	Direct ionization	JILA Database (2005)
H_3^+/H_2	Elastic scattering	Šimko et al. (1997)
	Conversion to H^+	Phelps (1990)
	Conversion to H_2^+	Phelps (1990)
H_2^+/H_2	Charge-exchange	Phelps (1990)
	Conversion to H_3^+	Phelps (1990)
H^+/H_2	Elastic scattering	Phelps (1990)
H^+/H	Charge-exchange	Eletskii (1997)
H^-/H_2	Elastic scattering	Phelps (1990)
	Detachment	Phelps (1990)
H^-/H	Detachment	Gorse et al. (1992)
	Charge-exchange	Eletskii (1997)
H^-/H_3^+	Neutralization	Gorse et al. (1992)

8.5.2 Solutions to Reduce the Computational Effort

A variance reduction technique can be applied to face the problem of particle species which small mole fraction which would be represented in the simulation by very few particles.

Two different values for the different weights of simulated particles W_s are used by applying the technique in order to reduce the statistical error over macroscopic quantities calculated for minority ionic species. The technique is straightforward but must be applied carefully in order to avoid errors. For example, to increase the number of simulated negative ions H^- by a factor 10 the W_- is 10 times lower than that of electrons W_e . Any time an electron produces a negative ion, the electron disappears but 10 simulated particles are produced. Coherently, a process in which H^- generates an electron (i.e. detachment) must produce 1/10 of electron. To implement this, one electron is randomly generated only in a case out of 10. These ratios and specific routines to handle them must be included in the code.

In the calculations presented hereafter $W(H^+)/W(e) = 0.1$ and the same for H_2^+ and H^- .

Negative ions, as mentioned earlier, need a very long time to reach a steady state density arising from the balance of pseudo zero-order production channel α (attachment) and pseudo first-order consumption channels $\beta n(H^-)$ (detachment, recombination), i.e. $\alpha = \beta n(H^-)$. The relaxation time $1/\beta$ is often very long with respect to the other plasma time scales (these last as high as 0.01 s and even sometimes much higher, as mentioned). A special technique has been devised to speed up the convergence of the negative ion density: the technique consists in scaling both α and β to $k\alpha$ and $k\beta$ respectively, with $k > 1$, while keeping $n(H^-) = \alpha/\beta$ constant (Diomede et al. 2005). This implies scaling the cross sections for attachment.

8.5.3 Test Case

As a test case, we consider a pure hydrogen RF discharge plasma produced by the parallel-plate configuration, i.e. one plane electrode surface ($x = 0$) is kept at electric potential $V = 0$ (grounded), while the opposite one ($x = d$) is assumed to be driven by an external generator to an oscillating potential. The PIC mesh has 400 cells, while the neutral reaction/diffusion equation mesh has 50 cells. The PIC time step is 0.05 ns, fitting the Courant condition. The code was run for 10^6 PIC time steps with 5 PIC/kinetics iterations in order to reach a steady state solution. The main bottleneck is the (albeit scaled) negative ion density relaxation. The values for physical quantities are: gas temperature $T_g = 300$ K, voltage amplitude 200 V, gas pressure $p = 0.1$ Torr, discharge frequency 13.56 MHz, discharge gap $d = 0.06$ m, DC voltage (bias) 0 V.

8.5.4 Some Results for Hydrogen

Figures 8.1 and 8.2 show a snapshot of the results. In particular:

Figure 8.1a shows the results obtained for the number densities of charged particles. It can be seen that the role of negative ions in the central region of the plasma is not negligible, contrary to the implicit assumption of most of the literature in the field.

Figures 8.1b and 8.2a show the eedf and the vibrational distribution function (vdf) in different positions in the discharge. For both it is confirmed a non equilibrium character. As already well known the vdf is characterized by a plateau due to EV excitation processes (i.e. high threshold processes with a singlet intermediate) occurring in the sheath/bulk boundary region where the electron energy deposition is larger. Figure 8.2b shows a comparison between our PIC/MC code results and those obtained with the fluid modeling based SIGLO-RF code in the same physical conditions and using mostly the same input data. This code, however, neglects the negative ion and the vibrational kinetics. It can be noticed a satisfactory agreement for the density of the majority positive ion. The comparison is better in the case of

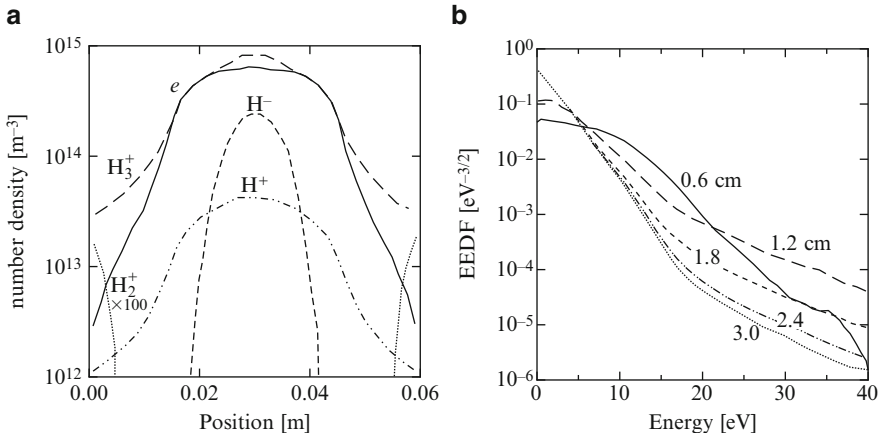


Fig. 8.1 (a) Number density of charged particles at the steady state for the test case. (b) eedf at different positions in the discharge

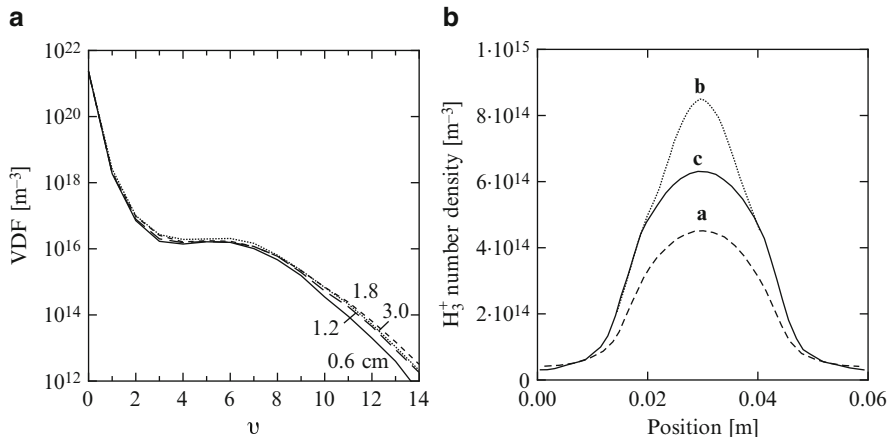


Fig. 8.2 (a) vdf at different positions in the discharge. (b) Comparison between H₃⁺ number density, as a function of position, calculated by SIGLO-RF fluid model code, **a**, and PIC/MC model taking into account, **b**, and neglecting, **c**, H⁻ ion production

the code run neglecting negative ions, as expected. These results could be obtained at the cost of 10.5 h on a Pentium 4, 1.7 GHz PC. The most remarkable point on this respect is the success of the negative ion time scale technique, which allowed to reduce the CPU time by a factor of ten without affecting the overall results in any sensible way. Since there is no need for a particle/mesh list, the approach is not only highly suitable for parallelization but possibly, with some modifications, for a GRID network implementation. Of course the computational cost of a fluid model run is by far lower, but this last is less informative as regards the electron energy distribution, since it considers local field conditions based on the calculated local electron energy,

and therefore cannot reproduce kinetic tails, like in Fig. 8.1b, which are due to fast electron diffusion. Besides, for the same reason, the fluid approach is not applicable to more rarefied cases, which are easily accessed by particle models like the one presented here.

A more detailed comparison of PIC and fluid models describing H₂ plasmas in capacitively RF discharges can be found in Diomede et al. (2008). A sample of results describing time-averaged vdf and eedf in the discharge center and at 0.2 cm from the electrode are reported in Figs. 8.3 and 8.4. Inspection of these figures shows a qualitative agreement for vdf, while large differences are present in the corresponding eedf.

8.5.5 Ion Energy Distribution Functions (iedf) in H₂ RF Discharge

In the last few years remarkable achievements have been produced in the reproduction of the experimental iedf's of different positive ions in RF discharges in hydrogen. These comparisons show the high level of precision of model predictions, in spite of the complexity of the multiple ion kinetics in hydrogen plasmas and witness the high level of the present state of art in these systems, which provides a starting point for future researches. It is known that the iedf in the sheath of RF plasmas as well as of the ions impacting on electrode surfaces have a complex shape build around systems of peaks. These peaks are explained by the Wild-Koidl mechanism (Wild and Koidl 1991) as iedf singularities associated to inversion points of an oscillating dynamics, that of ions falling through the oscillating field of the

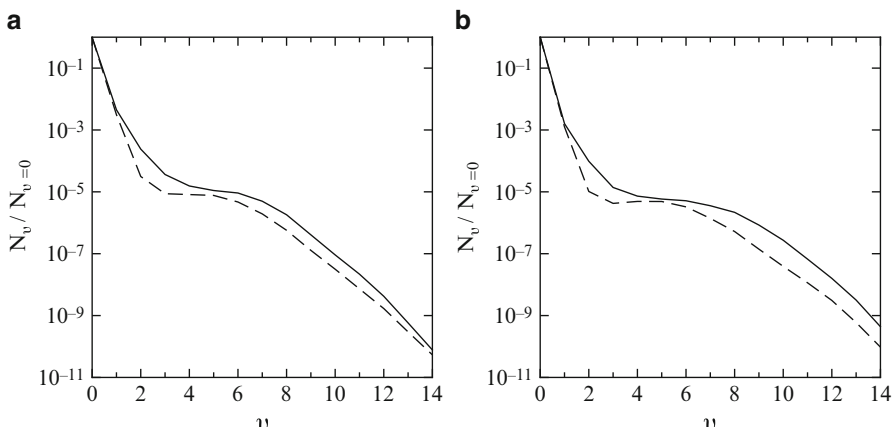


Fig. 8.3 Comparison between the vdf obtained from the kinetic (dashed line) and the fluid (solid line) model at 133 Pa, in two regions of the plasma. (a) In the discharge center; (b) at 0.2 cm from the electrode (From Diomede et al. 2008)

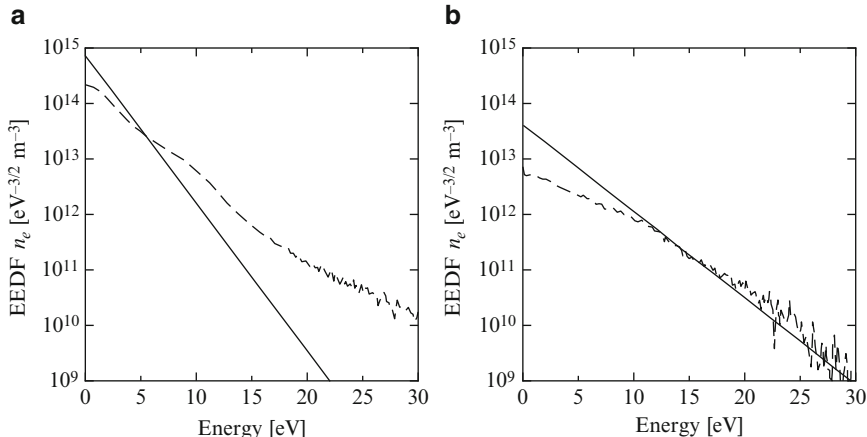


Fig. 8.4 Electron energy distribution function calculated at 70 Pa by the kinetic model (dashed line) in the plasma sheath region, compared to the Maxwellian distribution for the local electron density and temperature obtained by the fluid model (solid line). **(a)** In the discharge center; **(b)** at 0.2 cm from the electrode (From Diomede et al. 2008)

sheath, in the reference frame of the trajectory for a time averaged sheath field. Elaborations on this concept shows that the energy difference between the couple of peaks associated to this oscillating motion is related to the ion transit time in the sheath, and therefore to the ion mass (Kawamura et al. 1999). The Wild-Koidl mechanism clarifies the role of charge-exchange collisions which stop the ions at random times in the course of their passage through the sheath and provide a clue to the iedf shape, but it cannot describe iedf details when processes other than charge-exchange are important and, even more, where ion conversion reactions occur in the sheath region. In the case of H₂ discharges, as seen earlier, both circumstances are relevant. Concerning collision processes, in the case of the most important ion in H₂ discharge plasmas, namely, H₃⁺ elastic collision with H₂ neutrals play the most important role, unlike e.g. Ar⁺/Ar as in Ar RF discharges. Furthermore, ion conversion reactions are very important. In the case of H₃⁺, collisions with neutral H₂ start to produce H⁺ at about 10 eV and H₂⁺ at energies little above this. H₂⁺ ions, which are a minority in the bulk plasma because of their very fast collisional conversion to H₃⁺, can survive in the passage though the sheath if the ion energy is increased fast enough by the field, since the cross sections of the just mentioned reaction drops fast with the ion energy (following close a Langevin law at energies below 1 eV). At the same time, this reaction, although being the most important at low energy, does not hinder the formation of a sharp peak structure since it removes H₂⁺ ions from the plasma, instead of randomizing their velocity as in the case of elastic scattering. Above about 5 eV the most relevant channel is charge-exchange (producing thermal H₂⁺ and fast H₂) which fits well into the Wild-Koidl mechanism. While fast H₂⁺ can perform ion conversion reactions (to H⁺) above the threshold of 5.6 eV, the related cross sections is constantly below charge-exchange one by

an order of magnitude. For H^+ the highest cross section with neutral H_2 at low energy is momentum transfer with significant rotational excitation of the target, while vibrational excitation is very important in the critical energy range 10-few 100's eV. Ion conversion to H_2^+ may occur above the threshold of about 2 eV but it is not the most important process until very high energies of several hundreds eV are reached.

In this complex tableau of ion collisions and conversions, kinetic numerical models which include Monte Carlo treatment of collision processes, as discussed elsewhere in this volume, may provide insight and help interpreting experimental results of the iedf obtained through ion energy analyzers placed on the electrode surface. In particular, the model described in this chapter has been applied (Longo and Diomede 2009) to study the space-energy behavior of H^+ , H_2^+ and H_3^+ ions during their passage through oscillating fields of a RF discharge in H_2 . Concerning H^- , these ions, being negative, are trapped by the ambipolar potential in the bulk plasma, as mentioned earlier, therefore their passage through the sheath is not to be studied. The model included all the processes mentioned above with energy dependent cross section.

An application of this kind of model is to iedf tailoring. This concept arises in the field of material processing, where the effect of ions, of different species, hitting the growing substrate, is strongly dependent on the ion energy. Diomede et al. (2012) recently proposed detailed numerical modeling of a modified H_2 RF discharges where a sudden discharge voltage step is applied with different time delays to discharge on and discharge off (post-discharge) cases. In the same paper a close agreement with experimental results for the iedf of H_3^+ and H_2^+ is demonstrated. H_2^+ ion is that with the less predictable behavior, in view of its production in the sheath from other ion species. Furthermore, in Longo and Diomede (2009) it has been shown that this ion is the most sensitive to discharge asymmetry produced using double voltage following the concept proposed by Heil et al. (2008) and Donkó et al. (2009).

A sample of results is reported in Fig. 8.5 (Longo and Diomede 2009). It is clear that ions performs slowing down collisions able to concentrate the iedf around peaks, which at the same time are displaced to higher energies in the course of the fall. A leading edge of ions "following the wave" of most favorable voltage phase while skipping collision processes is seen in both cases, as well as a pronounced component of very low energy which follows the "relay model" of acceleration-collision (Golant et al. 1980). Figure 8.6 (Diomede et al. 2012), shows instead the agreement which is obtained using this model between model results and experiments, for the two cases of H_3^+ and H_2^+ . In the cited paper the features displayed by both theoretical and experimental iedfs in the two cases are related to the ion mass and collision processes.

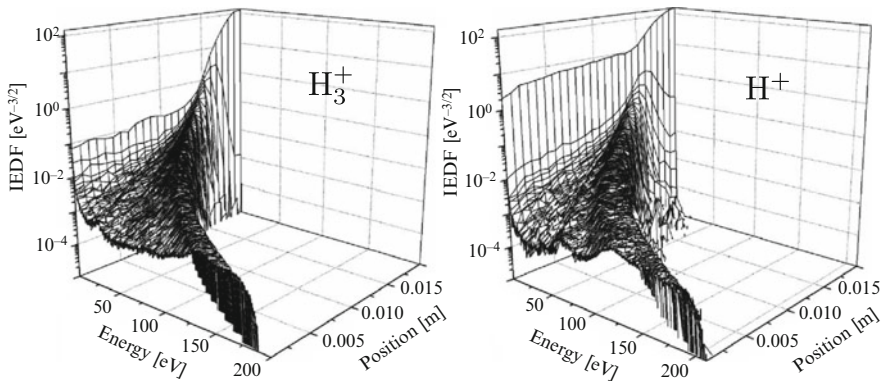


Fig. 8.5 Samples of iedf for H_3^+ (left) and H^+ (right) ions in a RF discharge as a function of energy and position, time averaged (From Longo and Diomede 2009)

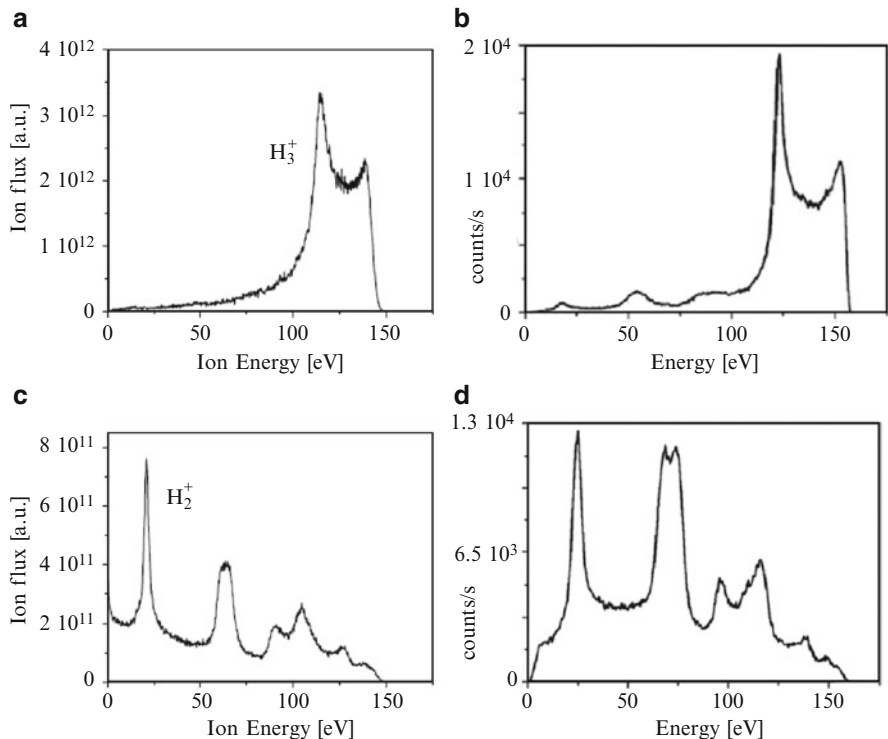


Fig. 8.6 Samples of iedf for H_3^+ , (a) and (b), and H_2^+ , (c) and (d), ions hitting the electrodes of a RF discharge and compared to experimental results (b) and (d) (O'Connell et al. 2007) (From Diomede et al. 2012)

References

- Birdsall CK (1991) Particle-in-cell charged-particle simulations, plus Monte Carlo collisions with neutral atoms, PIC-MCC. *IEEE Trans Plasma Sci* 19(2):68–85
- Birdsall CK, Langdon AB (1985) *Plasma physics via computer simulation*. McGraw-Hill, New York
- Boeuf J, Marode E (1982) A Monte Carlo analysis of an electron swarm in a nonuniform field: the cathode region of a glow discharge in helium. *J Phys D Appl Phys* 15(11):2169
- Capitelli M, Celiberto R, Caciato M (1994) Needs for cross sections in plasma chemistry. *Adv Atomic Mol Opt Phys* 33:321–372
- Capitelli M, Bruno D, Laricchiuta A (2013) *Fundamental aspects of plasma chemical physics: transport*. Springer series on Atomic, optical, and plasma physics, vol 74. Springer, New York
- Celiberto R, Janev RK, Laricchiuta A, Capitelli M, Wadehra JM, Atoms DE (2001) Cross section data for electron-impact inelastic processes of vibrationally excited molecules of hydrogen and its isotopes. *Atomic Data Nucl Data Tables* 77(2):161–213
- Chen FF, Chang JP (2003) *Lecture notes on principles of plasma processing*. Springer Science & Business Media Springer US
- Diomede P, Capitelli M, Longo S (2005) Effect of discharge voltage on capacitively coupled, parallel plate RF hydrogen plasmas. *Plasma Sources Sci Technol* 14:459
- Diomede P, Hassouni K, Longo S, Capitelli M (2007) Self-consistent modeling of the effect of wall-neutral reactions on parallel plate radio frequency discharge plasma in pure hydrogen. *IEEE Trans Plasma Sci* 35(5):1241–1246
- Diomede P, Michau A, Redolfi M, Morscheidt W, Hassouni K, Longo S, Capitelli M (2008) Fluid and kinetic models of the low temperature H₂ plasma produced by a radio-frequency reactor. *Phys Plasmas* 15(10):103505
- Diomede P, Economou DJ, Donnelly VM (2011) Particle-in-cell simulation of ion energy distributions on an electrode by applying tailored bias waveforms in the afterglow of a pulsed plasma. *J Appl Phys* 109(8):083302
- Diomede P, Longo S, Economou DJ, Capitelli M (2012) Hybrid simulation of a dc-enhanced radio-frequency capacitive discharge in hydrogen. *J Phys D Appl Phys* 45(17):175204
- Donkó Z (2011) Particle simulation methods for studies of low-pressure plasma sources. *Plasma Sources Sci Technol* 20(2):024001
- Donkó Z, Schulze J, Heil B, Czarnetzki U (2009) PIC simulations of the separate control of ion flux and energy in CCRF discharges via the electrical asymmetry effect. *J Phys D Appl Phys* 42(2):025205
- Eletskii AV (1997) Elementary processes in gases and plasmas. In: Grigoriev IS, Meilikov EZ, Radzig AA (eds) *Handbook of physical quantities*. CRC Press, Taylor & Francis, UK
- Fabrikant I, Wadhera J, Xu Y (2002) Resonance processes in e-H₂ collisions: dissociative attachment and dissociation from vibrationally and rotationally excited states. *Phys Scr* 2002(T96):45
- Fiala A, Pitchford LC, Boeuf JP (1994) Two-dimensional, hybrid model of low-pressure glow discharges. *Phys Rev E* 49:5607–5622
- Golant VE, Zhilinskii AP, Sakharov IE (1980) *Fundamentals of plasma physics*. Wiley series in plasma physics, John Wiley & Sons, New York
- Gorse C, Capitelli M, Bretagne J, Bacal M (1985) Vibrational excitation and negative-ion production in magnetic multicusp hydrogen discharges. *Chem Phys* 93(1):1–12
- Gorse C, Capitelli M, Bacal M, Bretagne J, Laganà A (1987) Progress in the non-equilibrium vibrational kinetics of hydrogen in magnetic multicusp H⁻ ion sources. *Chem Phys* 117(2):177–195
- Gorse C, Celiberto R, Caciato M, Laganà A, Capitelli M (1992) From dynamics to modeling of plasma complex systems: negative ion (H⁻) sources. *Chem Phys* 161(1):211–227
- Heil BG, Czarnetzki U, Brinkmann RP, Mussenbrock T (2008) On the possibility of making a geometrically symmetric RF-CCP discharge electrically asymmetric. *J Phys D Appl Phys* 41(16):165202

- Hockney RW, Eastwood JW (1991) Computer simulation using particles. Adam Hilger, Bristol
- JILA Database (2005) http://jila.colorado.edu/~avp/collision_data/electronneutral/ELECTRON.TXT
- Kae-Nune P, Perrin J, Jolly J, Guillon J (1996) Surface recombination probabilities of H on stainless steel, a-Si: H and oxidized silicon determined by threshold ionization mass spectrometry in H₂ RF discharges. *Surface Sci* 360(1):L495–L498
- Kawamura E, Vahedi V, Lieberman MA, Birdsall CK (1999) Ion energy distributions in RF sheaths; review, analysis and simulation. *Plasma Sources Sci Technol* 8(3):R45
- Kim YK, Rudd ME (1994) Binary-encounter-dipole model for electron-impact ionization. *Phys Rev A* 50(5):3954
- Kushner MJ (1983) Monte-Carlo simulation of electron properties in RF parallel plate capacitively coupled discharges. *J Appl Phys* 54(9):4958–4965
- Kushner MJ (2009) Hybrid modelling of low temperature plasmas for fundamental investigations and equipment design. *J Phys D Appl Phys* 42(19):194013
- Lieberman MA, Lichtenberg AJ (1994) Principles of plasma discharges and materials processing. *MRS Bull* 30:899–901
- Longo S (2000) Monte Carlo models of electron and ion transport in non-equilibrium plasmas. *Plasma Sources Sci Technol* 9:468
- Longo S (2006) Monte Carlo simulation of charged species kinetics in weakly ionized gases. *Plasma Sources Sci Technol* 15(4):S181
- Longo S, Diomede P (2009) Modeling of capacitively coupled RF plasmas in H₂. *Plasma Process Polym* 6(5):370–379
- Longo S, Capitelli M, Hassouni K (1997) The coupling of PIC/MCC models of discharge plasmas with vibrational and electronic kinetics. *J de Physique IV* C4:271
- Loureiro J, Ferreira C (1989) Electron and vibrational kinetics in the hydrogen positive column. *J Phys D Appl Phys* 22(11):1680
- O'Connell D, Zorat R, Ellingboe AR, Turner MM (2007) Comparison of measurements and particle-in-cell simulations of ion energy distribution functions in a capacitively coupled radio-frequency discharge. *Phys Plasmas* 14(10):103510
- Panarese A, Diomede P, Longo S (2013) Kinetic modelling of atom production and thermalization in CCRF discharges in H₂. *Plasma Sources Sci Technol* 22(4):045017
- Phelps A (1990) Cross sections and swarm coefficients for H⁺, H₂⁺, H₃⁺, H, H₂, and H⁻ in H₂ for energies from 0.1 eV to 10 keV. *J Phys Chem Ref Data* 19(3):653–675
- Pitchford LC, Phelps AV (1982) Comparative calculations of electron-swarm properties in N₂ at moderate *E/N* values. *Phys Rev A* 25:540
- Šimko T, Martišovič V, Bretagne J, Gousset G (1997) Computer simulations of H⁺ and H₃⁺ transport parameters in hydrogen drift tubes. *Phys Rev E* 56(5):5908
- Tskhakaya D, Matyash K, Schneider R, Taccogna F (2007) The Particle-In-Cell method. *Contrib Plasma Phys* 47(8–9):563–594
- Vahedi V, Surendra M (1995) A Monte Carlo collision model for the particle-in-cell method: applications to argon and oxygen discharges. *Comput Phys Commun* 87(1–2):179
- Wild C, Koidl P (1991) Ion and electron dynamics in the sheath of radio-frequency glow discharges. *J Appl Phys* 69(5):2909–2922

Chapter 9

Self-Consistent Kinetics of Molecular Plasmas: The Nitrogen Case

Nitrogen containing plasmas are continuously investigated due to their importance in laboratory and atmospheric plasma conditions. Since the pioneering work by Nighan (1970), showing the effect of Boltzmann vibrational distributions on the form of the electron energy distribution functions (eedf), a lot of theoretical works appeared in the literature to show the connection between the kinetics of excited states and the eedf under different discharge and post-discharge conditions. The first studies were dedicated to the construction of a time-dependent Boltzmann equation coupled to a vibrational kinetics to quantify the effect of second-kind electron vibrational collisions on eedf (Cacciatore et al. 1982). This code was then improved by adding a kinetics of the most important electronic states of nitrogen ($A^3\Sigma_u^+$, $B^3\Pi_g$, $C^3\Pi_u$) to understand the role of second-kind collisions between cold electrons and electronically excited states on structuring eedf (Gorse et al. 1988; Capitelli 1986; Capitelli et al. 2000; Nagpal and Ghosh 1990, 1991). A parallel effort was done by the Lisbon group, basically developing a stationary code for getting similar informations and applying their refined codes to many non equilibrium conditions (Loureiro and Ferreira 1986; Loureiro et al. 1990, 2011; Loureiro 1991). Russian groups (Dyatko et al. 1993, 2002, 2003, 2010; Kosyai et al. 1992; Son 1990; Gordiets et al. 1988) also performed very interesting studies on the coupling of kinetics and eedf emphasizing the experimental aspects and trying to estimate the electric field necessary to sustain the discharge, a point also considered by the Lisbon group. Despite the enormous efforts made by the different groups in the development of accurate models, the large number of elementary processes involving electron-molecule and heavy-particle collisions still require a profound reconsideration especially for the dependence of elementary processes on vibrational quantum number. Moreover the electronically excited state kinetics is based on rate coefficients from semi-empirical approaches which can hopefully yield quantities accurate to an order of magnitude.

Nowadays a lot of work is being made on the VT rates for atom-diatom energy exchange $N-N_2(v,j)$ and dissociation processes (Esposito and Capitelli 1999, 2006; Esposito et al. 2006a; Laganà et al. 1987; Garcia and Laganà 1997; Caridade et al. 2010a; Galvão and Varandas 2011; Galvão et al. 2013, 2014; Wang et al. 2003b; Panesi et al. 2013) as well as on eV rates¹ (Laporta et al. 2012, 2014), while VV rates are continuously updated (Macheret and Adamovich 2000; Caciato et al. 2005; Lino da Silva et al. 2009; Adamovich 2014) after the pioneering work by Billing (Billing and Fisher 1979; Billing 1982, 1986).

These last studies, while improving rate coefficients of elementary processes important for the coupled kinetics, warn us also on the number of vibrational levels to be considered in the N_2 vibrational kinetics. In particular the large majority of plasma chemical codes consider 45 levels in the vibrational ladder, while the recent dynamics studies consider the number of vibrational levels ranging from 58 to 68 depending on the used PEC, introducing a new problem in the kinetics (Armenise and Esposito 2015; Capitelli et al. 2012).

In this chapter we will report the most significative results obtained by our group from the first paper on non-equilibrium vibrational kinetics appeared about 40 years ago (Capitelli et al. 1977) to the more recent ones.

9.1 Database of N_2 Processes

The knowledge on elementary processes constructed exploiting the modern accurate approaches in quantum molecular dynamics can significantly affect the predictive capability of kinetic models, allowing to conduct numerical experiments that not only give a reliable estimation of macroscopic plasma parameters, but also shed light on the collisional mechanisms at microscopic level. A number of different open-access web-databases are nowadays available (LXcat 2015; ALADDIN 2013; GASPAR 2013; NIFS 2013), where dynamical information has been collected and shared with the modeling community and, due to the present asserting of the state-to-state kinetics, also state-specific cross sections and rate coefficients of elementary processes involving ground and excited chemical species, with resolution on the electronic, vibrational and rotational degrees of freedom (Phys4Entry 2013; STELLAR 2013).

For N_2 the investigation on the dynamics involving vibrationally excited molecules and the processes responsible for the vibrational pumping/de-activation mechanisms, including the dissociative/recombination channels, have been quite extensive. As for the resonant vibrational excitations, promoted by low-energy electrons, the cross sections have been recently recalculated and the main results reported in Chap. 1. However at higher collision energies different channels open

¹The vibrational excitation processes, known as eV processes in the plasma modeling community, correspond to RVE discussed in Chap. 1.

and electron-impact induced dissociation through electronically excited states could be considered the relevant in the kinetics, either by direct or by predissociative mechanisms. Cosby (1993) gave experimental evidence of the large predissociation branching ratio in the vibronic excitation of singlet terms in the nitrogen energy diagram. Theoretical vibrationally-resolved cross sections were obtained, in the frame of the semiclassical Gryzinski method, for a number of excitation transitions ($(X^1\Sigma_g^+, v) \rightarrow a^1\Pi_g, v' > 6; b^1\Pi_u; b'^1\Sigma_u^+; c^1\Pi_u; c'^1\Sigma_u^+; o^1\Pi_u; B^3\Pi_g, v' > 12; C^3\Pi_u, v' > 4$) involving both triplets and singlets and, in a farther step, combined with predissociation probability for the derivation of a global dissociative cross section (Capitelli et al. 2001; Capitelli and Celiberto 1998). The enhancement of the cross section absolute value for excitations initiated from vibrationally excited molecules, accompanied by the lowering of the process threshold in the low-energy region, both contribute to increase the global dissociation rate. The satisfactory agreement with experimental results (Cosby 1993), restricted to the $v=0$ case, can be appreciated in Fig. 9.1.

The N-N₂ collisional dissociation and energy transfer, reported in Chap. 2, represent also relevant channels, contributing to determine the shape of the vibrational distribution. In this case assessing the accuracy of the QCT dataset goes through the comparison with theoretical results, obtained following the dynamics on accurate ab-initio PESs, able to describe with higher accuracy both the energetics and the topology of the surface in proximity of the transition state with respect to the phenomenological LEPS adopted in the past (Laganà et al. 1987). Rotationally averaged dissociation and VT rate coefficients, for mono-quantum de-excitations, $v \rightarrow v - 1$, in N-N₂ collisions, assuming a Boltzmann distribution for rotational

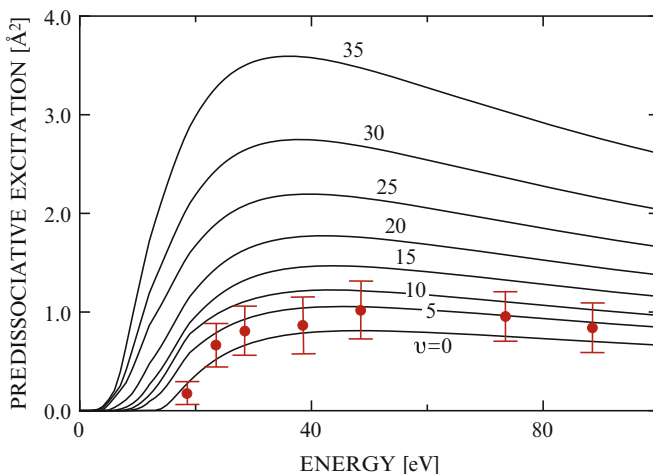


Fig. 9.1 State-specific global predissociation cross section as a function of collision energy for selected values of the initial vibrational quantum number (Capitelli et al. 2001; Capitelli and Celiberto 1998; Phys4Entry 2013), compared with experimental results for $v=0$ (markers) (Cosby 1993)

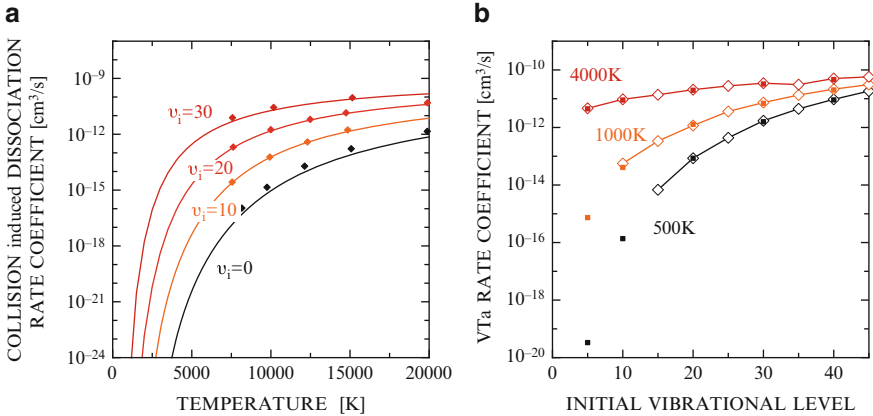


Fig. 9.2 (a) Rate coefficients for dissociation of N₂ induced by N collisions as a function of temperature for different initial vibrational levels (*solid lines*) (Esposito and Capitelli 1999, 2006; Phys4Entry 2013) compared with results obtained with QCT dynamics on the accurate N₃ PES (markers) (Bourdon et al. 2008). (b) Rate coefficients for mono-quantum de-excitations in N-N₂ collisions as function of the initial vibrational quantum number for selected values of temperature (*close markers*) (Esposito et al. 2006b; Esposito and Capitelli 2006; Phys4Entry 2013) compared with results by Laganà et al. (1996) on the LEPS (Laganà et al. 1987) (*open markers and lines*)

levels at translational temperature, are shown in Fig. 9.2 (Esposito and Capitelli 2006). The temperature profile of collision-induced dissociation rates for selected values of the initial N₂ vibrational level satisfactorily compares with QCT results obtained at NASA Ames with the ab initio PES developed by Wang et al. (2003a, 2004) and, as expected, the vibrational profiles of mono-quantum de-excitation rate coefficients, displayed for selected temperatures in Fig. 9.2b, nicely agree with results by Laganà et al. (1996) calculated with the same PES (Laganà et al. 1987). Recently new exchange and non-reactive energy transfer rate coefficients have been obtained, in the frame of the QCT method, by Caridade et al. (2010b) on a new ab initio PES, however considering only the first vibrational levels, thus limiting the comparison.

Finally, in Fig. 9.3 the vibrational dependence of the VV and VT energy transfer exothermic mono-quantum processes in N₂-N₂ collisions is displayed, comparing different approaches, i.e. the forced-harmonic oscillator (FHO) method, a semiclassical non-perturbative approach that allows analytical solutions for the process probability, and the accurate close-coupling method by Billing and Fisher (1979). The results were fitted by a suitable analytical expression for mono-quantum exothermic processes (Colonna et al. 2008). Inspection of Fig. 9.3 clearly show that VT_M energy transfers govern the high temperature region and are more efficient than VV for higher vibrational levels, regardless the temperature value. It should be pointed out that recently complete sets of rates, in a wide temperature range, for VT_M (mono- and multi-quantum transitions), for N₂-N₂ as well as for different

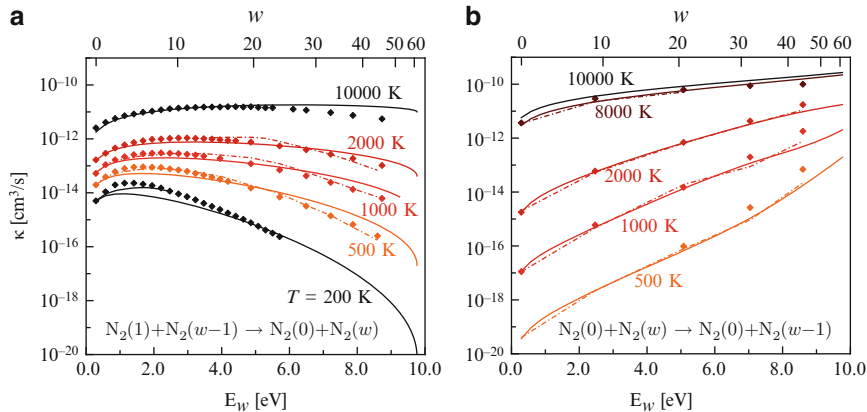


Fig. 9.3 (a) VV exothermic ($1,w-1 \rightarrow 0,w$) in N_2 - N_2 collisions rate coefficients as a function of final vibrational excited level. (b) VT_M mono-quantum de-excitation rates in N_2 - N_2 collisions as a function of initial vibrational level at different temperatures. (Solid line) (Colonna et al. 2008), (markers) FHO results (Adamovich et al. 1998), (dashed-dotted lines) semiclassical method (Billing and Fisher 1979)

collisional pairs, have been obtained with FHO method (Lino da Silva et al. 2009) and are available through the web-access DB (STELLAR 2013), these results accounting for the role of vibrationally excitation of both N_2 molecules.

9.2 Excited State Kinetics and eedf Under Discharge Conditions

In this section we want to present peculiar results describing the coupling between eedf and kinetics of excited states under discharge and post-discharge conditions. The time-dependent Boltzmann equation is coupled to the vibrational kinetics and the kinetics of electronically excited states of N_2 (in particular the states $A^3\Sigma_u^+$, $B^3\Pi_g$, $C^3\Pi_u$). Details of the considered elementary processes and the sources of cross sections and rates can be found in Caciato et al. (1982) and Gorse and Capitelli (1987). The vibrational ladder contained 45 levels, the last one miming the dissociation process.

The discharge results, here presented, have been obtained by fixing the gas temperature ($T = 300\text{ K}$), the pressure (3 Torr), the electron density (10^{10} cm^{-3}) and the reduced electric field ($E/N = 3 \times 10^{-16}\text{ V cm}^2$). As initial conditions at time $t = 0$ all vibrational concentration was put in the $v = 0$ level, while the initial concentration of electronic states and of nitrogen atoms was considered null. The initial eedf was that one corresponding to the *cold gas* approximation, i.e. depending only on the fixed E/N value.

Fig. 9.4 Temporal evolution of N_2 vibrational distribution under discharge conditions ($E/N = 3 \cdot 10^{-16} \text{ V cm}^2$, $T = 500 \text{ K}$, $p = 3 \text{ Torr}$, $n_e = 10^{10} \text{ cm}^{-3}$, t_d : residence time in the discharge) (From Capitelli and Gorse 1990)

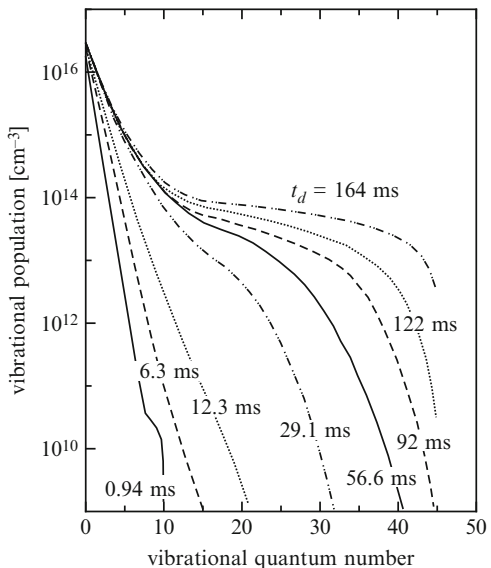


Figure 9.4 (Capitelli and Gorse 1990) shows the time evolution of the vibrational distribution starting from $t = 0.94$ to 164 ms. The reported curves are typical of the interplay between eV processes that pump vibrational energy on the low-lying vibrational levels of N_2 and the redistribution of these quanta by VV energy transfer collisions. In these conditions the role of VT processes promoted by molecules and formed atoms, considered having the same rates, is small. As a consequence we can observe at the quasi-stationary conditions ($t = 164$ ms) a long plateau created by the VV processes and a small tail at the gas temperature created by VT ones. These distributions were able to promote the dissociation and ionization processes through the so called pure vibrational mechanisms. On the other hand Fig. 9.5a, b shows the time evolution of eedf due to the second-kind collisions which are able to transport cold electrons to high energy portion of eedf. In particular Fig. 9.5a reports the effect of second-kind collisions from both vibrational (SVC) and electronic states (SEC), while Fig. 9.5b reports the eedf in the presence only of second-kind collisions from vibrational states. Comparison of the two figures can be taken as an indication of the importance of the two types of collisions in affecting eedf. In particular SVC strongly enlarge eedf up to approximately 10 eV, while SEC act from 10 eV on. These effects of course can be modified under different plasma conditions as emphasized in Chap. 5. The peculiar characteristics reported in the previous figures, confirmed by other researchers, can be recovered also in recent studies which make use of more refined sets of state-to-state cross sections as well a more refined kinetics involving electronically excited states of nitrogen molecules. As an example Fig. 9.6 (Capitelli et al. 2013) shows the time evolution of vdf and eedf for N_2 discharge characterized by the different kinetics represented in Tables 1 and 2 of the same Capitelli et al. (2013). In this case however we have solved also

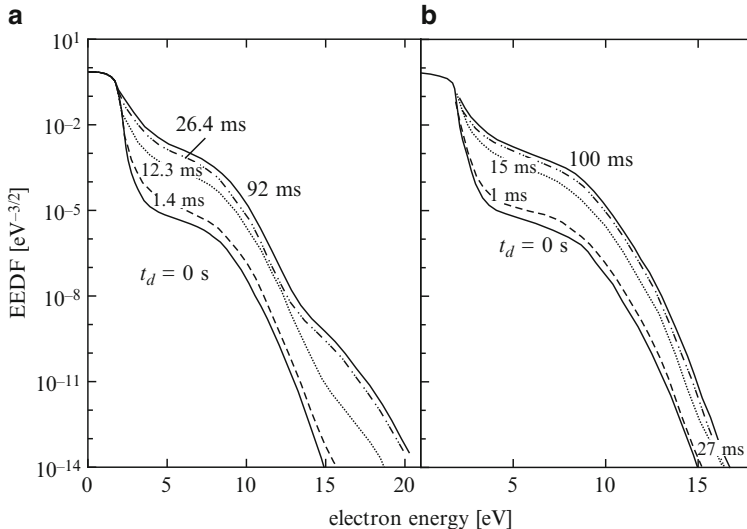


Fig. 9.5 Temporal evolution of eedf of pure N_2 under discharge conditions ($E/N = 3 \cdot 10^{-16} \text{ V cm}^2$, $T = 500 \text{ K}$, $p = 3 \text{ Torr}$, $n_e = 10^{10} \text{ cm}^{-3}$, t_d : residence time in the discharge), (a) with SEC and SVC (b) with SVC only (From Capitelli and Gorse 1990)

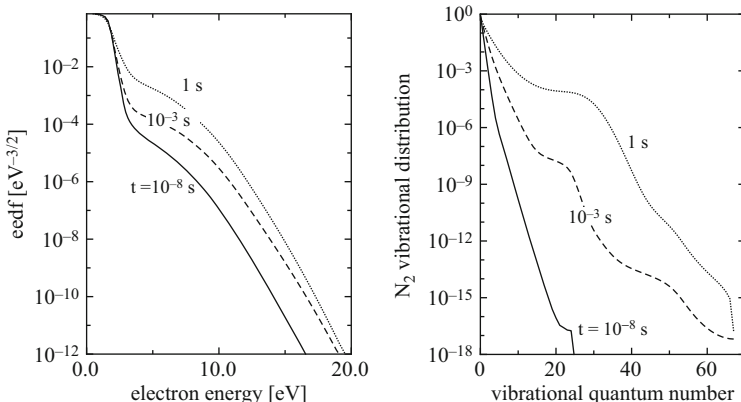
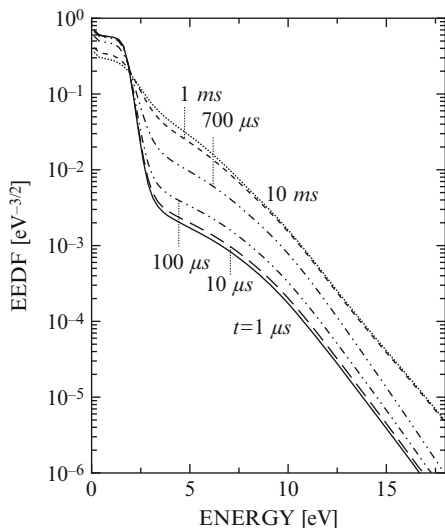


Fig. 9.6 (Left) eedf and (right) vdf in the N_2 discharge for a reduced electric field $E/N = 30 \text{ Td}$ calculated according to a *full* model including a complete set of inelastic and superelastic cross sections, including vibrationally excited states (From Capitelli et al. 2013)

an ionization kinetics with an initial electron density of about 10^{12} cm^{-3} ending at the end of evolution to $n_e(t = 1 \text{ s}) = 5 \times 10^8 \text{ cm}^{-3}$. Qualitatively the results follow those previously described, i.e. an increase of vdf and eedf due to the mutual strong coupling of the two distributions. We can note that at $t = 1 \text{ s}$ the use of a 68 level ladder is such to anticipate the tail in vdf due to the increased importance of VT rates involving atomic nitrogen. Figure 9.7 (Capitelli et al. 2012) shows the

Fig. 9.7 Vibrational population distribution of N_2 ground state for different time-shots in the discharge phase (From Capitelli et al. 2012)



time evolution of eedf for the same conditions of the previous figures with the only exception of E/N value (i.e. $E/N = 60 \text{ Td}$). In this case the time evolution of electron density is much more smooth than in the previous case starting from $5 \times 10^{11} \text{ cm}^{-3}$ ($t = 0$) to about $6 \times 10^{11} \text{ cm}^{-3}$ ($t = 0.1 \text{ s}$). These conditions generate much higher concentrations of vibrationally and electronically excited states with strong consequences on eedf. Again the role of SVC and SEC in affecting eedf is evident.

The results reported in Figs. 9.6–9.7 have been obtained by imposing a gas temperature of 1,000 K, which accelerates the VT processes decreasing the length of plateau in the vdf. This point can be understood in Fig. 9.8 (Capitelli et al. 2013), where the vibrational distributions obtained at a fixed molar fraction of electrons ($\chi_e = 10^{-6}$) and similar other conditions ($p = 5.6 \text{ Torr}$, $E/N = 60 \text{ Td}$) are reported for $T = 500 \text{ K}$ and $1,000 \text{ K}$. We can see that the length and the magnitude of plateau strongly increases at low temperature, presenting however an anticipation of the tail with respect to the 45 ladder model.

In Fig. 9.9 (Capitelli et al. 2014) shows that after 10^{-7} s the contribution from $v = 0$ and the global one are approximately the same (*cold gas approximation*, i.e. a condition where eedf depends only on E/N at fixed gas temperature). Then the two quantities start diverging, due to the contribution of vibrationally excited molecules in affecting the dissociation process, as well as the eedf (*hot gas approximation*, i.e. eedf depends not only on E/N but also on the population of vibrational and electronic states through the action of the relevant superelastic collisions (Loureiro et al. 1990; Capitelli et al. 2013)). Both the $v = 0$ contribution and the global one reach a stationary condition in times of the order of $0.1\text{--}1 \text{ s}$.

The state-specific kinetic rates for electron-impact induced resonant and dissociative excitation channels of N_2 are displayed at two different points in the temporal evolution, corresponding to the *cold gas approximation* and to the stationary

Fig. 9.8 vdf at $t = 0.1$ s in the N_2 discharge for a reduced electric field $E/N = 60$ Td and fixed electron molar fraction $\chi_e = 10^{-6}$, calculated for $T = 500$ K (dashed line) and $1,000$ K (solid line) (From Capitelli et al. 2013)

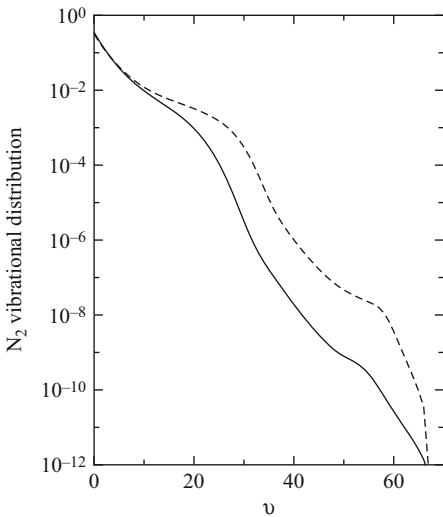
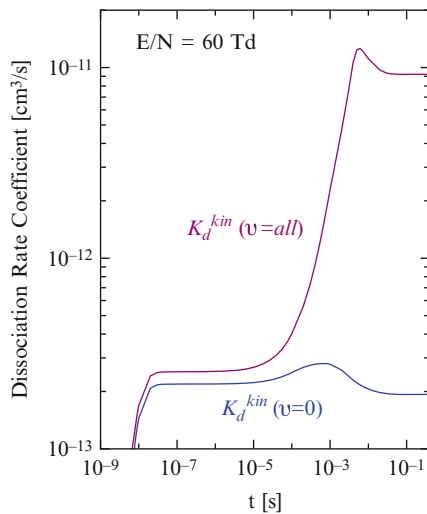


Fig. 9.9 Temporal evolution of the dissociation rate from $v = 0$ and the global one from all vibrational levels, at $E/N = 60$ Td and $T = 1,000$ K (From Capitelli et al. 2014)



condition (Figs. 9.10 and 9.11). Large deviations occur in the relevant rates as consequence of superelastic collisions in affecting the eedf.

The stationary values of the global dissociation rates for different channels are reported as a function of E/N in Fig. 9.12 and compared with the experimental rates by Polak et al. (1975). In this case the role of vibrationally excited states is well evident bringing the theoretical global rates in the same scale of experimental ones for $E/N > 60$ Td. Theoretical and experimental results however do not agree for $E/N < 50$ Td. In this last case the theoretical results not only are lower than the experimental ones but also do not reproduce the flat behavior of the experimental dissociation rate as a function of E/N . A flat behavior is indeed shown by quantity $K_d^{(\text{ulPVM})}$ as a function of T_e (i.e. to a first approximation as a function of E/N).

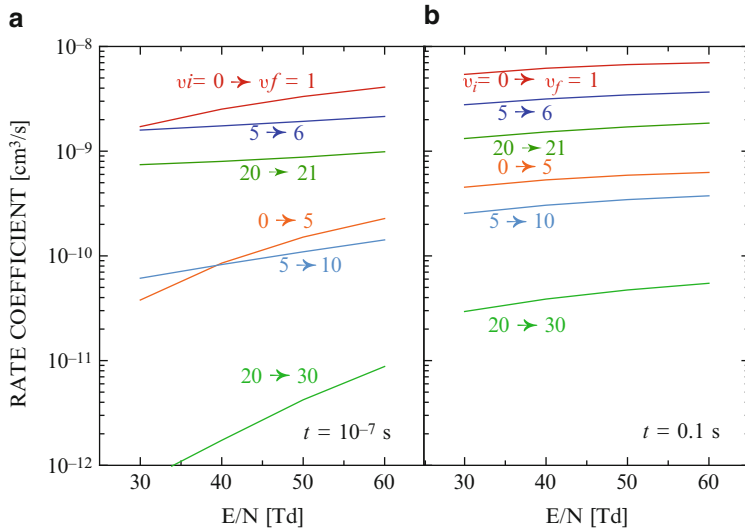


Fig. 9.10 Kinetic rate coefficients as a function of E/N , for selected mono and multi-quantum resonant vibrational excitations in $e\text{-N}_2(v)$ collisions, from cross sections by Laporta et al. (2012). (a) $t = 10^{-7}$ s and (b) $t = 10^{-1}$ s

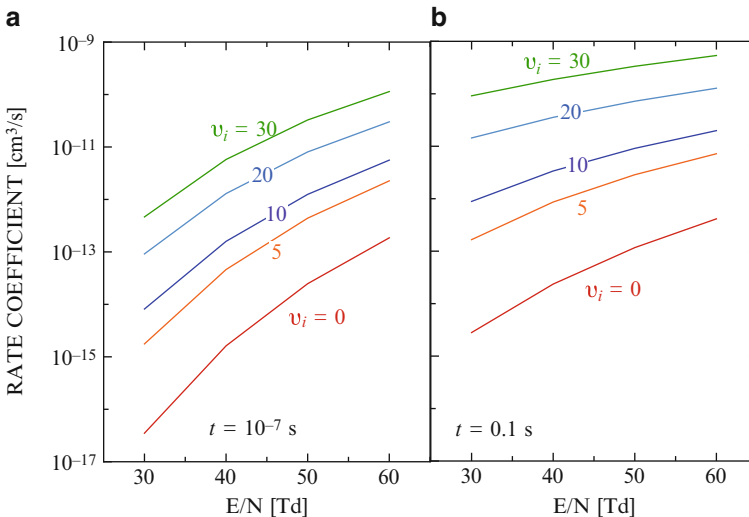


Fig. 9.11 Kinetic rate coefficients as a function of E/N , for dissociative excitation in $e\text{-N}_2(v)$ collisions, from cross sections by Capitelli et al. (2001) and Capitelli and Celiberto (1998). (a) $t = 10^{-7}$ s and (b) $t = 10^{-1}$ s

$K_d^{(\text{ulPVM})}$ is defined as

$$K_d^{(\text{ulPVM})} = \frac{1}{v_{\max}} \sum_{v=1}^{v_{\max}} v k_{\text{ev}}(0 \rightarrow v) \quad (9.1)$$

where $k_{\text{ev}}(0 \rightarrow v)$ is the rate coefficient of the $0 \rightarrow v$ excitation process and v_{\max} the number of vibrational levels in the N_2 ground state ladder. This quantity can be considered as an upper limit to the pure vibrational mechanism and more than two orders of magnitude higher than the experimental results, as reported in Fig. 1 of Capitelli et al. (2014). Moreover the old PVM rates reported in Cacciatore et al. (1982) for $E/N = 30$ and 60 Td seem to fill the gap between theoretical and experimental values reported in Fig. 9.12.

Going beyond the possibility of the dissociation from the last bound level of nitrogen we could assume a vibrational mechanism (Guerra et al. 2003, 2004) involving vibrationally and electronically excited molecules, specifically

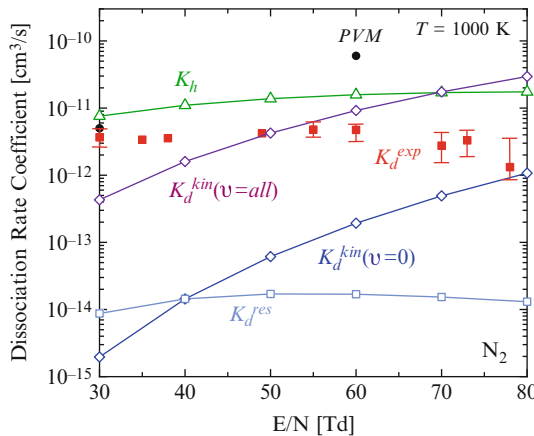
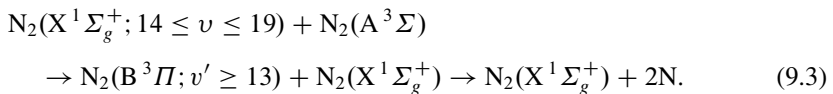
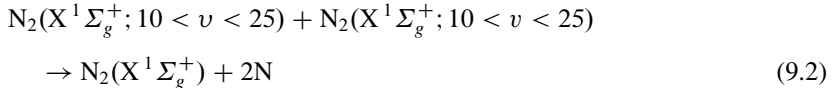


Fig. 9.12 Nitrogen dissociation rates as a function of reduced electric field E/N , at $p = 5.6$ Torr and $T = 1,000$ K, calculated according to different models. (close squares) experimental dissociation rate with error bars (Polak et al. 1975), (open diamonds) results from kinetics with dissociation from $v = 0$ and from all vibrational levels ($t = 10^{-1}$ s in the time evolution) (Capitelli et al. 2014), (close circles) pure vibrational mechanism PVM (Capitelli and Dilonardo 1977, 1978; Capitelli et al. 1980), (open triangles) total rate coefficient of the heavy-particle impact dissociation processes, (9.2) and (9.3), (open squares) rate coefficient of the resonant dissociation process, (9.6) (From Capitelli et al. 2014)

The global rate coefficients of these processes have been calculated considering the population of individual vibrational levels in the range reported in (9.2), (9.3) and the population of $\text{N}_2(\text{A}^3\Sigma)$ and using the corresponding values $k_d^{vv} = 3.5 \cdot 10^{-15} \text{ cm}^3/\text{s}$ and $k_d^{vA} = 4.5 \cdot 10^{-11} \exp(-1765/T) \text{ cm}^3/\text{s}$ as reported in Guerra et al. (2003)

$$\begin{aligned} K_d^{vv} &= \frac{k_d^{vv}}{\chi_e N^2} \sum_{v=11}^{24} \sum_{w=11}^{24} N_v N_w \\ K_d^{vA} &= \frac{k_d^{vA} N_A}{\chi_e N^2} \sum_{v=14}^{19} N_v \\ K_h &= K_d^{vv} + K_d^{vA} \end{aligned} \quad (9.4)$$

where N_v , N_w and N_A are the populations of the v, w vibrational levels and of the $\text{N}_2(\text{A}^3\Sigma)$ electronic state of the N_2 molecule respectively, N is the total number density of N_2 and $\chi_e = 10^{-6}$ is the electron molar fraction.

It should be noted that, in the present conditions, mechanism (9.2) prevails on (9.3). This mechanism, first proposed by Guerra et al. (2003) and later used by Dyatko et al. (2010) and Capitelli et al. (2013), involves the intermediate portion of vdf as well as of metastable nitrogen molecules instead of the last vibrational level as in the original PVM model.

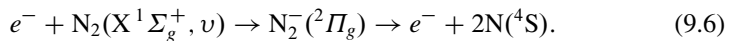
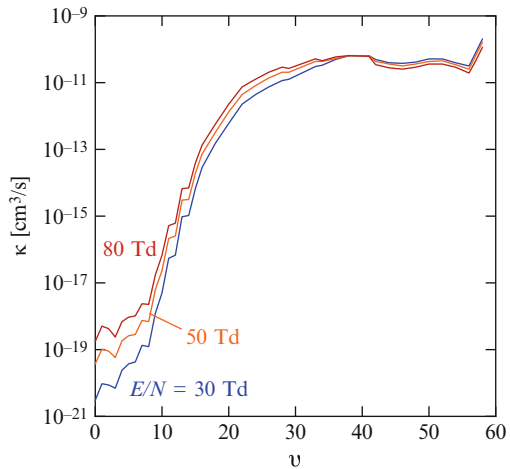
The rate coefficient K_h at stationary conditions ($t = 0.1\text{--}1 \text{ s}$), divided by the electron molar fraction $\chi_e = 10^{-6}$ to obtain a pseudo-electron impact rate coefficient, is reported in Fig. 9.12 and compared with the different models and with the experimental results. In this case the rates are in qualitative agreement with the experimental ones in the whole E/N range. In particular they fill the gap between experimental values and theoretical ones based on electron impact dissociation rates for $E/N < 50 \text{ Td}$. Note that the flat behavior of K_h is due to the fact that the quasistationary vibrational distributions, calculated with the complete vibrational and electronically excited state kinetics, including the VT energy transfer and neglecting surface processes, and N_A metastable concentration shows a much weaker dependence on the E/N compared to K_d^{kin} and $K_d^{\text{kin}}(v=0)$ as can be appreciated in Fig. 9.12. These last quantities, in fact depend on the high-energy region of eedf, which is more affected by E/N values (Capitelli et al. 2014).

In Fig. 9.12 we have also reported the global dissociation rate due to the resonant dissociation mechanism described by (9.6) which is calculated using the following average over the vibrational distribution

$$K_d^{\text{res}} = \sum_{v=0}^{v_{\text{max}}} k_d^{\text{res}}(v) \frac{N_v}{N_{\text{tot}}} \quad , \quad (9.5)$$

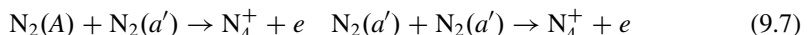
where $k_d^{\text{res}}(v)$ are the vibrationally resolved resonant dissociation rate coefficients, i.e. the process

Fig. 9.13 vibrationally resolved rate coefficients for the resonant dissociation process described by (9.6), calculated using the eedf at steady state at different values of the reduced electric field E/N , at $p = 5.6$ Torr and $T = 1,000$ K (From Capitelli et al. 2014)

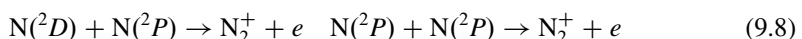


A sample of these rates have been reported in Fig. 9.13 at different E/N values as a function of vibrational quantum number, showing that the resonant dissociation rates are important only for high-lying vibrational levels, the $\nu = 0$ level being insignificant for the process. The global resonant dissociation rate is reported in Fig. 9.12. The new mechanism, while presenting a flat dependence on E/N , shows however very low values not competitive with the other mechanisms. It should be noted that the K_d^{res} increases by an order of magnitude if use is made of a Maxwell eedf with electron temperature T_e obtained by the average energy $\bar{\varepsilon} = \frac{3}{2}k_B T_e$ of the actual eedf.

Similar considerations can be made for the ionization process, the ionization rates calculated including all vibrational ladder exceeding the $\nu = 0$ contribution up to a factor 5 (Capitelli et al. 2013). This increase is not sufficient to explain the ionization rates under many experimental conditions, so that one is obliged to introduce other processes involving vibrationally excited states (Polak et al. 1975; Caciato et al. 1982) as well as electronically excited states. A recent work (Dyatko and Napartovich 2010) suggests in addition to associative ionization for nitrogen molecular states, i.e.



the same process involving atomic metastable states



It is worth noting that $N(^2D, ^2P)$ can also play a role in affecting the eedf under expansion conditions (Colonna and Capitelli 2001). Moreover the recent dynamic

calculations for the N(²D)-N₂(v) collisional system (Galvão et al. 2013, 2014) indicate a possible importance of this process in the N₂ vibrational kinetics.

The main results obtained in this section can be summarized as follows:

- The coupling between vdf and eedf generates distribution functions very far from the equilibrium ones
- The use of the 68 level ladder seems to rule out the possibility of pure vibrational mechanisms, involving the last vibrational levels of N₂, in the dissociation and ionization processes
- The intermediate portion of vdf can help the dissociation processes through electron-transitions from vibrationally excited states as well as from heavy-particle collisions involving vibrationally excited states
- Metastable states can be important for both dissociation and ionization.

Future improvements of these results should take into account a revisit of heavy-particle dissociation and ionization processes.

To validate these results one should compare them with dedicated experiments. Unfortunately the experimental situation for N₂ did not progress too much from the situation presented in different books. Still now a clear indication of the existence of plateaux in nitrogen discharges does not exist at least at the level of our knowledge of the experimental vibrational distributions of carbon monoxide system under discharge and post-discharge conditions (see Chap. 7). In this connection we want to emphasize that the previous model developed (Cacciatore et al. 1982) were able to reproduce to a satisfactory accuracy the experimental CARS distributions obtained by Massabieaux et al. which unfortunately sampled only the first 12 vibrational levels of nitrogen (Massabieaux et al. 1987).

The recent review paper by Adamovich (Lempert and Adamovich 2014) reports several experimental determination of vibrational distributions of N₂, however limited to the low-lying vibrational levels.

9.3 Excited State Kinetics and eedf Under Post-discharge (Afterglow) Conditions

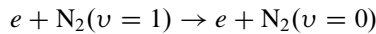
The post-discharge conditions of nitrogen plasmas have been studied by different authors (Gorse and Capitelli 1987; Gorse et al. 1988; Guerra et al. 2007; Loureiro et al. 2011; Dyatko et al. 2002, 2003) due to their importance in the plasma-surface remote interaction. Nowadays it becomes also important in the so called *plasma-assisted* combustion when a high voltage is applied to an atmospheric combustion system for a short time followed by a post-discharge period to create important precursors for the combustion ignition.

The coupling between excited state kinetics and eedf strongly depends on the initial condition assigned to the post-discharge regime. As a general rule the effect of second-kind collisions can be hidden by the presence of large vibrational

distribution functions which are able to maintain high electron temperatures on eedf. This situation occurs for continuous discharges at high electron-density and long residence times. On the other hand pulsed discharges with very small time duration represent an environment poor of vibrationally excited states and rich of electronically excited states, i.e. an environment which can generate a lot of structures in eedf. These qualitative considerations can be better understood by quantifying the time (τ) necessary to form a well-developed vibrational distribution function, which can be estimated by the simple equation

$$\tau = (n_e k_{1,0})^{-1} \quad (9.9)$$

where n_e is the electron density and $k_{1,0}$ is the rate coefficient of the process



Taking into account that under many discharge conditions $k_{1,0} \approx 10^{-8} \text{ cm}^3/\text{s}$ we can calculate τ at different electron densities ranging from 10^{-3} to 10^{-6} s for $n_e = 10^{11}$ and 10^{14} cm^{-3} . These characteristic times should be taken into account in examining the reported results.

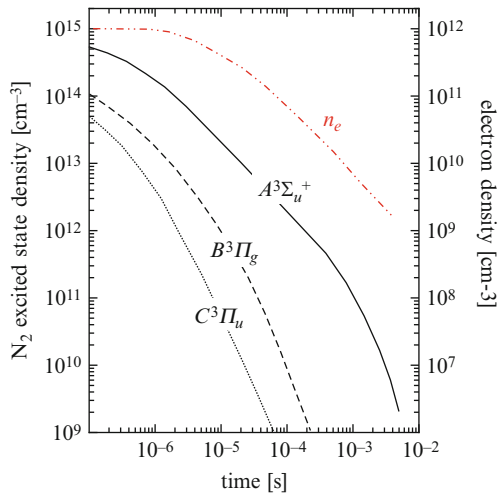
9.3.1 Short Time Pulsed Discharges

A lot of calculations have been performed on the coupling of eedf and excited state populations in the post-discharge regime of short time pulsed discharges. Usually these calculations are reported for high pressure situations; in these last years this subject increases its importance on plasma assisted combustion technology. The results we report have been obtained under experimental conditions from GTE (General Telephone & Electronics Corporation). Briefly an high pressure (300 Torr) nitrogen discharge with a current density of about 100 A/cm^2 is sustained for approximately 200 ns. The following state densities at the end of discharge at 300 Torr are estimated from a Boltzmann calculation for the rate coefficients assuming a nominal E/N value of 300 Td:

$$\begin{aligned} N_2(A^3\Sigma_u^+) &= 5 \times 10^{14} \text{ cm}^{-3} \\ N_2(B^3\Pi_g) &= 1 \times 10^{14} \text{ cm}^{-3} \\ N_2(C^3\Pi_u) &= 5 \times 10^{13} \text{ cm}^{-3} \\ T_v &= 400 K \quad n_e = 10^{12} \text{ cm}^{-3} \end{aligned}$$

The low vibrational temperature is due to the fact that length of pulse 200 ns is much lower than the eV relaxation time 10^{-4} s . Therefore we should expect a strong coupling of eedf and concentration of metastable state (in particular the A state) in the afterglow.

Fig. 9.14 The solid lines show the temporal evolution of the concentration of the electronically excited N_2 states $A^3\Sigma_u^+$, $B^3\Pi_g$ and $C^3\Pi_u$ and the electron density in the afterglow (From Gorse and Capitelli 1987)



This is the case as shown in Figs. 9.14–9.15a, b (Gorse and Capitelli 1987). In particular Fig. 9.14 reports the concentrations of electrons and metastable states in the afterglow regime showing a large decrease of all concentrations with the time. Figure 9.15a shows the corresponding behavior of eedf which presents an hole in the energy range 2–4 eV due to the lack of inelastic processes in this energy range as well as the lack of superelastical vibrational collisions. On the other hand it is well evident the role of the superelastical electronic collisions from the A state in forming the maximum at 6 eV, which decays with the time. The effect of second-kind collisions is well evident comparing the results of Fig. 9.15a with the corresponding ones of Fig. 9.15b, the last obtained without considering superelastical collisions. At early times the eedf preserves the hole in the eedf which disappears at $t = 10^{-7}$ s. It should be noted that the hole in the eedf has been experimentally observed by Bazhenov et al. in steady hollow-cathode glow discharge in N_2 (Bazhenov et al. 2001).

Finally it should be noted that the results reported in Fig. 9.15 are strongly dependent on the eV rates, as recently shown by Colonna et al. (2015).

9.3.2 Nitrogen Afterglow Following Continuous Discharges

The second example we consider has been recently presented in Guerra et al. (2007) and Loureiro et al. (2011), by considering the afterglow of nitrogen excited by a discharge operating at the stationary conditions in a pyrex tube of diameter 0.8 cm ($p = 2$ Torr, $T = 1,000$ K), with a corresponding E/N value of 135 Td. The estimated electron density in the discharge is $5 \times 10^{11} \text{ cm}^{-3}$ and the calculated vibrational temperature is very high, i.e. 21,000 K. Under these conditions one should expect that a strong role of vibrational superelastical collisions in affecting the low-energy

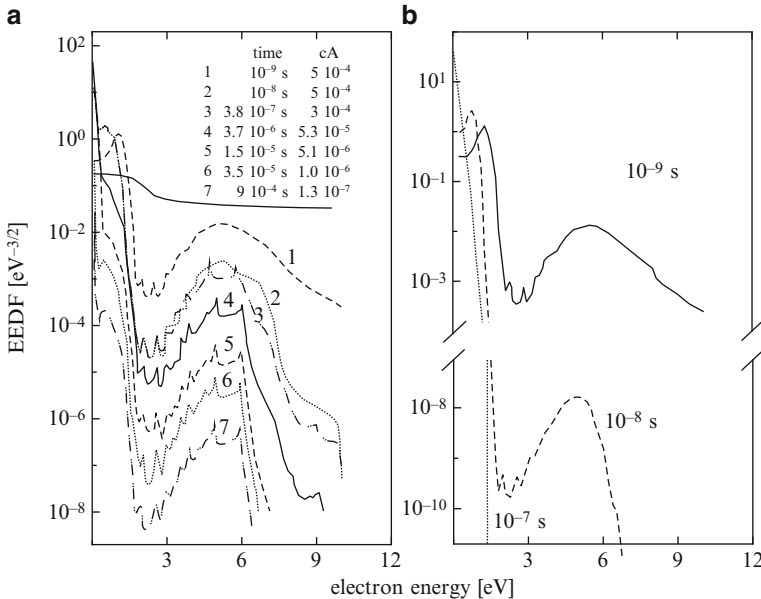


Fig. 9.15 Electron energy distribution functions at various times in the afterglow including (a) and neglecting (b) the superelastic collisions (From Gorse and Capitelli 1987)

part of eedf and the small role of superelastic collisions from the metastable states of nitrogen in affecting eedf. This is indeed the case as can be understood by looking at Fig. 9.16, where it is shown the time evolution of eedf in the afterglow regime starting at $t = 0$ from a well developed eedf created in the discharge. We can see that eedf is rapidly depopulated at earlier instants $t > 10^{-7}$ s due the inelastic losses, while for times $t > 10^{-6}$ s the eedf attains a quasistationary regime in the range 0.3–3.8 eV due to the compensation of inelastic and superelastic eV collisions (see also Gorse et al. 1988; Capitelli and Gorse 1990).

On the other hand Fig. 9.17 reports the time evolution of vibrational distributions of N₂ in the afterglow regime for conditions not too far from those of the previous case. We can see that the vdf in the afterglow start presenting the plateau due to VV up pumping regime only after $t > 10^{-3}$ s, a result not too far from that one reported by Capitelli et al. in the 1980s (Capitelli et al. 1981). In the same figure have been also reported experimental results obtained in Supiot et al. (1999) and Macko et al. (2001) which are consistent with the theoretical values.

In addition to the vibrational distributions the code of the Lisbon group contains a kinetics of metastable states of molecular nitrogen coupled with the vibrational kinetics through the so called VE (vibration-electronic) energy exchange processes. This kinetics contains also a lot of heavy-particle collisions leading to ionization.

Figure 9.18 reports the concentration of the metastable A state of nitrogen in the same afterglow conditions of Fig. 9.17, showing a very interesting theoretical

Fig. 9.16 eedf calculated in the post-discharge of a $\omega/(2\pi) = 2.45$ GHz discharge in N_2 , with $p = 2$ Torr and $n_e(0) = 5 \times 10^{11} \text{ cm}^{-3}$, for different instants in the afterglow (From Loureiro et al. 2011)

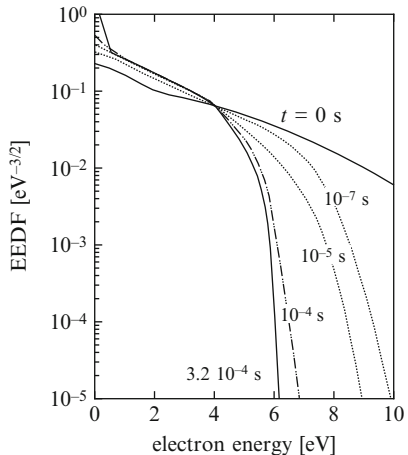


Fig. 9.17 vdf of $N_2(X^1\Sigma_g^+, v)$ molecules in the nitrogen afterglow of a $\omega/(2\pi) = 433$ MHz discharge at $p = 3.3$ Torr, in a cylindrical tube of inner radius $R = 1.9$ cm, for which $E/N = 4.6 \times 10^{-16} \text{ V.cm}^2$ and $T_v \approx 6,200$ K, at different instants in the afterglow. Experimental data (open circles) (Supiot et al. 1999), (close circles) (Macko et al. 2001) (From Guerra et al. 2007)

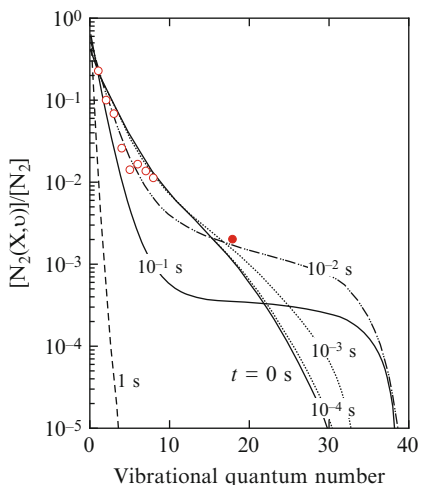


Fig. 9.18 Temporal evolution of the calculated and measured (close diamonds) (Eslami et al. 2002) absolute population of $N_2(A^3\Sigma_u^+)$ metastables, in the afterglow of a dc discharge at $\omega/(2\pi) = 433$ MHz with $p = 3.3$ Torr (From Guerra et al. 2007)

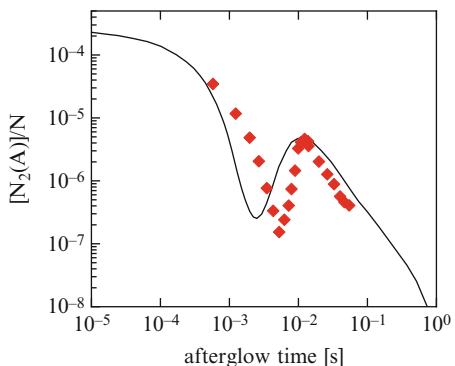
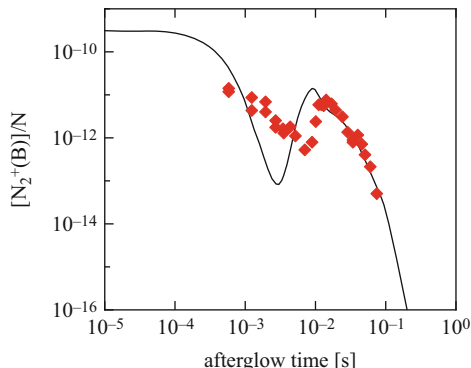


Fig. 9.19 Temporal evolution of the calculated and measured (*close diamonds*) (Eslami et al. 2004) absolute population of $N_2^+(B)$ state, in the afterglow of a dc discharge at $\omega/(2\pi) = 433$ MHz with $p = 3.3$ Torr (From Guerra et al. 2007)



reproduction of the non-monotonic trend of experimental results, in particular the presence of a maximum at late times. The same behavior can be observed in Fig. 9.19, where measured and calculated concentrations of $N_2^+(B)$ are reported as a function of afterglow time. Again we observe a maximum at $t = 10^{-2}$ s which has been explained taking into account electronically and vibrationally excited state collisions leading to ionization. It should be noted that a maximum in the ionization rate due to associative ionization of highly vibrationally excited states was observed in Capitelli et al. (1982). This maximum occurred at $t = 5$ and 25 ms for initial vibrational temperatures respectively of 8,500 and 4,400 K ($T = 500$ K, $p = 5$ Torr) intermediate of 10 ms obtained in Fig. 9.17 which considered an initial vibrational temperature of 6,200 K.

Nowadays the Lisbon group as well as the Troitsk group privilege the ionization involving electronically excited states even though we believe that the high-lying vibrational levels can take an important role. Moreover the importance of structured eedf in the post-discharge needs further experimental verification with consistent measurements of vibrationally and electronically excited states (De Benedictis and Dilecce 1995; Dilecce et al. 2007a,b; Simek et al. 1998).

References

- Adamovich IV (2014) Three-dimensional analytic probabilities of coupled vibrational-rotational-translational energy transfer for DSMC modeling of nonequilibrium flows. *Phys Fluids* 26(4):046102
- Adamovich IV, Macheret SO, Rich JW, Treanor CE (1998) Vibrational energy transfer rates using a forced harmonic oscillator model. *J Thermophys Heat Transf* 12(1):57–65
- ALADDIN (2013) Numerical database maintained by the IAEA nuclear data section A+M data unit. <https://www-amdis.iaea.org/ALADDIN/>
- Armenise I, Esposito F (2015) N_2 , O_2 , NO state-to-state vibrational kinetics in hypersonic boundary layers: the problem of rescaling rate coefficients to uniform vibrational ladders. *Chem Phys* 446:30–46

- Bazhenov VY, Ryabtsev AV, Soloshenko IA, Terent'eva AG, Khomich VA, Tsiolkov VV, Shchedrin AI (2001) Investigation of the electron energy distribution function in hollow-cathode glow discharges in nitrogen and oxygen. *Plasma Phys Rep* 27(9):813–818
- Billing GD (1982) Semiclassical calculation of rate constants for energy transfer between the asymmetric stretch mode of CO₂ and N₂. *Chem Phys Lett* 89(4):337–340
- Billing GD (1986) VV and VT energy transfer including multiquantum transitions in atom-diatom and diatom-diatom collisions. In: Capitelli M (ed) Nonequilibrium vibrational kinetics. Springer series topics in current physics, vol 39. Springer-Verlag, Berlin Heidelberg, pp 85–111
- Billing GD, Fisher ER (1979) VV and VT rate coefficients in N₂ by a quantum-classical model. *Chem Phys* 43(3):395–401
- Bourdon A, Panesi M, Brandis A, Magin TE, Chaban G, Huo W, Jaffe R, Schwenke DW (2008) Simulation of flows in shock-tube facilities by means of a detailed chemical mechanism for nitrogen excitation and dissociation. In: Proceedings of the summer program, Center for Turbulence Research, Stanford
- Cacciatore M, Capitelli M, Gorse C (1982) Non-equilibrium dissociation and ionization of nitrogen in electrical discharges: the role of electronic collisions from vibrationally excited molecules. *Chem Phys* 66(1–2):141–151
- Cacciatore M, Kurnosov A, Napartovich A (2005) Vibrational energy transfer in N₂-N₂ collisions: a new semiclassical study. *J Chem Phys* 123(17):174315
- Capitelli M (ed) (1986) Nonequilibrium vibrational kinetics. Springer series topics in current physics, vol 39. Springer-Verlag, Berlin Heidelberg
- Capitelli M, Celiberto R (1998) Electron-molecule cross sections for plasma applications: the role of internal energy of the target. In: Becker KH (ed) Novel aspects of electron-molecule collisions. World Scientific, Singapore/River Edge, pp 283–323
- Capitelli M, Dilonardo M (1977) Nonequilibrium vibrational populations of diatomic species in electrical discharges: effects on the dissociation rates. *Chem Phys* 24(3):417–427
- Capitelli M, Dilonardo M (1978) Non-equilibrium dissociation of nitrogen. *Rev Phys Appl (Paris)* 13(3):115–123
- Capitelli M, Gorse C (1990) Non equilibrium plasma kinetics. In: Capitelli M, Bardsley J (eds) Nonequilibrium processes in partially ionized gases. NATO ASI series, vol 220. Springer, US pp 45–61
- Capitelli M, Dilonardo M, Molinari E (1977) A theoretical calculation of dissociation rates of molecular hydrogen in electrical discharges. *Chem Phys* 20(3):417–429
- Capitelli M, Gorse C, Billing G (1980) V-V pumping up in non-equilibrium nitrogen: effects on the dissociation rate. *Chem Phys* 52(3):299–304
- Capitelli M, Gorse C, Ricard A (1981) Relaxation of the vibrational distribution function in N₂ time varying discharges. *J Phys Lett* 42(9):185–188
- Capitelli M, Gorse C, Ricard A (1982) Non equilibrium dissociation and ionization of N₂ in decaying plasmas. *J Phys Lett* 43(12):417–423
- Capitelli M, Ferreira CM, Gordiets BF, Osipov AI (2000) Plasma kinetics in atmospheric gases. Springer series on atomic, optical, and plasma physics, vol 31. Springer, Berlin/Heidelberg
- Capitelli M, Celiberto R, Eletskii A, Laricchiuta A (2001). Electron-molecule dissociation cross sections of H₂, N₂ and O₂ in different vibrational levels. Atomic and plasma-material interaction data for fusion, vol 9. IAEA, Vienna, p 47
- Capitelli M, Armenise I, Bisceglie E, Bruno D, Celiberto R, Colonna G, D'Ammando G, De Pascale O, Esposito F, Gorse C, Laporta V, Laricchiuta A (2012) Thermodynamics, transport and kinetics of equilibrium and non-equilibrium plasmas: a state-to-state approach. *Plasma Chem Plasma Process* 32(3):427–450
- Capitelli M, Colonna G, D'Ammando G, Laporta V, Laricchiuta A (2013) The role of electron scattering with vibrationally excited nitrogen molecules on non-equilibrium plasma kinetics. *Phys Plasmas* 20(10):101609
- Capitelli M, Colonna G, D'Ammando G, Laporta V, Laricchiuta A (2014) Nonequilibrium dissociation mechanisms in low temperature nitrogen and carbon monoxide plasmas. *Chem Phys* 438:31–36

- Caridade PJSB, Galvão BRL, Varandas AJC (2010a) Quasiclassical trajectory study of atom-exchange and vibrational relaxation processes in collisions of atomic and molecular nitrogen. *J Phys Chem A* 114(19):6063–6070
- Caridade PJSB, Galvão BRL, Varandas AJC (2010b) Quasiclassical trajectory study of atom-exchange and vibrational relaxation processes in collisions of atomic and molecular nitrogen. *J Phys Chem A* 114(19):6063–6070
- Colonna G, Capitelli M (2001) The influence of atomic and molecular metastable states in high enthalpy nozzle expansion nitrogen flows. *J Phys D: Appl Phys* 34:1812–1818
- Colonna G, Pietanza LD, Capitelli M (2008) Recombination-assisted nitrogen dissociation rates under nonequilibrium conditions. *J Thermophys Heat Transf* 22(3):399–406
- Colonna G, Laporta V, Celiberto R, Capitelli M, Tennyson J (2015) Non equilibrium vibrational and electron energy distribution functions in atmospheric nitrogen ns discharges: the role of electron-molecule vibrational excitation scaling laws. *Plasma Sources Sci Technol* 24:035004
- Cosby PC (1993) Electron-impact dissociation of nitrogen. *J Chem Phys* 98(12):9544–9553
- De Benedictis S, Dilecce G (1995) Relaxation of excited species in He/N₂ pulsed RF discharges: kinetics of metastable species. *Plasma Sources Sci Technol* 4(2):212
- Dilecce G, Ambrico PF, De Benedictis S (2007a) N₂(A³Σ_u⁺) density measurement in a dielectric barrier discharge in N₂ and N₂ with small O₂ admixtures. *Plasma Sources Sci Technol* 16(3):511
- Dilecce G, Ambrico PF, De Benedictis S (2007b) New N₂(C³Π_u, v) collision quenching and vibrational relaxation rate constants: 2. PG emission diagnostics of high-pressure discharges. *Plasma Sources Sci Technol* 16(1):S45
- Dyatko N, Napartovich A (2010) Ionization mechanisms in Ar: N₂ glow discharge at elevated pressures. AIAA paper 2010-4884
- Dyatko NA, Kochetov IV, Napartovich AP (1993) Electron energy distribution function in decaying nitrogen plasmas. *J Phys D: Appl Phys* 26(3):418
- Dyatko N, Kochetov I, Napartovich A (2002) Electron temperature in nitrogen afterglow: dependence of theoretical results on the adopted set of cross sections and on the type of molecular distribution over vibrational levels. *Plasma Phys Rep* 28(11):965–971
- Dyatko NA, Ionikh YZ, Kolokolov NB, Meshchanov AV, Napartovich AP (2003) Experimental and theoretical studies of the electron temperature in nitrogen afterglow. *IEEE Trans Plasma Sci* 31(4):553–563
- Dyatko N, Ionikh Y, Meshchanov A, Napartovich A, Barzilovich K (2010) Specific features of the current-voltage characteristics of diffuse glow discharges in Ar:N₂ mixtures. *Plasma Phys Rep* 36(12):1040–1064
- Eslami E, Foissac C, Campargue A, Supiot P, Sadeghi N (2002) Vibrational and rotational distributions in N₂(A³Σ_u⁺) metastable state in the short-lived afterglow of a flowing nitrogen microwave plasma. In: Proceedings of the XVIth Europhysics conference on atomic and molecular physics of ionized gases (ESCAPEIG)-5th international conference on reactive plasmas (ICRP) joint meeting, Grenoble, pp 57–58
- Eslami E, Foissac C, Supiot P, Sadeghi N (2004) Determination of the absolute density of N(²P) metastable atoms and N₂(a¹Π_g) molecules in a flowing nitrogen microwave discharge. In: Proceedings of the XVIIth Europhysics conference on atomic and molecular physics of ionized gases (ESCAPEIG) Constanta, p 197
- Esposito F, Capitelli M (1999) Quasiclassical molecular dynamic calculations of vibrationally and rotationally state selected dissociation cross-sections: N+N₂(v,j)→3N. *Chem Phys Lett* 302(1):49–54
- Esposito F, Capitelli M (2006) QCT calculations for the process N₂(v)+N→N₂(v')+N in the whole vibrational range. *Chem Phys Lett* 418(4):581–585
- Esposito F, Armenise I, Capitelli M (2006a) N-N₂ state to state vibrational-relaxation and dissociation rates based on quasiclassical calculations. *Chem Phys* 331(1):1–8
- Esposito F, Armenise I, Capitelli M (2006b) N-N₂ state to state vibrational-relaxation and dissociation rates based on quasiclassical calculations. *Chem Phys* 331(1):1–8

- Galvão BRL, Varandas AJC (2011) Ab initio based double-sheeted DMBE potential energy surface for $N_3(^2A')$ and exploratory dynamics calculations. *J Phys Chem A* 115(44):12390–12398
- Galvão B, Varandas A, Braga J, Belchior J (2013) Vibrational energy transfer in collisions: a quasiclassical trajectory study. *Chem Phys Lett* 577:27–31
- Galvão B, Braga J, Belchior J, Varandas A (2014) Electronic quenching in $N(^2D)+N_2$ collisions: a state-specific analysis via surface hopping dynamics. *J Chem Theory Comput* 10(5):1872–1877
- Garcia E, Laganà A (1997) Effect of varying the transition state geometry on $N+N_2$ vibrational deexcitation rate coefficients. *J Phys Chem A* 101(26):4734–4740
- GASPAR (2013) GAS and Plasma radiation database. <http://esther.ist.utl.pt/gaspar/>
- Gordiets B, Osipov A, Shelepin L (1988) Kinetic processes in gases and molecular lasers. Gordon and Breach Science Publishers, US
- Gorse C, Capitelli M (1987) Coupled electron and excited-state kinetics in a nitrogen afterglow. *J Appl Phys* 62(10):4072–4076
- Gorse C, Cacciatore M, Capitelli M, De Benedictis S, Dilecce G (1988) Electron energy distribution functions under N_2 discharge and post-discharge conditions: a self-consistent approach. *Chem Phys* 119(1):63–70
- Guerra V, Galiaskarov E, Loureiro J (2003) Dissociation mechanisms in nitrogen discharges. *Chem Phys Lett* 371:576–581
- Guerra V, Sá PA, Loureiro J (2004) Kinetic modeling of low-pressure nitrogen discharges and post-discharges. *Eur Phys J Appl Phys* 28:125–152
- Guerra V, Sá PA, Loureiro J (2007) Nitrogen pink afterglow: the mystery continues. *J Phys: Conf Ser* 63:012007
- Kossyi IA, Kostinsky AY, Matveyev AA, Silakov VP (1992) Kinetic scheme of the non-equilibrium discharge in nitrogen-oxygen mixtures. *Plasma Sources Sci Technol* 1(3):207
- Laganà A, Garcia E, Ciccarelli L (1987) Deactivation of vibrationally excited nitrogen molecules by collision with nitrogen atoms. *J Phys Chem* 91(2):312–314
- Laganà A, Ochoa De Aspuru G, Garcia E (1996) Temperature dependence of quasiclassical and quantum rate coefficients for $N + N_2$. Dipartimento di Chimica, Università di Perugia Perugia, Italy
- Laporta V, Celiberto R, Wadehra JM (2012) Theoretical vibrational-excitation cross sections and rate coefficients for electron-impact resonant collisions involving rovibrationally excited N_2 and NO molecules. *Plasma Sources Sci Technol* 21(5):055018
- Laporta V, Little DA, Celiberto R, Tennyson J (2014) Electron-impact resonant vibrational excitation and dissociation processes involving vibrationally excited N_2 molecules. *Plasma Sources Sci Technol* 23(6):065002
- Lempert WR, Adamovich IV (2014) Coherent anti-Stokes Raman scattering and spontaneous Raman scattering diagnostics of nonequilibrium plasmas and flows. (Topical Review) *J Phys D: Appl Phys* 47(43):433001
- Lino da Silva M, Guerra V, Loureiro J (2009) A review of non-equilibrium dissociation rates and models for atmospheric entry studies. *Plasma Sources Sci Technol* 18(3):034023
- Loureiro J (1991) Dissociation rate and $N(^4S)$ atom concentrations in a N_2 glow-discharge. *Chem Phys* 157(1–2):157–168
- Loureiro J, Ferreira CM (1986) Coupled electron energy and vibrational distribution functions in stationary N_2 discharges. *J Phys D: Appl Phys* 19(1):17
- Loureiro J, Ferreira CM, Capitelli M, Gorse C, Cacciatore M (1990) Non-equilibrium kinetics in nitrogen discharges: a comparative analysis of two theoretical approaches. *J Phys D: Appl Phys* 23(11):1371
- Loureiro J, Guerra V, Sá PA, Pintassilgo CD, Lino da Silva M (2011) Non-equilibrium kinetics in N_2 discharges and post-discharges: a full picture by modelling and impact on the applications. *Plasma Sources Sci Technol* 20(2):024007
- LXcat (2015) Plasma data exchange project Database. <http://fr.lxcat.net/home/>
- Macheret SO, Adamovich IV (2000) Semiclassical modeling of state-specific dissociation rates in diatomic gases. *J Chem Phys* 113(17):7351

- Macko P, Cunge G, Sadeghi N (2001) Density of $N_2(X^1\Sigma_g^+, v=18)$ molecules in a DC glow discharge measured by cavity ringdown spectroscopy at 227 nm; validity domain of the technique. *J Phys D: Appl Phys* 34(12):1807
- Massabieaux B, Gousset G, Lefebvre M, Pealat M (1987) Determination of $N_2(X)$ vibrational level populations and rotational temperatures using CARS in a D.C. low pressure discharge. *J Phys Fr* 48(11):1939–1949
- Nagpal R, Ghosh PK (1990) Electron energy distribution functions and vibrational population densities of excited electronic states in DC discharges through nitrogen. *J Phys D: Appl Phys* 23(12):1663
- Nagpal R, Ghosh PK (1991) Role of excited electronic states in the kinetics of electrons in nitrogen post-discharges. *J Phys B: At Mol Opt Phys* 24(14):3295
- NIFS (2013) National Institute for fusion science database. <http://dbshino.nifs.ac.jp/>
- Nighan WL (1970) Electron energy distributions and collision rates in electrically excited N_2 , CO, and CO_2 . *Phys Rev A* 2(5):1989
- Panesi M, Jaffe RL, Schwenke DW, Magin TE (2013) Rovibrational internal energy transfer and dissociation of $N_2(^1\Sigma_g^+)$ -N(4S_u) system in hypersonic flows. *J Chem Phys* 138(4):044312
- Phys4Entry database (2013) <http://phys4entrydb.ba.imip.cnr.it/Phys4EntryDB/>
- Polak LS, Sergeev PA, Slovenskii DI, Todesaite RD (1975) Proceedings 12th international conference on phenomena in ionized gases, Part 1, Eindhoven (1975)
- Simek M, Babický V, Clupek M, DeBenedictis S, Dilecce G, Sunka P (1998) Excitation of $N_2(C^3\Pi_u)$ and NO ($A^2\Sigma^+$) states in a pulsed positive corona discharge in N_2 , N_2-O_2 and N_2 -NO mixtures. *J Phys D: Appl Phys* 31(19):2591
- Son E (1990) Electrons in low-temperature plasmas. All-Union Correspondence Polytechnic Institute, Moscow (in Russian)
- STELLAR database (2013) <http://esther.ist.utl.pt/pages/stellar.html>
- Supiot P, Blois D, De Benedictis S, Dilecce G, Barj M, Chapput A, Dessaux O, Goudmand P (1999) Excitation of $N_2(B^3\Pi_g)$ in the nitrogen short-lived afterglow. *J Phys D: Appl Phys* 32(15):1887
- Wang D, Huo WM, Dateo CE, Schwenke DW, Stallcop JR (2003a) Reactive resonances in the N-N₂ exchange reaction. *Chem Phys Lett* 379(1–2):132–138
- Wang D, Stallcop JR, Huo WM, Dateo CE, Schwenke DW, Partridge H (2003b) Quantal study of the exchange reaction for N+N₂ using an ab initio potential energy surface. *J Chem Phys* 118(5):2186
- Wang D, Huo WM, Dateo CE, Schwenke DW, Stallcop JR (2004) Quantum study of the N+N₂ exchange reaction: state-to-state reaction probabilities, initial state selected probabilities, Feshbach resonances, and product distributions. *J Chem Phys* 120(13):6041–6050

Chapter 10

Negative Ion H⁻ Kinetics for Fusion

The production of negative H⁻/D⁻ ions is an important topics started with the experimental observation of Bacal and Hamilton (1979) of the existence of large concentrations of these ions under non equilibrium plasmas. Since then different international groups (Fukumasa and Mori 2005; Fukumasa et al. 2009; Benmeziane et al. 2005; Baksht et al. 2005; Bacal et al. 1999; Goretsky et al. 2007; Velasco and Dougar-Jabon 2004; Toader 2004) developed dedicated experimental devices and sophisticated models to better understand the origin of the formation of negative hydrogen ions particularly in multipole magnetic plasma configurations. This kind of basic research lasted approximately 20 years practically till the end of the twentieth century. A renewed interest on the other hand started again in the twenty-first century when it was decided that negative ion beams accelerated and neutralized could be used in tokamak devices for heating the fuel at temperatures necessary for promoting the fusion process. Again a large interest has been devoted toward the complete understanding of the physics and chemistry of these sources for optimization purposes (Bacal 2006; Capitelli et al. 2006; Svarnas et al. 2006), including construction of accurate databases of cross sections and rates for electron-impact induced processes in H₂(v) (Celiberto et al. 2001, 2002; Shakhmatov and Lebedev 2011; Capitelli et al. 2002; Laricchiuta et al. 2006; Janev et al. 2003). From our point of view the formation of negative ions represents an ideal situation, where state-to-state kinetics and their coupling with the electron energy distribution function represents a condition sine qua non it is practically impossible to understand the relevant phenomenology. This point comes from the accepted idea that the formation of negative ions is due to dissociative attachment from vibrationally excited hydrogen molecules implying the importance of their distribution in affecting the yield of negative ions. A lot of elementary processes are important in the formation of the vibrational distribution of molecular hydrogen and these processes must be defined by considering each vibrational state as a separate species with its own cross sections. The processes occur either in gas phase or in

gas surface interaction so that one can understand the role of atomic and molecular physics in the optimization of negative ion sources. This chapter is devoted (1) to the efforts made in these years to understand the physics of negative ion formation in multipole magnetic discharges operating in stationary and pulsed modes; (2) to the recent developments made in the last few years to using Monte Carlo methods for the transport of neutrals along the expansion region and of negative ions from the expansion region to the extraction one (Boeuf et al. 2012; Fubiani and Boeuf 2013; Diomede and Longo 2010; Taccogna et al. 2007, 2008b, 2010, 2013). Negative ion production has been recently considered in the global models by Hassouni et al. (2010), Gaboriau and Boeuf (2014), and Huh et al. (2015).

10.1 The Kinetic Model

Different chemical physical models were built in the last 30 years to describe the phenomenology occurring in multipole magnetic H₂/D₂ plasmas (Hiskes 1980; Hiskes and Karo 1984; Hiskes et al. 1985; Gorse et al. 1985, 1987, 1992; Bretagne et al. 1985; Capitelli 2005; Fukumasa 1989). Time-dependent and stationary approaches were used to this end. The models included the following sub-models

- The non-equilibrium vibrational kinetics responsible for the population of vibrationally excited states
- A time-dependent Boltzmann equation for the electron energy distribution function
- The dissociation kinetics
- The negative ion kinetics
- The ionization and recombination kinetics
- The interaction of molecules, atoms, electrons and ions with the reactor surface

Figure 10.1 represents the multipole source composed by a cylindrical chamber in which the discharge is produced by thermoionic electrons emitted from two filaments and accelerated in many cases up to 90 eV. The magnetic multicusp arrangement is produced by mounting several magnets around the cylindrical chamber wall and two magnets on the top end plate forming the magnetic filter.

In implicit form, the vibrational kinetics can be written as

$$\begin{aligned} \left(\frac{dN_v}{dt} \right) = & \left(\frac{dN_v}{dt} \right)_{eV} + \left(\frac{dN_v}{dt} \right)_{EV} + \left(\frac{dN_v}{dt} \right)_{VV} + \left(\frac{dN_v}{dt} \right)_{VT} + \left(\frac{dN_v}{dt} \right)_{eD} \\ & + \left(\frac{dN_v}{dt} \right)_{el} + \left(\frac{dN_v}{dt} \right)_{DA} + \left(\frac{dN_v}{dt} \right)_{eE} + \left(\frac{dN_v}{dt} \right)_{wall} \end{aligned} \quad (10.1)$$

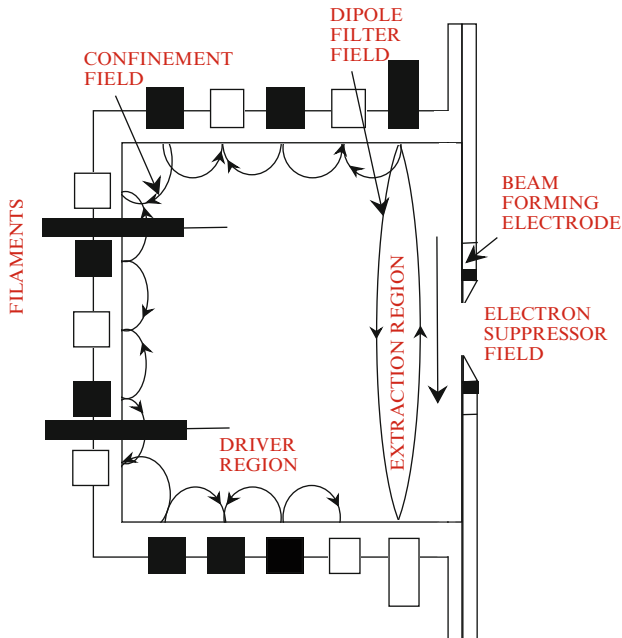


Fig. 10.1 Scheme of a Multicusp Negative Ion source

The terms on the right side represent the gain or the loss of the v th vibrational level due to vibrational excitation (eV¹ and EV processes), vibration-vibration (VV) and vibration-translation (VT) energy exchange processes, electron-impact-induced dissociation (eD) and ionization (eI), dissociative electron attachment (DA), electronic-excitation (eE) and surface processes (wall). Table 10.1 reports the elementary processes considered in Pagano et al. (2007).

The electron kinetics is represented by means of the electron Boltzmann equation that provides the temporal evolution of the density of the electrons having energy in a certain interval $[\varepsilon, \varepsilon + d\varepsilon]$. In the case of multicusp ion sources, it is characterized by a source term describing the injection of electrons in the source volume (Bretagne et al. 1985, 1986)

$$\frac{\partial n(\varepsilon, t)}{\partial t} = - \left(\frac{\partial J_{el}}{\partial \varepsilon} \right)_{eM} - \left(\frac{\partial J_{el}}{\partial \varepsilon} \right)_{ee} + \text{in} + \text{ion} + \text{sup} + S - L \quad (10.2)$$

where $S = I_d / (V_{\text{source}} e \Delta \varepsilon)$, I_d is the current of the injected electrons, V_{source} is the source volume, and $\Delta \varepsilon$ is the energy spreading of the injected electrons. The other terms are associated with all the other collisional processes occurring in the

¹The resonant vibrational excitation processes, known as eV processes in the plasma modeling community, correspond to RVE discussed in Chap. 1.

Table 10.1 List of processes included to model multicusp ion sources (Pagano et al. 2007)

Process	Description	References
$e + H_2(X^1\Sigma_g^+, v) \rightarrow H_2^*(B^1\Sigma_u^+, C^1\Pi_u) + e$ $\rightarrow H_2(X^1\Sigma_g^+, w) + e + h\nu$	EV: excitation-radiative decay vibrational excitation	Celiberto et al. (2001)
$e + H_2(X^1\Sigma_g^+, v) \rightarrow H_2(^2\Sigma_u^+) \rightarrow H_2(w) + e$	eV: vibrational excitation	Celiberto et al. (2001)
$e + H_2(X^1\Sigma_g^+, v) \rightarrow H_2^*(D,D'^1\Pi_u,B,B'^1\Sigma_u^+) + e$	eE: electronic excitation	Celiberto et al. (2001)
$e + H_2(X^1\Sigma_g^+, v) \rightarrow H_2^+ + e + e$	el: molecular ionization	Celiberto et al. (2001)
$e + H_2(X^1\Sigma_g^+, v) \rightarrow H_2(a^3\Sigma_g^+, b, e^3\Sigma_u^+, c^3\Pi_u) + e$ $\rightarrow H + H + e$ $e + H_2(X^1\Sigma_g^+, v) \rightarrow H_2^+(X^2\Sigma_g^+, \Sigma_u^+) + 2e$ $\rightarrow H + H^+ + 2e$	eD: dissociation	Celiberto et al. (2001)
$e + H_2(X^1\Sigma_g^+, v) \rightarrow H_2(^2\Sigma_u^+) \rightarrow H + H^-$	eDI: dissociative ionization	Celiberto et al. (2001)
$e + H_2(X^1\Sigma_g^+, v) \rightarrow H + H(n=2,3) + e$	DA: dissociative attachment	Celiberto et al. (2001)
$e + H(n=1,2,3) \rightarrow H^+ + e + e$	eD: dissociation	Celiberto et al. (2001)
$e + H(n=1,2,3) \rightarrow e + H(n)$	el: atomic ionization	Celiberto et al. (2001) and Kim and Rudd (1994)
$H_2(v) + H_2(w) \rightarrow H_2(v-1) + H_2(w+1)$	eE: atomic electronic excitation	Celiberto et al. (2001)
$H_2(v) + H_2 \rightarrow H_2(w) + H_2$	VV: vibration-vibration energy exchange	Matveyev and Siliakov (1995)
$H_2(v) + H \rightarrow H_2(w) + H$	VT _M : vibration-translation energy exchange	Cacciatore et al. (1989) and Matveyev and Siliakov (1995)
$H_2^+ + H_2 \rightarrow H_3^+ + H$ $H_2^+ + H \rightarrow H^+ + H_2$ $H^+ + H_2(v) \rightarrow H + H_2^+$	VT _a : vibration-translation energy exchange H ₃ ⁺ formation Ion conversion Ion conversion	Capitelli et al. (2002) Bowers et al. (1969) Karpas et al. (1979) Ichihara et al. (2000)

$H^+ + e \rightarrow H + h\nu$	Radiative recombination	Kramers (1923)
$H^+ + e + e \rightarrow H + e$	Three-body recombination	Bogaerts et al. (1998)
$H_2^+ + e \rightarrow neutrals$	Dissociative recombination	Tawara et al. (1990) and Janev et al. (2003)
$H_3^+ + e \rightarrow neutrals$	Dissociative recombination	Tawara et al. (1990) and Janev et al. (2003)
$H^- + e \rightarrow H + e + e$	Electron detachment	IAEA (2013)
$H^- + H^+ \rightarrow H + H(n = 3)$	Mutual neutralization	Matveyev and Silakov (1995)
$H^- + H_2^+ \rightarrow H_2 + H$	Mutual neutralization	Matveyev and Silakov (1995)
$H^- + H_3^+ \rightarrow H_2 + H_2$	Mutual neutralization	Matveyev and Silakov (1995)
$H(n) \rightarrow H(n') + h\nu$	Excited atom radiative decay	NIST (2013)
$H + wall \rightarrow 1/2H_2$	Atomic wall recombination	Gorse et al. (1985) and Gorse et al. (1987)
$H_2(v) + wall \rightarrow H_2(w)$	Vibrational deactivation	Gorse et al. (1987) and Hiskes and Karo (1989)
$H^+ + wall \rightarrow H$	Ion wall recombination	Zorat et al. (2000)
$H_2^+ + wall \rightarrow H_2$	Ion wall recombination	Zorat et al. (2000)
$H_3^+ + wall \rightarrow H_2 + H$	Ion wall recombination	Zorat et al. (2000)

plasma: $-\left(\frac{\partial J_{el}}{\partial \varepsilon}\right)_{eM}$ accounts for the flux of electrons along the energy axis due to elastic collisions, $-\left(\frac{\partial J_{el}}{\partial \varepsilon}\right)_{ee}$ for that due to electron-electron Coulomb collisions, and the other terms represent the contribution to the time variation of density of electrons with energy within a certain interval due to inelastic (in), ionizing (ion), and superelastic (sup) collisions and electron losses due to gas-phase recombination and on the wall (L).

In the first studies the term L (Bretagne et al. 1985) was written as

$$L = \frac{1}{4}n(\varepsilon)v(\varepsilon)\frac{A}{V}\left(1 - \frac{2eV_p}{m_e v^2(\varepsilon)}\right) + n(\varepsilon)n_+v(\varepsilon)\sigma_r(\varepsilon) = L'' + L_r \quad (10.3)$$

$v(\varepsilon)$ is the electron velocity, A is an effective area representing the sum of the unmagnetised conducting area and the equivalent leakage area through the magnetised wall (Bacal et al. 1984), V_p is the plasma potential, taken from the experiments to be 2 V. The wall loss is assumed to be equal to zero when $\varepsilon < eV_p$. In the hybrid magnetic multicusp discharge studied, the loss to the unmagnetised conducting part of the wall (one of the end plates) dominates the wall losses. Therefore A/V was taken to be approximately constant and equal to 0.07 cm^{-1} . n_+ is the ion density and $\sigma_r(\varepsilon)$ is the cross-section for the recombination process.

To calculate the rates of elementary processes involving heavy-particle collisions we use the relevant temperatures as parameters. We distinguish between atom and molecule temperatures. In particular we assume

$$T_H = T_{H^+} = T_{H^-} \quad \text{and} \quad T_{H_2} = T_{H_2^+} = T_{H_3^+} \quad (10.4)$$

while a reduced temperature is defined for atom-molecule interaction i.e.

$$T^* = \frac{m_H T_{H_2} + m_{H_2} T_H}{m_H + m_{H_2}} \quad (10.5)$$

On the other hand the electron impact rates are directly calculated by using the self-consistent eddf.

The surface processes like ion wall recombination and electron wall losses were calculated in the old models by introduction of parameters like the surface (A_{surf}) and the volume of plasma (V_{plasma}) and the loss surface for electrons ($A_{\text{plasma}}^{\text{el}}$). These parameters represented the surface and the volume seen by charged species and were introduced in order to take into account the magnetic confinement of the plasma. In the present model the ion wall losses rate coefficient is written as

$$k_{\text{wall}}^{\text{ion}} = u_{B,\text{ion}} \frac{A_{\text{eff}}}{V_{\text{source}}} \quad (10.6)$$

and calculated as described in Pagano et al. (2007). A similar equation was written for the loss of atomic species for surface recombination

$$k_{\text{wall}}^{\text{H}} = \frac{1}{4} \frac{A_{\text{source}}}{V_{\text{source}}} v_{\text{H}} \gamma_{\text{H}} \quad (10.7)$$

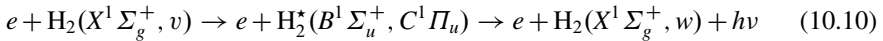
where v_{H} is the thermal velocity of atoms

$$v_{\text{H}} = \sqrt{\frac{8k_B T}{m_{\text{H}} \pi}} \quad (10.8)$$

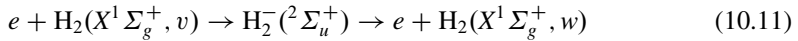
Before examining the results we want to remind that the negative ion production is formed by dissociative attachment from vibrationally excited molecules



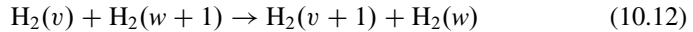
The vibrational distribution function to a first approximation is formed by eV and EV processes. In particular, the vibrational excitation generated first by high-energy electrons (mainly present during the first time steps in the discharge) through EV processes



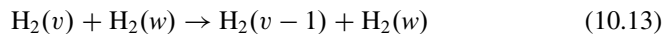
and then by low-energy electrons through eV processes



is redistributed by the so-called VV and VT processes. While VV processes determine the exchange of vibrational quanta between molecules



VT processes can involve molecules (VT_M) and atoms (VT); in both cases, the vibrational quanta of a molecule are converted to translational energy of another molecule or of an atom



Atomic hydrogen indeed is also important in destroying negative ions through detachment i.e.



Concerning the eedf we must remind that it is formed by the thermalization of electrons emitted by a filament and accelerated by an applied voltage V_d .

The corresponding eedf is similar to an electron beam which is transformed in a bi-maxwellian eedf through inelastic, superelastic and elastic collisions. A long plateau is therefore expected in the corresponding eedf followed by a low electron temperature maxwellian distribution dominated by low threshold energy loss of inelastic collisions. In general the high energy plateau is such to promote EV elementary processes creating in turn a plateau in the vibrational distribution function. The low-energy portion of eedf is such to activate the dissociative attachment processes characterized by low energy thresholds. An example of vdf and eedf in multicusp magnetic plasmas is reported in Figs. 10.2 and 10.3 (Pagano et al. 2007) for low and high current intensities (0.5 and 10 A).

The peculiarities of both distributions previously anticipated can be recovered in the two figures. In particular it is well evident the plateau in vdf created by EV processes, whose magnitude increases with the corresponding increase of the filament current, i.e. of the electron density. On the other hand the eedf presents the beam source at about 100 eV, followed by the long plateau and the low energy bulk maxwellian eedf. Moreover the increase of current intensity I_d strongly increases the magnitude of plateau in eedf. These points can be also recovered in the recent results by Shibata et al. (2013), obtained by using a Monte Carlo approach for the eedf in a multicusp arc discharge source. Similar considerations are found in the vdf of Fig. 10.3a, b (Pagano et al. 2007) which also present a satisfactory comparison of theoretical and experimental vdf, the last obtained by vacuum ultraviolet laser spectroscopy (Mosbach et al. 2000; Mosbach 2005). For $I_d = 0.5$ A the theoretical vibrational distribution overestimates the corresponding experimental curve in the plateau region, the reverse occurring in the low and high energy part of the distribution. A similar trend is also present for $I_d = 10$ A, even though in this case the vibrational distribution presents a Boltzmann behaviour up to an energy of 3 eV;

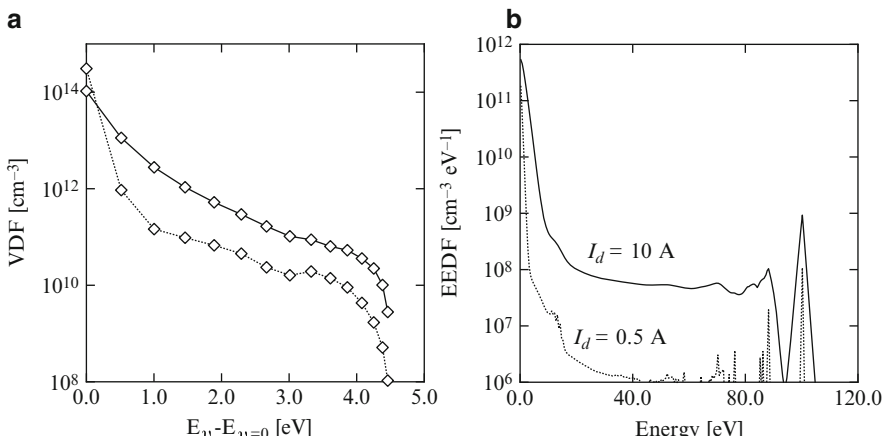


Fig. 10.2 Stationary vdf (a) and eedf (b) for different discharge currents, (solid line) $I_d = 10$ A (dotted line) $I_d = 0.5$ A, for $p = 1.5$ Pa and $V_d = 100$ V (From Pagano et al. 2007)

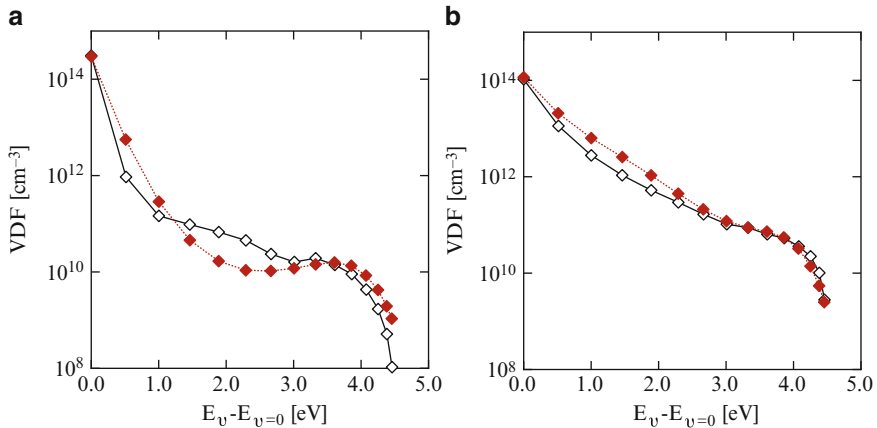
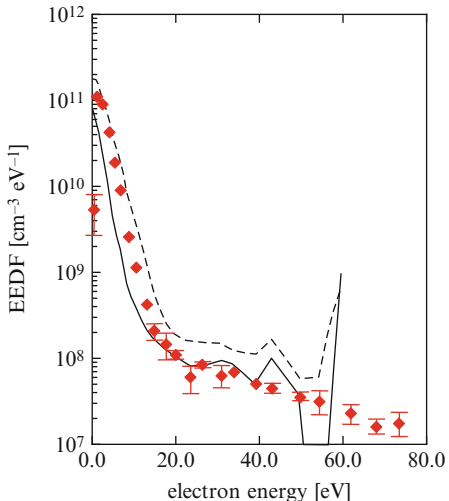


Fig. 10.3 Comparison of stationary vdfs calculated by Pagano et al. (2007) (open diamonds) and experimental results by Mosbach (2005) (close squares) for (a) $I_d = 0.5 \text{ A}$ and (b) $I_d = 10 \text{ A}$

Fig. 10.4 Electron energy distribution function: (markers) experimentally measured, calculated with surface area to volume ratio = 0.033 (solid line) and 0.004 (dashed line). (Discharge current $I_d = 10 \text{ A}$, discharge voltage $V_d = 60 \text{ V}$, gas pressure $p = 4.7 \text{ mTorr}$, $T_{\text{H}_2} = 500 \text{ K}$ and atomic fraction=0.07) (From Bretagne et al. 1991)



the plateau zone is strongly reduced as a result of eV transitions. Concerning the eedf a good agreement was found with similar theoretical results and experimental ones obtained by the second derivative of I_d/V_d probe curves as can be appreciated in Fig. 10.4 (Bretagne et al. 1991).

It is interesting to note that the behavior of the eedf reported in Figs. 10.2b–10.4 is similar to the experimental eedf found in helicon plasmas operating at low pressure (Blackwell and Chen 2001) (see Fig. 10.5).

Atomic hydrogen in general is considered as a killer of vibrationally excited molecules and therefore of the negative ion concentration. Selection of the material surface is therefore very important for establishing its concentration. Materials with

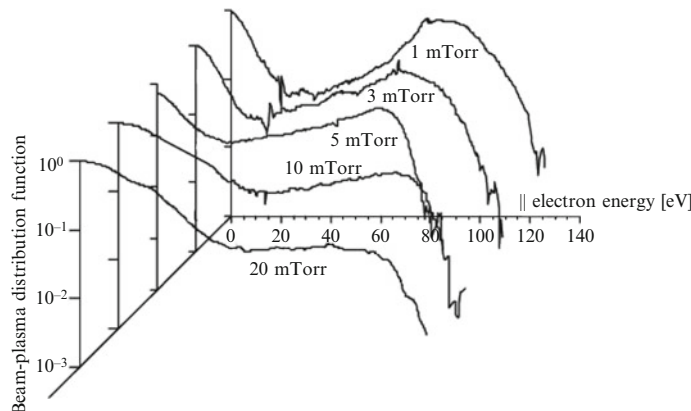
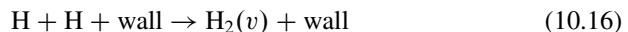


Fig. 10.5 Evolution of the beam-plasma distribution function in a magnetic field with increasing neutral gas pressure at a distance of 5 cm from the electron gun. The gun is dc biased at -80 V with the anode removed. The beam electrons, characterized by the bump, become depleted by ionizing collisions and raise the temperature of the bulk plasma as pressure is increased (From Blackwell and Chen 2001)

large recombination coefficients, γ_H , therefore decrease the concentration of atomic hydrogen increasing at the same time the plateau of the vibrational distribution and therefore the negative ion production. This point can be understood by looking at the results (Pagano et al. 2006) obtained by parametrizing the heterogeneous recombination coefficient of atomic hydrogen in a multicusp reactor characterized by $p = 4.5$ mTorr, $I_d = 10$ A, $T_H = 4,000$ K and $T_{H_2} = 500$ K (see Pagano et al. 2006).

Figure 10.6a (Pagano et al. 2006) reports the increase on the plateau of vibrational distribution function with the increase of the recombination coefficient γ_H , while Fig. 10.6b reports the corresponding increase as a function of γ_H of the concentration of negative ions. The heterogeneous recombination has an other effect on the negative ion production depending on the selective pumping of vibrational levels during the process (Eenshuistra et al. 1988; Hall et al. 1988) i.e.



An increase of a factor 2.5 in the concentration of negative ion is observed passing from no pumping of vibrational quanta, i.e. $\text{H}_2(v = 0)$ in Eq. (10.16), up to $\text{H}_2(v = 0 - 10)$ pumping (Fig. 10.7a, b). Similar results have been obtained by Diomede et al. (2005, 2007) in radiofrequency discharges for both atomic hydrogen and negative ion concentration parametrizing both atomic hydrogen recombination coefficient and selective pumping of vibrational levels during the recombination process.

The results in Figs. 10.6 and 10.7 should stimulate further experimental and theoretical studies on γ_H and on rates for the process (10.16).

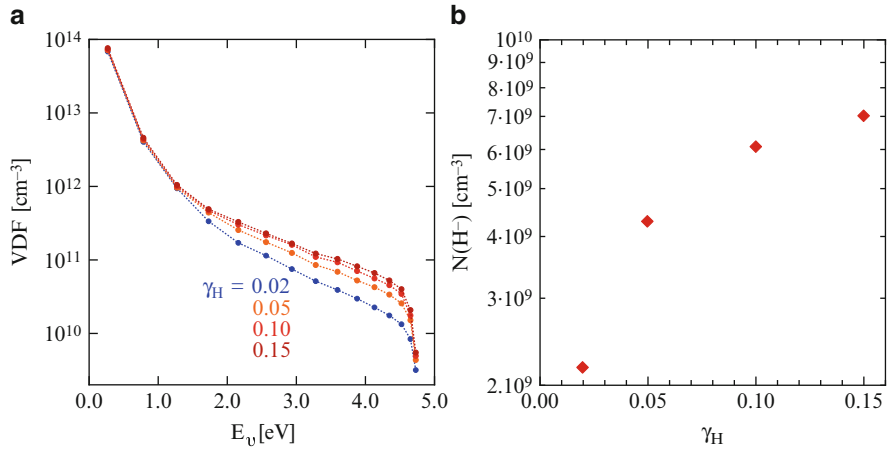


Fig. 10.6 Stationary vdf (a) and negative ion density (b) for different values of γ_H (From Pagano et al. 2006)

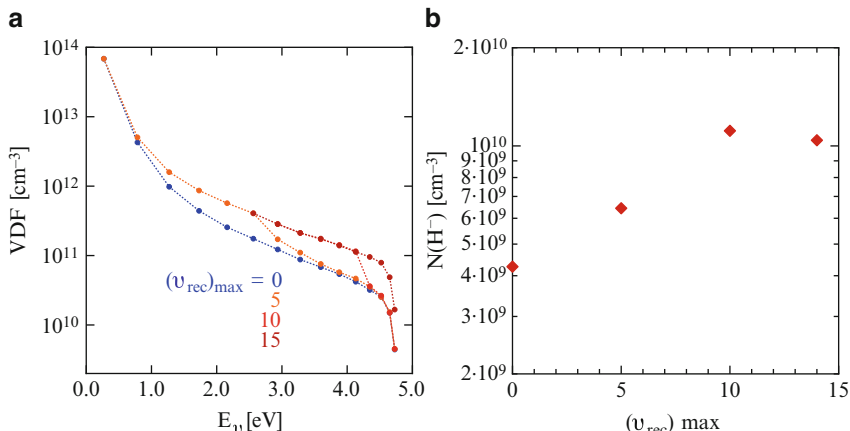


Fig. 10.7 Stationary vdf (a) and negative ion density (b) calculated distributing the recombination up to the v -th vibrational level (From Pagano et al. 2006)

10.2 Time-Dependent Pulsed Discharges

The time-dependent simulation of multipole discharges showed that switching on the discharge, both negative ion $n(H^-)$ and atom $n(H)$ densities rise with time (Gorse et al. 1985, 1987, 1992; Capitelli and Gorse 2005). However, at around $100 \mu\text{s}$, the negative ion density reaches a maximum, then decreases. This behavior was explained with the increased importance of associative detachment in collision with atoms, whose density continues to rise. If in a repetitive discharge, the current would be switched off as soon as the $n(H^-)$ density reaches its maximum value and

for a period sufficiently long to affect the atom density, one would obtain a higher mean value of $n(\text{H}^-)$.

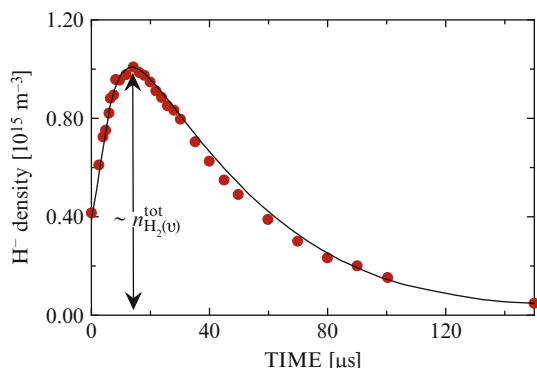
It should be noted that this procedure is correct as long as the atom life time, controlled by surface recombination, is shorter than that of either negative ions or vibrationally excited molecules. A second aspect of discharge modulation is related to the primary energetic electrons. As soon as the discharge is switched off their production stops and their density rapidly drops. Then also the fast electron detachment is halted. A third aspect is linked to the temporal behavior of the low energy part of eedf that can find a temporal window, in the post-discharge, for increasing the dissociative attachment rates.

Because of the similarity with the magnetic filter, in which there is a separation between fast and slow electrons, Hopkins and Mellon (1991) called “temporal filter” the procedure of separating in time the required hot and cold electron distributions. Different experiments (Hopkins and Mellon 1991; Hopkins et al. 1991; Hopman and Heeren 1992; Mosbach et al. 1998; Fukumasa and Shinoda 1998) show the enhancement of $n(\text{H}^-)$ in the post-discharge regime. As an example, Hopkins and Mellon show an enhancement by a factor 3 in the extracted H⁻ current, the enhancement lasting for about 200 μs .

Similar results (enhancement by a factor 2.5, time duration of about 100 μs) were obtained by Mosbach et al. (1998) (see Fig. 10.8), who also developed a phenomenological model to explain the experimental results, and by Fukumasa and Shinoda (1998) (enhancement by a factor 4 and duration of approximately 100 μs). On the other hand, the code developed in Bari was used (Gorse and Capitelli 1992) to qualitatively reproduce the complex phenomenology of pulsed discharges.

The results are summarized in Fig. 10.9a–d (Gorse and Capitelli 1992). In particular, Fig. 10.9a reports the relaxation of eedf at several times t_{pd} in the post-discharge. We can see that the relaxation of eedf is such to increase the number of electrons with low energy, enhancing those rate coefficients characterized by a low-energy threshold energy. In particular the dissociative attachment rates from highly vibrationally excited states can increase during the relaxation as can be appreciated from Fig. 10.9b. Note that in D₂ system, this behavior occurs for $v > 12$. On the other hand, Fig. 10.9c shows the relaxation of the vibrational distribution N_v , that

Fig. 10.8 Comparison of the measured (markers) and calculated (solid line) temporal behaviour of the H⁻ density in the post-discharge ($V_d = 90 \text{ V}$, $I_d = 4 \text{ A}$, $p = 0.25 \text{ Pa}$, pulse duration 250 μs , pause duration 250 μs) (Mosbach et al. 1998)



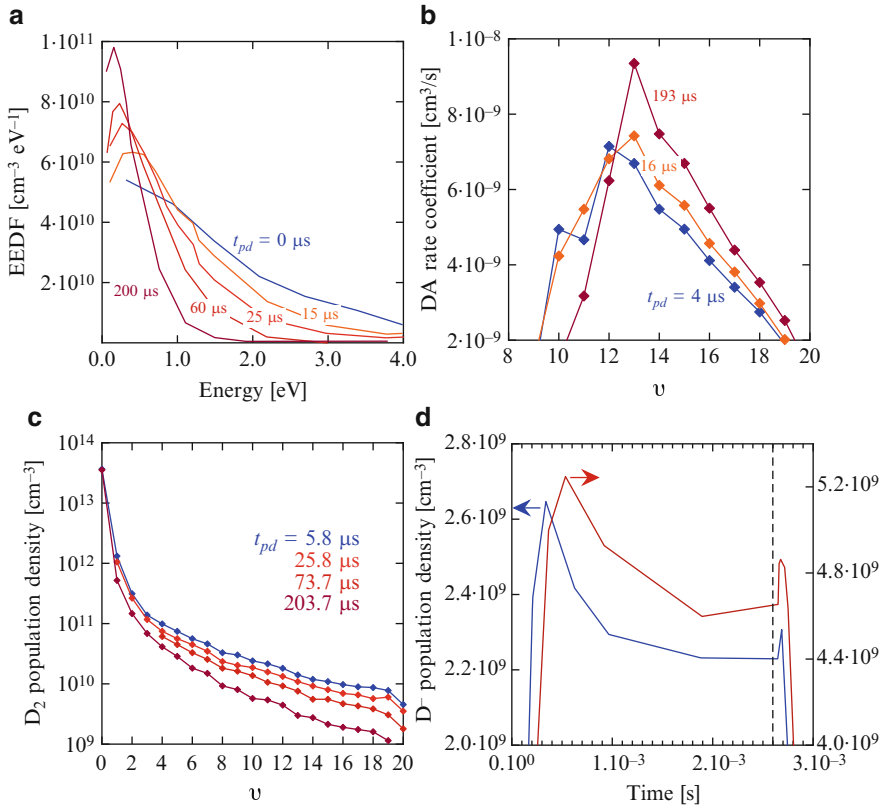


Fig. 10.9 Relaxation of several quantities. [(a) eedf. (b) DA rate coefficient. (c) $N_v^{D_2}$. (d) D^- density] in the D_2 post-discharge regime. In (d), the dashed line has been obtained by decreasing by a factor 8 the rate coefficient for the deactivation of vibrationally excited molecules on the metallic walls, the vertical dashed line indicating the onset of the post-discharge regime that lasts for about $200 \mu\text{s}$ (From Gorse and Capitelli 1992)

starts decreasing after $100 \mu\text{s}$. The D^- maximum in the post-discharge can take place due to a favorable interplay between the relaxation of eedf and, therefore, of the dissociative attachment rates, the relaxation of N_v and the decrease of D^- losses in the post-discharge regime. This is indeed the case, as reported in Fig. 10.9d, that shows the time dependence of negative ion concentration under discharge and post-discharge conditions.

These results have been, to a given extent, confirmed by a more recent PIC/MCC simulation on the formation of H^- in hydrogen post-discharge plasma obtained by turning off the potential in a capacitively parallel RF discharge (Diomede et al. 2006). In a recent paper by Ji-Zhong et al. (2012) the hydrogen discharge driven by the combined radio-frequency (RF)/short pulse sources has been investigated, in the same theoretical frame, demonstrating the role of the short pulse in enhancing the production of vibrationally excited molecules and, in turn, of H^- .

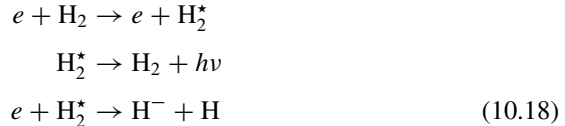
10.3 Rydberg States

So far we have considered dissociative attachment from vibrationally excited as the only mechanism for forming negative ions. However in Pinnaduwage and Christoprou (1993) and Datskos et al. (1997) a new mechanism is proposed for producing negative ions based on dissociative attachment on Rydberg states



where H_2^* represents a generic Rydberg state.

In a first paper (Pinnaduwage and Christoprou 1993) found an experimental value of $10^{-6} \text{ cm}^3 \text{ s}^{-1}$ for the corresponding rate. A new value of $6 \times 10^{-5} \text{ cm}^3 \text{ s}^{-1}$ was found by the same group in a subsequent publication (Datskos et al. 1997). The first value, i.e. $10^{-6} \text{ cm}^3 \text{ s}^{-1}$, was used in Garscadden and Nagpal (1995) in a simplified kinetic scheme



for estimating the concentration of negative ions through this mechanism. Insertion of this channel gives an enhancement of negative ion concentration by a factor 10 as compared with the concentration of negative ions obtained by the dissociative attachment mechanism from vibrationally excited states. This result was also confirmed, even though to a minor extent, in Gorse et al. (1996) by introducing the channel in the self-consistent model previously described.

These results were however criticized by Hiskes (1996a,b), who after decreasing by a factor 100 the lifetime of Rydberg states found a corresponding decrease of negative ion production through the Rydberg mechanism ruling out the corresponding channel. Hiskes however was using the first experimental value of Pinnaduwage and Christoprou (1993), a factor 60 lower than the last experimental value. This point pushed Hassouni et al. (1998) to reconsider the role of Rydberg states in affecting the production of negative ions in multicusp plasmas as well as in microwave plasmas. In the case of multicusp plasmas the authors used a new kinetic code (Hassouni et al. 1999) for H_2 plasmas containing also a collisional-radiative model for both molecular and atomic hydrogen. In particular the collisional-radiative model for molecules was able to yield the concentration of Rydberg states important for understanding their role in affecting the production of negative ions. The results we are presenting have been obtained by running the new kinetic model inserting in it the eedf of a typical experimental situation ($I_d = 10 \text{ A}$, $V_d = 100 \text{ V}$) calculated by Gorse et al. (1992). The calculations showed that the insertion of the Rydberg mechanism yields values of negative ion concentration 2.7 higher than the

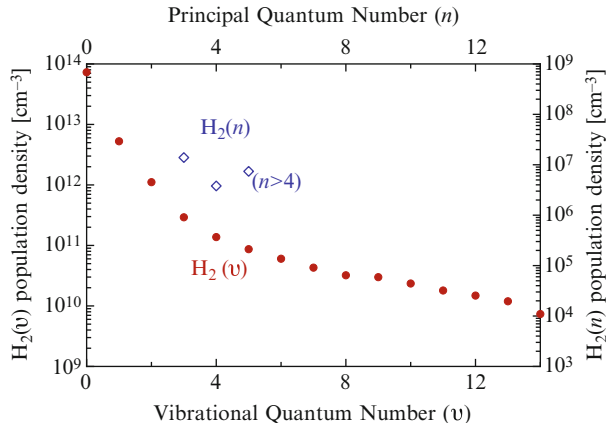


Fig. 10.10 $H_2(v)$ vibrational (Gorse et al. 1992) and $H_2^*(n)$ Rydberg state (Capitelli and Gorse 2005) (open markers from Hassouni et al. (1998)) population density versus vibrational and principal quantum numbers, respectively

case which does not consider this mechanism. To understand better this result we report in Fig. 10.10 the vibrational distribution and the concentration of Rydberg states obtained in this study.

Future work should be addressed to the development of a more detailed collisional-radiative model for Rydberg states as well as a new formulation of the dependence of dissociative attachment on the specific principal quantum number describing the excited Rydberg state. In the calculations by Hassouni et al. (1998) all excited states with $n > 2$ were considered as having a dissociative attachment rate of $6 \times 10^{-5} \text{ cm}^3 \text{ s}^{-1}$ very far from the proposed scaling law of Pinnaduwage et al. (1999). These authors proposed the following scaling law for the dependence of dissociative attachment on the principal quantum number of the Rydberg state

$$k_{\text{da}}(n) = 10^{-8} n^{7/2} \quad (10.19)$$

which corresponds to a value of about 5×10^{-5} for $n > 12$.

Equation (10.19) was used by Mosbach (2002) with a new collisional-radiative model for Rydberg states. The new calculations rule out the importance of the Rydberg mechanism as compared with the vibrational one.

A further study of the dissociative attachment from Rydberg states has been proposed some years ago (Capitelli et al. 2001). The idea is to consider the dissociative attachment reaction

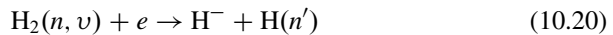
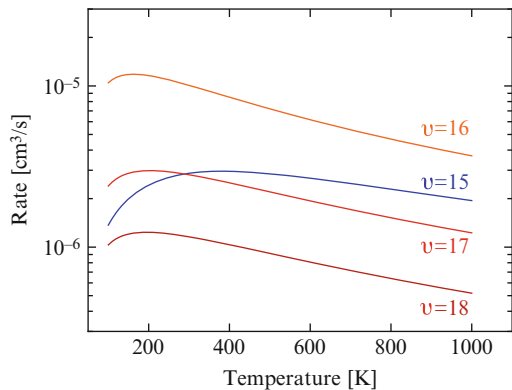
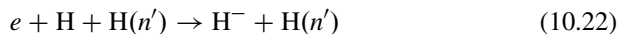
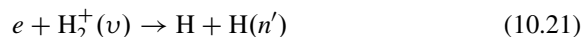


Fig. 10.11 Dissociative recombination rate coefficients as a function of temperature for different vibrational level of molecular ion (From Capitelli et al. 2001)



(here n is the effective principal quantum number for the Rydberg state, v is the vibrational quantum number and n' is the principal quantum number of the product atom) as the sum of two reactions



The $\text{H}(n)$ Rydberg state is regarded as a small-size hydrogen molecular ion H_2^+ surrounded by a *cloud* of the weakly-bound electron having the average radius as large as n^2 . Reactions (10.21) and (10.22) can be considered acting independently; therefore the cross sections of the dissociative attachment (10.20) should be proportional (or equal) to that for dissociative recombination. The corresponding dissociative recombination rates obtained by integrating the corresponding cross sections (Chibisov et al. 1997) have been reported in Fig. 10.11 for different vibrational level of molecular ion. The calculated rates reach very high values for the vibrational quantum number of molecular ion $v = 16$ of the same order of magnitude of the experimental value found by Pinnaduwage. No attempts have been made to insert these data in an appropriate collisional-radiative model including also the dependence of the rates on vibrational quantum number. We can conclude that in order to definitively assess the importance of Rydberg states a new theoretical approach for confirming Eq. (10.19) becomes mandatory.

10.4 RF Coupled Negative Ion Sources

Figure 10.12 (Taccogna et al. 2008a) shows a negative ion source composed by (1) the driver (2) the expansion region (3) the extraction region. The cylindrical driver are powered by the RF coils which are coupled to the H_2 gas to generate the plasma; the rectangular expansion region, where the plasma expands into the actual source body; and the extraction region, consisting of three grids, namely, the plasma grid PG, the extraction grid EG, and the grounded grid AG. The expansion and extraction

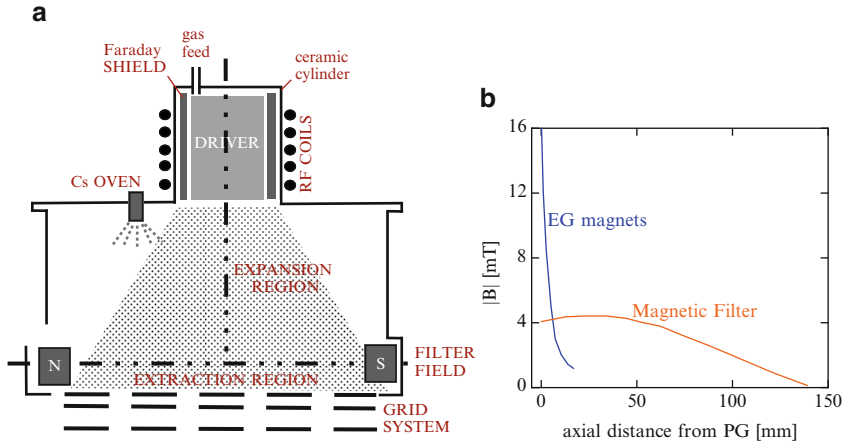


Fig. 10.12 (a) Scheme of the radio-frequency inductively coupled negative-ion source developed at Max-Planck IPP in Garching. (b) Magnetic field as a function of the axial distance from the plasma grid created by the electron deflection magnets inserted into the extraction grid EG and by the magnetic filter (From Taccogna et al. 2008a)

regions are separated by a nonhomogeneous magnetic field parallel to the plasma grid on the order of 5–7 mT, the filter field. The expansion chamber is crucial in the formation of a non-equilibrium vibrational distribution function due to the interplay of the elementary processes acting in the plasma (see Table 2 in Taccogna et al. 2008a).

In the expansion region, the plasma is continuously replenished from the driver region. Therefore, the plasma subsystem is considered as a fixed background. An axial decay due to plasma expansion is implemented using the following fitting formula from the experimental measurements of electron density (in m^{-3}) and temperature (in eV) (Bandyopadhyay 2004):

$$n_e(z) = n_{e,0} e^{-z/0.13} \quad (10.23)$$

$$T_e(z) = T_{e,0} e^{-z/0.23} \quad (10.24)$$

where z is in meters and $n_{e,0} = 10^{18} \text{ m}^{-3}$; $T_{e,0} = 8 \text{ eV}$ are the values at the driver exit plane. The molar fractions of the ion species H_x^+ is estimated for the operative conditions typical in the radio-frequency negative-ion source (Taccogna et al. 2011), as follows:

$$\chi(\text{H}^+) = 0.4 \quad \chi(\text{H}_2^+) = 0.4 \quad \chi(\text{H}_3^+) = 0.2 \quad (10.25)$$

while the ion temperature is fixed at $T_{i,0} = 0.8 \text{ eV}$. The same axial decay laws, i.e. Eqs. (10.23) and (10.24), are used for the ions' density and temperature. Through this plasma background, neutral pseudoparticles of H and H_2 are launched from

the source line [driver exit plane see Fig. 10.12a] with a half Maxwellian velocity distribution and with a Boltzmann vibrational population for a fixed temperature (translational temperature $T_{\text{transl}} = 1,200 \text{ K}$ equal to the vibrational temperature T_{vib} (Fantz et al. 2006b,a):

$$n_{\text{H}_2(v)} = n_{\text{H}_2} (1 - e^{-\varepsilon_v/k_B T_{\text{vib}}}) e^{-\varepsilon_v/k_B T_{\text{vib}}} \quad (10.26)$$

where $n_{\text{H}_2} = P/k_B T_{\text{transl}}$ is the total density of molecular hydrogen and ε_v is the energy of the vibrational level v , calculated using the Morse anharmonic oscillator. A ratio of $n_{\text{H}}/n_{\text{H}_2} = 0.2$ (Fantz et al. 2006b,a) between atomic and molecular density is defined at the source. The measurements reported in Fantz et al. (2006a) indicate a vibrational temperature sensibly (a factor two to three) higher than the translational temperature. However, results have shown a weak dependence on this assumption. An open-boundary condition is implemented on the right side of the simulation domain (particles crossing this line are deleted from the list). The neutral kinetics including the whole vibrational ladder and the atomic hydrogen in the expansion region is followed by a Direct Monte Carlo method.

Figure 10.13a (Taccogna et al. 2008a) reports the axial profiles of $\text{H}_2(v)$ for selected v levels and H densities along the expansion region. We note that in general from $z = 0$ the densities of vibrational levels increase, while the $\text{H}_2(v = 0)$ follows an opposite trend from 0.01 m on. As a result a well pumped vibrational distribution is appearing as can be appreciated from Fig. 10.13b displaying the vdf at the end of expansion region.

Figure 10.14a, b (Capitelli et al. 2011) report the pumping and deactivation rates at the end of expansion region. eV and surface processes control pumping and destruction of the vibrational levels. It should be noted that under these conditions

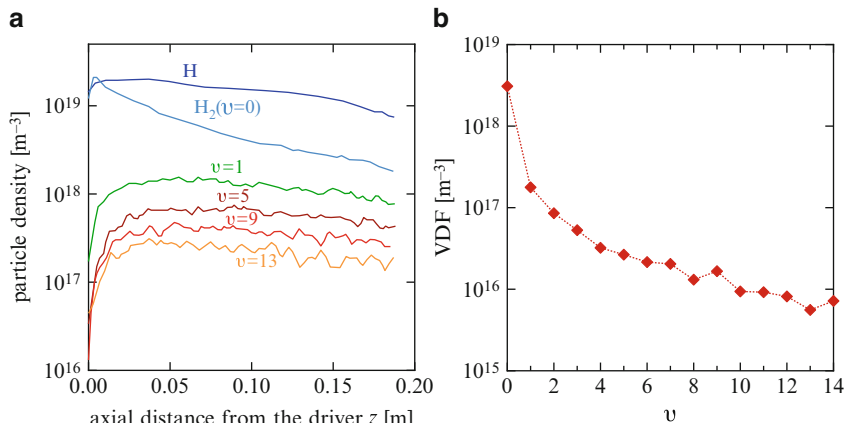


Fig. 10.13 (a) Axial profiles of H and $\text{H}_2(v)$ density for selected v levels (From Taccogna et al. 2008a). (b) Total density of vibrational states at the exit of the expansion region ($z \approx 0.2 \text{ m}$) (From Taccogna et al. 2011)

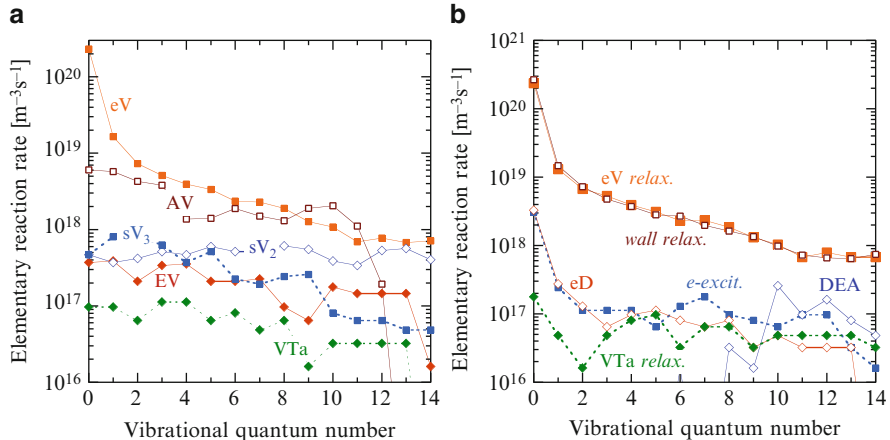
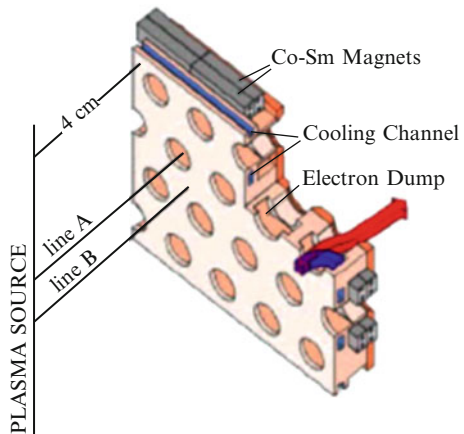


Fig. 10.14 Elementary reaction rates of the most important processes leading to (a) formation and (b) destruction of a vibrational state as a function of the vibrational state *v* in the last cell of the simulation domain (From Capitelli et al. 2011 and Taccogna et al. 2011)

Fig. 10.15 Schematic diagram of the simulation model showing the two different axial lines considered (From Taccogna et al. 2008a)



the EV processes loose their role in pumping vibrational energy as a result of the Maxwell distribution function existing along the *z* coordinate implying the lack of the long plateau in eedf existing in multicusp magnetic plasmas and to a given extent in multicusp ECR sustained plasmas (Béchu et al. 2013).

Let us now consider the extraction region (see Fig. 10.15). The simulation domain extends 4 cm from the PG. Two different axial lines are simulated: line A, which ends on the extraction hole, and line B, which ends on the caesiated molybdenum PG surface. The complete motion of electrons and ions (H^+ , H_2^+ , H_3^+) is calculated in the selfconsistent electric and applied magnetic fields by solving the equation of motion, including collisional effects via different Monte Carlo techniques and using a spatial grid (cell of the order of Debye length) for the

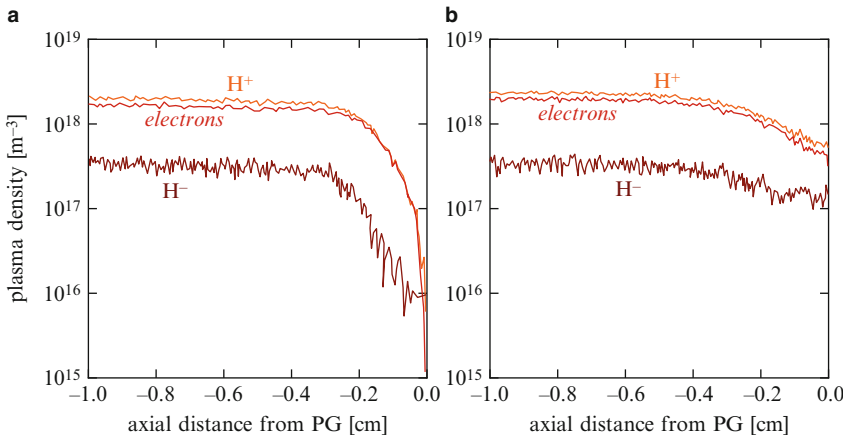


Fig. 10.16 Axial profiles of plasma density for the two lines considered. **(a)** Extraction hole, Line A and **(b)** plasma grid, Line B with PG biased at 0 V (From Taccogna et al. 2008a)

potential calculations as in typical particle in cell (PIC) cycle. In this module only charged particles are moved and the code does not follow the dynamics of neutrals but rather treats the latter as a fixed background with density and velocities profiles from the previous iteration of the neutral module, the same used in the expansion region. When the particles cross the opening in the PG (line A) they are extracted and lost. On the contrary when ions reach the PG surface among the different processes occurring (reflection, neutralization, recombination and dissociation) the activation of high vibrational states AV and the formation of negative ions by electron capture from the wall are the most important, because they are directly related to the negative ion production.

Figure 10.16a, b (Taccogna et al. 2008a) shows the profiles of electron, positive and negative ions along the axial distance from PG for the two lines reported in Fig. 10.15. The negative ion density increases by an order of magnitude in the case with surface production (Fig. 10.16b) as compared with the extraction hole situation.

10.5 Negative Ion Energy Distribution Function

The knowledge of the negative ion temperature is thus very important and much effort has been done, both from the theoretical and from the experimental point of view, in order to explain the mechanisms that determine the ion energy distribution function (iedf) (Hatayama et al. 2004; Bacal 2006; Diomede and Longo 2008). A few years ago a method suitable for exact treatment of ion transport in gases has been developed. The method is a Monte Carlo solution of the linear Boltzmann equation for the transport of particles diluted in a bulk gas. It is based on a constructive demonstration as mentioned in Chap. 4 and therefore formally demonstrated

to provide an exact solution of the linear problem. Being based on the complete form of the Boltzmann collision term including the thermal speed distribution of target particles, this method is accurate, as requested in such cases, down to thermal energy. The starting point is the expression of the real collision frequency for a H particle moving with velocity \mathbf{v} , given by

$$\nu(\mathbf{v}) = \int d^3w \alpha(g)f(\mathbf{w}) \quad (10.27)$$

where f is the velocity distribution function of target particles and α is the collision pair frequency defined as

$$\alpha = \sigma g n_b. \quad (10.28)$$

σ is the total cross section, $g = |\mathbf{v} - \mathbf{w}|$ is the relative speed of the collision pair and n_b is the target particle density.

By replacing $g\sigma(g)$ with $(g\sigma(g))_{max}$ in the integral expression (10.27) this last can be rewritten into the form $\nu(\mathbf{v}) = \alpha_{max}$ where

$$\alpha_{max} = (g\sigma(g))_{max} n_b. \quad (10.29)$$

Since α_{max} is not a function of g , the time to next collision after any test particle collision can be generated as a function of the random η sampled from a uniform distribution in $]0, 1]$ by the known formula

$$t_c = -(1/\alpha_{max})\ln(\eta) \quad (10.30)$$

which can be actually derived from a formal solution of the transport equation (Longo 2000).

A fraction of the collisions contributing to α_{max} is not real and is be removed as shown later to obtain the exact solution.

This time is re-calculated after any collision based on the statistical distribution $p(t)$ of free-flight-time using an excess-estimated collision frequency ω , i.e.

$$p(t) = \omega \exp(-\omega t)$$

The simulation proceeds to the nearest possible event in time: those of the j -th ion for which $t_c(j)$ is the lowest. Now the velocity $\mathbf{v}(j)$ is changed taking into account the electric field E , i.e. by adding the velocity change given by

$$\Delta\mathbf{v} = e\mathbf{v}E t_c(j)/m$$

A possible collision partner (atom or molecule) is randomly generated with a velocity \mathbf{w} which is selected from a Maxwell distribution at the gas temperature.

For this purpose velocity component v_i along each i -direction of a target particle are sampled by consecutive uses of the following formula

$$v_i = (-2k_B T_g \ln \eta_1 / m_{bulk})^{1/2} \sin(2\pi \eta_2) \quad (10.31)$$

which uses two random numbers η_1 and η_2 sampled from uniform distributions in the range $[0, 1]$.

The collision event occurs with a probability given by

$$P(g) = g n \sigma_{mt}(g) / \omega$$

where g is the relative speed of the pair

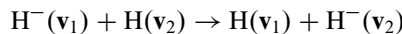
$$g = |\mathbf{v} + \Delta\mathbf{v} - \mathbf{w}|$$

In order to remove the extra collision events used to equalize the collision frequency to α_{max} , a further random number η_3 is compared to the fraction of real collisions given by α/α_{max} . If η_3 is smaller than this quantity, the collision is effective.

After an effective collision, the relative speed of the pair is rotated in space based on an isotropic distribution. Otherwise, no velocity variation occurs: in both cases a new collision time is generated for the ion. The proposed collision partner is forgotten. ω is empirically adjusted in order to obtain a negligible proportion of unphysical events for which P is greater than 1.

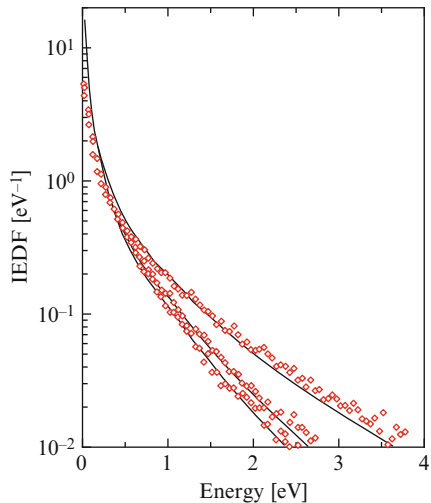
Let us see how a practical simulation works. A large ensemble of simulated particles is set initially at zero energy, or random distributed at thermal energy, whatever initial condition is considered sound, since one looks for steady-state results and the initial condition is not important. Then the ensemble is allowed to evolve for a time long enough to forget the initial conditions, which must be evaluated by monitoring the evolution of a sensible statistical estimator, e.g. the fraction of particles the ensemble with a kinetic energy higher than a few times the thermal energy.

An account of the iedf can be obtained by a simplified model where assume a uniform plasma model, where the iedf is supposed to result from the collisional kinetics of negative ions in the weakly ionized plasma with neutral particles, here H atoms since we can assume that the gas is fully dissociated as an approximation (in the expansion region, or plasma cooling region of real devices the fraction of molecules is about 0.3) and the most important collision process is the symmetric charge-exchange



The cross section used is that of Diomede and Longo (2008) where more details on a similar calculation are reported. In Fig. 10.17 the results of the MC simulation and the curve obtained by using an analytical model described in Diomede and

Fig. 10.17 H^- ion energy distribution function (iedf) as a function of energy as obtained from the analytical model (full line) and a test particle Monte Carlo simulation (markers). The two distributions are characterized by the same average kinetic energy



Longo (2008) are compared for different values of the reduced electric field E/N . An excellent agreement is obtained in the high energy region of the distribution, which is mostly determined by high energy ion removal due to exchange process, while the thermal bulk is sensibly different from the prediction of the simple model, being determined by the thermal background of molecules, contrary to the assumption $T_g = 0$ of the simple analytical model. The high energy regions is also seen to be roughly approximated as a two-T distribution, as mentioned earlier. It must be noted that, under conditions where the analytical model is appropriate, the ion distribution is very far from an equilibrium one: this is specially true from the point of view of angle distribution. When ions are basically created, accelerated and slowed down to thermal, the velocity distribution, with the exception of the very low energy range, is strongly unidirectional, realizing the exact opposite of the hypothesis of weak anisotropy which is the basis of the calculations in Chap. 4. The convergence of an expansion of the velocity distribution $f(\mathbf{v})$ into spherical harmonics for a given ion speed v is also extremely slow.

References

- Bacal M (2006) Physics aspects of negative ion sources. Nucl Fusion 46(6):S250–S259
- Bacal M, Hamilton GW (1979) H^- and D^- production in plasmas. Phys Rev Lett 42(23):1538
- Bacal M, Bruneteau AM, Nachman M (1984) Negative ion production in hydrogen plasmas confined by a multicusp magnetic field. J Appl Phys 55(1):15–24
- Bacal M, Baksht F, Ivanov V (1999) Increase of the effective rate constant of the dissociative attachment of electrons to hydrogen molecules due to the H_2 vibrational excitation in a hydrogen stream flowing in the channel. J Phys D Appl Phys 32(22):2886–2889
- Baksht FG, Ivanov VG, Shkol'nik SM, Bacal M (2005) Volume production of high negative hydrogen ion density in low-voltage caesium-hydrogen discharge. AIP Conf Proc 763(1):138–142

- Bandyopadhyay M (2004) Studies of an inductively coupled negative hydrogen ion radio frequency source through simulations and experiments. PhD thesis Technische Universität München, Max-Planck-Institut für Plasmaphysik, Garching
- Béchu S, Soum-Glaude A, Bès A, Lacoste A, Svartnas P, Aleiferis S, Ivanov AA, Bacal M (2013) Multi-dipolar microwave plasmas and their application to negative ion production. *Phys Plasmas* (1994-present) 20(10):101601
- Benmeziane K, Ferdinand R, Gobin R, Gousset G, Sherman JD (2005) 2D PIC-MCC code for Electron-Hydrogen gas interaction study in H⁻ ion sources. *AIP Conf Proc* 763:107–121
- Blackwell DD, Chen FF (2001) Time-resolved measurements of the electron energy distribution function in a helicon plasma. *Plasma Sources Sci Technol* 10(2):226
- Boeuf J, Chaudhury B, Garrigues L (2012) Physics of a magnetic filter for negative ion sources. I. Collisional transport across the filter in an ideal, 1D filter. *Phys Plasmas* 19(11):113509
- Bogaerts A, Gijbels R, Vleek J (1998) Collisional-radiative model for an argon glow discharge. *J Appl Phys* 84(1):121–136
- Bowers MT, Elleman DD, King J (1969) Analysis of the Ion-Molecule reactions in gaseous H₂, D₂, and HD by ion cyclotron resonance techniques. *J Chem Phys* 50(11):4787–4804
- Bretagne J, Delouya G, Gorse C, Capitelli M, Bacal M (1985) Electron energy distribution functions in electron-beam-sustained discharges: application to magnetic multicusp hydrogen discharges. *J Phys D Appl Phys* 18(5):811
- Bretagne J, Delouya G, Capitelli M, Gorse C, Bacal M (1986) On electron energy distribution functions in low-pressure magnetic multicusp hydrogen discharges. *J Phys D Appl Phys* 19(7):1197
- Bretagne J, Graham WG, Hopkins MB (1991) A comparison of experimental and theoretical electron energy distribution functions in a multicusp ion source. *J Phys D Appl Phys* 24(5):668
- Cacciato M, Capitelli M, Billing GD (1989) Vibration-to-translation energy exchanges in H₂ colliding with highly vibrationally excited H₂ molecules. *Chem Phys Lett* 157(4):305–308
- Capitelli M (2005) Twenty five years of vibrational kinetics and negative ion production in H₂ plasmas: modelling aspects. *AIP Conf Proc* 763:66–80
- Capitelli M, Gorse C (2005) Open problems in the physics of volume H⁻-D⁻ sources. *IEEE Trans Plasma Sci* 33(6):1832–1844
- Capitelli M, Celiberto R, Eletskii A, Laricchiuta A (2001) Electron-molecule dissociation cross-sections of H₂, N₂ and O₂ in different vibrational levels. *Atomic Plasma-Mater Interact Data Fusion (APID)* 9:47–64
- Capitelli M, Celiberto R, Esposito F, Laricchiuta A, Hassouni K, Longo S (2002) Elementary processes and kinetics of H₂ plasmas for different technological applications. *Plasma Sources Sci Technol* 11(3A):A7
- Capitelli M, Cacciato M, Celiberto R, De Pascale O, Diomede P, Esposito F, Gicquel A, Gorse C, Hassouni K, Laricchiuta A, Longo S, Pagano D, Rutigliano M (2006) Vibrational kinetics, electron dynamics and elementary processes in H₂ and D₂ plasmas for negative ion production: modelling aspects. *Nucl Fusion* 46(6):S260–S274
- Capitelli M, Celiberto R, Colonna G, D'Ammando G, De Pascale O, Diomede P, Esposito F, Gorse C, Laricchiuta A, Longo S, Pietanza LD, Taccogna F (2011) Plasma kinetics in molecular plasmas and modeling of reentry plasmas. *Plasma Phys Control Fusion* 53(12):124007
- Celiberto R, Janev R, Laricchiuta A, Capitelli M, Wadehra J, Atems D (2001) Cross section data for electron-impact inelastic processes of vibrationally excited molecules of hydrogen and its isotopes. *Atomic Data Nucl Data Tables* 77(2):161–213
- Celiberto R, Capitelli M, Laricchiuta A (2002) Towards a cross section database of excited atomic and molecular hydrogen. *Phys Scr* 2002(T96):32
- Chibisov MI, Mitchell JBA, Van der Donk PJT, Yousif FB, Morgan TJ (1997) Dissociative recombination of vibrationally excited H₂⁺ ions: high-Rydberg-state formation. *Phys Rev A* 56:443–456
- Datskos PG, Pinnaduwage LA, Kielkopf JF (1997) Photophysical and electron attachment properties of ArF-excimer-laser irradiated H₂. *Phys Rev A* 55(6):4131–4142

- Diomede P, Longo S (2008) Velocity distribution of H^- ions in low temperature hydrogen plasma. *IEEE Trans Plasma Sci* 36(4):1600–1606
- Diomede P, Longo S (2010) Monte Carlo Cs^+ transport from a point source in negative ion sources: effect of the deuterium flow. *Plasma Sources Sci Technol* 19(1):015019
- Diomede P, Longo S, Capitelli M (2005) Vibrational excitation and negative ion production in radio frequency parallel plate H_2 plasmas. *Eur Phys J D* 33(2):243–251
- Diomede P, Longo S, Capitelli M (2006) Charged particle dynamics and molecular kinetics in the hydrogen postdischarge plasma. *Phys Plasmas* 13(11):113505
- Diomede P, Hassouni K, Longo S, Capitelli M (2007) Self-consistent modeling of the effect of wall-neutral reactions on parallel plate radio frequency discharge plasma in pure hydrogen. *IEEE Trans Plasma Sci* 35(5):1241–1246
- Eenshuistra PJ, Bonnie JHM, Los J, Hopman HJ (1988) Observation of exceptionally high vibrational excitation of hydrogen molecules formed by wall recombination. *Phys Rev Lett* 60:341–344
- Fantz U, Falter H, Franzen P, Wunderlich D, Berger M, Lorenz A, Kraus W, McNeely P, Riedl R, Speth E (2006a) Spectroscopy—a powerful diagnostic tool in source development. *Nucl Fusion* 46(6):S297
- Fantz U, Falter HD, Franzen P, Speth E, Hemsworth R, Boilson D, Krylov A (2006b) Plasma diagnostic tools for optimizing negative hydrogen ion sources. *Rev Sci Instrum* 77(3):03A516
- Fubiani G, Boeuf JP (2013) Role of positive ions on the surface production of negative ions in a fusion plasma reactor type negative ion source—Insights from a three dimensional particle-in-cell Monte Carlo collisions model. *Phys Plasmas* 20(11):113511
- Fukumasa O (1989) Numerical studies on the optimisation of volume-produced H^- ions in the single-chamber system. *J Phys D Appl Phys* 22(11):1668
- Fukumasa O, Mori S (2005) Isotope effect of H^-/D^- volume production in Low-Pressure H_2/D_2 plasmas – negative ion densities versus plasma parameters. *AIP Conf Proc* 763:57–65
- Fukumasa O, Shinoda M (1998) Pulse modulation for plasma parameter control and optimization of volume H^- ion source. *Rev Sci Instrum* 69(2):938–940
- Fukumasa O, Nakano T, Mori S, Oohara W, Tsumori K, Takeiri Y, Surrey E, Simonin A (2009) Enhancement of D^- negative ion volume production in pure deuterium plasmas. *AIP Conf Proc* 1097:118–126
- Gaboriau F, Boeuf JP (2014) Chemical kinetics of low pressure high density hydrogen plasmas: application to negative ion sources for ITER. *Plasma Sources Sci Technol* 23(6):065032
- Garscadden A, Nagpal R (1995) Non-equilibrium electronic and vibrational kinetics in H_2-N_2 and H_2 discharges. *Plasma Sources Sci Technol* 4(2):268
- Goretsky VP, Ryabtsev AV, Soloshenko IA, Shchedrin AI (2007) Research of the negative ion source based on reflective discharge with and without addition of cesium. *AIP Conf Proc* 925:58–68
- Gorse C, Capitelli M (1992) Enhanced production of negative ions in low-pressure hydrogen and deuterium pulsed discharges: theoretical calculations. *Phys Rev A* 46(4):2176–2177
- Gorse C, Capitelli M, Bretagne J, Bacal M (1985) Vibrational excitation and negative-ion production in magnetic multicusp hydrogen discharges. *Chem Phys* 93(1):1–12
- Gorse C, Capitelli M, Bacal M, Bretagne J, Laganà A (1987) Progress in the non-equilibrium vibrational kinetics of hydrogen in magnetic multicusp H^- ion sources. *Chem Phys* 117(2):177–195
- Gorse C, Celiberto R, Cacciatore M, Laganà A, Capitelli M (1992) From dynamics to modeling of plasma complex systems: negative ion (H^-) sources. *Chem Phys* 161(1–2):211–227
- Gorse C, Capitelli M, Celiberto R, Iasillo D, Longo S (1996) Recent advances in H_2/D_2 plasma kinetics. *AIP Conf Proc* 380:109–117
- Hall RI, Čadež I, Landau M, Pichou F, Schermann C (1988) Vibrational excitation of hydrogen via recombinative desorption of atomic hydrogen gas on a metal surface. *Phys Rev Lett* 60:337–340
- Hassouni K, Gicquel A, Capitelli M (1998) The role of dissociative attachment from Rydberg states in enhancing H^- concentration in moderate- and low-pressure H_2 plasma sources. *Chem Phys Lett* 290(4–6):502–508

- Hassouni K, Gicquel A, Capitelli M, Loureiro J (1999) Chemical kinetics and energy transfer in moderate pressure H₂ plasmas used in diamond MPACVD processes. *Plasma Sources Sci Technol* 8(3):494
- Hassouni K, Silva F, Gicquel A (2010) Modelling of diamond deposition microwave cavity generated plasmas. *J Phys D Appl Phys* 43(15):153001
- Hatayama A, Makino K, Sakurabayasi T, Miyamoto K, Ogasawara M, Bacal M (2004) Numerical analysis of negative ion temperature in a negative ion source. *Rev Sci Instrum* 75(5):1650–1652
- Hiskes JR (1980) Cross sections for the vibrational excitation of the H₂(X¹Σ_g⁺) state via electron collisional excitation of the higher singlet states. *J Appl Phys* 51(9):4592–4594
- Hiskes JR (1996a) Molecular Rydberg states in hydrogen negative ion discharges. *Appl Phys Lett* 69(6):755
- Hiskes JR (1996b) The role of high Rydberg states in the generation of negative ions in negative-ion discharges. *AIP Conf Proc* 380:61–75
- Hiskes JR, Karo AM (1984) Generation of negative ions in tandem high-density hydrogen discharges. *J Appl Phys* 56(7):1927–1938
- Hiskes JR, Karo AM (1989) Analysis of the H₂ vibrational distribution in a hydrogen discharge. *Appl Phys Lett* 54(6):508–510
- Hiskes JR, Karo AM, Willmann PA (1985) Optimum extracted negative-ion current densities from tandem high-density systems. *J Appl Phys* 58(5):1759–1764
- Hopkins MB, Mellon KN (1991) Enhanced production of negative ions in low-pressure hydrogen and deuterium discharges. *Phys Rev Lett* 67(4):449–452
- Hopkins MB, Bacal M, Graham WG (1991) Enhanced volume production of negative ions in the post discharge of a multicusp hydrogen discharge. *J Appl Phys* 70(4):2009–2014
- Hopman H, Heeren R (1992) Negative ion source technology. In: Capitelli M, Gorse C (eds) *Plasma technology*. Springer US, pp 185–201
- Huh SR, Kim NK, Jung BK, Chung KJ, Hwang YS, Kim GH (2015) Global model analysis of negative ion generation in low-pressure inductively coupled hydrogen plasmas with bi-maxwellian electron energy distributions. *Phys Plasmas* 22(3):033506
- IAEA (2013) Atomic and Molecular Data Unit. www-amdis.iaea.org
- Ichihara A, Iwamoto O, Janev RK (2000) Cross sections for the reaction H⁺ + H₂(v=0-14) → H+H₂⁺ at low collision energies. *J Phys B Atomic Mol Opt Phys* 33(21):4747
- Janev RK, Reiter D, Samm U (2003) Collisional processes in low temperature hydrogen plasmas. Institut für Plasmaphysik, Jülich, Germany Forschungszentrum Jülich Rep. 4105
- Ji-Zhong S, Xian-Tao L, Jing B, De-Zhen W (2012) Using short pulses to enhance the production rate of vibrationally excited hydrogen molecules in hydrogen discharge. *Chin Phys B* 21(5):055205
- Karpas Z, Anicich V, Huntress WT (1979) An ion cyclotron resonance study of reactions of ions with hydrogen atoms. *J Chem Phys* 70(6):2877–2881
- Kim YK, Rudd ME (1994) Binary-encounter-dipole model for electron-impact ionization. *Phys Rev A* 50(5):3954–3967
- Kramers HA (1923) XCIII. On the theory of x-ray absorption and of the continuous x-ray spectrum. *Philosophical Magazine Series 6* 46(275):836–871
- Laricchiuta A, Celiberto R, Esposito F, Capitelli M (2006) State-to-state cross sections for H₂ and its isotopic variants. *Plasma Sources Sci Technol* 15(2):S62
- Longo S (2000) Monte Carlo models of electron and ion transport in non-equilibrium plasmas. *Plasma Sources Sci Technol* 9(4):468
- Matveyev AA, Silakov VP (1995) Kinetic processes in a highly-ionized non-equilibrium hydrogen plasma. *Plasma Sources Sci Technol* 4(4):606
- Mosbach T (2002) Do hydrogenic Rydberg molecules represent an efficient channel for the production of H⁻ ions in low temperature plasmas? Conference paper 16th European conference on atomic and molecular physics of ionized gases (ESCAPEIG16), Grenoble, France pp 231–232
- Mosbach T (2005) Population dynamics of molecular hydrogen and formation of negative hydrogen ions in a magnetically confined low temperature plasma. *Plasma Sources Sci Technol* 14(3):610

- Mosbach T, Katsch HM, Döbele HF (1998) Temporal behaviour of the H⁻ density in a pulsed multipole discharge investigated by the photodetachment technique. *Plasma Sources Sci Technol* 7(1):75
- Mosbach T, Katsch HM, Döbele HF (2000) In situ diagnostics in plasmas of electronic-ground-state hydrogen molecules in high vibrational and rotational states by laser-induced fluorescence with vacuum-ultraviolet radiation. *Phys Rev Lett* 85(16):3420
- NIST (2013) Atomic spectra database and lines. physics.nist.gov/cgi-bin/AtData/lines_form
- Pagano D, Gorse C, Capitelli M (2006) Atomic wall recombination and volume negative ion production. *Rev Sci Instrum* 77(3):03A505
- Pagano D, Gorse C, Capitelli M (2007) Modeling multicusp negative-ion sources. *IEEE Trans Plasma Sci* 35(5):1247–1259
- Pinnaduwage LA, Christophorou LG (1993) H⁻ formation in laser-excited molecular hydrogen. *Phys Rev Lett* 70(6):754–757
- Pinnaduwage LA, Ding WX, McCorkle DL, Lin SH, Mebel AM, Garscadden A (1999) Enhanced electron attachment to Rydberg states in molecular hydrogen volume discharges. *J Appl Phys* 85(10):7064–7069
- Shakhatov V, Lebedev Y (2011) Collisional-radiative model of hydrogen low-temperature plasma: processes and cross sections of electron-molecule collisions. *High Temp* 49(2):257–302
- Shibata T, Kashiwagi M, Inoue T, Hatayama A, Hanada M (2013) Numerical study of atomic production rate in hydrogen negative ion sources with the effect of non-equilibrium electron energy distribution function. *J Appl Phys* 114(14):143301
- Svartnas P, Breton J, Bacal M, Mosbach T (2006) Pressure optimization for H⁻ ion production in an electron cyclotron resonance-driven and a filamented source. *Rev Sci Instrum* 77(3):03A532
- Taccogna F, Schneider R, Longo S, Capitelli M (2007) Modeling of a negative ion source. I. Gas kinetics and dynamics in the expansion region. *Phys Plasmas* 14(7):073503
- Taccogna F, Longo S, Capitelli M, Schneider R (2008a) Negative-ion-source modeling: from expansion to extraction region. *IEEE Trans Plasma Sci* 36(4):1589–1599
- Taccogna F, Schneider R, Longo S, Capitelli M (2008b) Modeling of a negative ion source. II. Plasma-gas coupling in the extraction region. *Phys Plasmas* 15(10):103502
- Taccogna F, Minelli P, Longo S, Capitelli M, Schneider R (2010) Modeling of a negative ion source. III. Two-dimensional structure of the extraction region. *Phys Plasmas* 17(6):063502
- Taccogna F, Minelli P, Diomede P, Longo S, Capitelli M, Schneider R (2011) Particle modelling of the hybrid negative ion source. *Plasma Sources Sci Technol* 20(2):024009
- Taccogna F, Minelli P, Longo S (2013) Three-dimensional structure of the extraction region of a hybrid negative ion source. *Plasma Sources Sci Technol* 22(4):045019
- Tawara H, Itikawa Y, Nishimura H, Yoshino M (1990) Cross sections and related data for electron collisions with hydrogen molecules and molecular ions. *J Phys Chem Ref Data* 19(3):617–636
- Toader EI (2004) Production of negative hydrogen ions using a low-pressure reflex discharge source. *Nukleonika* 51(1):29–35
- Velasco AJC, Dougar-Jabon V (2004) Electron cyclotron resonance discharge as a source for hydrogen and deuterium ions production. 12th International congress on plasma physics, 25–29 Oct 2004, Nice, arXiv:physics/0411128
- Zorat R, Goss J, Boilson D, Vender D (2000) Global model of a radiofrequency H₂ plasma in DENISE. *Plasma Sources Sci Technol* 9(2):161

Chapter 11

Non Equilibrium Plasma in High Enthalpy Flows

Thermal and chemical non-equilibrium is a necessary assumption to understand the complex phenomenology of space vehicle entering a planetary atmosphere. The main requirement is to estimate the heat flux on the vehicle surface, which must account not only for the Fourier contribution (thermal conductivity) but also for radiation heating and surface processes. Another important aspect is the disturbance of the plasma to radio-communications, strongly affected by the ionization degree around the body. The extreme conditions inside the shock layer formed during the atmospheric entry makes extremely difficult to measure these quantities directly. Expensive ground test facilities (plasma wind tunnels) are of fundamental importance to reproduce the environment of an hypersonic object entering planetary atmospheres as well as astrophysical jets and strong explosions.

Different theoretical models have been proposed to investigate the role of non-equilibrium in high enthalpy flows, such as the supersonic expansion through converging-diverging nozzles of various geometries or shock wave formation. During gas expansion, its thermal energy is converted into kinetic one leading to an increase of velocity and a decrease in density, pressure and thermal translational energy enhancing recombination process of atomic species, forming molecules in highly excited vibrational states, resulting in strong non equilibrium vibrational distributions.

During shock formation, the gas temperature abruptly increases and the speed decreases as the flow crosses the shock front. However, the molecular vibration needs time to be heated, in order to activate chemical processes, such as dissociation, resulting in underpopulation of the vibrational distribution tails. Depending on the higher temperature in the flow field, the gas mixtures can be composed, in addition to molecules and atoms, of free electrons and ions.

Multi-temperature approaches (Park 2012), commonly used to model non-equilibrium among translation, internal and electron temperatures, considers Boltzmann and Maxwell distributions for internal degrees of freedom and free electrons

respectively, characterized by their own independent temperatures. In this approach, rate coefficients are expressed as a function of the temperatures of the degrees of freedom involved in the reaction. A commonly used model consider Arrhenius-type rates function of an effective temperature calculated as the geometrical mean of relevant temperatures. This kind of approach reproduces with good accuracy the behavior of the distribution at low vibrational quantum number, but cannot take into account the non-Boltzmann distribution for high v and only a state-to-state approach seems capable to describe the whole features of the vibrational distributions in high enthalpy flows.

The main problem in using the state-to-state kinetics in modeling hypersonic flows is the large number of mass continuity equations, that, with few exception (Giordano et al. 1997; Cutrone et al. 2015; Tuttafesta 2014), has been used only in 1D calculations (Colonna et al. 1999b, 2000a; Colonna and Capitelli 2001a,b; Munafò et al. 2012; Starik et al. 2010; Kadochnikov et al. 2013).

To overcome this problem, more refined treatments considered Treanor-type distributions at the local gas and vibrational temperatures (Nagnibeda and Kustova 2009) and, very recently, developments are being considered for reducing state-to-state approach to simplified models (Colonna et al. 2006, 2008; Guy et al. 2013), trying to account for the same features as the extended vibrational kinetic scheme.

This Chapter is devoted to describe the results obtained essentially by our group in modeling high enthalpy flows in 1D approximation and in particular in nozzle expansion and shock wave formation.

11.1 Fluid Dynamic Model for State-to-State Kinetics

In this section, we will briefly describe the general model for a reacting flow through a converging-diverging nozzle in the quasi one-dimensional approximation and in stationary conditions (Anderson 2000). The fluid dynamics is described by Euler equations, which assume the form:

$$\begin{aligned}
 \frac{d(\rho u A)}{dx} &= 0 && \text{mass conservation} \\
 \frac{dP}{dx} + \rho u \frac{du}{dx} &= 0 && \text{momentum conservation} \\
 u \frac{du}{dx} + \frac{dh_T}{dx} + \frac{dh_v}{dx} &= 0 && \text{energy conservation} \\
 \frac{d(\rho_{iv} u A)}{dx} &= \dot{\rho}_{iv} && \text{chemical reactions} \\
 P &= \frac{\rho R T}{\bar{m}} && \text{state equation}
 \end{aligned} \tag{11.1}$$

where x is the position coordinate along the nozzle axis, A is the nozzle section, ρ is the total mass density, and ρ_{iv} is the mass density of the i th species in the v th level, $\dot{\rho}_{iv}$ is the density production rate due to chemical processes, u is the flow speed, P is the hydrostatic pressure, T is the translational temperature, h_T and h_v are respectively the translational and the internal specific enthalpies, R is the ideal gas universal constant, and \bar{m} is the mean molar mass. The translational enthalpy h_T is proportional to the gas temperature according to the relation:

$$h_T = \frac{c_P}{\bar{m}} = \alpha \frac{RT}{\bar{m}} T = \frac{RT}{\bar{m}} \sum_i c_i \alpha_i \quad (11.2)$$

where c_p is the constant pressure molar specific heat, $\alpha_i = c_{p,i}/R$, where $c_{p,i}$ is the constant pressure specific heat¹ of the i th species, and c_i is the molar fraction of the i th species. The specific heat must be calculated considering only the contribution of the translational degrees of freedom and of other degrees of freedom in equilibrium with it. The internal enthalpy h_v takes into account the degree of freedom in non-equilibrium, such as chemical and internal contributions (in our case, molecular vibration):

$$h_v = \frac{1}{\bar{m}} \sum_{iv} c_i \chi_{iv} (H_i^f + \varepsilon_{iv}) \quad (11.3)$$

where H_i^f is the molar formation enthalpy of the i th species and χ_{iv} and ε_{iv} are the internal distribution and the energy of the levels.

At the nozzle inlet the flow is very slow, while temperature and pressure are very high. Close to the throat the flow velocity is close to the local speed of sound, becoming supersonic at the nozzle exit. Pressure and temperature are decreasing function of the nozzle position, reaching low values at the exit. As a consequence, the gas passes from local equilibrium in the converging part of the nozzle, where the characteristic time of the processes is much larger than the flow residence time, to strong non-equilibrium at the exit, where the flow is considered chemically and thermally frozen.

The classical approach to solve the nozzle equations (Colonna et al. 2001) consists in writing all the macroscopic quantities as a function of the flow speed, which is calculated by solving the following differential equation

¹This result is valid only if the single species specific heat is constant. For atomic species this assumption is valid because α_i includes only the translational degrees of freedom. For molecular species, because α_i includes also the rotational degrees of freedom, this relation holds only if the temperature is sufficiently high to neglect quantum effects in molecular rotation. The electronic excitation of both atoms and molecules are to be considered as non-equilibrium degrees of freedom. In general the dependence of h_T on the temperature can be a complex expression.

$$\frac{du}{udx} = \frac{\frac{dA}{Adx} + \frac{d\alpha}{\alpha dx} + \frac{1}{(\alpha-1)c_s^2} \frac{dh_v}{dx}}{M^2 - 1} \quad (11.4)$$

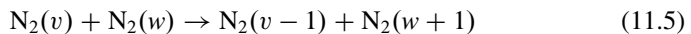
where c_s is the speed of sound and $M = u/c_s$ is the Mach number. The numerator of the right side fraction contains one term depending on the geometry of the nozzle ($\frac{dA}{Adx}$) and the other two depends on the chemical processes and internal distribution relaxation ($\frac{dh_v}{dx}$). Considering only the geometrical term, the solution exists only if the $M = 1$ in the throat. The other two terms are less than or equal to zero, moving the sonic point somewhere in the divergent part. While temperature and pressure are given at the nozzle inlet, the inlet speed must be determined with the condition that numerator and denominator becomes null in the same position. Numerical solution of Eq. (11.4) presents some numerical instabilities.

An alternative approach has been proposed, rearranging the Euler equations as proposed in Colonna et al. (2001), which avoids the numerical problems in Eq. (11.4), giving also a criteria to find the initial velocity and the sonic point position.

The same set of equations can be used to solve the shock tube problem, considering constant the section of the nozzle. Moreover, the supersonic inlet conditions must be imposed, with low pressure and temperature, considering a sudden increase of temperature and pressure as the flow crosses the shock front, determining the post-shock conditions using the Rankine-Hugoniot relations neglecting chemical processes and the relaxation of internal degrees of freedom.

11.2 N₂ Vibrational Kinetics in Nozzle

The simplest case of state-to-state model is the vibrational kinetics of pure gases. In this section we will focus on N₂/N mixture, considering in this case 68 vibrational levels for nitrogen molecules. The kinetic model includes internal transitions, i.e. VV (vibration-vibration), VT_M (vibration-translation by molecules) and VT (vibration-translation by atoms) exchanges processes, in the order



and dissociation-recombination processes by molecule-molecule and molecule-atom collisions



The behavior of different dissociation-recombination models (direct dissociation or ladder climbing, see Sect. 7.1.3) has been investigated, comparing results obtained with these dissociation rates of the process (11.9)

QCT Dissociation rates have been calculated using QCT data taken from Capitelli et al. (2004)

LC Dissociation rates have been obtained extrapolating the VT rates to a virtual level above the dissociation limit (ladder climbing)

These two models have been applied to the expansion through the conic nozzle reported in Fig. 11.1, considering as reservoir conditions $P_0 = 1 \text{ atm}$ and $T_0 = 8,000 \text{ K}$. In these conditions, the inlet dissociation degree (in equilibrium) is around 90 %, so that recombination is the leading process for high energy vibrational levels (see Chap. 7) and as a consequence results obtained with the two dissociation-recombination models should present large differences. In general, the vibrational kinetics weakly affects the macroscopic quantities such as flow speed, temperature, and pressure profiles because the energy exchanged with the translational degrees of freedom in vibrational processes is small, this point being confirmed by the present calculations. As an example, we can observe that the temperature axial profile, reported in Fig. 11.2 normalized by T_0 , shows very small differences between the two dissociation models.

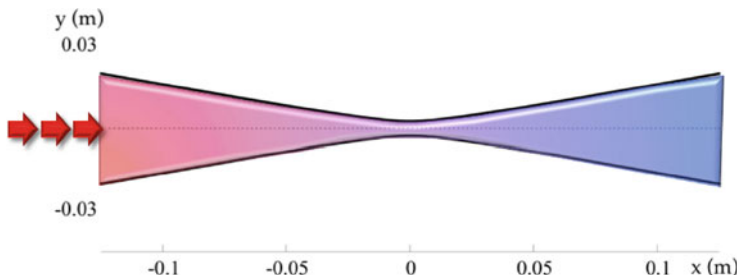
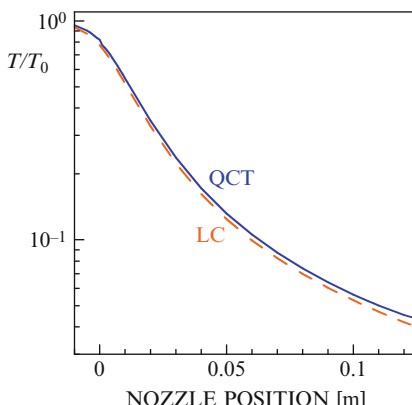


Fig. 11.1 Longitudinal section and reference frame of the conic nozzle, borrowed from the work of Shizgal in an oxygen mixture (Shizgal and Lordet 1996)

Fig. 11.2 Temperature profile in the nozzle outlet for QCT and LC models.
 $T_0=8,000 \text{ K}$.
 $P_0=1 \text{ atm}$ (Capitelli et al. 2004)



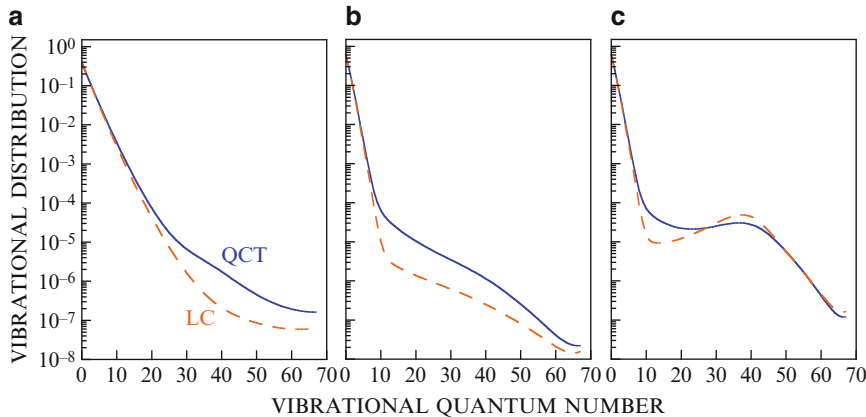


Fig. 11.3 N_2 vibrational distributions for QCT and LC models, at different positions in the nozzle: (a) nozzle throat ($x = 0$); (b) $x = 0.05$ m; (c) $x = 0.1$ m. $T_0 = 8,000$ K. $P_0 = 1$ atm (Capitelli et al. 2004)

Larger effects can be observed in the vibrational distributions, reported in Figs. 11.3a–c, for different nozzle positions. The reported behavior shows a large dependence of the results on the adopted model (LC, QCT). Qualitatively, the two models show the same trend emphasizing large non-equilibrium vibrational distributions far from the nozzle throat. In particular, at the exit of the nozzle we can observe a long plateau in the vibrational distribution created by the recombination process, a result widely discussed in our previous calculations (Colonna et al. 2001; Colonna and Capitelli 2001a) (see also Sect. 7.2.1).

The differences in the vibrational distributions are reflected on the global dissociation rate, calculated as

$$k_d^{\text{N}/\text{N}_2} = \sum_{v=0} \chi_{\text{N}_2,v} k_{v \rightarrow c}^{\text{N}/\text{N}_2} \quad (11.10)$$

where $k_{v \rightarrow c}^{\text{N}/\text{N}_2}$ is the state-specific dissociation rate, either by atomic or molecular collisions. This rate is strongly affected by non-equilibrium behavior of the distribution, being the dissociation process favored from highly excited states. Let us now examine the global dissociation rate of N_2 molecules induced by collisions with atomic nitrogen ($k_{v \rightarrow c}^{\text{N}}$) along the nozzle axis (see Fig. 11.4), drawing these values as a function of the inverse of the local translational temperature in an Arrhenius-type plot. The results, which are strongly dependent on the adopted model, show non-Arrhenius behavior of the dissociation rates as a consequence of non-Boltzmann vibrational distributions reported in Fig. 11.3. Note in fact that the dissociation rate increases as the translational temperature decreases, this behavior being much more important with the LC model. The consequence of this result is that along the divergent part of the nozzle there is no correlation between the global rate and

Fig. 11.4 Arrhenius plot of the global dissociation rate for process (11.9) for QCT and LC models.
 $T_0 = 8,000$ K.
 $P_0 = 1$ atm (Capitelli et al. 2004)

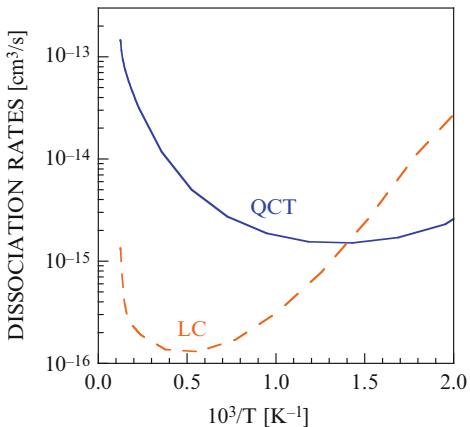
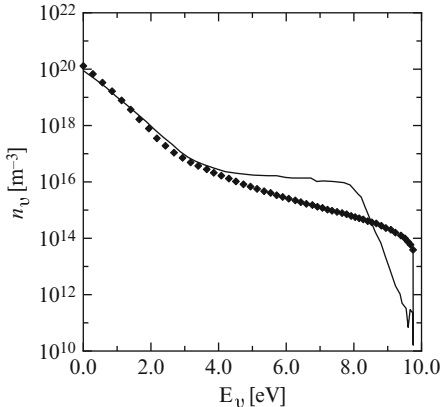


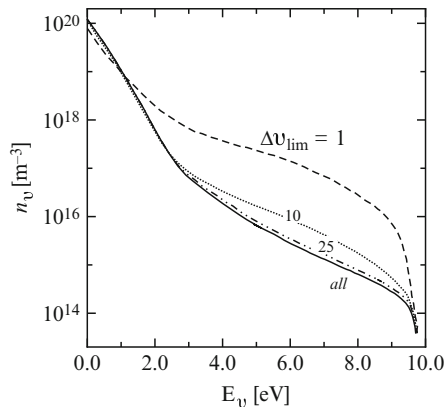
Fig. 11.5 Population of N₂ vibrational energy levels at $x = 0.083$ m. (solid line)
NASA ARC VT rate coefficients (Chaban et al. 2008; Jaffe et al. 2008, 2009; Schwenke 2008), (markers)
VT rate coefficients by Esposito et al. (2006)
(From Munafò et al. 2012)



the translational temperature. The global rate loses the correlation also with the vibrational temperature, which is a decreasing function of the nozzle position.

A similar approach has been used by Munafò et al. (2012) to investigate the dependence of vibrational distributions along the nozzle on the selection of VT rates (see process (11.7)), one set described in Esposito et al. (2006) and the other set from Chaban et al. (2008), Jaffe et al. (2008), Schwenke (2008) and Jaffe et al. (2009). The EAST facility nozzle has been used for the simulation, choosing as reservoir conditions $P_0 = 1$ atm and $T_0 = 10,000$ K, in order to neglect the N₂+N₂ VT rates. The comparison is reported in Fig. 11.5, where the non equilibrium vibrational distributions calculated with the two sets of VT rates have been compared at the nozzle exit ($x = 0.083$ m). Inspection of the figure shows a satisfactory agreement between the two calculations, the Nasa Ames results presenting a more pronounced tail in the high-lying portion of vdf. Both distributions contain also the role of multi-quantum VT rates, which play an important role in shaping the relevant vdf's. This point has been recently emphasized by Guy et al. (2013) (see Fig. 11.6).

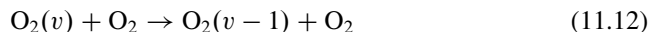
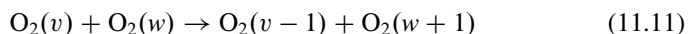
Fig. 11.6 Effect of varying the maximum allowed multi-quantum jump $\Delta v = |v' - v| \leq \Delta v_{\text{lim}}$ for atomic impact vibrational excitation and de-excitation by VT process on the N_2 vdf at the nozzle outlet.
 $T_0 = 10,000$ K. $P_0 = 1$ atm.
N mass fraction = 0.9867
(From Guy et al. 2013)



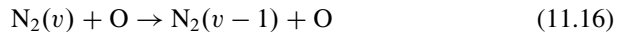
It is worth noting that the results of Fig. 11.5 are similar to those reported in Fig. 11.3c (Capitelli et al. 2004), despite the different nozzle geometries and different initial conditions. Moreover the reader can reflect on the similarity of these results with those shown in Chap. 7 for the vibrational kinetics in the boundary layer of re-entry bodies.

11.3 Air Vibrational Kinetics in Nozzle

A further step in developing state-to-state model is to extend the kinetic model to air mixture, N_2/O_2 , discussed by our group (Colonna et al. 1999b), adding to the kinetic model described in the previous section the vibrational kinetics of oxygen



VT relaxation of N_2 by atomic oxygen



and the first Zeldovich reaction



In this specific case, 46 vibrational levels have been considered for N₂ and 33 for O₂. Only mono-quantum transitions have been considered for relaxation processes involving oxygen. The dissociation rates have been calculated considering the ladder climbing approach, using rates from Armenise et al. (1996), Capitelli et al. (1997) and Colonna and Capitelli (1996), while the state-to-state dynamics of Zeldovich reactions being investigated in Bose and Candler (1996, 1997). The calculations have been performed for 1-m-long parabolic nozzle having cylindrical symmetry with the following radius equation

$$r(x) = 3.5x^2 - 3.5x + 1 \quad (11.18)$$

with x and r expressed in meters ($x_{\text{throat}} = 0.5$ m). The reservoir pressure is 1 atm while the reservoir temperature ranges from 4,000 to 8,000 K.

The vibrational distributions of both O₂ and N₂ as a function of vibrational quantum number at different nozzle positions have been reported in Fig. 11.7a–b in Colonna et al. (1999b). In both cases the non equilibrium character of vdf is evident; in particular the N₂ distribution presents a strong overpopulation at the nozzle exit.

The non Boltzmann character of N₂ vdf is reflected in the formation rate of NO (see Eq. (11.17)). Figure 11.8 reports the NO formation rate as a function of the local $1/T$ values in the F4 nozzle (Walpot et al. 1996) for different values of reservoir temperature. In the same figure is also reported the thermal experimental NO formation rate (Monat et al. 1978). We can see that the theoretical values follow the experimental Arrhenius values for low $1/T$ values (i.e. at high temperature) presenting an anti-Arrhenius behavior at low temperature.

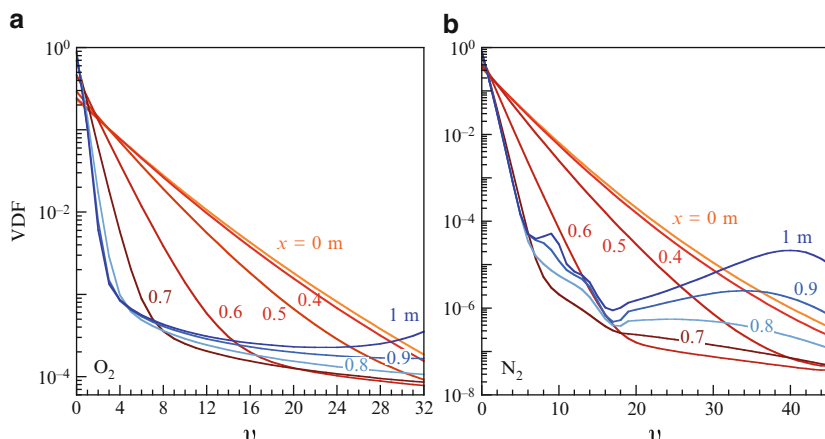


Fig. 11.7 Vibrational distribution functions (vdfs) at $T_0 = 8,000$ K, for different positions along the axis of a parabolic nozzle (From Colonna et al. 1999b)

Fig. 11.8 NO global production rate for the reaction $\text{N}_2 + \text{O} \rightarrow \text{NO} + \text{N}$, for different reservoir temperatures T_0 in F4 nozzle (Walpot et al. 1996). (markers) experimental results (Monat et al. 1978); (dashed line) Arrhenius fit (From Colonna et al. 1999b)

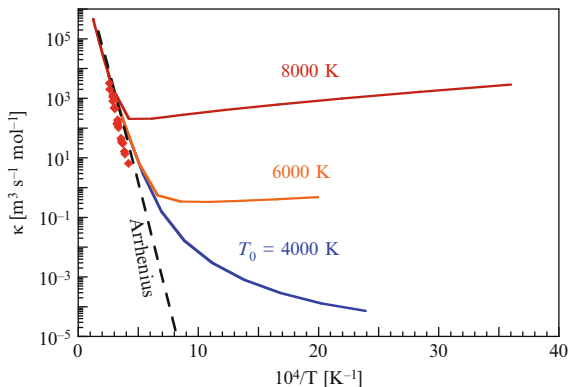
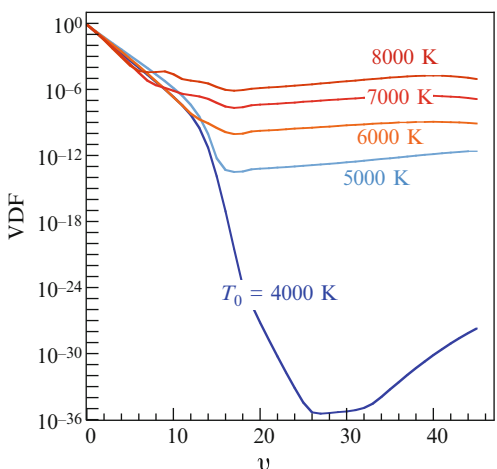


Fig. 11.9 N_2 vibrational distribution function (vdf) as a function of vibrational quantum number at the parabolic nozzle outlet ($x = 1 \text{ m}$) for different reservoir temperatures T_0 (Colonna et al. 1999a)

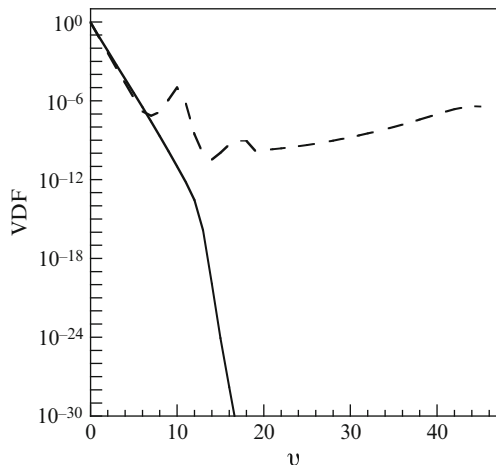


The reported results of course depend on the kinetic scheme as well as on the used rates and also on the nozzle geometry. As an example insertion of the second Zeldovich reaction



in the whole kinetics does not alter the N_2 vibrational distribution in the parabolic nozzle (see Fig. 11.9) (Colonna et al. 1998, 1999a), having however dramatic destructive effects on the vibrational distributions of N_2 in the F4 nozzle facility, as displayed in Fig. 11.10 (Colonna et al. 2000b).

Fig. 11.10 Vibrational distribution functions of N_2 at the outlet ($x = 4 \text{ m}$) of the F4 nozzle calculated with (solid line) and without (dashed line) reaction (11.19)
(From Colonna et al. 2000b)



11.4 Ionizing Nitrogen Mixture

Vibrational kinetics is sufficient to describe high enthalpy flows for orbital atmospheric entry. Re-entry from lunar or even from outer planets involve higher energy content, so that state-to-state model in high enthalpy flows should be extended to include the ionization and electronically excited states. In this section we want to show the role of electrons in affecting the non equilibrium properties in nozzle expansion.

To investigate this problem we have coupled the self-consistent plasma kinetics presented in Chap. 9 with the fluid dynamic equations according to the scheme reported in Fig. 11.11 (Colonna and Capitelli 2001b). To this end we have constructed a complete kinetic scheme adding to the reactions in Eqs. (11.8)–(11.9) the kinetics for ionized species (N_2^+ , N^+) and for electronically excited states (Colonna and Capitelli 2001b). In addition electron impact dissociation and ionization processes from each vibrational state and electron-molecule resonant vibrational transitions are introduced in the complete kinetics. The electron impact rate coefficients are calculated from the electron energy distribution function obtained from the solution of the Boltzmann equation.

This kinetic model has been applied to the conic nozzle in Fig. 11.1 for inlet conditions $P_0=1 \text{ atm}$ and $T_0=10,000 \text{ K}$, the last assumption implying a large ionization degree. Figures 11.12–11.13 (Colonna and Capitelli 2001b) report respectively vibrational and free electron distributions at different values of the nozzle coordinate, observing large deviations from Boltzmann and Maxwell distributions. It should be noted that the large electron molar fraction ($\approx 10^{-2}$), almost constant along the nozzle coordinate, is not sufficient to eliminate the plateaux present in eedf generated by second-kind collisions involving low energy electrons and metastable molecular states. These plateaux increase by three orders of magnitude if the electron-electron Coulomb collisions are not considered in the Boltzmann equation

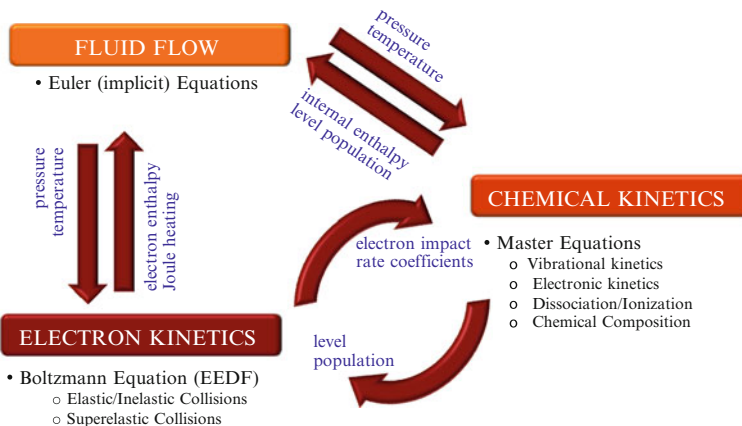
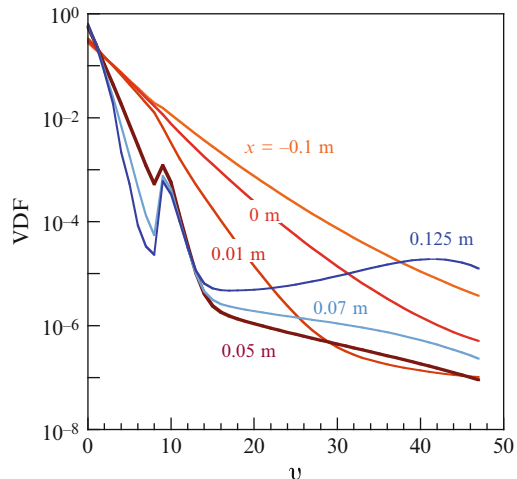


Fig. 11.11 Scheme of the self-consistent coupling between, heavy particle, electron kinetics, and Euler equations

Fig. 11.12 vdfs in different nozzle positions calculated with a complete kinetic scheme (From Colonna and Capitelli 2001b)



(see Fig. 11.14), warning about the use of an electron temperature to describe the phenomenology of high temperature reservoirs. Moreover, to understand the role of electrons in the vibrational kinetics, Fig. 11.15 compares the vdf from the complete model with the corresponding one obtained by considering the vibrational kinetics with processes (11.8)–(11.9) only (i.e. without electrons and metastable states). We see that vdf tail, in this last case, is two orders of magnitude higher than the corresponding one from the complete model. Electrons appear to strongly deactivate the vibrational distribution. The peak around $v = 10$ is due to transitions involving electronically excited states of N₂ (Colonna and Capitelli 2001b) in the process

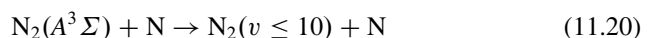


Fig. 11.13 eedf in different nozzle positions calculated with a complete kinetic scheme (From Colonna and Capitelli 2001b)

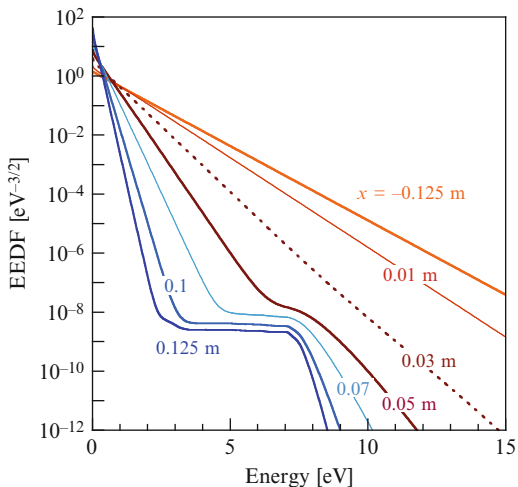
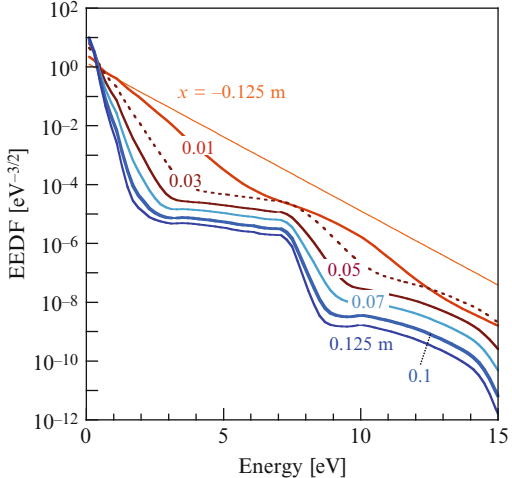


Fig. 11.14 eedf, in different nozzle positions calculated with a complete kinetic scheme, neglecting elastic electron-electron collisions (From Colonna and Capitelli 2001b)



Obviously, effects due to free electrons decrease at lower reservoir temperatures as the electron density decreases. As an example we report vdf and eedf in the F4 nozzle in Figs. 11.16 and 11.17 (Colonna and Capitelli 2001a). This case study has been obtained by considering $P_0 = 1 \text{ atm}$ and $T_0 = 7,000 \text{ K}$ and by adding to the complete kinetics an additional kinetics involving the low-lying 2P and 2D atomic nitrogen metastables. In this case the electron molar fraction (4×10^{-4}) is not able to deactivate the concentrations of vibrationally excited states as well as to Maxwellize the corresponding eedf.

The results reported in these sessions underline the importance of state-to-state models for understanding the phenomenology occurring in nozzle expansion in particular the formation of long plateau in the corresponding vdf. Very recent

Fig. 11.15 vdf at nozzle exit calculated with a complete kinetic scheme (solid line) or a simplified dissociation-recombination regime (dashed line)
(From Colonna and Capitelli 2001b)

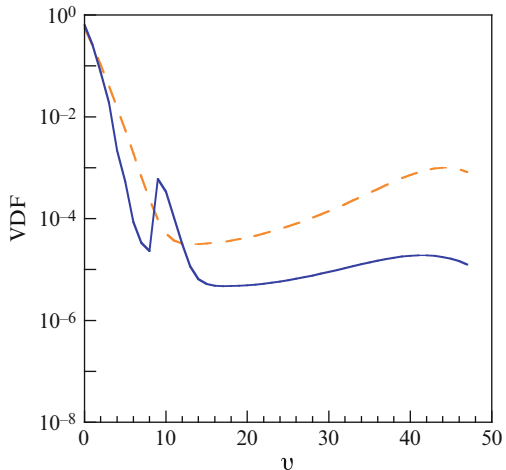
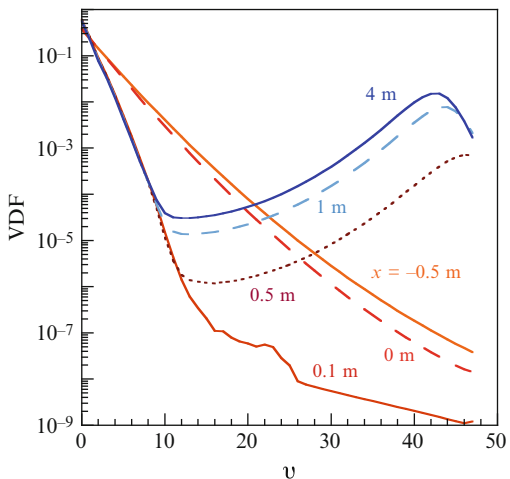


Fig. 11.16 vdf as a function of vibrational quantum number at different nozzle positions ($T_0 = 7,000$ K; $P_0=1$ atm) (From Colonna and Capitelli 2001a)



papers (Loukhovitski and Starik 2009; Starik et al. 2010; Arsentiev et al. 2012; Kadocchnikov et al. 2013) confirm to a given extent our results, in addition showing that the coupling of vibrational distributions of ground and excited electronically states strongly affect the plateau of ground electronic state.

11.5 Nozzle Expansion in the Presence of Electric and Magnetic Field

The self-consistent model reported in Fig. 11.11 can be improved to include the contribution of applied electric and magnetic fields, adding some terms in the Boltzmann equation for free electrons and energy and momentum source terms in

Fig. 11.17 eedf as a function of vibrational quantum number at different nozzle positions ($T_0 = 7,000$ K; $P_0 = 1$ atm) (From Colonna and Capitelli 2001a)

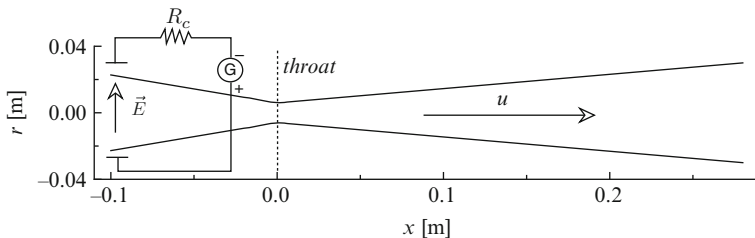
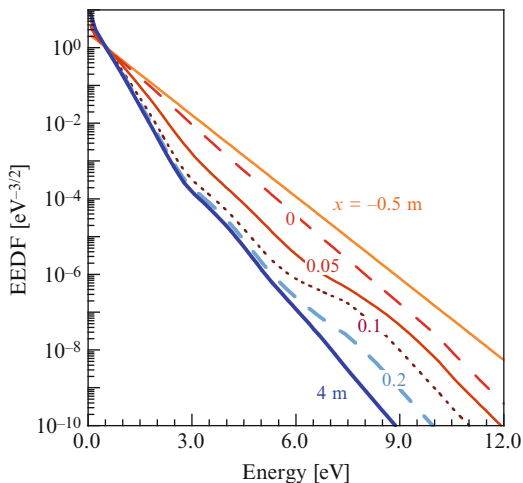


Fig. 11.18 Nozzle profile and external circuit (From Colonna and Capitelli 2008)

the Euler equations. This model can be useful for modeling plasma jets and MHD effects. The theory has been developed in Colonna and Capitelli (2008) and reported in Sect. 4.1.

Figure 11.18 reports the nozzle profile considered in this case study, at the inlet of which ($x = -0.1$ m with respect to the throat) is applied the electric field, the nozzle exit placed at 0.28 m. Inlet pressure and temperature were respectively 1 atm and 1,000 K and inlet ionization degree was 10^{-5} . A polarization circuit is included in the model with a resistance to limit the current density when the electrical field is on. The reduced electric field (E/N)₀ in absence of current ranges from 0 to 40 Td. Argon is considered as working fluid. The following microscopic processes are considered

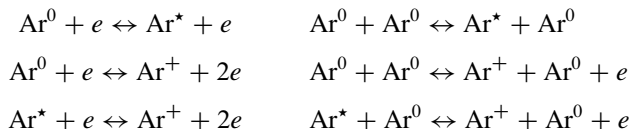


Fig. 11.19 Gas temperature, electron and metastable argon molar-fraction profiles for different applied electric field (From Colonna and Capitelli 2008)

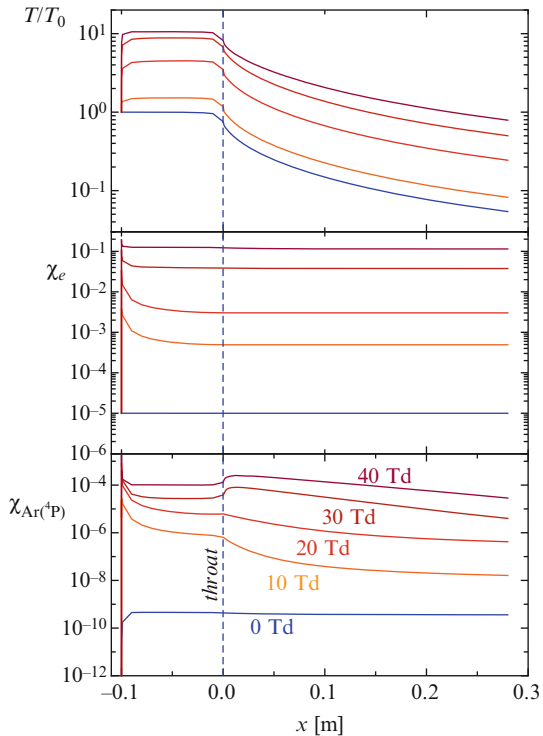


Figure 11.19 reports the profiles of gas temperature, electron molar fraction and argon metastable molar fraction for different $(E/N)_0$ values. The applied field energize the electron which return part of the energy to heavy particles, by increasing the gas temperature through the Joule heating and by exciting atomic metastable state and ionizing gas. The field is active in a small region close to the inlet, corresponding to the part with rapid increase of all the quantities in Fig. 11.19. In the rest of the nozzle the field is null, and the expansion proceed as usual. This approach allows to simulate inlet non-equilibrium when the nozzle is heated by electric arc.

Figure 11.20 reports the eedf at the throat and at the exit of nozzle for different reduced electric fields. At the throat the plateau in eedf formed by superelastic collisions involving low energy electrons and the metastable argon are destroyed $(E/N)_0 \geq 30$ Td because of thermalizing action of electron-electron collisions. On the other hand, at the nozzle exit, the action of superelastic collisions is exalted due to the decrease of the electron temperature reproducing post-discharge conditions as discussed in Chap. 5.

We have also examined another configuration, to investigate the effects of electric and magnetic fields in an high speed region. With the same nozzle used in the previous case, an electric and a magnetic fields have been applied in a small region after the throat (see Fig. 11.21). The direction of the fields has been chosen to have

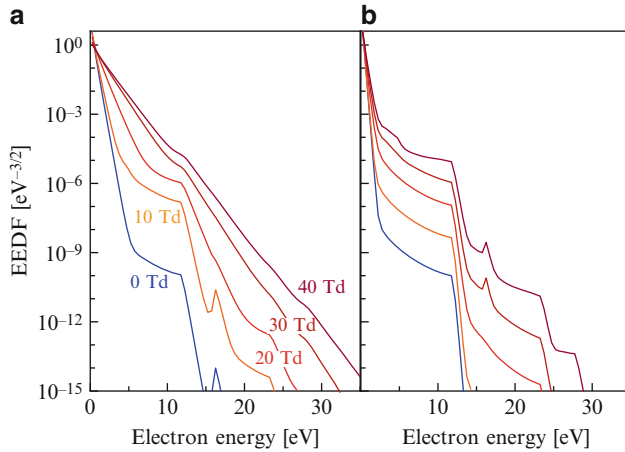


Fig. 11.20 Electron energy distributions at the throat (a) and at the exit of the nozzle (b), for different values of the electric field (From Colonna and Capitelli 2008)

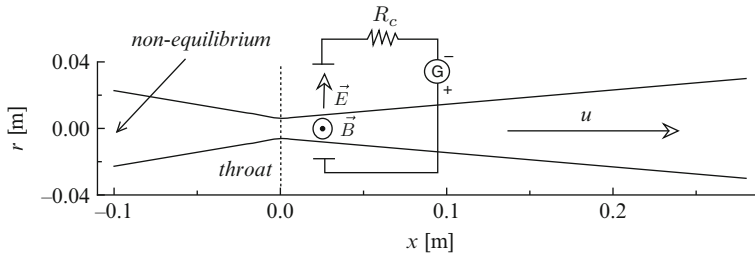


Fig. 11.21 Nozzle profile, external circuit and magnetic field (entering the paper). The E and B fields are applied in the region $0.01\text{--}0.02$ m (From Colonna and Capitelli 2008)

$\mathbf{E} \wedge \mathbf{B}$ oriented in the positive x direction. To mimic the effect of inlet electric field, we have considered non-equilibrium inlet condition $P_0=1$ atm, $T_0=7,000$ K, $T_e=T_{Ar}=10,000$ K, $\chi_e=10^{-2}$. In this configuration the ionization fraction is not influenced by the presence of the field, because the flow speed in the field region is high.

Figure 11.22 reports the eedf at $x=0.02$ m (end of field region) for different values of the magnetic field for $E/N=0$ (a) and $E/N=60$ Td (b). In the first case, the eedf is heated by the magnetic field due to the Faraday electromotive force (see Eq. (4.43)) as a real electric field is applied, and the distribution becomes more energetic as B increases. When $E/N=60$ Td, we observe a non-monotonic dependence on the magnetic field. For $B \leq 0.1$ T, electric and magnetic field have synergic effects, showing large variation also for $B=0.01$ T, contrarily to the case with $E/N=0$. For $B=1$ T, the eedf is cooled down, becoming similar to that obtained for $B=0.01$ T, and electric and magnetic fields act in opposition due to complex interaction between the Faraday and MHD force (see Eq. (4.44)).

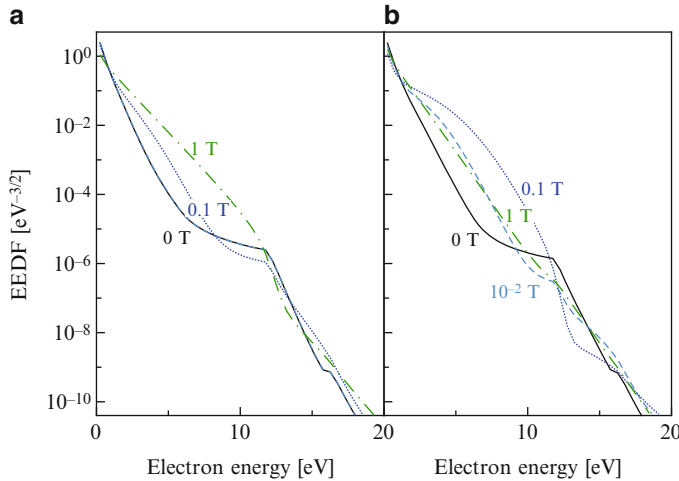


Fig. 11.22 Electron energy distributions at $x = 0.02$ m (upper limit of the E and B field region) for different magnetic field magnitude. **(a)** $E/N = 0$ and **(b)** $E/N = 60$ Td (From Colonna and Capitelli 2008)

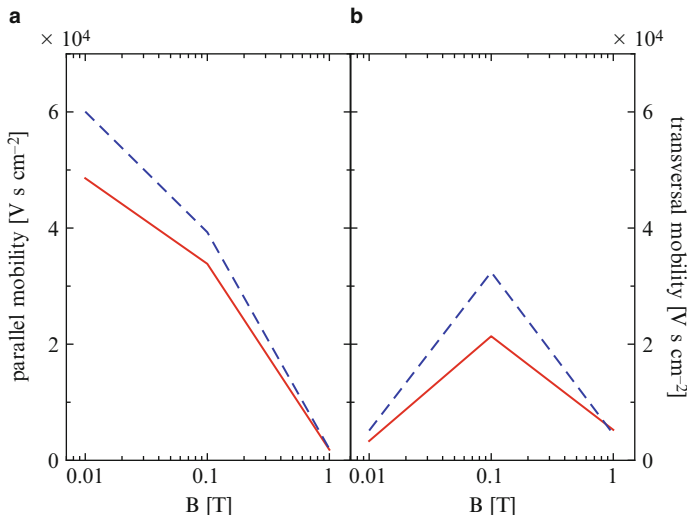


Fig. 11.23 Parallel **(a)** and transversal **(b)** electron mobility at $x = 0.02$ m (upper limit of the E and B field region) as a function of magnetic field magnitude for two different values of E/N . $E/N = 0$ (solid line) and 60 Td (dashed line)

It is worth noticing the dependence of the electron mobility at the end of the field region. In the presence of a magnetic field, the electron mobility is not parallel to the electric field, but presents a transversal component in the direction $\mathbf{E} \wedge \mathbf{B}$. In Fig. 11.23 we report the parallel and transversal components of the mobility at

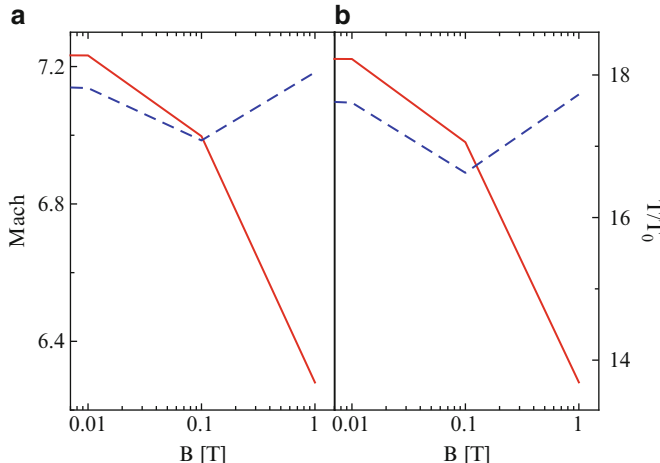


Fig. 11.24 Mach number (a) and reduced temperature (b) at the nozzle exit, as a function of magnetic field magnitude for two different values of E/N . $E/N = 0$ (solid line) and 60 Td (dashed line)

$x = 0.02$ m as a function of the magnetic field for two values of the electric field. The parallel mobility, as expected, is a decreasing function of B and the influence of E is relevant for the small value of B diminishing as B increases. On the other hand, the transversal mobility presents a weak dependence on B at small and high values while the influence on E is largest for $B = 0.1$ T, reflecting the behavior of the eedf.

The effect of the fields applied close to the throat propagates to the nozzle exit on macroscopic quantities. As an example Mach number and translational temperature at the nozzle exit have been reported in Fig. 11.24 as a function of the B field in the same conditions as previous figures. It should be noted that similar behavior has been observed for the electron mobility. This is not a coincidence, because the mechanical force on the flow exerted by the magnetic field is a function of the current and as a consequence of the mobility.

11.6 The Role of Radiation in High Enthalpy Flows

11.6.1 Shock Tube

Another important aspect where state-to-state kinetics can play a fundamental role is in the characterization of radiative flows. During atmospheric entry, the shock wave formed in front of the vehicle can lose energy through radiation, partly is dispersed, partly reach the vehicle surface contributing to the total heat flux (Surzhikov 2004, 2008, 2010; Colonna et al. 2014). To determine plasma emissivity, it is necessary to know the distribution of electronic and vibrational levels (D’Ammando

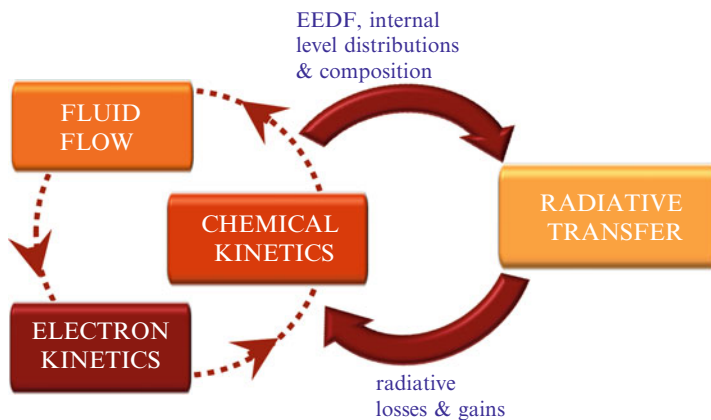
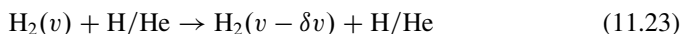
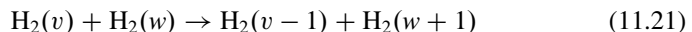


Fig. 11.25 Scheme of the self-consistent coupling including radiation transport

et al. 2010; Laux et al. 2003, 2012). To calculate absorption coefficients it is necessary to determine the photon density and flux, solving the Boltzmann equation for the photon distribution, a function of the position, direction, frequency and time (Zel'dovich and Raizer 1966). The problem is very complex and can be solved only approximatively (Mihalas and Weibel Mihalas 1984; Modest 2003).

To investigate the role of non-equilibrium in radiative shock waves, we have coupled the self-consistent model in Fig. 11.11 with the radiation transport equation in 1D approximation using the ray tracing method (Colonna et al. 2012, 2015). This approach improves the collisional-radiative models in Chap. 6, substituting the escape factor with the absorption coefficient calculated self-consistently with the composition and internal distribution, according to the scheme in Fig. 11.25.

This model has been applied to characterize a shock tube operating with pure hydrogen (Colonna et al. 2012) and Jupiter atmosphere (hydrogen-helium) (Colonna et al. 2015; Capitelli et al. 2013). The kinetic model in Chap. 6 has been extended including the vibrational relaxation processes for the He/H₂ mixture



and atom-atom collisions for atomic excitation and ionization

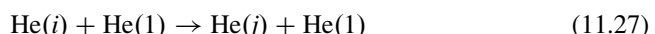
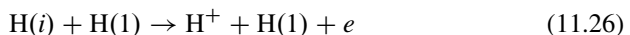
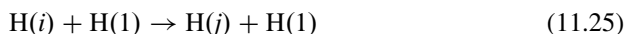
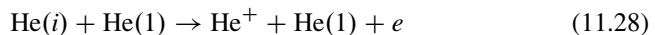


Table 11.1 Molar fractions of H atoms (χ_H) and electrons (χ_e), H atom temperature T_H and electron temperature T_e in given positions of the post-shock region for Mach 20 (From Colonna et al. 2012)

Points	Distance [m]	χ_H	χ_e	T_H [K]	T_e [K]
0	0	$1.0 \cdot 10^{-10}$	$2.0 \cdot 10^{-10}$	300	300
1	$1.00 \cdot 10^{-4}$	$1.0 \cdot 10^{-10}$	$2.0 \cdot 10^{-10}$	8,756	2,950
2	$1.00 \cdot 10^{-3}$	$4.4 \cdot 10^{-10}$	$2.0 \cdot 10^{-10}$	8,706	6,768
3	$5.00 \cdot 10^{-3}$	$3.6 \cdot 10^{-4}$	$3.3 \cdot 10^{-10}$	8,884	8,332
4	$1.00 \cdot 10^{-2}$	$1.2 \cdot 10^{-2}$	$5.9 \cdot 10^{-7}$	10,308	10,035
5	$2.00 \cdot 10^{-2}$	$1.4 \cdot 10^{-1}$	$5.2 \cdot 10^{-4}$	11,052	10,676
6	$2.85 \cdot 10^{-2}$	$4.7 \cdot 10^{-1}$	$3.5 \cdot 10^{-3}$	9,643	11,002
7	$3.00 \cdot 10^{-2}$	$5.6 \cdot 10^{-1}$	$3.9 \cdot 10^{-3}$	9,200	10,945
8	$3.30 \cdot 10^{-2}$	$7.3 \cdot 10^{-1}$	$4.1 \cdot 10^{-3}$	8,163	10,446
9	$4.00 \cdot 10^{-2}$	$9.3 \cdot 10^{-1}$	$3.5 \cdot 10^{-3}$	8,000	7,596
10	$1.00 \cdot 10^{-1}$	$9.9 \cdot 10^{-1}$	$2.6 \cdot 10^{-3}$	8,400	6,328
11	$3.00 \cdot 10^0$	$9.9 \cdot 10^{-1}$	$2.7 \cdot 10^{-4}$	7,830	6,332



These last processes are very important just after the shock tube, when the density of free electrons is low.

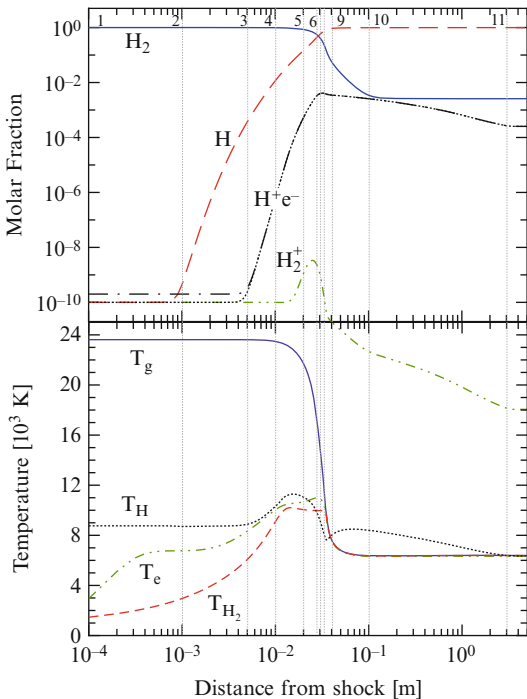
As a first test case let us consider a Mach = 20 free stream conditions, in pure hydrogen, in a very high enthalpy shock tube, reproducing Jupiter entry conditions of the Galileo probe between 90 and 80 Km altitude (Milos 1999).

In Table 11.1, atomic and electron molar fractions, together with they temperatures, have been listed at some distances from the shock front. A complex trend can be observed in molar fractions and temperatures profiles (Fig. 11.26), and some critical points have been evidenced, listed in Table 11.1, corresponding to different kinetic regimes.

Just after the shock front, the pressure jumps to a very high value (of the order of one atmosphere) and $T_g \approx 24,000$ K. Internal distributions² and gas composition are the same as in the free stream. Then, the vibrational relaxation starts driven by VT_M processes and the vibrational temperature increases reaching $T_{\text{H}_2} = 3,000$ K after $d = 1$ mm from the shock (2), where the dissociation process starts. At $d = 5$ mm (3), the atomic molar fraction is about $3.6 \cdot 10^{-4}$ and the H+H ionization becomes effective, while the vibrational temperature keeps growing at an higher rate due to the H₂+H VT_A transfer until about 1 cm (4). In this region T_g does not change, because the energy transferred to vibration is always small and the activation of s other degrees of freedom or to chemical processes is negligible, being the atomic and free electron molar fractions respectively 10^{-2} and 6×10^{-7} .

²In this case the free stream gas is formed only by H₂ molecules and therefore only the vibrational temperature is meaningful.

Fig. 11.26 Spatial profiles of molar fractions and temperatures as a function of the distance from the shock for free stream velocity Mach = 20. The *marked points* refer to the labels in Table 11.1 (From Colonna et al. 2012)



In the next 2 mm (5–7) the kinetic scheme completely changes: T_H reaches its maximum (5) and the electron induced processes overwhelm the contribution of $H+H$ collisions. As the electron molar fraction grows, the electron impact ionization becomes the dominant process for atomic levels, determining the decreasing of the T_H , while T_e reaches its maximum (6) due to elastic collisions, and soon after (7) the maximum of ionization degree is observed. The energy lost by atoms due to ionization is not balanced by the up-pumping due to electron impact excitation, and therefore the atomic temperature decreases reaching a minimum value (8). At this point, the plasma is almost completely atomic and the gas and electron temperatures have reached the equilibrium value, and, passing from the ionization regime to the recombination one, the atomic temperature reaches a new maximum (9) higher than the gas and electron temperature. After 10 cm, also the dissociation process is in equilibrium (10), while the atomic temperature now decreases due to electron collisions and to radiative losses, stabilizing at a stationary value nearly equal to the gas temperature.

This trend is reflected to the eedf and to the distribution of atomic energy levels (see Figs. 11.27 and 11.28) which show non-equilibrium shapes. Both distributions present an heating phase (left), corresponding to the ionization regime, and a cooling one (right), corresponding to the recombination regime. The distributions in the three points (5),(6),(7), i.e. between the maximum of the atomic temperature and the maximum of electron molar fractions are practically constant. In previous points

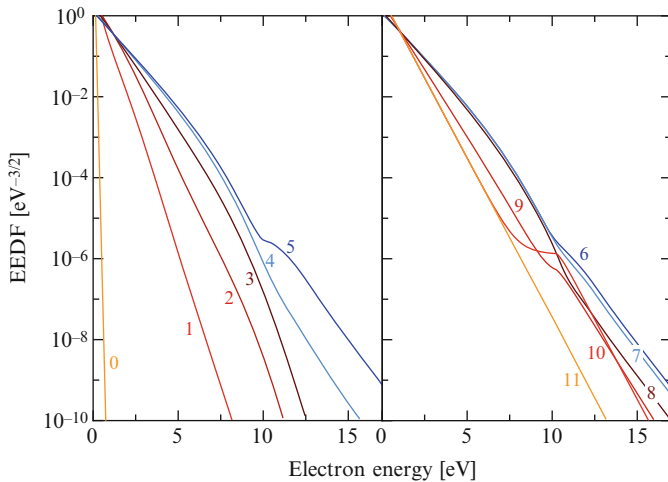


Fig. 11.27 Electron energy distribution at different distances from the shock front for Mach = 20. The curve levels refers to points in Table 11.1 (From Colonna et al. 2012)

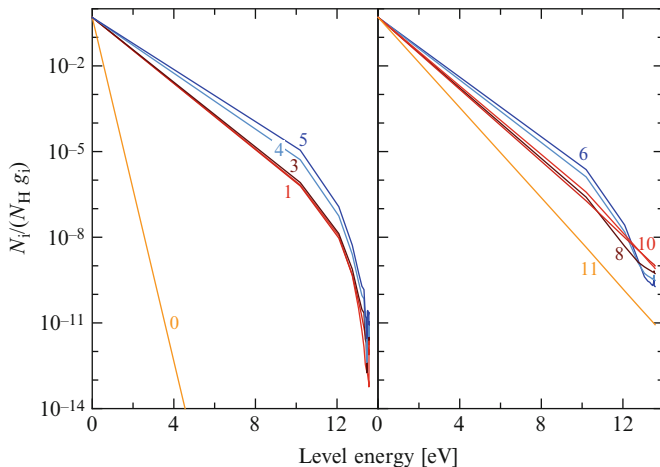
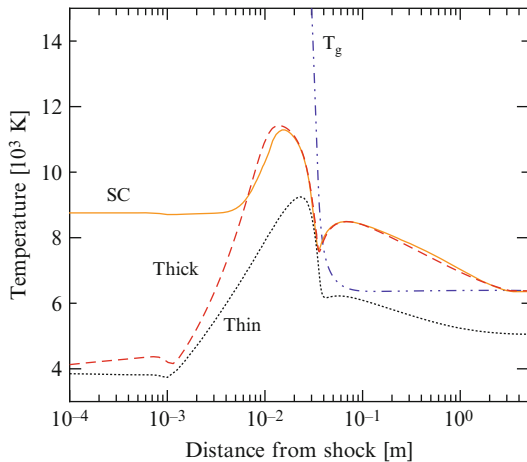


Fig. 11.28 H atom level distribution at different distances from the shock front for Mach = 20. The curve levels refers to points in Table 11.1 (From Colonna et al. 2012)

(1–4) the T_e is heated by elastic collisions, while the eedf tail is underpopulated, being inelastic collisions dominant. In the points (5–7) the distribution tail is overpopulated by superelastic collisions, transferring energy from the H($n = 2$) to electrons, and a step appear in the eedf. This character is present up to point (10), while for longer distances (11) the distribution is nearly Maxwellian.

The level distribution, being connected to the eedf by electron-atom inelastic collisions, shows similar evolution: in the points (1–5) H($n = 2$) state is heated, while higher excited states are underpopulated by the ionization process. On the

Fig. 11.29 H atom internal temperature at different distances from the shock front for Mach = 20. Self-consistent (SC) results compared with thin and thick approximations (gas temperature is reported as reference). (From Colonna et al. 2012)



other hand, points (6–10) are dominated by the $e+H^+$ recombination, producing atoms in high energy states while low energy states are cooled down by superelastic collisions. At the last point (11) the level distribution is a Boltzmann, because the local thermodynamic equilibrium has been reached. The analysis of the distributions shows that non-equilibrium survives for a time longer than predicted by considering the composition of majority species and internal temperatures. In these conditions, H_2 vibrational distribution is very close to Boltzmann in all the shock layer, being the vibrational kinetics governed by VT processes.

In order to understand the role of radiation, in Fig. 11.29 the temperature of atomic hydrogen obtained with the self-consistent approach (SC) has been compared with the thin³ and thick⁴ calculations. It can be observed that the thick curve is a good approximation of the SC value, except in a short range, where SC is much larger than thin and thick curves. This is the consequence of the radiation emitted by the region when the atomic distribution is hot and reabsorbed at short distance, where the distribution is not heated by collisions.

11.6.2 Nozzle Flow

It is also interesting to investigate the role of radiation during the supersonic expansion through a converging-diverging nozzle (Colonna et al. 2015). For this geometry the radiation transport has not been considered, and therefore only thin and thick cases have been compared. The case studied have been carried out in the

³All the radiation escapes.

⁴All the radiation is locally reabsorbed, i.e. radiative processes are neglected.

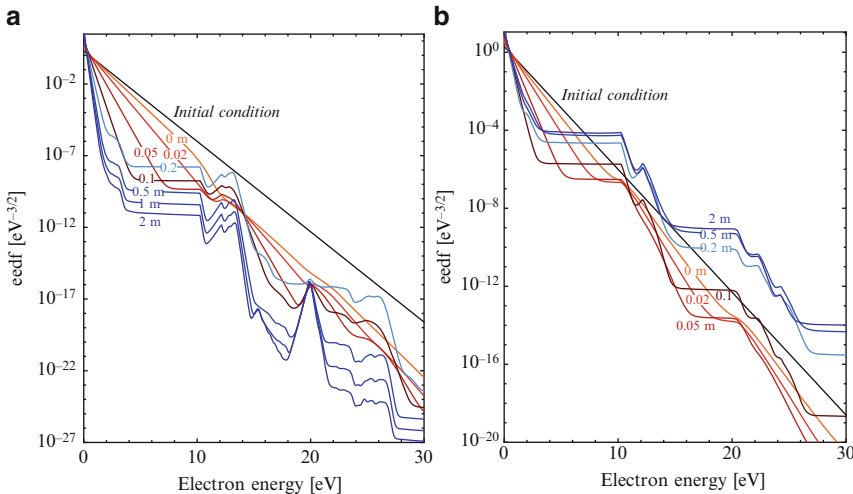


Fig. 11.30 Evolution of the eedf at different positions along the nozzle axis obtained imposing $P_0 = 1 \text{ atm}$ and $T_0 = 8,000 \text{ K}$ in the reservoir in the optically thin (**a**) and thick (**b**) cases (From Colonna et al. 2015)

F4 nozzle (Walpot et al. 1996; Colonna et al. 2015), for inlet pressure $P_0 = 1 \text{ atm}$ and $T_0 = 8,000 \text{ K}$ and for the Jupiter atmosphere (89 % H₂, 11 % He). The profile of the vibrational distribution of H₂ molecules is similar to that observed in the case of the ionizing nitrogen, discussed in Sect. 11.4, and they are poorly affected by the radiation model (Colonna et al. 2015).

At a first glance, comparing the eedf obtained in the present case (Fig. 11.30) with the results for pure nitrogen (see Fig. 11.12) in similar conditions, we observe the same step structure due to superelastic collisions.

The radiation model has a great influence on the eedf. The thick model presents very regular steps, separated by an energy interval $\Delta\epsilon \approx 10 \text{ eV}$, while in the thin case some peaks are superimposed to the steps, with the extreme case of a peak at $\epsilon = 20 \text{ eV}$ emerging from the plateaux as the distance from the throat increases. In the thin case, the plateaux appear around $x = 2 \text{ cm}$. Their height degreases until $x = 10 \text{ cm}$, then it changes the trend, growing until $x = 20 \text{ cm}$ to decrease again up to the exit. In the thick case the plateaux appear at $x = 5 \text{ cm}$ increasing until $x = 50 \text{ cm}$.

The reason of these differences between the two cases is the consequence of the respective evolution of atomic level distributions, reported in Fig. 11.31. In the first region (left viewgraphs), the distribution grows, while in the second region they decreases, influencing the behavior of the plateaux in the eedf. However, the most interesting result is the difference in the distribution shape. While for very high levels the distribution are decreasing with the level energy in both thin and thick cases, low and intermediate levels behaves differently. In the thin case spontaneous emission depopulate the levels, equilibrating with the recombination

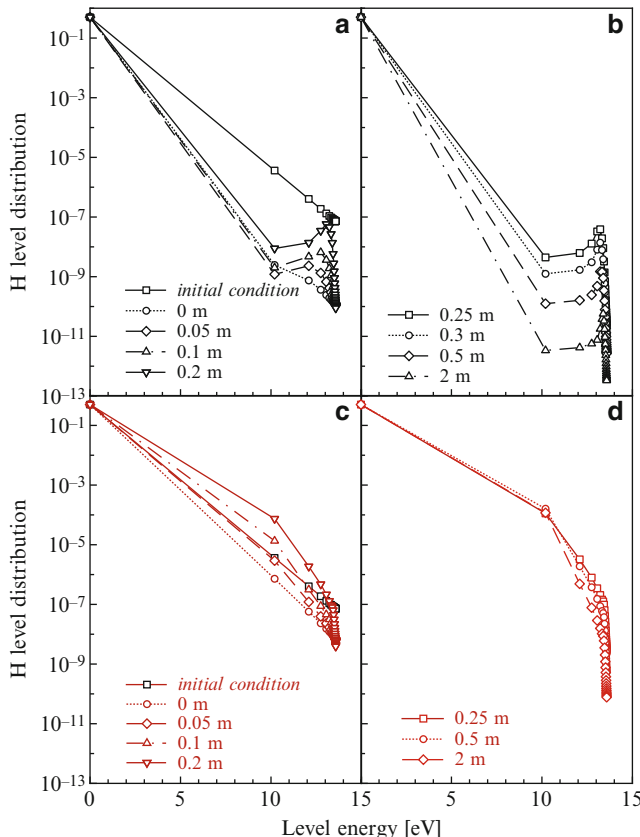


Fig. 11.31 Evolution of the H internal electronic distribution at different positions along the nozzle axis obtained imposing $P_0 = 1 \text{ atm}$ and $T_0 = 8,000 \text{ K}$ in the reservoir in the *optically thin*, (a) and (b), and *optically thick*, (c) and (d), cases (From Colonna et al. 2015)

processes, mainly radiative recombination, this last dominating for intermediate levels, resulting in a population inversion. In the thick case, the energy levels can be depleted only by superelastic collisions with low energy electrons. However, the superelastic collisions produce the long plateaux in the eedf, favoring electron impact excitation and ionization. As a consequence, the plateaux in the thick case are much higher than in the thin case. The peak at $\varepsilon \approx 20 \text{ eV}$ is produced by superelastic collisions with the He metastable state.

Electron molar fraction (Fig. 11.32) is slightly decreasing in the thin case and as a consequence the contribution of electron-electron collisions is reduced. In the thick case the first excited state of atoms is increasing because of electron ion recombination with a small minimum around the throat due to the collisional cooling. In the thin case, $H(n=2)$ is depleted at the beginning, to equilibrate the radiative losses with collisional processes. After the throat this state is linked to the

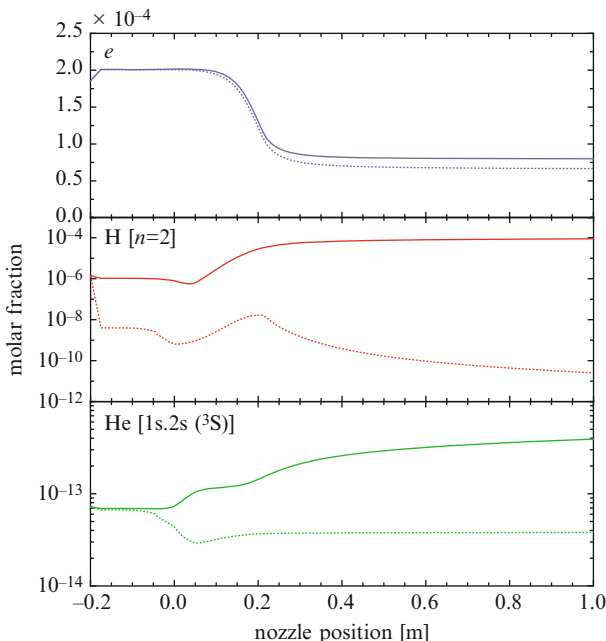


Fig. 11.32 Evolution of the molar fraction of free electrons, of $H(n = 2)$ and of $He(^3S)$ along the nozzle axis obtained imposing $P_0 = 1$ atm and $T_0 = 8,000$ K in optically thin (dotted lines) and optically thick (solid lines) cases

plateaux of the eedf, presenting a maximum, coincident with the maximum of the plateaux in the eedf. The He metastable is cooled down by collisions with electrons and after that value its concentration grows again, populated by higher triplet states decaying by spontaneous emission.

References

- Anderson JD (2000) Hypersonic and high temperature gas dynamics. AIAA, Reston
 Armenise I, Capitelli M, Gorse C (1996) Nonequilibrium vibrational kinetics in the boundary layer of re-entering bodies. *J Thermophys Heat Transf* 10(3):397–405
 Arsentiev I, Loukhovitski B, Starik A (2012) Application of state-to-state approach in estimation of thermally nonequilibrium reaction rate constants in mode approximation. *Chem Phys* 398:73–80
 Bose D, Candler GV (1996) Thermal rate constants of the $N_2 + O \rightarrow NO + N$ reaction using ab initio $^3A''$ and $^3A'$ potential energy surfaces. *J Chem Phys* 104(8):2825–2833
 Bose D, Candler GV (1997) Thermal rate constants of the $O_2 + N \rightarrow NO + O$ reaction using ab initio $^2A'$ and $^4A'$ potential energy surfaces. *J Chem Phys* 107(16):6136–6145
 Capitelli M, Armenise I, Gorse C (1997) State-to-state approach in the kinetics of air components under re-entry conditions. *J Thermophys Heat Transf* 11(4):570–578

- Capitelli M, Colonna G, Esposito F (2004) On the coupling of vibrational relaxation with the Dissociation-Recombination kinetics: from dynamics to aerospace applications. *J Phys Chem A* 108(41):8930–8934
- Capitelli M, Colonna G, Pietanza LD, D'Ammando G (2013) Coupling of radiation, excited states and electron energy distribution function in non equilibrium hydrogen plasmas. *Spectrochim Acta Part B* 83–84:1–13
- Chaban G, Jaffe R, Schwenke D, Huo W (2008) Dissociation cross sections and rate coefficients for nitrogen from accurate theoretical calculations. 46th AIAA aerospace sciences meeting and exhibit, aerospace sciences meetings, Reno. American Institute of Aeronautics and Astronautics AIAA paper 2008–1209
- Colonna G, Capitelli M (1996) Electron and vibrational kinetics in the boundary layer of hypersonic flow. *J Thermophys Heat Transf* 10(3):406–412
- Colonna G, Capitelli M (2001a) The influence of atomic and molecular metastable states in high-enthalpy nozzle expansion nitrogen flows. *J Phys D Appl Phys* 34(12):1812
- Colonna G, Capitelli M (2001b) Self-consistent model of chemical, vibrational, electron kinetics in nozzle expansion. *J Thermophys Heat Transf* 15(3):308–316
- Colonna G, Capitelli M (2008) Boltzmann and master equations for magnetohydrodynamics in weakly ionized gases. *J Thermophys Heat Transf* 22(3):414–423
- Colonna G, Tuttafesta M, Capitelli M, Giordano D (1998) NO formation in one dimensional nozzle air flow with state-to-state non-equilibrium vibrational kinetics. AIAA/ASME Joint Thermophysics and Heat Transfer Conference, Albuquerque
- Colonna G, Tuttafesta M, Capitelli M, Giordano D (1999a) NO formation in one dimensional air nozzle flow with state-to-state vibrational kinetics- the influence of $O_2(v)+N \rightarrow NO + O$ reaction. AIAA paper 99–3685
- Colonna G, Tuttafesta M, Capitelli M, Giordano D (1999b) Non-Arrhenius NO formation rate in one-dimensional nozzle airflow. *J Thermophys Heat Transf* 13(3):372–375
- Colonna G, Armenise I, Catella M, Capitelli M (2000a) Non equilibrium effects in plasma expansion flows. *J Tech Phys* 41(1):203–214
- Colonna G, Tuttafesta M, Capitelli M, Giordano D (2000b) Influence of $O_2(v)+N \rightarrow NO + O$ on NO formation in one-dimensional air nozzle flow. *J Thermophys Heat Transf* 14(3):455–456
- Colonna G, Tuttafesta M, Giordano D (2001) Numerical methods to solve Euler equations in one-dimensional steady nozzle flow. *Comput Phys Commun* 138(3):213–221
- Colonna G, Armenise I, Bruno D, Capitelli M (2006) Reduction of state-to-state kinetics to macroscopic models in hypersonic flows. *J Thermophys Heat Transf* 20(3):477–486
- Colonna G, Pietanza LD, Capitelli M (2008) Recombination-assisted nitrogen dissociation rates under nonequilibrium conditions. *J Thermophys Heat Transf* 22(3):399–406
- Colonna G, Pietanza LD, D'Ammando G (2012) Self-consistent collisional-radiative model for hydrogen atoms: atom-atom interaction and radiation transport. *Chem Phys* 398:37–45
- Colonna G, D'Ammando G, Dikalyuk A, Panesi M, Pietanza LD, Surzhikov ST (2014) Advanced models in shock waves. *Open Plasma Phys J* 7(Suppl 1:M1):101–113
- Colonna G, D'Ammando G, Pietanza LD, Capitelli M (2015) Excited-state kinetics and radiation transport in low-temperature plasmas. *Plasma Phys Control Fusion* 57(1):014009
- Cutrone L, Tuttafesta M, Capitelli M, Schettino A, Pascazio G, Colonna G (2014) 3D nozzle flow simulations including state-to-state kinetics calculation. In: Proceedings of the XXIX international symposium on rarefied gas dynamics, AIP Conf. Proc. 1628:1154
- D'Ammando G, Pietanza LD, Colonna G, Longo S, Capitelli M (2010) Modelling spectral properties of nonequilibrium atomic hydrogen plasma. *Spectrochim Acta B* 65(2):120–129
- Esposito F, Armenise I, Capitelli M (2006) N-N₂ state to state vibrational-relaxation and dissociation rates based on quasiclassical calculations. *Chem Phys* 331(1):1–8
- Giordano D, Bellucci V, Colonna G, Capitelli M, Armenise I, Bruno C (1997) vibrationally relaxing flow of N₂ past an infinite cylinder. *J Thermophys Heat Transf* 11(1):27–35
- Guy A, Bourdon A, Perrin MY (2013) Consistent multi-internal-temperatures models for nonequilibrium nozzle flows. *Chem Phys* 420:15–24

- Jaffe R, Schwenke D, Chaban G, Huo W (2008) Vibrational and rotational excitation and relaxation of nitrogen from accurate theoretical calculations. 46th AIAA aerospace sciences meeting and exhibit, aerospace sciences meetings, Reno. American Institute of Aeronautics and Astronautics AIAA paper 2008-1208
- Jaffe R, Schwenke D, Chaban G (2009) Theoretical analysis of N₂ collisional dissociation and rotation-vibration energy transfer. 47th AIAA aerospace sciences meeting including The New Horizons forum and aerospace exposition, aerospace sciences meetings, Orlando. American Institute of Aeronautics and Astronautics AIAA paper 2009-1569
- Kadochnikov IN, Loukhovitski BI, Starik AM (2013) Kinetics of plasmachemical processes in the expanding flow of nitrogen plasma. *Physica Scripta* 88(5):058306
- Laux CO, Spence TG, Kruger CH, Zare RN (2003) Optical diagnostics of atmospheric pressure air plasmas. *Plasma Sources Sci Technol* 12:125
- Laux CO, Pierrot L, Gessman RJ (2012) State-to-state modeling of a recombining nitrogen plasma experiment. *Chem Phys* 398:46–55
- Loukhovitski B, Starik A (2009) Modeling of vibration–electronic–chemistry coupling in the atomic–molecular oxygen system. *Chem Phys* 360(1–3):18–26
- Mihalas D, Weibel Mihalas B (1984) Foundations of radiation hydrodynamics. Oxford University Press, New York
- Milos FS (1999) Analysis of Galileo probe heatshield ablation and temperature data. *J Spacecr Rockets* 36(3):298–306
- Modest MF (2003) Radiative heat transfer. Academic Press, Amsterdam London New York
- Monat JP, Hanson RK, Kruger CH (1978) Shock tube determination of the rate coefficient for the reaction N₂+O→NO+N. In: Proceedings of 17th symposium (international) on combustion, Combustion Inst., University of Leeds, Leeds, pp 543–552
- Munafò A, Panesi M, Jaffe RL, Colonna G, Bourdon A, Magin TE (2012) QCT-based vibrational collisional models applied to nonequilibrium nozzle flows. *Eur Phys J D* 66(7):188
- Nagnibeda E, Kustova E (2009) Non-equilibrium reacting gas flows: kinetic theory of transport and relaxation processes. Springer series heat and mass transfer. Springer, Berlin/Heidelberg
- Park C (ed) (2012) Nonequilibrium hypersonic aerothermodynamics. Wiley-Interscience, John Wiley & Sons, New York
- Schwenke DW (2008) Dissociation cross-sections and rates for nitrogen. In: Non-equilibrium gas dynamics: from physical models to hypersonic flights. von Karman institute for fluid dynamics lecture series. RTO-EN-AVT-162. Rhode St. Genèse, Belgium
- Shizgal BD, Lordet F (1996) Vibrational nonequilibrium in a supersonic expansion with reaction: application to O₂-O. *J Chem Phys* 104(10):3579–3597
- Starik AM, Titova NS, Arsentiev IV (2010) Comprehensive analysis of the effect of atomic and molecular metastable state excitation on air plasma composition behind strong shock waves. *Plasma Sources Sci Technol* 19(1):015007
- Surzhikov ST (2004) Radiative-gasdynamic model of martian descent space vehicle AIAA paper 2004–1355
- Surzhikov ST (2008) A study of the influence of kinetic models on calculations of the radiation-conductive heating of a space vehicle in Fire-II flight experiment. *Russ J Phys Chem B* 2(5):814–826
- Surzhikov ST (2010) Coupled radiation-gasdynamic model for sturdust aerothermodynamic data AIAA paper 2010-4521
- Tuttafesta M (2014) Theoretical aspects of reactive gas dynamics aided by massive parallel computing. PhD thesis, PhD School of Physics, Bari University
- Walpot L, Simeonides G, Muylaert J, Bakker P (1996) High enthalpy nozzle flow sensitivity study and effects on heat transfer. *Shock Waves* 6(4):197–204
- Zel'dovich YB, Raizer YP (1966) Physics of shock waves and high-temperature hydrodynamic phenomena, vol 1. Academic Press, New York and London

Chapter 12

Toward the Activation of Polyatomic Molecules by eV Processes: The CO₂ Case Study

Plasma-processing of CO₂ under non-equilibrium conditions is nowadays considered a promising substitute to conventional routes to specifically tackle the rate-limiting dissociation into CO (Taylan and Berberoglu 2015; Goede et al. 2014; Kozak and Bogaerts 2014; Silva et al. 2014). The idea to use *cold*, i.e. non equilibrium plasmas, for the CO₂ dissociation has a long history started with the works of Russian (Fridman 2012; Legasov et al. 1977) and Italian groups (Capazzuto et al. 1976; Capitelli and Molinari 1980), at the beginning of plasma-chemistry activities. The basic idea was the impossibility to rationalize experimental dissociation rates of CO₂ by using the direct electron impact dissociation process. On the contrary, especially at low electron temperature (T_e of the order of 1 eV), the input of electrical energy goes through the excitation of vibrational modes of CO₂ (in particular the asymmetric one) followed by VV energy exchange processes able to spread the low-lying vibrational quanta over the whole vibrational ladder of CO₂, ending in the dissociation process. The upper limit to the dissociation rate of this mechanism, called pure vibrational mechanism, can be obtained by the following equation

$$K_d^{(\text{ulPVM})} = \frac{1}{v_{\max}} k_{\text{eV}}(000 \rightarrow 001) \quad (12.1)$$

where $k_{\text{eV}}(000) \rightarrow (001)$ is the rate of the resonant vibrational excitation process and v_{\max} the number of vibrational quanta contained in the vibrational ladder of CO₂ (to a first approximation we can imagine to pump vibrational energy selectively on the asymmetric mode of CO₂) as in the case of nitrogen (Capitelli et al. 2014; Sergeev and Slovensky 1983). This rate can be several orders of magnitude higher than the corresponding dissociation process induced by electron impact. These simple considerations are at the basis of the numerous experimental attempts to use vibrational energy in the dissociation process rather than the direct electronic process with the belief that the activation energy of the vibrational excitation process

is much less than the corresponding electron impact process. Unfortunately the situation is much more complicated than that given by Eq. (12.1), which completely disregards the relaxation of vibrational energy by VT energy exchange processes. Moreover the possible enhancement of the direct electron impact dissociation process due to the presence of excited molecules should be taken into account. The last has a twofold effect on the direct dissociation process

- it enlarges the electron energy distribution function (eedf) through the effect of superelastic vibrational and electronically excited state collisions, increasing at the same time the direct dissociation rate,
- it increases the dissociation rate due to the lowering of the energy threshold of dissociation, decreasing with vibrational quantum number.

The first point has been considered in the past to understand the dissociation of CO₂ in laser mixtures (Capitelli et al. 1981), this aspect being reiterated more recently for the same aim (Kumar et al. 2013). The second point has been recently reinvestigated in the case of nitrogen plasmas (Capitelli et al. 2013).

To better understand these points we have studied the dissociation rate of CO₂ as a function of vibrational temperature in different approximations

1. According to Eq. (12.1)
2. Considering only the direct electronic excitation-dissociation from the CO₂ ground state, $k_d(000)$
3. Including the effect of vibrational levels in direct dissociation

$$K_d(\text{all}) = \sum_v^{v_{\max}} \exp \left[\frac{\varepsilon_{00v}}{k_B} \left(\frac{1}{T_e} - \frac{1}{T_v} \right) \right] k_d(000) \quad (12.2)$$

v_{\max} being the maximum value of vibrational levels in the asymmetric stretching ladder, i.e. 21 according to Kozák and Bogaerts (2014). This equation results from the crude assumption of a shift of cross section threshold for excited vibrational levels, and Boltzmann distribution function of vdf and eedf at T_v and T_e temperatures respectively, reducing to $K_d(\text{all}) = v_{\max} k_d(000)$ for the case $T_v = T_e$, as reported by Park (2008).

4. Including the effect of vibrational levels in the pure vibrational mechanism

$$K_d^{\text{(ulPVM)}}(\text{all}) = \frac{1}{v_{\max}} \sum_{n=1}^8 \frac{\varepsilon_{v_n}}{\varepsilon_{v_8}} k_{\text{ev}}(0 \rightarrow v_n) \quad (12.3)$$

where v_n are the excited vibrational levels belonging to different normal CO₂ modes, as reported in Table 12.1. Note that Eq. (12.3) normalizes the input of vibrational quanta to the asymmetric mode.

$k_d(000)$ and $k_{\text{ev}}(0 \rightarrow v_n)$ rate coefficients have been calculated from the solution of the Boltzmann equation including vibrational and electronic superelastic collisions, considering a parametric change of the temperatures associated to the

Table 12.1 Channels in CO₂ kinetics

Notation	State	Energy [eV]	Channel
CO ₂ (v ₀)	(000)	0.000	
CO ₂ (v ₁)	(010)	0.083	Vib-excitation
CO ₂ (v ₂)	(020)+(100)	0.167	Vib-excitation
CO ₂ (v ₃)	(030)+(110)	0.252	Vib-excitation
CO ₂ (v ₄)	(0n0)+(n00)	0.339	Vib-excitation
CO ₂ (v ₅)	(0n0)+(n00)	0.442	Vib-excitation
CO ₂ (v ₆)	(0n0)+(n00)	0.505	Vib-excitation
CO ₂ (v ₇)	(0n0)+(n00)	2.500	Vib-excitation
CO ₂ (v ₈)	(001)	0.291	Vib-excitation
CO ₂ (e ₁)		7.000	Direct dissociation
CO ₂ (e ₂)		10.500	Electronic excitation
CO ₂ ⁺		13.300	ionization

different vibrational normal modes, T_v for the asymmetric stretching and T'_v for the symmetric and bending modes, imposing $T_v > T'_v$ following what observed in CO₂ laser physics. Moreover the concentration of the CO₂(e₂) electronically excited state has been estimated from Boltzmann distribution at T'_v , while, only in the post-discharge regime, a fixed concentration of 10⁻⁵ has been imposed. Finally the electron-electron (*e-e*) Coulomb collisions have been inserted with different electron ionization degrees. All the cross section data entering the Boltzmann equation have been taken from Lowke et al. (1973), while superelastic cross sections have been derived by detailed balance principle. Note that in the corresponding database (Lowke et al. 1973) the 7-eV threshold process is considered as a dissociative channel, while the electronic excitation is limited to a process with energy threshold of 10.5 eV. The addition of further excitation and dissociation levels (Fridman 2012; Kozák and Bogaerts 2014) can improve the accuracy of the present results, without altering their qualitative validity.

Figure 12.1a reports the eedf at different vibrational temperatures, calculated accounting for *e-e* collisions. We have selected an ionization degree of 10⁻³ which can be considered as the lower limit for the action of *e-e* collisions in affecting eedf under conditions of Fig. 12.1. We note the effect of superelastic vibrational collisions in enlarging the eedf and its thermalization due to *e-e* collisions. This last point can be better understood by looking at Fig. 12.1b displaying the corresponding electron energy distributions when *e-e* collisions are neglected. A minor role is on the contrary played by superelastic electronic collisions due to the low concentration of the 10.5 eV excited state.

Figure 12.2 reports the corresponding rates as a function of T_v obtained accounting and neglecting for the *e-e* collisions. The inclusion of *e-e* collisions does not have an appreciable effect on the rates, except for low values of the vibrational temperatures, reflecting the differences in the corresponding electron energy distribution functions (Fig. 12.1) at energy values that correspond to the thresholds for

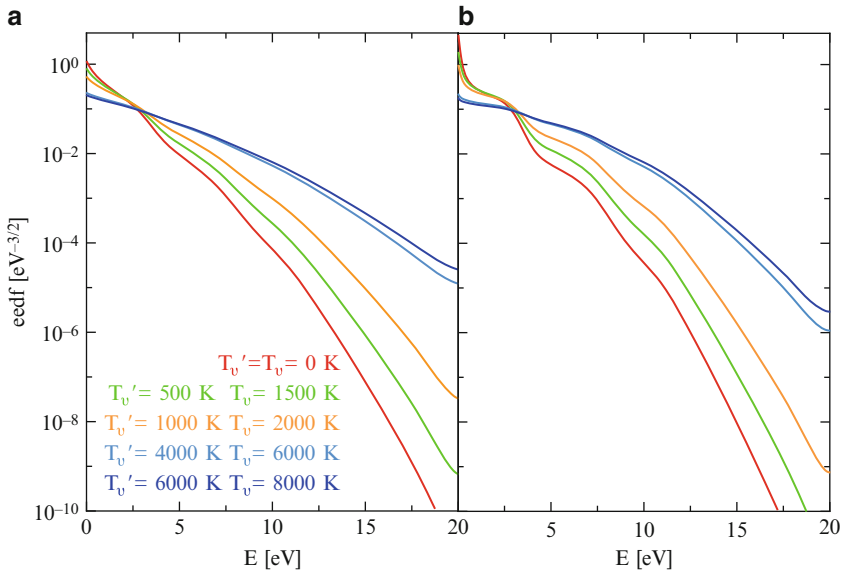
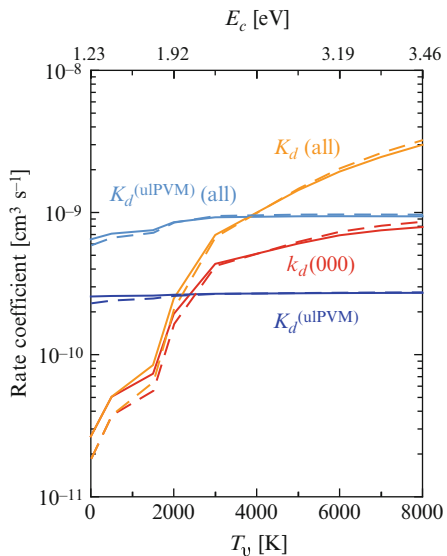


Fig. 12.1 Electron energy distribution function at $E/N=30$ Td for different selected values of the temperatures of symmetric/bending (T'_v) and asymmetric (T_v) normal modes. **(a)** Including ($\chi_e = 10^{-3}$) and **(b)** neglecting electron-electron collisions

Fig. 12.2 Rate coefficients for dissociation channels in CO_2 plasma, as a function of vibrational temperature of asymmetric mode (on the upper axis the corresponding values of characteristic energy E_c are reported), at $E/N = 30$ Td, including (solid lines) and neglecting (dashed lines) $e\text{-}e$ collisions



the different channels. In fact, while the dissociative cross section from the ground vibrational level is peaked at ~ 9 eV, the threshold associated to the vibrational mechanism is located at low energies. The pure vibrational mechanisms including

all vibrational channels are dominant at lower T_v vibrational temperature, while direct dissociation channels become competitive at higher vibrational temperatures. In any case, at $E/N = 30 \text{ Td}$, direct dissociation strongly increases with T_v as a result of the corresponding behavior of the eedf (see Fig. 12.1a). At the same time the pure vibrational mechanisms become more and more important as the reduced field decreases ($E/N < 30 \text{ Td}$), the reverse being true for $E/N > 30 \text{ Td}$. These points should be taken into account when trying to rationalize the experimental results of CO_2 dissociation. Attempt in this direction should take into account the strong coupling between eedf and non-equilibrium vibrational kinetics, including electronic (dissociative and excitation) transitions involving vibrational excited states as shown in Fig. 12.2. The above reported scenario applies mainly in the low-electron temperature plasmas dominated by the excitation of vibrational modes, a situation which can occur in microwave (Mw) discharges operating at moderate pressures. Microwave (Mw) driven CO_2 plasma at sub-atmospheric pressures can reach energy efficiencies as high as 60 % at low specific injected energies (around 1 eV/molecule CO_2) thus confirming the importance of vibrational excitation in the dissociation process (Silva et al. 2014). The use of atmospheric DBD pulsed discharges revealed an energy efficiency of about 10 % (Silva et al. 2014; Kozák and Bogaerts 2014).

Another interesting case could be the use of nanosecond high-voltage discharges operating at atmospheric pressure. The situation in this case is completely different from the Mw case because during the pulse one creates very elevate electron temperatures, able to excite electronic states of CO_2 rather than vibrational states. In the post-discharge following the pulse, the electronically excited states can create structures in the eedf due to superelastic collisions between cold electrons and electronically excited states, increasing the dissociation rate of CO_2 also in the post-discharge regime (Colonna et al. 1991). In Fig. 12.3a we report the electron energy distribution function at different vibrational temperatures in the post-discharge regime. We can see that superelastic electronic collision from the excited electronic level $\text{CO}_2(e_2)$ forms a source of electrons at the threshold energy for the excitation process, i.e. 10.5 eV, which is transformed in a plateau by elastic and inelastic relevant collisions, including e - e collisions not considered by Colonna et al. (1991). The results consider an ionization degree of 10^{-3} which is not able to destroy the long plateau at low T_v created by superelastic electronic collisions. The plateau length strongly decreases with the increase of vibrational temperatures. It should be pointed out that in ns pulsed discharges the realistic values of vibrational temperatures do not exceed 1,000 K, while the selected values of the electronic state concentrations (10^{-5}) can be considered typical of ns pulsed discharges. On the contrary the selected ionization degree, probably overestimated, has been selected to better understand the role of e - e collisions in the afterglow. Figure 12.3b reports the eedf for the same conditions without the presence of e - e collisions. In this case we observe a large number of structures, not smoothed by the action of Coulomb collisions.

In Fig. 12.4, the rate coefficients for the dissociative channels are reported in the post-discharge regime ($E/N = 0 \text{ Td}$), showing the corresponding values

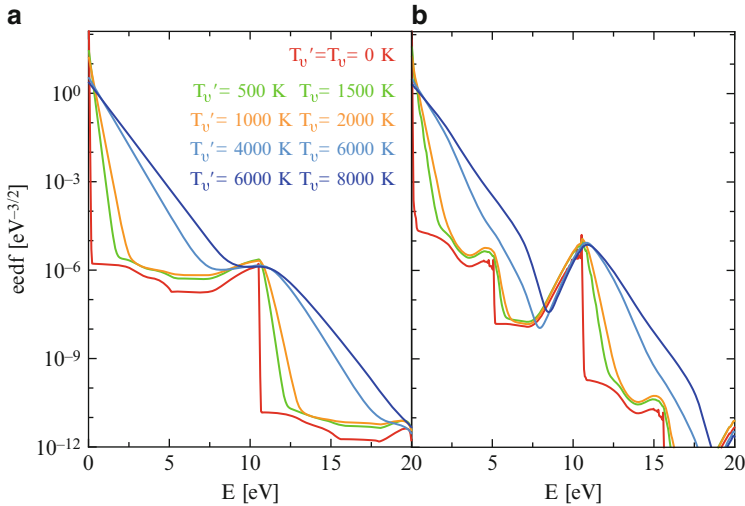
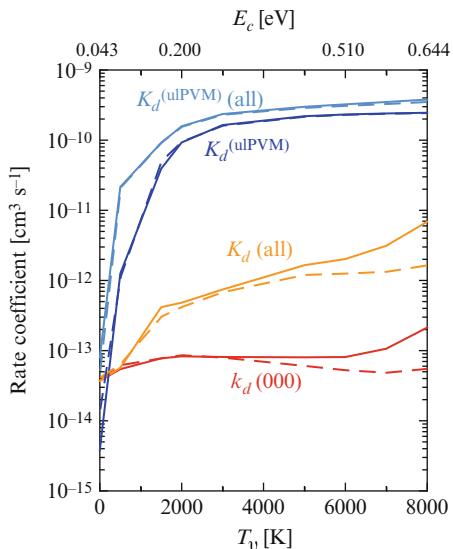


Fig. 12.3 Electron energy distribution function in the post-discharge regime ($E/N = 0 \text{ Td}$), with $\chi_{\text{CO}_2(e_2)} = 10^{-5}$, for different selected values of the temperatures of symmetric/bending (T'_v) and asymmetric (T_v) normal modes. **(a)** Including ($\chi_e = 10^{-3}$) and **(b)** neglecting electron-electron collisions

Fig. 12.4 Rate coefficients for dissociation channels in CO_2 plasma, as a function of vibrational temperature of asymmetric mode (on the upper axis the corresponding values of characteristic energy E_c are reported), in the post-discharge regime ($E/N = 0 \text{ Td}$), with $\chi_{\text{CO}_2(e_2)} = 10^{-5}$ and $\chi_e = 10^{-3}$, including (solid lines) and neglecting (dashed lines) $e\text{-}e$ collisions



calculated by including or neglecting $e\text{-}e$ collisions. In the post-discharge, the pure vibrational mechanisms dominate the direct dissociation channels in the whole T_v vibrational temperature range. In any case, the direct dissociation channels cannot be neglected and should be included in the description of post-discharge regime, taking into account that the pure vibrational mechanism rate coefficients represent upper

limits to the actual rates. It should be noted that the high vibrational temperatures considered in Figs. 12.3 and 12.4 can be considered as representative of situations obtained by turning off the electrical field in continuous discharge after several ms residence times. The differences in the rates obtained by including or not the *e-e* collisions are, in the post-discharge, appreciable only for the direct electron impact dissociation channels and in the higher vibrational temperature range. The eedf is strongly depleted at energy near the dissociation threshold, while the structure is smoothed away when *e-e* collisions are accounted for, this effect being more efficient at higher vibrational temperatures, thus leading to higher values of the eedf and, in turn, of dissociation rates. These results, while confirming the main ideas discussed in the literature, should be considered for the CO₂ model still at a qualitative level. Improvements of the vibrational ladder as well as of the dynamical information for the corresponding inelastic channels should require a not trivial effort. On the other hand a state-to-state vibrationally and electronically excited state kinetics coupled to a self-consistent Boltzmann equation should be developed. Particular care should be devoted to the VV and VT processes involving a more realistic vibrational CO₂ ladder (Armenise and Kustova 2013). Moreover we should insert these modules in a more complex one describing the plasma chemistry occurring in the discharge (Aerts et al. 2014; Kozák and Bogaerts 2014; Bultel and Annaloro 2013). Dedicated experiments are then expected to validate the theoretical model to transform it in a predictive tool.

References

- Aerts R, Snoeckx R, Bogaerts A (2014) In-situ chemical trapping of oxygen in the splitting of carbon dioxide by plasma. *Plasma Process Polym* 11(10):985–992
- Armenise I, Kustova E (2013) State-to-state models for CO₂ molecules: from the theory to an application to hypersonic boundary layers. *Chem Phys* 415:269–281
- Bultel A, Annaloro J (2013) Elaboration of collisional-radiative models for flows related to planetary entries into the Earth and Mars atmospheres. *Plasma Sources Sci Technol* 22(2):025008
- Capezzuto P, Cramarossa F, D'Agostino R, Molinari E (1976) Contribution of vibrational excitation to the rate of carbon dioxide dissociation in electrical discharges. *J Phys Chem* 80(8):882–888
- Capitelli M, Molinari E (1980) Kinetics of dissociation processes in plasmas in the low and intermediate pressure range. in *Plasma Chemistry II*, Springer Series Topics in Current Chemistry, vol. 90, pp. 59–109. Springer, Berlin Heidelberg
- Capitelli M, Gorse C, Berardini M, Braglia G (1981) Influence of second-kind collisions on electron energy distributions, transport coefficients and the rate coefficients in the laser mixture CO₂-N₂-He-CO. *Lettore Al Nuovo Cimento Series 2* 31(6):231–237
- Capitelli M, Colonna G, D'Ammando G, Laporta V, Laricchiuta A (2013) The role of electron scattering with vibrationally excited nitrogen molecules on non-equilibrium plasma kinetics. *Phys Plasmas* 20(10):101609
- Capitelli M, Colonna G, D'Ammando G, Laporta V, Laricchiuta A (2014) Nonequilibrium dissociation mechanisms in low temperature nitrogen and carbon monoxide plasmas. *Chem Phys* 438:31–36

- Colonna G, Capitelli M, De Benedictis S, Gorse C, Paniccia F (1991) Electron energy distribution functions in CO₂ laser mixture: the effects of second kind collisions from metastable electronic states. *Contrib Plasma Phys* 31(6):575–579
- Fridman A (2012) Plasma chemistry. Cambridge University Press, Cambridge
- Goede A, Bongers WA, Graswinckel MF, van de Sanden MCM, Leins M, Kopecki J, Schulz A, Walker M (2014) Chemical energy storage by CO₂ plasmolysis. XARMAE Workshop, Barcelona, Jan 2014
- Kozák T, Bogaerts A (2014) Splitting of CO₂ by vibrational excitation in non-equilibrium plasmas: a reaction kinetics model. *Plasma Sources Sci Technol* 23(4):045004
- Kumar M, Biswas A, Bhargav P, Reghu T, Sahu S, Pakhare J, Bhagat M, Kukreja L (2013) Theoretical estimation and experimental studies on gas dissociation in TEA CO₂ laser for long term arc free operation. *Opt Laser Technol* 52:57–64
- Legasov VA, Givotov VK, Krashennikov EG, Rusanov VD, Fridman A (1977) Sov Phys Doklady 238:66
- Lowke JJ, Phelps AV, Irwin BW (1973) Predicted electron transport coefficients and operating characteristics of CO₂-N₂-He laser mixtures. *J Appl Phys* 44(10):4664–4671
- Park C (2008) Rate parameters for electronic excitation of diatomic molecules 1. Electron-impact processes. AIAA paper 2008–1206
- Sergeev P, Slovetsky D (1983) vibrationally excited molecules and mechanisms of chemical and physical processes in non-equilibrium plasmas. *Chem Phys* 75(2):231–241
- Silva T, Britun N, Godfroid T, Snyders R (2014) Optical characterization of a microwave pulsed discharge used for dissociation of CO₂. *Plasma Sources Sci Technol* 23(2):025009
- Taylan O, Berberoglu H (2015) Dissociation of carbon dioxide using a microhollow cathode discharge plasma reactor: effects of applied voltage, flow rate and concentration. *Plasma Sources Sci Technol* 24(1):015006

Index

A

ad-atoms, 72, 75
ad-species, 72, 74, 75
afterglow, 71, 117, 118, 138, 236–241, 309
anti-Arrhenius
 behavior, 192, 283
Arrhenius
 behavior, 192
 fit, 284
 plot, 280, 281
 rate, 276
associative detachment, 257
associative ionization, 137, 138, 235, 241

B

Boltzmann equation, 79, 80, 84, 95, 98, 102, 107, 114, 122, 125, 127, 134, 143, 144, 163, 176, 205, 249, 285, 288, 294, 306
collision terms, 89, 267
discretized, 94
homogeneous, 113
linear, 266
local approximation, 117
multi-term, 80
time-dependent, 131, 136, 223, 227, 248
two-term (P_1), 79–81, 90, 99, 105, 108
Born-Bethe approximation (BB), 18, 19, 151
boundary layer, 175, 186, 191–194

C

catalysis, 71, 75

chemisorption, 58, 59, 61, 64
 energy, 67
 well, 58, 61, 66
cold gas approximation, 118, 227, 231
collision frequency, 86, 102, 103, 105, 108, 109, 132, 210, 267, 268
collisional-radiative model (CR), 143, 144, 146, 148, 149, 151, 157, 162, 163, 169, 260–262, 294
collisions
 atom-molecule, 31, 34, 35, 37, 41, 45
 charge-exchange, 218, 268
 elastic, 81, 105, 108, 120, 127, 167, 212, 252, 254, 297
 electron-electron Coulomb, 81, 86, 89, 99, 108, 109, 114, 121, 123–127, 133, 136, 137, 169, 181, 252, 285, 287, 290, 300, 307–311
 electron-molecule, 1, 2, 17, 102, 186, 210, 211, 223
 heavy-particle, 175, 223, 236, 239, 252, 278
 inelastic, 81, 105, 114, 115, 120, 121, 124, 128, 130, 133, 167, 169, 254, 297
 molecule-molecule, 176, 182
 second-kind or superelastic, 79, 81, 114–116, 118–120, 122, 124, 125, 127, 128, 130, 131, 135–138, 167, 169, 197, 223, 228, 231, 236, 239, 254, 285, 290, 297–300
 electronic, 125, 132, 223, 228, 238, 306, 307, 309
 vibrational, 113, 114, 118, 125, 132, 228, 238, 306
Coulomb logarithm, 109

- cross section
 Coulomb, 123
 DEA $e\text{-H}_2(v)$, 25, 26
 direct dissociation $e\text{-CO}_2$, 308
 direct dissociation $e\text{-H}_2(v)$, 213
 dissociation $\text{N}\text{-N}_2(v)$, 38
 dissociative recombination $e\text{-H}_2^+(v)$, 262
 elastic, 206
 elastic differential, 103, 104
 electronic excitation $e\text{-N}_2(v)$, 225
 excitation $e\text{-H}(n)$, 153
 ionization $e\text{-H}(n)$, 154
 momentum transfer, 86, 104, 105
 momentum transfer $e\text{-Ar}$, 100
 momentum transfer for screened Coulomb interaction, 109
 non-resonant excitation $e\text{-BeH}$, 18, 23, 24
 non-resonant excitation $e\text{-BeH}^+$, 18, 21
 non-resonant excitation $e\text{-CH}$, 18–20
 predissociation $e\text{-N}_2(v)$, 225
 RVE $e\text{-CO}(v)$, 16
 RVE $e\text{-CO}_2(v, 0, 0)$, 17
 RVE $e\text{-H}_2(v)$, 25–27
 RVE $e\text{-N}_2(v)$, 7, 8, 10
 RVE $e\text{-NO}(v)$, 12–15
 RVE $e\text{-O}_2(v)$, 11
 superelastic, 115, 116
 VT $\text{N}\text{-N}_2(v)$, 38, 39, 42
 VT $\text{O}\text{-N}_2(v)$, 39, 43
 current density, 96, 237, 289
- D**
 databases, 131, 151, 153, 154, 224, 247, 307
 detailed balance principle, 25, 80, 147, 150, 177, 179–182, 197, 199, 202, 307
 DFT, 59, 61, 70
 diffusion, 87, 95, 211, 212
 ambipolar, 206
 coefficient, 210, 212
 equation, 206, 210, 215
 radial, 212
 surface, 57
 discharge
 capacitively coupled RF
 parallel plate reactor, 114, 205, 211, 215, 217, 259
 tubular reactor, 188
 DBD pulsed, 309
 dc or continuous, 237, 238, 240, 241, 311
 hollow-cathode, 124, 125, 238
 magnetic multicusp, 252, 254
 microwave (Mw), 309
 nanosecond (ns) pulsed, 237, 309
- pulsed, 257, 258
 radiofrequency (RF), 131, 208, 211, 217–220, 256
 RLC, 135
 discharge current, 125, 138, 249, 254, 255, 257
 dissociation-recombination, 175, 176, 181, 191, 192, 194, 278, 279, 288
 dissociative electron attachment (DEA), 2, 6, 18, 24, 25, 67, 247, 249, 250, 253, 254, 258–260
 from Rydberg states, 260, 261
 through Rydberg states, 25
 distribution
 Boltzmann, 38, 67, 74, 80, 192, 196, 198, 199, 202, 223, 225, 254, 264, 275, 285, 298, 306
 Maxwell, 2, 8, 79, 81, 95, 96, 100, 109, 117, 122, 124, 139, 143, 145, 151, 152, 165, 167, 211, 218, 235, 254, 264, 265, 267, 275, 285
 Saha-Boltzmann, 161
 Treanor, 74, 75, 121, 181, 200, 276
 divertor, 1, 17, 18, 25
- E**
 Einstein coefficient of spontaneous emission, 147, 148, 155
 Einstein theorem, 96
 electron current, 81, 87, 89
 electron density, 124, 128, 129, 137, 147, 150, 157, 159, 161, 162, 164, 165, 168, 169, 196, 218, 227, 229, 230, 237, 238, 254, 263, 287
 electron diffusion, 217
 coefficient, 95
 electron energy distribution function (eedf), 2, 90, 101, 113, 117, 145, 208
 afterglow plasma, 138
 Ar plasma, 123
 Ar plasma with magnetic field, 291
 CO plasma, 119
 CO_2 plasma, 308, 310
 CO-He plasma, 121
 Cs vapor, 138
 decaying Ar/NF₃ plasma, 101
 excimer laser, 135
 expansion conditions, 235
 experimental, 123, 131, 133, 138
 experimental in HCD, 124
 F4 nozzle expansion, 287
 H plasma, 143, 163
 H₂ capacitively coupled parallel plate RF discharge, 216, 218

- H**
- He plasma, 120, 124
 - He/Ar/Xe/H₂ plasma, 139
 - helicon plasma, 255
 - Hg afterglow plasma, 139
 - ionizing H plasma, 170
 - multicusp source, 254, 265
 - N₂ afterglow, 236, 239
 - N₂ plasma, 126, 133, 223, 228, 229
 - Ne/Xe/HCl mixture, 107, 108, 135, 136
 - negative ion source, 254, 255
 - non-local effects, 114, 117, 118
 - nozzle expansion, 285, 287, 299
 - periodic behavior, 132
 - photo-resonant plasma, 138
 - plateaux, 117, 127, 300
 - recombining H plasma, 168
 - relaxation, 107, 109, 258, 259
 - shock tube, 297
 - stationary, 2, 125
 - stationary in multicusp source, 254
 - structures, 119–121, 123, 137, 237
 - tail, 135, 137
 - time dependent, 136
 - time evolution, 122
 - electron mobility, 96, 100, 292, 293
 - electron plasma frequency, 206, 208
 - electron-hole pair excitation, 67, 75
 - electronically excited states, 113
 - Ar^{*}, 122
 - CO₂^{*}, 307, 309
 - H^{*}, 147, 297
 - H₂^{*}, 212, 261
 - N₂, 223, 225, 227, 228, 286
 - energy accommodation coefficient, 57
 - escape factor, 147, 148, 294
 - excited state relaxation, 139, 143
- F**
- Faraday current, 95
 - fixed nuclei approximation, 4
 - fluid model, 205, 216
 - forced-harmonic oscillator method (FHO), 37, 46, 48–52, 226
- G**
- gaunt factor, 156
 - global rate
 - formation NO, 284
 - pseudo first-order, 182
 - golden rule, 116, 122, 123
 - Gryzinski approach, 225
- H**
- Hall current, 97
 - heterogeneous recombination, 57, 60, 66, 72, 74, 75, 191, 194, 195, 251, 252, 256–258
 - coefficient, 57, 59, 63, 70, 256
 - dynamics, 65
 - H in Cu, 66
 - H on Cu
 - H₂ vdf, 66
 - H on graphite, 62
 - H₂ rotational distribution, 63
 - H₂ vdf, 62, 65
 - H on Ta
 - H₂ vdf, 75
 - H on W, 67
 - H₂ vdf, 68
 - isotopic effect, 63, 64, 66
 - mechanisms, 57, 58
 - Eley-Rideal (ER), 57, 58, 60, 69–71
 - hot atom, 58, 67
 - Langmuir-Hinshelwood (LH), 57, 64, 69
 - N on β -cristobalite, 70
 - N₂ vdf, 71
 - O on β -cristobalite
 - O₂ vdf, 69
 - probability, 59, 61, 62, 64, 66, 67
 - ro-vibrational distribution, 57, 59, 64, 65
 - vdf, 64, 73–75
 - high-enthalpy flow, 184, 275, 285, 293
 - hypersonic body, 186, 191, 275
 - hypersonic flows, 175, 276
- I**
- infinite order sudden approximation, 35
 - ion energy distribution function
 - RF discharges, 217
 - isotope scaling, 37
 - isotopic effect, 63, 64
 - H+H₂ collisional system, 37
 - isotropic scattering, 104, 105
- K**
- kinetic rate coefficient
 - dissociation e-N₂(v), 232
 - dissociation CO₂, 308–310
 - RVE e-N₂(v), 232
 - kinetics
 - dissociation, 248
 - excited-state, 147, 223, 227, 228, 234, 236, 239, 287

- kinetics (*cont.*)

 free electron, 84, 93, 95, 98, 99, 127, 181, 206, 249

 ionization, 229

 ionization/recombination, 248

 ionized species, 285

 neutral species, 264

 non-equilibrium vibrational, 31, 175, 176, 184, 194, 195, 198, 206, 211, 212, 215, 223, 224, 236, 239, 248, 279, 285, 286, 298, 309

 in boundary layer, 191

 in discharges, 227

 in nozzle, 278, 282

 plasma, 134, 176, 205, 206

 state-to-state, 31, 79, 99, 206, 209, 224, 276, 311

 in N₂ afterglow, 236

 in negative ion sources, 247

 in shock tube, 293

 surface, 59, 74
- L**

 ladder climbing model, 182, 183, 192, 194, 279, 283

 laser, 137

 CO pumping, 175, 186

 CO₂, 306, 307

 excimer, 108, 131, 134–136

 IR vibrational pumping, 175, 186, 187, 198

 power, 138

 pulse, 143, 198

 VUV spectroscopy, 254

 laser-plasma interaction, 183, 198

 local complex-potential model (LCP), 6, 7, 9, 14, 25

 low-lying excited states, 139, 157, 161, 186, 287
- M**

 master equation, 99, 150, 183, 186, 198, 202

 metastable states, 117, 118, 122, 124, 151, 285, 286

 Ar, 290

 CO, 117–121

 He, 117, 118, 120, 124, 125, 300, 301

 N, 235, 287

 N₂, 71, 234, 236–240

 Ne, 136

 Xe, 136

 mobile ad-layer, 72

 Monte Carlo method, 80, 100–102, 104, 248, 254, 265, 266, 269
- Direct Monte Carlo, 38, 264

 Monte Carlo Flux, 107, 108

 multi-fluid models, 89
- N**

 negative conductivity, 100

 negative ion, 206, 211

 negative ion conductivity, 138

 negative ion H[−], 212, 214, 247, 256, 257, 259, 260, 266

 energy distribution function, 266, 269

 beams, 247

 density, 215, 257

 kinetics, 247, 248

 magnetic multicusp source, 248–250, 252, 254, 256, 260, 265

 RF coupled source, 262

 driver, 262–264

 expansion region, 248, 262–264, 266, 268

 extraction region, 262, 265

 sources, 25, 248

 yield, 247

 negative molecular ion H₂[−], 25, 250

 non-Arrhenius

 behavior, 280

 normal vibrational modes

 CO₂, 306

 nozzle, 93, 94, 275–278, 280, 298

 axis, 277, 280

 EAST, 281

 exit, 94, 277, 280, 281

 expansion, 99, 276, 285, 287

 F4, 283–285, 287

 flow, 93–95, 171

 geometry, 278, 282

 conic, 279

 parabolic, 283, 284

 inlet, 94, 277, 278

 outlet, 279, 282

 section, 277

 throat, 280

 with electric and magnetic fields, 289, 290, 293
- O**

 optically thick plasma, 149, 167–170, 298–300

 optically thin plasma, 149, 161, 167–170, 298–300
- P**

 particle models, 206, 207

- PIC, 207, 208, 215, 266
 PIC MCC, 114, 214, 259
 Penning ionization, 122, 137, 138
 PES, 33, 38, 43, 50, 51, 53, 58, 61, 64, 67, 69, 70, 225
 BKMP2, 36
 LEPS, 31, 37, 39, 50
 LSTH, 34
 photoresonant plasmas, 137
 physisorption, 58, 59, 61, 64, 66
 Planck spectral distribution, 146
 plasma potential, 252
 Poisson equation, 134, 207, 208
 post-discharge, 99, 117, 118, 122, 123, 125, 139, 185, 188, 197, 219, 223, 227, 236, 237, 241, 258, 259, 290, 307, 309–311
 power
 gain, 130, 136
 injected, 128
 loss, 130, 136
 pure vibrational mechanism, 228, 233, 236, 305, 306, 308–310
- Q**
 QCT, 31, 32, 34–36, 42, 46, 48–51, 184, 225, 226, 279, 281
 quantum statistics, 80
 quasi-steady state (QSS), 89, 98, 143, 151, 157, 161, 162, 164, 185
- R**
 R-matrix, 8, 9, 13–16, 18, 19, 22, 23
 radiation transport, 149, 294, 298
 Ramsauer minimum, 100
 random variables, 33, 36, 100, 102, 218, 267, 268
 rate
 formation CO₂, 190
 rate coefficient
 DEA *e*-H₂(*v*), 26
 direct dissociation *e*-CO₂, 305, 306
 dissociation *e*-N₂(*v*), 233
 experimental, 233
 dissociation N₂-N₂, 182
 dissociation N-N₂(*v*), 182, 224, 226
 excitation *e*-H(*n*), 154
 global recombination, 159
 ionization *e*-H(*n*), 155
 non-resonant excitation *e*-BeH, 18, 24
 non-resonant excitation *e*-BeH⁺, 18, 22
 non-resonant excitation *e*-CH, 18, 20
 pseudo first-order, 73, 182, 192, 193
 pure vibrational mechanism *e*-N₂(*v*), 233
 resonant dissociation *e*-N₂(*v*), 233–235
 RVE *e*-CO(*v*), 16
 RVE *e*-CO₂, 305
 RVE *e*-CO₂(*v*, 0, 0), 17
 RVE *e*-H₂(*v*), 27
 RVE *e*-N₂(*v*), 10
 RVE *e*-NO(*v*), 15
 RVE *e*-O₂(*v*), 11
 VT *e*-H₂(*v*)
 non-reactive, 45
 reactive, 45
 VT *e*-N₂(*v*)
 non-reactive, 49
 reactive, 49
 VT *e*-O₂(*v*)
 non-reactive, 51
 reactive, 51
 VT N-N₂(*v*), 224, 281
 mono-quantum de-excitation, 226
 VT_M N₂-N₂
 mono-quantum de-excitation, 227
 VT_MN₂-N₂, 184
 VV N₂-N₂, 184, 227
 reactions
 pseudo-first order, 210
 recombination, 17, 25, 93, 125, 159, 161, 163, 169, 175, 184, 185, 191, 213, 252, 256, 275, 279, 280, 299, 300
 e-proton, 169
 coefficient (α), 159, 161
 dissociative, 251, 262
 gas-phase, 191, 192
 global rate coefficient, 159
 radiative, 137, 149, 156, 158, 161, 251, 300
 regime, 169, 171
 three-body, 35, 137, 148, 158, 161, 251
 reduced electric field (*E/N*), 108, 113, 121, 127, 129, 130, 135–137, 186, 227, 229–233, 235, 269, 289, 290, 309
 relaxation time, 130, 148, 149, 157, 178, 193, 196, 215, 237
 resonance theory, 2
 resonance width, 5, 8, 10, 12, 13
 resonant nuclear equation
 local, 6
 non-local, 5
 resonant vibrational excitation (RVE), 2, 6–8, 12–14, 18, 24, 25, 224, 232
 through Rydberg states, 25
 Rydberg states, 260–262
 resonant, 18, 25, 26

S

- Saha equation, 144, 145, 150
 self-consistent model, 99, 134, 143, 206, 209, 223, 260, 285, 286, 288, 294, 298, 311
 semiclassical approach, 34, 36, 39, 40, 59, 61, 65, 69, 227
 semiclassical collisional method, 60
 shock tube, 278, 293–295
 stationary state, 129, 130
 surface
 catalytic, 60, 175, 191, 194, 195
 catalyticity, 57, 195
 fully-catalytic, 57
 non-catalytic, 57, 175, 191, 194, 195

T

- thermal diffusion, 95
 coefficient, 96
 threshold-modified Mott&Massey approximation (TMMM), 23
 trajectories
 non-reactive, 36, 42, 44, 46, 48–51
 non-recrossing, 44, 50
 purely non-reactive (PNR), 45, 46, 49–51
 reactive, 36, 42, 47, 49, 51
 recrossing, 42, 46–48
 transitions
 mono-quantum, 44, 176, 178, 184, 201, 202, 213, 225–227
 multi-quantum, 2, 7, 14, 44, 51, 52, 176, 177, 183, 185, 202, 213, 226, 232, 281–283

V

- VE energy exchange, 186, 239
 vibrational distribution (vdf), 38, 178, 184, 237, 282
 CO, 121, 186–189, 198, 199
 experimental, 236
 H₂
 in nozzle, 299
 in RF discharge, 216, 217
 H₂(v), 247, 253, 254, 261
 plateau, 215, 254, 256

- N₂, 129, 185, 192, 194, 195, 225, 228, 229, 231, 234, 239, 280
 experimental, 236
 in nozzle, 283, 284

- N₂(v)
 in F4 nozzle, 287
 in nozzle, 283, 284
 non-equilibrium, 175, 191–195, 199, 263, 275, 276, 280, 281, 288
 in boundary layer, 194

- O₂, 195
 in nozzle, 283
 quasi-stationary, 234
 relaxation, 258
 stationary in multicusp magnetic plasmas, 254, 257, 264
 tail, 286

- Treanor, 74, 75, 121, 181, 200, 276
 vibrational relaxation, 183, 184, 196, 294, 295
 vibrationally excited states, 113, 197

- CO, 118, 120
 CO₂, 309
 H₂, 248
 N₂, 229, 231, 236, 241, 287
 VL energy exchange
 N-N₂, 74
 VT energy exchange, 175, 176, 178, 183, 196, 306
 H-H₂(v), 45, 212, 253
 He-CO(v), 186
 N-N₂(v), 49, 224, 225, 228, 229, 278
 O-N₂, 282
 O-O₂(v), 51

- VT_M energy exchange
 CO-N₂, 198
 H₂-H₂, 212, 250
 N₂-N₂, 184, 226, 278, 281
 VV energy exchange, 74, 175, 176, 178, 179, 181, 183, 196, 200, 305
 CO-CO, 186
 CO-N₂, 198
 H₂-H₂, 213, 253
 N₂-N₂, 184, 185, 224, 226–228, 239, 278
 quasi-resonant, 199
 resonant, 180, 199

Z

- Zeldovich reactions, 282–284